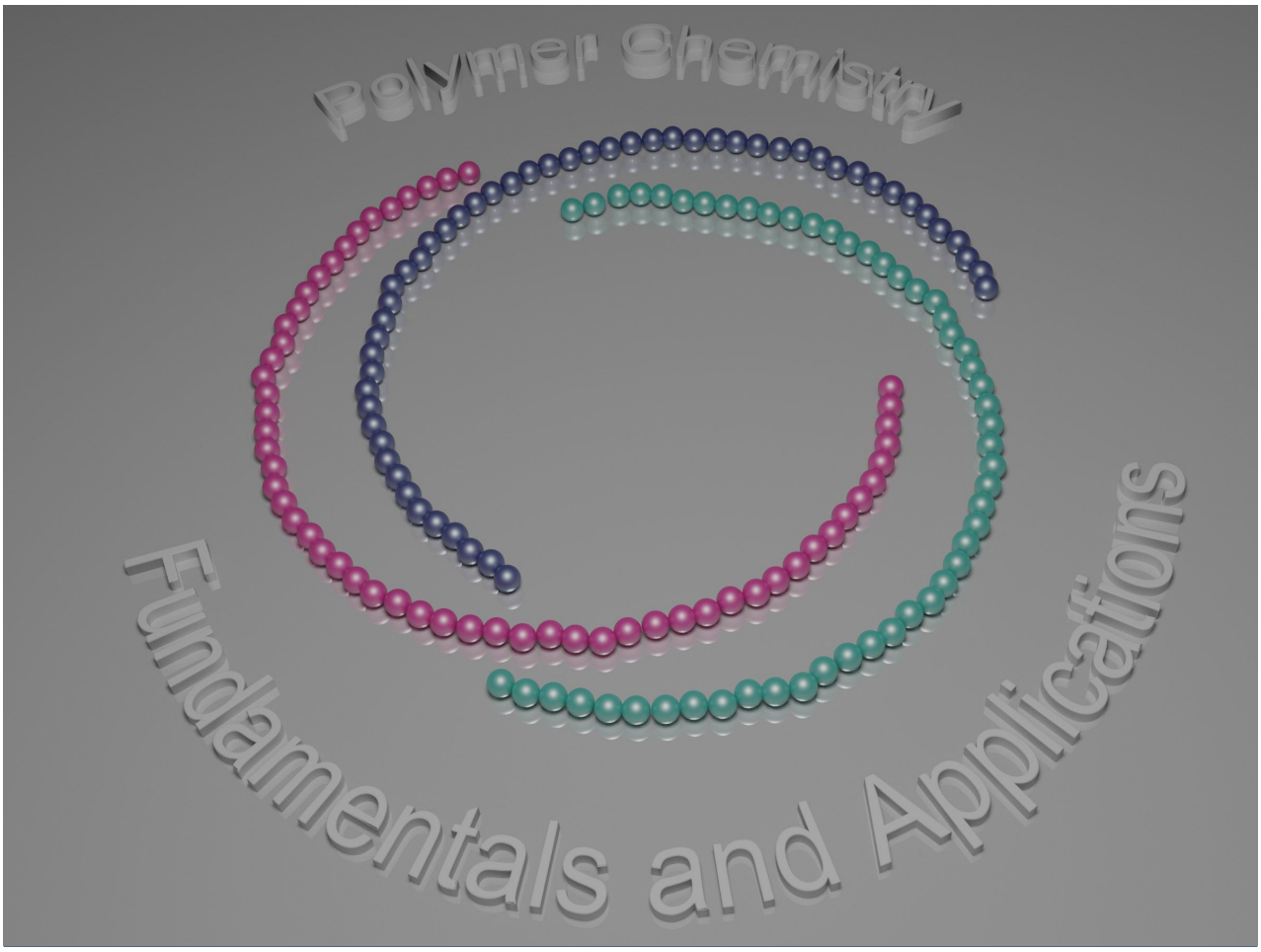
BEILSTEIN JOURNAL OF ORGANIC CHEMISTRY

Polymer chemistry: fundamentals and applications

Edited by Bernhard V. K. J. Schmidt



Generated on 03 November 2026, 11:44

Imprint

Beilstein Journal of Organic Chemistry
www.bjoc.org
ISSN 1860-5397
Email: journals-support@beilstein-institut.de

The *Beilstein Journal of Organic Chemistry* is published by the Beilstein-Institut zur Förderung der Chemischen Wissenschaften.

Beilstein-Institut zur Förderung der Chemischen Wissenschaften
Trakehner Straße 7–9
60487 Frankfurt am Main
Germany
www.beilstein-institut.de

The copyright to this document as a whole, which is published in the *Beilstein Journal of Organic Chemistry*, is held by the Beilstein-Institut zur Förderung der Chemischen Wissenschaften. The copyright to the individual articles in this document is held by the respective authors, subject to a Creative Commons Attribution license.

The cover image, copyright 2021 Bernhard V. K. J. Schmidt, is licensed under the Creative Commons Attribution 4.0 license (https://creativecommons.org/licenses/by/4.0). The reuse, redistribution or reproduction requires that the author, source and license are credited.

BEILSTEIN JOURNAL OF ORGANIC CHEMISTRY

Polymer chemistry: fundamentals and applications

Bernhard V. K. J. Schmidt

Editorial

Open Access

Address:
School of Chemistry, University of Glasgow, G12 8QQ Glasgow, UK

Email:
Bernhard V. K. J. Schmidt - bernhard.schmidt@glasgow.ac.uk

Keywords:
polymer chemistry

Beilstein J. Org. Chem. **2021,** *17,* 2922–2923.
https://doi.org/10.3762/bjoc.17.200

Received: 15 November 2021
Accepted: 24 November 2021
Published: 14 December 2021

This article is part of the thematic issue "Polymer chemistry: fundamentals and applications".

Guest Editor: B. V. K. J. Schmidt

© 2021 Schmidt; licensee Beilstein-Institut.
License and terms: see end of document.

Ever since the introduction of the term macromolecule and the early days of polymer science [1], organic chemistry and polymer chemistry have been closely related [2]. It only seems to be a logical step to give room for a thematic issue on polymer chemistry in the *Beilstein Journal of Organic Chemistry*. The connection between organic and polymer chemistry has been highlighted frequently [3,4], up to the point where one can talk about macroorganic chemistry, where oligomers bring molecular precision from organic chemistry together with materials properties from polymer chemistry [5]. Especially in the challenge of transformation to a more sustainable polymer science, organic chemistry can give significant support in the development of greener polymer materials [6].

This thematic issue covers a broad range of current topics in polymer chemistry, from synthesis to materials and applications. In the area of synthetic methods, the use of click photochemistry in polymer and organic molecule synthesis is presented, as well as the combination of polymers with supramolecular chemistry for the assembly of polymer fibers and the synthesis of well-defined polysaccharides. In the direction of materials, cryogels and reinforced hydrogels are discussed, as well as 3D-printed poly(caprolactone) biomaterials. In addition, properties of thermoresponsive materials and self-healing materials are presented in this thematic issue. Finally, the use of polymerization-induced self-assembly for the synthesis of drug carriers is presented. The issue also shows the multidisciplinary character of polymer science, for example when supramolecular motifs, organic coupling reactions or photocatalysis are employed in the development of new polymer materials in order to address specific applications.

Overall, I hope the thematic issue “Polymer chemistry: fundamentals and applications” highlights the breadth of current polymer research and enables the reader to dive into this fascinating area of chemistry. I want to express my gratitude to all authors who showcase their excellent work in this thematic issue and the Editorial Team for the magnificent organization.

Bernhard V. K. J. Schmidt

Glasgow, November 2021

References

1. Staudinger, H. *Ber. Dtsch. Chem. Ges.* **1920,** *53,* 1073–1085. doi:10.1002/cber.19200530627
2. Mülhaupt, R. *Angew. Chem., Int. Ed.* **2004,** *43,* 1054–1063. doi:10.1002/anie.200330070

3. Sumerlin, B. S.; Vogt, A. P. *Macromolecules* **2010,** *43,* 1–13. doi:10.1021/ma901447e
4. Hawker, C. J.; Wooley, K. L. *Science* **2005,** *309,* 1200–1205. doi:10.1126/science.1109778
5. van Genabeek, B.; Lamers, B. A. G.; Hawker, C. J.; Meijer, E. W.; Gutekunst, W. R.; Schmidt, B. V. K. J. *J. Polym. Sci.* **2021,** *59,* 373–403. doi:10.1002/pol.20200862
6. Llevot, A.; Dannecker, P.-K.; von Czapiewski, M.; Over, L. C.; Söyler, Z.; Meier, M. A. R. *Chem. – Eur. J.* **2016,** *22,* 11510–11521. doi:10.1002/chem.201602068

License and Terms

This is an open access article licensed under the terms of the Beilstein-Institut Open Access License Agreement (https://www.beilstein-journals.org/bjoc/terms), which is identical to the Creative Commons Attribution 4.0 International License (https://creativecommons.org/licenses/by/4.0). The reuse of material under this license requires that the author(s), source and license are credited. Third-party material in this article could be subject to other licenses (typically indicated in the credit line), and in this case, users are required to obtain permission from the license holder to reuse the material.

The definitive version of this article is the electronic one which can be found at: https://doi.org/10.3762/bjoc.17.200

BEILSTEIN JOURNAL OF ORGANIC CHEMISTRY

Photoinduced post-modification of graphitic carbon nitride-embedded hydrogels: synthesis of 'hydrophobic hydrogels' and pore substructuring

Cansu Esen and Baris Kumru*

Full Research Paper

Open Access

Address:
Max Planck Institute of Colloids and Interfaces, Department of Colloid Chemistry, Am Mühlenberg 1, 14476 Potsdam, Germany

Email:
Baris Kumru* - baris.kumru@mpikg.mpg.de

* Corresponding author

Keywords:
hydrophobic hydrogel; photoactive hydrogels; photomodification; pore modification; soft materials

Beilstein J. Org. Chem. **2021,** *17,* 1323–1334.
https://doi.org/10.3762/bjoc.17.92

Received: 21 March 2021
Accepted: 14 May 2021
Published: 21 May 2021

This article is part of the thematic issue "Polymer chemistry: fundamentals and applications".

Associate Editor: P. J. Skabara

© 2021 Esen and Kumru; licensee Beilstein-Institut.
License and terms: see end of document.

Abstract

Hydrogels are a special class of crosslinked hydrophilic polymers with a high water content through their porous structures. Post-modifications of hydrogels propose an attractive platform so that a variety of fresh functions, which are not arising from initial monomers, could be accessible on a parental network. Photoinduced post-modification of hydrogels by embedding semiconductor nanosheets would be of high interest and novelty. Here, a metal-free semiconductor graphitic carbon nitride (g-CN)-embedded hydrogel as an initial network was synthesized via redox-couple initiation under dark conditions. Post-photomodification of so-formed hydrogel, thanks to the photoactivity of the embedded g-CN nanosheets, was exemplified in two scenarios. The synthesis of 'hydrophobic hydrogel' is reported and its application in delayed cation delivery was investigated. Furthermore, pores of the initial hydrogel were modified by the formation of a secondary polymer network. Such a facile and straightforward synthetic protocol to manufacture functional soft materials will be of high interest in near future by the means of catalysis and agricultural delivery.

Introduction

Popularity of hydrogels arises from their structural similarity to natural tissues, meaning that they are stable networks with high water content [1-3]. The simplest synthesis of hydrogels can be conducted in an aqueous solution of a water-soluble monomer and crosslinker (bi- or more functional) in the presence of an initiator (generally radical initiation). Since then, many synthetic routes have been developed in order to synthesize artificial matter that mimics the performance of natural tissues. Therefore, many reinforcement methods have been suggested, i.e., host–guest interactions [4,5], double network formation [6-8], and reinforcer addition [9-12]. The potential of hydrogels is beyond biomaterials, currently these aqueous soft materials are

prime candidates in agricultural delivery systems as well [13,14].

In the era of sustainability, utilization of sunlight is of great importance [15]. Metal-containing and mostly toxic and non-sustainable semiconductors are slowly being replaced by a new generation of semiconductors. Graphitic carbon nitride (g-CN) is a metal-free polymeric semiconductor that is mainly composed of carbon and nitrogen elements by tri-*s*-triazine, triazine imide, or heptazine repeating units [16-18]. g-CN represents a family of materials where variety of synthetic routes can be applied to form photoactive matter with altered properties, i.e., monomer supramolecular assembly to attain a monomer complex prior to carbonization results in enhanced porosity and photoactivity since ordered structures are formed, and a detailed overview has been reported by Shalom et.al. [19]. Facile tunability has rendered g-CN to be applied in visible-light-induced catalytic reactions such as water splitting [20-22], pollutant degradation [23-26], CO_2 reduction [27-29], photonics [30,31] and polymer synthesis [32-35].

Integration of g-CN into hydrogels has been popularized in the last four years, where g-CN nanosheets can be implemented into hydrogels through embedding [36] or covalent binding [37,38] for the target application such as reinforced hydrogels [39] and hydrogels for photoredox-based applications [40,41].

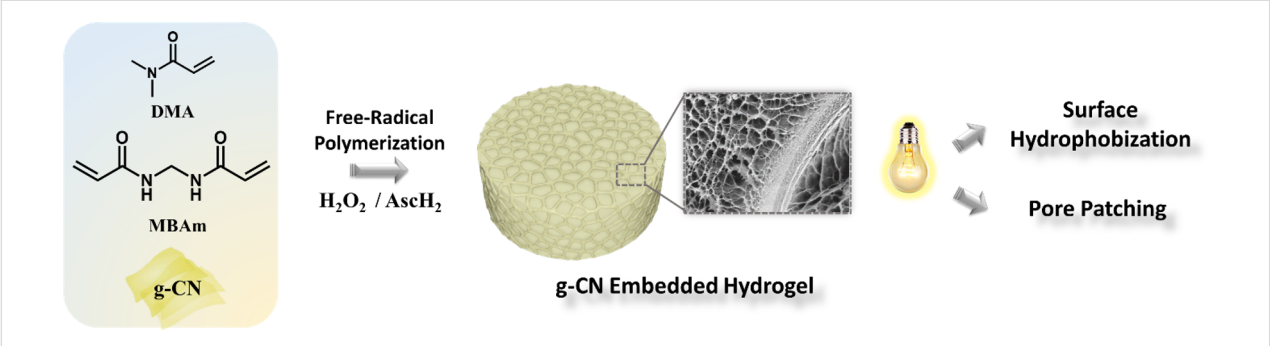
Hydrogel post-modification via semiconductors induced by visible light would be an appealing haven. Herein, we demonstrate the photoactive g-CN nanosheet addition to hydrogels through embedding, which will be the anchoring point that grants an access to photoinduced post-modification methods. The effectiveness of this strategy will be demonstrated via a photoinduced transformation of a hydrophilic skeleton to a hydrophobic network. Furthermore, freeze-dried hydrogel will be subjected to a subsequent photoinduced pore patching (Scheme 1).

Results and Discussion

Under the scope of this study, which is divided into two parts, the hydrogel denoted as HGCM was utilized as the main substrate for both sections. To prepare HGCM, firstly graphitic carbon nitride was synthesized from the thermal treatment of a cyanuric acid–melamine supramolecular complex (CM) [42]. The resulting yellow powder was ultrasonicated in water to obtain a g-CN aqueous colloidal dispersion. The freshly prepared CM/water colloidal dispersion was mixed with water-soluble monomer (*N*,*N*-dimethylacrylamide, DMA) and crosslinker (*N*,*N*'-methylenebisacrylamide, MBA) followed by the addition of the redox couple, ascorbic acid/hydrogen peroxide, respectively. The mixture was immediately placed in a Petri dish to complete the gelation via free radical polymerization under dark conditions. After 3 hours, the resulting hydrogel was purified with water to remove the unreacted species (monomers and redox mediators), then it was freeze-dried overnight (HGCM). Despite the fact that g-CN-based hydrogels are appealing as g-CN nanosheets can be employed as photoinitiators to form covalent species, in this study external initiators were employed to embed g-CN nanosheets within hydrogel network [36]. In addition, a comparative sample was prepared by the same procedure in the absence of g-CN.

Hydrophobic hydrogels

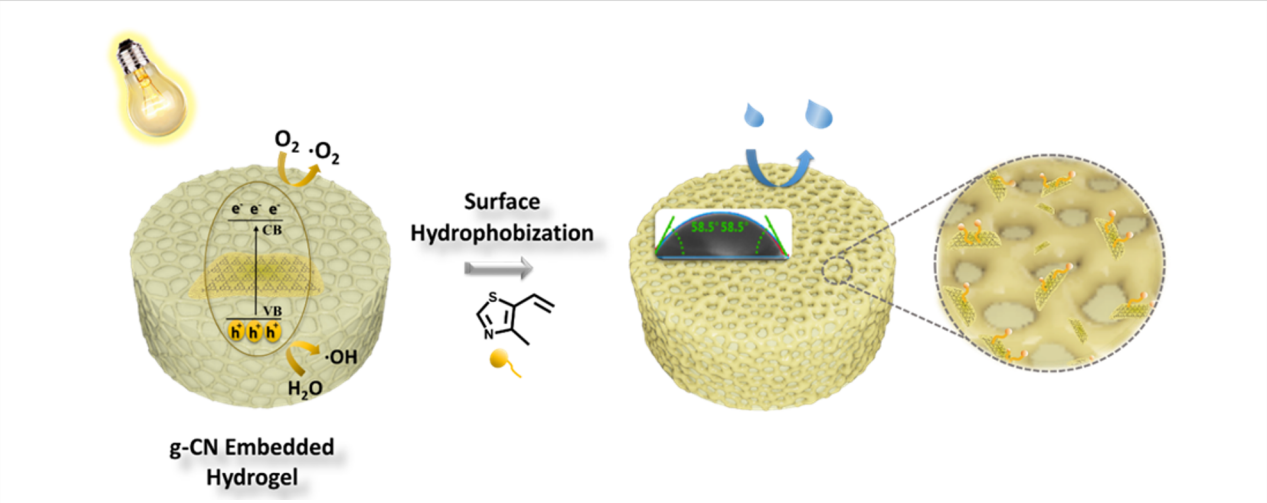
Recently, utilization of hydrogels in nutrient delivery in agricultural science and long-term drug delivery exhibits a significant interest [43]. Most of these methods require aqueous formulations to be delivered over a certain amount of time, yet a hydrophobicity for a long-term open-air application must be possessed in order to prevent the drying and a loss of a part [44]. Hydrophobic hydrogel is a novel concept that administers the surface properties of the initial network. In this section, we will propose a straightforward photo-based surface modification to introduce hydrophobicity on a hydrophilic network by taking advantage of the photoactive g-CN nanosheets. As explained in the preparation section, the resulting HGCM was immersed in the hydrophobic monomer 4-methyl-5-vinylthia-



Scheme 1: Schematic overview of g-CN-embedded hydrogel fabrication and its subsequent photoinduced post-modifications.

zole, denoted as vTA, then exposed to visible light irradiation to initiate an in situ surface photomodification. Extensive studies over the last years demonstrated photoinduced g-CN surface modification methods through a photoredox system. vTA, which is a common food additive to donate a nutty taste, has previously shown a significant hydrophobization effect on bulk g-CN [45], so that a similar strategy is targeted for the present case in hydrogel systems (Scheme 2). After adequate light irradiation followed by a facile purification step, the resulting sample (HGCM-vTA) and HGCM were investigated via solid-state analysis to evaluate the vTA incorporation, and microscopy techniques were employed to examine the impact on their morphology. In terms of applicability, water contact angle measurement, equilibrium swelling ratio analysis, and dye releasing efficiency experiment were also conducted.

All hydrogel samples were characterized via FTIR analysis to elucidate structural footprints of CM embedding and vTA photographing. The broad peak in the range from 3639 cm^{-1} to 3136 cm^{-1} corresponds to the hydrogen bonding between carboxyl and hydroxy groups with amide functionality of the hydrogel backbone. Significant stretching at 1620 cm^{-1} is typical for carbonyl groups of amides (Figure 1a). Thereupon, characteristic hydrogel vibrations explicitly vary according to the applied processes. The major difference between HG and HGCM is the significant peak sharpness around 3274 cm^{-1},



Scheme 2: Hydrophobic hydrogel via photoinduced surface modification over embedded g-CN nanosheets in hydrogel network.

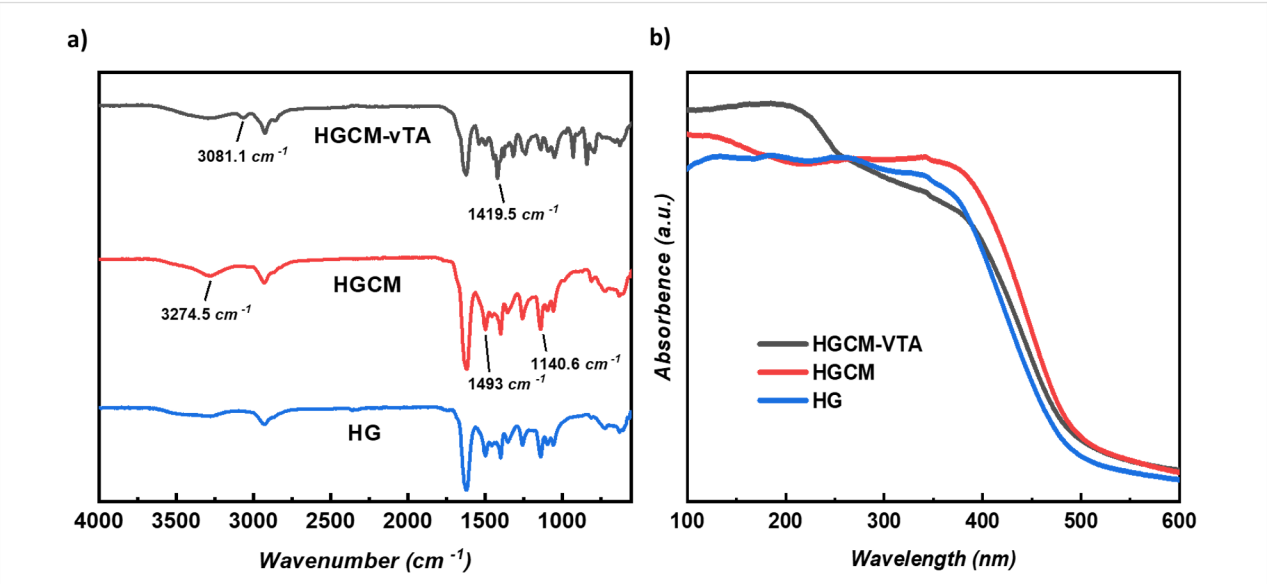


Figure 1: a) FTIR spectra of freeze-dried HGCM-vTA, HGCM and HG. b) UV spectra of freeze-dried HGCM-vTA, HGCM and HG.

which can be related to $-NH_2$ functional group stretching relying on buried g-CN structure in hydrogel network. The vTA photografting can be revealed via distinctive signals such as the emergent peak at 3081 cm^{-1}, corresponding to C–H aromatic stretchings arising from the thiazole ring, the neck at 1687 cm^{-1} signifies the C=N vibration band, and at last the intensified peak at 1419 cm^{-1} indicates a C–N stretching of the thiazole ring.

Proceeding the examination by UV–vis spectroscopy, overlaid absorption spectra of the samples revealed the photophysical differences as expected, since HG does not consist of photoactive g-CN particles in contrast to HGCM and HGCM-vTA. Moreover, the altered HGCM absorbance after surface modification provides enhanced absorption in deep UV range (Figure 1b). In addition, digital images of HG, HGCM, HGCM-vTA under UV light irradiation also reveal their emissive properties (Supporting Information File 1, Figure S1).

Scanning electron microscopy was performed to investigate the morphology of freeze-dried HGCM and HGCM-vTA. As shown in Figure 2a, HGCM exhibits a significantly porous and uniform morphology. Formation of accessible pores for vTA was the key point to reach in order to activate g-CN nanosheets buried in the hydrogel to perform a photoinduced modification. It must be mentioned that the light transmission is limited since the hydrogel substrate is not fully transparent, and this envisions the importance of porosity as a key factor to diffuse and reflect the incoming light that can reach embedded g-CN nanosheets to enhance the modification.

Surface transformation has drastically changed the parental hydrogel morphology. Closure of pores (Figure 2) are the supportive evidences for a successful modification as they are not observed in parental hydrogel (Figure 2a). Besides, elemental mapping results of HGCM-vTA are exhibiting a sulfur content allocation in accordance with the nitrogen atom distribution in a fair amount of abundance (Figure 2b). Determination of the sulfur content is a facile approval for the surface modification as neither monomers nor g-CN from HGCM are possessing a sulfur atom (Figure 2a).

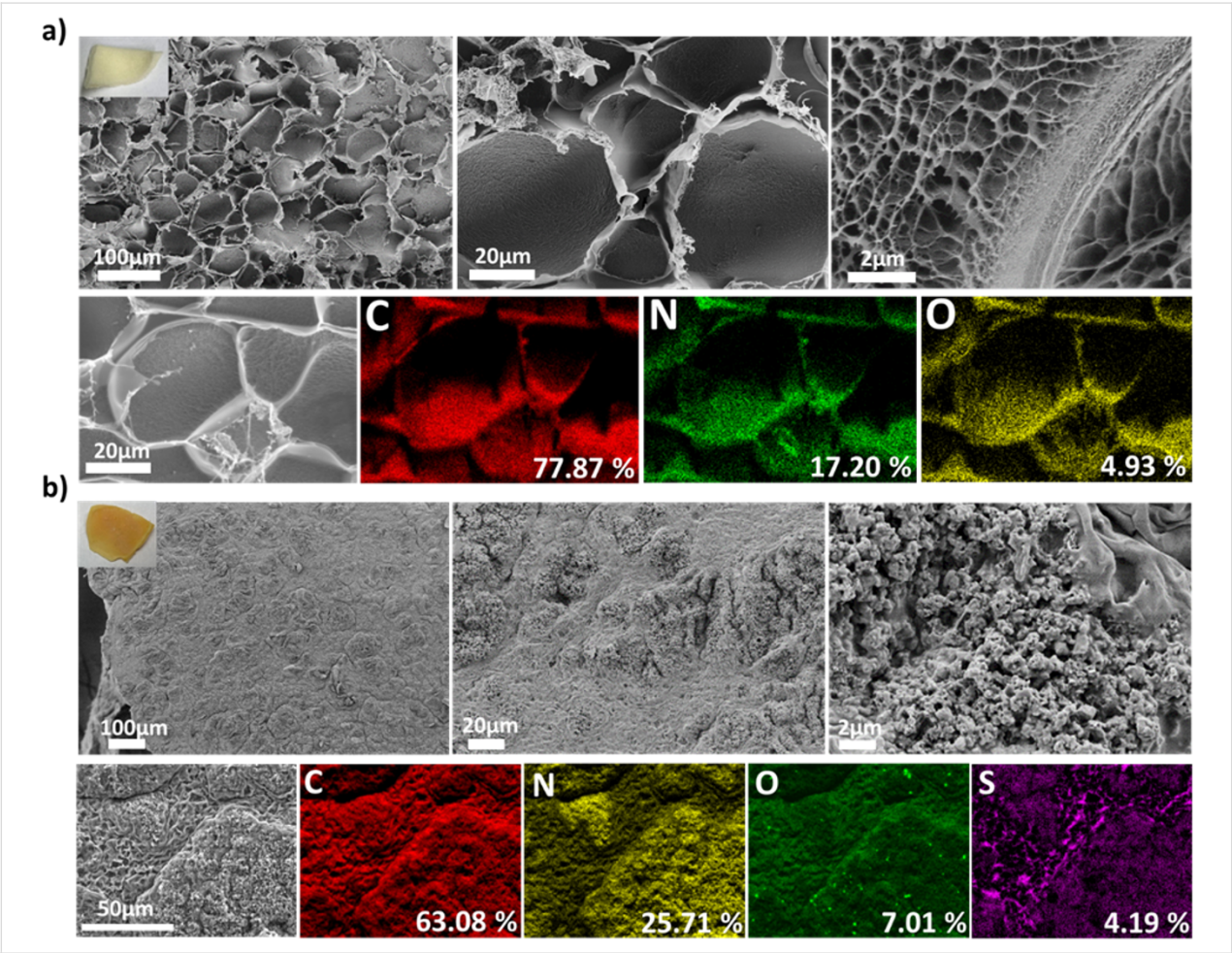


Figure 2: Scanning electron microscopy (SEM) images of a) HGCM and b) HGCM-vTA in combination with their elemental mapping results via EDX.

As we attempted to modify HGCM surface from hydrophilic to hydrophobic, the corresponding material surface wettability is expected to be influenced. To investigate this, wet forms of HGCM and HGCM-vTA were subjected to a water contact angle (WCA) measurement by utilizing multiple contact points (Supporting Information File 1, Figure S2). The most stable result in terms of smooth and unwrinkled contact point of HGCM-vTA has resulted in 58.5° over 40 seconds, and the other spots have resulted in 77.8° and 68.3°. On the other hand, HGCM showed a super hydrophilic character by imbibing the water with high-speed that even imaging was not possible (see the video provided as Supporting Information File 2).

It is known that the competition between the hydrophobic and hydrophilic character of hydrogels has a role in affecting water absorption and retention. In this regard, synthesized hydrogels were subjected to a swelling measurement to reveal their overall water affinity and then a TGA measurement was conducted to examine the water retention performances. The swelling ratio results showed that the surface hydrophobization led to a significant decrease, nearly a half performance, compared to unmodified samples (Figure 3a). Following that, water retention performances of HGCM and HGCM-vTA were investigated after leaving the samples to dry at room temperature for 2 days before conducting the TGA measurement (Figure 3b). TGA profiles did not indicate a significant difference for water retention, but thermal stability of HGCM-vTA within the range of 150 °C to 318 °C has improved. Considering the water retention, the first trials of the hydrophobization process were designed to perform the hydrophobization with the swollen sample instead of using freeze-dried versions to take the advantage of entrapped water that might provide the opportunity to control the water retention. Unfortunately, during the photomodification, diffusion of vTA molecules has driven the water mole-

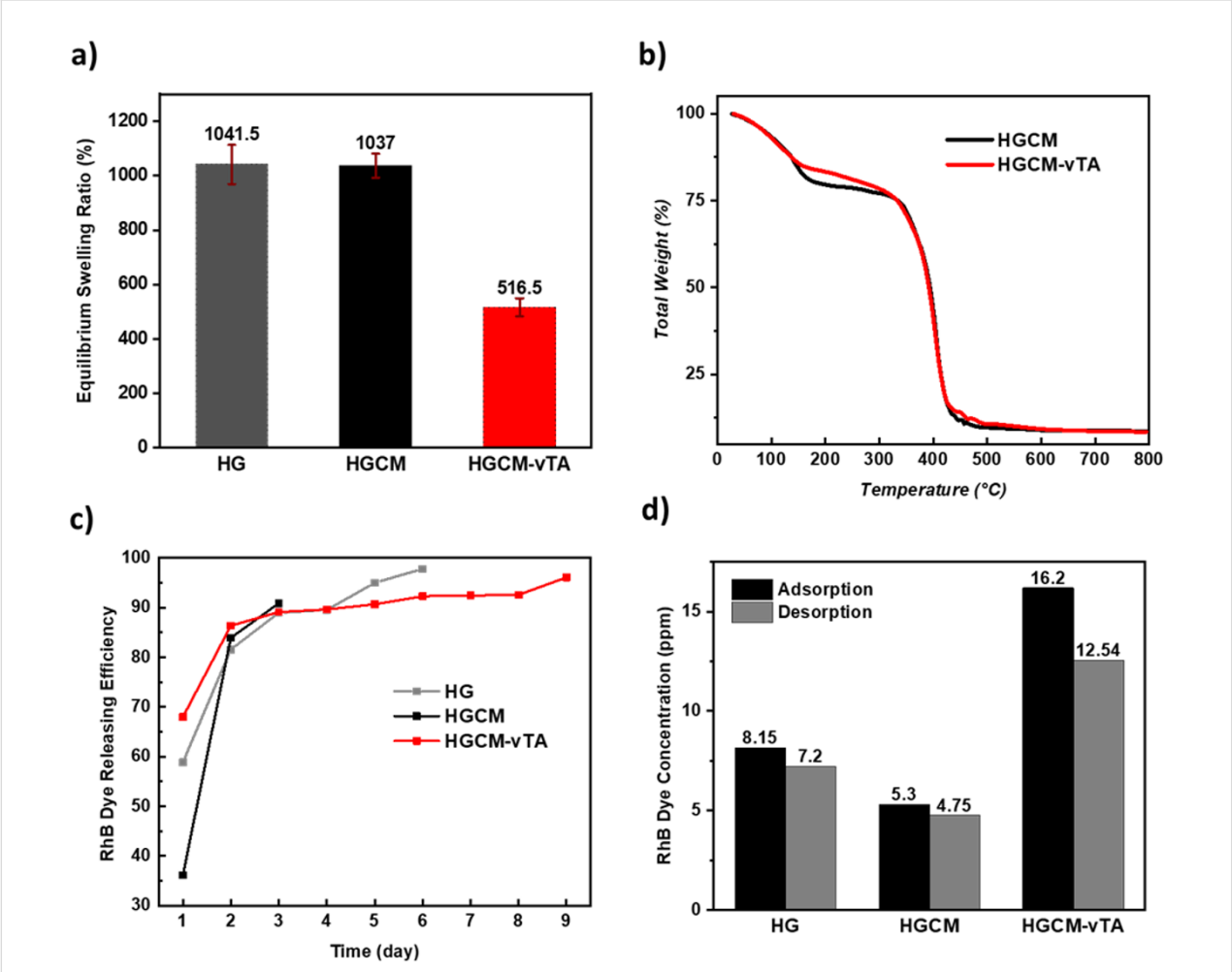


Figure 3: a) Equilibrium swelling ratios of HG, HGCM, HGCM-vTA at specified time intervals. b) Thermogravimetric analysis of HGCM and HGCM-vTA. c) RhB dye releasing efficiency versus time plot of HG, HGCM, and HGCM-vTA. d) RhB dye adsorption/desorption concentrations of HG, HGCM, HGCM-vTA.

cules outside the network. Despite this fact, the wet-modified sample resulted in a fair water contact angle result, but, however, not enhanced water retention. Another parameter on the water swelling was the effect of g-CN presence. It was observed that the presence of g-CN in hydrogel did not affect the water swelling ratio compared to the reference hydrogel, which is reasonable in terms of the physicochemical nature of hydrophilic hydrogels.

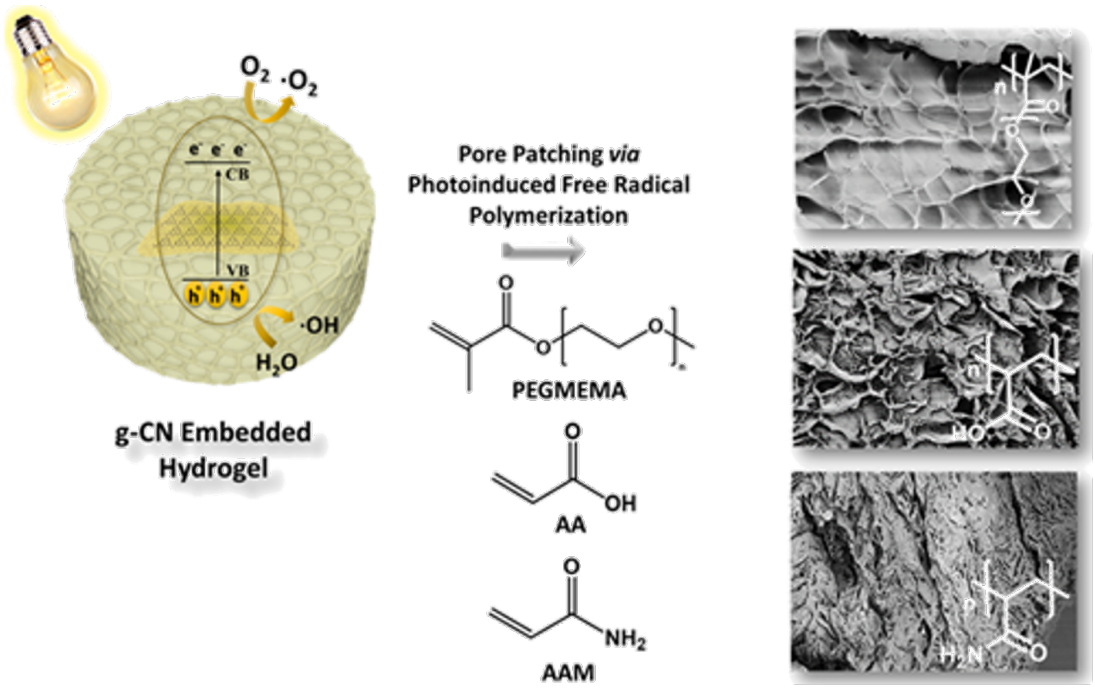
After the swelling experiment, samples were contacted to an aqueous RhB dye solution to investigate their dye releasing efficiency by gradually washing out the samples, in order to mimic a drug or nutrient release. One of the attractive applications of g-CN relies on the adsorption and/or photodegradation of dyes. In general, these performances are reported on bulk g-CN materials, such as the on a self-standing ultra-long porous g-CN wires exhibiting outstanding RhB adsorption values by minimized solvent uptakes [46]. In our case, we focus on the RhB releasing profiles of RhB swollen hydrogels. HG, HGCM, and HGCM-vTA have been immersed in RhB solution for 24 hours, then washed with distilled water every 24 hours, and all collected samples were investigated by UV–vis spectroscopy until reaching the minimum dye absorbance (Figure 3c,d, Supporting Information File 1, Figure S4). According to released RhB dye concentration versus time plots of all samples, HGCM-vTA completed dye releasing with the longest time period of 9 days. It was followed by HG, which resulted in 6 days whereas HGCM was accomplishing the process in 3 days (Figure 3c). Besides, according to periodically collected RhB dye concentrations summed up and compared with adsorption concentrations for each sample (stock RhB concentration: 40 ppm), HG released 88% of adsorpt RhB dye in 6 days, HGCM 89% in 3 days, and HGCM-vTA 77% in 9 days (Figure 3d). In addition to RhB dye, albumin–fluorescein isothiocyanate and fluorescein isothiocyanate–dextran fluorescent probes were subjected to HGCM and HGCM-vTA samples with a comparatively shorter releasing experiment than the one performed for RhB dye (Supporting Information File 1, Figure S4a). The static experiment principally relies on physical adsorption/releasing performance being under the control of intermolecular interactions. Hydrophobization might enhance the hydrophobic interactions between the dye core and the polymer network, thus releasing can be achieved in a longer term. As a last simulative experiment, cation (K^+, Ca^{2+}, Mg^{2+}) releasing performances of HGCM and HGCM-vTA after an overnight immersion in separately prepared stock solutions were analysed via ICP-OES (Supporting Information File 1, Figure S4b). HGCM shows higher cation releasing which might be driven by osmosis, however, HGCM-vTA retains cations thus offering a slower release which is highly beneficial for agricultural delivery systems.

The grand outcome of embedded g-CN-based surface photomodification has significant advantages in terms of its non-toxic process and cost-efficient material resources.

Pore substructuring

In porous materials, the functionality of the pores is responsible for the main catalytic activity, such as in carbonaceous materials [47,48]. When a network with full functionality cannot be formed easily, one can form a rigid neutral host and modify the pores subsequently. Herein, the nanoporous system is magnified to macropores in hydrogel systems as a representative synthetic approach to modulate porous structures of hydrogels with secondary polymers via visible-light-induced reaction. The photoactivity of g-CN materials are attractive in this sense since covalent modification of the surface of g-CN has offered a versatile post modification platform [49]. The as-prepared hydrogel network (HGCM) was immersed in various acrylic monomers. Following that, photoinduced free radical polymerization of employed monomers performed under visible light irradiation by taking advantage of embedded g-CN nanosheets in HGCM. According to literature, g-CN as an organic semiconductor is utilized in polymerization processes as a photoinitiator by generation of reactive radical species ($O_2^{-\bullet}$, $HO^\bullet$, $HO_2^\bullet$) under convenient light illumination. The ability of g-CN to initiate polymerization and act as a polymerization locus for a covalent polymer growth have been investigated in detail in literature [37,50]. Inspired by these, we now attempt to conduct a pore modification on g-CN-embedded hydrogels by visible-light-induced reaction. HGCM was a host network and the variety of monomers were swollen in the network, polymerized, and purified (Scheme 3). After the polymerization was completed, polymer networks were purified as delineated in the experimental section. Altered pore morphology was investigated by SEM, and functional group analysis was achieved by FTIR.

Enrichment of the hydrogel network with subsequent radical polymerization using various acrylic monomers possessing different functional groups were explicitly confirmed via FTIR (Figure 4). Regarding the polyacrylic acid-based system (PAA), the broadened signal from 2730 cm^{-1} to 3703 cm^{-1} and sharp signal at 3303 cm^{-1} corresponds to O–H stretching of the carboxylic acid group. The peak appearing at 1723 cm^{-1} can be attributed to asymmetric C=O group stretching vibrations of carboxylic acid groups on PAA chains. The polyacrylamide-based (PAAM) pore substructure spectrum is exhibiting the typical –NH stretching vibrations at 3420 cm^{-1} and the band at 1656 cm^{-1} is corresponding to the strong primary amide C=O stretching vibration of the amide group. The strong signals at 1558 and 1404 cm^{-1} are originated from amine N–H bending and scissoring $–CH_2–$ vibrations, respectively. At last, the poly(ethylene glycol) methyl ether methacrylate (PEGMEMA)-



Scheme 3: Overview of pore substructuring via photoinduced free radical polymerization over embedded g-CN nanosheets in hydrogel network.

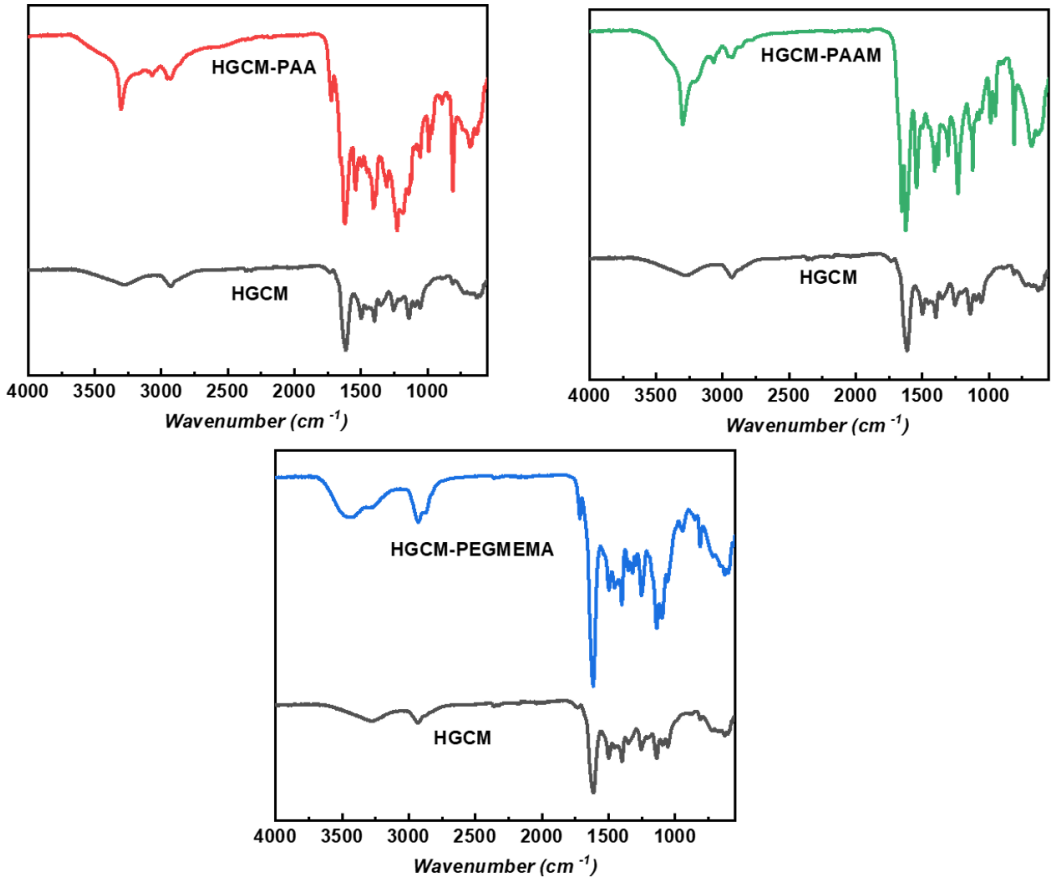


Figure 4: FTIR spectra of freeze-dried HGCM-PAA, HGCM-PAAM, HGCM-PEGMEMA in comparison with HGCM.

based network displays O–H stretching from 3106 cm^{-1} to 3710 cm^{-1} relying on pendant hydroxy groups of the PEG structure, the signal at 1719 cm^{-1} is corresponding to the C=O group stretching and the more pronounced intensities from 980 cm^{-1} to 1202 cm^{-1} are attributed to C–H bending and C–O stretching vibrations. Consequently, all FTIR spectra results confirm the photoinduced polymerization within the hydrogel network.

Visible light irradiation leads to a polymerization of monomers within the three-dimensional hydrogel network, thus one can expect altered pore morphologies. In that regard, SEM images are useful to explore the pore substructuring for each type of polymer, which are compacted and attached to the hydrogel skeleton (Figure 5). The morphology of HGCM as a main substructure was already investigated in the previous chapter. Considering the HGCM porous structure as a reference point, HGCM derived hydrogels demonstrated altered pore structures based on the type of the interpenetrated polymer. While PAA and PEGMEMA formations mostly bound intrinsically surface-attached, PAAM exhibited comb-like strands by connecting two junction points on the substrate. The reason of this might be both topological selectivity of polymers and the arbitrary photo-polymerization process. In addition, we were not able to identify free polymer chains during the purification process, which indicates a covalent growth of polymers on a hydrogel host.

It is expected that pore modification on networks will influence the thermal stability of the initial substrate. Regarding this, thermogravimetric analysis results confirmed the enhanced thermal stability for each employed polymer network compared to the initial substrate (Figure 6a). The HGCM curve is indicating the evaporation of entrapped water (up to 150 °C) followed by structural decomposition starting from 307 °C and ending up with 8.44% total weight at 800 °C, at first place. HGCM-PAA maintained thermal stability up to 305 °C with 8.4% mass change and resulted in 12.6% total weight whereas HGCM-PAAM was stable up to 250 °C with 7% mass change ending up with 13.4% total weight. At last, HGCM-PEGMEMA exhibited thermal stability up to 307 °C with 13% mass change and resulted in 8.5% total weight. When the temperature range between 160 °C and 300 °C is subjected for all curves, it can be concluded that the occupied pores by subsequent polymer networks are providing the thermal stability to parental HGCM substrate.

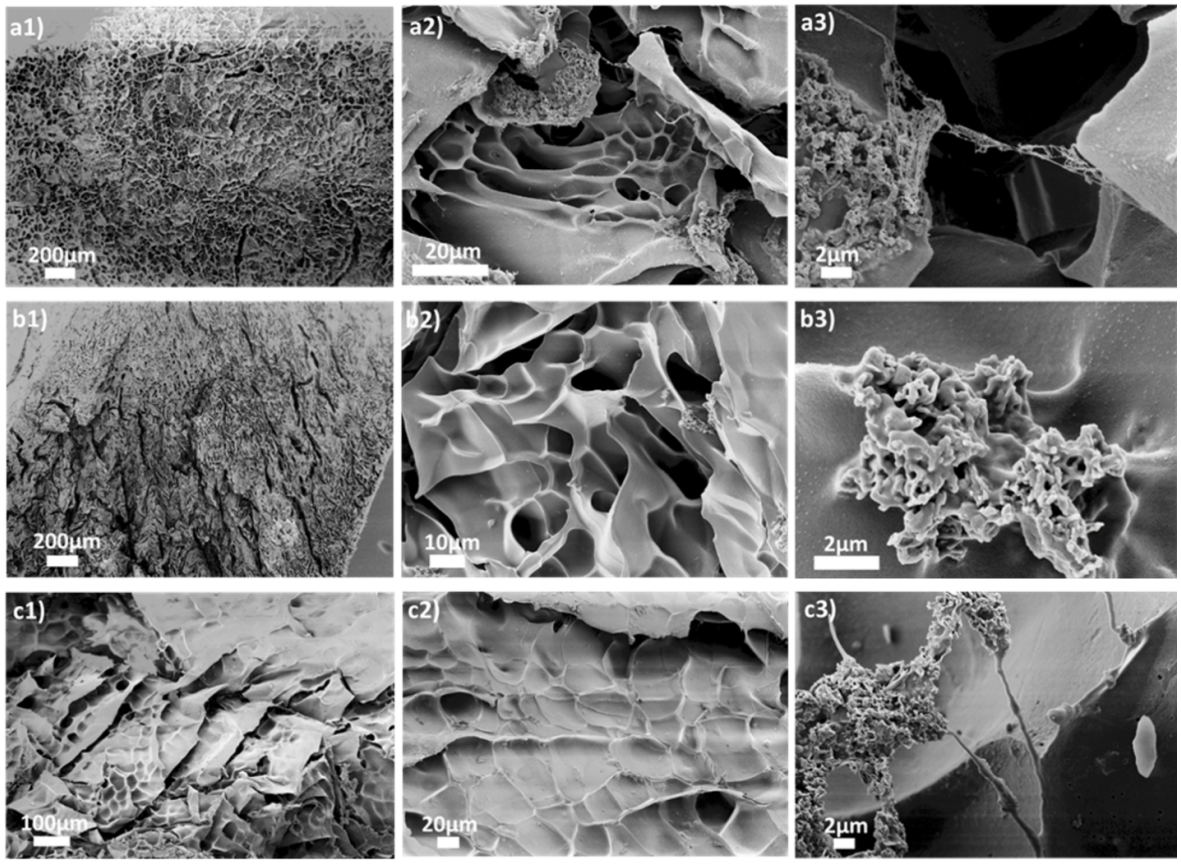


Figure 5: Scanning electron microscopy (SEM) images of a) HGCM-PAA, b) HGCM-PAAM, and c) HGCM-PEGMEMA.

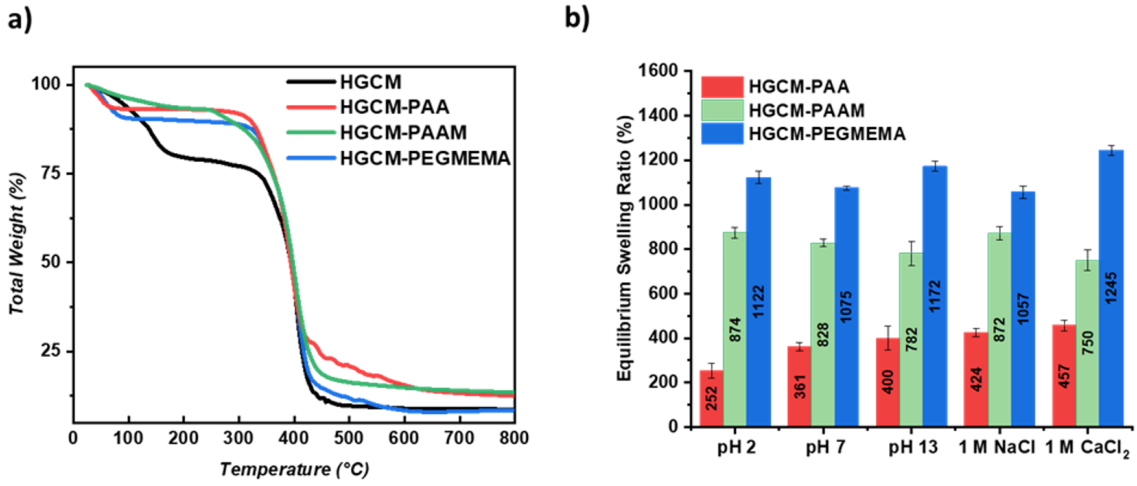


Figure 6: a) Thermogravimetric analysis of HGCM, HGCM-PAA, HGCM-PAAM and HGCM-PEGMEMA. b) Equilibrium swelling ratio results of HGCM-PAA, HGCM-PAAM, HGCM-PEGMEMA in various conditions; pH 2, pH 7, pH 13, 1 M NaCl, 1 M $CaCl_2$.

Employing a diverse set of monomers to HGCM network can have an influence on the swelling properties as well. Regarding this, swelling performances of so-formed networks were examined via swelling process at equilibrium state in various conditions (Figure 6b). The first overall interpretation is that the condition variety did not drastically affect ESR results of each sample. HGCM-PEGMEMA has the highest ESR in every condition that is in good agreement with the nonionic and highly flexible structure of PEG that can resist electrolytes and pH stimuli.

On the other hand, PAAM and PAA depicted significantly decreased ESR results, which are confirming the subsequent network formation by occupying the pores. The gap between the ESR results in each network could be considered as their patching efficiency. HGCM-PAAM performed a slight decrease from low pH to high pH value due to amine groups' protonation on the polymer backbone via electrostatic attraction, and it responded to monovalent electrolyte with a higher ESR. With the increased pH, HGCM-PAA eventuated with enhanced ESR results arising from the dissociation of carboxylic acid groups. Swelling in saltwater conditions demonstrated similar results, yet significantly lower compared to previous examples.

In addition, the error margins of equilibrium swelling behavior were affected by isotropic accretion of polymer networks over the substrate. It is important to underline that the presented polymerization process relies on a light access in the porous network, so conducting the reaction on thin substrates is favored.

Conclusion

Embedding photoactive g-CN nanosheets in hydrogels could be an advanced trick to access photoinduced post-modification techniques. The pores of the dried hydrogel can be filled with the precursor of a secondary network, and a visible light illumination forms an extended network with interlocked character. Alternatively, hydrophobization of a hydrogel can be attained by visible-light-induced photografting of vinylthiazole groups. In the present paper, two straightforward synthetic pathways for hydrogel post-modification are presented, and final products could be of great interest from the materials science perspective. Visible-light-induced post modification technology by semiconductors on porous networks could be extended to other porous systems as well, such as carbonecous networks.

Experimental

Materials: 4-Methyl-5-vinylthiazole (vTA, 97%, Sigma-Aldrich), L-(+)-ascorbic acid (AsA, 98+%, Alfa Aesar), *N*,*N*-dimethylacrylamide (99.0+%, TCI), *N*,*N*′-methylenebis(acrylamide) (MBA, 99%, Sigma-Aldrich), acrylic acid (AA, 99%, Sigma-Aldrich), acrylamide (AAM, 98.5%, Acros), albumin–fluorescein isothiocyanate conjugate (FITC-Albumin, Sigma-Aldrich), calcium chloride ($CaCl_2$, 97%, Alfa Aesar), cyanuric acid (98%, Sigma-Aldrich), fluoresceinisothiocyanat-dextran (FITC–Dextran, 10.000 M_w), hydrochloric acid (HCl, 37%, Sigma-Aldrich), hydrochloric acid (1 M solution, Sigma-Aldrich), hydrogen peroxide (30% aqueous solution, Merck), magnesium chloride ($MgCl_2$, 99%, Merck), melamine (99%, Sigma-Aldrich), poly(ethylene glycol) dimethacrylate (PEGDMA, M_n 550, Sigma-Aldrich), poly(ethylene glycol) methyl ether methacrylate (PEGMEMA, M_n 300, Sigma-

Aldrich), potassium chloride (KCl, 99%, Merck), rhodamine B (RhB, 95%, Sigma-Aldrich), sodium chloride (NaCl, 99%, Sigma-Aldrich), sodium hydroxide (1 M solution, Sigma-Aldrich). DMA, PEGDMA, PEGMEMA and were passed through basic alumina column prior to use.

Synthesis of g-CN: g-CN was synthesized from cyanuric acid–melamine supramolecular complex as reported in literature [42]. Cyanuric acid (1.29 g) and melamine (1.26 g, 1:1 molar ratio) were mixed in 50 mL distilled water overnight to form cyanuric acid–melamine complex, then the solid was filtered and dried in vacuum overnight. The dried product was transferred into a capped crucible and put into an N_2-protected oven at 550 °C for 4 hours, with a heating rate of 2.3 °C /min. The resulting yellow powder is labeled as g-CN (CM).

Synthesis of g-CN nanosheets embedded hydrogel (HGCM): 150 mg as-prepared CM was dispersed in 30 mL distilled water and sonicated 3 times for 30 minutes to exfoliate g-CN nanosheets (CM-W). 9 g freshly prepared CM-W, 0.8 g DMA, 0.150 g MBA and 0.150 g AsA were weighted into a flask, mixed for 5 minutes, then sonicated for 20 seconds. Following that, 1.5 mL hydrogen peroxide solution was injected into the mixture and placed in a Petri dish after mixing thoroughly. The Petri dish was capped and left for 3 hours to obtain a gelation via redox-induced free radical polymerization. Afterwards, it was washed with distilled water to remove the unreacted species and freeze dried for 24 hours. The resulting light and brittle g-CN nanosheets embedded hydrogel was ready for further usage. In addition, a comparative sample was prepared with the same procedure in the absence of CM, then the final hydrogel is denoted as (HG).

Synthesis of hydrophobic hydrogels (HGCM-vTA): 100 mg as-prepared HGCM and 5 mL vTA were put in a glass vial and left for 30 minutes to complete adsorption–desorption equilibrium. Afterwards, it was placed between two visible light sources (10 cm distance each) for 5 hours to perform in situ photomodification based on the photoactivity of embedded g-CN nanosheets within the hydrogel network. After 5 hours, hydrophobized HD-CM was placed in a Petri dish and washed with 20 mL acetone to remove the remaining vTA, then left in a fume hood for drying overnight.

Pore substructuring of HGCM by photoinitiation: 100 mg as-prepared HGCM and certain amounts of patching monomer (consisting 10 mol % crosslinker) were added into a capped glass vial containing 2 g distilled water and left for 2 hours to complete adsorption–desorption equilibrium. After 2 hours, monomer swollen hydrogel was replaced into another capped glass vial and set between two visible light sources (10 cm distance each) overnight to accomplish photopolymerization. Afterwards, it was purified by immersing in 20 mL distilled water refreshed repeatedly every 2 hours for 3 times and then left in a fume hood for drying overnight. This procedure was repeated for each substructuring monomer categorized as acidic AA (10 mol % MBA), cationic AAM (10 mol % MBA), and neutral PEGMEMA (10 mol % PEGDMA).

Rhodamine B dye releasing experiment: 40 mg HD, HGCM and HGCM-vTA were weighted separately in a capped glass vial containing 4 mL RhB dye solution (4×10^{-2} M) and left for 24 hours. Afterwards, all samples were replaced in another glass vial containing 4 mL distilled water to follow the dye releasing progress spectroscopically every 24 h. The RhB dye releasing efficiency was calculated by using the following formula for each sample:

$$\text{releasing efficiency } (\%) = \frac{c_t - c_0}{c_0} \times 100$$

c_0: initial RhB dye concentration, c_t: RhB dye concentration at specified time.

FTIC-albumin and FTIC-dextran releasing experiment: 40 mg HGCM and HGCM-vTA were weighted separately in a capped glass vial containing 4 mL FTIC-albumin (2000 ppm) and FTIC-dextran (2000 ppm) solutions and left overnight. Afterwards, all samples were placed in another glass vial containing 4 mL distilled water to spectroscopically monitor the labeled molecule release process after 24 h.

Cation releasing experiment: 100 mg HGCM and HGCM-vTA were separately immersed in freshly prepared KCl, $CaCl_2$ and $MgCl_2$ stock solutions (corresponding concentration for each cation, K^+, Ca^{2+} and Mg^{2+} = 1000 ppm) overnight. Afterwards, samples were placed in a capped glass vial containing 10 mL distilled water, respectively, and left overnight. Released contents of each cation were analyzed via ICP-OES.

Characterization: Fourier transform infrared (FTIR) spectra were acquired on a Nicolet iS 5 FT-IR spectrometer. Solid-state ultraviolet−visible (UV−vis) spectroscopy for grinded samples was performed via a Cary 500 Scan spectrophotometer equipped with an integrating sphere. Thermogravimetric analysis (TGA) was performed via TG 209 Libra from Netzsch under nitrogen atmosphere with a heating rate 10 K min^{-1} using aluminum crucible for samples. Trace analysis of potassium, calcium and magnesium cations were performed via inductively coupled plasma optical emission spectroscopy (ICP-OES Optima 8000). Scanning electron microscopy (SEM) and EDX

elemental mapping were performed using a JSM-7500F (JEOL) microscope equipped with an Oxford Instruments X-Max 80 mm^2 detector for the determination of both elemental composition and morphology. The CM/water suspension was prepared in a sonication bath at 50% amplitude from Elma (Transsonic T310). Freeze drying was applied to hydrogels for 24 hours (LSC, Christ, Germany) in order to obtain solid samples with protected porous architectures for further investigations. Water contact angle measurement was performed using a Krüss contact angle measuring system G10 and recorded via Krüss official software. The sample with ideally flat surface is placed in front of a camera which records the water drop on the surface and estimates the angle between water droplet and surface. This method is useful to determine surface properties, such as hydrophilicity and hydrophobicity in the present case.

Swelling ratio analysis of the samples were calculated with the following procedure: 40 mg dried hydrogels (*Wd*) were put into separate vials containing 4 mL of deionized water at pH 2, pH 7, and pH 13 (prepared from 1 M HCL and 1 M NaOH stock solutions), 1 M NaCl solution and 1 M $CaCl_2$ solution, respectively. The vials are then capped and left for different time intervals taking into consideration of equilibrium swelling point at room temperature. Relative standard deviation was calculated based on the measurement of 3 samples. Hydrogels treated with solutions were weighted separately (*Ws*), and the swelling ratio was calculated by using the following formula for each sample:

$$\text{swelling ratio } (\%) = \frac{Ws - Wd}{Wd} \times 100$$

Supporting Information

Supporting Information File 1

Four supporting figures.
[https://www.beilstein-journals.org/bjoc/content/supplementary/1860-5397-17-92-S1.pdf]

Supporting Information File 2

Water contact angle video.
[https://www.beilstein-journals.org/bjoc/content/supplementary/1860-5397-17-92-S2.avi]

Acknowledgements

We thank Prof. Dr. Dr. Markus Antonietti for a continuous support. Ms. Antje Völkel is acknowledged for TGA measurements.

Funding

The authors greatly acknowledge the Max Planck Society for funding.

ORCID® iDs

Cansu Esen - https://orcid.org/0000-0002-1400-2950

References

1. Caló, E.; Khutoryanskiy, V. V. *Eur. Polym. J.* **2015,** *65,* 252–267. doi:10.1016/j.eurpolymj.2014.11.024
2. Li, L.; Yan, B.; Yang, J.; Huang, W.; Chen, L.; Zeng, H. *ACS Appl. Mater. Interfaces* **2017,** *9,* 9221–9225. doi:10.1021/acsami.6b16192
3. Yuk, H.; Lin, S.; Ma, C.; Takaffoli, M.; Fang, N. X.; Zhao, X. *Nat. Commun.* **2017,** *8,* 14230. doi:10.1038/ncomms14230
4. Murakami, T.; Schmidt, B. V. K. J.; Brown, H. R.; Hawker, C. J. *Macromolecules* **2015,** *48,* 7774–7781. doi:10.1021/acs.macromol.5b01713
5. Li, T.; Kumru, B.; Al Nakeeb, N.; Willersinn, J.; Schmidt, B. V. K. J. *Polymers (Basel, Switz.)* **2018,** *10,* 576. doi:10.3390/polym10060576
6. Chen, Q.; Chen, H.; Zhu, L.; Zheng, J. *J. Mater. Chem. B* **2015,** *3,* 3654–3676. doi:10.1039/c5tb00123d
7. Li, Z.; Su, Y.; Xie, B.; Liu, X.; Gao, X.; Wang, D. *J. Mater. Chem. B* **2015,** *3,* 1769–1778. doi:10.1039/c4tb01653j
8. Haque, M. A.; Kurokawa, T.; Gong, J. P. *Polymer* **2012,** *53,* 1805–1822. doi:10.1016/j.polymer.2012.03.013
9. Gao, G.; Du, G.; Cheng, Y.; Fu, J. *J. Mater. Chem. B* **2014,** *2,* 1539–1548. doi:10.1039/c3tb21554g
10. Wang, Q.; Hou, R.; Cheng, Y.; Fu, J. *Soft Matter* **2012,** *8,* 6048. doi:10.1039/c2sm07233e
11. Djonlagic, J.; Lancuski, A.; Nikolic, M. S.; Rogan, J.; Ostojic, S.; Petrovic, Z. *J. Appl. Polym. Sci.* **2017,** *134,* 44535. doi:10.1002/app.44535
12. Liu, L.; Li, L.; Qing, Y.; Yan, N.; Wu, Y.; Li, X.; Tian, C. *Polym. Chem.* **2016,** *7,* 7142–7151. doi:10.1039/c6py01652a
13. Klein, M.; Poverenov, E. *J. Sci. Food Agric.* **2020,** *100,* 2337–2347. doi:10.1002/jsfa.10274
14. Sampathkumar, K.; Tan, K. X.; Loo, S. C. J. *iScience* **2020,** *23,* 101055. doi:10.1016/j.isci.2020.101055
15. Nayak, P. K.; Mahesh, S.; Snaith, H. J.; Cahen, D. *Nat. Rev. Mater.* **2019,** *4,* 269–285. doi:10.1038/s41578-019-0097-0
16. Kumru, B.; Antonietti, M. *Adv. Colloid Interface Sci.* **2020,** *283,* 102229. doi:10.1016/j.cis.2020.102229
17. Liao, G.; He, F.; Li, Q.; Zhong, L.; Zhao, R.; Che, H.; Gao, H.; Fang, B. *Prog. Mater. Sci.* **2020,** *112,* 100666. doi:10.1016/j.pmatsci.2020.100666
18. Gaddam, S. K.; Pothu, R.; Boddula, R. *Polym. Compos.* **2020,** *41,* 430–442. doi:10.1002/pc.25410
19. Barrio, J.; Shalom, M. *ChemCatChem* **2018,** *10,* 5573–5586. doi:10.1002/cctc.201801410
20. Liu, Q.; Wang, X.; Yang, Q.; Zhang, Z.; Fang, X. *Appl. Surf. Sci.* **2018,** *450,* 46–56. doi:10.1016/j.apsusc.2018.04.175
21. Luo, B.; Song, R.; Geng, J.; Jing, D.; Zhang, Y. *Appl. Catal., B* **2018,** *238,* 294–301. doi:10.1016/j.apcatb.2018.07.039
22. Han, Q.; Wang, B.; Zhao, Y.; Hu, C.; Qu, L. *Angew. Chem., Int. Ed.* **2015,** *54,* 11433–11437. doi:10.1002/anie.201504985

23. Yang, Y.; Zeng, G.; Huang, D.; Zhang, C.; He, D.; Zhou, C.; Wang, W.; Xiong, W.; Song, B.; Yi, H.; Ye, S.; Ren, X. *Small* **2020,** *16,* 2001634. doi:10.1002/smll.202001634
24. Xu, G.; Xu, Y.; Zhou, Z.; Bai, Y. *Diamond Relat. Mater.* **2019,** *97,* 107461. doi:10.1016/j.diamond.2019.107461
25. Sun, J.; Xu, J.; Grafmueller, A.; Huang, X.; Liedel, C.; Algara-Siller, G.; Willinger, M.; Yang, C.; Fu, Y.; Wang, X.; Shalom, M. *Appl. Catal., B* **2017,** *205,* 1–10. doi:10.1016/j.apcatb.2016.12.030
26. Cao, Q.; Amini, S.; Kumru, B.; Schmidt, B. V. K. J. *ACS Appl. Mater. Interfaces* **2021,** *13,* 4643–4651. doi:10.1021/acsami.0c18064
27. Qin, J.; Wang, S.; Ren, H.; Hou, Y.; Wang, X. *Appl. Catal., B* **2015,** *179,* 1–8. doi:10.1016/j.apcatb.2015.05.005
28. Lin, J.; Pan, Z.; Wang, X. *ACS Sustainable Chem. Eng.* **2014,** *2,* 353–358. doi:10.1021/sc4004295
29. Gong, X.; Yu, S.; Guan, M.; Zhu, X.; Xue, C. *J. Mater. Chem. A* **2019,** *7,* 7373–7379. doi:10.1039/c8ta09801h
30. Giusto, P.; Cruz, D.; Heil, T.; Arazoe, H.; Lova, P.; Aida, T.; Comoretto, D.; Patrini, M.; Antonietti, M. *Adv. Mater. (Weinheim, Ger.)* **2020,** *32,* 1908140. doi:10.1002/adma.201908140
31. Giusto, P.; Kumru, B.; Zhang, J.; Rothe, R.; Antonietti, M. *Chem. Mater.* **2020,** *32,* 7284–7291. doi:10.1021/acs.chemmater.0c01798
32. Kiskan, B.; Zhang, J.; Wang, X.; Antonietti, M.; Yagci, Y. *ACS Macro Lett.* **2012,** *1,* 546–549. doi:10.1021/mz300116w
33. Fu, Q.; Ruan, Q.; McKenzie, T. G.; Reyhani, A.; Tang, J.; Qiao, G. G. *Macromolecules* **2017,** *50,* 7509–7516. doi:10.1021/acs.macromol.7b01651
34. Kumru, B.; Cruz, D.; Heil, T.; Antonietti, M. *Chem. Mater.* **2020,** *32,* 9435–9443. doi:10.1021/acs.chemmater.0c03616
35. Kumru, B.; Mendoza Mesa, J.; Antonietti, M.; Al-Naji, M. *ACS Sustainable Chem. Eng.* **2019,** *7,* 17574–17579. doi:10.1021/acssuschemeng.9b05351
36. Sun, J.; Schmidt, B. V. K. J.; Wang, X.; Shalom, M. *ACS Appl. Mater. Interfaces* **2017,** *9,* 2029–2034. doi:10.1021/acsami.6b14879
37. Liu, J.; An, T.; Chen, Z.; Wang, Z.; Zhou, H.; Fan, T.; Zhang, D.; Antonietti, M. *J. Mater. Chem. A* **2017,** *5,* 8933–8938. doi:10.1039/c7ta02923c
38. Ye, B.; Yao, C.; Yan, M.; Zhang, H.; Xi, F.; Liu, J.; Li, B.; Dong, X. *Macromol. Mater. Eng.* **2019,** *304,* 1800500. doi:10.1002/mame.201800500
39. Kumru, B.; Molinari, V.; Hilgart, M.; Rummel, F.; Schäffler, M.; Schmidt, B. V. K. J. *Polym. Chem.* **2019,** *10,* 3647–3656. doi:10.1039/c9py00505f
40. Thurston, J. H.; Clifford, A. J.; Henderson, B. S.; Smith, T. R.; Quintana, D.; Cudworth, K. F.; Lujan, T. J.; Cornell, K. A. *ACS Appl. Bio Mater.* **2020,** *3,* 1681–1689. doi:10.1021/acsabm.9b01240
41. Hu, C.; Lin, Y.-R.; Yang, H.-C. *ChemSusChem* **2019,** *12,* 1794–1806. doi:10.1002/cssc.201802257
42. Shalom, M.; Inal, S.; Fettkenhauer, C.; Neher, D.; Antonietti, M. *J. Am. Chem. Soc.* **2013,** *135,* 7118–7121. doi:10.1021/ja402521s
43. Zhou, X.; Zhang, P.; Zhao, F.; Yu, G. *ACS Mater. Lett.* **2020,** *2,* 1419–1422. doi:10.1021/acsmaterialslett.0c00439
44. Sikder, A.; Pearce, A. K.; Parkinson, S. J.; Napier, R.; O'Reilly, R. K. *ACS Appl. Polym. Mater.* **2021,** *3,* 1203–1217. doi:10.1021/acsapm.0c00982
45. Kumru, B.; Cruz, D.; Heil, T.; Schmidt, B. V. K. J.; Antonietti, M. *J. Am. Chem. Soc.* **2018,** *140,* 17532–17537. doi:10.1021/jacs.8b08956
46. Barrio, J.; Shalom, M. *ACS Appl. Mater. Interfaces* **2018,** *10,* 39688–39694. doi:10.1021/acsami.8b13873
47. de Oliveira Ferreira, M. E.; Vaz, B. G.; Borba, C. E.; Alonso, C. G.; Ostroski, I. C. *Microporous Mesoporous Mater.* **2019,** *277,* 208–216. doi:10.1016/j.micromeso.2018.10.034
48. Yu, Y.; Miyawaki, J. *Carbon* **2020,** *170,* 380–383. doi:10.1016/j.carbon.2020.07.050
49. Barrio, J.; Volokh, M.; Shalom, M. *J. Mater. Chem. A* **2020,** *8,* 11075–11116. doi:10.1039/d0ta01973a
50. Yandrapalli, N.; Robinson, T.; Antonietti, M.; Kumru, B. *Small* **2020,** *16,* 2001180. doi:10.1002/smll.202001180

License and Terms

This is an Open Access article under the terms of the Creative Commons Attribution License (https://creativecommons.org/licenses/by/4.0). Please note that the reuse, redistribution and reproduction in particular requires that the author(s) and source are credited and that individual graphics may be subject to special legal provisions.

The license is subject to the *Beilstein Journal of Organic Chemistry* terms and conditions: (https://www.beilstein-journals.org/bjoc/terms)

The definitive version of this article is the electronic one which can be found at: https://doi.org/10.3762/bjoc.17.92

BEILSTEIN JOURNAL OF ORGANIC CHEMISTRY

Progress and challenges in the synthesis of sequence controlled polysaccharides

Giulio Fittolani[1,2], Theodore Tyrikos-Ergas[1,2], Denisa Vargová[1], Manishkumar A. Chaube[1] and Martina Delbianco[*1]

Review

Open Access

Address:
[1]Department of Biomolecular Systems, Max Planck Institute of Colloids and Interfaces, Am Mühlenberg 1, 14476 Potsdam, Germany and [2]Department of Chemistry and Biochemistry, Freie Universität Berlin, Arnimallee 22, 14195 Berlin, Germany

Email:
Martina Delbianco[*] - martina.delbianco@mpikg.mpg.de

* Corresponding author

Keywords:
enzymes; glycans; polysaccharides; synthesis; well-defined polymers

Beilstein J. Org. Chem. **2021,** *17,* 1981–2025.
https://doi.org/10.3762/bjoc.17.129

Received: 21 May 2021
Accepted: 22 July 2021
Published: 05 August 2021

This article is part of the thematic issue "Polymer chemistry: fundamentals and applications".

Guest Editor: B. V. K. J. Schmidt

© 2021 Fittolani et al.; licensee Beilstein-Institut.
License and terms: see end of document.

Abstract

The sequence, length and substitution of a polysaccharide influence its physical and biological properties. Thus, sequence controlled polysaccharides are important targets to establish structure–properties correlations. Polymerization techniques and enzymatic methods have been optimized to obtain samples with well-defined substitution patterns and narrow molecular weight distribution. Chemical synthesis has granted access to polysaccharides with full control over the length. Here, we review the progress towards the synthesis of well-defined polysaccharides. For each class of polysaccharides, we discuss the available synthetic approaches and their current limitations.

Introduction

Polysaccharides are an abundant class of natural polymers that play important roles in the biosphere by structurally supporting plants, providing energy to animals, and regulating a variety of biological processes [1]. Their versatility and diversity result in a wide range of properties exploited for commercial purposes. Chemical modifications permit to broaden their applications even further. Additionally, polysaccharides can be converted into useful chemicals upon biodegradation [2,3], contributing to the sustainable development of future materials.

Despite polysaccharides' utility, there are limitations associated with their exploitation. Extraction from natural sources is laborious, low yielding, and provides heterogeneous mixtures that hamper characterization, reproducibility, and quality control. Small contaminations can heavily affect the polysaccharides' material and biological properties. This issue became dramatic when contaminated batches of heparin caused many deaths during the so called "heparin crisis" in 2008 [4].

In addition, the heterogeneity of naturally sourced samples poses a severe bottleneck to the molecular characterization of polysaccharides that dwarfs in comparison to other biomolecules like peptides and nucleic acids. Establishing structure–property correlations is key to understanding polysaccharides' function in nature and translate this knowledge into tailor-made materials.

Synthesis (i.e., chemical, enzymatic, or through polymerization) offers the opportunity to access polysaccharides with well-defined composition, length, and substitution. These compounds are ideal probes to study polysaccharides at the molecular level and identify structure–property correlations. Access to synthetic polysaccharides facilitated the correlation of chemical structure with molecular conformations [5,6], intermolecular interactions [7,8], and biological response [9]. Nevertheless, the complexity and diversity of polysaccharides makes synthetic processes extremely laborious and time consuming. Several aspects are crucial to plan a successful polysaccharide synthesis. Properly designed starting materials and/or catalysts are required to ensure regio- and stereocontrol during glycosidic bond formation. Control over the polysaccharide length (degree of polymerization, DP) and regioselective insertion of modifications or branches are additional challenges. Three main approaches are available (Figure 1): A) enzymatic polymerization [10-17], B) chemical polymerization [18], C) chemical synthesis.

The use of enzymes has undeniable advantages because it offers the possibility to use unprotected sugars as substrates and guarantees remarkable control of the regio- and stereoselectivity during glycosylation. Mono- or oligosaccharides bearing a reactive leaving group (LG, e.g., phosphate, fluoride, nucleotide) are polymerized by the enzyme to form the desired polysaccharide (Figure 1A). Several classes of enzymes are available, including hydrolases, phosphorylases, sucrases, glycosyltransferases, and glycosynthases [19-22]. An excellent overview of the enzymes available for polysaccharide synthesis and their mode of action was recently published [11]. Despite the numerous advantages of this approach, limited enzyme availability as well as their high specificity narrowed the substrate scope. Generally, the highly specific enzyme reactive site tolerates only small modifications, hampering the formation of unnatural polymers. Low glycosylation yields and product hydrolysis represent additional hurdles associated with enzymatic synthesis of polysaccharides [23]. With this approach, homopolymers are often obtained as non-uniform samples, because the enzymes cannot distinguish between acceptors with different lengths in the reaction mixture.

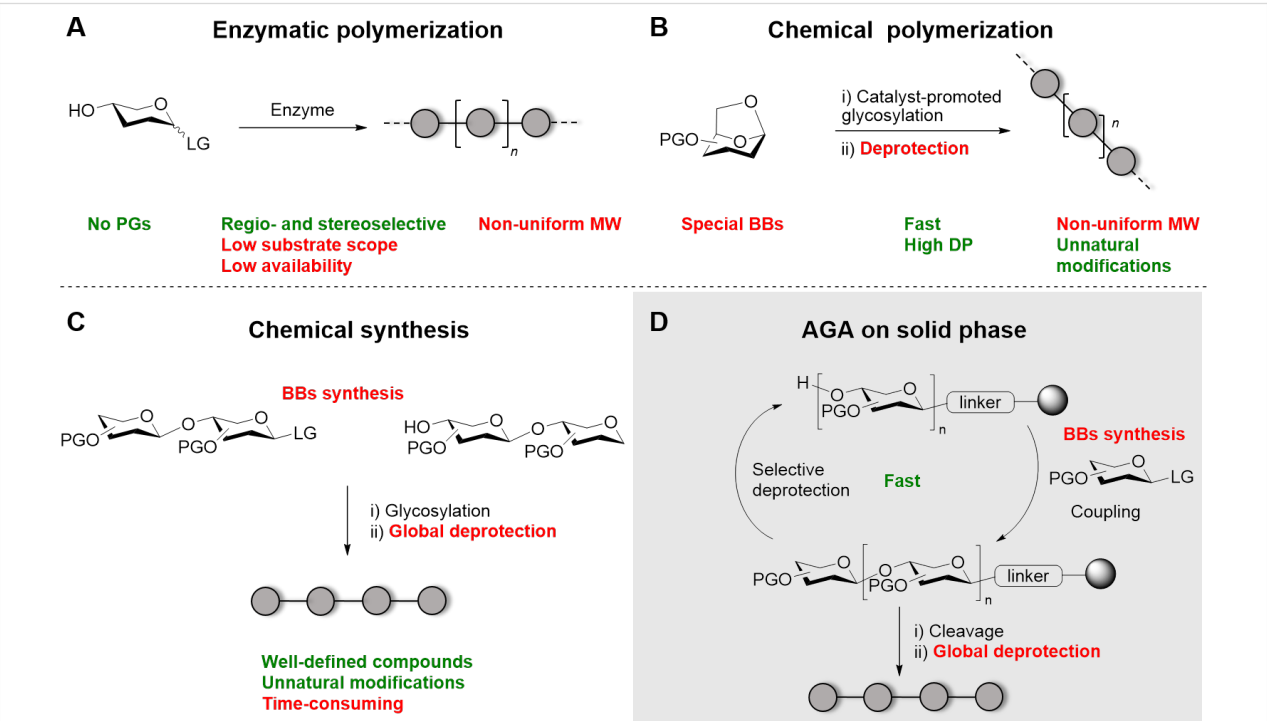


Figure 1: Overview of the methods available for the synthesis of polysaccharides. For each method, advantages (green) and disadvantages (red) are highlighted. Polymerization techniques (A and B) generate mixtures of compounds with non-uniform distribution of molecular weight (MW). In contrast, chemical synthesis (C) produces well-defined polysaccharides, but it is time-consuming. Automated Glycan Assembly (AGA) increases the efficiency of chemical synthesis by automating cycles of coupling and deprotection on a solid support (D).

Chemical polymerization is often performed by ring-opening of the respective anhydrosugar (Figure 1B) or polycondensation reactions. This approach is highly valuable to generate long chains in short time, allowing for the introduction of unnatural modifications. However, the control over the length and substitution pattern remains poor. To ensure good regio- and stereoselectivity, the starting material, often a polycyclic compound, has to be designed with suitable protecting groups (PGs). These structures can be quite challenging to prepare. Moreover, problems can occur during the removal of the PGs, since partially deprotected compounds can generate insoluble aggregates [24]. Incomplete deprotection and residual PGs can largely affect the properties of the obtained polymer.

Chemical synthesis provides compounds with well-defined length and substitution pattern (Figure 1C), but requires a substantial synthetic effort. For this reason, only few examples of long polysaccharides prepared by chemical synthesis are available. Properly designed building blocks (BBs) are needed, often prepared following numerous synthetic steps. In general, BBs are equipped with a reactive anomeric LG to allow for glycosylation and suitable PGs to ensure regio- and stereocontrol [25]. Even though, in most cases, BB preparation follows straightforward protection/deprotection strategies, the low selectivity and yield of certain transformations [26,27] can limit the scope of this approach. The desired polysaccharide is generally assembled following a linear or a convergent approach. In the former, the desired BBs are added sequentially to the growing polysaccharide chain via a series of glycosylation reactions. In contrast, a convergent approach (also known as fragment coupling) allows connecting pre-assembled oligosaccharide blocks. To decrease the synthetic time required for the chemical synthesis of polysaccharides, automated techniques have been developed [28-31]. Automated glycan assembly (AGA) connects monosaccharide BBs on a solid support following a linear approach (Figure 1D). Cycles of glycosylation and selective deprotection are iteratively performed to access the desired polysaccharide with full control over the length and the monosaccharide sequence [32]. Upon completion of the assembly, the desired product is released from the solid support and subjected to global deprotection. Similar to chemical polymerization, the removal of the PGs is a significant bottleneck. Additionally, several transformations remain challenging due to the poor reactivity or limited stereocontrol of certain BBs [33-37].

To overcome some limitations of the individual methods, a combination of methods is sometimes exploited. A classic example is chemoenzymatic synthesis, in which synthetic BBs are employed to direct the enzymatic synthesis towards the desired polysaccharide target.

In this review, we discuss the recent efforts towards the synthesis of well-defined polysaccharides, with particular focus on how to control the length and the substitution pattern. Each section describes a class of polysaccharides based on a particular monosaccharide backbone (Figure 2). For each class, we discuss the specific challenges associated with their synthesis and we highlight the methods that were developed to overcome such bottlenecks. We aim to provide guidelines for the synthesis of a target polysaccharide, as well as to identify the remaining bottlenecks associated with each class of polysaccharides. For this reason, the synthesis of polysaccharides based on a highly heterogeneous backbone will not be discussed [38-40]. Such syntheses are specific to the single polysaccharide target and only applicable to that particular sequence.

Each chapter focuses on recent literature describing the synthesis of oligo- and polysaccharides longer than hexasaccharides. Shorter oligomers are discussed when they represent a key step towards the synthesis of the corresponding polysaccharide. Polymers based on a sugar backbone connected via glycosidic linkages are analyzed, excluding glycopolymers and other mimetics. Extraction methodologies or post-extraction modifications are not discussed.

Review

Glucose-based polysaccharides

Cellulose

Cellulose is a polymer consisting of glucose units connected by β(1–4) glycosidic bonds. It is mainly found in two allomorphs – Cellulose I (natural) and Cellulose II (synthetic) – that differ in the orientation of the individual chains and in the number of hydrogen bonds in the crystalline structures [42,43]. In Cellulose I, the chains are oriented parallel, whereas in Cellulose II antiparallel. Natural cellulose is produced by cellulose synthases [44-46]. As the chain gets elongated, microfibrils are formed. Such fibrils are the main structural components of the plant cell-wall, together with hemicelluloses [47]. Because of the high abundance and biodegradability [48-52], cellulosic materials have found multiple industrial applications [53].

Synthesis and utilization, as well as a better understanding of cellulose's properties are hindered by its poor solubility in most solvents. Relatively short oligomers with DPs of 6–10 tend to aggregate and precipitate out of solution [54], making isolation of pure samples troublesome. Much effort has been put to tune the synthetic conditions and produce long and uniform polysaccharides. Solvent systems like DMAc/LiCl or quaternary ammonium electrolytes are able to dissolve cellulose and could overcome the precipitation issues during synthesis [55,56]; however, these systems are not always compatible with reaction conditions [57]. The developments of synthetic cellulose

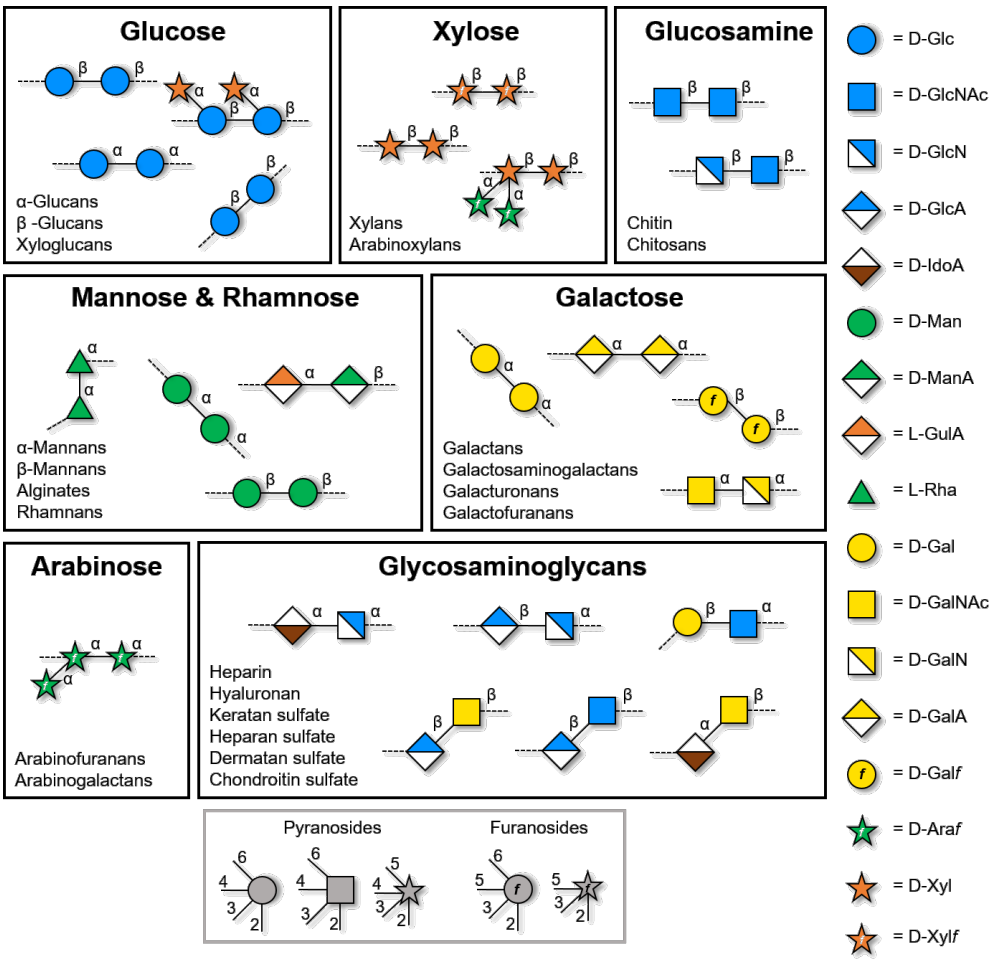


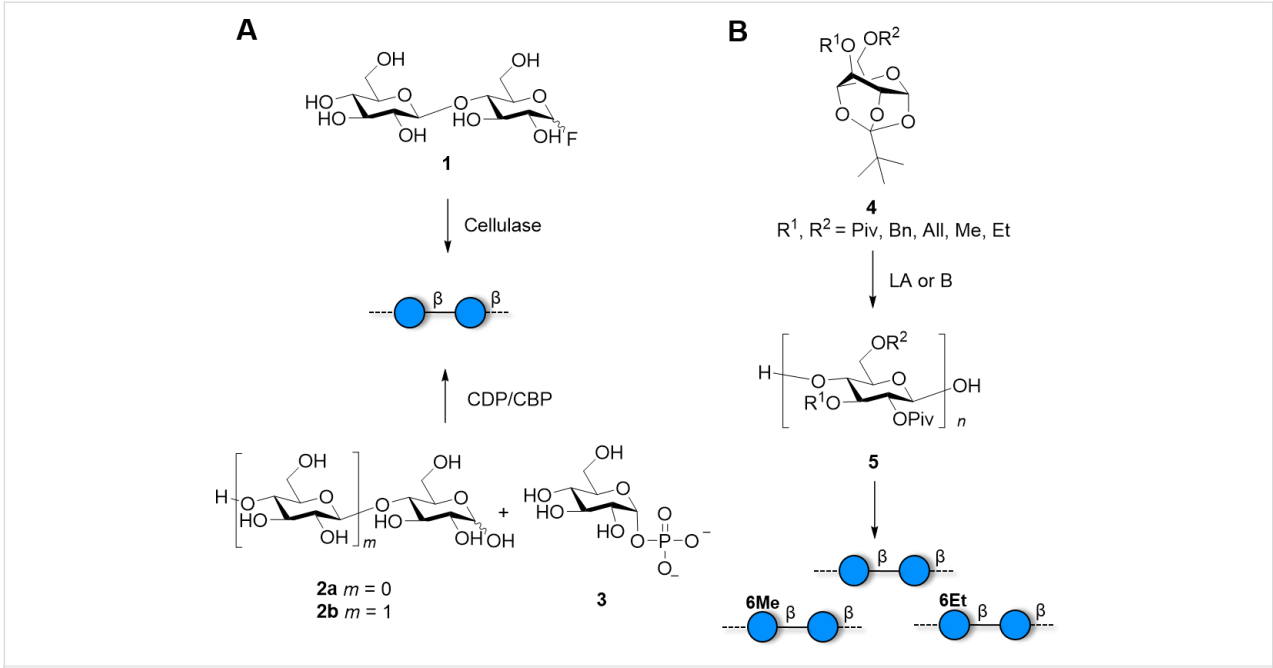
Figure 2: Overview of the classes of polysaccharides discussed in this review. Each section deals with polysaccharides built on the same monosaccharide backbone. Representation following the Symbol Nomenclature For Glycans (SNFG) [41].

until the year 2005 were discussed in a previous review [58], therefore we will focus only on recent reports. A detailed discussion on the synthesis of cellulose oligomers by enzymatic depolymerization [59] and phosphorylase [60] can be found elsewhere.

The first successful enzymatic synthesis of cellulose was reported by Kobayashi in 1991 [61]. Since then, a plethora of enzymes [62] and substrates [63] were developed, aiming to narrow the dispersion of molecular weight (MW), increase the DP, or control the molecular organization of the resulting material (Scheme 1). Enzymatic polymerization of cellobiose fluoride **1** was achieved using a cellulase produced from *Trichoderma viride* (Scheme 1A). The DP of the acetylated product was shown to be at least 22. Using a purified version of this enzyme, it was possible to obtain a synthetic analogue of Cellulose I [64].

A rough control of DPs (between 5 and 14) could be obtained tuning the concentration of glucose (**2a**) or cellobiose (**2b**) primer acceptor [65]. Polymerization conducted under macromolecular crowding conditions using water-soluble polymers produced hydrogels consisting of cellulose and gelatin networks [54,66-69]. A study of the self-assembly of cellulose chains at the active site of the enzyme suggested that diffusion of the aggregated molecules and the monomers around the active center dictates the DP that can be obtained by enzymatic polymerization [70,71]. This could be the reason causing enzymatic reactions to stop after a certain chain length, as the active site becomes overcrowded. Thus, by modifying the reaction medium, a better control over the DP may be achieved.

Longer cellulose chains (DP > 100) were obtained using DMAc/LiCl as reaction solvent and a cellulose surfactant complex, even though in low yields (2–5%). This approach circum-



Scheme 1: Enzymatic and chemical polymerization approaches provide cellulose oligomers with a non-uniform distribution of MW. A) Cellulose oligomers can be synthesized using cellobiose fluoride **1** and cellulase. Other enzymes like cellodextrin phosphorylase (CDP) or cellobiose phosphorylase (CBP) use glucose (**2a**) or cellobiose (**2b**) primer respectively and glucose phosphate **3**. B) Synthesis of cellulose by ROP from protected orthoester **4** promoted by Lewis acid (LA) or base (B).

vented the precipitation of the water-insoluble oligomers and allowed for chain elongation [72,73]. This methodology was improved employing a protic co-catalyst system to yield DP > 120 in a 26% conversion [74]. Generally, an acid catalyst would promote the hydrolysis of the glycosidic bond. In this system, the SEE was hydrolytically inactive and the acid catalysis activated the C-1 at the reducing end efficiently to promote chain-elongation.

Immobilized catalysis provided cellulose analogues with very high crystallinity. A synthetic mutant enzyme of endoglucanase II [75] was cross-linked by bis-nitrilotriacetic acid yielding fibrous cellulose [76]. Cross-linked enzymes are believed to arrange their catalytic core domains and promote the formation of cellulose with high crystallinity. A similar principle was also demonstrated on a self-assembled monolayer [77]. Mimicking the natural cellulose synthases machinery can be foreseen to provide synthetic Cellulose I.

Some enzymes offer the flexibility to produce modified cellulose structures. Cellulose oligomers with fluorine substitution at C-2, C-3 or C-6 position were prepared by cellodextrin phosphorylases [78]. Mono- or multi-fluorinated compounds were obtained in good yields (30–47%) with average DPs ranging from 9 to 15. The multifluorinated compound crystallized in a new cellulose allomorph. AFM and TEM images confirmed the formation of long platelets for monofluorinated compounds, similar to those observed for cellulose [67,79], while the multifluorinated compound formed considerably shorter platelets. Cellulose–xylan [80] and cellulose–chitin [81] hybrids were also obtained upon enzymatic polymerization of the respective dimers. An amino or azido functionality in the C-6 position allows for further modifications, for example by click-chemistry [82]. These results show that enzymatic methods can be powerful approaches also to create unnatural polysaccharide materials. Nevertheless, the inherent selectivity of the enzymes limits these approaches to particular patterns and modifications.

To access a broader scope of cellulose modifications, chemical polymerization is a more suitable option. Ring-opening polymerization (ROP) of orthoesters **4** (Scheme 1B) is an established procedure for the synthesis of β(1–4)-glucopyranan structures. The first chemical synthesis of stereoregular cellulose was achieved by ROP of 3,6-dibenzyl-protected **4** catalyzed by Ph_3CBF_4 [83]. The protected polymer **5** was obtained in 2 h in 62% yield and an average DP of 19.3. The benzyl (Bn) group seems to be essential for the selective transformation [84]. Several derivatives were prepared in a similar fashion (Scheme 1B), including the 6-deoxy [85], ^{13}C-labelled [24], L-Glc [86], and ethyl/methyl analogues [87-89]. Depending on the methyl/ethyl content, it was possible to tune the solubility of the polymer in water. 6-*O*-Methyl- and 6-*O*-ethyl-celluloses were poorly soluble in water, in contrast to heterogeneous polymers with an increased content of ethyl groups. Even though the

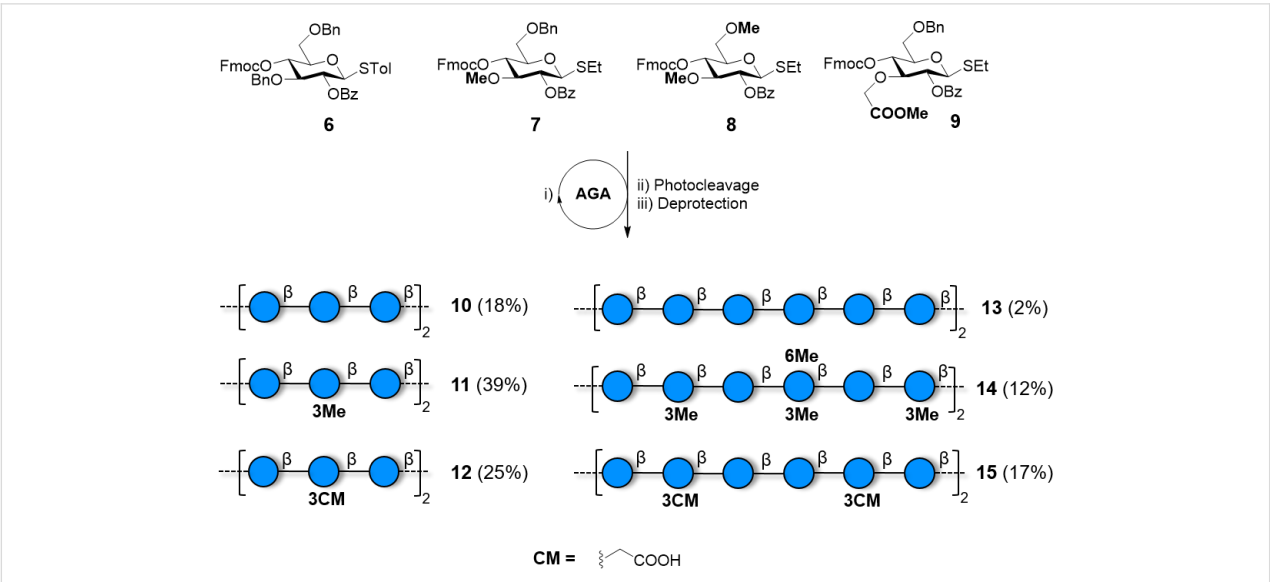
methyl/ethyl content could be adjusted using different ratios of the respective BBs, no control over the substitution pattern could be achieved. Removal of the Bn PG posed a bottleneck, requiring repeated treatments at high pressures and temperatures. Allyl groups provided a valid alternative and could be removed with palladium chloride at 60 °C in 4 hours [90].

Chemical synthesis grants full control over the polymer length, avoiding non-uniform dispersions of MW obtained by polymerization. Polymers with virtually any possible pattern of modification can be prepared. Strategically introduced PGs can be selectively removed to insert a branch or a chemical modification. However, to date, this approach has suffered dramatically from the severe aggregation and insolubility of cellooligosaccharides, permitting to obtain only relatively short structures in low yields. To overcome this issue, the products were converted and studied as their acetate analogues, as in the case of a cellulose 20mer obtained with a convergent approach [91,92]. To date, the longest well-defined cellulose analogue produced via chemical synthesis is a 12mer (**13**, Scheme 2), obtained in a 2% yield due to formation of insoluble aggregates during the deprotection step, resulting in loss of product during purification [93]. **13** was obtained by AGA as part of a collection of substituted compounds, obtained in much higher yields. Specifically placed substituents including methyl, fluorine, and carboxymethyl groups, prevented the formation of insoluble aggregates by disrupting hydrogen-bond networks. Dramatic differences in the conformation (e.g., radius of gyration and glycosidic bond conformation) and aggregation behaviour (i.e., crystallinity and solubility) were observed for compounds with the same degree but different pattern of substitution, underscoring the importance of pure and well-defined polysaccharides for proper structure–property characterization. For example, compounds with an alternated methylation pattern resulted in quasi-linear structures, whereas more bent geometries were observed with a block wise arrangement of methyl groups. As chemical synthesis offers high flexibility in terms of manipulation, non-carbohydrate moieties can be exploited to guide the geometry of the resulting compounds. β(1–4)-Linked glucose chains were connected parallel via an anthraquinone moiety to give synthetic Cellulose I [94].

Overall, enzymatic synthesis is an established procedure to obtain non-uniform cellulose oligo- and polysaccharides. Some success was achieved using additives and molecular crowding conditions; however, this approach remains limited by product insolubility and enzyme flexibility. ROP allowed for the introduction of modifications in the structure, thus providing a first step towards structure–properties correlations. Yet, the substitution pattern remains random. Cellulose analogues were obtained with full control over the length and substitution pattern by chemical synthesis, albeit in low yields. Selective disruption of intra- and intermolecular hydrogen bonds suggested that modifications can be designed to prevent precipitation and guide cellulose assembly.

Xyloglucans

Xyloglucans (XGs) are based on a β(1–4)-Glc backbone decorated with xylopyranose branches, which can be further substituted at the C-2 position by a β-linked galactose or a α-L-fucose



Scheme 2: AGA of a collection of cellulose analogues obtained using BBs **6**–**9**. Specifically placed modifications prevented the formation of insoluble aggregates resulting in higher isolated yields. The AGA cycle includes coupling (NIS/TfOH), capping (Ac_2O) and Fmoc deprotection (piperidine or Et_3N).

unit (Figure 3). XGs are abundant components of the plant cell-wall, where they are believed to interact with cellulose promoting the integrity of the plant wall [95]. However, a recent study suggested that XGs are not essential for the creation of the cellulose network [96].

The complexity and diversity of XGs hinder isolation from natural sources and complicates their description. A significant effort was put towards the development of enzymes for selective introduction of the side chains [97,98]. A detailed overview of the enzymatic strategies to generate artificial plant cell wall polymers was recently published [11,99]. Here, we describe the methods available to access well-defined XG oligo- and polysaccharides.

The first solution phase synthesis of a nonasaccharide repeating unit was realized using a convergent approach [101]. The process was later simplified using AGA and several XG oligosaccharides were prepared [102]. Representative examples are **19** and **20** (Scheme 3) [103], as well as the galactose-containing compounds **21** and **22** [104]. These compounds permitted to study XG recognition by plant cell-wall antibodies. To avoid performing the challenging 1,2-*cis* glycosylation that would generate a mixture of anomers in AGA, the α(1–6) linkage between glucose and xylose was pre-installed in the disaccharide BB **16** (Scheme 3, highlighted in red) [104]. The orthogonal levulinoyl (Lev) and *p*-methoxybenzyl (PMB) PGs could be selectively cleaved to allow for chain elongation and for introduction of the Gal unit at the C-2 of the xylopyranose, respectively.

An alternative approach utilized natural sourced XLLG tetrasaccharide, which was obtained from tamarind seed XG via enzymatic digestion. This compound was then chemically transformed to the corresponding glycosyl donors (4-methoxyphenyl- or fluoro-glycoside) to chemoenzymatically produce complex XGs. Compounds with different substitution patterns were obtained using a glycosynthase from *Humicola insolens* [105,106]. This approach produced polysaccharides with controlled substitution, but no control over the length [107].

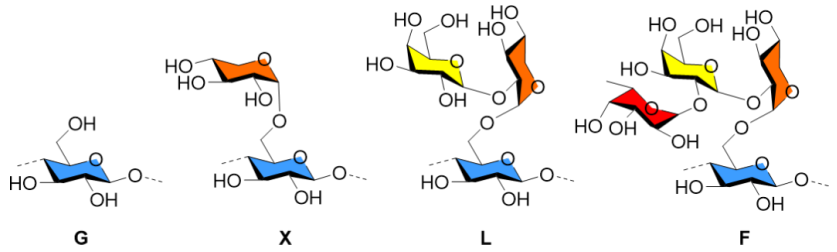
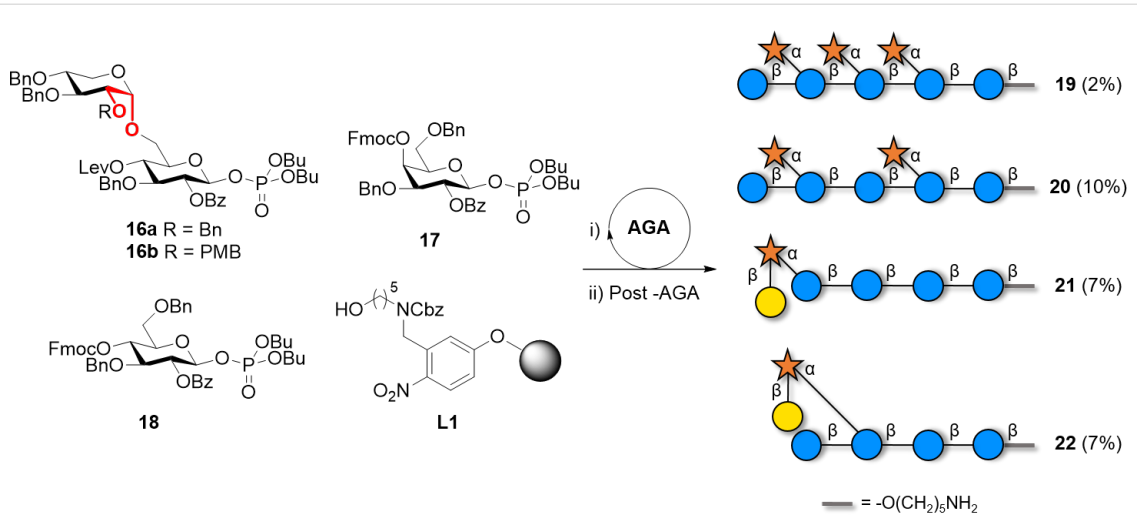


Figure 3: Chemical structure of the different branches G, X, L, F commonly found in XGs. Names are given following the established nomenclature [100].



Scheme 3: AGA of XG analogues with defined side chains. The AGA cycle includes coupling (TMSOTf), Fmoc deprotection (Et_3N), PMB deprotection (DDQ) and Lev deprotection (hydrazine).

Similarly, XG fragments prepared by enzymatic degradation of XGs were converted to the fluoride donors and used in the subsequent glycosynthase-catalyzed transformations. $(XXXG)_3$, $(XLLG)_3$, and XXXG-GGGG-XXXG were prepared to study interactions with bacterial microcrystalline cellulose [108]. The glycosyl fluoride donors were also polymerized to give $(XXXG)_n$ and $(XLLG)_n$ with MW up to 12000 [109]. The synthesis of the highly branched $(XLFG)_n$ polysaccharides required the additional fucosyltransferase *At*FUT1 to introduce the fucose residues [110].

Even though the complexity of plant polysaccharides hinders their synthesis, these compounds are highly desirable to dissect the different interactions taking place in the plant cell-wall. Recognition of the branched oligomers by glycosynthases proved to be limited and more enzymes are needed to broaden applications and generate uniform polymers. Chemoenzymatic methods provided XG oligo- and polymers, but are laborious, requiring several synthetic steps for the synthesis of the glycosyl donors.

β(1–3)-Glucans

β(1–3)-Glucans, linear or with β(1–6) appendances, are present in the cell-wall of fungi and yeasts, and are major polysaccharides in brown seaweeds (laminarins) [111]. Due to their immunostimulating, antibacterial and antitumor activities, linear and branched β(1–3)-glucans have become interesting synthetic targets. Since several reports highlighted the correlation between chain length and biological activity, significant effort has been put to chemically synthesize β(1–3)-glucans with well-defined lengths.

In contrast to β(1–4)-glucans (i.e., cellulose), β(1–3)-glucans with a DP up to 20 can be dissolved in water [112], simplifying the synthetic process. Several oligosaccharides have been prepared to identify the best PG pattern ensuring a proper balance between BB reactivity, stereoselectivity, and simplicity of deprotection [113-125]. Ester groups are commonly employed at C-2 position to ensure anchimeric assistance during glycosylation (Figure 4). However, the *O*-2 acyl group on the glycosyl acceptor hinders the 3-*O*-glycosylation sterically and electronically [126]. The decreased nucleophilicity of the C-3 hydroxy acceptor could lead to poor stereoselectivity [127]. This issue becomes even more dramatic when 2,4-di-*O*-acyl groups are present, sometimes leading to exclusive formation of α-anomers [128,129]. PGs like 2-*O*-ADMB (4-acetoxy-2,2-dimethylbutanoate) [130] or 2,2'-*O*-benzylidene [131] were introduced to solve this issue. Several reports highlighted the importance of the 4,6-*O*-benzylidene group on the glycosyl donor and the acceptor for the stereoselective formation of the β(1–3) linkage (Figure 4) [132].

Interestingly, oligomers bearing several 4,6-*O*-benzylidene groups show anomalously small coupling constants for some of the C-1 hydrogens. NMR [133] and X-ray [134] studies revealed that, for some residues, the 4,6-*O*-benzylidene group stabilizes a boat conformation ($^{1,4}B$ or $B_{2,5}$), in contrast to the standard chair ($^4C_1$). This unexpected conformation did not affect the stereoselectivity of the glycosylation, permitting the preparation of linear β(1–3)-glucans of different lengths (6mer, 8mer, 10mer and 12mer) following a convergent preactivation-based iterative strategy [135]. These compounds were subsequently conjugated to keyhole limpet hemocyanin, revealing that the length of the glucans affected the immunogenic properties. A pre-activation-based iterative one-pot glycosylation method was also employed to access different branched structures having β(1–3)- and β(1–6)-linked Glc appendances on a β(1–3) backbone [136].

To date, the longer β(1–3)-glucans [137,138] were obtained using a 2-*O*-acylated donor, to ensure β-selectivity, followed by deacylation and use of the resulting 2,3-diol as acceptor in the following glycosylation [131]. A regioselective glycosylation strategy was developed to obtain a collection of linear glucans

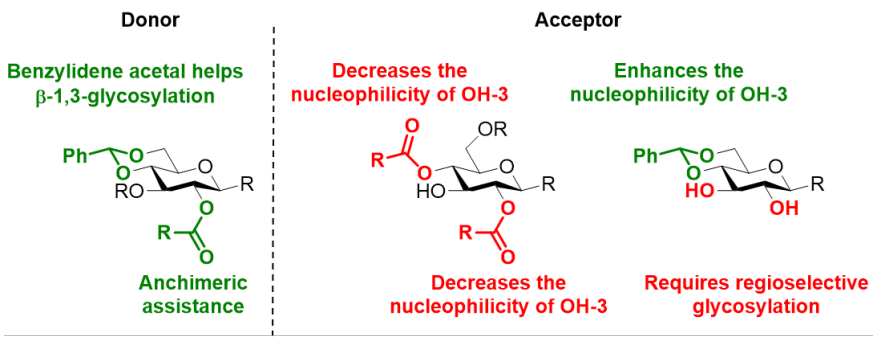


Figure 4: Synthetic strategies and issues associated to the formation of the β(1–3) linkage.

(8mer to 16mer) (Scheme 4), as well as a branched 9mer and 17mer [137,138]. A similar strategy based on the regioselective glycosylation of a 2,3-diol 4,6-*O*-benzylidene acceptor permitted to access various β(1–3)-glucans, ranging from trimer to 13mer [126]. Regioselectivity was also achieved using a gold-catalyzed glycosylation, to give a linear β(1–3)-linked 11mer and a branched 14mer in a convergent manner [139].

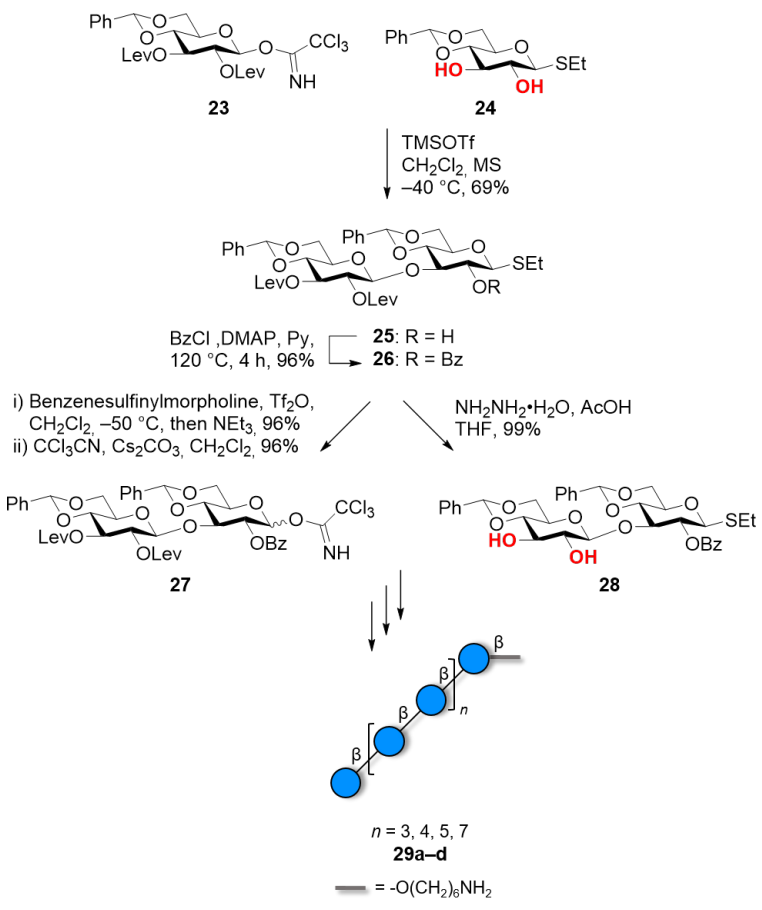
Collection of linear as well as branched β(1–3)-glucans with defined lengths could be prepared by AGA [140-142]. The poor nucleophilicity of the C-3 hydroxy group on the glycosyl acceptor required the use of more reactive glycosyl phosphate donors and, in some cases, a double glycosylation cycle [118,143].

Longer structures, albeit with no control over the DP, could be prepared via chemoenzymatic polymerization of α-laminaribiosyl fluoride donors catalyzed by the mutated barley β(1–3)-glucanase [144,145]. Linear β(1–3)-glucans with DP of 30–40 appeared as lamellar, hexagonal crystals. Electron and X-ray diffraction studies revealed that long β(1–3)-glucan structures adopt a parallel, triple helical structures [146]. A glycosynthase derived from *Bacillus licheniformis* could polymerize glycosyl fluoride donors to prepare artificial mixed linkage β-glucans with an average molecular mass of 10–15 kDa [147].

The better solubility of β(1–3)-glucans, compared to the β(1–4) analogues, has permitted the chemical or enzymatic synthesis of long polysaccharides. Still, the poor nucleophilicity of the hydroxy group at C-3, in the presence of a C-2 ester PG, could decrease the efficiency of chemical synthesis. Hence, there is scope for new strategies to provide anchimeric assistance, without affecting the nucleophilicity of the hydroxy group at C-3.

β(1–6)-Glucans

The formation of the β(1–6)-glycosidic bond poses less synthetic challenges than the β(1–3) bond. The primary C-6 hydroxy group is more nucleophilic than the secondary hydroxy group at C-3 and β-selectivity is easily achieved with the help of



Scheme 4: Convergent synthesis of β(1–3)-glucans using a regioselective glycosylation strategy.

anchimeric assistance provided by a 2-*O*-acyl functionality. Despite these advantages, the synthesis of β(1–6)-Glc polysaccharides appears only in few reports [148,149], with short oligomers being prepared mainly to prove new methodologies [31,150-155].

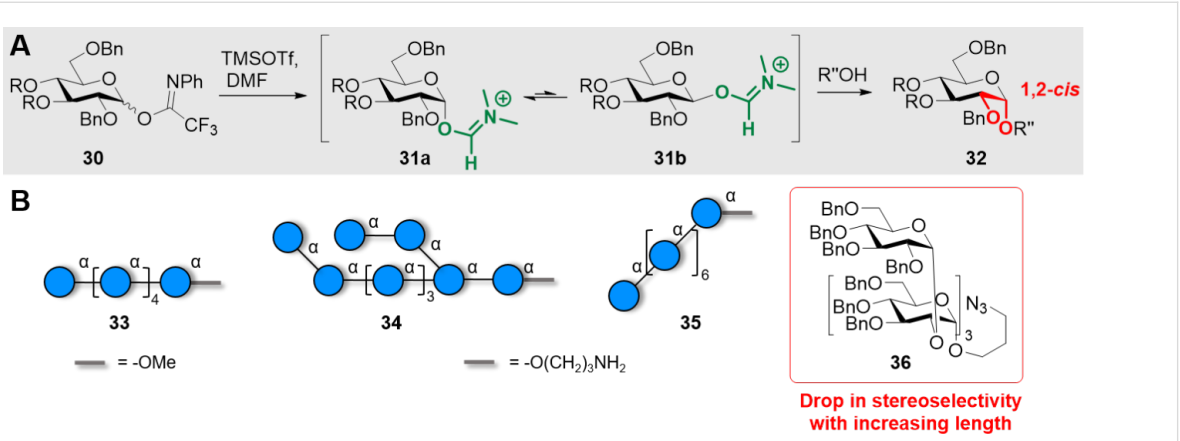
The synthesis of structures longer than hexasaccharides suffered from poor solubility during the deprotection step, likely due to the formation of aggregates resulting from particular secondary structures adopted by the partially protected intermediates [156]. The replacement of a single Glc unit with a Man unit was sufficient to disrupt this secondary structure and significantly increased the isolated yield of the final compounds. Molecular dynamic (MD) simulations predicted a compact helical conformation for the fully deprotected compound, confirmed by NMR studies on a collection of ^{13}C-labelled hexamers [157]. Similar issues during deprotections were not observed when the β(1–6) backbone was substituted with β(1–3) branches [158-166] and long oligomers could be synthesized on solid support [157,166] or in solution phase using block coupling [165].

α-Glucans

In contrast to the relatively simple formation of a 1,2-*trans* glycosidic bond using participating group at C-2, the construction of 1,2-*cis* glycosidic bonds is a long-standing challenge in the field of glycochemistry [167]. The formation of 1,2-*cis* Glc linkages is particularly relevant, as α(1–4)-glucans form the backbone of starch, with the linear amylose and the branched amylopectin, and α(1–3)-glucans are related to fungal pathogenicity in plants [168]. Only few options can aid the stereoselective construction of 1,2-*cis* glycosidic bonds. In general, stereocontrol can be obtained either by fine tuning of PGs at C-3, C-4 or C-6 positions, or by making use of participating solvents [37,167]. 3-*O*-acyl and 6-*O*-acyl groups are commonly employed to remotely participate in the glycosylation and promote α-selectivity [169,170]. This strategy permitted to prepare oligosaccharides having multiple α-glycosidic linkages by AGA [171].

Additional strategies include the dehydrative glycosylation of glucosyl hemiacetal [172] or the halide-catalyzed in situ anomerization of glucosyl iodide donors that yielded α(1–6)-hexaglucans [173]. The halide-catalyzed in situ anomerization approach was efficient in solid phase as well as in solution phase synthesis. The participating (*S*)-(phenylthiomethyl) benzyl chiral auxiliary at the C-2 position of the glucosyl donor permitted the solid phase synthesis of a branched pentaglucan having a α(1–3) branch on an α(1–6) backbone [174]. Boron-mediated aglycon delivery (BMAD) with the use of a diboron catalyst allowed for regio-, as well as stereoselective glycosylation to achieve an α(1-3)-pentaglucoside [175]. Regioselective 1,2-*cis*-glycosylation could also be achieved by boron-catalyzed coupling via a S_Ni-type mechanism [176]. Hydrogen bond-mediated aglycon delivery (HAD) with the aid of a 4-*O*-picoloyl (Pico) group offered an interesting method to achieve multiple α-glucosidic linkages. However, the efficacy of the HAD diminished with the increased bulk of the glycosyl acceptor [177].

In general, even though several elegant approaches were reported, the construction of multiple α-linkages remains challenging, in particular with the increasing size of the acceptor. The nucleophilic additive glycosylation-based approach (Scheme 5A) offers the opportunity to install multiple 1,2-*cis* glycosidic bonds by converting the glycosyl donor **30** into a less reactive adduct **31**. DMF-mediated glycosylations permitted access to long structures based on multiple α(1–4) linkages **33** and **34** [178] and α(1–3) linkages **35** [179] (Scheme 5B). The short oligosaccharide **36** having α(1–2) linkages was also prepared, however, in this case, the stereoselectivity diminished



Scheme 5: DMF-mediated 1,2-*cis* glycosylation. A) General mechanism and B) examples of α-glucans prepared using this approach.

with the increasing length of the oligosaccharide, possibly due to steric hindrance [180].

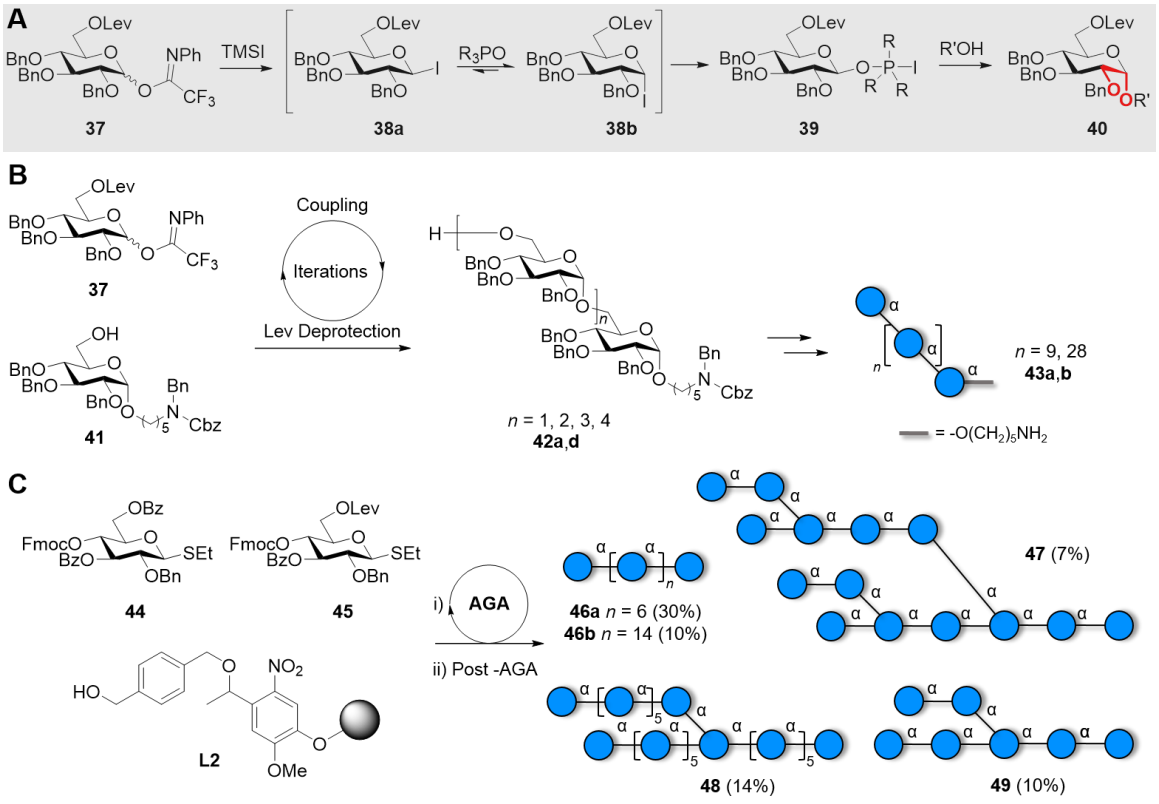
The nucleophilic modulation strategy in combination with the *O*-6-Lev remote anchimeric assistance could further improve the stereoselectivity of the 1,2-*cis* glycosylations, leading to the synthesis of long linear α-glucans **43** (11mer and 30mer) having multiple 1,2-*cis* glycosidic linkages (Scheme 6A and 6B) [181]. The remote anchimeric assistance from ester groups at C-3 and C-6 on thioglucoside BBs **44** and **45** permitted the AGA of linear **46a**,**b** and branched **47–49** glucans with multiple 1,2-*cis* linkages (Scheme 6C) [182].

To avoid the chemical formation of this challenging bond, natural compounds containing 1,2-*cis* linkages could be exploited. α-, β- and γ-cyclodextrins offered a good starting material to prepare stereoselectively a 6-*O*-methylated α(1–4)-glucopolysaccharides consisting of 6–20 monomer units [183,184]. As alternative, stereoselectivity can be achieved with enzymes. Glucan phosphorylase is commonly employed to produce linear amylose polysaccharides with the desired average MW by changing the glucose monophosphate/amylose primer ratio [185]. This approach permitted the preparation of amylose with narrow MW distribution, amylose hybrids, and amylose-functionalized materials [186]. Linear and branched oligosaccharides with mixed α(1–3) and α(1–4) linkages were synthesized using a glucansucrase from *Lactobacillus reuteri* [187,188].

Even though several chemical methods are available for the formation of 1,2-*cis* linkages, only few are unaffected by the increasing size of the target molecule. The recently published synergistic approach that combines remote anchimeric assistance and nucleophilic modulation permitted access to long linear α-glucans [181]. The implementation of a similar strategy in AGA has already shown promising results [182] and could fuel the production of well-defined polysaccharides based on multiple 1,2-*cis*-glycosidic linkages.

Xylose-based polysaccharides

Xylans are abundant polysaccharides mainly found in plants or in mammalian cells as proteoglycans [189,190]. They participate in the formation of the cell-wall by interacting with cellulose microfibrils [191], however, these interactions lack a mo-



Scheme 6: Synergistic glycosylation strategy employing a nucleophilic modulation strategy (TMSI and Ph_3PO) in combination with the *O*-6-Lev remote anchimeric assistance. A) General glycosylation mechanism. B) Synthesis of linear α(1–6)-glucan 11mer and 30mer. C) AGA of starch and glycogen oligo- and polysaccharides. The AGA cycle includes coupling (NIS/TfOH), capping (Ac_2O), Fmoc deprotection (Et_3N), and Lev deprotection (hydrazine).

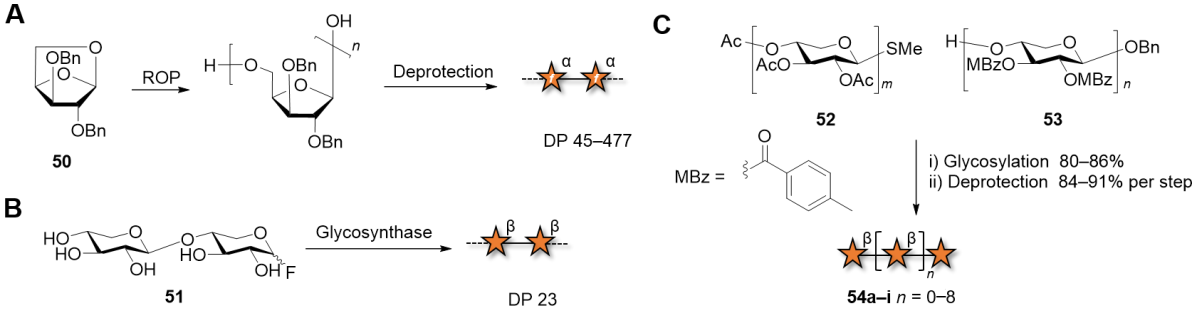
lecular description [192]. Some evidences suggest that the xylan–cellulose interaction depends on the xylan substitution pattern [193].

Natural xylans contain β(1–4), β(1–3) or a combination of β(1–4)- and β(1–3)-linked β-D-xylopyranosyl units. Rarely, α(1–3) glycosidic linkages are present [194]. These backbones are often partially acetylated or appended with sugar side chains, mainly L-arabinose, fucose, galactose and 4-*O*-methylglucuronic acid [195]. In general, low substituted xylans are forming insoluble aggregates, whereas heavily substituted xylans are highly soluble in water [196,197]. Minor changes to the xylan structure can dramatically affect their crystallinity and solubility [198], highlighting the importance of obtaining well-defined samples.

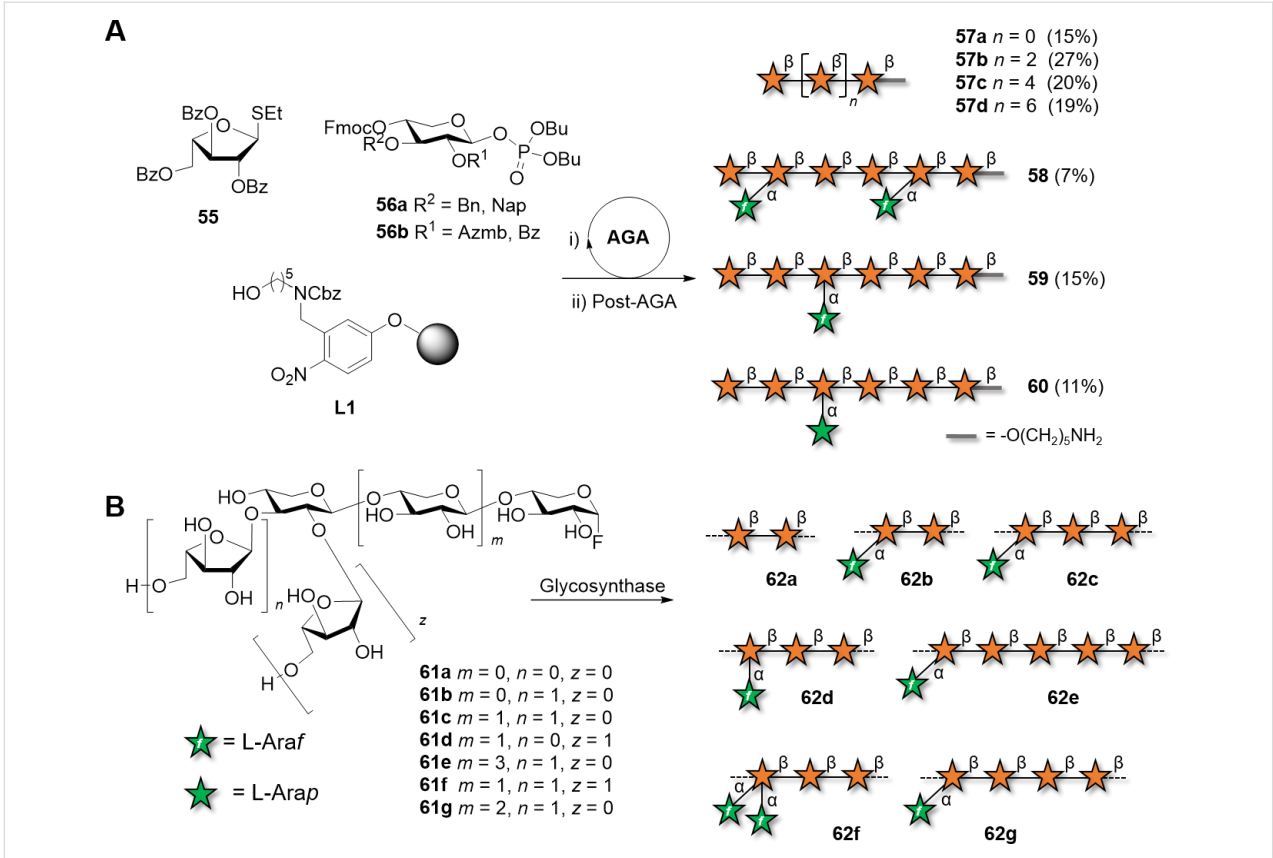
Cationic ROP of anhydrosugars was the pioneering approach for the preparation of synthetic, unnatural xylans. Polyxylofurans with (1–5) and (3–5) linkages were described [199,200]. In most cases, non-uniform polysaccharides were obtained, as in the case of α(1–5)-xylans, prepared in up to 93% yields and DP between 45 to 477 (Scheme 7A) [201]. Enzymatic polymerization is generally performed using glycosyl fluorides as substrates, which are structurally related to the natural glycosyl enzyme intermediate [202]. β-Xylobiosyl fluoride donors, selectively recognized by the cellulase from *Trichoderma viride,* afforded xylans containing exclusively β(1–4) linkages in 72% yield [203]. Compounds with DP higher than 23 constituted the insoluble fraction (37% yield) (Scheme 7B). The combination of XynB2-catalyzed dimerization of α-D-xylopyranosyl fluoride and subsequent polymerization by XynA helped to overcome the bottleneck of poor substrate-recognition of longer oligosaccharides by glycosynthases [204]. Still, the polymer was obtained with a wide range of DP between 6–100. Shorter Xyl chains with up to 12 units were reported using a retaining xylanase from *Cellulomonas fimi* [202].

Well-defined xylan oligosaccharides were obtained by chemical synthesis following convergent or sequential glycosylation approaches. These well-defined xylans allowed establishing correlations between the substitution pattern, length, and macroscopic properties (i.e., crystallinity, solubility, interactions with other polysaccharides). To date, the longest xylans reported are 10mers [205], although there is in principle no reason hindering the synthesis of longer structures. A convergent approach is often employed to avoid tedious purification of unreacted acceptors from the products, resulting from incomplete glycosylation. Peracetylated thioglycoside donors **52** were reacted with 4-methylbenzoylated (MBz) acceptors **53**, following NIS/AgOTf activation (Scheme 7C). Upon global deprotection, a collection of well-defined oligoxylans with 4–10 monosaccharide units was obtained [205]. A convergent approach was also employed to prepare a β(1–3)-Xyl hexamer, an analogue of xylans found in algae cell-walls [206]. TMSOTf promoted the glycosylation of the Bz-protected disaccharide acceptor with the Bz-protected tetrasaccharide trichloroacetimidate donor. Although not yet reported, the authors suggested that this method can be extended to the synthesis of longer oligomers in a gram-scale.

To avoid purifications after each glycosylation step, oligoxylans were produced by AGA on solid support (Scheme 8A) [207,208]. The iterative addition of monosaccharide BBs and the use of orthogonal PGs permitted to control the length and pattern of substitution. A collection of linear β(1–4)-D-xylan chains and with α(1–3)-L-arabinofuranosyl branches was quickly assembled to identify the binding epitopes of monoclonal antibodies. These oligomers, together with other well-defined analogues obtained by chemoenzymatic synthesis, were converted to the respective glycosyl fluoride and used for enzymatic polymerization catalyzed by XynAE265G (Scheme 8B) [7]. This approach generated polymers **62a–g** with well-defined substitution patterns. Differences in solubility were observed for



Scheme 7: Different approaches to produce xylans. A) Polymerization techniques including ROP, and B) enzymatic polymerization yielded non-uniform homopolymers. C) Chemical synthesis following a convergent approach provided short oligomers with control over DP.



Scheme 8: A) Synthesis of arabinofuranosyl-decorated xylan oligosaccharides using AGA. Representative compounds are reported. The AGA cycle includes coupling (NIS/TfOH for thioglycosides and TMSOTf for glycosyl phosphates), Fmoc deprotection (Et_3N) and Nap deprotection (DDQ). Azmb = 2-(azidomethyl)benzoyl. B) Chemoenzymatic synthesis of arabinofuranosyl-decorated xylan polymers with well-defined substitution patterns.

certain patterns, affecting the efficiency of polymerization and the DPs of the resulting polymers. Linear xylan precipitated with a MW of 9.2 kDa. Arabinofuranosyl xylans substituted at the C-2 or C-3 position of every third residue, formed crystalline aggregates. The authors speculated that a threefold helical screw conformation might enable the regular interaction of individual chains. The arabinose pattern also played a role in the interaction with cellulose, with the crystalline compound **62c** that did not adsorb to cellulose, in contrast to **62b**, which adsorbed irreversibly. The high adsorption of **62b** was associated with its twofold helical screw conformation, only accessible with this substitution pattern.

Overall, chemical and enzymatic polymerization are faster than chemical synthesis, however, non-uniform xylans are always generated. The chemoenzymatic approach permitted to prepare, for the first time, arabinose-substituted polymers with a defined substitution pattern. Although still lacking control over the polymer length, these compounds underscored the importance of well-defined polysaccharides to understand the microscopic properties of natural xylans and fuel advancements in plant cell-wall biology [102].

Glucosamine-based polysaccharides

Chitin and chitosan

Chitin is a linear polysaccharide composed of β(1–4)-linked 2-acetamido-2-deoxy-D-glucopyranose (GlcNAc) repeating units, which mainly exists in the exoskeleton of crustaceans and insects, as well as in the cell-wall of fungi [209,210]. Chitosan, its partially *N*-deacetylated analogue, has vast industrial applications in coating materials, cosmetics and pharmaceuticals [211]. Owing to their superior biological and mechanical properties, chitin and chitosan are used in fibers, gels, sponges, films, beads, and nanoparticles [212]. Tunable stiffness, solubility, and transparency can be obtained by tuning of the DP and fraction of acetylation (FA).

Chitooligosaccharides (COS: β(1–4)-linked oligomers of GlcNAc and/or GlcN) have gained popularity due to their exceptional antimicrobial, antitumor, and immune modulatory activities [29,213-217]. Methods to obtain well-defined COS with controlled size and substitution pattern are highly desirable, because DP and FA affect the physicochemical properties of the COS [218,219]. A size-dependent immune recognition was verified in plant chitin receptors as well as in toll-like re-

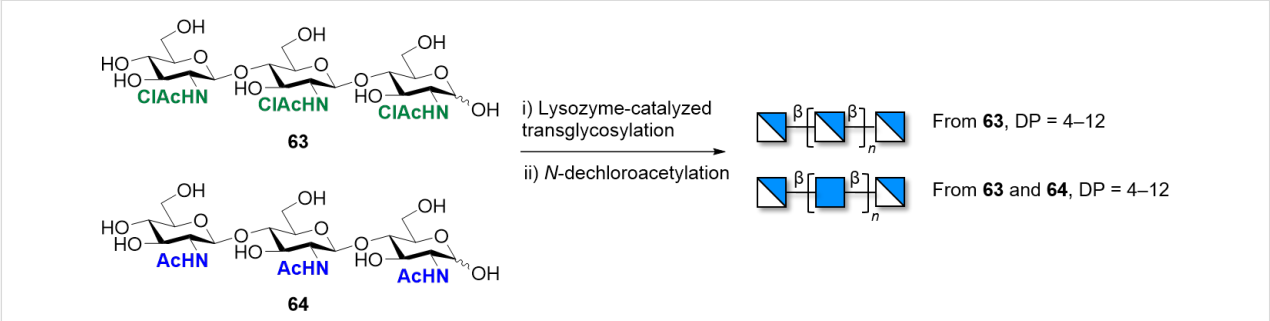
ceptors (TLR2) [220]. Moreover, the PA can tune the biological activity, as demonstrated using partially acetylated COS obtained by enzymatic degradation of chitosan promoted by hydrolases [221].

Chemical degradation of chitin promoted by acid treatment [222-228] or using chitinases and chitosanases [229-231] generates mixtures of short COS, which requires tedious purification steps. Furthermore, degradation of natural chitin often lacks proper control over the pattern of acetylation (PA). Acetolysis also often leads to heterogeneous mixtures [232-235]. A controlled acetolysis of chitin, followed by the one-pot *trans*-*N*-trifluoroacetylation of peracetylated chitooligomers, could efficiently generate 1,2-(2-trifluoromethyloxazoline) donors. These reactive compounds were employed to construct different length COS, from dimer to hexamer [236].

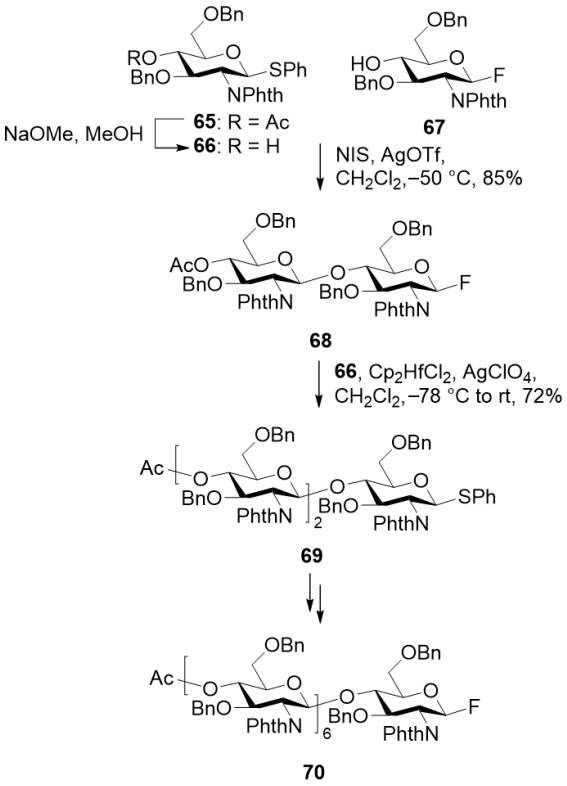
Synthetic COS were prepared following chemical or enzymatic polymerization, albeit with poor control over size and substitution pattern. Classical methods include chitinase-catalyzed assembly via ring-opening polyaddition of *N,N'*-diacetylchitobiose oxazoline derivatives [237-239] or self-condensation of *N*-phthalimide protected thioglycoside [240]. Enzymatic polymerization promoted by hydrolases is an interesting option to produce long COS from shorter oligomers [241]. After cleaving the glycosidic linkage, the enzyme remains attached to the new reducing end of the oligomer, releasing the cleaved part. Subsequently, the oligomer is transferred to another COS acceptor, forming a new glycosidic bond [216]. Various enzymes have been successfully employed, including β-*N*-acetylhexosaminidase [242], lysozyme (Scheme 9) [243], and endochitinase [244-246]. With these approaches, structures with a DP up to 13 could be accessed. Genetically engineered transglycosylating hydrolases were employed to polymerize chemically activated oligosaccharide substrates [216]. These chemoenzymatic approaches are often based on glycosynthase-type GH18 or GH19 chitinases and produce mixture of COS with different lengths [237,243,247-250].

Chemical synthesis offers the possibility to generate well-defined COS, but it is to date underexploited. The poor reactivity of the C-4 hydroxy group of the glucosamine BB, and the need of orthogonal PGs on the nitrogen atom to control the PA are the main bottlenecks [251]. The β-directing *N*-phthaloyl (*N*-Phth) PG was installed in trichloroacetimidate donors to synthesize fully deacetylated COS up to 12mer. After each glycosylation step, the 4-methoxyphenyl group at the anomeric position was oxidatively removed and the resulting hemiacetal was transformed into the trichloroacetimidate glycosyl donor for the next glycosylation step [252]. An orthogonal glycosylation strategy was developed to alternately stitch *N*-Phth-protected thioglycoside donors and *N*-Phth-protected fluoride donors to obtain COS up to 7mer (Scheme 10) [253]. Similarly, trichloroacetimidate and thioglycoside donors permitted the synthesis of short COS [254]. Upon assembly, the *N*-Phth PGs were removed with hydrazine under reflux and the free amino groups were acetylated to obtain the fully *N*-acetylated COS [255].

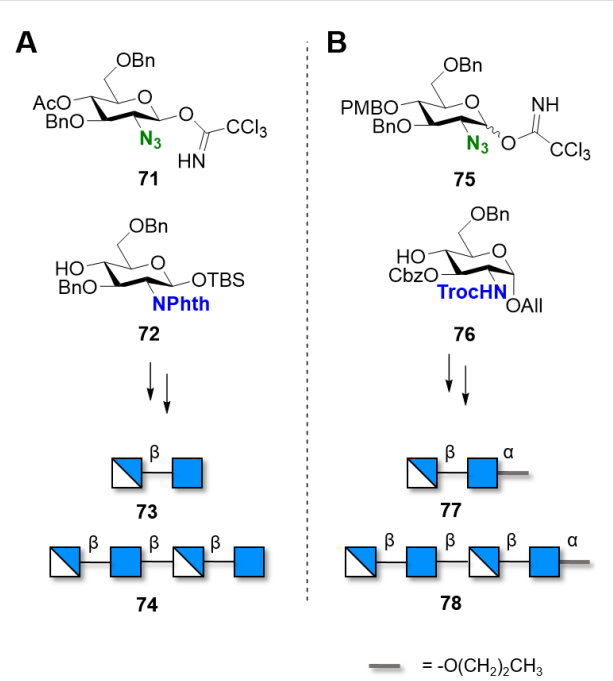
Control over the pattern of *N*-acetylation was for the first time achieved using two monosaccharides bearing an azido (N_3) and a *N*-Phth moieties as precursors of the free and *N*-acetylated amino group, respectively [256]. The stereoselectivity of the glycosylation reaction between the C-2 azido donor **71** and *N*-Phth **72** acceptor met with little success, lowering the yield of the desired anomer significantly. The obtained disaccharide was converted to the trichloroacetimidate donor and used in a [2 + 2] glycosylation, affording the tetramer **74** with an alternated *N*-acetyl pattern (Scheme 11A) [257]. Partially *N*-acetylated COS dimer and tetramer were obtained exploiting the orthogonality of the azide and *N*-Troc groups [258]. β-Selectivity during the glycosylation with the C-2 azido trichloroacetimidate donor **75** was controlled by S_N2 displacement of the α-trichloroacetimidate LG upon activation with $BF_3{\cdot}OEt_2$ in CH_2Cl_2/*n*-hexane (3:2) (Scheme 11B). The orthogonal *N*-trichloroacetyl (*N*-TCA) and *N*-benzyloxycarbonyl (*N*-Cbz) PGs permitted the synthesis of chitobioses with different PA.



Scheme 9: Chemoenzymatic synthesis of COS utilizing a lysozyme-catalyzed transglycosylation reaction followed by the deprotection of *N*-chloroacetate.



Scheme 10: Synthesis of COS using an orthogonal glycosylation strategy based on the use of two different LGs.

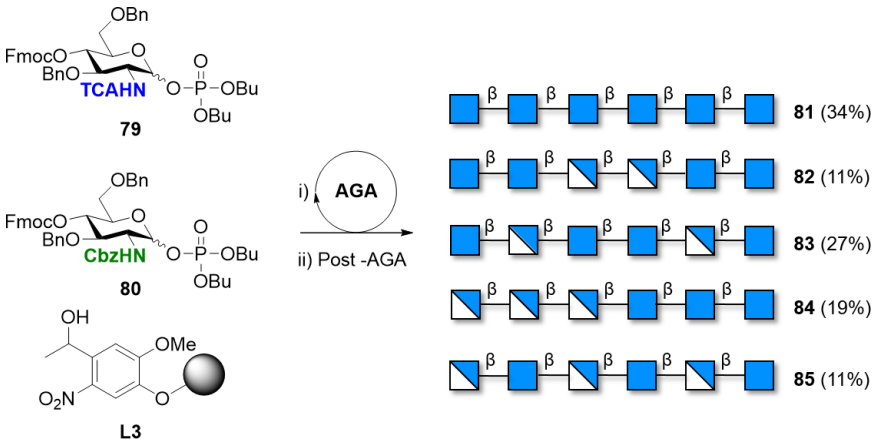


Scheme 11: Orthogonal *N*-PGs permitted the synthesis of COS with different PA.

N-TCA groups could be converted into *N*-acetates upon reduction with tributyltin hydride and azobisisobutyronitrile (AIBN), and the *N*-Cbz groups were removed to liberate the free amino groups during hydrogenolysis over Pd/C [259].

A collection of well-defined COS with defined DP and PA was prepared by AGA [93,157,260]. The automated solid-phase approach required only two BBs with the amino group protected either with the *N*-TCA **79** or with the *N*-Cbz group **80** (Scheme 12). Compounds **81**–**85** served as standards to explore the conformational space of COS with different PA. NMR analysis and MD simulations revealed the importance of the deacetylated residues, with the free amino group able to stabilize new geometries.

Many more *N*-protecting groups [217,261] are available and could generate COS with defined PA, however, to date most of



Scheme 12: AGA of well-defined COS with different PA using two orthogonally protected BBs. The AGA cycle includes coupling (TMSOTf), capping (Ac_2O), and Fmoc deprotection (piperidine).

them have shown significant drawbacks, decreasing the reactivity of the BB during glycosylation or complicating the deprotection steps. Orthogonality and stability become particularly crucial when the goal is the multistep synthesis of long COS.

Other glucosamine-based polysaccharides

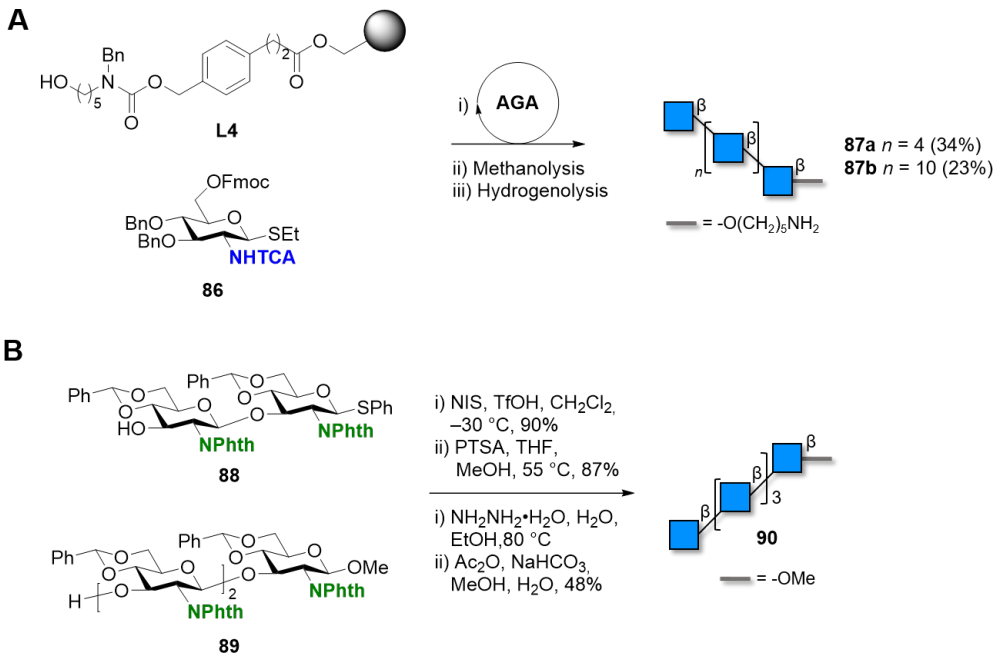
Other polymers of glucosamine based on the β(1–3) or β(1–6) linkages exist, but have gained less synthetic attention. Nevertheless, β(1–6)-linked GlcN oligosaccharides may act as potential antitumor and immunostimulating agents [262] and could become important synthetic targets. The synthesis of a β(1–6)-linked 9mer was demonstrated, using an isopropyl thioglycoside donor [262]. Convergent [262] as well as linear iterative [263] approaches were reported. A block coupling approach enabled access to a collection of free amino or *N*-acetylated structures up to 11mer [264]. Intramolecular glycosylation between a thioglycoside and a free C-6 hydroxy group at the non-reducing end enabled the synthesis of β(1–6)-glucosamine macrocyclic compounds [265]. The iterative glycosylation of *N*-Phth protected 2-deoxy-2-aminothioglycosides allowed for the combinatorial synthesis of short oligoglucosamines having β(1–6) and/or β(1–4)-linkages [263]. Automated solution-phase synthesis of β(1–6)-glucosamine oligosaccharides, ranging from tri- to hexasaccharide, was obtained via iterative electrochemical assembly [266]. A solid-phase automated approach delivered β(1–6)-glucosamine hexasaccharide **87a** and dodecasaccharide **87b** (Scheme 13A) [267]. β(1–3)-Oligomer **90** was prepared as chitin mimetics (Scheme 13B). Despite the subtle differences in the conformational behavior of the two analogues (β(1–3) vs β(1–4) oligomers), it was observed that the β(1–3)-mimetic was still recognized by wheat germ agglutinin and a chitinase enzyme, and could act as a moderate inhibitor of chitin hydrolysis [268].

Mannose- and rhamnose-based polysaccharides

Due to the structural analogies between Rha (both D and L) and Man, we describe the polysaccharides based on these two units in the same section. From a chemical point of view mannose and rhamnose are 'double-faced' monosaccharides, as chemically constructing α-linkage is relatively easy, whereas β-linkages are still considered a major challenge in carbohydrate chemistry (Figure 5). While long α-mannosides could be accessed either by chemical synthesis or by polymerization approaches, only relatively short β-mannan analogues could be synthesized to date. In addition, limited enzymatic approaches exist to assist with the synthesis of mannans and rhamnans.

α-Mannans

Mannans are widespread in nature, as constituents of the plant cell-wall (β-mannans, based on the β(1–4)-Man linkage), or on the surface of yeast and pathogens (α-mannans, where α(1–2), α(1–3), and α(1–6) linkages can be found). No enzyme has been reported for the synthesis of α-mannosides. Similarly, polymerization approaches remain to date underrepresented.



Scheme 13: A) AGA of β(1–6)-*N*-acetylglucosamine hexasaccharide and dodecasaccharide. AGA includes cycles of coupling (NIS/TfOH) and Fmoc deprotection (piperidine). B) Convergent synthesis of a β(1–3)-glucosamine pentasaccharide.

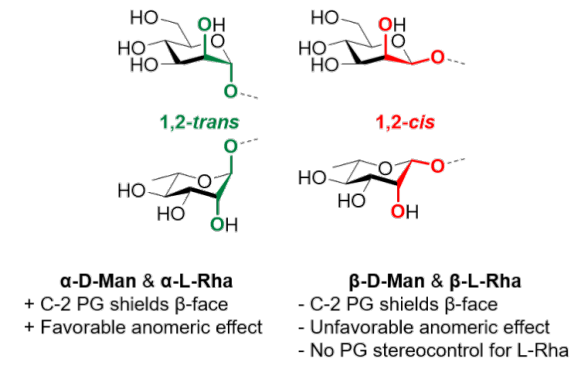


Figure 5: 'Double-faced' chemistry exemplified for D-Man and L-Rha. Constructing β-Man linkages is considerably more challenging than constructing α-Man. β-Rha linkages present an additional challenge as PG-directed 1,2-*cis* glycosylations are not viable.

α-Mannosides can be reliably prepared through chemical glycosylation, which is in general highly α-stereoselective. Construction of the 1,2-*trans* linkage of α-mannosides is conventionally achieved with [142,157,269], or even without [270], neighboring group participation (e.g., Ac, Bz). The favorable anomeric effect ensures efficient glycosylation reactions. The synthesis of α-mannosides is widely established, allowing the chemical synthesis of the longest polysaccharide to date (i.e., 151mer). To speed up and simplify the solution phase synthesis of long and well-defined polymannosides, iterative coupling strategies are generally adopted [271,272]. Two monosaccharides are coupled yielding a disaccharide, which is parted and converted to the new donor and acceptor. This process is repeated iteratively allowing for an exponential length growth, while maintaining control over the elongation. Beside more common LGs such as phosphates, thioethers, and imidates, ynenoate donors activated using Au(I) catalysis were successfully employed in an iterative strategy, enabling the synthesis of a 32mer [272]. The construction of α(1–6)-mannans (up to 10mer) bearing α(1–2)-Man branches was also accomplished using phosphate, *N*-phenyltrifluoroacetimidate or *n*-pentenyl-orthoester donors [273,274].

An approach using a (cationic) ROP method using tricyclic orthoester Man BBs considerably reduced the time needed for the stereoselective synthesis of linear α(1–6)-mannans (ranging from 5mer to 20mer) [275]. The biggest advantage of this approach is the easy scalability, up to a gram scale. However, this strategy is limited to one type of linkage (i.e., only α(1–6) linkages) and does not allow for access to mannans with defined length.

Total syntheses of mannose polysaccharides including a 30mer [276], 50mer [277] and 100mer [278] were achieved by AGA. Key optimizations including tuning of the PGs [277], adjustment of coupling time and temperature [278], and introduction of a capping step [279] permitted to drastically improve overall yields and to simplify the purification (Figure 6). The 100mer **93** was obtained with a calculated average stepwise yield of 98.75% (Scheme 14). Long α-mannosides have the advantageous feature of being highly soluble due to the high flexibility of α(1–6)-Man backbone, facilitating the deprotection and purification steps [157].

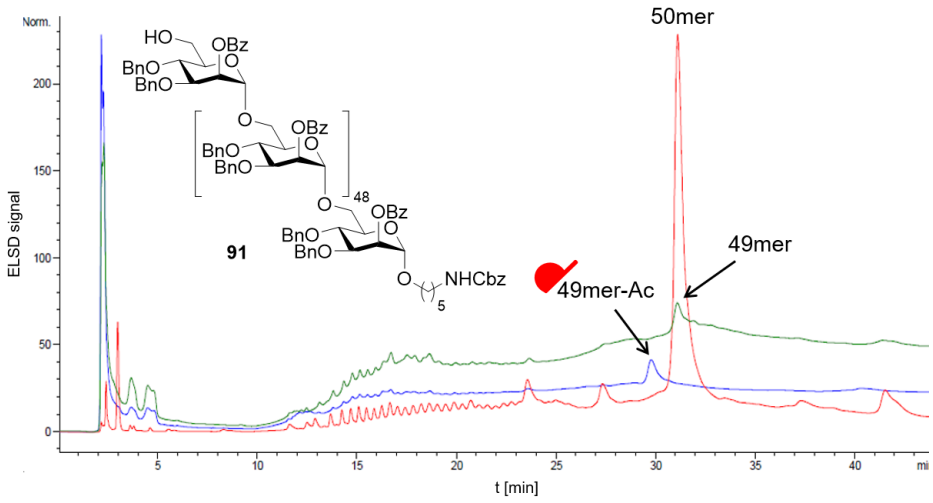
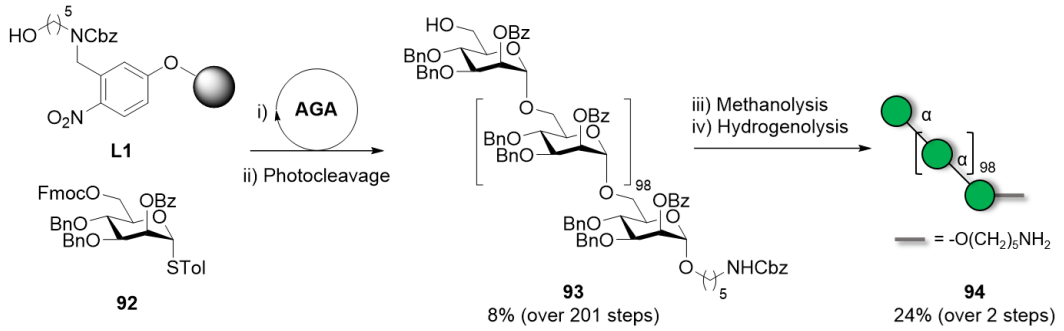


Figure 6: Implementation of a capping step after each glycosylation cycle for the AGA of a 50mer oligomannoside **91**. Uncapped 50mer and 49mer deletion sequence are eluted with virtually the same retention time. The capped 49mer (i.e., C-6 *O*-acetylated) is instead readily separated from the desired 50mer.

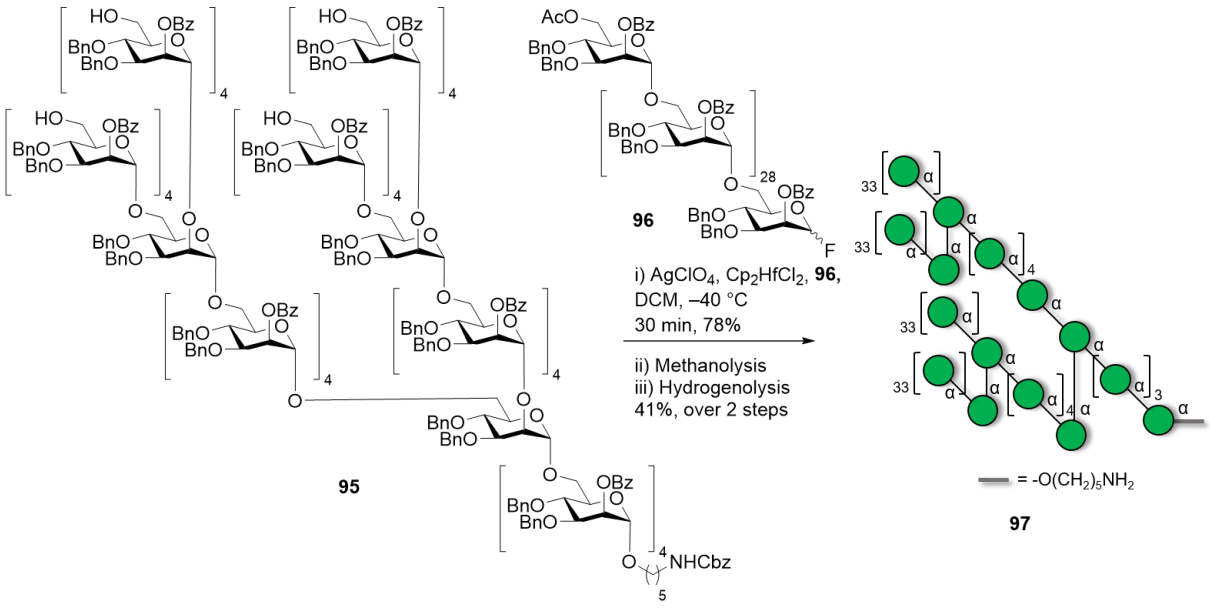


Scheme 14: AGA enabled the synthesis of a linear α(1–6)-mannoside 100mer **93** within 188 h and with an average stepwise yield of 98.75%. The AGA cycle includes glycosylation (NIS, TfOH), capping (Ac_2O), and Fmoc deprotection (piperidine).

Naturally occurring mannosides, such as lipomannans found on the cell surface of mycobacteria, normally consist of a α(1–6)-mannan core substituted with α(1–2) branches, commonly introduced exploiting orthogonal PGs (e.g., Fmoc and Lev) [269,280,281]. These compounds could be prepared entirely on a solid support, or following a solution-phase fragment (or block) coupling. In this case, the branch produced by AGA, employing a traceless linker [118], was converted into a glycosyl donor and coupled to the mannan acceptor to create a dendron-like structure. To overcome the high steric hindrance of both coupling partners, careful optimization of the LG and the reaction temperature was imperative [118,278,280,282]. A [31 + 30 + 30 + 30 + 30] fragment coupling allowed assembling a 151mer polymannoside **97**, the biggest synthetic polysaccharide obtained to date (Scheme 15). Switching from a *N*-trichloroacetimidate to a less reactive fluoride donor and screening of the suitable activator was key to the success of the coupling. As synthetic polymannosides have now reached the size of macromolecules, new challenges are arising in terms of purification and characterization. Gel permeation chromatography (GPC) and advanced high-resolution MS analysis are being developed to address the need of these new available compounds [278,283].

β-Mannans and β-mannuronans

In contrast to α-Man linkages, the construction of β-Man glycosidic linkages is a major challenge (Figure 5). Absence of the anomeric effect in the β-product and steric repulsion of the C-2 axial substituent make β-selectivity hard to achieve. Even though, several methods have been developed to construct



Scheme 15: The 151mer branched polymannoside was synthesized by a [30 + 30 + 30 + 30 + 31] fragment coupling. AGA enabled the synthesis of the α-mannoside 30mer donor fragment **96** and the branched 31mer acceptor fragment **95**.

β-Man glycosidic linkages, the majority of them focused on the construction of a single β-Man linkage [284,285]. Hydrogen-bond-mediated aglycone delivery (HAD) was recently employed to construct a β(1–3) 2-*O*-acetyl-6-deoxy-mannoheptopyranose 4mer with excellent β-selectivity [286]. PG stereocontrol by means of 4,6-*O*-benzylidene is to date the most applied chemical strategy to construct β-mannosides [270]. In a first stage, the donor (either a sulfoxide or a thioglycoside) is pre-activated at low temperature with triflate-based activators. After this step, the acceptor is added, leading to preferential formation of the β-mannoside [287]. The high stereoselectivity is thought to derive from the high stability of the α-triflate intermediate, which dissociates generating a contact ion pair (CIP). In the CIP, the triflate anion shields the α-face, allowing for the preferential attack of the nucleophile from the β-face (Figure 7A). The 4,6-*O*-benzylidene group disfavors the complete dissociation of the α-triflate to the corresponding solvent separated ion pair (SSIP), preventing the formation of the α-Man product [288,289].

Various β-mannosides (up to 8mer) with β(1–2), β(1–4) [290] as well as mixed linkages β(1–3)/β(1–4) [291] were prepared with high stereoselectivity (α:β ratio ca. 1:9) using PG stereocontrol (Figure 7B, **99**–**101**). Interestingly, the synthesis of β(1–2) analogues suffered from a drastic decrease in stereoselectivity (α:β ratio drop to ca. 1:4) and yield as the chain was elongated beyond the 3mer stage (Figure 7C). This observation was ascribed to the characteristic conformation of the protected β(1–2)-trisaccharide acceptor **103**, in which a compact helical structure caused severe hindrance impacting the reactivity and stereoselectivity [290,292]. This issue was not observed with the β(1–4)-mannosides due to their more linear rod-like shape.

Overall, the wide variety of β-mannosides prepared underscored the versatility of the 4,6-*O*-benzylidene directed β-mannosylation to construct the challenging β-Man linkage. Some limitations of the method occur when large Man donors are used, especially when bulky substituents are present at C-3 position (α:β ratio can drop to 1.5:1) [291]. To date, the sulf-

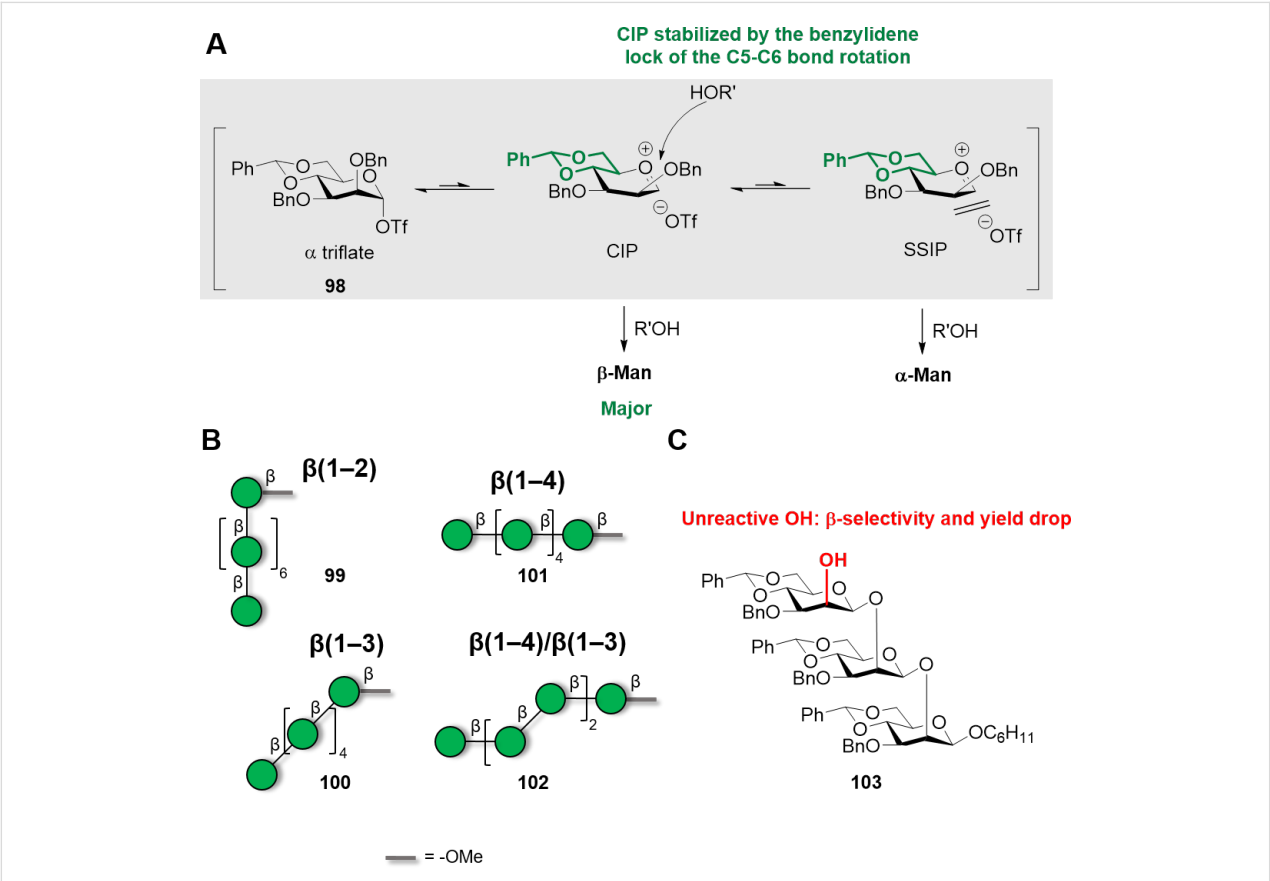
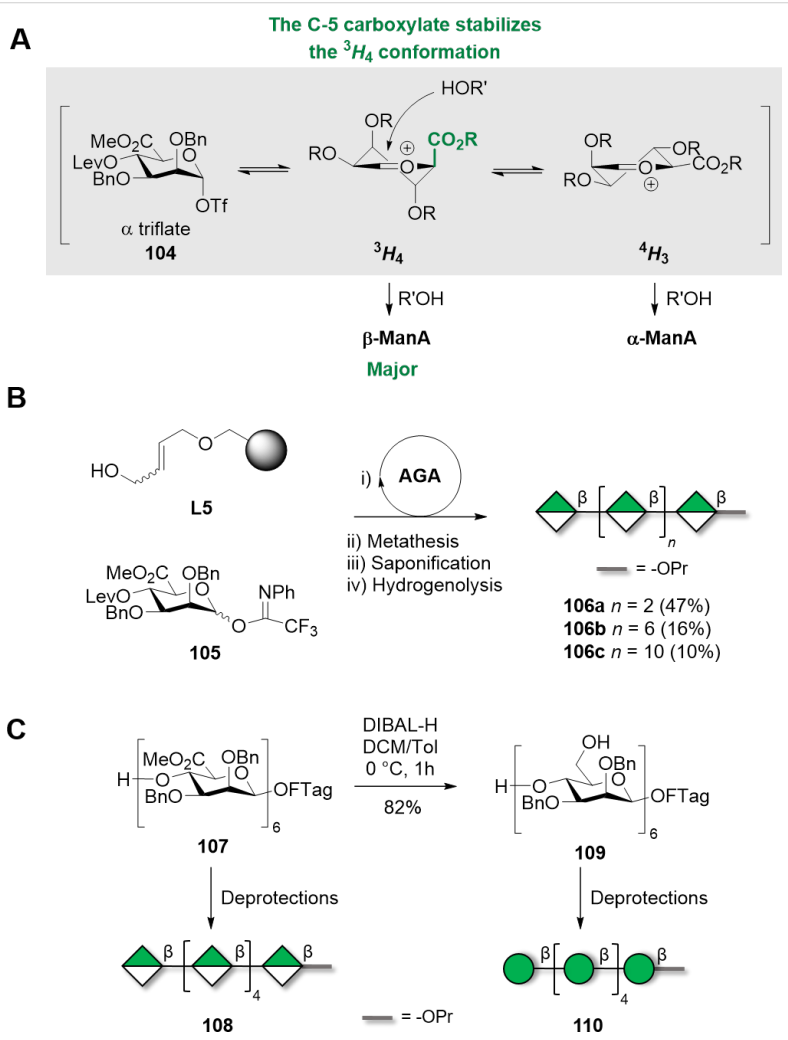


Figure 7: PG stereocontrol strategy to obtain β-mannosides. A) The mechanism of the β-mannosylation reaction is thought to proceed through a contact ion pair (CIP) in which the triflate anion shields the α-face favoring the nucleophile attack from the β-face. The solvent separated ion pair (SSIP) scenario is disfavored due to the benzylidene group locking the C5–C6 bond in the *tg* conformation which destabilizes the oxocarbenium ion. For a thorough explanation of the mechanism we refer to the original publication [289]. B) Examples of β-mannosides synthesized using the 4,6-*O*-benzylidene directed β-mannosylation strategy. C) Chain elongation beyond the trisaccharide level for β(1–2)-analogues presented a significant drop in yield and β-stereoselectivity due to the conformation of acceptor **103**.

oxide donor pre-activation protocol and the low temperatures needed (−78 to −60 °C) posed technical challenges to the implementation of this method in AGA. Thus, carboxybenzyl donors bearing a minimally intrusive PG at C-3 were employed in a protocol that does not require pre-activation [293]. However, only trisaccharides with β(1–4)/β(1–3) mixed linkage could be isolated after challenging purification steps, indicating that major limitations still exist for the AGA of β-mannosides.

Since stereoselectivity and yield are sensitive to the acceptor conformation and nucleophilicity, the synthesis of some classes of compounds remain hindered. To circumvent the challenge of β-mannosylation using large donors, an indirect approach was followed to construct β(1–4)-mannosides up to 8mer. The high β-stereoselectivity of β-glucosylation was exploited in a [4 + 4] fragment coupling. The subsequent C-2 epimerization, via an oxidation–reduction step, converted the β-Glc into a β-Man [294]. Similarly, an indirect approach using Glc orthoester donors was applied for the synthesis of a 8mer based on β(1–2)-Man linkages. The newly formed β-Glc was converted to β-Man by Swern oxidation of the hydroxy group at C-2, followed by reduction of the carbonyl group [295]. Other indirect methods to synthesize β(1–2)-mannosides were also reported using donors bearing a ketone functionality at C-2 (ulosyl donors) which require a reduction step to obtain Man [296,297].

High β-selectivities were observed for mannuronic acid (ManA) donors [298-301]. This result is thought to derive from the unusual $^3H_4$ conformation of the oxocarbenium ion intermediate, stabilized by the *pseudo*-axial C-5 carboxylate (Scheme 16A) [299,301]. The ManA donor enabled the convergent assembly of β(1–4)-ManA oligosaccharides up to 5mer,



Scheme 16: A) Mechanism of 1,2-*cis* stereoselective glycosylation using ManA donors. Once the ManA donor is activated, the C-5 carboxylate stabilizes the oxocarbenium ion in a $^3H_4$ conformation which favors formation of β-ManA linkages. B) Series of β(1–4)-oligomannuronates synthesized using AGA and ManA donors. The AGA cycle includes coupling (TfOH) and Lev deprotection (hydrazine). C) β(1–4)-Man and β(1–4)-ManA oligosaccharides prepared using fluorous-tag (FTag) assisted automated synthesis.

with a α:β ratio of about 1:10 (in 50–70% yields) [299]. Importantly, yield and β-stereoselectivity were not affected by the size of the coupling partners, a key feature that makes this methodology attractive to access long polysaccharides. This approach was implemented in AGA to generate a collection of mannuronic acid oligomers, ranging from 4mer to 12mer (Scheme 16B, **106a–c**) [302]. Key steps were the choice of the temporary PGs (i.e., Lev), the LG (*N*-phenyltrifluoroacetimidate), activation system (TfOH), and the coupling temperatures (−40 °C) used for BB **105**. An average 90% yield per step with excellent β-stereoselectivity was observed. A solution-phase approach allowed to reduce the amount of required donor (1–2 equiv compared to 9 equiv) and to couple big fragments (i.e., [4 + 4] and [8 + 8] glycosylations) without a significant loss in β-stereoselectivity. A β(1–4)-ManA 16mer was prepared using this highly convergent and iterative approach [303].

The high β-stereoselectivity of ManA donors was capitalized to access β(1–4)-Man 6mer **110**, after reduction of carboxylate moieties of β(1–4)-ManA 6mer **107** (Scheme 16C) [304]. The fast assembly of a β(1–4)-ManA 6mer **107** (75% average yield per step) was achieved by automated solution-phase synthesis with the help of fluorous solid phase extraction (FSPE). Reduction of the carboxylic acid moieties was achieved by diisobutylaluminium hydride (DIBAL-H) treatment.

Enzymatic approaches to access β-mannans are scarce in the literature. The enzymatic synthesis of β(1–4)-mannans (up to DP 7) was reported using glycosynthase mutants of the β-mannanase from *Cellvibrio japonicas*. α-Mannobiosyl fluoride donors were coupled to a Glc acceptor, to obtain the desired product, albeit in a relatively low yield (5% for the 7mer) [305]. Recently, β(1–4)-mannans were synthesized using a thermoactive glycoside phosphorylase from *Thermotoga maritima* that catalyzed the reversible degradation of mannosides by phosphorolysis. An initial screening of temperature and pH, using the α-D-mannose 1-phosphate donor (αMan1P) and D-mannose as the acceptor, identified optimal conditions (pH 6.0 and 60 °C), yielding mixtures of oligomers with a DP of 2 to 6. When a β(1–4)-mannoside 6mer was employed as acceptor, higher DP could be reached. The longest oligomers (DP between 7 and 16) precipitated into lamellar crystals with a diffraction pattern typical of mannan I [306].

ManA-based polysaccharides are abundant component of alginates, often found as mixed polymers with α(1–4)-L-GulA (i.e., guluronic acid). These naturally occurring anionic polysaccharides are found in algae and some bacteria [307]. The two monosaccharides can be arranged in the polymer in different patterns (i.e., MM, GG, or MG domains where M stands for ManA and G for GulA). To date chemical synthesis is the only way to access well-defined alginate oligosaccharides as enzymatic synthesis has suffered from the complexity of the enzymes involved [308]. The chemical construction of α(1–4)-L-Gul linkages is facilitated by the intrinsic tendency of Gul donors to form 1,2-*cis* glycosidic linkages (α:β ratios >10:1). The $^4H_3$ conformation adopted preferentially by the Gul oxocarbenium intermediate favors the attack of the nucleophile from the α-face, leading to a 1,2-*cis* glycosylation (Figure 8A). In contrast, GulA donors were found to be less α-stereoselective [301,309,310]. Therefore, the most frequently adopted strategies involve highly α-stereoselective glycosylations using Gul donors and subsequent oxidation to obtain GulA [310]. With this strategy, alginate oligomers (i.e., 7mer) with mixed sequence were prepared. The solution phase synthesis was performed by sequential addition of a disaccharide BB **111** with the α(1–4) GulA glycosidic linkage pre-installed (α(1–4) gulosylation followed by C-6 oxidation). The ManA unit provided high β-stereoselectivity (α:β >1:20) (Figure 8B). This strategy, while avoiding late-stage oxidations, suffered from the poor re-

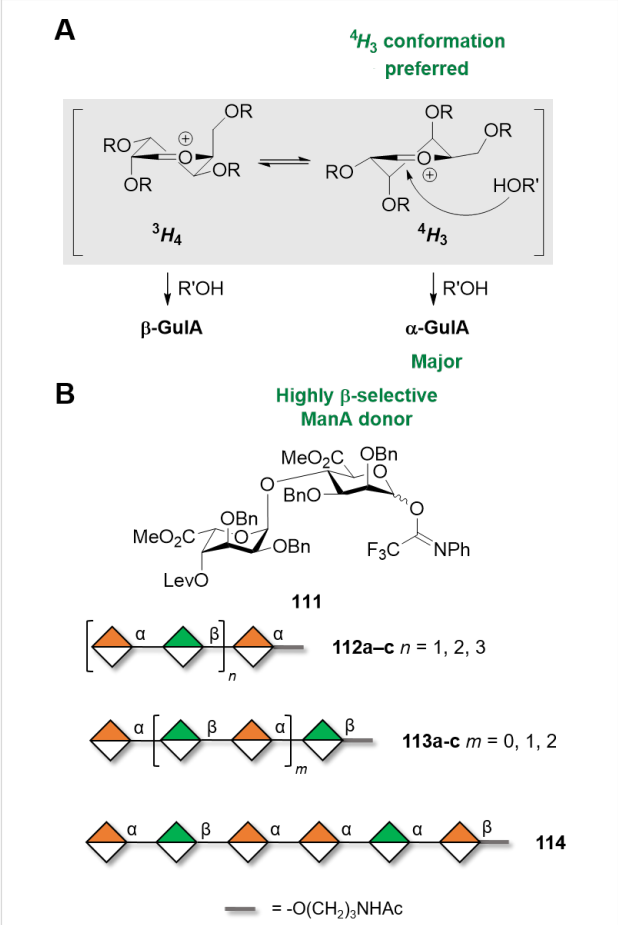


Figure 8: A) The preferred $^4H_3$ conformation of the gulosyl oxocarbenium ion favors the attack of the alcohol from the α-face. B) Key disaccharide BB **111** used for the solution phase synthesis of alginate oligosaccharides and representative structures obtained.

activity of the axial OH-4 of GulA resulting in low glycosylation yields for longer analogues (i.e., 30–42%). In addition, the acceptor reactivity was found to be highly sensitive to subtle modifications in remote positions of the acceptor [309,311], highlighting the importance of the – often overlooked – acceptor three-dimensional structure.

Rhamnans

Long repetitive polysaccharides constituted of L-Rha (i.e., rhamnans) are found in bacteria, plants, and algae but are absent in animals [312]. The enantiomer D-Rha is less common, only found in the capsule of some bacterial species. Linear repetitive rhamnans can be classified in type I (alternated α(1–3)/α(1–2) L-Rha residues) or type II (linear α(1–3)-L-Rha residues) and can be variously sulfated.

Very few examples of enzymatic or polymerization methods have been reported to prepare this class of compounds. In contrast, from a chemical standpoint constructing α-rhamnans does not present significant challenges. Similar to Man, Rha donors benefit from the favorable anomeric effect and neighboring group participation, generally achieved with C-2 *O*-acyl groups (e.g., Ac, Bz, Piv), which secures highly stereoselective 1,2-*trans* glycosylations (Figure 5) [270,313-318]. Even in absence of neighboring group participation α-stereoselectivity is achieved [319,320].

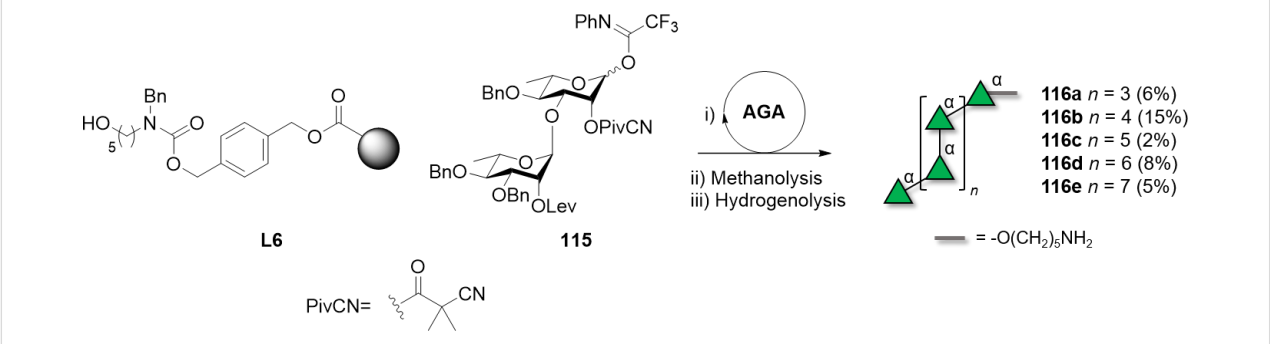
α-Rhamnans chemical synthesis suffers from PG migration. This issue has been observed when constructing α(1–3) linkages, since C-2 *O*-Ac groups are prone to migrate from the axial O-2 to the equatorial O-3 of L-Rha [313,314,321,322]. Replacing the Ac group with benzoyl (Bz) [315], pivaloyl (Piv), or cyano-pivaloyl (CNPiv) [313,314] groups prevented acyl migration. In particular, CNPiv was developed to avoid the harsh conditions generally required for Piv removal and could be easily cleaved either by hydrogenolysis [313] or methanolysis [314]. Type I rhamnans up to 16mer (**116a–e**) were prepared by AGA using disaccharide BB **115** (Scheme 17) [314]. Type I and II α-rhamnans were also successfully assembled following solution-phase approaches by stepwise elongation of the rhamnan chain using orthogonally protected disaccharide BBs. The range of orthogonal PGs used (i.e., PMB, Bz, Nap, Bn) suggested the possibility to generate rhamnan structures with different sulfation patterns [315,316]. Orthogonality of PGs was also exploited to introduce β(1–3)-GlcNAc branches on a type I rhamnan 8mer backbone, common in bacterial α-rhamnans [317].

In analogy to mannose, β-rhamnosylation is a highly challenging reaction. However, while the β-mannosylation reaction can benefit from 4,6-*O*-benzylidene PG stereocontrol, β-rhamnosylation cannot [323]. To date, only few reports of successful β-rhamnans synthesis are available, mostly limited to short oligosaccharides [324].

Polysaccharides based on a mixed mannose–rhamnose backbone

The lack of enzymatic approaches to construct the often unique linkages found in bacterial polysaccharides makes chemical synthesis the only amenable way to access these molecules. Generally, the repeating unit containing the challenging linkage is prepared and used in iterative glycosylation approaches enabling exponential growth, while maintaining control over the polysaccharide length.

Recently, the synthesis of large bacterial polysaccharides containing D-Man, and D/L-Rha mixed structures was reported [325,326]. The *O*-antigen of *Bacteroides vulgatus* consisted of alternating α(1–3)-L-Rha and β(1–4)-D-Man linkages. The efficient α-rhamnosylation reaction was exploited to elongate the chain by iterative glycosylations, while the challenging β(1–4)-Man was installed at the disaccharide level (**117**) using the 4,6-*O*-benzylidene directed β-mannosylation (Figure 9A). The exponential growth, up to the 128mer (**118a–h**), was enabled by



Scheme 17: AGA of type I rhamnans up to 16mer using disaccharide BB **115** and CNPiv PG. The AGA cycle includes coupling (TfOH) and Lev deprotection (hydrazine).

o-alkynylbenzoate donors [327] and the use of two orthogonal PG at the reducing and non-reducing end (i.e., *p*-methoxyphenyl (PMP) and *tert*-butyldimethylsilyl (TBS) groups, respectively). The glycosylation reactions proved robust, with only a slight drop in yield (i.e., 74% compared to ca. 90%) for the [64 + 64] glycosylation. Issues during the final deprotection steps, due to poor solubility and reducing end degradation [294], lowered the isolated yield to 15% for the longest analogues [325].

The capsular polysaccharide (CPS) of *Clostridium bolteae,* consisting of alternating α(1–4)-D-Man and β(1–3)-D-Rha, was targeted to showcase a methodology to construct β-D-Rha linkages. Similar to the above approach, the disaccharide BB **119** including the challenging β(1–3)-D-Rha glycosidic linkage was initially prepared (Figure 9B). The efficient α-mannosylation reaction was exploited to further elongate the chain in a sequential manner. Three different strategies were screened for the construction of the dimer: i) β-rhamnosylation through a pre-activation strategy, ii) 4,6-*O*-benzylidene directed β-mannosylation and subsequent C-6 deoxygenation to provide D-Rha, iii) indirect approach using 6-deoxy-D-Glc in a 1,2-*trans* glycosylation and subsequent C-2 epimerization to give D-Rha. Strategies ii) and iii) successfully formed the β(1–3)-D-Rha linkage of the disaccharide BB. A series of sequential glycosylations enabled the solution-phase assembly of oligosaccharides up to 18mer (**120a–i**) in excellent yields (80–90% per coupling). The deprotection (i.e., methanolysis and hydrogenolysis) proved to be challenging for longer analogues due to the degradation of the oligosaccharides in the acidic solvent chosen for hydrogenolysis. A neutral solvent mixture permitted to obtain the compounds, even though in low yield compared to shorter analogues [326].

Galactose-based polysaccharides

Enzymatic and polymerization approaches are not so common for galactopyranose-based polysaccharides and are limited to the construction of single glycosidic linkages [328]. In contrast, bacterial enzymes capable of constructing galactofuranose-based polysaccharides have been widely studied and offer the unique possibility to tune the chain length. Additionally, chemical synthesis can reliably afford both α-Gal and β-Gal polysaccharides.

β-Galactans

Galactans and arabinogalactans, together with arabinans, are the three types of side chains in the pectin RG-I domain [99,329,330]. The backbone of type I galactans is made of β(1–4)-linked Gal residues, while type II galactans are highly branched polysaccharides composed of β(1–3)- or β(1–6)-linked Gal residues [99].

β-Galactosylation is easily achieved by neighboring group participation. The main challenge of type I galactans is the low reactivity of the axial hydroxy group at C-4 of the Gal residues. Type I galactans up to 7mer (**121a–c**) have been prepared employing C-2 *O*-Piv or *O*-Ac PG and either *n*-pentenyl or thioglycoside LG (Figure 10) [331-333]. Steric bulk around the unreactive C-4 OH was minimized by using Bn or allyl (All) ethers at C-3 and C-6 positions [331]. Removal of Piv, despite requiring harsh conditions (LiOH in MeOH under reflux or Et_4NOH in THF under reflux), yielded the desired product in good yield (70–90%). In contrast, removal of allyl (All) PG was more challenging, requiring extensive optimization [331]. The use of Nap to mask the hydroxy groups at C-4 or C-6 allowed for the late-stage installation of arabinan side chains [332]. AGA was employed to assemble a collection of type I galactans using three

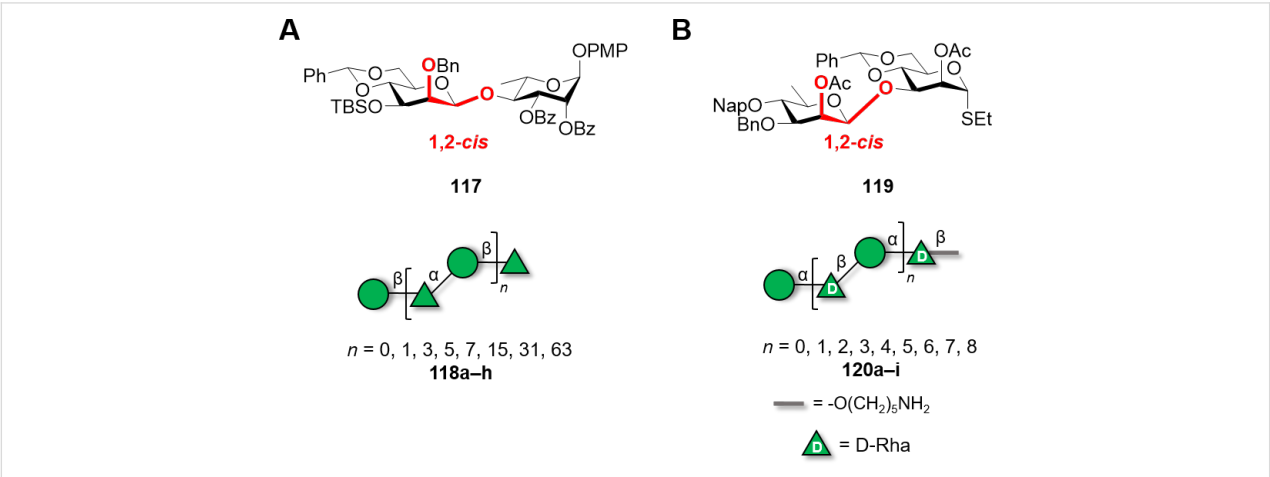


Figure 9: Key BBs for the synthesis of the *O*-antigen of *Bacteroides vulgatus* up to a 128mer (A) and the CPS of *Clostridium bolteae* up to 18mer (B). The most challenging 1,2-*cis* glycosidic linkage is installed in the key BBs and highly stereoselective 1,2-*trans* α-rhamnosylation or α-mannosylation were exploited for elongation.

different Gal BBs equipped with Fmoc as a temporary PG to allow for chain elongation. Lev could be selectively removed to install L-arabinose branches at the C-3. The low reactivity of the hydroxy group at C-4 required a double cycle of glycosylation and negatively impacted the final yields [334].

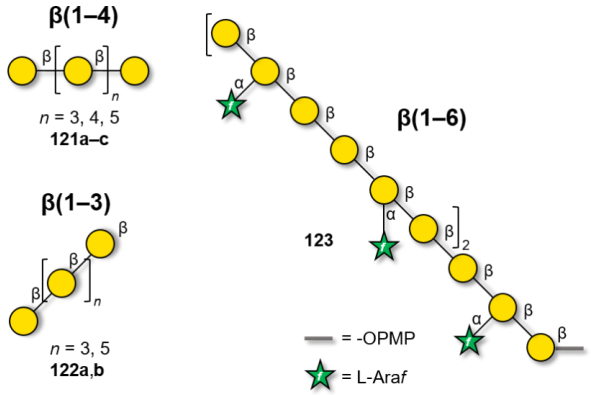


Figure 10: Examples of type I and type II galactans synthesized to date.

The easy formation of β-Gal linkages and the excellent reactivity of the primary hydroxy group at C-6 considerably simplified the synthesis of type II galactans. Solution-phase synthesis provided long β(1–6)-galactans, bearing α(1–2)- or α(1–3)-linked L-arabinofuranose side-chains [335-338]. A stepwise elongation (i.e., [4 + 12] then [4 + 16]) proved successful to construct a 20mer β(1–6)-galactan, bearing arabinose side chains [338] (**123**, Figure 10).

Only shorter synthetic oligomers based on a β(1–3)-Gal backbone could be obtained (**122a,b**). A collection of linear and branched type II galactans was synthesized by solution-phase methods. To minimize PG migration, the use of thioglycoside disaccharide donors bearing a participating Piv ester at C-2 position was the key [339]. Similar structures were obtained by AGA [340]. In both cases, orthogonal PG were necessary for the installation of either β(1–6)-Gal or α(1–3)-Ara*f* branches.

α-Galactans and α-galactosaminogalactans

In contrast to the challenging formation of other 1,2-*cis* linkages, α-galactosylation can be reliably obtained using Kiso's di-*tert*-butylsilylene (DTBS)-directed α-stereoselective methodology (Figure 11A). Upon activation, the galacto-type oxocarbenium adopts a $^4H_3$ conformation, preferentially attacked from the α-face in a S_N1 mechanism due to the steric bulk of the DTBS group. The $^4H_3$ conformation is stabilized by through-space electron donation from the DTBS group. Complete α-stereoselectivity is often preserved, even in presence of C-2 participating PGs [341,342].

This methodology was elegantly implemented for the synthesis of galactosaminogalactans, linear heteropolysaccharide found in the cell-wall of the fungus *Aspergillus fumigatus* (Figure 11B) [343,344]. Natural galactosaminogalactans are composed of Gal, GalN, and GalNAc arranged in a random pattern impeding their isolation from natural sources. A sequential strategy using BBs **124**, **125**, and **126** afforded a collection of α(1–4)-Gal, α(1–4)-GalN, α(1–4)-GalNAc, including mixed structures. The

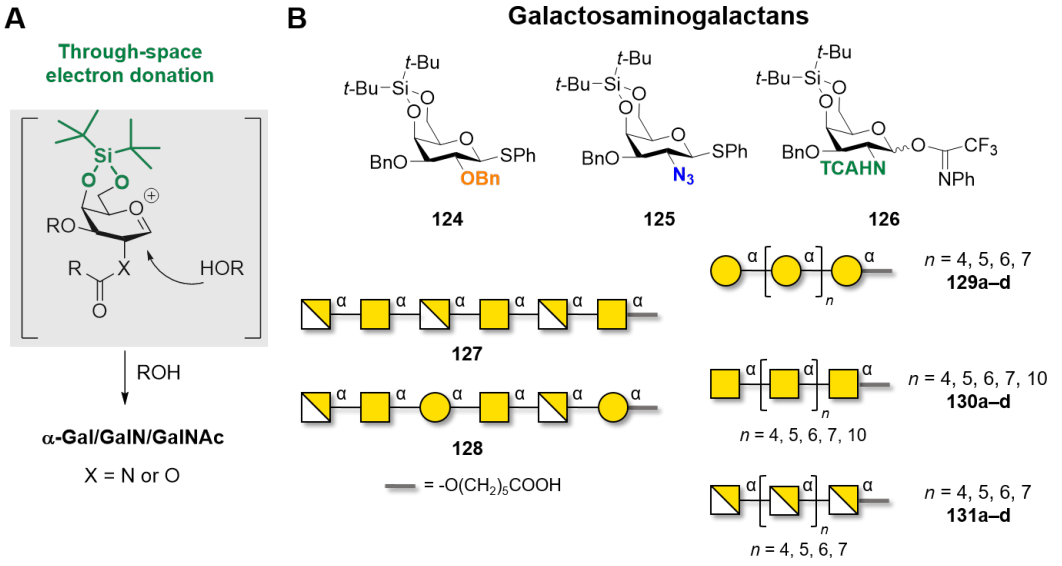


Figure 11: A) The DTBS PG stabilizes the $^3H_4$ conformation of the Gal oxocarbenium ion favoring the attack of the alcohol from the α-face in a S_N1 manner. B) Key BBs used in the synthesis of galactosaminogalactans bearing the α-directing DTBS PG.

use of the highly reactive *N*-phenyltrifluoroacetimidate glycosyl donors **126** proved to be crucial to generate long oligosaccharides. Chain elongation was achieved by DTBS removal and selective benzoylation of the OH at C-6, yielding the free C-4 hydroxy group to be used as acceptor in the next glycosylation. Good yields (80–90%) and excellent α-stereoselectivities were obtained for the construction of oligomers up to 12mer (**127**, **128**, **129a–d**, **130a–d**, **131a–d**). The deprotection of α(1–4)-Gal 8mer and 9mer suffered from low yields (20–30%), due to low solubility in water. Higher yields were obtained for more soluble analogues [343,344].

The pectin domain homogalacturonan (HG) consists of a linear backbone of α(1–4)-GalA residues in which the C-6 carboxylate moiety can exist as methyl ester, generating different patterns [99,329,330]. While the stereoselective construction of the α(1–4) linkages did not pose a significant challenge, the poor acceptor reactivity due to the presence of the carboxylate moiety often translated into low yield [99]. HG analogues (up to a 12mer, **132a**,**b**) were successfully synthesized by solution-phase synthesis (Figure 12). Solvent participation with Gal fluoride donors (activated with $SnCl_2$, $AgClO_4$) ensured high α-stereoselectivities. The Gal residues were converted to GalA by selective hydrolysis of the Ac ester at C-6 and a two-step oxidation (i.e., Swern oxidation followed by treatment with $NaClO_2$ in aqueous acidic conditions) [345,346]. An alternative oxidation protocol (Dess–Martin periodinane/$NaClO_2$) was applied to synthesize HG fragments with different methylation patterns (**134a–d**). Two orthogonal PGs (Ac and PMP) were installed at C-6 of the α(1–4)-Gal fragments, allowing for selective oxidation (Figure 12). Methylation (with $TMSCHN_2$) or benzylation (with $PhCHN_2$) of the carboxylic acid allowed to differentiate between the carboxylic acids and obtain the methyl ester or the carboxylic acid, respectively [347,348]. Overall, while requiring more PG manipulations, the post-glycosylation oxidation strategy proved to be higher yielding compared to a procedure using GalA donors [349].

Galactofuranose-based polysaccharides

The cell wall of mycobacteria contains galactofuranose (Gal*f*)-based polysaccharides that play various functional roles based on their length [350]. These polymers are biosynthesized in a length-controlled manner by complex enzymatic machineries. However, to date, the molecular mechanism for chain length control remains poorly understood [351].

The galactan found in *Mycobacterium tuberculosis* is composed of 20–40 Gal*f* residues connected via alternated β(1–5)- and β(1–6)-linkages. The in vitro enzymatic synthesis of these galactans has been reported using galatofuranosyltransferase (GlfT2) from *Mycobacterium tuberculosis,* UPD-Gal*f* donor, and acceptor **135c** (Figure 13). The resulting polysaccharide showed a product distribution unbalanced towards larger polymers (up to 27mer), with a narrow distribution centered on the 21mer. The nature and length of the lipidic part was a key parameter to control the in vitro polymerization. While **135a** and **135b** did not function as efficient acceptors, longer galactans with distribution centered on the 41mer could be obtained tuning the lipid length (acceptor **135d**) [352]. The mechanism of galactan length control may differ consistently between the in vitro and in vivo setting as the interplay between the GlfT2 enzyme, the plasma membrane and other proteins involved in transport across the membrane play a crucial role in length control [353,354]. Recently, it was reported that a mutation on the GlfT2 enzyme enabled the regulation of the galactan chain length (4mer or 11mer with a relatively narrow distribution) [350]. These examples suggest a potential avenue to produce length-controlled polysaccharides via glycoengineering [351,354,355].

The main challenges associated to the chemical construction of alternated β(1–5)- and β(1–6)-linked D-Gal*f* residues are the complexity of Gal*f* BB synthesis. Especially for Gal*f*, the lower thermodynamic stability compared to its pyranosic counterpart, makes BBs synthesis more complex [356-359]. Common ap-

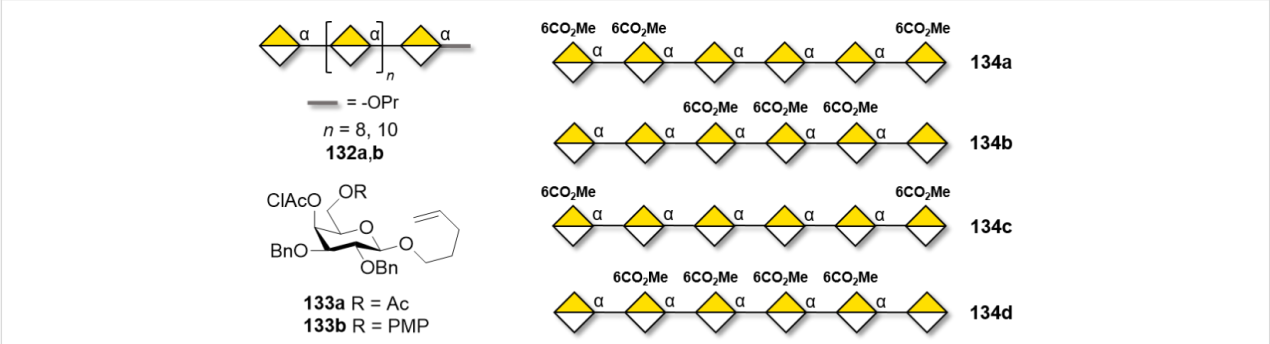


Figure 12: Homogalacturonan oligosaccharides synthesized to date. Access to different patterns of methyl-esterification could be controlled using BBs **133a** and **133b** bearing different C-6 PGs (i.e., Ac or PMP).

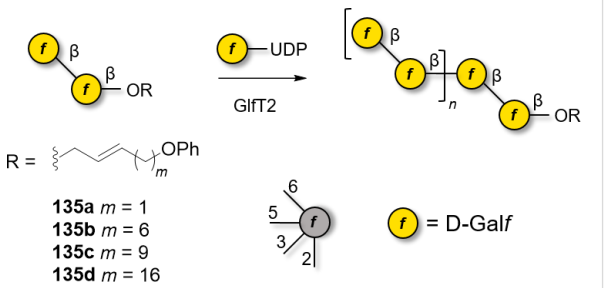


Figure 13: GlfT2 from *Mycobacterium tuberculosis* catalyzes the sequential addition of UPD-Gal*f* donor to a growing galactan chain composed of alternated β(1–5)- and β(1–6)-linked D-Gal*f*.

proaches to access Gal in the furanose form involved dithioacetal cyclization using iodine and an alcohol [358] or a recently reported pyranoside-into-furanoside (PIF) rearrangement [360]. Frequent O-5→O-6 ester migration is observed in basic media. The migration could be reduced by using morpholine, instead of piperidine, during the Fmoc deprotection permitting the synthesis of a 7mer upon stepwise chain elongation [358,359]. Other approaches employing Lev as a temporary PG yielded a 14mer galactan [361]. Interestingly, while a good reactivity of acceptor **136** was observed, the poor reactivity of acceptor **137** hindered the stepwise synthesis of the linear backbone, already at the 3mer stage (Figure 14). This poor reactivity was ascribed to the unfavorable conformation adopted by **137**. This problem was solved by building the galactan backbone from the non-reducing end to the reducing end [358].

Galactan fragments, up to 20mer, were prepared by AGA (Scheme 18). When BBs **138a** and **139a** were used, several problems were encountered such as poor solubility, aggregation of the growing chain on the solid support and instability. Switching to BBs **138b** and **139b** bearing disarming Bz groups solved the issue and enabled the assembly of galactans up to 20mer **140** [362].

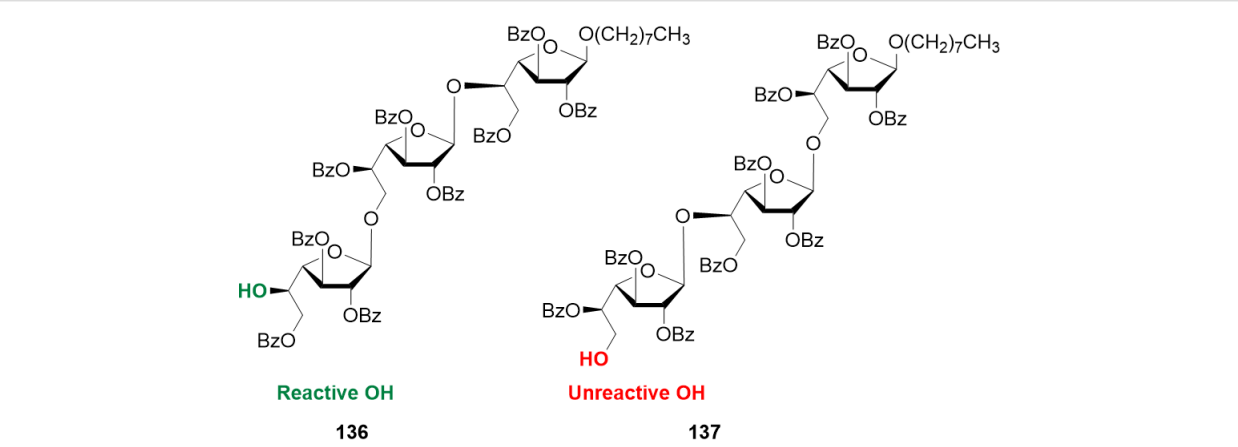
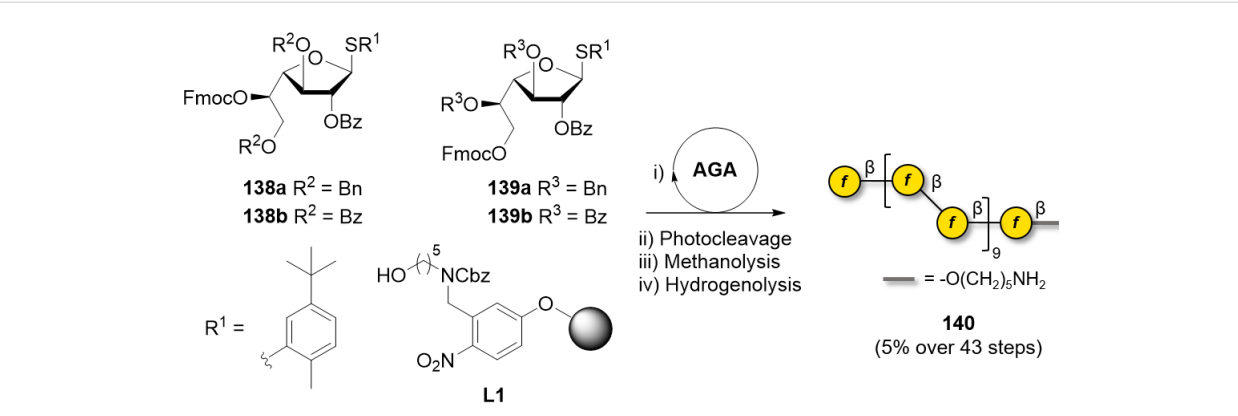


Figure 14: The poor reactivity of acceptor **137** hindered a stepwise synthesis of the linear galactan backbone at the 3mer stage. In contrast, acceptor **136** proved to be more reactive.



Scheme 18: AGA of a linear β(1–5) and β(1–6)-linked galactan 20mer. The AGA cycle includes coupling (NIS/TfOH), capping (Ac_2O) and Fmoc deprotection (DBU).

Fucose-based polysaccharides

Fucans are a class of ionic polysaccharides present on the cell wall of marine brown algae, mainly constituted of repeating L-fucose units [363]. They are heavily sulfated and connected through α(1–3) or α(1–4) linkages [364]. Several orthogonal PGs are required to access different sulfation patterns present in fucans. Long structures (up to 16mer) with α(1–3) connectivity were obtained by iterative couplings of dimers and tetrasaccharides units [365]. Donors bearing 4-*O*-benzoyl, in combination with the 3-*O*-Ac and 2-*O*-Bn groups, enhanced the α-selectivity through remote participation. To date, only short tetramers containing both types of α-linkages have been reported [366].

Arabinose-based polysaccharides

Arabinans, repetitive polysaccharides containing arabinofuranose (Ara*f*), are major constituents of both plant cell-wall and of mycobacterial cell-wall, with the important difference that plants contain L-Ara*f,* while bacteria D-Ara*f* [367]. Mycobacterial arabinans are composed of a linear backbone of α(1–5)-D-Ara*f* with α(1–3) branches, which can be further elongated with linear α(1–5)-D-Ara*f* residues. Similarly, plant arabinans consist of α(1–5)-L-Ara*f* bearing α(1–3) and/or α(1–2) branches.

A variety of strategies have been reported to synthesize these compounds. Most of them show several common features. Bz groups are the most commonly used neighboring participating groups to ensure stereoselectivity, affording the linear α(1–5)-D-Ara*f* backbone. Convergent strategies are commonly employed [368]. As an alternative approach, cationic ROP using 1,2,5-orthobenzoate BBs and Lewis acid catalysis (i.e., $SnCl_4$ or TMSOTf) could generate mixtures of linear α(1–5)-arabinans (up to 25mer) [369-371]. Using 1,2,5-orthopivaloate BBs, linear α(1–5) arabinans with DP up to 91 could be prepared [372]. Tuning the polymerization conditions gave mono-, di-, and trisaccharide thioglycoside Ara*f* BBs, that were used to assemble defined linear arabinans (up to 8mer) [373].

When constructing branched arabinans, convergent approaches involving fragment coupling, rather than sequential elongation, are preferred. Steric hindrance at the arabinan acceptor was found to be the limiting factor during the installation of the α(1–3)-arabinan branches. Small Ara*f* donors enabled the installation of C-3 branches in a 12mer [374,375]. Larger structures (up to 22mer) were synthesized by convergent fragment coupling [376,377]. Key to the success of these syntheses was the early stage installation of the α(1–3) branches and the single β(1–2)-linked Ara*f* at the non-reducing end. Trichloroacetimidates were chosen as reactive LGs for the most challenging couplings (i.e., [12 + 3 + 3], and [12 + 5 + 5]). To avoid the removal of a large number of Bn groups at the last stage of the synthesis, Bz groups were chosen as the sole PGs for the fragments [376]. The reactivity of Ara*f* permitted the implementation of milder glycosylation conditions; 1,2-propargyl orthoester donors and alkynyl carbonate donors, activated using a Au(I) catalyst in presence of AgOTf, were employed in the convergent synthesis of a 25mer. The glycosylation could be carried out at room temperature [368,378-380]. Shorter branched structures (up to 6mer) could be assembled by AGA using thioglycoside donors [281,381].

Fewer examples exist for the chemical synthesis of L-arabinans. A convergent assembly of a α(1–5)-linked 8mer was accomplished with L-Ara*f* *N*-trichloroacetimidate donors. Regioselective glycosylation of the primary alcohol at C-5 on partially protected acceptors was possible, simplifying BB preparation. However, this reaction was shown to be highly acceptor-dependent and worked best only for Ara*f* acceptors [382,383].

Recently, the synthesis of the whole complex arabinogalactan polysaccharide 92mer was reported. A linear 30mer backbone of alternated β(1–5)- and β(1–6)-linked D-Gal*f* residues bearing two branched 31mer arabinan was assembled in a convergent approach. Two equivalents of a branched arabinan donor (bearing α(1–5) and α(1–3) linkages) were coupled to a linear galactofuranose (30mer) backbone acceptor in a [31 + 31 + 30] glycosylation step (Figure 15).

The three fragments were assembled following one-pot protocols, in which the donor was pre-activated at low temperature (stoichiometric *p*TsCl/AgOTf at −78 °C) and then the acceptor was added [154]. Upon completion of the reaction, the newly formed compound was subjected to the same pre-activation protocol and employed in the following step without intermediate purification. In this way, the alternated linear β(1–5)- and β(1–6)-linked D-Gal*f* 30mer fragment was quickly obtained via a five-component one-pot glycosylation [6 + 6 + 6 + 6 + 6]. Each 6mer was itself generated via a six-component one-pot protocol. Similarly, branched arabinofuranose fragment **145** was assembled following a six-component one-pot glycosylation [7 x 2 + 5 + 6 + 6] (Scheme 19). To avoid late-stage installation of challenging linkages, the β(1–2)-Ara*f* terminal residues were installed at an early stage using a 3,5-TIPDS protected (3,5-O-tetraisopropyldisiloxanylidene) Ara*f* donor [384].

The three fragments were finally connected using the benzenesulfinylmorpholine/triflic anhydride (BSM/Tf_2O) activator system. Despite the impressive size of the molecule, no issues were encountered in the final deprotection steps (75% yield), permitting to obtain 92mer arabinogalactan polysaccharide **140** [385].

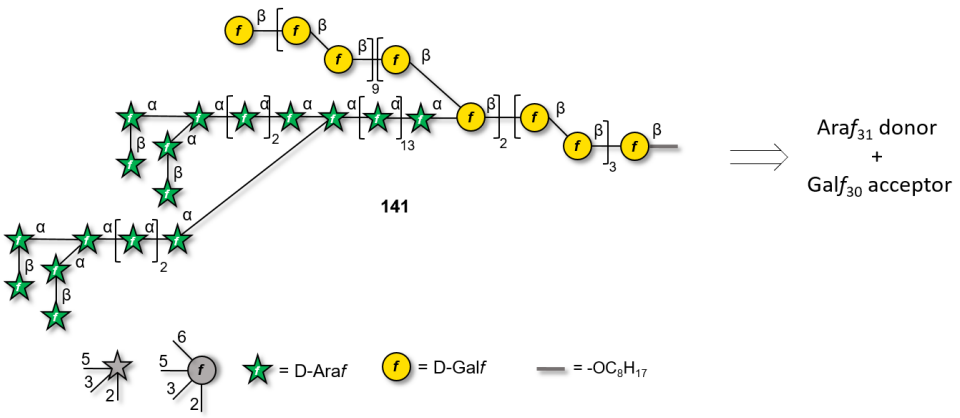
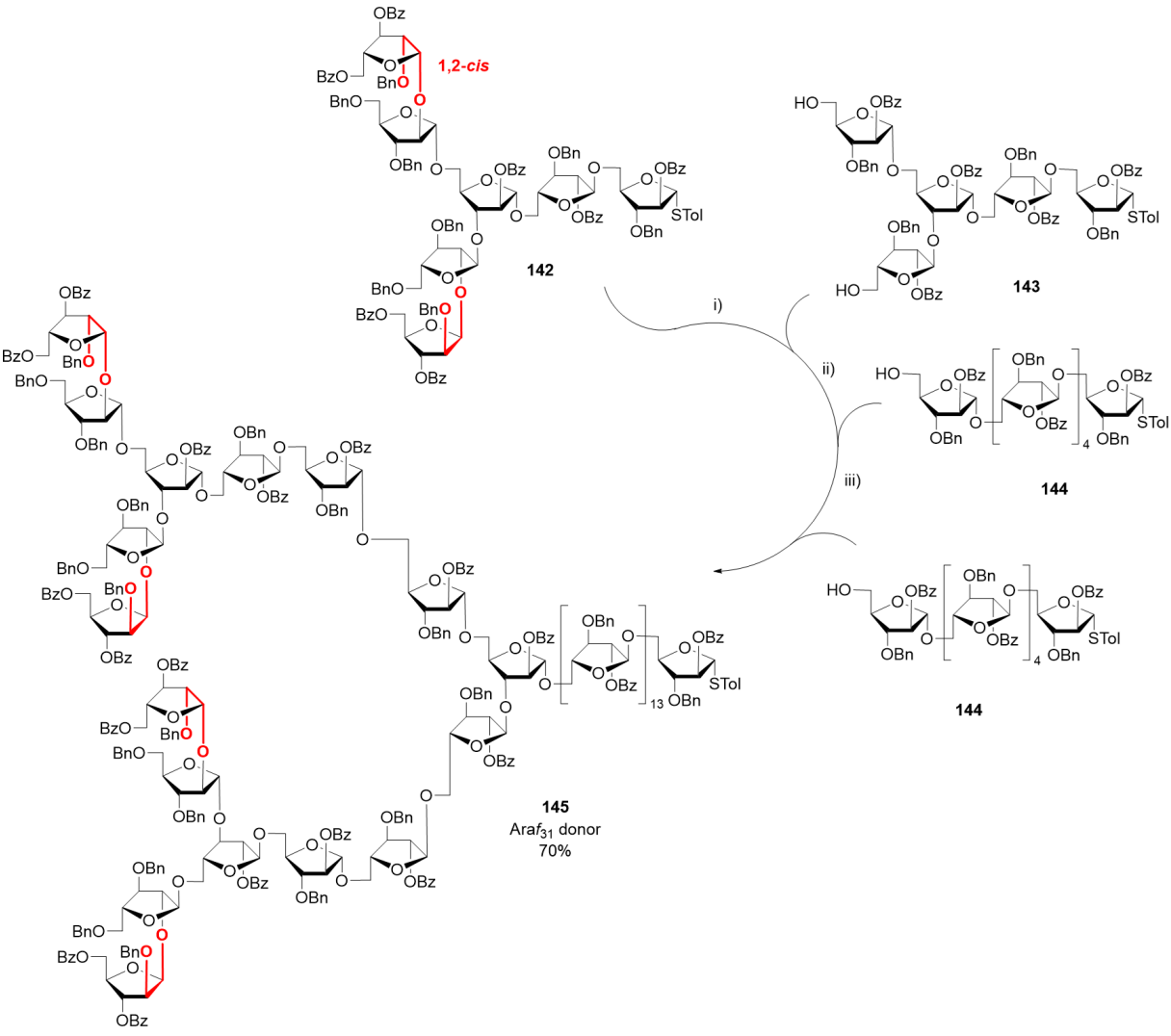


Figure 15: The 92mer arabinogalactan was synthesized using a [31 + 31 + 30] fragment coupling between a 31mer arabinan donor (Araf_{31}) and a 30mer galactan acceptor (Galf_{30}).



Scheme 19: Synthesis of the branched arabinofuranose fragment using a six component one-pot synthesis. i) TTBP, 4 Å MS, DCM, *p*TolSCl, AgOTf then **143**, −78 °C to room temperature. ii) *p*TolSCl, AgOTf then **144**, −78 °C to room temperature. iii) *p*TolSCl, AgOTf then **144**, −78 °C to room temperature.

Glycosaminoglycans (GAGs)

Ionic polysaccharides are ubiquitous in living organisms where they regulate a multitude of cell functions. The ionic moieties control the shape of such compounds by promoting repulsive and attractive interactions [9]. Glycosaminoglycans (GAGs) are the major structural components of the extracellular matrix (ECM) in mammals. GAGs are linear, negatively charged polysaccharides composed mainly of repeating disaccharide units (Figure 16A) [386]. The anionic backbone, bearing sulfate moieties (except for hyaluronans), is responsible for their interactions with a plethora of proteins and the regulation of a large number of biological processes [387-389]. GAGs are water retaining polysaccharides, thus modulating the hydration and the water homeostasis in tissues [390].

GAGs can be obtained from animal sources (e.g., chondroitin sulfate is extracted from shark cartilage), albeit in heterogeneous mixtures that hampered quality control and reproducibility [391]. The heterogeneous nature of these samples is particularly problematic because the spatial orientation of the sulfate groups (sulfation code) [392,393] and the length of the polysaccharide chain affects the structural and biological features of GAGs. This became obvious during the "heparin crisis" in 2008, when batches of heparin, contaminated with oversulfated chondroitin sulfate, entered the marketplace causing the life of hundreds of people [4]. This episode underscored the urgency to develop reliable methods to access well-defined GAGs, with full control over substitution pattern and chain length. Well-defined GAGs are also valuable standards to uncover the mech-

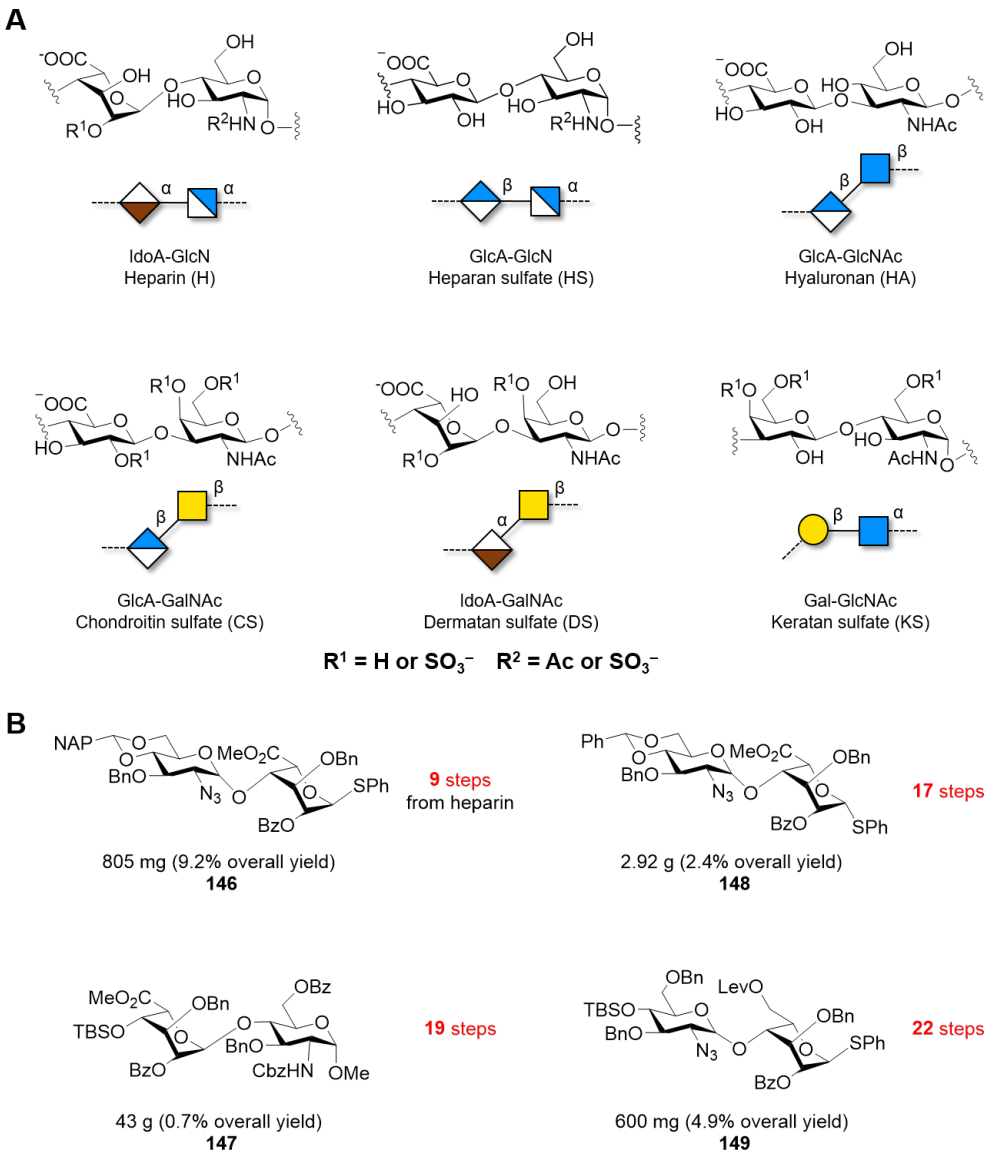


Figure 16: A) Chemical structure and SNFG of the representative disaccharide units forming the GAG backbones, and B) representative examples of synthetic disaccharides used for the preparation of HS analogues.

anism of action of heparin-like drugs (e.g., fondaparinux) [394,395].

Heparin and heparan sulfate

Among GAGs, heparin (H), heparan sulfate (HS), and heparin-like structures have been studied extensively due to their biological relevance [389]. HS binds to over hundred proteins depending on sulfation pattern and chain length. Generally, a minimal length (in most cases an octasaccharide) is required to trigger specific biological events, including interaction with cytokines and chemokines growth factors [396].

Due to their structural complexity, the synthesis of H/HS poses multiple challenges (Figure 17) [397]. The formation of the 1,2-*cis* linkage in the GlcN-GlcA repeating units cannot be directed with neighboring group participation. A plethora of PGs has been used to ensure or enhance α-stereoselectivity, through remote participation and/or electronic effects. In addition, orthogonal PGs should also be strategically placed to allow for the subsequent regioselective sulfation. This requirement becomes particularly challenging considering the multiple steps needed to generate the rare L-idose unit. Another bottleneck arises from the lability of the sulfate groups in both acidic and basic conditions, limiting PG manipulations or functional group transformations. Thus, the removal of the PG must be carefully planned to avoid small pH fluctuations. Not last, purification and detection of highly sulfated structures is troublesome [398,399].

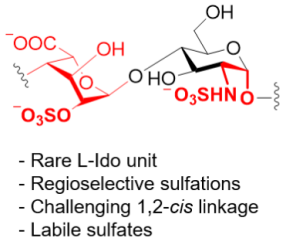
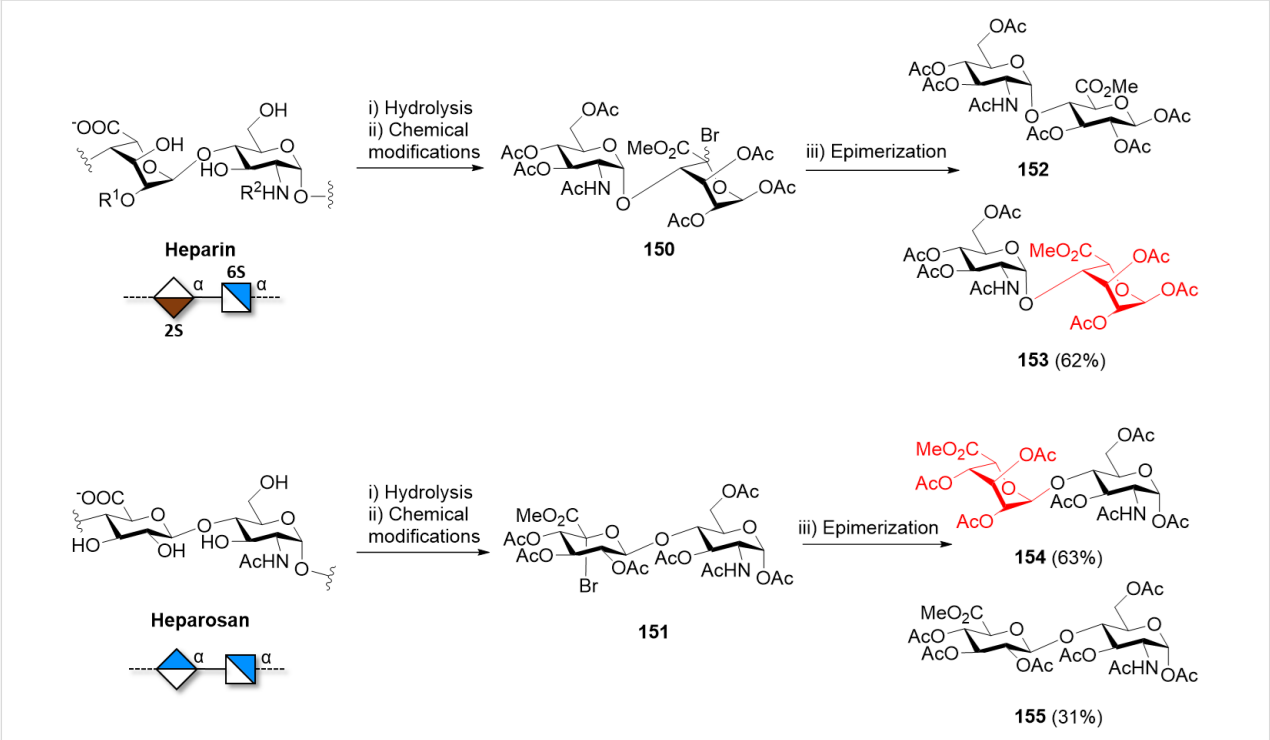


Figure 17: Synthetic challenges associated to the H/HS synthesis.

The significant efforts of the last 20 years resulted in synthetic methods to access various BBs for the assembly of heparin and heparan oligosaccharides. Considerable success has been obtained in making the core dimers IdoA-GlcN that can be further assembled to give longer oligomers [400-404]. Still, most methods suffered from lengthy and laborious processes (18–29 steps) and low yields that precluded scalability (Figure 16B).

Recently, a clever approach suggested the controlled hydrolysis of commercially available heparin and heparosan polymers to overcome the challenges associated with the chemical synthesis of the disaccharide cores (Scheme 20) [405]. NMR spectrosco-

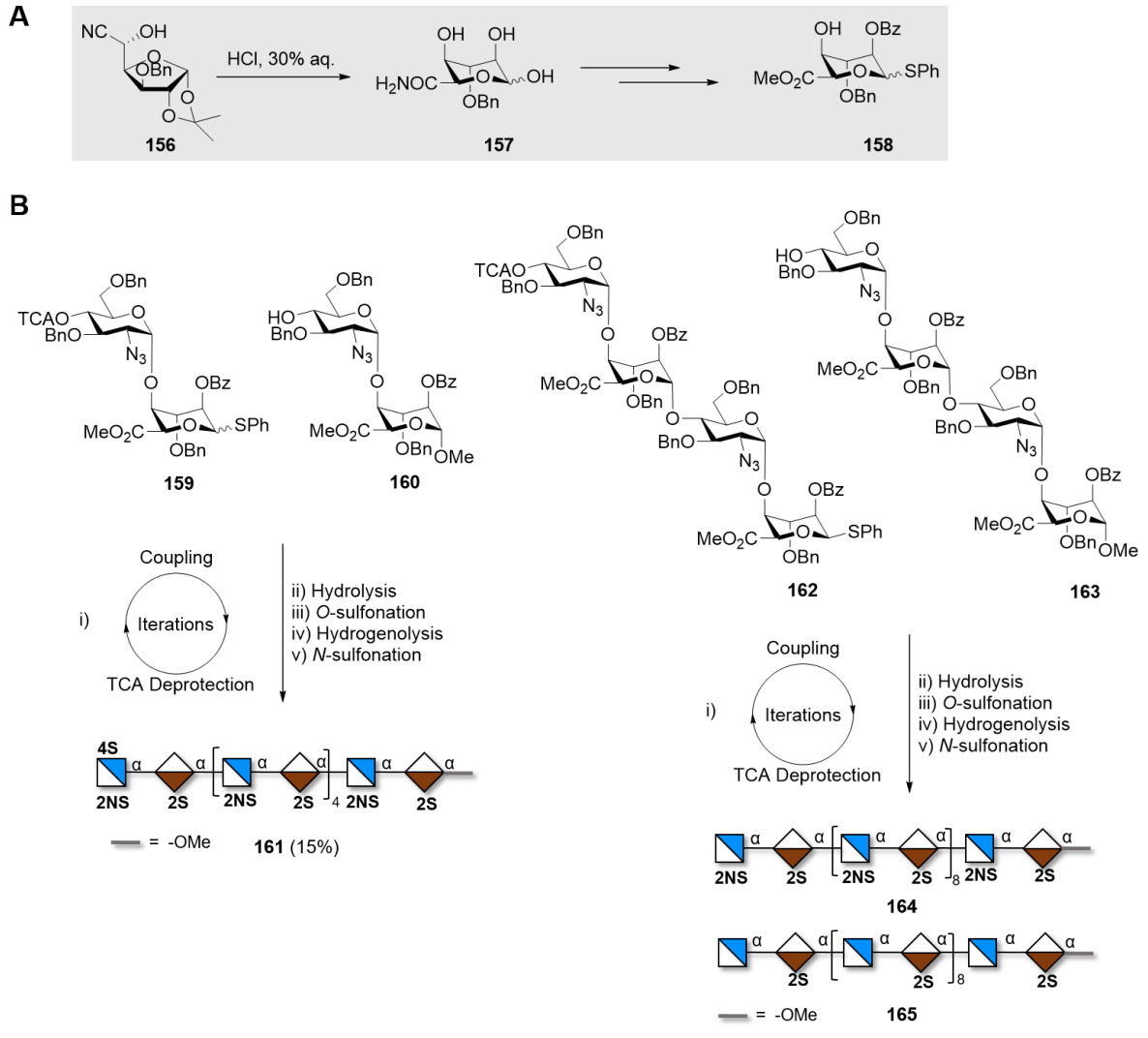


Scheme 20: Degradation of natural heparin and heparosan generated valuable disaccharides **150** and **151** that can be further converted into four disaccharide BBs **152–155** to assemble well-defined structures.

py revealed that, after acid hydrolysis, both polymers produced one type of dimer as the major product (e.g., A-B or B-A). Epimerization strategies (i.e., GlcA→IdoA) granted access to the other two dimers present in HS. The introduction of orthogonal PGs and selective sulfation, provided a set of disaccharides in high yields (9% overall) to be used in the synthesis of well-defined heparin-like structures. To date, this scalable and efficient approach was applied to the synthesis of tetramers.

Impressive results in terms of scalability were achieved starting from the diastereomerically pure cyanohydrin **156** that was quantitatively converted to L-iduronamide **157** [406]. Upon suitable PG manipulations, compound **157** was transformed into acceptor **158** that enabled the formation of the challenging α(1–4) glycosidic linkage with the 2-azidoglucoside donor (Scheme 21). The synthesis of a 12mer was achieved using iterative couplings of compound **159**. Cleavage of the ester PGs, *O*-sulfonation, azide reduction and debenzylation, followed by final *N*-sulfonation permitted the first gram-scale synthesis of a heparin-related 12mer **161** [407].

A similar iterative strategy, using tetrasaccharide BB **162** [408], led to the successful synthesis of a collection of protected HS analogues, from 16mer to 40mer [409]. The use of tetrasaccharide **162** permitted to reduce the number of purification steps after each iterative coupling and improve the overall yields. From this collection, the 20mer was further transformed into two homogeneous HS-like oligosaccharides **164** and **165** with different sulfation patterns (Scheme 21B).



Scheme 21: A) The one-step conversion of cyanohydrin **156** to L-iduronamide **157** represent the key step for the synthesis of BB **158.** B) Synthesis of long heparin-like structures using iterative coupling strategies.

Despite these impressive results, chemical methods based on repetitive coupling steps, deprotections, and purifications are extremely labor demanding. Enzymatic synthesis offers an alternative approach to shorten these lengthy procedures. Nevertheless, a purely enzymatic approach has been proven inadequate for the synthesis of long GAGs, because it generates ill-defined mixtures of oligomers with different lengths [410]. A chemoenzymatic approach could be the ideal solution to prepare well-defined heparin structures [399]. Key to a successful chemoenzymatic route is to design a sequence that resembles the in vivo biosynthesis. Bacterial glycosyltransferases (GTases) KfiA and PmHS2 are commonly used for the elongation of a starting disaccharide using UDP-GlcNAc **169** and UDP-GlcA **168** activated sugar donors [411]. *N*- and *O*-sulfotransferases (STases) catalyze the regioselective insertion of the sulfate moieties using 3'-phosphoadenosine 5'-phosphosulfates (PAPS). To facilitate the detection and the purification steps, the acceptor could be covalently attached to a UV detectable chromophore, such as *para*-nitrophenol [412] (*p*-NP), or a fluorous tag [413]. Chemical modifications, tolerated by the enzyme, were used to overcome particular bottlenecks of the purely enzymatic approach. For example, while the natural substrate for KfiA (UDP-GlcNAc **168**) proved very stable to *N*-deacetylation, the unnatural donor [414,415] UDP-GlcNTFA **167** could be efficiently *N*-deacylated under mild basic conditions, permitting subsequent regioselective *N*-sulfation. Variation on the chemical backbone were catalyzed by C5-epimerase (C5-epi), able to convert GlcA into IdoA and vice versa [416]. Recent studies revealed that C5-epi recognizes specific binding domains, promoting reversible or irreversible epimerization [417]. Following these paths, low-molecular-weight heparins (LMWH) were produced in a gram scale. Longer structures (up to 21mer, **172a–d**) were also accessible (Scheme 22A) [418]. Still, the preparation of structures containing a large number of IdoA2S-GlcNS6S remains problematic. A random epimerization may happen in the presence of C5-epi, leading to ill-defined mixtures of GlcA and IdoA in the final product. A pioneering strategy demonstrated that epimerization could be successfully controlled with the selective introduction of a 6-*O*-methyl ether on a GlcN residue (Scheme 22B) [419]. Three model hexasaccharides **173**, **174**, and **175** demonstrated how single site substitutions can be key to direct enzymatic modifications and generate knowledge on enzyme specificity.

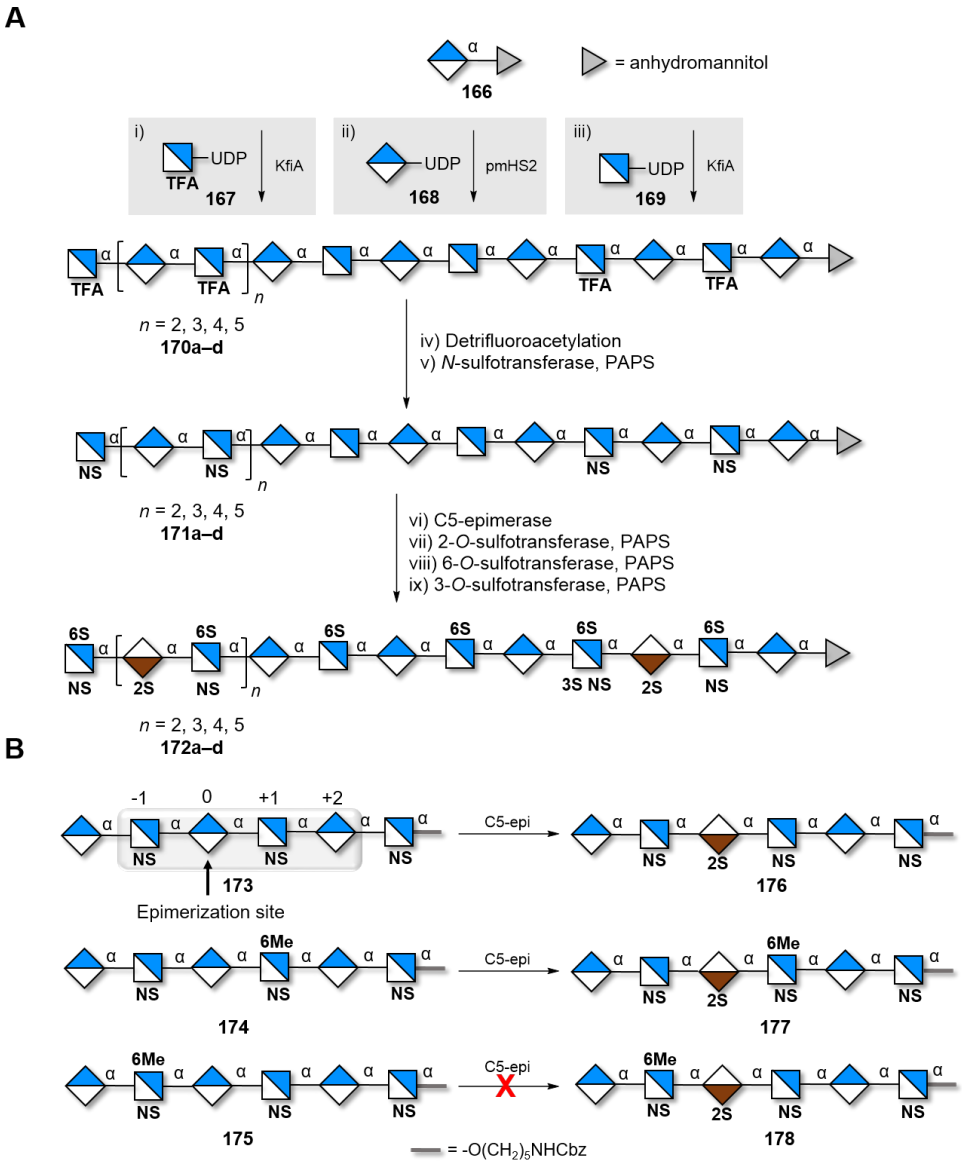
Others GAGs

Chondroitin sulfate (CS) is comprised of β(1–4)-linked *N*-acetyl-D-galactosamine (D-GalNAc) and β(1–3)-linked D-glucuronic acid (D-GlcA) repeating units (Figure 16A). Dermatan sulfate, also named chondroitin sulfate B, is an analogue of CS, having IdoA instead of the GlcA repeating unit. In analogy to heparin and HS, the sulfation pattern dictates the interaction with other biomolecules resulting in important biological functions such as cell proliferation, tissue morphogenesis, and wound repair [420].

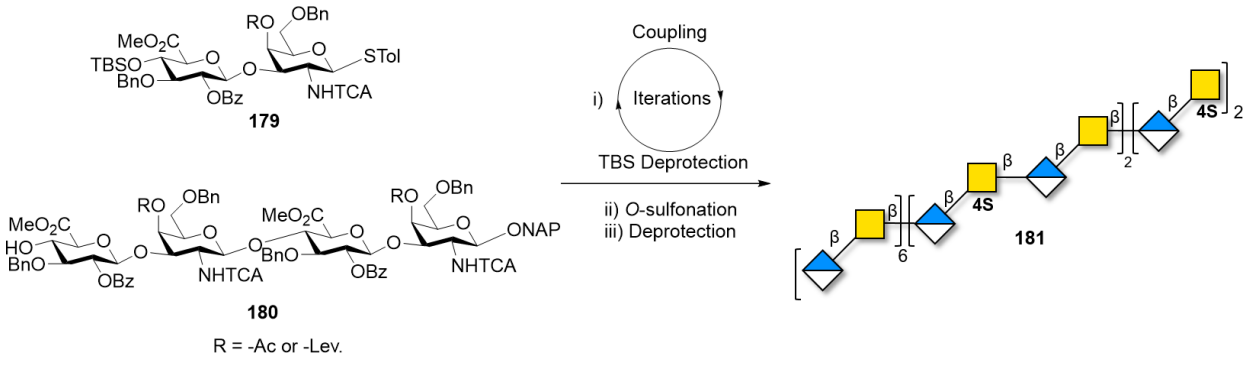
To date, the longest CS chain chemically synthesized was a 24mer [421]. To ensure stereocontrol, the nitrogen on the GalN unit was equipped with a participating PG, which can be afterwards easily removed to release the free amine. The screening of different disaccharide donors revealed that the di-4,6-*O*-acetylated GalNTFA gave the desired β-selectivity. However, the formation of a stable oxazoline side-product during the glycosylation of bigger and less reactive acceptors limited this approach. Replacement of TFA with TCA and use of Bn groups instead of the electron withdrawing esters limited the formation of the oxazoline side-product. Iterative couplings of dimer **179** allowed for the synthesis of the protected 24mer (Scheme 23). The cleavage of the Lev groups liberated the hydroxy groups that were sulfated using $SO_3{\cdot}NEt_3$. Different methods were attempted for the removal of the TCA groups, which proved to be very stable. Finally, a concentrated ammonia solution permitted the cleavage of the twelve TCA moieties to give compound **181**, after hydrogenolysis.

A total of 15 CS oligosaccharides with different sulfation patterns, ranging from trisaccharides to nonasaccharides, were enzymatically synthesized to investigate their biological function [422]. The glycosyl transferase KfoC [423], extracted from the *E. coli* K4 strain, permitted to transfer both UDP-GalNAc and UDP-GlcA. The backbone could be prepared in a gram scale, thanks to the UDP-sugars obtained from cheap starting materials. This approach proved to be highly divergent, because KfoC tolerated the unnatural substrate GalNTFA, which could be chemically transformed to either an amine or an azide for further functionalization. A collection of well-defined oligosaccharides with natural and unnatural sulfation patterns were produced on multi-milligram scales.

Hyaluronic acid (HA) is the only non-sulfated GAG and is composed of alternating GlcA and GlcNAc residues connected through β(1–3) and β(1–4) glycosidic linkages, respectively (Figure 16A). HA is a major component of the extracellular matrix and is involved in many essential biological processes [424] such as cell adhesion, cell migration, and wound healing. Its mode of action is length-dependent; thus much effort has been put to obtain defined hyaluronans of different lengths. The low reactivity of the GlcA as glycosyl donor is the major synthetic challenge, generally overcome by the use of the more reactive Glc donor followed by a post-glycosylation oxidation to convert it to GlcA. Issues associated to GlcNAc concern the protection of the amino group: TCA, commonly used to direct the formation of the β-linkages through participation, often led



Scheme 22: A) Chemoenzymatic synthesis of heparin structures, using different types of UDP activated natural and unnatural monosaccharides. The steps follow the in vivo biosynthesis of such compounds. B) Selective epimerization of hexasaccharides **173**, **174**, and **175** revealed how single-site methylation can affect the function of C5-epi.



Scheme 23: Synthesis of the longest synthetic CS chain **181** (24mer) using donor **179** and acceptor **180** in an iterative approach.

to the formation of less reactive oxazolines. The use of TMSOTf suppressed the formation of this side product and allowed for the synthesis of a 10mer in moderate yields [425].

A collection of hyaluronans, ranging from trimers to 15mer, has been synthesized in an automated fashion on a solid-support [426]. Disaccharide **182** was prepared in a multigram scale from compound **183**. The C-4 and C-6 hydroxy groups of GlcNAc were masked as silyl ethers, providing ketals with excellent stability to acidic conditions. A first glycosylation with monomer **183** ensured high yield of the first coupling to the solid support. Iterative couplings with dimer **182** gave the protected hyaluronans with well-defined lengths that were liberated from the solid support and subjected to global deprotection to give **184a–c** (Scheme 24).

HA oligomers were prepared chemoenzymatically, using PmHAS, a unique class of bacterial enzymes that catalyze the addition of both UDP-GlcNAc and UDP-GlcA monosaccharides [427]. Short oligomers (2-4mers) were obtained after stepwise enzymatic couplings, controlling the acceptor/donor molar ratio. These oligomers served as synthons for the one-pot polymerization. HA polymers formed from short length acceptors displayed a very narrow MW distribution, as confirmed by multi-angle light scattering experiments. The same strategy was applied for the synthesis of homogeneous chondroitin polymers and other derivatives [428].

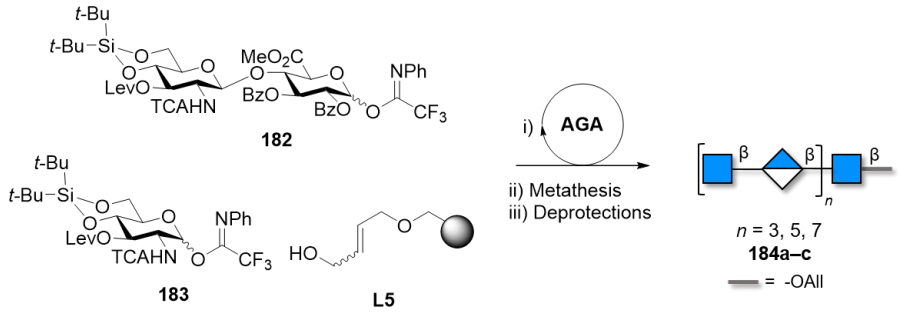
Keratan sulfate (KS) consists of a *N*-acetyllactosamine backbone (Figure 16) [429]. Different types of KS are present in the cornea, cartilage, and brain, named KS I, KS II and KS III, respectively [430]. Despite some encouraging results, the synthesis of long KS is, to date, not reported. A chemoenzymatic approach allowed for the step-by-step elongations of the backbone, but remained limited to tetrasaccharides [431]. Hexasaccharides with different sulfation pattern were obtained by AGA [432]. The low reactivity of the donor and the acceptor as the chain length increases has limited the formation of longer structures.

Overall, GAGs with well-defined composition, patterns and lengths are needed to unlock the "sulfation code" and establish structure–function correlations. Recent advances in chemical and chemoenzymatic synthesis permitted the preparation of impressive targets. Still, most procedures are lengthy and low yielding, suffering from low reactivity or poor selectivity as the polysaccharide chain grows. New automated procedures as well as highly selective enzymatic transformations should be implemented to provide valuable alternatives to naturally sourced GAGs.

Conclusion

Exploitation of polysaccharides has always relied on mixtures of compounds extracted from natural sources. Much effort has been put to understand how sequence, length, and substitution pattern affect polysaccharides' biological and material properties [93,221,350]. Therefore, well-defined polysaccharide samples become essential probes to establish structure–property correlations and for reproducible biological studies [93,221,350]. Polysaccharides with well-defined chemical structures can be prepared synthetically following three main approaches: i) enzymatic methods, ii) polymerization, and iii) chemical synthesis. These approaches are complementary to each other, offering advantages and limitations. Thus, in most cases, the choice of the more suitable methods depends on the desired application.

Enzymatic and chemoenzymatic methods showed enormous potential for the synthesis of some classes of polysaccharides (i.e., GAGs). The main advantages are the simple synthetic protocols (no PGs required) and the high regio- and stereoselectivity, typical of enzymes. In contrast, the high specificity of the enzymes hampers the introduction of unnatural moieties and limits the scope of these methods. To date, not all glycosidic linkages are accessible and repetitive polymers are often ob-



Scheme 24: AGA of a collection of HA with different lengths. The AGA cycle includes coupling (TfOH) and Lev deprotection (hydrazine).

tained as mixtures with a non-uniform dispersion of MW. The combination of enzymatic methods with chemical strategies (i.e., chemoenzymatic methods) offers a valuable alternative to generate precision polysaccharides [399]. Synthetically produced oligomers can be enzymatically polymerized to obtain artificial polymers with well-defined branching pattern [7]. Being able to control the polysaccharide length remains the next challenge. The inspiration could come from length-controlled biosynthetic pathways [351,354,355].

Polymerization approaches allowed growing large synthetic polysaccharides in short time and are easily scalable. However, only few types of glycosidic linkages are accessible and mixtures of different chain lengths are often generated. Recently reported methods for polymerization in confined space could improve the control over the chain length [433-435].

Chemical synthesis enabled the preparation of well-defined polysaccharides, but is labor-intensive, requiring several protected monosaccharide BBs and, to date, it suffered from poor scalability. Recently achieved total syntheses (i.e., 92mer [385] and 128mer [325]) showed that long and well-defined polysaccharides could be accessed. With automated platforms, long polysaccharides could be obtained routinely (i.e., 100mer and 151mer [278]), considerably reducing the lengthy synthetic protocols traditionally needed for solution phase methods. Still, only some classes of polysaccharides have been synthesized, often relying on the relatively easy installation of 1,2-*trans* glycosidic bonds. In contrast, the formation of multiple 1,2-*cis* glycosidic bonds remains highly challenging. New highly selective methods have been developed [167,178,285], however, only few proved to be applicable to the synthesis of long polysaccharides. Additionally, the low reactivity of particular BBs (e.g., uronic acids for the synthesis of GAGs) hampered the establishment of efficient synthetic protocols. A major limitation encountered in many reports of polysaccharide total synthesis is the decreased reactivity of large donors and acceptors. This issue is, to date, poorly predictable, due to the little knowledge on the conformation of protected glycans. Computational methods are expected to help the understanding of the reactivity for such complex molecules. While chemical ligation protocols enabled the total synthesis of proteins [436], similar methods are still lacking for polysaccharides and fragment coupling often requires broad screenings of LGs, solvents, and activation systems.

Aggregation is another major bottleneck that can drastically decrease the yield of polysaccharide synthesis and can occur either at the fully protected stage, during an intermediate stage [156,157] (i.e., semiprotected stage) or at the final deprotected stage [93,344].

Upon assembly of the protected polysaccharide target, either by polymerization or chemical synthesis, the removal of the PGs often proved to be challenging. Aggregation [93,156,157,437], degradation (both during methanolysis [93] and hydrogenolysis [294,325,326]), substituent migration [322,438] or cleavage are among the most common issues encountered. The development of better PGs that can be removed quantitatively is highly desirable. Particular effort should be put towards the development of novel N-PGs considering the many drawbacks of the currently employed ones [251,261]. Novel PGs [439] and more suitable solvent systems [440] could alleviate some of these problems.

The purification and characterization of long polysaccharides poses an additional challenge, especially for ionic polysaccharides [398,441]. As the size of synthetic polysaccharides approaches the size of macromolecules, the implementation of novel analytical and purifications techniques becomes necessary [283].

Overall, structural precision has become an important goal in polymer science as it is crucial to achieve novel properties or to fully understand complex architectures [442,443]. Automated techniques and solid-phase methods have become popular to generate polymers with full control over the sequence, length, and substitution [444,445]. These approaches, despite being time consuming and in most cases not yet scalable, represent the only amenable way to obtain structure–property correlations. Oligomers able to maintain the properties of longer polymeric structures could become a valuable target to fill the gap between small molecule and polymer science [446]. The same trend is true for polysaccharides. Well-defined polysaccharides could become essentials in biology where batch-to-batch reproducibility is imperative. Oligosaccharides with controlled lengths will be required to induce particular biological responses and automated techniques could grant access to collection of pure compounds for screening. Full control on the polysaccharide length and sequence will also be key to control the aggregation of these compounds and create nanomaterials with defined dimensions [447].

Funding

We thank the Max Planck Society, the MPG-FhG Cooperation Project Glyco3Dysplay and the German Federal Ministry of Education and Research (BMBF, grant number 13XP5114) for generous financial support.

ORCID® iDs

Giulio Fittolani - https://orcid.org/0000-0001-6201-3454
Denisa Vargová - https://orcid.org/0000-0001-9923-7080
Manishkumar A. Chaube - https://orcid.org/0000-0001-9027-5275
Martina Delbianco - https://orcid.org/0000-0002-4580-9597

References

1. Varki, A.; Cummings, R. D.; Esko, J. D.; Stanley, P.; Hart, G. W.; Aebi, M.; Darvill, A. G.; Kinoshita, T.; Packer, N. H.; Prestegard, J. H.; Schnaar, R. L.; Seeberger, P. H. *Essentials of Glycobiology,* 3rd ed.; Cold Spring Harbor Laboratory Press: Cold Spring Harbor, NY, USA, 2017.
2. de Moura, F. A.; Macagnan, F. T.; da Silva, L. P. *Int. J. Food Sci. Technol.* **2015,** *50,* 275–281. doi:10.1111/ijfs.12681
3. Verendel, J. J.; Church, T. L.; Andersson, P. G. *Synthesis* **2011,** 1649–1677. doi:10.1055/s-0030-1260008
4. Guerrini, M.; Beccati, D.; Shriver, Z.; Naggi, A.; Viswanathan, K.; Bisio, A.; Capila, I.; Lansing, J. C.; Guglieri, S.; Fraser, B.; Al-Hakim, A.; Gunay, N. S.; Zhang, Z.; Robinson, L.; Buhse, L.; Nasr, M.; Woodcock, J.; Langer, R.; Venkataraman, G.; Linhardt, R. J.; Casu, B.; Torri, G.; Sasisekharan, R. *Nat. Biotechnol.* **2008,** *26,* 669–675. doi:10.1038/nbt1407
5. Anggara, K.; Zhu, Y.; Delbianco, M.; Rauschenbach, S.; Abb, S.; Seeberger, P. H.; Kern, K. *J. Am. Chem. Soc.* **2020,** *142,* 21420–21427. doi:10.1021/jacs.0c09933
6. Wu, X.; Delbianco, M.; Anggara, K.; Michnowicz, T.; Pardo-Vargas, A.; Bharate, P.; Sen, S.; Pristl, M.; Rauschenbach, S.; Schlickum, U.; Abb, S.; Seeberger, P. H.; Kern, K. *Nature* **2020,** *582,* 375–378. doi:10.1038/s41586-020-2362-1
7. Senf, D.; Ruprecht, C.; Kishani, S.; Matic, A.; Toriz, G.; Gatenholm, P.; Wågberg, L.; Pfrengle, F. *Angew. Chem., Int. Ed.* **2018,** *57,* 11987–11992. doi:10.1002/anie.201806871
8. Kittle, J. D.; Qian, C.; Edgar, E.; Roman, M.; Esker, A. R. *ACS Omega* **2018,** *3,* 14004–14012. doi:10.1021/acsomega.8b01750
9. Zhang, Q.; Gimeno, A.; Santana, D.; Wang, Z.; Valdés-Balbin, Y.; Rodríguez-Noda, L. M.; Hansen, T.; Kong, L.; Shen, M.; Overkleeft, H. S.; Vérez-Bencomo, V.; van der Marel, G. A.; Jiménez-Barbero, J.; Chiodo, F.; Codée, J. D. C. *ACS Cent. Sci.* **2019,** *5,* 1407–1416. doi:10.1021/acscentsci.9b00454
10. Armstrong, Z.; Withers, S. G. *Biopolymers* **2013,** *99,* 666–674. doi:10.1002/bip.22335
11. Smith, P. J.; Ortiz-Soto, M. E.; Roth, C.; Barnes, W. J.; Seibel, J.; Urbanowicz, B. R.; Pfrengle, F. *ACS Sustainable Chem. Eng.* **2020,** *8,* 11853–11871. doi:10.1021/acssuschemeng.0c03622
12. Perugino, G.; Cobucci-Ponzano, B.; Rossi, M.; Moracci, M. *Adv. Synth. Catal.* **2005,** *347,* 941–950. doi:10.1002/adsc.200505070
13. Kobayashi, S.; Uyama, H.; Kadokawa, J., Eds. *Enzymatic Polymerization towards Green Polymer Chemistry;* Green Chemistry and Sustainable Technology; Springer International Publishing: Singapore, 2019. doi:10.1007/978-981-13-3813-7
14. Faijes, M.; Planas, A. *Carbohydr. Res.* **2007,** *342,* 1581–1594. doi:10.1016/j.carres.2007.06.015
15. Shoda, S.-i.; Uyama, H.; Kadokawa, J.-i.; Kimura, S.; Kobayashi, S. *Chem. Rev.* **2016,** *116,* 2307–2413. doi:10.1021/acs.chemrev.5b00472
16. Kobayashi, S.; Makino, A. *Chem. Rev.* **2009,** *109,* 5288–5353. doi:10.1021/cr900165z
17. Kadokawa, J.-i. *Chem. Rev.* **2011,** *111,* 4308–4345. doi:10.1021/cr100285v
18. Xiao, R.; Grinstaff, M. W. *Prog. Polym. Sci.* **2017,** *74,* 78–116. doi:10.1016/j.progpolymsci.2017.07.009
19. Mackenzie, L. F.; Wang, Q.; Warren, R. A. J.; Withers, S. G. *J. Am. Chem. Soc.* **1998,** *120,* 5583–5584. doi:10.1021/ja980833d
20. Danby, P. M.; Withers, S. G. *ACS Chem. Biol.* **2016,** *11,* 1784–1794. doi:10.1021/acschembio.6b00340
21. Hayes, M.; Pietruszka, J. *Molecules* **2017,** *22,* 1434. doi:10.3390/molecules22091434
22. Cobucci-Ponzano, B.; Moracci, M. *Nat. Prod. Rep.* **2012,** *29,* 697. doi:10.1039/c2np20032e
23. Wang, L.-X.; Huang, W. *Curr. Opin. Chem. Biol.* **2009,** *13,* 592–600. doi:10.1016/j.cbpa.2009.08.014
24. Adelwöhrer, C.; Takano, T.; Nakatsubo, F.; Rosenau, T. *Biomacromolecules* **2009,** *10,* 2817–2822. doi:10.1021/bm9006612
25. Tokatly, A. I.; Vinnitskiy, D. Z.; Ustuzhanina, N. E.; Nifantiev, N. E. *Russ. J. Bioorg. Chem.* **2021,** *47,* 53–70. doi:10.1134/s1068162021010258
26. Kaeothip, S.; Demchenko, A. V. *Carbohydr. Res.* **2011,** *346,* 1371–1388. doi:10.1016/j.carres.2011.05.004
27. Jeanneret, R. A.; Johnson, S. E.; Galan, M. C. *J. Org. Chem.* **2020**. doi:10.1021/acs.joc.0c02045
28. Pardo-Vargas, A.; Delbianco, M.; Seeberger, P. H. *Curr. Opin. Chem. Biol.* **2018,** *46,* 48–55. doi:10.1016/j.cbpa.2018.04.007
29. Panza, M.; Pistorio, S. G.; Stine, K. J.; Demchenko, A. V. *Chem. Rev.* **2018,** *118,* 8105–8150. doi:10.1021/acs.chemrev.8b00051
30. Hsu, C.-H.; Hung, S.-C.; Wu, C.-Y.; Wong, C.-H. *Angew. Chem., Int. Ed.* **2011,** *50,* 11872–11923. doi:10.1002/anie.201100125
31. Panza, M.; Stine, K. J.; Demchenko, A. V. *Chem. Commun.* **2020,** *56,* 1333–1336. doi:10.1039/c9cc08876h
32. Seeberger, P. H. *Acc. Chem. Res.* **2015,** *48,* 1450–1463. doi:10.1021/ar5004362
33. Chang, C.-W.; Lin, M.-H.; Chan, C.-K.; Su, K.-Y.; Wu, C.-H.; Lo, W.-C.; Lam, S.; Cheng, Y.-T.; Liao, P.-H.; Wong, C.-H.; Wang, C.-C. *Angew. Chem., Int. Ed.* **2021,** *60,* 12413–12423. doi:10.1002/anie.202013909
34. van der Vorm, S.; Hansen, T.; Overkleeft, H. S.; van der Marel, G. A.; Codée, J. D. C. *Chem. Sci.* **2017,** *8,* 1867–1875. doi:10.1039/c6sc04638j
35. Crich, D. *J. Am. Chem. Soc.* **2021,** *143,* 17–34. doi:10.1021/jacs.0c11106
36. Fraser-Reid, B.; Cristóbal López, J., Eds. *Reactivity Tuning in Oligosaccharide Assembly;* Topics in Current Chemistry, Vol. 301; Springer: Berlin, Heidelberg, 2011. doi:10.1007/978-3-642-20914-7
37. Hettikankanamalage, A. A.; Lassfolk, R.; Ekholm, F. S.; Leino, R.; Crich, D. *Chem. Rev.* **2020,** *120,* 7104–7151. doi:10.1021/acs.chemrev.0c00243
38. Matsuzaki, Y.; Ito, Y.; Nakahara, Y.; Ogawa, T. *Tetrahedron Lett.* **1993,** *34,* 1061–1064. doi:10.1016/s0040-4039(00)77492-2
39. Petitou, M.; Duchaussoy, P.; Driguez, P.-A.; Hérault, J.-P.; Lormeau, J.-C.; Herbert, J.-M. *Bioorg. Med. Chem. Lett.* **1999,** *9,* 1155–1160. doi:10.1016/s0960-894x(99)00155-9
40. Pozsgay, V. *Tetrahedron: Asymmetry* **2000,** *11,* 151–172. doi:10.1016/s0957-4166(99)00553-4
41. Varki, A.; Cummings, R. D.; Aebi, M.; Packer, N. H.; Seeberger, P. H.; Esko, J. D.; Stanley, P.; Hart, G.; Darvill, A.; Kinoshita, T.; Prestegard, J. J.; Schnaar, R. L.; Freeze, H. H.; Marth, J. D.; Bertozzi, C. R.; Etzler, M. E.; Frank, M.; Vliegenthart, J. F.; Lütteke, T.; Perez, S.; Bolton, E.; Rudd, P.; Paulson, J.; Kanehisa, M.; Toukach, P.; Aoki-Kinoshita, K. F.; Dell, A.; Narimatsu, H.; York, W.; Taniguchi, N.; Kornfeld, S. *Glycobiology* **2015,** *25,* 1323–1324. doi:10.1093/glycob/cwv091

42. Rojas, O. J. In *Cellulose Chemistry and Properties: Fibers, Nanocelluloses and Advanced Materials;* Rojas, O. J., Ed.; Advances in Polymer Science, Vol. 271; Springer International Publishing: Cham, Switzerland, 2016. doi:10.1007/978-3-319-26015-0
43. O'Sullivan, A. C. *Cellulose* **1997,** *4,* 173–207. doi:10.1023/a:1018431705579
44. Atalla, R. H. *Science* **1998,** *282,* 591. doi:10.1126/science.282.5389.591a
45. Delmer, D. P. *Annu. Rev. Plant Physiol. Plant Mol. Biol.* **1999,** *50,* 245–276. doi:10.1146/annurev.arplant.50.1.245
46. Brown, R. M., Jr. *J. Macromol. Sci., Part A: Pure Appl. Chem.* **1996,** *33,* 1345–1373. doi:10.1080/10601329608014912
47. Rajinipriya, M.; Nagalakshmaiah, M.; Robert, M.; Elkoun, S. *ACS Sustainable Chem. Eng.* **2018,** *6,* 2807–2828. doi:10.1021/acssuschemeng.7b03437
48. Klemm, D.; Kramer, F.; Moritz, S.; Lindström, T.; Ankerfors, M.; Gray, D.; Dorris, A. *Angew. Chem., Int. Ed.* **2011,** *50,* 5438–5466. doi:10.1002/anie.201001273
49. Habibi, Y.; Lucia, L. A.; Rojas, O. J. *Chem. Rev.* **2010,** *110,* 3479–3500. doi:10.1021/cr900339w
50. Moon, R. J.; Martini, A.; Nairn, J.; Simonsen, J.; Youngblood, J. *Chem. Soc. Rev.* **2011,** *40,* 3941–3994. doi:10.1039/c0cs00108b
51. Thomas, B.; Raj, M. C.; B, A. K.; H, R. M.; Joy, J.; Moores, A.; Drisko, G. L.; Sanchez, C. *Chem. Rev.* **2018,** *118,* 11575–11625. doi:10.1021/acs.chemrev.7b00627
52. Schurz, J. *Prog. Polym. Sci.* **1999,** *24,* 481–483. doi:10.1016/s0079-6700(99)00011-8
53. Li, T.; Chen, C.; Brozena, A. H.; Zhu, J. Y.; Xu, L.; Driemeier, C.; Dai, J.; Rojas, O. J.; Isogai, A.; Wågberg, L.; Hu, L. *Nature* **2021,** *590,* 47–56. doi:10.1038/s41586-020-03167-7
54. Serizawa, T.; Fukaya, Y.; Sawada, T. *Polym. J.* **2018,** *50,* 799–804. doi:10.1038/s41428-018-0057-3
55. Burchard, W. *Cellulose* **2003,** *10,* 213–225. doi:10.1023/a:1025160620576
56. Potthast, A.; Rosenau, T.; Buchner, R.; Röder, T.; Ebner, G.; Bruglachner, H.; Sixta, H.; Kosma, P. *Cellulose* **2002,** *9,* 41–53. doi:10.1023/a:1015811712657
57. Kostag, M.; Gericke, M.; Heinze, T.; El Seoud, O. A. *Cellulose* **2019,** *26,* 139–184. doi:10.1007/s10570-018-2198-0
58. Kobayashi, S. *J. Polym. Sci., Part A: Polym. Chem.* **2005,** *43,* 693–710. doi:10.1002/pola.20662
59. Billès, E.; Coma, V.; Peruch, F.; Grelier, S. *Polym. Int.* **2017,** *66,* 1227–1236. doi:10.1002/pi.5398
60. Nidetzky, B.; Zhong, C. *Biotechnol. Adv.* **2020,** 107633. doi:10.1016/j.biotechadv.2020.107633
61. Kobayashi, S.; Kashiwa, K.; Kawasaki, T.; Shoda, S.-i. *J. Am. Chem. Soc.* **1991,** *113,* 3079–3084. doi:10.1021/ja00008a042
62. Hiraishi, M.; Igarashi, K.; Kimura, S.; Wada, M.; Kitaoka, M.; Samejima, M. *Carbohydr. Res.* **2009,** *344,* 2468–2473. doi:10.1016/j.carres.2009.10.002
63. Hattori, T.; Ogata, M.; Kameshima, Y.; Totani, K.; Nikaido, M.; Nakamura, T.; Koshino, H.; Usui, T. *Carbohydr. Res.* **2012,** *353,* 22–26. doi:10.1016/j.carres.2012.03.018
64. Lee, J. H.; Brown, R. M.; Kuga, S.; Shoda, S.-i.; Kobayashi, S. *Proc. Natl. Acad. Sci. U. S. A.* **1994,** *91,* 7425–7429. doi:10.1073/pnas.91.16.7425
65. Pylkkänen, R.; Mohammadi, P.; Arola, S.; de Ruijter, J. C.; Sunagawa, N.; Igarashi, K.; Penttilä, M. *Biomacromolecules* **2020,** *21,* 4355–4364. doi:10.1021/acs.biomac.0c01162
66. Hata, Y.; Sawada, T.; Marubayashi, H.; Nojima, S.; Serizawa, T. *Langmuir* **2019,** *35,* 7026–7034. doi:10.1021/acs.langmuir.9b00850
67. Yataka, Y.; Sawada, T.; Serizawa, T. *Langmuir* **2016,** *32,* 10120–10125. doi:10.1021/acs.langmuir.6b02679
68. Serizawa, T.; Fukaya, Y.; Sawada, T. *Langmuir* **2017,** *33,* 13415–13422. doi:10.1021/acs.langmuir.7b03653
69. Hata, Y.; Kojima, T.; Koizumi, T.; Okura, H.; Sakai, T.; Sawada, T.; Serizawa, T. *ACS Macro Lett.* **2017,** *6,* 165–170. doi:10.1021/acsmacrolett.6b00848
70. Hashimoto, T.; Tanaka, H.; Koizumi, S.; Kurosaki, K.; Ohmae, M.; Kobayashi, S. *Biomacromolecules* **2006,** *7,* 2479–2482. doi:10.1021/bm0605255
71. Tanaka, H.; Koizumi, S.; Hashimoto, T.; Kurosaki, K.; Kobayashi, S. *Macromolecules* **2007,** *40,* 6304–6315. doi:10.1021/ma070699u
72. Egusa, S.; Kitaoka, T.; Goto, M.; Wariishi, H. *Angew. Chem., Int. Ed.* **2007,** *46,* 2063–2065. doi:10.1002/anie.200603981
73. Egusa, S.; Kitaoka, T.; Igarashi, K.; Samejima, M.; Goto, M.; Wariishi, H. *J. Mol. Catal. B: Enzym.* **2010,** *67,* 225–230. doi:10.1016/j.molcatb.2010.08.010
74. Egusa, S.; Goto, M.; Kitaoka, T. *Biomacromolecules* **2012,** *13,* 2716–2722. doi:10.1021/bm3006775
75. Nakamura, I.; Makino, A.; Sugiyama, J.; Ohmae, M.; Kimura, S. *Int. J. Biol. Macromol.* **2008,** *43,* 226–231. doi:10.1016/j.ijbiomac.2008.05.007
76. Nakamura, I.; Makino, A.; Horikawa, Y.; Sugiyama, J.; Ohmae, M.; Kimura, S. *Chem. Commun.* **2011,** *47,* 10127–10129. doi:10.1039/c1cc14202j
77. Nakamura, I.; Horikawa, Y.; Makino, A.; Sugiyama, J.; Kimura, S. *Biomacromolecules* **2011,** *12,* 785–790. doi:10.1021/bm101394j
78. Andrade, P.; Muñoz-García, J. C.; Pergolizzi, G.; Gabrielli, V.; Nepogodiev, S. A.; Iuga, D.; Fábián, L.; Nigmatullin, R.; Johns, M. A.; Harniman, R.; Eichhorn, S. J.; Angulo, J.; Khimyak, Y. Z.; Field, R. A. *Chem. – Eur. J.* **2021,** *27,* 1374–1382. doi:10.1002/chem.202003604
79. Serizawa, T.; Kato, M.; Okura, H.; Sawada, T.; Wada, M. *Polym. J.* **2016,** *48,* 539–544. doi:10.1038/pj.2015.125
80. Fujita, M.; Shoda, S.-i.; Kobayashi, S. *J. Am. Chem. Soc.* **1998,** *120,* 6411–6412. doi:10.1021/ja980893j
81. Kobayashi, S.; Makino, A.; Matsumoto, H.; Kunii, S.; Ohmae, M.; Kiyosada, T.; Makiguchi, K.; Matsumoto, A.; Horie, M.; Shoda, S.-I. *Biomacromolecules* **2006,** *7,* 1644–1656. doi:10.1021/bm060094q
82. Codera, V.; Edgar, K. J.; Faijes, M.; Planas, A. *Biomacromolecules* **2016,** *17,* 1272–1279. doi:10.1021/acs.biomac.5b01453
83. Nakatsubo, F.; Kamitakahara, H.; Hori, M. *J. Am. Chem. Soc.* **1996,** *118,* 1677–1681. doi:10.1021/ja953286u
84. Kamitakahara, H.; Hori, M.; Nakatsubo, F. *Macromolecules* **1996,** *29,* 6126–6131. doi:10.1021/ma960488h
85. Hori, M.; Nakatsubo, F. *Macromolecules* **2001,** *34,* 2476–2481. doi:10.1021/ma001652a
86. Yagura, T.; Ikegami, W.; Kamitakahara, H.; Takano, T. *Cellulose* **2020,** *27,* 9755–9766. doi:10.1007/s10570-020-03512-z
87. Kamitakahara, H.; Funakoshi, T.; Nakai, S.; Takano, T.; Nakatsubo, F. *Cellulose* **2009,** *16,* 1179–1185. doi:10.1007/s10570-009-9339-4
88. Kamitakahara, H.; Funakoshi, T.; Takano, T.; Nakatsubo, F. *Cellulose* **2009,** *16,* 1167–1178. doi:10.1007/s10570-009-9332-y
89. Sakakibara, K.; Takano, T.; Nakatsubo, F. *Cellulose* **2011,** *18,* 105–115. doi:10.1007/s10570-010-9461-3
90. Karakawa, M.; Kamitakahara, H.; Takano, T.; Nakatsubo, F. *Biomacromolecules* **2002,** *3,* 538–546. doi:10.1021/bm015656e
91. Nishimura, T.; Nakatsubo, F. *Cellulose* **1997,** *4,* 109–130. doi:10.1023/a:1018423503762

92. Nishimura, T.; Nakatsubo, F. *Tetrahedron Lett.* **1996,** *37,* 9215–9218. doi:10.1016/s0040-4039(96)02186-7
93. Yu, Y.; Tyrikos-Ergas, T.; Zhu, Y.; Fittolani, G.; Bordoni, V.; Singhal, A.; Fair, R. J.; Grafmüller, A.; Seeberger, P. H.; Delbianco, M. *Angew. Chem., Int. Ed.* **2019,** *58,* 13127–13132. doi:10.1002/anie.201906577
94. Murty, K. V. S. N.; Xie, T.; Bernet, B.; Vasella, A. *Helv. Chim. Acta* **2006,** *89,* 675–730. doi:10.1002/hlca.200690068
95. Hayashi, T.; Marsden, M. P. F.; Delmer, D. P. *Plant Physiol.* **1987,** *83,* 384–389. doi:10.1104/pp.83.2.384
96. Kuki, H.; Yokoyama, R.; Kuroha, T.; Nishitani, K. *Plants* **2020,** *9,* 629. doi:10.3390/plants9050629
97. Culbertson, A. T.; Ehrlich, J. J.; Choe, J.-Y.; Honzatko, R. B.; Zabotina, O. A. *Proc. Natl. Acad. Sci. U. S. A.* **2018,** *115,* 6064–6069. doi:10.1073/pnas.1801105115
98. Urbanowicz, B. R.; Bharadwaj, V. S.; Alahuhta, M.; Peña, M. J.; Lunin, V. V.; Bomble, Y. J.; Wang, S.; Yang, J.-Y.; Tuomivaara, S. T.; Himmel, M. E.; Moremen, K. W.; York, W. S.; Crowley, M. F. *Plant J.* **2017,** *91,* 931–949. doi:10.1111/tpj.13628
99. Kinnaert, C.; Daugaard, M.; Nami, F.; Clausen, M. H. *Chem. Rev.* **2017,** *117,* 11337–11405. doi:10.1021/acs.chemrev.7b00162
100. Fry, S. C.; York, W. S.; Albersheim, P.; Darvill, A.; Hayashi, T.; Joseleau, J.-P.; Kato, Y.; Lorences, E. P.; Maclachlan, G. A.; McNeil, M.; Mort, A. J.; Grant Reid, J. S.; Seitz, H. U.; Selvendran, R. R.; Voragen, A. G. J.; White, A. R. *Physiol. Plant.* **1993,** *89,* 1–3. doi:10.1111/j.1399-3054.1993.tb01778.x
101. Sakai, K.; Nakahara, Y.; Ogawa, T. *Tetrahedron Lett.* **1990,** *31,* 3035–3038. doi:10.1016/s0040-4039(00)89019-x
102. Bartetzko, M. P.; Pfrengle, F. *ChemBioChem* **2019,** *20,* 877–885. doi:10.1002/cbic.201800641
103. Dallabernardina, P.; Schuhmacher, F.; Seeberger, P. H.; Pfrengle, F. *Org. Biomol. Chem.* **2016,** *14,* 309–313. doi:10.1039/c5ob02226f
104. Dallabernardina, P.; Ruprecht, C.; Smith, P. J.; Hahn, M. G.; Urbanowicz, B. R.; Pfrengle, F. *Org. Biomol. Chem.* **2017,** *15,* 9996–10000. doi:10.1039/c7ob02605f
105. Fauré, R.; Saura-Valls, M.; Brumer, H.; Planas, A.; Cottaz, S.; Driguez, H. *J. Org. Chem.* **2006,** *71,* 5151–5161. doi:10.1021/jo0525682
106. Fauré, R.; Cavalier, D.; Keegstra, K.; Cottaz, S.; Driguez, H. *Eur. J. Org. Chem.* **2007,** 4313–4319. doi:10.1002/ejoc.200700395
107. Piens, K.; Henriksson, A.-M.; Gullfot, F.; Lopez, M.; Fauré, R.; Ibatullin, F. M.; Teeri, T. T.; Driguez, H.; Brumer, H. *Org. Biomol. Chem.* **2007,** *5,* 3971–3978. doi:10.1039/b714570e
108. Lopez, M.; Fort, S.; Bizot, H.; Buléon, A.; Driguez, H. *Carbohydr. Polym.* **2012,** *88,* 185–193. doi:10.1016/j.carbpol.2011.11.085
109. Gullfot, F.; Ibatullin, F. M.; Sundqvist, G.; Davies, G. J.; Brumer, H. *Biomacromolecules* **2009,** *10,* 1782–1788. doi:10.1021/bm900215p
110. Spadiut, O.; Ibatullin, F. M.; Peart, J.; Gullfot, F.; Martinez-Fleites, C.; Ruda, M.; Xu, C.; Sundqvist, G.; Davies, G. J.; Brumer, H. *J. Am. Chem. Soc.* **2011,** *133,* 10892–10900. doi:10.1021/ja202788q
111. Descroix, K.; Ferrieres, V.; Jamois, F.; Yvin, J.-C.; Plusquellec, D. *Mini-Rev. Med. Chem.* **2006,** *6,* 1341–1349. doi:10.2174/138955706778993058
112. Ogawa, Y.; Noda, K.; Kimura, S.; Kitaoka, M.; Wada, M. *Int. J. Biol. Macromol.* **2014,** *64,* 415–419. doi:10.1016/j.ijbiomac.2013.12.027
113. Elsaidi, H. R. H.; Paszkiewicz, E.; Bundle, D. R. *Carbohydr. Res.* **2015,** *408,* 96–106. doi:10.1016/j.carres.2015.03.007
114. Adamo, R.; Hu, Q.-Y.; Torosantucci, A.; Crotti, S.; Brogioni, G.; Allan, M.; Chiani, P.; Bromuro, C.; Quinn, D.; Tontini, M.; Berti, F. *Chem. Sci.* **2014,** *5,* 4302–4311. doi:10.1039/c4sc01361a
115. Adamo, R.; Tontini, M.; Brogioni, G.; Romano, M. R.; Costantini, G.; Danieli, E.; Proietti, D.; Berti, F.; Costantino, P. *J. Carbohydr. Chem.* **2011,** *30,* 249–280. doi:10.1080/07328303.2011.604453
116. Huang, G.-L.; Mei, X.-Y.; Liu, M.-X. *Carbohydr. Res.* **2005,** *340,* 603–608. doi:10.1016/j.carres.2005.01.015
117. Huang, G.-L.; Mei, X.-Y.; Liu, M.-X.; Liu, T.-C. *Bioorg. Med. Chem. Lett.* **2004,** *14,* 6027–6029. doi:10.1016/j.bmcl.2004.09.076
118. Le Mai Hoang, K.; Pardo-Vargas, A.; Zhu, Y.; Yu, Y.; Loria, M.; Delbianco, M.; Seeberger, P. H. *J. Am. Chem. Soc.* **2019,** *141,* 9079–9086. doi:10.1021/jacs.9b03769
119. Yashunsky, D. V.; Tsvetkov, Y. E.; Nifantiev, N. E. *Carbohydr. Res.* **2016,** *436,* 25–30. doi:10.1016/j.carres.2016.11.005
120. Yang, G.; Kong, F. *Carbohydr. Res.* **2005,** *340,* 39–48. doi:10.1016/j.carres.2004.11.005
121. Zhao, W.; Yang, G.; Kong, F. *Carbohydr. Res.* **2003,** *338,* 2813–2823. doi:10.1016/j.carres.2003.08.003
122. Zeng, Y.; Kong, F. *Carbohydr. Res.* **2003,** *338,* 2359–2366. doi:10.1016/j.carres.2003.08.004
123. Tanaka, H.; Amaya, T.; Takahashi, T. *Tetrahedron Lett.* **2003,** *44,* 3053–3057. doi:10.1016/s0040-4039(03)00553-7
124. Yang, G.; Kong, F. *Synlett* **2000,** 1423–1426. doi:10.1055/s-2000-7646
125. Egusa, K.; Kusumoto, S.; Fukase, K. *Eur. J. Org. Chem.* **2003,** 3435–3445. doi:10.1002/ejoc.200300248
126. Yashunsky, D. V.; Tsvetkov, Y. E.; Grachev, A. A.; Chizhov, A. O.; Nifantiev, N. E. *Carbohydr. Res.* **2016,** *419,* 8–17. doi:10.1016/j.carres.2015.10.012
127. Yang, F.; He, H.; Du, Y.; Lü, M. *Carbohydr. Res.* **2002,** *337,* 1165–1169. doi:10.1016/s0008-6215(02)00122-2
128. Ning, J.; Zhang, W.; Yi, Y.; Yang, G.; Wu, Z.; Yi, J.; Kong, F. *Bioorg. Med. Chem.* **2003,** *11,* 2193–2203. doi:10.1016/s0968-0896(03)00118-4
129. Zeng, Y.; Ning, J.; Kong, F. *Tetrahedron Lett.* **2002,** *43,* 3729–3733. doi:10.1016/s0040-4039(02)00584-1
130. Yu, H.; Williams, D. L.; Ensley, H. E. *Tetrahedron Lett.* **2005,** *46,* 3417–3421. doi:10.1016/j.tetlet.2005.03.099
131. He, H.; Yang, F.; Du, Y. *Carbohydr. Res.* **2002,** *337,* 1673–1678. doi:10.1016/s0008-6215(02)00276-8
132. Takeo, K.; Maki, K.; Wada, Y.; Kitamura, S. *Carbohydr. Res.* **1993,** *245,* 81–96. doi:10.1016/0008-6215(93)80061-i
133. Jamois, F.; Ferrières, V.; Guégan, J.-P.; Yvin, J.-C.; Plusquellec, D.; Vetvicka, V. *Glycobiology* **2005,** *15,* 393–407. doi:10.1093/glycob/cwi020
134. Mo, K.-F.; Li, H.; Mague, J. T.; Ensley, H. E. *Carbohydr. Res.* **2009,** *344,* 439–447. doi:10.1016/j.carres.2008.12.014
135. Liao, G.; Zhou, Z.; Burgula, S.; Liao, J.; Yuan, C.; Wu, Q.; Guo, Z. *Bioconjugate Chem.* **2015,** *26,* 466–476. doi:10.1021/bc500575a
136. Liao, G.; Burgula, S.; Zhou, Z.; Guo, Z. *Eur. J. Org. Chem.* **2015,** 2942–2951. doi:10.1002/ejoc.201500229
137. Tanaka, H.; Kawai, T.; Adachi, Y.; Hanashima, S.; Yamaguchi, Y.; Ohno, N.; Takahashi, T. *Bioorg. Med. Chem.* **2012,** *20,* 3898–3914. doi:10.1016/j.bmc.2012.04.017
138. Tanaka, H.; Kawai, T.; Adachi, Y.; Ohno, N.; Takahashi, T. *Chem. Commun.* **2010,** *46,* 8249–8251. doi:10.1039/c0cc03153d
139. Hamagami, H.; Adachi, Y.; Ohno, N.; Tanaka, H. *Asian J. Org. Chem.* **2019,** *8,* 411–416. doi:10.1002/ajoc.201800726

140. Weishaupt, M. W.; Hahm, H. S.; Geissner, A.; Seeberger, P. H. *Chem. Commun.* **2017,** *53,* 3591–3594. doi:10.1039/c7cc00520b
141. Weishaupt, M. W.; Matthies, S.; Seeberger, P. H. *Chem. – Eur. J.* **2013,** *19,* 12497–12503. doi:10.1002/chem.201204518
142. Plante, O. J.; Palmacci, E. R.; Seeberger, P. H. *Science* **2001,** *291,* 1523–1527. doi:10.1126/science.1057324
143. Dallabernardina, P.; Schuhmacher, F.; Seeberger, P. H.; Pfrengle, F. *Chem. – Eur. J.* **2017,** *23,* 3191–3196. doi:10.1002/chem.201605479
144. Fairweather, J. K.; Hrmova, M.; Rutten, S. J.; Fincher, G. B.; Driguez, H. *Chem. – Eur. J.* **2003,** *9,* 2603–2610. doi:10.1002/chem.200304733
145. Montel, E.; Hrmova, M.; Fincher, G. B.; Driguez, H.; Cottaz, S. *Aust. J. Chem.* **2009,** *62,* 575. doi:10.1071/ch08517
146. Hrmova, M.; Imai, T.; Rutten, S. J.; Fairweather, J. K.; Pelosi, L.; Bulone, V.; Driguez, H.; Fincher, G. B. *J. Biol. Chem.* **2002,** *277,* 30102–30111. doi:10.1074/jbc.m203971200
147. Perez, X.; Faijes, M.; Planas, A. *Biomacromolecules* **2011,** *12,* 494–501. doi:10.1021/bm1013537
148. Yashunsky, D. V.; Karelin, A. A.; Tsvetkov, Y. E.; Nifantiev, N. E. *Carbohydr. Res.* **2018,** *455,* 18–22. doi:10.1016/j.carres.2017.11.001
149. Wang, H.-R.; Li, Z.-L.; Ning, J.; Kong, F.-Z. *Chin. J. Chem.* **2003,** *21,* 944–949. doi:10.1002/cjoc.20030210744
150. Sittel, I.; Tran, A.-T.; Benito-Alifonso, D.; Galan, M. C. *Chem. Commun.* **2013,** *49,* 4217–4219. doi:10.1039/c2cc37164b
151. Manmode, S.; Kato, M.; Ichiyanagi, T.; Nokami, T.; Itoh, T. *Asian J. Org. Chem.* **2018,** *7,* 1802–1805. doi:10.1002/ajoc.201800345
152. Smith, R.; Müller-Bunz, H.; Zhu, X. *Org. Lett.* **2016,** *18,* 3578–3581. doi:10.1021/acs.orglett.6b01572
153. Pistorio, S. G.; Nigudkar, S. S.; Stine, K. J.; Demchenko, A. V. *J. Org. Chem.* **2016,** *81,* 8796–8805. doi:10.1021/acs.joc.6b01439
154. Huang, X.; Huang, L.; Wang, H.; Ye, X.-S. *Angew. Chem., Int. Ed.* **2004,** *43,* 5221–5224. doi:10.1002/anie.200460176
155. Hashihayata, T.; Ikegai, K.; Takeuchi, K.; Jona, H.; Mukaiyama, T. *Bull. Chem. Soc. Jpn.* **2003,** *76,* 1829–1848. doi:10.1246/bcsj.76.1829
156. Yu, Y.; Gim, S.; Kim, D.; Arnon, Z. A.; Gazit, E.; Seeberger, P. H.; Delbianco, M. *J. Am. Chem. Soc.* **2019,** *141,* 4833–4838. doi:10.1021/jacs.8b11882
157. Delbianco, M.; Kononov, A.; Poveda, A.; Yu, Y.; Diercks, T.; Jiménez-Barbero, J.; Seeberger, P. H. *J. Am. Chem. Soc.* **2018,** *140,* 5421–5426. doi:10.1021/jacs.8b00254
158. Yi, Y.; Zhou, Z.; Ning, J.; Kong, F.; Li, J. *Synthesis* **2003,** 0491–0496. doi:10.1055/s-2003-37644
159. Tanaka, H.; Adachi, M.; Tsukamoto, H.; Ikeda, T.; Yamada, H.; Takahashi, T. *Org. Lett.* **2002,** *4,* 4213–4216. doi:10.1021/ol020150+
160. Nicolaou, K. C.; Winssinger, N.; Pastor, J.; DeRoose, F. *J. Am. Chem. Soc.* **1997,** *119,* 449–450. doi:10.1021/ja963482g
161. Yamada, H.; Harada, T.; Takahashi, T. *J. Am. Chem. Soc.* **1994,** *116,* 7919–7920. doi:10.1021/ja00096a068
162. Fügedi, P.; Birberg, W.; Garegg, P. J.; Pilotti, Å. *Carbohydr. Res.* **1987,** *164,* 297–312. doi:10.1016/0008-6215(87)80137-4
163. Ossowski, P.; Pilotti, A.; Garegg, P. J.; Lindberg, B. *J. Biol. Chem.* **1984,** *259,* 11337–11340. doi:10.1016/s0021-9258(18)90866-5
164. Ossowski, P.; Pilotti, Å.; Garegg, P. J.; Lindberg, B. *Angew. Chem., Int. Ed. Engl.* **1983,** *22,* 793–794. doi:10.1002/anie.198307931
165. Ning, J.; Yi, Y.; Kong, F. *Tetrahedron Lett.* **2002,** *43,* 5545–5549. doi:10.1016/s0040-4039(02)01143-7
166. Nicolaou, K. C.; Watanabe, N.; Li, J.; Pastor, J.; Winssinger, N. *Angew. Chem., Int. Ed.* **1998,** *37,* 1559–1561. doi:10.1002/(sici)1521-3773(19980619)37:11<1559::aid-anie1559>3.0.co;2-e
167. Nigudkar, S. S.; Demchenko, A. V. *Chem. Sci.* **2015,** *6,* 2687–2704. doi:10.1039/c5sc00280j
168. Geoghegan, I.; Steinberg, G.; Gurr, S. *Trends Microbiol.* **2017,** *25,* 957–967. doi:10.1016/j.tim.2017.05.015
169. Komarova, B. S.; Orekhova, M. V.; Tsvetkov, Y. E.; Beau, R.; Aimanianda, V.; Latgé, J.-P.; Nifantiev, N. E. *Chem. – Eur. J.* **2015,** *21,* 1029–1035. doi:10.1002/chem.201404770
170. Komarova, B. S.; Tsvetkov, Y. E.; Nifantiev, N. E. *Chem. Rec.* **2016,** *16,* 488–506. doi:10.1002/tcr.201500245
171. Hahm, H. S.; Hurevich, M.; Seeberger, P. H. *Nat. Commun.* **2016,** *7,* 12482. doi:10.1038/ncomms12482
172. Hirooka, M.; Koto, S. *Bull. Chem. Soc. Jpn.* **1998,** *71,* 2893–2902. doi:10.1246/bcsj.71.2893
173. Lam, S. N.; Gervay-Hague, J. *Carbohydr. Res.* **2002,** *337,* 1953–1965. doi:10.1016/s0008-6215(02)00227-6
174. Boltje, T. J.; Kim, J.-H.; Park, J.; Boons, G.-J. *Nat. Chem.* **2010,** *2,* 552–557. doi:10.1038/nchem.663
175. Tomita, S.; Tanaka, M.; Inoue, M.; Inaba, K.; Takahashi, D.; Toshima, K. *J. Org. Chem.* **2020,** *85,* 16254–16262. doi:10.1021/acs.joc.0c02093
176. Tanaka, M.; Nakagawa, A.; Nishi, N.; Iijima, K.; Sawa, R.; Takahashi, D.; Toshima, K. *J. Am. Chem. Soc.* **2018,** *140,* 3644–3651. doi:10.1021/jacs.7b12108
177. Yasomanee, J. P.; Demchenko, A. V. *Angew. Chem., Int. Ed.* **2014,** *53,* 10453–10456. doi:10.1002/anie.201405084
178. Wang, L.; Overkleeft, H. S.; van der Marel, G. A.; Codée, J. D. C. *J. Am. Chem. Soc.* **2018,** *140,* 4632–4638. doi:10.1021/jacs.8b00669
179. Wang, L.; Overkleeft, H. S.; van der Marel, G. A.; Codée, J. D. C. *Eur. J. Org. Chem.* **2019,** 1994–2003. doi:10.1002/ejoc.201800894
180. Wang, L.; Berni, F.; Enotarpi, J.; Overkleeft, H. S.; van der Marel, G.; Codée, J. D. C. *Org. Biomol. Chem.* **2020,** *18,* 2038–2050. doi:10.1039/d0ob00240b
181. Zhang, Y.; He, H.; Chen, Z.; Huang, Y.; Xiang, G.; Li, P.; Yang, X.; Lu, G.; Xiao, G. *Angew. Chem., Int. Ed.* **2021,** *60,* 12597–12606. doi:10.1002/anie.202103826
182. Zhu, Y.; Delbianco, M.; Seeberger, P. H. *J. Am. Chem. Soc.* **2021,** *143,* 9758–9768. doi:10.1021/jacs.1c02188
183. Meppen, M.; Wang, Y.; Cheon, H.-S.; Kishi, Y. *J. Org. Chem.* **2007,** *72,* 1941–1950. doi:10.1021/jo061990v
184. Cheon, H.-S.; Lian, Y.; Kishi, Y. *Org. Lett.* **2007,** *9,* 3327–3329. doi:10.1021/ol071334x
185. Ohdan, K.; Fujii, K.; Yanase, M.; Takaha, T.; Kuriki, T. *Biocatal. Biotransform.* **2006,** *24,* 77–81. doi:10.1080/10242420600598152
186. Nishimura, T.; Akiyoshi, K. *Wiley Interdiscip. Rev.: Nanomed. Nanobiotechnol.* **2017,** *9,* e1423. doi:10.1002/wnan.1423
187. Meng, X.; Pijning, T.; Dobruchowska, J. M.; Yin, H.; Gerwig, G. J.; Dijkhuizen, L. *Sci. Rep.* **2016,** *6,* 35261. doi:10.1038/srep35261
188. Meng, X.; Dobruchowska, J. M.; Gerwig, G. J.; Kamerling, J. P.; Dijkhuizen, L. *Carbohydr. Res.* **2015,** *414,* 85–92. doi:10.1016/j.carres.2015.07.011
189. Timell, T. E. *Adv. Carbohydr. Chem.* **1964,** *19,* 247–302. doi:10.1016/s0096-5332(08)60284-2

190. Thorsheim, K.; Siegbahn, A.; Johnsson, R. E.; Stålbrand, H.; Manner, S.; Widmalm, G.; Ellervik, U. *Carbohydr. Res.* **2015,** *418,* 65–88. doi:10.1016/j.carres.2015.10.004
191. Ebringerová, A.; Heinze, T. *Macromol. Rapid Commun.* **2000,** *21,* 542–556. doi:10.1002/1521-3927(20000601)21:9<542::aid-marc542>3.0.co;2-7
192. Busse-Wicher, M.; Grantham, N. J.; Lyczakowski, J. J.; Nikolovski, N.; Dupree, P. *Biochem. Soc. Trans.* **2016,** *44,* 74–78. doi:10.1042/bst20150183
193. Grantham, N. J.; Wurman-Rodrich, J.; Terrett, O. M.; Lyczakowski, J. J.; Stott, K.; Iuga, D.; Simmons, T. J.; Durand-Tardif, M.; Brown, S. P.; Dupree, R.; Busse-Wicher, M.; Dupree, P. *Nat. Plants (London, U. K.)* **2017,** *3,* 859–865. doi:10.1038/s41477-017-0030-8
194. Santibáñez, L.; Henríquez, C.; Corro-Tejeda, R.; Bernal, S.; Armijo, B.; Salazar, O. *Carbohydr. Polym.* **2021,** *251,* 117118. doi:10.1016/j.carbpol.2020.117118
195. Köhnke, T.; Ostlund, Å.; Brelid, H. *Biomacromolecules* **2011,** *12,* 2633–2641. doi:10.1021/bm200437m
196. Bosmans, T. J.; Stépán, A. M.; Toriz, G.; Renneckar, S.; Karabulut, E.; Wågberg, L.; Gatenholm, P. *Biomacromolecules* **2014,** *15,* 924–930. doi:10.1021/bm4017868
197. Linder, Å.; Bergman, R.; Bodin, A.; Gatenholm, P. *Langmuir* **2003,** *19,* 5072–5077. doi:10.1021/la0341355
198. Timell, T. E. *J. Am. Chem. Soc.* **1959,** *81,* 4989–4994. doi:10.1021/ja01527a054
199. Uryu, T.; Koyama, Y.; Matsuzaki, K. *J. Polym. Sci., Polym. Lett. Ed.* **1979,** *17,* 673–678. doi:10.1002/pol.1979.130171009
200. Uryu, T.; Koyama, Y.; Matsuzaki, K. *Makromol. Chem.* **1984,** *185,* 2099–2107. doi:10.1002/macp.1984.021851005
201. Uryu, T.; Yamanouchi, J.; Hayashi, S.; Tamaki, H.; Matsuzaki, K. *Macromolecules* **1983,** *16,* 320–326. doi:10.1021/ma00236a030
202. Kim, Y.-W.; Fox, D. T.; Hekmat, O.; Kantner, T.; McIntosh, L. P.; Warren, R. A. J.; Withers, S. G. *Org. Biomol. Chem.* **2006,** *4,* 2025. doi:10.1039/b601667g
203. Kobayashi, S.; Wen, X.; Shoda, S.-i. *Macromolecules* **1996,** *29,* 2698–2700. doi:10.1021/ma951552i
204. Ben-David, A.; Bravman, T.; Balazs, Y. S.; Czjzek, M.; Schomburg, D.; Shoham, G.; Shoham, Y. *ChemBioChem* **2007,** *8,* 2145–2151. doi:10.1002/cbic.200700414
205. Takeo, K.; Ohguchi, Y.; Hasegawa, R.; Kitamura, S. *Carbohydr. Res.* **1995,** *278,* 301–313. doi:10.1016/0008-6215(95)00259-6
206. Chen, L.; Kong, F. *Carbohydr. Res.* **2002,** *337,* 2335–2341. doi:10.1016/s0008-6215(02)00285-9
207. Schmidt, D.; Schuhmacher, F.; Geissner, A.; Seeberger, P. H.; Pfrengle, F. *Chem. – Eur. J.* **2015,** *21,* 5709–5713. doi:10.1002/chem.201500065
208. Senf, D.; Ruprecht, C.; de Kruijff, G. H. M.; Simonetti, S. O.; Schuhmacher, F.; Seeberger, P. H.; Pfrengle, F. *Chem. – Eur. J.* **2017,** *23,* 3197–3205. doi:10.1002/chem.201605902
209. Khoushab, F.; Yamabhai, M. *Mar. Drugs* **2010,** *8,* 1988–2012. doi:10.3390/md8071988
210. Kurita, K. *Mar. Biotechnol.* **2006,** *8,* 203–226. doi:10.1007/s10126-005-0097-5
211. Rinaudo, M. *Prog. Polym. Sci.* **2006,** *31,* 603–632. doi:10.1016/j.progpolymsci.2006.06.001
212. Azuma, K.; Izumi, R.; Osaki, T.; Ifuku, S.; Morimoto, M.; Saimoto, H.; Minami, S.; Okamoto, Y. *J. Funct. Biomater.* **2015,** *6,* 104–142. doi:10.3390/jfb6010104
213. Xu, H.; Shen, B.; Qiao, M.; Linhardt, R. J.; Zhang, X. *Carbohydr. Polym.* **2021,** *258,* 117672. doi:10.1016/j.carbpol.2021.117672
214. Shoueir, K. R.; El-Desouky, N.; Rashad, M. M.; Ahmed, M. K.; Janowska, I.; El-Kemary, M. *Int. J. Biol. Macromol.* **2021,** *167,* 1176–1197. doi:10.1016/j.ijbiomac.2020.11.072
215. Bonin, M.; Sreekumar, S.; Cord-Landwehr, S.; Moerschbacher, B. M. *Int. J. Mol. Sci.* **2020,** *21,* 7835. doi:10.3390/ijms21217835
216. Naqvi, S.; Moerschbacher, B. M. *Crit. Rev. Biotechnol.* **2017,** *37,* 11–25. doi:10.3109/07388551.2015.1104289
217. Yang, Y.; Yu, B. *Tetrahedron* **2014,** *70,* 1023–1046. doi:10.1016/j.tet.2013.11.064
218. Wattjes, J.; Sreekumar, S.; Richter, C.; Cord-Landwehr, S.; Singh, R.; El Gueddari, N. E.; Moerschbacher, B. M. *React. Funct. Polym.* **2020,** *151,* 104583. doi:10.1016/j.reactfunctpolym.2020.104583
219. Cord-Landwehr, S.; Richter, C.; Wattjes, J.; Sreekumar, S.; Singh, R.; Basa, S.; El Gueddari, N. E.; Moerschbacher, B. M. *React. Funct. Polym.* **2020,** *151,* 104577. doi:10.1016/j.reactfunctpolym.2020.104577
220. Fuchs, K.; Cardona Gloria, Y.; Wolz, O.-O.; Herster, F.; Sharma, L.; Dillen, C. A.; Täumer, C.; Dickhöfer, S.; Bittner, Z.; Dang, T.-M.; Singh, A.; Haischer, D.; Schlöffel, M. A.; Koymans, K. J.; Sanmuganantham, T.; Krach, M.; Roger, T.; Le Roy, D.; Schilling, N. A.; Frauhammer, F.; Miller, L. S.; Nürnberger, T.; LeibundGut-Landmann, S.; Gust, A. A.; Macek, B.; Frank, M.; Gouttefangeas, C.; Dela Cruz, C. S.; Hartl, D.; Weber, A. N. *EMBO Rep.* **2018,** *19,* e46065. doi:10.15252/embr.201846065
221. Basa, S.; Nampally, M.; Honorato, T.; Das, S. N.; Podile, A. R.; El Gueddari, N. E.; Moerschbacher, B. M. *J. Am. Chem. Soc.* **2020,** *142,* 1975–1986. doi:10.1021/jacs.9b11466
222. Osorio-Madrazo, A.; David, L.; Trombotto, S.; Lucas, J.-M.; Peniche-Covas, C.; Domard, A. *Biomacromolecules* **2010,** *11,* 1376–1386. doi:10.1021/bm1001685
223. Einbu, A.; Grasdalen, H.; Vårum, K. M. *Carbohydr. Res.* **2007,** *342,* 1055–1062. doi:10.1016/j.carres.2007.02.022
224. Einbu, A.; Vårum, K. M. *Biomacromolecules* **2007,** *8,* 309–314. doi:10.1021/bm0608535
225. Vårum, K. *Carbohydr. Polym.* **2001,** *46,* 89–98. doi:10.1016/s0144-8617(00)00288-5
226. Tømmeraas, K.; Vårum, K. M.; Christensen, B. E.; Smidsrød, O. *Carbohydr. Res.* **2001,** *333,* 137–144. doi:10.1016/s0008-6215(01)00130-6
227. Defaye, J.; Gadelle, A.; Pedersen, C. *Carbohydr. Res.* **1994,** *261,* 267–277. doi:10.1016/0008-6215(94)84023-7
228. Capon, B.; Foster, R. L. *J. Chem. Soc. C* **1970,** 1654–1655. doi:10.1039/j39700001654
229. Kidibule, P. E.; Santos-Moriano, P.; Jiménez-Ortega, E.; Ramírez-Escudero, M.; Limón, M. C.; Remacha, M.; Plou, F. J.; Sanz-Aparicio, J.; Fernández-Lobato, M. *Microb. Cell Fact.* **2018,** *17,* 47. doi:10.1186/s12934-018-0895-x
230. Vaaje-Kolstad, G.; Horn, S. J.; Sørlie, M.; Eijsink, V. G. H. *FEBS J.* **2013,** *280,* 3028–3049. doi:10.1111/febs.12181
231. Horn, S. J.; Sorbotten, A.; Synstad, B.; Sikorski, P.; Sorlie, M.; Varum, K. M.; Eijsink, V. G. H. *FEBS J.* **2006,** *273,* 491–503. doi:10.1111/j.1742-4658.2005.05079.x
232. Aam, B. B.; Heggset, E. B.; Norberg, A. L.; Sørlie, M.; Vårum, K. M.; Eijsink, V. G. H. *Mar. Drugs* **2010,** *8,* 1482–1517. doi:10.3390/md8051482

233. Nishimura, S.-I.; Kuzuhara, H.; Takiguchi, Y.; Shimahara, K. *Carbohydr. Res.* **1989,** *194,* 223–231. doi:10.1016/0008-6215(89)85021-9
234. Inaba, T.; OhgushiI, T.; Iga, Y.; Hasegawa, E. *Chem. Pharm. Bull.* **1984,** *32,* 1597–1603. doi:10.1248/cpb.32.1597
235. Barker, S. A.; Foster, A. B.; Stacey, M.; Webber, J. M. *J. Chem. Soc.* **1958,** 2218–2227. doi:10.1039/jr9580002218
236. Despras, G.; Alix, A.; Urban, D.; Vauzeilles, B.; Beau, J.-M. *Angew. Chem., Int. Ed.* **2014,** *53,* 11912–11916. doi:10.1002/anie.201406802
237. Alsina, C.; Faijes, M.; Planas, A. *Carbohydr. Res.* **2019,** *478,* 1–9. doi:10.1016/j.carres.2019.04.001
238. Makino, A.; Ohmae, M.; Kobayashi, S. *Macromol. Biosci.* **2006,** *6,* 862–872. doi:10.1002/mabi.200600128
239. Sakamoto, J.; Sugiyama, J.; Kimura, S.; Imai, T.; Itoh, T.; Watanabe, T.; Kobayashi, S. *Macromolecules* **2000,** *33,* 4155–4160. doi:10.1021/ma000230y
240. Hashimoto, H.; Abe, Y.; Horito, S.; Yoshimura, J. *J. Carbohydr. Chem.* **1989,** *8,* 307–311. doi:10.1080/07328308908048012
241. Crout, D. H. G.; Vic, G. *Curr. Opin. Chem. Biol.* **1998,** *2,* 98–111. doi:10.1016/s1367-5931(98)80041-0
242. Singh, S.; Gallagher, R.; Derrick, P. J.; Crout, D. H. G. *Tetrahedron: Asymmetry* **1995,** *6,* 2803–2810. doi:10.1016/0957-4166(95)00370-5
243. Akiyama, K.; Kawazu, K.; Kobayashi, A. *Carbohydr. Res.* **1995,** *279,* 151–160. doi:10.1016/0008-6215(95)00288-x
244. Purushotham, P.; Podile, A. R. *J. Bacteriol.* **2012,** *194,* 4260–4271. doi:10.1128/jb.06473-11
245. Madhuprakash, J.; Tanneeru, K.; Purushotham, P.; Guruprasad, L.; Podile, A. R. *J. Biol. Chem.* **2012,** *287,* 44619–44627. doi:10.1074/jbc.m112.400879
246. Usui, T.; Matsui, H.; Isobe, K. *Carbohydr. Res.* **1990,** *203,* 65–77. doi:10.1016/0008-6215(90)80046-6
247. Ohnuma, T.; Tanaka, T.; Urasaki, A.; Dozen, S.; Fukamizo, T. *J. Biochem.* **2019,** *165,* 497–503. doi:10.1093/jb/mvy123
248. Sirimontree, P.; Suginta, W.; Sritho, N.; Kanda, Y.; Shinya, S.; Ohnuma, T.; Fukamizo, T. *Biosci., Biotechnol., Biochem.* **2014,** *78,* 2014–2021. doi:10.1080/09168451.2014.948373
249. Ohnuma, T.; Fukuda, T.; Dozen, S.; Honda, Y.; Kitaoka, M.; Fukamizo, T. *Biochem. J.* **2012,** *444,* 437–443. doi:10.1042/bj20120036
250. Kohri, M.; Kobayashi, A.; Noguchi, M.; Kawaida, S.-i.; Watanabe, T.; Shoda, S.-i. *Holzforschung* **2006,** *60,* 485–491. doi:10.1515/hf.2006.080
251. Crich, D.; Dudkin, V. *J. Am. Chem. Soc.* **2001,** *123,* 6819–6825. doi:10.1021/ja010086b
252. Kuyama, H.; Nakahara, Y.; Nukada, T.; Ito, Y.; Nakahara, Y.; Ogawa, T. *Carbohydr. Res.* **1993,** *243,* C1–C7. doi:10.1016/0008-6215(93)84095-n
253. Kanie, O.; Ito, Y.; Ogawa, T. *J. Am. Chem. Soc.* **1994,** *116,* 12073–12074. doi:10.1021/ja00105a066
254. Yudina, O. N.; Tsvetkov, Y. E.; Nifantiev, N. E. *Russ. Chem. Bull.* **2015,** *64,* 2932–2941. doi:10.1007/s11172-015-1250-6
255. Yudina, O. N.; Tsvetkov, Y. E.; Nifantiev, N. E. *Russ. Chem. Bull.* **2016,** *65,* 2937–2942. doi:10.1007/s11172-016-1681-8
256. Kawada, T.; Yoneda, Y. *Monatsh. Chem.* **2009,** *140,* 1245–1250. doi:10.1007/s00706-009-0172-0
257. Kawada, T.; Yoneda, Y. *Monatsh. Chem.* **2009,** *140,* 1251–1256. doi:10.1007/s00706-009-0174-y
258. Bedini, E.; Cirillo, L.; Marchetti, R.; Basso, S.; Tufano, D.; Molinaro, A.; Parrilli, M. *Synlett* **2013,** *25,* 365–370. doi:10.1055/s-0033-1340323
259. Barroca-Aubry, N.; Pernet-Poil-Chevrier, A.; Domard, A.; Trombotto, S. *Carbohydr. Res.* **2010,** *345,* 1685–1697. doi:10.1016/j.carres.2010.05.010
260. Tyrikos-Ergas, T.; Bordoni, V.; Fittolani, G.; Chaube, M. A.; Grafmüller, A.; Seeberger, P. H.; Delbianco, M. *Chem. – Eur. J.* **2021,** *27,* 2321–2325. doi:10.1002/chem.202005228
261. Enugala, R.; Carvalho, L. C. R.; Dias Pires, M. J.; Marques, M. M. B. *Chem. – Asian J.* **2012,** *7,* 2482–2501. doi:10.1002/asia.201200338
262. Yang, F.; Du, Y. *Carbohydr. Res.* **2003,** *338,* 495–502. doi:10.1016/s0008-6215(02)00494-9
263. Yamago, S.; Yamada, T.; Maruyama, T.; Yoshida, J.-i. *Angew. Chem., Int. Ed.* **2004,** *43,* 2145–2148. doi:10.1002/anie.200353552
264. Gening, M. L.; Tsvetkov, Y. E.; Pier, G. B.; Nifantiev, N. E. *Carbohydr. Res.* **2007,** *342,* 567–575. doi:10.1016/j.carres.2006.08.010
265. Gening, M. L.; Titov, D. V.; Grachev, A. A.; Gerbst, A. G.; Yudina, O. N.; Shashkov, A. S.; Chizhov, A. O.; Tsvetkov, Y. E.; Nifantiev, N. E. *Eur. J. Org. Chem.* **2010,** 2465–2475. doi:10.1002/ejoc.200901275
266. Nokami, T.; Hayashi, R.; Saigusa, Y.; Shimizu, A.; Liu, C.-Y.; Mong, K.-K. T.; Yoshida, J.-i. *Org. Lett.* **2013,** *15,* 4520–4523. doi:10.1021/ol402034g
267. Kröck, L.; Esposito, D.; Castagner, B.; Wang, C.-C.; Bindschädler, P.; Seeberger, P. H. *Chem. Sci.* **2012,** *3,* 1617–1622. doi:10.1039/c2sc00940d
268. Morando, M.; Yao, Y.; Martín-Santamaría, S.; Zhu, Z.; Xu, T.; Cañada, F. J.; Zhang, Y.; Jiménez-Barbero, J. *Chem. – Eur. J.* **2010,** *16,* 4239–4249. doi:10.1002/chem.200902860
269. Hölemann, A.; Stocker, B. L.; Seeberger, P. H. *J. Org. Chem.* **2006,** *71,* 8071–8088. doi:10.1021/jo061233x
270. Cai, F.; Wu, B.; Crich, D. Stereocontrolled Synthesis of Mannans and Rhamnans. *Advances in Carbohydrate Chemistry and Biochemistry;* Elsevier: Amsterdam, Netherlands, 2009; pp 251–309. doi:10.1016/s0065-2318(09)00006-7
271. Cheon, H.-S.; Lian, Y.; Kishi, Y. *Org. Lett.* **2007,** *9,* 3323–3326. doi:10.1021/ol0713335
272. Li, X.; Li, C.; Liu, R.; Wang, J.; Wang, Z.; Chen, Y.; Yang, Y. *Org. Lett.* **2019,** *21,* 9693–9698. doi:10.1021/acs.orglett.9b03851
273. Jayaprakash, K. N.; Lu, J.; Fraser-Reid, B. *Angew. Chem.* **2005,** *117,* 6044–6048. doi:10.1002/ange.200500505
274. Sawettanai, N.; Leelayuwapan, H.; Karoonuthaisiri, N.; Ruchirawat, S.; Boonyarattanakalin, S. *J. Org. Chem.* **2019,** *84,* 7606–7617. doi:10.1021/acs.joc.8b02944
275. Leelayuwapan, H.; Kangwanrangsan, N.; Chawengkirttikul, R.; Ponpuak, M.; Charlermroj, R.; Boonyarattanakalin, K.; Ruchirawat, S.; Boonyarattanakalin, S. *J. Org. Chem.* **2017,** *82,* 7190–7199. doi:10.1021/acs.joc.7b00703
276. Calin, O.; Eller, S.; Seeberger, P. H. *Angew. Chem., Int. Ed.* **2013,** *52,* 5862–5865. doi:10.1002/anie.201210176
277. Naresh, K.; Schumacher, F.; Hahm, H. S.; Seeberger, P. H. *Chem. Commun.* **2017,** *53,* 9085–9088. doi:10.1039/c7cc04380e
278. Joseph, A. A.; Pardo-Vargas, A.; Seeberger, P. H. *J. Am. Chem. Soc.* **2020,** *142,* 8561–8564. doi:10.1021/jacs.0c00751
279. Yu, Y.; Kononov, A.; Delbianco, M.; Seeberger, P. H. *Chem. – Eur. J.* **2018,** *24,* 6075–6078. doi:10.1002/chem.201801023

280. Sahloul, K.; Lowary, T. L. *J. Org. Chem.* **2015,** *80,* 11417–11434. doi:10.1021/acs.joc.5b02083
281. Pardo-Vargas, A.; Bharate, P.; Delbianco, M.; Seeberger, P. H. *Beilstein J. Org. Chem.* **2019,** *15,* 2936–2940. doi:10.3762/bjoc.15.288
282. van der Vorm, S.; Hansen, T.; van Hengst, J. M. A.; Overkleeft, H. S.; van der Marel, G. A.; Codée, J. D. C. *Chem. Soc. Rev.* **2019,** *48,* 4688–4706. doi:10.1039/c8cs00369f
283. Nicolardi, S.; Joseph, A. A.; Zhu, Q.; Shen, Z.; Pardo-Vargas, A.; Chiodo, F.; Molinaro, A.; Silipo, A.; van der Burgt, Y. E. M.; Yu, B.; Seeberger, P. H.; Wuhrer, M. *Anal. Chem. (Washington, DC, U. S.)* **2021,** *93,* 4666–4675. doi:10.1021/acs.analchem.1c00239
284. Sasaki, K.; Tohda, K. *Tetrahedron Lett.* **2018,** *59,* 496–503. doi:10.1016/j.tetlet.2017.12.077
285. Li, Q.; Levi, S. M.; Jacobsen, E. N. *J. Am. Chem. Soc.* **2020,** *142,* 11865–11872. doi:10.1021/jacs.0c04255
286. Geng, X.; Wang, G.; Guo, Z.; Gu, G. *J. Org. Chem.* **2020,** *85,* 2369–2384. doi:10.1021/acs.joc.9b03085
287. Crich, D. *Acc. Chem. Res.* **2010,** *43,* 1144–1153. doi:10.1021/ar100035r
288. Crich, D.; Sun, S. *Tetrahedron* **1998,** *54,* 8321–8348. doi:10.1016/s0040-4020(98)00426-8
289. Crich, D.; Chandrasekera, N. S. *Angew. Chem., Int. Ed.* **2004,** *43,* 5386–5389. doi:10.1002/anie.200453688
290. Crich, D.; Banerjee, A.; Yao, Q. *J. Am. Chem. Soc.* **2004,** *126,* 14930–14934. doi:10.1021/ja047194t
291. Crich, D.; Li, W.; Li, H. *J. Am. Chem. Soc.* **2004,** *126,* 15081–15086. doi:10.1021/ja0471931
292. Crich, D.; Li, H.; Yao, Q.; Wink, D. J.; Sommer, R. D.; Rheingold, A. L. *J. Am. Chem. Soc.* **2001,** *123,* 5826–5828. doi:10.1021/ja015985e
293. Codée, J. D. C.; Kröck, L.; Castagner, B.; Seeberger, P. H. *Chem. – Eur. J.* **2008,** *14,* 3987–3994. doi:10.1002/chem.200701864
294. Ohara, K.; Lin, C.-C.; Yang, P.-J.; Hung, W.-T.; Yang, W.-B.; Cheng, T.-J. R.; Fang, J.-M.; Wong, C.-H. *J. Org. Chem.* **2013,** *78,* 6390–6411. doi:10.1021/jo4005266
295. Mathew, F.; Mach, M.; Hazen, K.; Fraser-Reid, B. *Synlett* **2003,** 1319–1322. doi:10.1055/s-2003-40350
296. Nitz, M.; Purse, B. W.; Bundle, D. R. *Org. Lett.* **2000,** *2,* 2939–2942. doi:10.1021/ol0061743
297. Nitz, M.; Bundle, D. R. *J. Org. Chem.* **2001,** *66,* 8411–8423. doi:10.1021/jo010570x
298. van den Bos, L. J.; Dinkelaar, J.; Overkleeft, H. S.; van der Marel, G. A. *J. Am. Chem. Soc.* **2006,** *128,* 13066–13067. doi:10.1021/ja064787q
299. Codée, J. D. C.; van den Bos, L. J.; de Jong, A.-R.; Dinkelaar, J.; Lodder, G.; Overkleeft, H. S.; van der Marel, G. A. *J. Org. Chem.* **2009,** *74,* 38–47. doi:10.1021/jo8020192
300. Hansen, T.; Lebedel, L.; Remmerswaal, W. A.; van der Vorm, S.; Wander, D. P. A.; Somers, M.; Overkleeft, H. S.; Filippov, D. V.; Désiré, J.; Mingot, A.; Bleriot, Y.; van der Marel, G. A.; Thibaudeau, S.; Codée, J. D. C. *ACS Cent. Sci.* **2019,** *5,* 781–788. doi:10.1021/acscentsci.9b00042
301. Dinkelaar, J.; de Jong, A. R.; van Meer, R.; Somers, M.; Lodder, G.; Overkleeft, H. S.; Codée, J. D. C.; van der Marel, G. A. *J. Org. Chem.* **2009,** *74,* 4982–4991. doi:10.1021/jo900662v
302. Walvoort, M. T. C.; van den Elst, H.; Plante, O. J.; Kröck, L.; Seeberger, P. H.; Overkleeft, H. S.; van der Marel, G. A.; Codée, J. D. C. *Angew. Chem., Int. Ed.* **2012,** *51,* 4393–4396. doi:10.1002/anie.201108744
303. Pan, D.; Zhang, L.; Hua, Q.; Yang, Y. *Org. Biomol. Chem.* **2019,** *17,* 6174–6177. doi:10.1039/c9ob01254k
304. Tang, S.-L.; Pohl, N. L. B. *Org. Lett.* **2015,** *17,* 2642–2645. doi:10.1021/acs.orglett.5b01013
305. Jahn, M.; Stoll, D.; Warren, R. A. J.; Szabó, L.; Singh, P.; Gilbert, H. J.; Ducros, V. M.-A.; Davies, G. J.; Withers, S. G. *Chem. Commun.* **2003,** 1327–1329. doi:10.1039/b302380j
306. Grimaud, F.; Pizzut-Serin, S.; Tarquis, L.; Ladevèze, S.; Morel, S.; Putaux, J.-L.; Potocki-Veronese, G. *Biomacromolecules* **2019,** *20,* 846–853. doi:10.1021/acs.biomac.8b01457
307. Pawar, S. N.; Edgar, K. J. *Biomaterials* **2012,** *33,* 3279–3305. doi:10.1016/j.biomaterials.2012.01.007
308. Beswick, L.; Ahmadipour, S.; Dolan, J. P.; Rejzek, M.; Field, R. A.; Miller, G. J. *Carbohydr. Res.* **2019,** *485,* 107819. doi:10.1016/j.carres.2019.107819
309. Zhang, Q.; van Rijssel, E. R.; Overkleeft, H. S.; van der Marel, G. A.; Codée, J. D. C. *Eur. J. Org. Chem.* **2016,** 2393–2397. doi:10.1002/ejoc.201600336
310. Dinkelaar, J.; van den Bos, L. J.; Hogendorf, W. F. J.; Lodder, G.; Overkleeft, H. S.; Codée, J. D. C.; van der Marel, G. A. *Chem. – Eur. J.* **2008,** *14,* 9400–9411. doi:10.1002/chem.200800960
311. Zhang, Q.; van Rijssel, E. R.; Walvoort, M. T. C.; Overkleeft, H. S.; van der Marel, G. A.; Codée, J. D. C. *Angew. Chem., Int. Ed.* **2015,** *54,* 7670–7673. doi:10.1002/anie.201502581
312. Giraud, M.-F.; Naismith, J. H. *Curr. Opin. Struct. Biol.* **2000,** *10,* 687–696. doi:10.1016/s0959-440x(00)00145-7
313. Geert Volbeda, A.; Reintjens, N. R. M.; Overkleeft, H. S.; van der Marel, G. A.; Codée, J. D. C. *Eur. J. Org. Chem.* **2016,** 5282–5293. doi:10.1002/ejoc.201600956
314. Geert Volbeda, A.; van Mechelen, J.; Meeuwenoord, N.; Overkleeft, H. S.; van der Marel, G. A.; Codée, J. D. C. *J. Org. Chem.* **2017,** *82,* 12992–13002. doi:10.1021/acs.joc.7b02511
315. Tanaka, H.; Hamaya, Y.; Nishiwaki, N.; Ishida, H. *Carbohydr. Res.* **2018,** *455,* 23–31. doi:10.1016/j.carres.2017.11.005
316. Kohout, V. R.; Pohl, N. L. B. *Carbohydr. Res.* **2019,** *486,* 107829. doi:10.1016/j.carres.2019.107829
317. Zhang, J.; Kong, F. *Tetrahedron* **2003,** *59,* 1429–1441. doi:10.1016/s0040-4020(03)00075-9
318. Palmacci, E. R.; Plante, O. J.; Hewitt, M. C.; Seeberger, P. H. *Helv. Chim. Acta* **2003,** *86,* 3975–3990. doi:10.1002/hlca.200390331
319. Bedini, E.; Parrilli, M.; Unverzagt, C. *Tetrahedron Lett.* **2002,** *43,* 8879–8882. doi:10.1016/s0040-4039(02)02237-2
320. Bedini, E.; De Castro, C.; Erbs, G.; Mangoni, L.; Dow, J. M.; Newman, M.-A.; Parrilli, M.; Unverzagt, C. *J. Am. Chem. Soc.* **2005,** *127,* 2414–2416. doi:10.1021/ja0452166
321. Werz, D. B.; Seeberger, P. H. *Angew. Chem., Int. Ed.* **2005,** *44,* 6315–6318. doi:10.1002/anie.200502615
322. Govindarajan, M. *Carbohydr. Res.* **2020,** *497,* 108151. doi:10.1016/j.carres.2020.108151
323. Rai, D.; Kulkarni, S. S. *Org. Biomol. Chem.* **2020,** *18,* 3216–3228. doi:10.1039/d0ob00297f
324. Crich, D.; Bowers, A. A. *Org. Lett.* **2006,** *8,* 4327–4330. doi:10.1021/ol061706m
325. Zhu, Q.; Shen, Z.; Chiodo, F.; Nicolardi, S.; Molinaro, A.; Silipo, A.; Yu, B. *Nat. Commun.* **2020,** *11,* 4142. doi:10.1038/s41467-020-17992-x
326. Cai, J.; Hu, J.; Qin, C.; Li, L.; Shen, D.; Tian, G.; Zou, X.; Seeberger, P. H.; Yin, J. *Angew. Chem., Int. Ed.* **2020,** *59,* 20529–20537. doi:10.1002/anie.202007209

327. Yu, B. *Acc. Chem. Res.* **2018,** *51,* 507–516. doi:10.1021/acs.accounts.7b00573
328. Koeller, K. M.; Wong, C.-H. *Chem. Rev.* **2000,** *100,* 4465–4494. doi:10.1021/cr990297n
329. Pfrengle, F. *Curr. Opin. Chem. Biol.* **2017,** *40,* 145–151. doi:10.1016/j.cbpa.2017.09.010
330. Nepogodiev, S. A.; Field, R. A.; Damager, I. Approaches to Chemical Synthesis of Pectic Oligosaccharides. *Annual Plant Reviews;* Wiley-Blackwell: Oxford, UK, 2010; Vol. 41, pp 65–92. doi:10.1002/9781444391015.ch3
331. Lichtenthaler, F. W.; Oberthür, M.; Peters, S. *Eur. J. Org. Chem.* **2001,** 3849–3869. doi:10.1002/1099-0690(200110)2001:20<3849::aid-ejoc3849>3.0.co;2-q
332. Andersen, M. C. F.; Kračun, S. K.; Rydahl, M. G.; Willats, W. G. T.; Clausen, M. H. *Chem. – Eur. J.* **2016,** *22,* 11543–11548. doi:10.1002/chem.201602197
333. Andersen, M. C. F.; Boos, I.; Kinnaert, C.; Awan, S. I.; Pedersen, H. L.; Kračun, S. K.; Lanz, G.; Rydahl, M. G.; Kjærulff, L.; Håkansson, M.; Kimbung, R.; Logan, D. T.; Gotfredsen, C. H.; Willats, W. G. T.; Clausen, M. H. *Org. Biomol. Chem.* **2018,** *16,* 1157–1162. doi:10.1039/c7ob03035e
334. Bartetzko, M. P.; Schuhmacher, F.; Seeberger, P. H.; Pfrengle, F. *J. Org. Chem.* **2017,** *82,* 1842–1850. doi:10.1021/acs.joc.6b02745
335. Zeng, Y.; Li, A.; Kong, F. *Tetrahedron Lett.* **2003,** *44,* 8325–8329. doi:10.1016/j.tetlet.2003.08.087
336. Li, A.; Kong, F. *Carbohydr. Res.* **2004,** *339,* 1847–1856. doi:10.1016/j.carres.2004.05.007
337. Li, A.; Zeng, Y.; Kong, F. *Carbohydr. Res.* **2004,** *339,* 673–681. doi:10.1016/j.carres.2003.11.006
338. Li, A.; Kong, F. *Bioorg. Med. Chem.* **2005,** *13,* 839–853. doi:10.1016/j.bmc.2004.10.035
339. Andersen, M. C. F.; Boos, I.; Ruprecht, C.; Willats, W. G. T.; Pfrengle, F.; Clausen, M. H. *J. Org. Chem.* **2017,** *82,* 12066–12084. doi:10.1021/acs.joc.7b01796
340. Bartetzko, M. P.; Schuhmacher, F.; Hahm, H. S.; Seeberger, P. H.; Pfrengle, F. *Org. Lett.* **2015,** *17,* 4344–4347. doi:10.1021/acs.orglett.5b02185
341. Imamura, A.; Ando, H.; Korogi, S.; Tanabe, G.; Muraoka, O.; Ishida, H.; Kiso, M. *Tetrahedron Lett.* **2003,** *44,* 6725–6728. doi:10.1016/s0040-4039(03)01647-2
342. Imamura, A.; Matsuzawa, N.; Sakai, S.; Udagawa, T.; Nakashima, S.; Ando, H.; Ishida, H.; Kiso, M. *J. Org. Chem.* **2016,** *81,* 9086–9104. doi:10.1021/acs.joc.6b01685
343. Kazakova, E. D.; Yashunsky, D. V.; Krylov, V. B.; Bouchara, J.-P.; Cornet, M.; Valsecchi, I.; Fontaine, T.; Latgé, J.-P.; Nifantiev, N. E. *J. Am. Chem. Soc.* **2020,** *142,* 1175–1179. doi:10.1021/jacs.9b11703
344. Zhang, Y.; Gómez-Redondo, M.; Jiménez-Osés, G.; Arda, A.; Overkleeft, H. S.; Marel, G. A.; Jiménez-Barbero, J.; Codée, J. D. C. *Angew. Chem., Int. Ed.* **2020,** *59,* 12746–12750. doi:10.1002/anie.202003951
345. Nakahara, Y.; Ogawa, T. *Carbohydr. Res.* **1989,** *194,* 95–114. doi:10.1016/0008-6215(89)85010-4
346. Nakahara, Y.; Ogawa, T. *Carbohydr. Res.* **1990,** *205,* 147–159. doi:10.1016/0008-6215(90)80135-p
347. Clausen, M. H.; Madsen, R. *Chem. – Eur. J.* **2003,** *9,* 3821–3832. doi:10.1002/chem.200204636
348. Clausen, M. H.; Jørgensen, M. R.; Thorsen, J.; Madsen, R. *J. Chem. Soc., Perkin Trans. 1* **2001,** 543–551. doi:10.1039/b006981g
349. van den Bos, L. J.; Codée, J. D. C.; Litjens, R. E. J. N.; Dinkelaar, J.; Overkleeft, H. S.; van der Marel, G. A. *Eur. J. Org. Chem.* **2007,** 3963–3976. doi:10.1002/ejoc.200700101
350. Justen, A. M.; Hodges, H. L.; Kim, L. M.; Sadecki, P. W.; Porfirio, S.; Ultee, E.; Black, I.; Chung, G. S.; Briegel, A.; Azadi, P.; Kiessling, L. L. *Sci. Adv.* **2020,** *6,* eaba4015. doi:10.1126/sciadv.aba4015
351. King, J. D.; Berry, S.; Clarke, B. R.; Morris, R. J.; Whitfield, C. *Proc. Natl. Acad. Sci. U. S. A.* **2014,** *111,* 6407–6412. doi:10.1073/pnas.1400814111
352. May, J. F.; Splain, R. A.; Brotschi, C.; Kiessling, L. L. *Proc. Natl. Acad. Sci. U. S. A.* **2009,** *106,* 11851–11856. doi:10.1073/pnas.0901407106
353. Wheatley, R. W.; Zheng, R. B.; Richards, M. R.; Lowary, T. L.; Ng, K. K. S. *J. Biol. Chem.* **2012,** *287,* 28132–28143. doi:10.1074/jbc.m112.347484
354. Savková, K.; Huszár, S.; Baráth, P.; Pakanová, Z.; Kozmon, S.; Vancová, M.; Tesařová, M.; Blaško, J.; Kaliňák, M.; Singh, V.; Korduláková, J.; Mikušová, K. *Proc. Natl. Acad. Sci. U. S. A.* **2021,** *118,* e2023663118. doi:10.1073/pnas.2023663118
355. Woodward, R.; Yi, W.; Li, L.; Zhao, G.; Eguchi, H.; Sridhar, P. R.; Guo, H.; Song, J. K.; Motari, E.; Cai, L.; Kelleher, P.; Liu, X.; Han, W.; Zhang, W.; Ding, Y.; Li, M.; Wang, P. G. *Nat. Chem. Biol.* **2010,** *6,* 418–423. doi:10.1038/nchembio.351
356. Peltier, P.; Euzen, R.; Daniellou, R.; Nugier-Chauvin, C.; Ferrières, V. *Carbohydr. Res.* **2008,** *343,* 1897–1923. doi:10.1016/j.carres.2008.02.010
357. Houseknecht, J. B.; Lowary, T. L. *Curr. Opin. Chem. Biol.* **2001,** *5,* 677–682. doi:10.1016/s1367-5931(01)00265-4
358. Completo, G. C.; Lowary, T. L. *J. Org. Chem.* **2008,** *73,* 4513–4525. doi:10.1021/jo800457j
359. Argunov, D. A.; Krylov, V. B.; Nifantiev, N. E. *Org. Lett.* **2016,** *18,* 5504–5507. doi:10.1021/acs.orglett.6b02735
360. Krylov, V. B.; Argunov, D. A.; Vinnitskiy, D. Z.; Verkhnyatskaya, S. A.; Gerbst, A. G.; Ustyuzhanina, N. E.; Dmitrenok, A. S.; Huebner, J.; Holst, O.; Siebert, H.-C.; Nifantiev, N. E. *Chem. – Eur. J.* **2014,** *20,* 16516–16522. doi:10.1002/chem.201405083
361. Joe, M.; Lowary, T. L. *Can. J. Chem.* **2016,** *94,* 976–988. doi:10.1139/cjc-2016-0416
362. Sabbavarapu, N. M.; Seeberger, P. H. *J. Org. Chem.* **2021,** *86,* 7280–7287. doi:10.1021/acs.joc.1c00505
363. Mourão, P. *Trends Cardiovasc. Med.* **1999,** *9,* 225–232. doi:10.1016/s1050-1738(00)00032-3
364. Berteau, O.; Mulloy, B. *Glycobiology* **2003,** *13,* 29R–40R. doi:10.1093/glycob/cwg058
365. Ustyuzhanina, N.; Krylov, V.; Grachev, A.; Gerbst, A.; Nifantiev, N. *Synthesis* **2006,** 4017–4031. doi:10.1055/s-2006-950333
366. Arafuka, S.; Koshiba, N.; Takahashi, D.; Toshima, K. *Chem. Commun.* **2014,** *50,* 9831–9834. doi:10.1039/c4cc03544e
367. Liu, K.; Wang, L.; Guo, Z. *J. Carbohydr. Chem.* **2019,** *38,* 414–469. doi:10.1080/07328303.2019.1630841
368. Mishra, B.; Manmode, S.; Panda, R. R. A.; Hotha, S. *Eur. J. Org. Chem.* **2017,** 4794–4802. doi:10.1002/ejoc.201700712
369. Podvalnyy, N. M.; Abronina, P. I.; Zdorovenko, E. L.; Chizhov, A. O.; Zinin, A. I.; Torgov, V. I.; Kononov, L. O. *Russ. Chem. Bull.* **2014,** *63,* 497–500. doi:10.1007/s11172-014-0459-0
370. Podvalnyy, N. M.; Chizhov, A. O.; Zinin, A. I.; Kononov, L. O. *Carbohydr. Res.* **2016,** *431,* 25–32. doi:10.1016/j.carres.2016.05.009
371. Leelayuwapan, H.; Ruchirawat, S.; Boonyarattanakalin, S. *Carbohydr. Polym.* **2019,** *206,* 262–272. doi:10.1016/j.carbpol.2018.10.048

372. Hori, M.; Nakatsubo, F. *Macromolecules* **2000,** *33,* 1148–1151. doi:10.1021/ma9915172
373. Panova, M. V.; Podvalnyy, N. M.; Okun, E. L.; Abronina, P. I.; Chizhov, A. O.; Kononov, L. O. *Carbohydr. Res.* **2018,** *456,* 35–44. doi:10.1016/j.carres.2017.11.002
374. Lu, J.; Fraser-Reid, B. *Chem. Commun.* **2005,** 862–864. doi:10.1039/b413694b
375. Fraser-Reid, B.; Lu, J.; Jayaprakash, K. N.; López, J. C. *Tetrahedron: Asymmetry* **2006,** *17,* 2449–2463. doi:10.1016/j.tetasy.2006.09.008
376. Joe, M.; Bai, Y.; Nacario, R. C.; Lowary, T. L. *J. Am. Chem. Soc.* **2007,** *129,* 9885–9901. doi:10.1021/ja072892+
377. Ishiwata, A.; Ito, Y. *J. Am. Chem. Soc.* **2011,** *133,* 2275–2291. doi:10.1021/ja109932t
378. Thadke, S. A.; Mishra, B.; Islam, M.; Pasari, S.; Manmode, S.; Rao, B. V.; Neralkar, M.; Shinde, G. P.; Walke, G.; Hotha, S. *Nat. Commun.* **2017,** *8,* 14019. doi:10.1038/ncomms14019
379. Islam, M.; Shinde, G. P.; Hotha, S. *Chem. Sci.* **2017,** *8,* 2033–2038. doi:10.1039/c6sc04866h
380. Pasari, S.; Manmode, S.; Walke, G.; Hotha, S. *Chem. – Eur. J.* **2018,** *24,* 1128–1139. doi:10.1002/chem.201704009
381. Kandasamy, J.; Hurevich, M.; Seeberger, P. H. *Chem. Commun.* **2013,** *49,* 4453–4455. doi:10.1039/c3cc00042g
382. Du, Y.; Pan, Q.; Kong, F. *Synlett* **1999,** 1648–1650. doi:10.1055/s-1999-3170
383. Du, Y.; Pan, Q.; Kong, F. *Carbohydr. Res.* **2000,** *329,* 17–24. doi:10.1016/s0008-6215(00)00159-2
384. Ishiwata, A.; Akao, H.; Ito, Y. *Org. Lett.* **2006,** *8,* 5525–5528. doi:10.1021/ol062198j
385. Wu, Y.; Xiong, D.-C.; Chen, S.-C.; Wang, Y.-S.; Ye, X.-S. *Nat. Commun.* **2017,** *8,* 14851. doi:10.1038/ncomms14851
386. Mende, M.; Bednarek, C.; Wawryszyn, M.; Sauter, P.; Biskup, M. B.; Schepers, U.; Bräse, S. *Chem. Rev.* **2016,** *116,* 8193–8255. doi:10.1021/acs.chemrev.6b00010
387. Yu, M.; Zhang, T.; Zhang, W.; Sun, Q.; Li, H.; Li, J.-p. *Front. Mol. Biosci.* **2021,** *7,* 628551. doi:10.3389/fmolb.2020.628551
388. Zhang, Q.; Chen, C. Z.; Swaroop, M.; Xu, M.; Wang, L.; Lee, J.; Wang, A. Q.; Pradhan, M.; Hagen, N.; Chen, L.; Shen, M.; Luo, Z.; Xu, X.; Xu, Y.; Huang, W.; Zheng, W.; Ye, Y. *Cell Discovery* **2020,** *6,* 80. doi:10.1038/s41421-020-00222-5
389. Ricard-Blum, S.; Lisacek, F. *Glycoconjugate J.* **2017,** *34,* 339–349. doi:10.1007/s10719-016-9747-2
390. Mattson, J. M.; Turcotte, R.; Zhang, Y. *Biomech. Model. Mechanobiol.* **2017,** *16,* 213–225. doi:10.1007/s10237-016-0811-4
391. Badri, A.; Williams, A.; Linhardt, R. J.; Koffas, M. A. G. *Curr. Opin. Biotechnol.* **2018,** *53,* 85–92. doi:10.1016/j.copbio.2017.12.018
392. Gama, C. I.; Tully, S. E.; Sotogaku, N.; Clark, P. M.; Rawat, M.; Vaidehi, N.; Goddard, W. A., III; Nishi, A.; Hsieh-Wilson, L. C. *Nat. Chem. Biol.* **2006,** *2,* 467–473. doi:10.1038/nchembio810
393. Habuchi, H.; Habuchi, O.; Kimata, K. *Glycoconjugate J.* **2004,** *21,* 47–52. doi:10.1023/b:glyc.0000043747.87325.5e
394. Zhang, X.; Pagadala, V.; Jester, H. M.; Lim, A. M.; Pham, T. Q.; Goulas, A. M. P.; Liu, J.; Linhardt, R. J. *Chem. Sci.* **2017,** *8,* 7932–7940. doi:10.1039/c7sc03541a
395. Wang, Z.; Hsieh, P.-H.; Xu, Y.; Thieker, D.; Chai, E. J. E.; Xie, S.; Cooley, B.; Woods, R. J.; Chi, L.; Liu, J. *J. Am. Chem. Soc.* **2017,** *139,* 5249–5256. doi:10.1021/jacs.7b01923
396. Arnold, K.; Liao, Y.-E.; Liu, J. *Biomedicines* **2020,** *8,* 503. doi:10.3390/biomedicines8110503
397. Lee, J.-C.; Lu, X.-A.; Kulkarni, S. S.; Wen, Y.-S.; Hung, S.-C. *J. Am. Chem. Soc.* **2004,** *126,* 476–477. doi:10.1021/ja038244h
398. Miller, R. L.; Guimond, S. E.; Schwörer, R.; Zubkova, O. V.; Tyler, P. C.; Xu, Y.; Liu, J.; Chopra, P.; Boons, G.-J.; Grabarics, M.; Manz, C.; Hofmann, J.; Karlsson, N. G.; Turnbull, J. E.; Struwe, W. B.; Pagel, K. *Nat. Commun.* **2020,** *11,* 1481. doi:10.1038/s41467-020-15284-y
399. Liu, J.; Linhardt, R. J. *Nat. Prod. Rep.* **2014,** *31,* 1676–1685. doi:10.1039/c4np00076e
400. Hu, Y.-P.; Lin, S.-Y.; Huang, C.-Y.; Zulueta, M. M. L.; Liu, J.-Y.; Chang, W.; Hung, S.-C. *Nat. Chem.* **2011,** *3,* 557–563. doi:10.1038/nchem.1073
401. Muñoz-García, J. C.; López-Prados, J.; Angulo, J.; Díaz-Contreras, I.; Reichardt, N.; de Paz, J. L.; Martín-Lomas, M.; Nieto, P. M. *Chem. – Eur. J.* **2012,** *18,* 16319–16331. doi:10.1002/chem.201202770
402. Dai, X.; Liu, W.; Zhou, Q.; Cheng, C.; Yang, C.; Wang, S.; Zhang, M.; Tang, P.; Song, H.; Zhang, D.; Qin, Y. *J. Org. Chem.* **2016,** *81,* 162–184. doi:10.1021/acs.joc.5b02468
403. Zong, C.; Venot, A.; Li, X.; Lu, W.; Xiao, W.; Wilkes, J.-S. L.; Salanga, C. L.; Handel, T. M.; Wang, L.; Wolfert, M. A.; Boons, G.-J. *J. Am. Chem. Soc.* **2017,** *139,* 9534–9543. doi:10.1021/jacs.7b01399
404. Dey, S.; Wong, C.-H. *Chem. Sci.* **2018,** *9,* 6685–6691. doi:10.1039/c8sc01743c
405. Pawar, N. J.; Wang, L.; Higo, T.; Bhattacharya, C.; Kancharla, P. K.; Zhang, F.; Baryal, K.; Huo, C.-X.; Liu, J.; Linhardt, R. J.; Huang, X.; Hsieh-Wilson, L. C. *Angew. Chem., Int. Ed.* **2019,** *58,* 18577–18583. doi:10.1002/anie.201908805
406. Hansen, S. U.; Baráth, M.; Salameh, B. A. B.; Pritchard, R. G.; Stimpson, W. T.; Gardiner, J. M.; Jayson, G. C. *Org. Lett.* **2009,** *11,* 4528–4531. doi:10.1021/ol901723m
407. Hansen, S. U.; Miller, G. J.; Jayson, G. C.; Gardiner, J. M. *Org. Lett.* **2013,** *15,* 88–91. doi:10.1021/ol303112y
408. Hansen, S. U.; Miller, G. J.; Cole, C.; Rushton, G.; Avizienyte, E.; Jayson, G. C.; Gardiner, J. M. *Nat. Commun.* **2013,** *4,* 2016. doi:10.1038/ncomms3016
409. Hansen, S. U.; Miller, G. J.; Cliff, M. J.; Jayson, G. C.; Gardiner, J. M. *Chem. Sci.* **2015,** *6,* 6158–6164. doi:10.1039/c5sc02091c
410. Zhang, X.; Lin, L.; Huang, H.; Linhardt, R. J. *Acc. Chem. Res.* **2020,** *53,* 335–346. doi:10.1021/acs.accounts.9b00420
411. Xu, Y.; Masuko, S.; Takieddin, M.; Xu, H.; Liu, R.; Jing, J.; Mousa, S. A.; Linhardt, R. J.; Liu, J. *Science* **2011,** *334,* 498–501. doi:10.1126/science.1207478
412. Xu, Y.; Cai, C.; Chandarajoti, K.; Hsieh, P.-H.; Li, L.; Pham, T. Q.; Sparkenbaugh, E. M.; Sheng, J.; Key, N. S.; Pawlinski, R.; Harris, E. N.; Linhardt, R. J.; Liu, J. *Nat. Chem. Biol.* **2014,** *10,* 248–250. doi:10.1038/nchembio.1459
413. Zong, C.; Venot, A.; Dhamale, O.; Boons, G.-J. *Org. Lett.* **2013,** *15,* 342–345. doi:10.1021/ol303270v
414. Masuko, S.; Bera, S.; Green, D. E.; Weïwer, M.; Liu, J.; DeAngelis, P. L.; Linhardt, R. J. *J. Org. Chem.* **2012,** *77,* 1449–1456. doi:10.1021/jo202322k
415. Weïwer, M.; Sherwood, T.; Green, D. E.; Chen, M.; DeAngelis, P. L.; Liu, J.; Linhardt, R. J. *J. Org. Chem.* **2008,** *73,* 7631–7637. doi:10.1021/jo801409c
416. Li, J.-p.; Hagner-McWhirter, Å.; Kjellén, L.; Palgi, J.; Jalkanen, M.; Lindahl, U. *J. Biol. Chem.* **1997,** *272,* 28158–28163. doi:10.1074/jbc.272.44.28158
417. Sheng, J.; Xu, Y.; Dulaney, S. B.; Huang, X.; Liu, J. *J. Biol. Chem.* **2012,** *287,* 20996–21002. doi:10.1074/jbc.m112.359885

418. Xu, Y.; Pempe, E. H.; Liu, J. *J. Biol. Chem.* **2012,** *287,* 29054–29061. doi:10.1074/jbc.m112.358523
419. Lu, W.; Zong, C.; Chopra, P.; Pepi, L. E.; Xu, Y.; Amster, I. J.; Liu, J.; Boons, G.-J. *Angew. Chem., Int. Ed.* **2018,** *57,* 5340–5344. doi:10.1002/anie.201800387
420. Yamada, S.; Sugahara, K. *Curr. Drug Discovery Technol.* **2008,** *5,* 289–301. doi:10.2174/157016308786733564
421. Ramadan, S.; Li, T.; Yang, W.; Zhang, J.; Rashidijahanabad, Z.; Tan, Z.; Parameswaran, N.; Huang, X. *ACS Cent. Sci.* **2020,** *6,* 913–920. doi:10.1021/acscentsci.9b01199
422. Li, J.; Su, G.; Liu, J. *Angew. Chem., Int. Ed.* **2017,** *56,* 11784–11787. doi:10.1002/anie.201705638
423. Sugiura, N.; Shimokata, S.; Minamisawa, T.; Hirabayashi, J.; Kimata, K.; Watanabe, H. *Glycoconjugate J.* **2008,** *25,* 521–530. doi:10.1007/s10719-008-9105-0
424. Köwitsch, A.; Zhou, G.; Groth, T. *J. Tissue Eng. Regener. Med.* **2018,** *12,* e23–e41. doi:10.1002/term.2398
425. Lu, X.; Kamat, M. N.; Huang, L.; Huang, X. *J. Org. Chem.* **2009,** *74,* 7608–7617. doi:10.1021/jo9016925
426. Walvoort, M. T. C.; Volbeda, A. G.; Reintjens, N. R. M.; van den Elst, H.; Plante, O. J.; Overkleeft, H. S.; van der Marel, G. A.; Codée, J. D. C. *Org. Lett.* **2012,** *14,* 3776–3779. doi:10.1021/ol301666n
427. Fu, X.; Shang, W.; Wang, S.; Liu, Y.; Qu, J.; Chen, X.; Wang, P. G.; Fang, J. *Chem. Commun.* **2017,** *53,* 3555–3558. doi:10.1039/c6cc09431g
428. Wang, Y.; Li, S.; Xu, X.; Tan, Y.; Liu, X.-w.; Fang, J. *Carbohydr. Polym.* **2020,** *232,* 115822. doi:10.1016/j.carbpol.2019.115822
429. Pomin, V. H. *Int. J. Biol. Macromol.* **2015,** *72,* 282–289. doi:10.1016/j.ijbiomac.2014.08.029
430. Ohmae, M.; Yamazaki, Y.; Sezukuri, K.; Takada, J. *Trends Glycosci. Glycotechnol.* **2019,** *31,* E129–E136. doi:10.4052/tigg.1830.1e
431. Ohmae, M.; Sakaguchi, K.; Kaneto, T.; Fujikawa, S.-i.; Kobayashi, S. *ChemBioChem* **2007,** *8,* 1710–1720. doi:10.1002/cbic.200700252
432. Hahm, H. S.; Broecker, F.; Kawasaki, F.; Mietzsch, M.; Heilbronn, R.; Fukuda, M.; Seeberger, P. H. *Chem* **2017,** *2,* 114–124. doi:10.1016/j.chempr.2016.12.004
433. Kobayashi, Y.; Horie, Y.; Honjo, K.; Uemura, T.; Kitagawa, S. *Chem. Commun.* **2016,** *52,* 5156–5159. doi:10.1039/c6cc01357k
434. Holerca, M. N.; Peterca, M.; Partridge, B. E.; Xiao, Q.; Lligadas, G.; Monteiro, M. J.; Percec, V. *J. Am. Chem. Soc.* **2020,** *142,* 15265–15270. doi:10.1021/jacs.0c07912
435. Begum, S.; Hassan, Z.; Bräse, S.; Tsotsalas, M. *Langmuir* **2020,** *36,* 10657–10673. doi:10.1021/acs.langmuir.0c01832
436. Dawson, P. E.; Kent, S. B. H. *Annu. Rev. Biochem.* **2000,** *69,* 923–960. doi:10.1146/annurev.biochem.69.1.923
437. Kuir, D.; Guillemineau, M.; Auzanneau, F.-I. *J. Org. Chem.* **2015,** *80,* 5004–5013. doi:10.1021/acs.joc.5b00405
438. Lassfolk, R.; Rahkila, J.; Johansson, M. P.; Ekholm, F. S.; Wärnå, J.; Leino, R. *J. Am. Chem. Soc.* **2019,** *141,* 1646–1654. doi:10.1021/jacs.8b11563
439. Asano, S.; Tanaka, H.-N.; Imamura, A.; Ishida, H.; Ando, H. *Org. Lett.* **2019,** *21,* 4197–4200. doi:10.1021/acs.orglett.9b01372
440. El Seoud, O. A.; Koschella, A.; Fidale, L. C.; Dorn, S.; Heinze, T. *Biomacromolecules* **2007,** *8,* 2629–2647. doi:10.1021/bm070062i
441. Shi, X.; Huang, Y.; Mao, Y.; Naimy, H.; Zaia, J. *J. Am. Soc. Mass Spectrom.* **2012,** *23,* 1498–1511. doi:10.1007/s13361-012-0429-4
442. Solleder, S. C.; Schneider, R. V.; Wetzel, K. S.; Boukis, A. C.; Meier, M. A. R. *Macromol. Rapid Commun.* **2017,** *38,* 1600711. doi:10.1002/marc.201600711
443. Aksakal, R.; Mertens, C.; Soete, M.; Badi, N.; Du Prez, F. *Adv. Sci.* **2021,** *8,* 2004038. doi:10.1002/advs.202004038
444. Martens, S.; Van den Begin, J.; Madder, A.; Du Prez, F. E.; Espeel, P. *J. Am. Chem. Soc.* **2016,** *138,* 14182–14185. doi:10.1021/jacs.6b07120
445. Al Ouahabi, A.; Charles, L.; Lutz, J.-F. *J. Am. Chem. Soc.* **2015,** *137,* 5629–5635. doi:10.1021/jacs.5b02639
446. Genabeek, B.; Lamers, B. A. G.; Hawker, C. J.; Meijer, E. W.; Gutekunst, W. R.; Schmidt, B. V. K. J. *J. Polym. Sci. (Hoboken, NJ, U. S.)* **2021,** *59,* 373–403. doi:10.1002/pol.20200862
447. Govindaraju, T.; Avinash, M. B. *Nanoscale* **2012,** *4,* 6102–6117. doi:10.1039/c2nr31167d

License and Terms

This is an Open Access article under the terms of the Creative Commons Attribution License (https://creativecommons.org/licenses/by/4.0). Please note that the reuse, redistribution and reproduction in particular requires that the author(s) and source are credited and that individual graphics may be subject to special legal provisions.

The license is subject to the *Beilstein Journal of Organic Chemistry* terms and conditions: (https://www.beilstein-journals.org/bjoc/terms)

The definitive version of this article is the electronic one which can be found at: https://doi.org/10.3762/bjoc.17.129

BEILSTEIN JOURNAL OF ORGANIC CHEMISTRY

An initiator- and catalyst-free hydrogel coating process for 3D printed medical-grade poly(ε-caprolactone)

Jochen Löblein[‡1], Thomas Lorson[‡1], Miriam Komma[1], Tobias Kielholz[2], Maike Windbergs[2], Paul D. Dalton[*,‡3] and Robert Luxenhofer[*,‡1,4]

Full Research Paper

Open Access

Address:
[1]Polymer Functional Materials, Chair for Advanced Materials Synthesis, Institute for Functional Materials and Biofabrication, Department of Chemistry and Pharmacy, Julius-Maximilians-University Würzburg, Würzburg, Germany, [2]Institute of Pharmaceutical Technology and Buchmann Institute for Molecular Life Sciences, Goethe University, Frankfurt am Main, Germany, [3]Knight Campus for Accelerating Scientific Impact, University of Oregon, 1505 Franklin Blvd, Eugene, 97403 Oregon, USA and [4]Soft Matter Chemistry, Department of Chemistry and Helsinki Institute of Sustainability Science, Faculty of Science, University of Helsinki, 00014 Helsinki, Finland

Email:
Paul D. Dalton[*] - pdalton@uoregon.edu; Robert Luxenhofer[*] - robert.luxenhofer@helsinki.fi

* Corresponding author ‡ Equal contributors

Keywords:
additive manufacturing; light-induced polymerization; self-initiated photografting and photopolymerization; surface-initiated polymerization; surface modification

Beilstein J. Org. Chem. **2021,** *17,* 2095–2101.
https://doi.org/10.3762/bjoc.17.136

Received: 09 June 2021
Accepted: 02 August 2021
Published: 19 August 2021

This article is part of the thematic issue "Polymer chemistry: fundamentals and applications".

Guest Editor: B. V. K. J. Schmidt

© 2021 Löblein et al.; licensee Beilstein-Institut.
License and terms: see end of document.

Abstract

Additive manufacturing or 3D printing as an umbrella term for various materials processing methods has distinct advantages over many other processing methods, including the ability to generate highly complex shapes and designs. However, the performance of any produced part not only depends on the material used and its shape, but is also critically dependent on its surface properties. Important features, such as wetting or fouling, critically depend mainly on the immediate surface energy. To gain control over the surface chemistry post-processing modifications are generally necessary, since it's not a feature of additive manufacturing. Here, we report on the use of initiator and catalyst-free photografting and photopolymerization for the hydrophilic modification of microfiber scaffolds obtained from hydrophobic medical-grade poly(ε-caprolactone) via melt-electrowriting. Contact angle measurements and Raman spectroscopy confirms the formation of a more hydrophilic coating of poly(2-hydroxyethyl methacrylate). Apart from surface modification, we also observe bulk polymerization, which is expected for this method, and currently limits the controllability of this procedure.

Introduction

Additive manufacturing, commonly referred to as three-dimensional (3D) printing, is an approach to create physical objects using layer-by-layer [1] or voxel-by-voxel fabrication [2]. 3D printed materials can be used for a broad spectrum of applications, including medical devices where implants can be personalized to improve outcomes in patients [3]. Here, compliance to the regulatory pathway [4,5] is important, which favors solvent-free processing technologies of medical-grade raw materials. Solvent-free 3D printing approaches such as electron beam melting [6], micro-extrusion [7] and selective laser sintering have all been used to fabricate clinical implants [6,7].

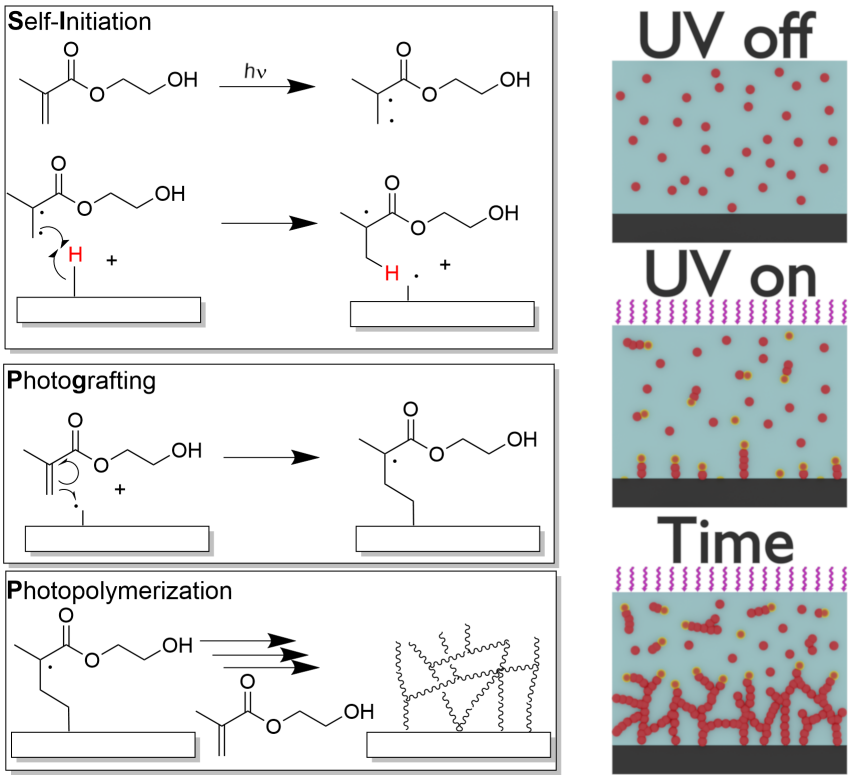
Other emerging 3D printing technologies can also fit the prerequisites described above, including melt electrowriting (MEW) [8]. This technology is based on the direct-writing of ultra-fine (800 nm to 10 µm) and micro-scale filaments onto a collector with repeat fiber deposition to build up a micro-scale 3D object, with build heights in the range of several millimeters [9-11]. In MEW, the polymer jet is electrostatically drawn from a nozzle, resulting in a considerable reduction of the final fiber diameter. The direct-writing onto a flat collector or on a rotating/translating mandrel enables the printing of flat [11,12] or tubular [13] scaffolds, respectively.

While medical-grade poly(ε-caprolactone) (PCL) is the most commonly used material for MEW, due to its favorable thermal and mechanical properties, cytocompatibility, biodegradability, and good printing properties [8,14,15], it is a hydrophobic polymer and immersion into fluids can result in air bubble capture within the scaffold structure, biofouling and non-specific cell interactions [16]. Protein adsorption and denaturation on the hydrophobic surface can lead to fibrous encapsulation of medical implants [17,18]. Accordingly, it would be beneficial for PCL implants to have a hydrophilic, non-fouling surface while avoiding factors that complicate the regulatory path to the clinic. So far, the wettability could be improved by a variety of methods like plasma treatment, NaOH hydrolysis treatment or a micro deposition system. This study outlines a potential approach to coat medical-grade PCL with a thin hydrogel that requires no initiator or catalyst – just a deoxygenated aqueous monomer solution and UV light. We demonstrate this surface modification using a hydrogel, poly(2-hydroxyethyl methacrylate) (PHEMA) [19]. However, this approach should have broad utility for a spectrum of monomers and macromonomers susceptible to radical polymerization onto (almost) any surface featuring C–H bonds. This hydrogel coating is achieved with self-initiated photografting and photopolymerization (SIPGP, Scheme 1).

SIPGP is a simple, solvent-free bulk/surface photografting first introduced by Deng et al. grafting maleic anhydride [20] and styrene [21] onto low-density poly(ethylene) films. Later, this was extended for other monomers and many other substrates including ultra-nanocrystalline diamond, graphene and silicon carbide [22-30]. Even bottle-brush brushes could be prepared via SIPGP on various substrates for different applications [31-33].

Results and Discussion

Here, we introduce SIPGP for the coating of 3D printed PCL microfiber scaffolds, investigate the range of suitable parameters and characterize the change in the properties of the coated scaffolds. PCL scaffolds with a hatch spacing of either 150 µm or 500 µm were fabricated, with the fiber diameter being 12.1 ± 3.3 µm. The experimental setup consisted of a closed chamber, which was equipped with a valve for argon supply and a slot for the UV lamp (Supporting Information File 1, Figure S1). Initially, static conditions were used to determine the influence of exposure time, distance between light source and substrate on the PHEMA coating and monomer concentration (Supporting Information File 1, Figure S2). As the next step, scaffolds were investigated with respect to their wettability. In order to simulate aqueous conditions in cell culture medium or after implantation, samples were immersed in water for 0, 10, 20 and 30 min (Figure 1A and Figure 1B; t = 0, 10, 20, 30 [min]) before analysis. Based on contact angle measurements, the wettability of PCL scaffolds notably changed after SIPGP modification (Figure 1). The hydrophobicity of untreated PCL MEW scaffolds (500 µm hatch spacing) is also affected by the macrostructure of the hatches, with a high contact angle of at least 127.9° (Figure 1A, t = 0 [min]) (compared to 66° reported for a smooth PCL film [34]) that remains almost unchanged over time. SIPGP-modified PCL scaffolds, however, revealed a significantly lower initial contact angle. For 500 µm hatch spacing, an initial contact angle of 83.2° (t = 0 [min]) was measured and decreased until a final value of 64.9° after 300 s (Figure 1B). The decrease in contact angle is more rapid compared to the uncoated PCL scaffold, because further water is adsorbed by the hydrophilic PHEMA coating, resulting in enhanced wettability. However, both graphs also show a time-dependent wettability decrease in the first 30 min after the withdrawal from immersion which might be in consequence of a hydration loss through water evaporation. Interestingly, this tendency is only followed by the dried PHEMA-coated sample and not by the dried pristine PCL scaffold. An explanation for this observation might be PHEMA´s ability to absorb water as well as the relative indistinct hydration state of PCL compared to PHEMA when fully hydrated.



Scheme 1: Schematic representation of the self-initiated photografting and photopolymerization (SIPGP) of 2-hydroxyethyl methacrylate (HEMA) including intersystem crossing from singlet to triplet state which is mandatory for the formation of a biradical (left). Cartoon how SIPGP leads to surface-initiated polymerization and bulk polymerization (monomer red, active species red/yellow halo) (right).

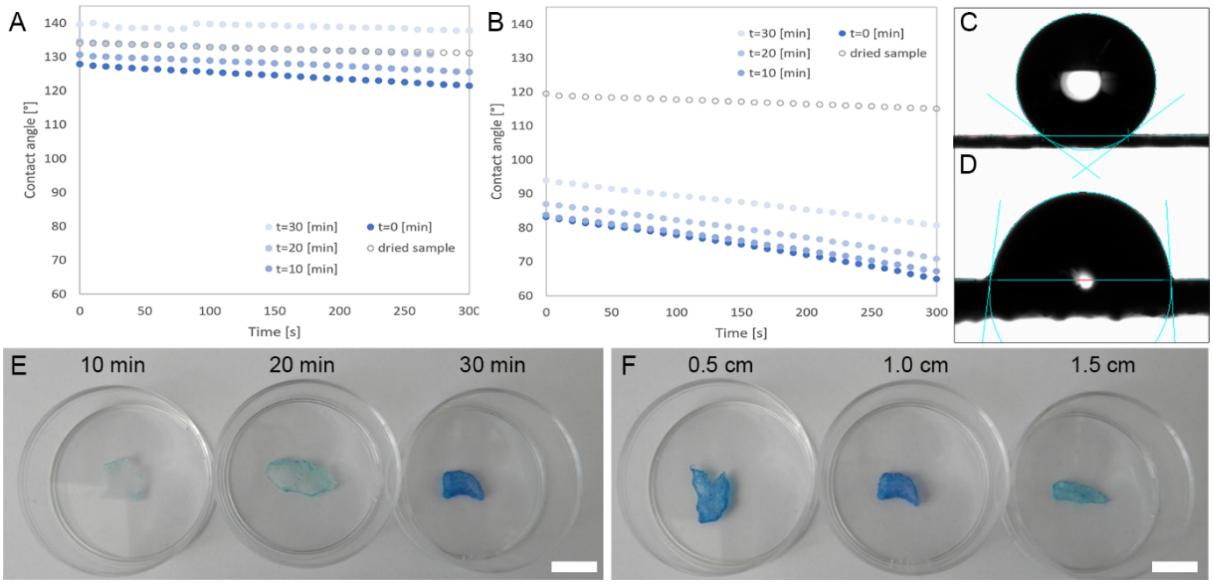


Figure 1: A) Graph showing change in the static contact angle with time on a pristine PCL scaffold with a 500 µm hatch spacing and B) on a SIPGP-coated scaffold with a 500 µm hatch spacing. The measured samples were immersed in water for different periods of time t = 0, 10, 20, 30 [min]. C) Photograph of a 2 µL water drop on a pristine PCL scaffold immediately after droplet deposition and D) on a SIPGP-modified scaffold immediately after droplet deposition. E and F) toluidine blue staining of PCL scaffolds coated with PHEMA via SIPGP showing the variation with E) the UV-reaction time and F) the distance between light source and substrate. Scale bar for E and F is 1 cm.

Toluidine blue staining was used as a rapid, colorimetric readout as it selectively binds to PHEMA. Results for three negative controls (cleaned scaffold, scaffold irradiated without monomer solution, and scaffold immersed in monomer solution without irradiation) can be found in Supporting Information File 1, Figure S3, and have no staining. The irradiation time was varied between 10 min, 20 min, and 30 min (Figure 1E) and the intensity of the blue coloration is proportional to reaction time resulting in a complete coating of the PCL fibers after 30 min. The distance between the UV source and the scaffold was varied from 0.5 cm, 1.0 cm, and 1.5 cm (Figure 1F) and, as the intensity decreases inversely in proportion to the square of the distance, a larger working distance should result in less pronounced coating.

Wang and Brown reported a polymerization conversion of 90% after 50 s for HEMA (0.30 mm ± 0.04 mm) [22] which is significantly faster than the values investigated in the present study. However, the authors used UV-C light with an intensity of 0.024 W/cm^2 compared to UV-A light with a calculated intensity of 0.079 W/cm^2 at a distance of 1.0 cm used in the present study. After SIPGP, a thin, heterogeneous material can be seen spanning large proportion of the pores (Figure 2A and Figure 2B), however, this morphology is highly irregular. A change in wetting behavior could be demonstrated, and toluidine blue staining indicates successful SIPGP of HEMA on PCL scaffolds. However, to prove that this material is indeed PHEMA, we performed confocal Raman microscopy on the samples, which allows a spatially resolved polymer identification based on chemical functionalities. A unique peak at 1111 cm^{-1} was identified and is attributed to backbone stretching of aliphatic chains [ν(C–C)] in PCL. Also, a characteristic band at 829 cm^{-1} was detected which can be assigned to PHEMA and refers to the symmetrical stretching vibration [ν(C–O–C)] of ester groups (Figure 2C, blue and red circles). With Raman imaging and the corresponding spectra, the presence of PHEMA on the PCL MEW scaffolds was clearly verified (Figure 2C and Figure 2D), especially regarding the material spanning the boxes.

Unfortunately, the high PCL signal intensity covers most of the signals originating from the thin PHEMA coating directly deposited on fibers (Supporting Information File 1, Figure S4; a 3D Raman reconstruction is provided in Supporting Information File 2). Scanning electron microscopy (SEM) corroborates this fiber coating and corroborates the inhomogeneous distribution of PHEMA inside the boxes (Figure 3). Compared to the pristine scaffold (Figure 3A and Figure 3B), the PHEMA coat can be clearly distinguished both as a thin coat on the fibers as well as in form of films between fibers and spanning boxes (Figure 3C). On unmodified scaffolds, rough patches on the bottom-most fibers are discernible (Figure 3B, white arrows), which originate from the contacting of the first fibers with the collector. After coating, these rough patches are covered by more smooth material, but only partially (Figure 3D, orange arrows). The coating is clearly irregular, even where fibers are fully coated, with seemingly thicker strands of PHEMA covering the PCL scaffold (Figure 3C and Figure 3E, yellow arrow). We assume that these thicker strands may originate from UV-induced HEMA polymerization in solution which are then deposited on the scaffold. Interestingly, profound webbing of PHEMA between the fibers can be observed (Figure 3F, red arrow), but also rather inhomogeneous membranous deposi-

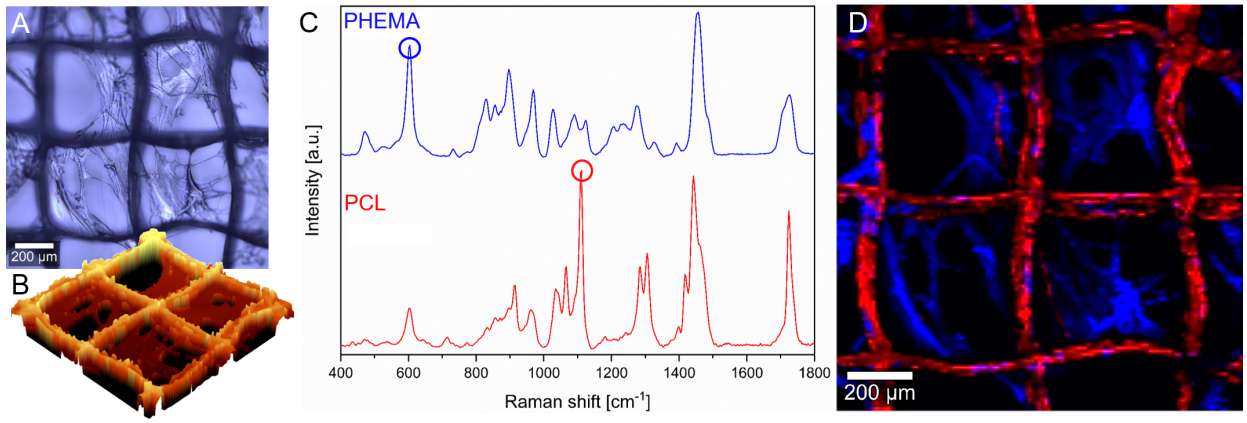


Figure 2: A) Optical photograph of an SIPGP-coated sample. B) 3D topography reconstruction of the SIPGP-coated scaffold. C) Raman spectra depicting the fingerprint region of PHEMA and PCL with the two significant peaks of PHEMA (829 cm^{-1}) and PCL (1111 cm^{-1}) marked with circles. (D) Shows these peaks as False-color Raman image of PCL fibers (red) and PHEMA coating (blue).

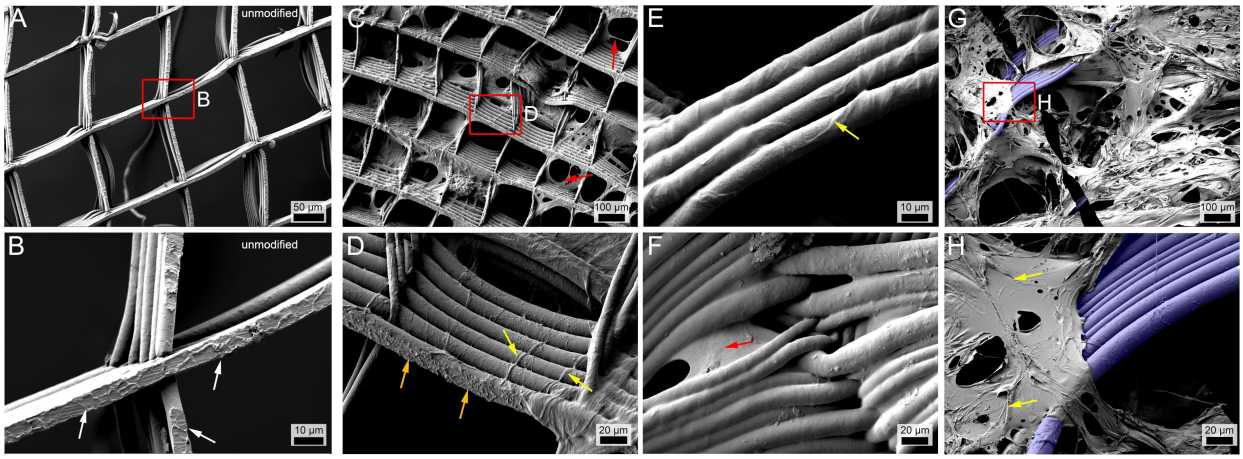


Figure 3: A) SEM image of pristine, uncoated PCL MEW scaffolds with a hatch spacing of 150 µm × 200 µm and inset (B), where the white arrows show embossing of the first printed layer on the bottom of the scaffold. C) PHEMA coated scaffolds (prominent spots of PHEMA coating marked with red arrows) of the same hatch spacing, irradiated from a distance of 1 cm for 30 min with a wavelength of 365 nm with inset shown in (D), where the yellow arrows point at PHEMA strands, in contrast to the irregularities caused by the printing (orange arrows). E and F) SEM images of scaffolds with a hatch spacing of 500 µm under the same conditions as C). The yellow arrow in (E) points at a border line of PHEMA and the red arrow in (F) at pure PHEMA in between fibers. G) SEM image of a scaffold with a hatch spacing of 500 µm under the same conditions as C), but freeze dried, with inset shown in (H), where the yellow arrows point at irregularities within the PHEMA coating. False colored blue for G and H indicates the exposed PCL fibers in the PHEMA-filled MEW scaffolds.

tions on larger sections of the scaffolds (Figure 3G and Figure 3H).

Even though MEW has been carried out predominantly using PCL, other non-conductive polymers like water-soluble poly(2-ethyl-2-oxazoline) (PEtOx) [35], polypropylene (PP) [36,37] photo-cross-linkable and biodegradable poly(L-lactide-*co*-ε-caprolactone-*co*-acryloyl carbonate) [38], or thermoplastic elastomers [39] have successfully been processed via MEW [40]. Interestingly, PCL frames made with MEW were used to build up soft network composites [41-43] with outstanding mechanical properties, also with weak matrices of interest for tissue engineering applications [44].

Conclusion

SIPGP is an interesting complementary technique to modify the surface of MEW printed scaffolds, which may be required for suitable interaction with cells or other materials. SIPGP does not require special equipment other than a UV lamp or special reagents. As a proof-of-concept, we demonstrated the feasibility using HEMA as monomer, but essentially any monomer polymerizable by free radical polymerization should be feasible. At this point, the coating of the fibrous scaffolds is rather inhomogeneous, as the surface-initiated polymerization is confounded by polymerization in bulk. Therefore, we are currently working on a slightly modified experimental setup, which utilizes a flow setup, constantly removing the bulk materials and facilitating a more homogeneous surface coating.

Supporting Information

Supporting Information File 1

Experimental section and additional images.
[https://www.beilstein-journals.org/bjoc/content/supplementary/1860-5397-17-136-S1.pdf]

Supporting Information File 2

3D Raman reconstruction.
[https://www.beilstein-journals.org/bjoc/content/supplementary/1860-5397-17-136-S2.mp4]

Acknowledgements

Technical support by Simon Ziegler is greatly appreciated. MEW scaffolds were kindly provided by Dr. Gernot Hochleitner.

Funding

We gratefully acknowledge financial support by the Volkswagen Stiftung (Grant# 93 417).

ORCID® iDs

Jochen Löblein - https://orcid.org/0000-0002-2155-9300
Tobias Kielholz - https://orcid.org/0000-0001-5945-8495
Paul D. Dalton - https://orcid.org/0000-0001-9602-4151
Robert Luxenhofer - https://orcid.org/0000-0001-5567-7404

References

1. Campbell, I.; Bourell, D.; Gibson, I. *Rapid Prototyping J.* **2012,** *18,* 255–258. doi:10.1108/13552541211231563
2. Bernal, P. N.; Delrot, P.; Loterie, D.; Li, Y.; Malda, J.; Moser, C.; Levato, R. *Adv. Mater. (Weinheim, Ger.)* **2019,** *31,* 1904209. doi:10.1002/adma.201904209
3. Ligon, S. C.; Liska, R.; Stampfl, J.; Gurr, M.; Mülhaupt, R. *Chem. Rev.* **2017,** *117,* 10212–10290. doi:10.1021/acs.chemrev.7b00074
4. Youssef, A.; Hollister, S. J.; Dalton, P. D. *Biofabrication* **2017,** *9,* 012002. doi:10.1088/1758-5090/aa5766
5. Pashuck, E. T.; Stevens, M. M. *Sci. Transl. Med.* **2012,** *4,* 160sr4. doi:10.1126/scitranslmed.3002717
6. Regis, M.; Marin, E.; Fedrizzi, L.; Pressacco, M. *MRS Bull.* **2015,** *40,* 137–144. doi:10.1557/mrs.2015.1
7. Probst, F. A.; Hutmacher, D. W.; Müller, D. F.; Machens, H.-G.; Schantz, J.-T. *Handchir. Mikrochir. Plastische Chir.* **2010,** *42,* 369–373. doi:10.1055/s-0030-1248310
8. Robinson, T. M.; Hutmacher, D. W.; Dalton, P. D. *Adv. Funct. Mater.* **2019,** *29,* 1904664. doi:10.1002/adfm.201904664
9. Ristovski, N.; Bock, N.; Liao, S.; Powell, S. K.; Ren, J.; Kirby, G. T. S.; Blackwood, K. A.; Woodruff, M. A. *Biointerphases* **2015,** *10,* 011006. doi:10.1116/1.4914380
10. Jungst, T.; Muerza-Cascante, M. L.; Brown, T. D.; Standfest, M.; Hutmacher, D. W.; Groll, J.; Dalton, P. D. *Polym. Int.* **2015,** *64,* 1086–1095. doi:10.1002/pi.4948
11. Wunner, F. M.; Wille, M.-L.; Noonan, T. G.; Bas, O.; Dalton, P. D.; De-Juan-Pardo, E. M.; Hutmacher, D. W. *Adv. Mater. (Weinheim, Ger.)* **2018,** *30,* 1706570. doi:10.1002/adma.201706570
12. Muerza-Cascante, M. L.; Shokoohmand, A.; Khosrotehrani, K.; Haylock, D.; Dalton, P. D.; Hutmacher, D. W.; Loessner, D. *Acta Biomater.* **2017,** *52,* 145–158. doi:10.1016/j.actbio.2016.12.040
13. McColl, E.; Groll, J.; Jungst, T.; Dalton, P. D. *Mater. Des.* **2018,** *155,* 46–58. doi:10.1016/j.matdes.2018.05.036
14. Woodruff, M. A.; Hutmacher, D. W. *Prog. Polym. Sci.* **2010,** *35,* 1217–1256. doi:10.1016/j.progpolymsci.2010.04.002
15. Bartnikowski, M.; Dargaville, T. R.; Ivanovski, S.; Hutmacher, D. W. *Prog. Polym. Sci.* **2019,** *96,* 1–20. doi:10.1016/j.progpolymsci.2019.05.004
16. Khampieng, T.; Yamassatien, V.; Ekabutr, P.; Pavasant, P.; Supaphol, P. *Adv. Polym. Technol.* **2018,** *37,* 2030–2042. doi:10.1002/adv.21861
17. Zhang, L.; Cao, Z.; Bai, T.; Carr, L.; Ella-Menye, J.-R.; Irvin, C.; Ratner, B. D.; Jiang, S. *Nat. Biotechnol.* **2013,** *31,* 553–556. doi:10.1038/nbt.2580
18. Swartzlander, M. D.; Barnes, C. A.; Blakney, A. K.; Kaar, J. L.; Kyriakides, T. R.; Bryant, S. J. *Biomaterials* **2015,** *41,* 26–36. doi:10.1016/j.biomaterials.2014.11.026
19. Hicks, C.; Crawford, G.; Chirila, T.; Wiffen, S.; Vijayasekaran, S.; Lou, X.; Fitton, J.; Maley, M.; Clayton, A.; Dalton, P.; Platten, S.; Ziegelaar, B.; Hong, Y.; Russo, A.; Constable, I. *Prog. Retinal Eye Res.* **2000,** *19,* 149–170. doi:10.1016/s1350-9462(99)00013-0
20. Deng, J.-P.; Yang, W.-T. *J. Polym. Sci., Part A: Polym. Chem.* **2001,** *39,* 3246–3249. doi:10.1002/pola.1307
21. Deng, J.-P.; Yang, W.-T.; Rånby, B. *Macromol. Rapid Commun.* **2001,** *22,* 535–538. doi:10.1002/1521-3927(20010401)22:7<535::aid-marc535>3.0.co;2-3
22. Wang, H.; Brown, H. R. *Macromol. Rapid Commun.* **2004,** *25,* 1095–1099. doi:10.1002/marc.200400010
23. Fang, W.-H.; Liu, R.-Z. *J. Am. Chem. Soc.* **2000,** *122,* 10886–10894. doi:10.1021/ja0004579
24. Steenackers, M.; Lud, S. Q.; Niedermeier, M.; Bruno, P.; Gruen, D. M.; Feulner, P.; Stutzmann, M.; Garrido, J. A.; Jordan, R. *J. Am. Chem. Soc.* **2007,** *129,* 15655–15661. doi:10.1021/ja075378c
25. Steenackers, M.; Küller, A.; Stoycheva, S.; Grunze, M.; Jordan, R. *Langmuir* **2009,** *25,* 2225–2231. doi:10.1021/la803386c
26. Steenackers, M.; Gigler, A. M.; Zhang, N.; Deubel, F.; Seifert, M.; Hess, L. H.; Lim, C. H. Y. X.; Loh, K. P.; Garrido, J. A.; Jordan, R.; Stutzmann, M.; Sharp, I. D. *J. Am. Chem. Soc.* **2011,** *133,* 10490–10498. doi:10.1021/ja201052q
27. Steenackers, M.; Sharp, I. D.; Larsson, K.; Hutter, N. A.; Stutzmann, M.; Jordan, R. *Chem. Mater.* **2010,** *22,* 272–278. doi:10.1021/cm903051j
28. Yang, J.; Hou, L.; Xu, B.; Zhang, N.; Liang, Y.; Tian, W.; Dong, D. *Macromol. Rapid Commun.* **2014,** *35,* 1224–1229. doi:10.1002/marc.201400068
29. Yang, J.; Zhang, N.; Li, H.; Xu, B.; Tian, W.; Dong, D. *Polym. Int.* **2015,** *64,* 804–810. doi:10.1002/pi.4855
30. Bian, H.; Dong, X.; Chen, S.; Dong, D.; Zhang, N. *Chin. Chem. Lett.* **2018,** *29,* 171–174. doi:10.1016/j.cclet.2017.05.011
31. Zhang, N.; Steenackers, M.; Luxenhofer, R.; Jordan, R. *Macromolecules* **2009,** *42,* 5345–5351. doi:10.1021/ma900329y
32. Zhang, N.; Pompe, T.; Amin, I.; Luxenhofer, R.; Werner, C.; Jordan, R. *Macromol. Biosci.* **2012,** *12,* 926–936. doi:10.1002/mabi.201200026
33. Hou, L.; Wang, L.; Zhang, N.; Xie, Z.; Dong, D. *Polym. Chem.* **2016,** *7,* 5828–5834. doi:10.1039/c6py01008c
34. Cheng, Z.; Teoh, S.-H. *Biomaterials* **2004,** *25,* 1991–2001. doi:10.1016/j.biomaterials.2003.08.038
35. Hochleitner, G.; Hümmer, J. F.; Luxenhofer, R.; Groll, J. *Polymer* **2014,** *55,* 5017–5023. doi:10.1016/j.polymer.2014.08.024
36. Haigh, J. N.; Dargaville, T. R.; Dalton, P. D. *Mater. Sci. Eng., C* **2017,** *77,* 883–887. doi:10.1016/j.msec.2017.03.286
37. Florczak, S.; Lorson, T.; Zheng, T.; Mrlik, M.; Hutmacher, D. W.; Higgins, M. J.; Luxenhofer, R.; Dalton, P. D. *Polym. Int.* **2019,** *68,* 735–745. doi:10.1002/pi.5759
38. Chen, F.; Hochleitner, G.; Woodfield, T.; Groll, J.; Dalton, P. D.; Amsden, B. G. *Biomacromolecules* **2016,** *17,* 208–214. doi:10.1021/acs.biomac.5b01316
39. Hochleitner, G.; Fürsattel, E.; Giesa, R.; Groll, J.; Schmidt, H.-W.; Dalton, P. D. *Macromol. Rapid Commun.* **2018,** *39,* 1800055. doi:10.1002/marc.201800055
40. Kade, J. C.; Dalton, P. D. *Adv. Healthcare Mater.* **2021,** *10,* 2001232. doi:10.1002/adhm.202001232
41. Bas, O.; De-Juan-Pardo, E. M.; Chhaya, M. P.; Wunner, F. M.; Jeon, J. E.; Klein, T. J.; Hutmacher, D. W. *Eur. Polym. J.* **2015,** *72,* 451–463. doi:10.1016/j.eurpolymj.2015.07.034
42. Bas, O.; D'Angella, D.; Baldwin, J. G.; Castro, N. J.; Wunner, F. M.; Saidy, N. T.; Kollmannsberger, S.; Reali, A.; Rank, E.; De-Juan-Pardo, E. M.; Hutmacher, D. W. *ACS Appl. Mater. Interfaces* **2017,** *9,* 29430–29437. doi:10.1021/acsami.7b08617
43. Bas, O.; De-Juan-Pardo, E. M.; Meinert, C.; D'Angella, D.; Baldwin, J. G.; Bray, L. J.; Wellard, R. M.; Kollmannsberger, S.; Rank, E.; Werner, C.; Klein, T. J.; Catelas, I.; Hutmacher, D. W. *Biofabrication* **2017,** *9,* 025014. doi:10.1088/1758-5090/aa6b15
44. Schaefer, N.; Janzen, D.; Bakirci, E.; Hrynevich, A.; Dalton, P. D.; Villmann, C. *Adv. Healthcare Mater.* **2019,** *8,* 1801226. doi:10.1002/adhm.201801226

License and Terms

This is an Open Access article under the terms of the Creative Commons Attribution License (https://creativecommons.org/licenses/by/4.0). Please note that the reuse, redistribution and reproduction in particular requires that the author(s) and source are credited and that individual graphics may be subject to special legal provisions.

The license is subject to the *Beilstein Journal of Organic Chemistry* terms and conditions: (https://www.beilstein-journals.org/bjoc/terms)

The definitive version of this article is the electronic one which can be found at: https://doi.org/10.3762/bjoc.17.136

BEILSTEIN JOURNAL OF ORGANIC CHEMISTRY

Constrained thermoresponsive polymers – new insights into fundamentals and applications

Patricia Flemming[‡1,2], Alexander S. Münch[*,‡1], Andreas Fery[1,2] and Petra Uhlmann[*1,3]

Review

Open Access

Address:
[1]Leibniz-Institut für Polymerforschung Dresden e.V., Hohe Straße 6, 01069 Dresden, Germany, [2]Technische Universität Dresden, 01062 Dresden, Germany and [3]University of Nebraska-Lincoln, NE 68588, Lincoln, USA

Email:
Alexander S. Münch[*] - muench@ipfdd.de;
Petra Uhlmann[*] - uhlmannp@ipfdd.de

* Corresponding author ‡ Equal contributors

Keywords:
lower critical solution temperature (LCST); responsive coating; smart material; thermoresponsive polymer; upper critical solution temperature (UCST)

Beilstein J. Org. Chem. **2021,** *17,* 2123–2163.
https://doi.org/10.3762/bjoc.17.138

Received: 31 March 2021
Accepted: 10 August 2021
Published: 20 August 2021

This article is part of the thematic issue "Polymer chemistry: fundamentals and applications".

Guest Editor: B. V. K. J. Schmidt

© 2021 Flemming et al.; licensee Beilstein-Institut.
License and terms: see end of document.

Abstract

In the last decades, numerous stimuli-responsive polymers have been developed and investigated regarding their switching properties. In particular, thermoresponsive polymers, which form a miscibility gap with the ambient solvent with a lower or upper critical demixing point depending on the temperature, have been intensively studied in solution. For the application of such polymers in novel sensors, drug delivery systems or as multifunctional coatings, they typically have to be transferred into specific arrangements, such as micelles, polymer films or grafted nanoparticles. However, it turns out that the thermodynamic concept for the phase transition of free polymer chains fails, when thermoresponsive polymers are assembled into such sterically confined architectures. Whereas many published studies focus on synthetic aspects as well as individual applications of thermoresponsive polymers, the underlying structure–property relationships governing the thermoresponse of sterically constrained assemblies, are still poorly understood. Furthermore, the clear majority of publications deals with polymers that exhibit a lower critical solution temperature (LCST) behavior, with PNIPAAM as their main representative. In contrast, for polymer arrangements with an upper critical solution temperature (UCST), there is only limited knowledge about preparation, application and precise physical understanding of the phase transition. This review article provides an overview about the current knowledge of thermoresponsive polymers with limited mobility focusing on UCST behavior and the possibilities for influencing their thermoresponsive switching characteristics. It comprises star polymers, micelles as well as polymer chains grafted to flat substrates and particulate inorganic surfaces. The elaboration of the physicochemical interplay between the architecture of the polymer assembly and the resulting thermoresponsive switching behavior will be in the foreground of this consideration.

Introduction

During the last decades, the class of stimuli-responsive materials has entered the focus of scientific research and applied polymer science [1-9]. They are characterized primarily by their ability to adapt spontaneously and reversibly to changes of environmental conditions because of their characteristic physical and chemical properties. For this reason, they are also referred to as "smart materials". Due to their very flexibly designable organic structure, the physicochemical properties of polymers can be adjusted precisely, making them ideal chemical components for the generation of smart devices. Depending on the polymer structure, including backbone and functional groups [10], their properties can be reversibly influenced by external chemical (e.g., pH value [11,12], ionic strength [13], polarity of solvent [14]), biological (e.g., bacteria, biomolecules [15], enzymes [16]) or physical stimuli (e.g., light [17-19], temperature [12,18], mechanical forces, as well as electric [20,21] and magnetic fields [22-24]) [1,25,26]. As a result of these environmental triggers, smart materials exhibit a defined reversible change in their physicochemical properties (e.g., solubility, viscosity) and can respond to stimuli in several ways by altering light transmitting abilities, shape, color, conductivity, as well as wettability [27,28]. Therefore, such functional polymers have a huge potential in numerous areas of application including biomedicine [29,30], drug delivery [12,31], tissue engineering [32,33], analytic application [18], environmental applications [34,35], sensors [36-38], actuators [37-39] and other applications [5].

For many of these purposes, it is essential to tether such polymers to interfaces or arrange them into confined polymeric architectures, such as star polymers or micelles, in a defined way. All these arrangements have in common that the mobility, i.e., the degrees of freedom of movement of the polymer chains, is limited compared to free polymers in solution, which affects the responsiveness of the polymers. The switching behavior can thus be controlled not only by the chemical composition of the polymer and its chain length, but also by its specific arrangement, for example by varying the grafting density [40-42]. Therefore, a transfer of the physicochemical concepts valid for free polymer chains in solution is only conditionally applicable to constrained polymer topologies. The most commonly used stimulus to induce responsive behavior is the temperature [2,43-45]. The physicochemical basis for this is a temperature-dependent solubility of a polymer in one or a mixture of solvents. In solution, stimuli responsive polymers undergo a conformational, so-called coil-to-globule, transition. Depending on whether the solubility increases below (LCST for lower critical solution temperature [46-49]) or above (UCST for upper critical solution temperature [50-53]) a critical demixing temperature, this class of polymers can be divided into those with LCST or UCST behavior. Physicochemically, these temperature-dependent phase transitions and consequently the term UCST/LCST are exclusively defined for substances, like polymers, in solution. However, the related concepts have been extended to polymers attached to flat or particulate surfaces as well as polymers in star or micelle constitution in the last decades. Hence, thermoresponsive polymers are still intensively investigated regarding to theory, preparation and their potential use [2,43]. However, while polymers with an LCST type phase transition have been extensively studied over the past decades, interest in the equally promising but usually more complex and experimentally much less frequently observed UCST-based phase transitions of polymers has grown strongly in recent years.

The UCST-type thermoresponsive behavior of polymers is governed by oriented polymer–polymer interactions, such as hydrogen bonding or electrostatic interactions. As a function of temperature, these attractive interactions are formed and contribute to phase separation (T < UCST) or are increasingly destabilized and allow solvation of the polymer chains (T > UCST). Compared to an entropy-driven LCST behavior of polymers, the enthalpy-driven UCST thermoresponse is based on spatially highly directed forces between polymer segments [51,52,54,55]. Understanding the molecular mechanism and thus precisely controlling the complex interplay of attractive interactions enables fine-tuning of the phase transition temperature itself, as well as the sharpness, switching amplitude and reversibility of the transition for a desired application [6,50,51]. Today there are several excellent reviews offering synthetic guidelines for the design of novel thermoresponsive polymers exhibiting UCST type behavior. Seuring et al. [51,54], Niskanen et al. [50], Bansal et al. [52] or Zhao et al. [55] summarize known thermoresponsive building blocks based on their molecular structure and offer interesting design approaches supported by the underlying thermodynamic mixing theory. However, although the influence of certain molecular parameters such as chain length, concentration, pH or low molecular weight additives are discussed, the thermoresponsive behavior of polymers is exclusively considered as free polymer chains in solution. On the other hand, there are several reviews dealing with applications of thermoresponsive polymers. In this context, among others Zarrintaj et al. [56], Mokhtarinia et al. [57] and Sponchioni et al. [58] present a few novel applications of UCST polymers, especially in the biomedical field in comparison to LCST-based approaches [6,7,59-62]. However, these reviews and the summarized research papers mainly focus on the application itself. A systematic investigation of the underlying structure–property relationship of the thermoresponsive polymer has only been conducted to a very small extent.

Despite of first successful applications of UCST polymers, it is still poorly understood how the polymer's topology is effecting its thermoresponsive behavior until now. So far, there are neither sufficient theoretical models nor extensive experimental work that can comprehensively describe the influence of grafting density, degree of crosslinking or branching as well as the substrate's influence on the UCST phase transition of grafted polymers. Moreover, for polymers in solution, a generalized thermodynamic description and a standardized characterization of the macroscopic effects via turbidimetry (determination of the cloud point) is available. For thermoresponsive interfaces in the form of polymer brushes on a flat substrate or on nanoparticles, however, there are only very limited comparable analytical characterization methods, which consequently leads to a distortion of terminologies and makes it difficult to compare different studies. Nevertheless, based on selected studies, we want to highlight different topologies of UCST polymers in the subsequent discussion and work out their impact on the thermoresponsive phase transition. In contrast to a large number of previously published studies, the present review does not only focus on the molecular structure of thermoresponsive polymers and their synthesis but also discusses their phase transitions, in terms of structure–property relationships arising from the alignment of the polymer chains in assemblies of constrained mobility. Benefits as well as limitations of selected grafted or crosslinked architectures will be pointed out. However, based on the relatively small number of available studies and sometimes contradictory findings, it is evident that there is a big demand of academic research to develop generalized guidelines for the use of UCST-type polymer topologies especially within multicomponent systems.

The present review will be limited exclusively to stimuli-responsive polymer layers bonded to flat and particulate inorganic surfaces as well as to star polymers and polymer micelles. Only polymer layers that are covalently, i.e., chemically, bonded will be considered in contrast to non-bonded Langmuir–Blodgett or hydrogel films [63,64].

The following contribution is divided into three sections. The review will be preluded with a presentation of the physicochemical aspects of the phase transition of unhindered polymer chains in solution with an LCST or UCST behavior, followed by a consideration of grafted linear polymers, star polymers and micelles having such thermoresponsive characteristics. Because studies about systems with UCST behavior are underrepresented and only sporadically physicochemically analyzed, the focus will be on this type of phase transitions. Additionally, the knowledge about the LCST behavior of the mentioned polymer structures (micelles, star polymers) and grafted configurations (chains anchored on spheric and flat substrates) will be briefly summarized. This review article aims to outline the existing knowledge on thermosensitive polymers from a physicochemical rather than a synthetic point of view in order to gain a deeper understanding of the mechanisms involved in the phase transition with upper critical demixing point versus lower critical demixing point. The fundamental understanding of the polymer–solvent (–surface) interactions and the influence of the polymer morphology is essential for the generation of new polymer-equipped devices with tailored properties for specific applications. At the end of the review article all abbreviations are explained in a separate list.

Review

Theory of LCST and UCST

Fundamental thermodynamics of binary mixtures

The theoretical considerations about the mixing behavior of a polymer in a solvent, which is often characterized by a limited temperature-dependent miscibility due to the specific properties of macromolecules, is introduced with some fundamental remarks on the thermodynamics during the mixing process [65,66]. From the mathematical description of the law of energy conservation (1st law of thermodynamics) and the assumption that energy cannot be completely converted into work (2nd law of thermodynamics), a criterion for the spontaneity of processes in general, and the mixing processes discussed here, has been thermodynamically formulated. Mathematically, this description results in the Gibbs energy of mixing $\Delta_m G$, which is linked to the enthalpy of mixing $\Delta_m H$ and the entropy of mixing $\Delta_m S$ via the following well-known connection:

$$\Delta_m G = \Delta_m H - \Delta_m S \tag{1}$$

This means that for positive values of $\Delta_m G$, segregation occurs and for negative $\Delta_m G$, mixing occurs. For an ideal binary mixture of components A and B, this equation can be converted into the following form by comparing the Gibbs energy before and after mixing using the chemical potentials μ:

$$\Delta_m G = n \cdot R \cdot T \cdot \left(\varphi_A \cdot \ln \varphi_A + \varphi_B \cdot \ln \varphi_B\right) \tag{2}$$

with $n = n_A + n_B$. It should be noted that the essential property of an ideal mixture of liquids is not the exclusion of all interactions as it is assumed for the mixing of ideal gases. In an ideal solution, there are interactions between the components A and B, but the average interaction energy between A and B in the mixture is the same as the average energy of interaction between the single components in the pure liquids. Therefore, the enthalpy of mixing, the difference between the enthalpy of the mixture and the enthalpy of the pure components, $\Delta_m H$ is zero

and from the comparison of Equation 1 and Equation 2 we obtain for the entropy of mixing:

$$\Delta_m S = -R \cdot T \cdot \left(\varphi_A \cdot \ln \varphi_A + \varphi_B \cdot \ln \varphi_B\right) \quad (3)$$

Thus, the driving force of the mixing process is the increase in disorder due to the mixing of the particles of both species. $\Delta_m G$ is therefore always negative for ideal mixtures of any composition with a minimum at a certain ratio A–B and is always smaller than the Gibbs energy for a heterogeneous system over the entire concentration range (illustrated in Figure 1a, curve α). The Gibbs energy of mixing cannot be reduced by demixing, so that A and B are miscible with each other in any ratio. The mixture is always more stable than the pure components. In contrast, the curve γ shows an example for the behavior of $\Delta_m G$ of a real mixture. Here, the Gibbs energy of the single-phase state is always higher than the mixture of the two components. Therefore, the two liquids are immiscible with each other over the whole concentration range. On the molecular level, these real mixtures are characterized by interactions A–A, A–B as well as B–B, which are all different from each other. The mixing process is thus accompanied by an enthalpy change and possibly by an additional entropy contribution. The free energy of mixing can thus become positive (spontaneous segregation) if the mixing process is strongly endothermic (large positive value for $\Delta_m H$) and $\Delta_m S$ is negative (for example, due to reorganization of the molecules, which can lead to a more ordered system).

In addition to systems that are immiscible over the complete composition range, components A and B may also be miscible only in a specific range of possible compositions. This phenomenon is also called partially miscibility. In this case, a mixing gap is formed in which the binary system is characterized by instability (Figure 1, curve β). In this region, $\Delta_m G$ exhibits a maximum and two inflection points (E and F) as a function of composition. This region cannot be realized by "equilibrium" experiments and can only be captured mathematically. These points are also called spinodal points. In addition, two further minima exist. By applying the double tangent to these two points C and D, the composition of the coexisting phases of the hypothetical mixture with the composition x_m can be obtained. The region between C and D, also called binodal points, and the inflection points is a metastable region. Mathematically, this results in the following instability criterion:

$$\frac{\partial \Delta_m G}{\partial x} = 0; \quad \frac{\partial^2 \Delta_m G}{\partial x^2} = 0 \quad (4)$$

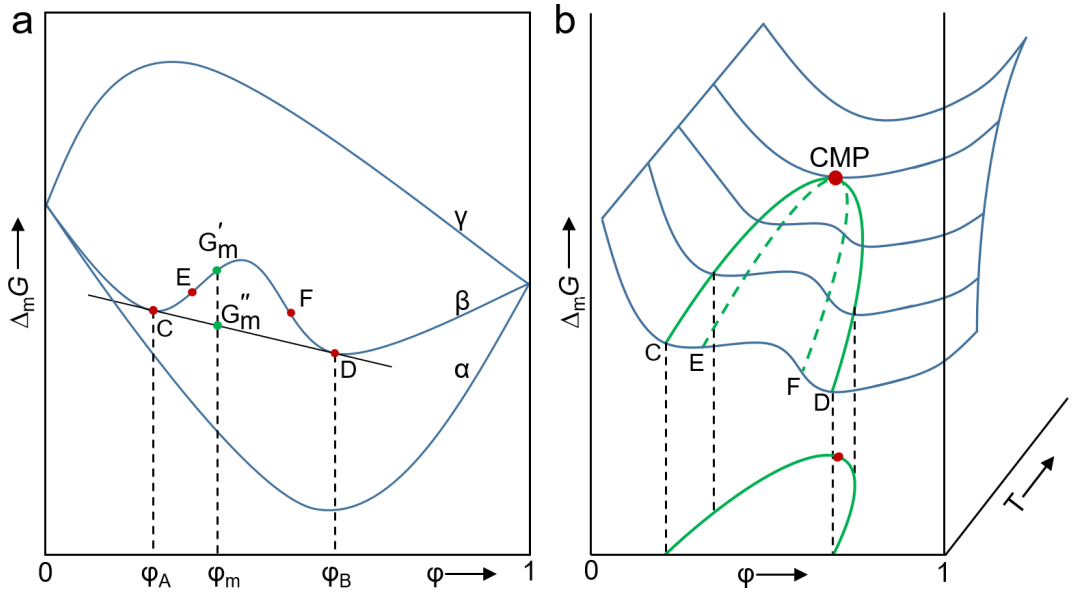


Figure 1: (a) Schematic representation of the phase stability of a binary mixture based on the free enthalpy of mixing $\Delta_m G$ as a function of composition at constant pressure and temperature. Function α shows the curve for an ideal mixture with complete miscibility. Curve β corresponds to a system with a miscibility gap. Here, for example, a mixture of composition φ_m decomposes into the corresponding phases A and B with the corresponding volume fractions φ_A and φ_B. The mixture can thereby lower its energy from G'_m to G''_m. The curve γ shows the behavior with complete immiscibility. (b) Schematic representation of the phase stability of a binary mixture with limited miscibility in a spatial φ–$\Delta_m G$–T diagram with projection of the Gibbs energy of mixing curves onto the φ–T plane for the construction of the known temperature-composition curves is exemplarily shown for a system with an upper critical demixing point and corresponding upper critical solution temperature (UCST).

These equations are valid for φ_1 as well as for φ_2. The point where binodals and spinodals touch, i.e., their values become equal, is called the critical point (Figure 1b). The criterion is that in this point the third derivative of the Gibbs energy after composition is zero:

$$\frac{\partial^3 \Delta_m G}{\partial x^3} = 0 \tag{5}$$

In many binary systems, the miscibility of two components is temperature dependent. Depending on whether a miscibility gap occurs above or below a certain temperature, a distinction is made between mixtures with an upper critical solution temperature (UCST) or a lower critical solution temperature (LCST). Figure 1b demonstrates the schematic projection of several functions of $\Delta_m G$ at different concentrations and temperatures into a commonly represented T–φ diagram using the example of a system with a UCST.

As described above, limited miscibility occurs whenever the mixture exhibits deviations from the ideal state. This means that $\Delta_m G$ is no longer exclusively dependent on the entropy of mixing (Equation 3). In addition, a value for the enthalpy of mixing $\Delta_m H$, which describes the energetic interactions, must be included in the consideration. Flory and Huggins did significant work on this field, which is widely used in the description of polymer solutions [67-70]. For the enthalpic description, they introduced the interaction parameter χ, which is defined over the intracomponent interactions ε_{AA} and ε_{BB} between the particles of the pure components and intercomponent interactions ε_{AB} between the components among each other. Whether limited miscibility occurs depends on the interplay between these inter- and intracomponent forces. According to Flory and Huggins the χ-parameter was derived via a lattice model of statistical thermodynamics and is defined as follows:

$$\chi = -\frac{z}{2kT} \cdot \left(\varepsilon_{AA} + \varepsilon_{BB} - 2\varepsilon_{AB}\right) \tag{6}$$

with k as the Boltzmann constant, z as the (average) number of contacts per molecule and T as the temperature. Accordingly, the following relationship is obtained for the enthalpy of mixing:

$$\Delta_m H = R \cdot T \cdot \chi \cdot \varphi_A \cdot \varphi_B \tag{7}$$

By combination of this equation with Equation 3 for the entropy and Equation 1, a mathematical relationship can be derived for $\Delta_m G$, which is also the mathematical description for the curves α, β, and γ in Figure 1. In the case of an ideal mixture, the χ-parameter is zero and curve α is obtained. Because of interactions between the components in nonideal two component systems, the χ-parameter takes positive or negative values depending on whether the intracomponent interaction is smaller or larger in comparison to the intercomponent interaction. The miscibility, i.e., whether $\Delta_m G$ becomes negative, is decided by the relationship between $\Delta_m H$ and $\Delta_m S$ and the temperature, which is illustrated in Figure 1.

Thermodynamics of polymer–solvent mixtures

Based on these fundamental considerations, these thermodynamic relationships for the mixing process of two liquids are now transferred to free polymer chains in a solvent. For simplicity, a monodisperse polymer is assumed, which, in a first approximation, should behave like a liquid in a solvent. The dissolution of polymers is characterized by strong interactions among the polymer chains and with the solvent molecules. For a polymer to dissolve well in a solvent, the intermolecular forces between the polymer chains on one side and between the solvent molecules on the other side must be smaller than the effective forces between polymer and solvent molecules among each other. If this condition is fulfilled, solvation of the polymer takes place. First, cohesive forces between the solvent molecules and the polymer chains must be overcome. At the same time, polymer chains come into contact with solvent molecules, which leads to the release of solvation energies or adhesion energies. If the Gibbs energy of the individual components (polymer and solvent) is higher than that of the homogeneous mixture, $\Delta_m G$ is less than zero. The components mix into each other. Conversely, if $\Delta_m G > 0$, complete dissolution of the polymer cannot occur. Coexisting, separate phases with a high and a low polymer content are formed. Experimental and theoretical studies show that there is both a concentration and temperature dependence of χ [71-74]. Consequently, for the exact description of complex phenomena of the dissolution of polymers, an extension of the basic theory is necessary, which results in a various number of tailored models [75-77], like the Flory–Huggins–van Santen (FHS) model. The FHS model shows that the combinatorial entropy of mixing is much smaller for macromolecules than for compounds with a low molar mass. For modelling of phase diagrams with LCST and/or UCST, it is common practice to replace χ by a semiempirical interaction parameter g, which is both temperature and concentration dependent [78,79] and can be modelled by using the following polynomial in φ_2 (with k as index of summation).

$$g = \sum_{k=o}^{n} g_k \cdot \varphi_2^k \qquad k = 0,1,2,3,...,n \tag{8}$$

$$g_k = g_{k0} + \frac{g_{k1}}{T} + g_{k2} \cdot k \qquad g_{k0}, g_{k1}, g_{k2} = const. \quad (9)$$

Due to a complex temperature dependency of g (denoted as gk in Equation 9) the polymer can show an upper or lower critical demixing point or a combination of both (Figure 2). In the discussion so far, it was assumed that the investigated polymer solution is strictly binary and consists only of a solvent and the polymer with one molar mass. However, this is not true for any real polymer solution. Every polymer always exhibits a molar mass distribution. Therefore, a quasi-binary mixture is usually considered. It is possible to measure the cloud-points, but the obtained cloud-point (T_{cp}) curve differs from a simple bimodal. Thus, the critical point (LCST or UCST) of one specific polymer with distinct P_n is not the extremum and is found at higher polymer concentrations in practice. The maximum of the cloud-point curve shifted to higher temperatures and to the solvent-rich region. The theoretical model was accordingly extended to account for polydispersity [80-82].

In general, the determination of cloud-points with respect to a thermally induced phase transition is a widely discussed phenomenon in the literature. At this point we would like to refer to an excellent work by Hoogenboom and co-workers [46]. We will only briefly discuss the definition of T_{cp} and how it differs from LCST and UCST. The T_{cp} is defined as the temperature at which the phase transition of a polymer solution at a certain concentration from the soluble state to the collapsed state occurs, accompanied by the turbidity of the solution. This temperature can be determined by various methods, such as turbidimetry [83], ^{1}H NMR spectrosocopy [84], and dynamic light scattering [85,86]. In this context, the cloud-point is the phase transition temperature at a certain polymer concentration, which can be located at any point on the binodal curve, and therefore, the polymer concentration must be specified sets in the cloud-point determination. It should be noted that T_{cp} is not equivalent with LCST or UCST, since LCST corresponds to the minimum temperature value or UCST corresponds to the maximum temperature value of the binodal curve. In other words, the LCST is the lowest value of T_{cp} in the phase diagram and the UCST is the highest value of T_{cp}. The cloud-point curve does not exactly match the binodal curve in the overall phase diagram [87]. This difference between cloud-points and the binodal curve is related to kinetic aspects of determining T_{cp} versus the thermodynamic binodal curve, as well as to the limitations of the turbidity measurement, since it only detects polymer agglomerates that are sufficiently dehydrated and large enough. In addition, the cloud-point depends on the method used for the determination. In addition to these differences between LCST/UCST and T_{cp} for polymers in solution, the differences to polymers grafted on surfaces must be considered. These include, in particular, the strong interaction between the grafted chains caused by their close distances to each other and the limitation in their degrees of freedom of movement due to the substrate geometry. In addition, each grafted film has a density- and thus a concentration profile, which makes it difficult to define a quantity corresponding to the T_{cp}. The exact concentration in a grafted polymer film is not known and can only be indirectly given by the grafting density. Thus, the phase transition temperature observed by methods such as in situ ellipsometry is by definition different from such temperatures determined in solution.

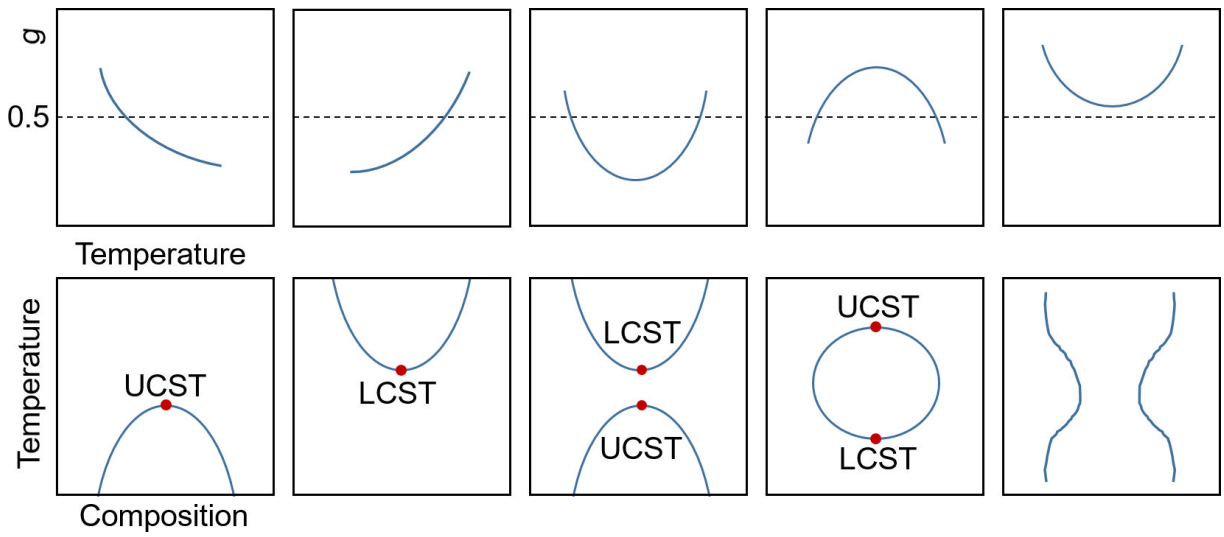


Figure 2: Illustration of the relationship between the type of miscibility gap and the temperature dependence on the g-parameter. In the temperature–composition diagrams the binodal lines are shown. Figure 2 redrawn from [51].

The critical points in the isobaric phase diagram, where temperature is plotted versus composition, are denoted as lower critical solution temperature or upper critical solution temperature. In the case of a polymer with a UCST, the polymer is in a phase-separated, collapsed state below this temperature. Heating increases the solubility until only one phase is present above the UCST. Schematically, the chains are in stretched conformation and soluble in all proportions. In contrast, the LCST is the temperature above which the polymer is insoluble (Figure 3).

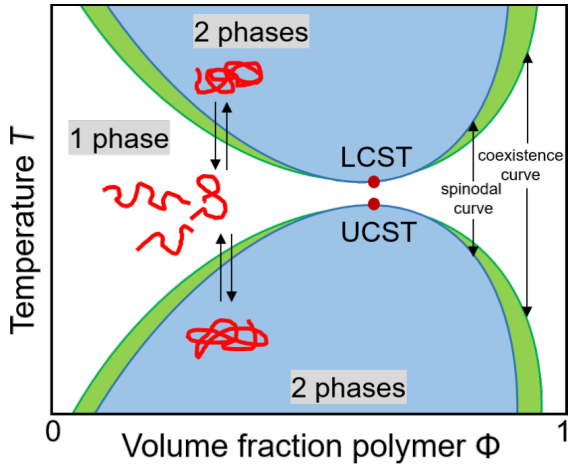


Figure 3: Schematically pictured phase diagram of a binary mixture composed of a dissolved polymer with a LCST and an UCST miscibility gap, respectively.

The reason of this described UCST behavior lies mainly in enthalpic effects [50,51]. From a thermodynamic point of view, Δ_mH and Δ_mS of the mixing process are positive for UCST polymers. If the temperature curve is considered, it can be seen that at a low temperature Δ_mH is larger than the $T{\cdot}\Delta_mS$ term. According to Equation 1, Δ_mG is positive and the polymer is insoluble. When the temperature is higher than the temperature of the associated binodal at a given composition, the expression $T{\cdot}\Delta_mS$ exeeds Δ_mH and Δ_mG becomes negative and the polymer dissolves. This phenomenon occurs for polymers whose interactions with the solvent or between the chains are characterized by strong dipol–dipol interactions, such as Coulomb forces, or by hydrogen bonds. Hence, on the one hand, strongly charged zwitterionic polymers, such as PDMAPS and its structural analogues [88-91], and on the other hand, polymers with strong hydrogen acceptor and donor units, like the uncharged PNAGA [92-96], show a pronounced UCST.

In contrast, the solubilization process of a polymer with LCST behavior is an entropic effect characterized by negative Δ_mH and Δ_mS values. The essential structural feature of such polymers is their amphiphilic structure of hydrophobic domains and hydrophilic groups, which can form hydrogen bonds with water. These interactions result in a highly ordered hydration shell when the macromolecule is in solution. The best known example of a phase transition with an LCST is PNIPAAm with its hydrophilic isopropyl groups interacting with water molecules [48,97-99]. From a thermodynamic point of view, the hydrogen bonds between the polymer and the water molecules lead to a negative value for Δ_mH and, due to the ordered hydration structures, to a negative entropy of mixing. As soon as the turbidity temperature is reached, the hydrophobic effect becomes dominant and water molecules are released, leading to a collapse of the hydration shell and a significant increase in entropy. The intra- and intermolecular interactions between polymer segments are favored and the polymer begins to precipitate. A comparison of the calorimetrically determined enthalpies of mixture Δ_mH for PNAGA and PNIPAAm reveals the different mechanisms. The entropically driven LCST phase transition of PNIPAAm has a substantially smaller value for Δ_mH (≈5 kJ/mol) [100,101] than the enthalpically based UCST transition of PNAGA (≈90 kJ/mol) [92], which additionally indicates stronger polymer–polymer interactions for UCST polymers.

Phase transition behavior of particular polymer architectures

The relationships described above concerning the segregation behavior of a polymer below or above a certain temperature and the associated formation of a miscibility gap were initially considered only for free polymer chains in solution. In the following section particular polymer arrangements and architectures will be briefly introduced concerning the relationship between their morphology and the temperature-induced phase transition. These polymer arrangements of constrained mobility include star polymers, micelles and grafted linear polymers on flat surfaces as well as on nanoparticles. In general, these four polymer arrangements are characterized by the fact that the mobility of the polymer chains is constrained, in contrast to free polymer chains in solution. Due to the substrate geometry in the case of grafted polymers or due to their arrangement through their structure in the case of micelles and star polymers, the polymers are forced into a certain structure and their degrees of freedom of movement are thus limited. As a result, extremely high segment densities are sometimes generated. In the case of grafted polymers, this depends on the grafting density and substrate geometry. In micelles, the local concentration depends on the total chain length, as in star polymers, and on the ratio of hydrophilic and hydrophobic components. A phase diagram, as described above, describes the mixing behavior over the entire concentration range, i.e., from 0 to 100%, which, however, is never completely reached in the four polymer arrangements studied. Therefore, we cannot speak here of phase diagrams in

the classical sense, as well as about a UCST and LCST in the strict sense. Nevertheless, the micelles, star polymers and grafted polymers show a responsive behavior, which will now be discussed in general. The main focus is on fundamental trends. Subsequently, these trends are applied to numerous UCST systems.

Definition and phase transition behavior of star polymers and polymeric micelles: So far, only the phase transition for free polymer chains in solution has been studied. The arrangement of polymer chains can form superstructures that have a direct influence on the physical properties, such as mobility and intermolecular interactions, and thus also on the position and width of the phase transition. A topologically simple way to restrict the mobility of the polymer chains is the radial, covalent fixation of at least three polymer chains around a core. If the dimension of the core is much smaller than the length of the arms, that is, the root-mean square end-to-end distance, this arrangement is called star polymer [102-107]. These "arms" extend into the surrounding solvent and can interact with it. If thermoresponsive polymers are used for this purpose, the swelling behavior can be thermo-induced. In combination with other nonresponsive polymers the corona of the star polymer can be modulated resulting in an intermolecular micellization [108], which is illustrated in Figure 4. In contrast to free polymer chains in solution, branched polymers have an enhanced segmental density with the same molar mass and are therefore more similar to the hard sphere model [109]. Due to the confined structure, star polymers possess distinct physicochemical properties such as a low viscosity, high density of polymer segments and functional groups as well as a smaller hydrodynamic radius and larger diffusion coefficient compared to linear polymer chains in solution.

Amphiphilic AB-type copolymers spontaneously form micelle structures above a critical concentration by self-assembly due to their structure consisting of hydrophilic and hydrophobic units [110-113]. In the case of rather large corona blocks compared to the core-forming blocks, such structures are usually star-shaped and spherically composed of many individual chains by noncovalent interchain interactions in contrast to star-shaped polymers. Thus, in a polar solvent, such as water, the hydrophobic block forms an anhydrous core. The hydrophilic chains stretch into the solvent in the shape of a swollen corona (Figure 5). The size, shape and dynamics of the micelle can be essentially tuned by the absolute length of the block copolymer and the relative length of the blocks to each other and the glass transition temperature. If a block is composed of a thermoresponsive polymer, the amphiphilic character and self-assembly ability can be altered by changing the temperature. The thermoresponsive block collapses or swells depending on the temperature resulting in a reversibly switching behavior of structure and shape of the micelle.

Definition and phase transition behavior of polymers grafted on flat and particular surfaces: For numerous applications, immobilization of the polymer chains is desirable. In solution, a phase diagram is uniquely defined and can be easily determined by turbidity measurements, for instance. On a surface, however, conventional segregation is not possible due to the hindered mobility of the polymer chains. In contrast, external triggers, such as temperature, can more or less switch between a stretched and a collapsed brush conformation, leading to a change in macroscopic properties, such as contact angle or layer thickness, in contrast to the cloud point for free polymer chains. The influence of covalent bonding on a flat or curved surface will be considered using the example of the polymer brush structure, which has been intensively studied both experimentally and theoretically [114-117]. In general, these influencing parameters include the curvature and general properties of the substrate, the grafting density and chain end effects. A polymer brush is defined as a dense array of flexible polymer chains chemically or physically attached to a surface through one end of the chain [118]. The distance between the

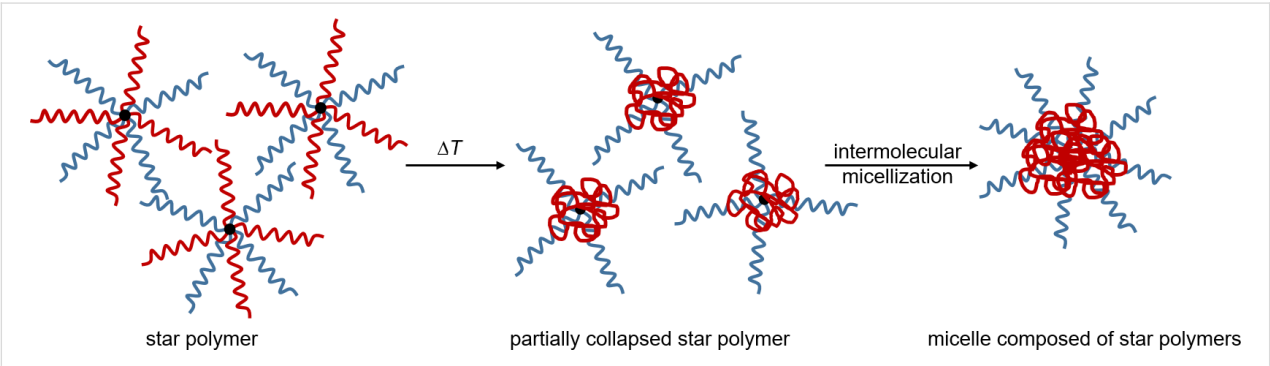


Figure 4: Schematic illustration of a thermo-induced swelling behavior of a star polymer composed of responsive (red) and nonresponsive (blue) polymer chains and their subsequent intermolecular micellization. Figure 4 redrawn from [108].

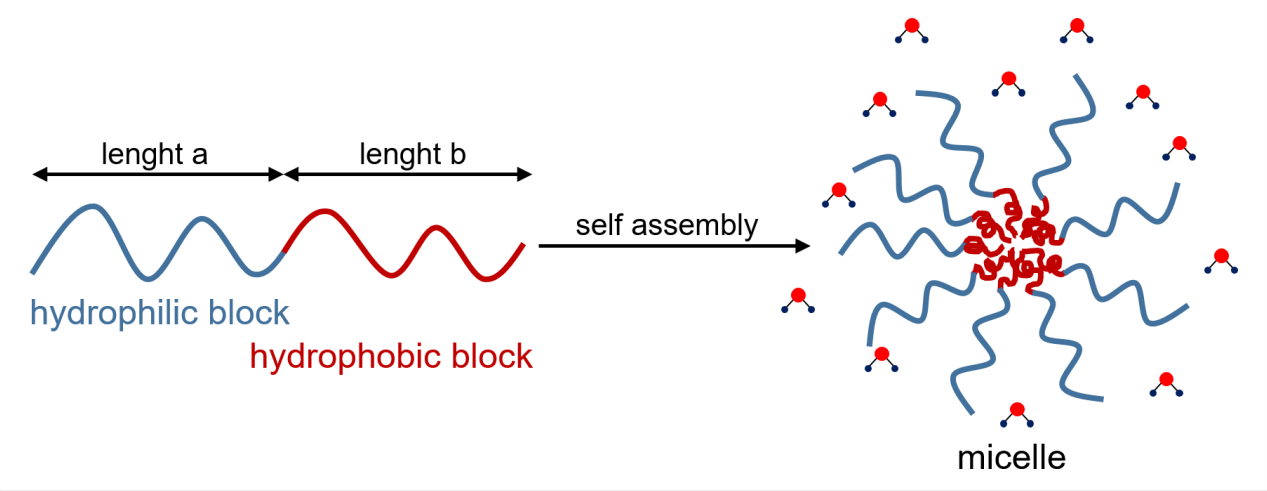


Figure 5: Schematic illustration of self-assembly of block copolymer amphiphiles in a polar medium.

attachment points is decisive for the properties of the polymer film and its differences from free polymer chains (Figure 6). If the average distance between the anchor points is smaller than the undisturbed gyration radius R_g of the free chains, the polymer chains stretch to the so-called polymer brush conformation, due to the repulsive segment–segment interaction, in contrast to the so called "mushroom regime". That means, the intermolecular interactions in the brush dominate over the intramolecular ones. As a result, the chain conformation within the brush structure is always stretched compared to unattached pendants.

The first theoretical investigations into the swelling behavior of polymer brushes based on the work of de Gennes [119,120] and Alexander [121]. In this theoretical work scaling laws were derived for uniformly stretched neutral polymer chains in nonpolar solvents that form a brush with fairly uniform density ("box-model"). The scaling laws allow the description of the swollen layer thicknesses as a function of the grafting density and the molecular weight of the polymers. Using the self-consistent field theory, it was possible to describe the nonequally and nonuniformly stretching behavior in order to minimize the whole conformational entropy loss [122,123]. Using further theoretic models and methods, such as the lattice density functional theory, the temperature-dependent swelling behavior of a polymer brush could be simulated in comparison to the corresponding phase diagrams of the free, unbound polymer chains in solution [124]. The corresponding diagrams are summarized in Figure 7 and show the typical thickness–temperature graphs for polymer brushes.

With regard to the interactions between the chains, a distinction is made between so-called classical polymer brushes, in which only van der Waals interactions dominate between the chains, nonclassical neutral brushes, in which additional specific interactions occur between the chains themselves and with the solvent including structuring effects in hydrogen bonding solvents, and polyelectrolyte brushes, whose behavior is additionally determined by long-range Coulomb interactions [114,116]. The main difference between classical and nonclassical polymer brushes is the role of the solvent, which has an influence on the internal structure of the polymer film. This leads to different

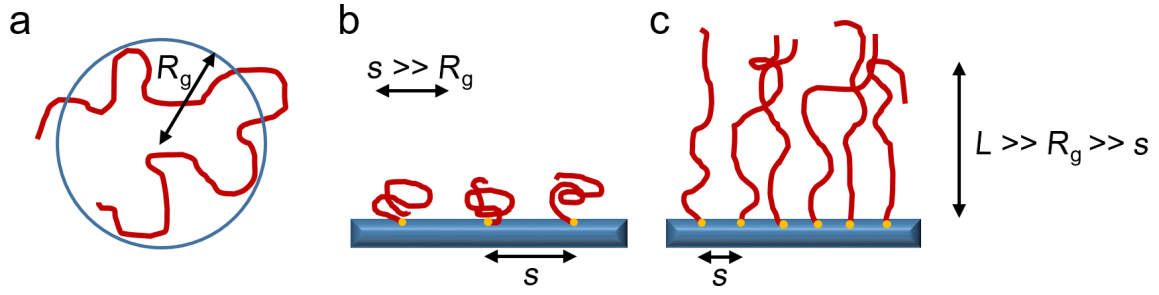


Figure 6: Schematic comparison of the size and conformation between free polymer chains (a), grafted polymer chains in mushroom regime (b) and polymer chains grafted on a surface in the brush conformation (R_g – radius of gyration, s – distance between grafting points, L – brush height). Figure 6 redrawn from [117].

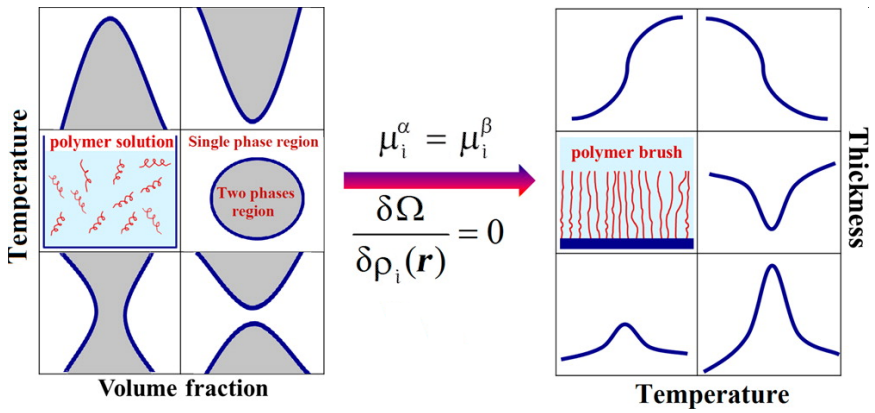


Figure 7: Comparison of the possible phase diagrams of a polymer in solution with partially miscibility and the corresponding temperature–thickness curve, showing the swelling behavior of the polymer brushes as a function of the temperature change (μ – chemical potential, *i* – component, Ω – potential of the grand canonical ensemble, *ρ* – density distribution, *r* – chain length). These graphs were simulated using lattice density functional theory. Figure 7 was reprinted with permission from [124]. Copyright 2014 American Chemical Society. This content is not subject to CC BY 4.0.

distributions of the polymer segments and therefore to different polymer profiles in vertical extension to the surface. This effect has a direct impact on the occurrence and width of phase separation with an LCST or UCST and its dependence on brush parameters, such as local concentration, and thus on its influenceability. It has often been shown experimentally that the most pronounced conformational response of polymer brushes is achieved at moderate grafting densities [125]. Furthermore, the collapse of end-tethered assemblies is generally weaker and broader due to the interaction between the chains compared to isolated chains in solution [123,126]. In the case of classical polymer brushes, i.e., nonpolar systems such as polystyrene brushes, the transition from a swollen state to a collapsed state is characterized by the change of the segment distribution from a parabolic to a step profile and a rearrangement of the chain ends [126]. This collapse can be described by the classical Flory–Huggins model. It follows that this vertical collapse above the LCST or below the UCST is merely a shrinkage and not a discontinuous transition [70,114,125,127]. Unlike free, unbound polymer chains, where the degree of dilution can achieve any composition in the phase diagram, the extent of dilution in brushes is limited and a function of grafting density and temperature. For phase segregation, the concentration of segments in a brush must be in the semi-dilute region. The associated concentration is generally much higher than required for the critical temperature. Hence, the contraction of the brush never crosses the coexistence curve with decreasing temperature [114]. Due to the special arrangement of the chains on a surface and the intermolecular interaction that occurs, vertical phase separation is suppressed in systems such as polystyrene in cyclohexane, in contrast to free dissolved chains [128]. However, at vanishingly small concentrations, classical brushes always exhibit a behavior resembling phase separation with UCST. Unlike this classical polymer brush, the χ-parameter for water-soluble polymers depends on both temperature and concentration as well as on φ [71-74,129,130]. This dependency results in a shift of the critical point and a change of the shape of the coexistence curve enveloping the two-phase region. Because of the specific interactions between water and polymer chains, water-soluble polymers can have a critical point at any concentration, which often corresponds to a miscibility gap with a LCST [74], in contrast to nonpolar brushes in an organic solvent (like polystyrene in cyclohexane), which always show an UCST. This critical point is usually located in the semi-dilute regime and the brush can contract discontinuously or continuously [114,131]. The more complex dependencies on χ leads to a bilayer-type profile, as has been shown for PNIPAAm [132,133], since the near-surface segments tend to segregate compared to the outer region. This results in a broadening of the temperature range in which the polymer chains collapse. The third class of brushes are films composed of polyelectrolytes in which long-range Coulomb interactions are dominant [134,135]. Here the charges of the polymer chains and therefore the intermolecular repulsions are compensated by counterions. Due to this counterion condensation, the majority of ions are located inside the brush. Therefore, the interface is in a charged state, viewed from the outside, which can be easily observed by, e.g., zeta potential measurements. Two scaling regimes can be defined as limiting cases using the specific localization of the counterions that results from additionally added salt: the salted brush and osmotic brush [136-138]. These additional counterions, in addition to pH changes, have significant influence on the swelling behavior in the case of weak polyelectrolytes. In a salted brush, the concentration outside and inside the brush is approximately the same and the swelling properties are determined by excluded volume interactions between the segments. In an osmotic brush, the concentration of trapped counterions inside the brush is greater than the concen-

tration outside. The resulting osmotic pressure depends on the interconnected polymer segments, the chain elasticity and the trapped counterions.

The previous remarks on the swelling behavior of polymer brushes on planar surfaces can essentially be transferred to curved surfaces, that is, to coated particles. Particulate systems [115,117] are characterized by the fact that a certain number of coated surfaces interact with each other. The temperature-dependent swelling influences the interactions between the functionalized particles. In addition to the described factors influencing the position and width of the critical point, the curvature must be considered for particulate systems. A general trend is that the cloud points of responsive nanoparticles are smaller than compared to free polymer chains [139]. The size of the nanoparticle core directly affects the thermal response. Thus, it was found that with increasing particle size, the LCST decreases [140]. The reason for this is the strong dependence of the free space per polymer chain at the same grafting density on the degree of curvature [115].

Responsive polymers with LCST behavior

The LCST behavior of the mentioned polymer arrangements is a very intensively studied phenomenon in the literature. There are many different polymers that exhibit a phase transition with LCST, such as PNIPAAm, PEGMA, POX, PDMAEMA, PDEAEMA, PDEAEAM, PMEMA and PDEAAM. The review of Roy et al. presents a comprehensive list of investigated polymers with a LCST-like behavior [2]. The influence of structure and properties of the polymers as well as their arrangement on the location and width of the phase transition has also been studied in numerous examples. Therefore, at this point we will only refer to published reviews on this topic. Table 1 summarizes the work on micellar

Table 1: Overview of the most significant polymers with LCST behavior ordered by the polymer arrangements star polymer, polymer micelles as well as polymers covalently grafted on nanoparticles and flat surfaces.

Polymer arrangements	Polymer	Object of research/highlighted application	reference
star polymers [102,103,106]	*PNIPAAm-based polymers* [102]		
	PNIPAAm-PDEAEMA	synthesis/analysis	[141,142]
	PNIPAAm-PS	synthesis/analysis	[143]
	PNIPAAm-PEG	synthesis/analysis	[108]
	PEG-PDEAEMA-PNIPAAm	synthesis/analysis	[144]
	PEG-PNIPAAm-Plys/PAA	synthesis/analysis	[145]
	PS-PCL-PNIPAA	synthesis/analysis	[146]
	PEG-PtBMA-PNIPAAm	synthesis/analysis	[147]
	PS-PNIPAAm-PDMAEMA	synthesis/analysis	[148]
	PNIPAAm-P4VP	synthesis/analysis	[149]
	PS-PNIPAAm-P4VP	synthesis/analysis	[102,149]
	PAA-PNIPAAm	nanocarrier/molecule delivery; synthesis	[105]
	PCL-PNIPAAm	nanocarrier/drug delivery, synthesis	[150]
	PTEGDA-PNIPAAm-PNMA	drug delivery, synthesis	[151]
	PNASME-PNIPAAm	synthesis/analysis	[152]
	POX-based star polymers		
	PBOX-PEtOX	synthesis/analysis	[153]
	PEtOX- PIPOX	synthesis/analysis	[154]
	PIPOX	synthesis/analysis	[155,156]
	PEG or PEG derivates-based star polymers		
	PEG-PDMAEMA	synthesis/analysis	[157]
	PCL-POEOMA-PMEO$_2$M	synthesis/analysis	[158]
	PDEGA-PHEA	synthesis/analysis	[159]
	P(DEGMA-OEGMA-GMA)	as nanolayers for controlled cell sheet detachment, synthesis	[160]
	PDMAEMA-PDEGA	synthesis/analysis	[161]
	other polymers		
	MPEP-PCL-PPE	synthesis/analysis	[162]
	PVAc-PNVCL-PNVP	synthesis/analysis	[163]

Table 1: Overview of the most significant polymers with LCST behavior ordered by the polymer arrangements star polymer, polymer micelles as well as polymers covalently grafted on nanoparticles and flat surfaces. (continued)

polymer micelles [4,59,164,165]	*PNIPAAm-based micelles*		
	P4VP-PNIPAAm	catalysis, synthesis	[166]
	PNIPAAm-PDMAAm	drug delivery, synthesis	[167]
	PNIPAAm-DNA	synthesis/analysis	[168]
	PNIPAAm-PHPMA-PEG	synthesis/analysis	[169]
	PNIPAAm-PBMA	drug delivery, synthesis	[170]
	PNIPAAm-PS	synthesis/analysis	[171,172]
	PNIPAAm-HPG		[173]
	POX-based micelles [174,175]		
	PEtOX-PPropOX	synthesis/analysis	[176]
	PIPOX-PAMPT	radionuclide delivery, synthesis	[177]
	PMeOX-PIPOX-PBuO	synthesis/analysis	[178]
	PBOX-PEtOX	drug delivery, synthesis	[153]
	PMeOX-PBuOX	synthesis/analysis	[179]
	other polymers		
	PDMAEMA-PCL	drug delivery, synthesis	[180]
	PEGMA-PMMA-PDEAEMA	synthesis/analysis	[181]
	PHPMA-PDEGMA	drug delivery, synthesis	[182]
polymers grafted on nanoparticles [4,115,117,164,183-185]	*PNIPAAm-based grafted nanoparticles*		
	PNIPAAm-	preparation/analysis	[186]
	PDMAAm@Fe_3O_4	preparation/analysis	[187]
	PNIPAAm-PNHMA@ Fe_3O_4	drug release, preparation	[188-191]
	PNIPAAm@SiO_2	molecule delivery, preparation	[191-194]
	PNIPAAm@Fe_3O_4	microfluidic separation and assay; sensing; drug release, preparation	[195-201]
	PNIPAAm@Au	fundamental investigation, preparation, cell up-take control	[200,202]
	PNIPAAm-PAm@Au PNIPAAm-PNVP@Fe_3O_4	cell up-take control drug delivery/cell separation, preparation	[203]
	PNIPAAm-PDMAEMA@Fe_3O_4/Au	catalysis, preparation	[204]
	PNIPAAm-PAA@UCNP	sensing, preparation	[205]
	PNIPAAm-PMAA-PVP@Fe_2O_3	drug delivery, preparation	[206]
	POX-based grafted nanoparticles [207]		
	PIPOX@Fe_3O_4	preparation/analysis	[208]
	PIPOX-PEtOX@SPION	cell up-take control	[209]
	PEtOX/PPropOX-PVIm/P4VP@Ag	preparation/analysis	[210]
	PEG or PEG derivates-based grafted nanoparticles [211]		
	PEG-PDMAEMA@Au	preparation/analysis	[212]
	PEGMA@Au	preparation/analysis	[151,213]
	$PMEO_2MA$-OEGMA@Au	protein adsorption, preparation	[214]
	PEGMA-PEG@SiO_2	catalysis, preparation	[215]
	PEG-PPO@SPIO	protein adsorption, preparation sensing, contrast agent	[216]
	PEG-PPO@ SiO_2	drug delivery	[217]
	other polymers		
	P(HPEI-IBAm)@Au	preparation/analysis	[218,219]

Table 1: Overview of the most significant polymers with LCST behavior ordered by the polymer arrangements star polymer, polymer micelles as well as polymers covalently grafted on nanoparticles and flat surfaces. (continued)

	PVME@Au	preparation/analysis	[220]
	PMDM@Au, glass or SiO_2	catalysis, sensing, preparation	[221-223]
	PTEGMMA-PMAPMA@SiO_2	protein adsorption, preparation	[224]
polymers grafted on flat surfaces [3,43,225,226]	*PNIPAAm-based grafted surface* [43,227]		
	PNIPAAm@different flat substrates, such as Au, Si-wafers, glass	preparation, theory, fundamental investigation of swelling behavior, cell/protein adhesion, sensing, environmental application	[132,228-255]
	PNIPAAm-PAA@SiO_2	protein adhesion, preparation	[256-259]
	PMMA-PBIEM-PNIPAAm	cell up-take control, preparation	[260]
	PNIPAAm-PLAMA@glass	preparation	[261]
	PNIPAAm-PDMAEMA@Al	preparatio	[262]
	PNIPAAm-PNTBA@glass	cell up-take control, preparation	[263]
	PNIPAAm-ODS@glass	microfluidic, preparation	[264]
	PNIPAAm-PEG@Au	cell up-take control, preparation	[265]
	POX-based grafted surface		
	PCPOX-PMeOX@SiO_2	preparation	[228]
	PPropOX@glass	cell up-take control, preparation	[266]
	PEG or PEG derivates-based grafted surfaces [43,211]		
	$PMEO_2MA$-PDEAEMA@SiO_2	preparation	[267]
	$PMEO_2MA$-POEGMA@SiO_2	protein adsorption, preparation	[268]
	other polymers		
	PMDM@glass	protein adsorption, preparation	[221]
	PVCL-PDMAEMA-PMPC@PDMS	controlled wettability self-cleaning, anti-microbial coating, preparation	[269]

structures, star polymers and polymers grafted on particles or on planar surfaces as well as their discussed application without the claim of completeness. Due to the large number of investigated polymers with LCST behavior, only a few examples are summarized in Table 1 to illustrate the focus of research, which lies on synthesis, fundamental understanding of the relationship between polymer arrangement and architecture and the phase transition behavior as well as on real application and their potential in different fields of biomedicine, sensing or catalysis, for instance. In addition, some review articles on the respective architectures and polymers in principle are listed.

Responsive polymers with UCST behavior

In this section, we would like to give the reader a brief overview and update of known polymeric building blocks exhibiting UCST behavior, highlighting in particular recently developed structures (Figure 8). Subsequently, their use in different topologies and assemblies such as star polymers, micelles as well as covalently grafted polymers on flat substrates and nanoparticles will be explained in more detail.

According to the type of supramolecular interactions governing the thermoresponsive behavior UCST type polymers can be classified into two categories. Although various molecular forces such as van der Waals interactions and hydrophobic effects contribute to the thermoresponsiveness of polymers, UCST type behavior is generally governed either by strong hydrogen bonding or by attractive electrostatic interactions [51,52,55].

UCST resulting from strong hydrogen bonding interactions. Increasing interest is focussed on nonionic polymers in water, whose UCST behavior is based on hydrogen bonding. Due to their tolerance towards added salt ions, they represent attractive candidates for biomedical applications [50-52]. Among the few known homopolymers of this type, PNAGA, whose UCST behavior was first characterized by Seuring and Agarwal in 2010, is the most widely studied [92-96]. In addition to UCST-type polymers such as poly(methacrylamide) and polyuracilacrylates, which have been known for some time [51,52], Zhang et al. recently presented the synthesis of a novel homopolymer with transiently thermoresponsive behavior [271]. Within a

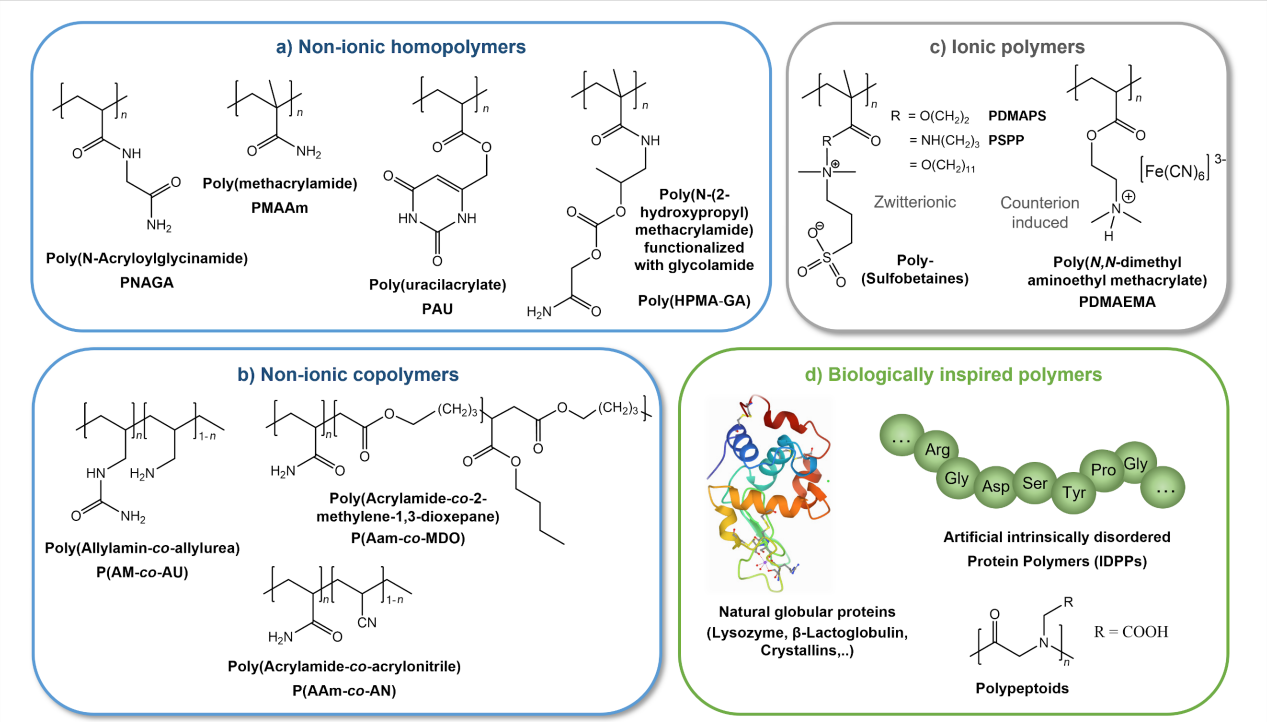


Figure 8: Selection of polymers exhibiting UCST behavior due to hydrogen bonding (blue) divided into homo- (a) and copolymers (b), as well as upon attractive electrostatic interactions (gray, c)). Furthermore, biologically inspired polymer structures with UCST behavior are shown (d), in which thermoresponsiveness arises from a variety of intermolecular interactions. The illustration is intended to highlight several polymer classes with confirmed UCST behavior, without making a claim to completeness. The crystal structure of hen egg white lysozyme in part d) is reprinted from the RCSB Protein Data Bank [270].

physiologically relevant window, the developed GA-polyHMPA initially exhibits UCST responsiveness, but can subsequently be slowly biodegraded to a fully water-soluble polymer (polyHMPA) via hydrolysis. Initial in vivo studies of a sustained release of either a hydrophilic model protein or a hydrophobic dye entrapped within the collapsed UCST polymer are promising and open new perspectives for the development of the next generation of smart, degradable biomaterials. In addition to the homopolymers mentioned above, more and more copolymers have been discovered, in which UCST behavior can be induced via hydrogen bonding. Interestingly, the individual monomers usually do not exhibit responsive properties. However, the combination within a copolymer leads to a pronounced thermoresponse. A prominent representative of such behavior is poly(acrylamide-*co*-acrylonitrile), which is assembled from a fully soluble, hydrophilic monomer (AAm) and the hydrophobic AN block [51,52,94]. Since the phase transition temperature of the copolymer can be adjusted over a wide temperature range via the ratio of the two monomers, it is frequently used for the development of novel drug release systems [272-276]. Due to the continuous development and improvement of polymerization techniques, more and more diverse copolymers can be synthesized. Very recently, Kertsomboon et al. succeeded in preparing a copolymer (poly(AAm-*co*-MDO)) of acrylamide and a degradable, hydrophobic monomer based on a ring opening polymerisation of cyclic ketene acetals [277]. This copolymer also showed a well-controllable reversible UCST behavior in aqueous solutions. In 2020, Zhao et al. reported that by incorporating azobenzene functionalities into polyacrylamide copolymers, the responsive UCST behavior was furthermore tuneable via light irradiation as well as by host molecule (α-cyclodextrin) complexation [278]. Due to the high number of proton acceptor/donor sites, ureido-modified copolymers such as poly(allylamine-*co*-allylurea) are also becoming more and more important. The critical phase transition temperature can often be finely tuned under physiologically relevant pH and salt conditions via the hydrophilicity of the co-monomers and their molar ratio [52,55,279].

UCST resulting from attractive electrostatic interactions. The thermoresponsive behavior of zwitterionic polymers, in contrast to the previously mentioned UCST type polymers, is based on attractive electrostatic interactions. In addition to poly(phosphobetaines) high attention is especially focused on poly(sulfobetaines) [280-282]. Extensive studies in aqueous solution have shown that the thermoresponsive behavior depends on a variety of parameters, such as concentration, ionic strength, as well as the molecular weight and the spacer length

between the charges of the monomers [50,51,283,284]. In particular, the influence of salt ions, which trigger a so-called antipolyelectrolyte effect by screening of the zwitterionic charges, was intensively investigated [285]. As intra- and intermolecular electrostatic interactions are strongly affected by screening, the increase of the ionic strength generally results in a remarkable drop of the phase transition temperature eventually resulting in a complete disappearance of the UCST-type behavior [50,285]. Although zwitterionic polymers display a very sharp phase transition in pure water, their use for biological applications is therefore limited. However, besides zwitterionic compounds, UCST behavior can also be induced in polyelectrolytes via suitable counterions [50]. Analogously, electrostatic interactions dominate the UCST behavior of such charged polymers, which can be manipulated via the hydrophobicity, polarizability, size, and especially the valency of the counterion [50,51]. While Flory et al. investigated the UCST behavior of PAA in the presence of large amounts of NaCl (c = 1.245 mol/L) already in 1954, nowadays more and more examples of counterion-induced thermoresponsiveness on charged homopolymers as well as copolymers have been revealed [50,51,286]. In addition to the thermoresponsive behavior of the branched polyelectrolyte polyethyleneimine (PEI) described by Noh et al. [287] in the presence of the halide anions Cl^-, Br^-, and I^-, respectively, UCST behavior can also be induced in polymeric ionic liquids by the addition of a suitable hydrophobic counterion, such as tetrafluoroborate BF_4^- [288,289]. In both cases, the critical phase transition temperature is strongly affected by the concentration of the polymer, but also by the nature of the anion as well as its concentration. Moreover, UCST behavior induced by BF_4^- was also detected in aqueous solutions of polypeptides, whose side chains contain charged pyridinium or imidazolium functionalities [290,291]. In contrast to single charged counterions, multivalent ions exert a particularly strong influence on polyelectrolytes due to their high charge density [292]. Plamper et al. [293] as well as Zhang et al. [294] demonstrated that in the presence of the triply negatively charged hexacyanoferrate $[Fe(CN)_6]^{3-}$, polycationic poly(dimethylaminoethyl methacrylate) (PDMAEMA) exhibits UCST behavior in aqueous solution. This is particularly interesting since the polymer initially exhibits LCST behavior in the absence of multivalent ions due to its amphiphilic polymer structure [295,296]. The switchable thermoresponsivity is furthermore complemented by a pH and ionic strength sensitivity [5,297]. The complex phenomenon is referred to as multiresponsivity and has already led to extensive research on PDMAEMA, especially with regard to biomedical applications [5,298,299]. While numerous studies have been performed on free polymer chains in solution, especially focussing on the LCST transition, we have recently shown that an UCST behavior can also be induced in PDMAEMA brushes, thereby generating a novel approach for controllable in situ nanostructuring on surfaces [300,301].

UCST resulting from biological inspired structures. In addition to synthetic polymers, thermoresponsivity can also be observed in biological structures and their derivatives. While LCST behavior is more frequently studied in synthetic polymers, the occurrence of UCST behavior predominates in aqueous solutions of proteins [302,303]. The thermoresponse of natural proteins such as β-lactoglobulin, lysozyme or crystallins is based on a complex interplay of various attractive forces such as hydrogen bonding, electrostatic as well as π–π interactions and hydrophobic effects [302,304,305] Several studies show that in the case of natural proteins multivalent ions also have a strong impact on thermoresponsiveness [302,303,305]. Exactly inverse to the behavior of synthetic PDMAEMA, Schreiber and colleagues demonstrate that in the presence of a low concentration of the multivalent salt YCl_3 (c < 2mM), solutions of the globular protein β-lactoglobulin show an unusual LCST behavior [302]. However, when the concentration of the added Y^{3+} ions is increased up to 5 mM, the original UCST-type behavior of the protein is detected again. Isothermal titration calorimetry shows an entropically driven cation binding with a disruption of the highly structured hydration shell of the protein, which governs the LCST behavior. Furthermore, the authors propose that bridging between proteins via the multivalent Y^{3+} ions significantly dominate the unusual LCST behavior. Conversely, however, for synthetic PDMAEMA, it was found that bridging between charged polymer chains via multivalent hexacyanoferrate ions $[Fe(CN)_6]^{3-}$ leads to an unusual UCST behavior of the polymer [294,300]. Thus, it becomes apparent that even supposedly similar intermolecular interactions such as ionic bridging can lead to different macroscopic outcomes depending on the spatial arrangement of the interacting functional groups.

Driven by the diverse thermoresponsiveness of natural proteins, Quiroz et al. 2015 presented the concept of artificially synthesized disordered proteins (IDPs) [306]. The identification of specific amino acid repeat motifs leading to a desired thermoresponsive outcome of the artificial protein (UCST or LCST) enables encoding a desired phase behavior at the sequential level. The demonstrated platform of, in particular, Pro- and Gly-rich IDPs allows the targeted generation of both LCST and UCST phase transitions, as well as tuning of the phase transition temperature in the range between 20–60 °C within physiologically relevant ionic strength and pH values. Furthermore, the authors show that the fusion of LCST and UCST encoding motifs within one IDP allows the generation of self-assembling structures like micelles. In addition to IDPs, polypeptoids based on an N-substituted glycine backbone, thus biomimetically

resembling polypeptides, also obtain high potential for smart biomedical applications [307]. By synthetically varying the charged side chain, Xing et al. recently succeeded in generating both UCST and LCST phase transitions with controllable transition temperature using a single homopolymer polypeptoid backbone [308].

After briefly introducing polymeric building blocks with UCST-type behavior, we will now discuss their use in different topologies in more detail. The analysis of structure–property relationships allows to gain a better understanding of UCST-type phase transitions and therefore reveals beneficial polymeric topologies to be considered for a desired application.

Star-shaped architectures

A star-shaped architecture represents a unique class of branched polymers consisting of a central core grafted with several polymer chains, which are forming so-called “arms” stretching into the surrounding solvent. While synthetic approaches for the formation of star polymers as well as their (self-)assembly into complex hierarchical topologies have been extensively studied in current research [309], the influence of branching on the thermoresponsive behavior of polymers is rarely considered [310]. While there are several studies for LCST star polymers (see Table 1), some of them are contradictory, the number of topological studies for UCST star polymers is very limited. However, we will use individual examples to explain the complex impact of the star topology on the thermoresponsive phase transition of polymers and subsequently derive topological advantages of the star architecture.

In a recent study Li et al. synthesized zwitterionic star shaped polymers showing a dual pH- and UCST-type thermoresponsiveness in aqueous solution [310]. Using an “arm-first” approach they prepolymerized PDMAPS as a macroRAFT agent. In a second RAFT polymerization the PDMAPS arms were subsequently assembled into a star architecture via the addition of a crosslinker. Li and colleagues thus succeeded in preparing 6-, 8- and 10-arm star polymers $(PDMAPS_{80})_x$, whose thermoresponsive behavior was thoroughly compared to linear analogues ($(PDMAPS_{80})$ and $(PDMAPS_{300})$). Turbidimetry at pH 7 shows an increase in the UCST-type transition temperature of the 6-arm to the 8-arm starPDMAPS from 16 °C to 23 °C (Figure 9, part A). The authors attribute this shift to an increased molecular weight of the polymers, thus resulting in enhanced intermolecular electrostatic attraction. This is consistent with studies on linear polymer chains in solution, which generally show an increase in the phase transition temperature of UCST-type polymers with increasing molecular weight due to a decreasing entropy of mixing [51,311]. Interestingly, the phase transition temperature of the 8-arm star polymer (T_c $(PDMAPS_{80})_8$ = 23 °C) is significantly lower than that of linear $PDMAPS_{300}$ (T_c $(PDMAPS_{300})$ = 39 °C), although the authors claim both polymers have a comparable molecular weight of ≈67 kDa [310]. Since DLS measurements confirm a lower hydrodynamic radius D_h and thus a denser arrangement of polymer chains in the star architecture, one might speculate that the M_n of the star polymer obtained via GPC measurements is still significantly underestimated. However, the increased local segment density surprisingly does not enhance attractive intermolecular interactions, thus leading to a decreased UCST of the star polymer. This example demonstrates very clearly that the influence of a polymer's architecture on its thermoresponsiveness is usually not easy to predict and should be carefully studied for each individual system. Moreover, the very sharp and fast phase transition of the PDMAPS star polymers even at high molecular weight is particularly noteworthy (Figure 9, part A). This topological advantage could be a promising strategy to avoid a broadening of the phase transition window with increasing molecular weight as observed for linear zwitterionic polymers by Shih et al. [311]. Furthermore, the relatively broad phase transition of linear UCST polymers, in contrast to well-known LCST systems, is still an urgent issue, which needs to be addressed in order to develop fast switching systems for novel actuator or sensor applications [38,51,311,312]. In addition, Li and co-workers were able to exploit the high density of functional groups within the star topology to tune the thermoresponsive behavior with a second external trigger. Carboxylic end-groups allowed the gradual increase of the UCST in the pH range from 3 to 10 by 18 °C for the 6-arm star polymer. By increasing the number of arms an even larger shift of up to 36 °C was achieved for the 10-arm star polymer, whereas for the linear polymer $PDMAPS_{80}$ T_c could only be tuned within a window of 10 °C (Figure 9, part A). In a comparable manner, Qi et al. were able to induce a so-called amplification effect using a hyperbranched thermoresponsive copolymer [313]. Herein RAFT polymerization of P(AAm-*co*-AN)-arms onto a branched hydrophobic core yielded the characteristic star architecture pictured in Figure 9, part B. Unlike charged zwitterionic polymers, hydrogen bonds control the thermoresponsive behavior of the neutral copolymer P(AAm-*co*-AN). Consequently, the system is less sensitive to ionic strength and shows a reversible, sharp phase transition in water as well as electrolyte solution. Variation of the AN content within the copolymer enables tuning of the cloud point, which is a feature also known from linear analogues [94]. Interestingly, the branched architecture showed a large shift of the UCST-type cloud point from 33 °C to ≈65 °C by very slightly increasing the AN fraction from 23 to 29%. Studies on the linear copolymer show a lower tunability and illustrate that a hyperbranched architecture can significantly enrich the thermoresponsive behavior [94,275,313]. To further study the effect of

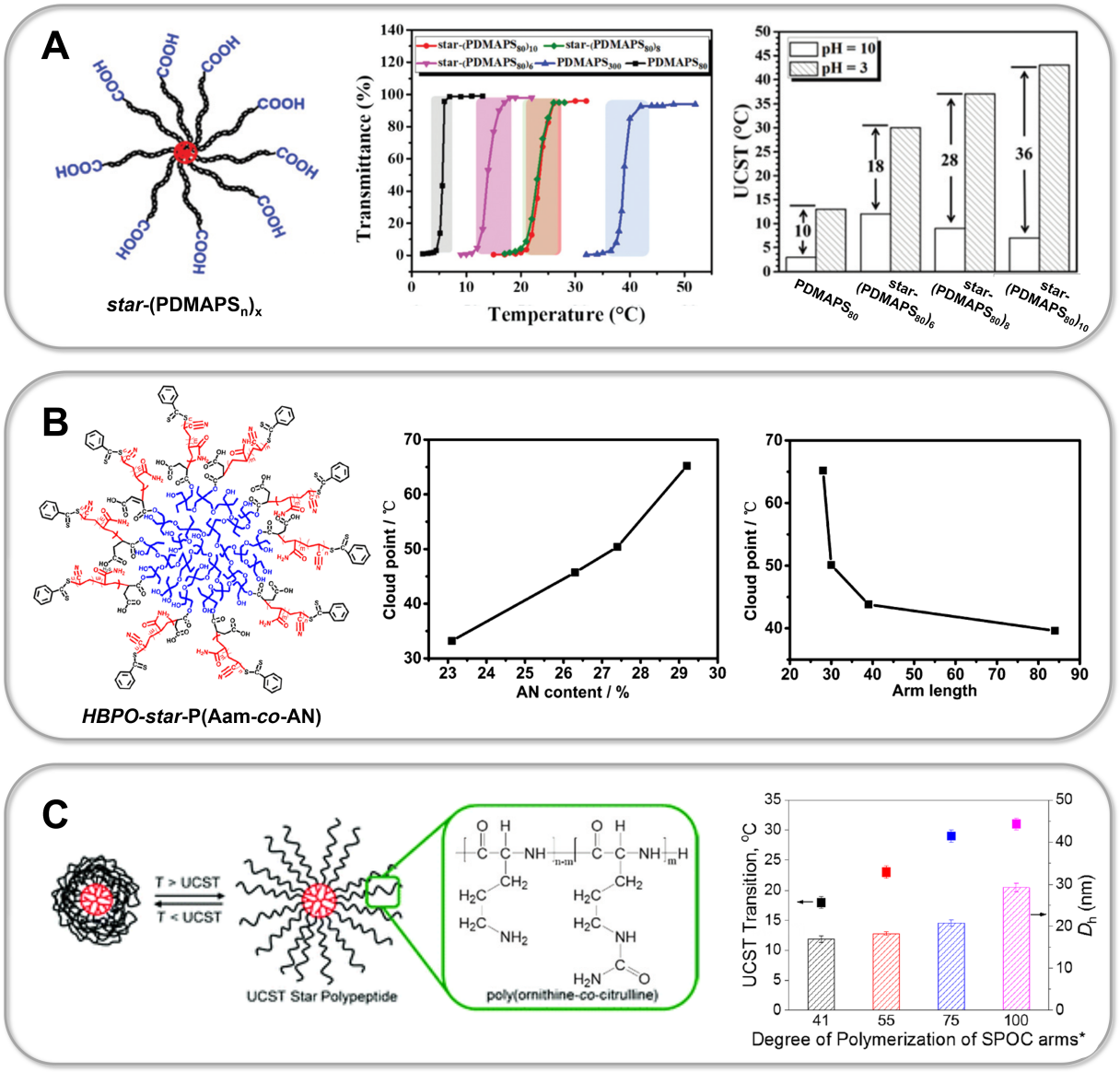


Figure 9: Part A shows the molecular structure of PDMAPS stars synthesized by Li et al. (left) demonstrating tunable UCST-type behavior upon changing the number of arms (middle) as well as changing of the pH value (right) [310]. The responsive behavior of star polymers (PDMAPS$_{80}$)$_x$ in aqueous solution was compared to linear analogs (PDMAPS$_{80}$ and PDMAPS$_{300}$) in order to understand the influence of the star topology. Part B pictures the hyperbranched architecture of P(AAm-*co*-AN)-based star polymers prepared by Qi et al. (left) [313], which demonstrate a characteristic (topologically amplified) dependence of the UCST type cloud point on the AN content of the copolymer as well as the arm length of the stars. Part C shows the UCST type swelling behavior of star polypeptides prepared from poly(ornithine-*co*-citrulline) by Zhou et al., which exhibit arm length dependent UCST transitions [314,317]. Figure 9A was adapted with permission of The Royal Society of Chemistry from [310] ("Synthesis of star-shaped polyzwitterions with adjustable UCST and fast responsiveness by a facile RAFT polymerization" by Z. Li et al., *Polym. Chem.*, vol. 11, issue 18, © 2020); permission conveyed through Copyright Clearing Center, Inc. This content is not subjected to CC BY 4.0. Figure 9B was adapted with permission from [313]. Copyright 2018 American Chemical Society. This content is not subject to CC BY 4.0. Figure 9C (left) was adapted with permission of The Royal Society of Chemistry from [314] ("Enzymatically degradable star polypeptides with tunable UCST transitions in solution and within layer-by-layer films" by Q. Zhou et al., *Polym. Chem.*, vol. 9, issue 40, © 2018); permission conveyed through Copyright Clearing Center, Inc. This content is not subjected to CC BY 4.0. Figure 9C (right) was adapted with permission from [317]. Copyright 2019 American Chemical Society. This content is not subject to CC BY 4.0.

molecular architecture, Qi et al. synthesized a set of star polymers containing a constant AN fraction of 29% with variable arm length. Increasing the degree of polymerization of the arms from 28 to 84 leads to a decrease in the cloud point from 65.2 °C to 39.6 °C [313]. This represents an inverse dependence compared to linear P(AAm-*co*-AN), where an increase in T_c is observed with an increase in molecular weight [274,275]. The authors propose that this inverse trend is based on a pro-

nounced hydration of long polymer arms, which leads to stretching into the surrounding solution away from the hydrophobic core. One might speculate as well that the sterically restricted geometry of the star polymer hampers the formation of intermolecular hydrogen bonds, which are crucial for the UCST-type response. However, Zhou et al. demonstrate that in the case of star-shaped polypeptides (star-poly(L-ornithin-*co*-L-citrullin) (SPOC), the increase in arm length from ≈60 kDa to ≈100 kDa results in an increase in the UCST-type phase transition temperature from 18 °C to 31 °C [314] (Figure 9, part C). Although analogous to the star-shaped P(PAAm-*co*-AN) of Qi et al., the UCST behavior is based on hydrogen bonding, the steric confinement of the polypeptide chains does not seem to hamper attractive intermolecular interactions in this case [313]. Moreover, it is demonstrated that the high local concentration of functional groups and therefore strong polymer–polymer interactions lead to a higher T_c of the star polypeptide compared to a linear analogue with matching polymer chain length and similar composition [314]. Interestingly, the dendritic topology of the star polypeptide revealed a very low concentration dependency of the phase transition temperature. While a T_c shift of more than 10 °C was detected for linear ureido-based polymers when the concentration was increased from 0.5 mg/mL to 2.5 mg/mL [315], the T_c varied only by a few degrees Celsius for the star polypeptides (<3 °C) [314]. The phase transition itself occurs within a remarkably small temperature window (<5 °C). Due to the conformational restriction of the polypeptide in the star architecture, the formation of secondary structures can be strongly inhibited. This contrasts with the increasing formation of β-sheets during multiple heating/cooling cycles of linear polypeptides, which can lead to irreversible precipitation [314,316]. In addition, Zhou et al. also succeeded in assembling star polypeptides via a layer-by-layer technique using hydrogen bond-forming tannic acid into a functional surface coating [314,317]. Importantly, for all thin films of the star polypeptides the UCST transition shifted to much higher temperatures than in solution. In particular, the T_c of the star-polypeptide $SPOC_{55}$-96 in solution increased from around 24 °C to around 44 °C, when assembled into a thin film with tannic acid via hydrogen bonding interactions. Furthermore, ellipsometric studies of the films show that in this physically crosslinked geometry, a much broader and thus slower phase transition of the star polypeptides occurs. This again illustrates that the spatial arrangement of thermoresponsive materials exerts a strong influence on the phase transition. This was also shown by Willcock and co-workers, who investigated the influence of branching on zwitterionic PDMAPS with molecular weights ranging from 5 to 500 kDa [318]. The introduction of bifunctional monomers leading to additional side chains of the zwitterionic polymers results in vastly reduced transition temperatures compared to their linear analogs. The shift of T_c to lower temperatures often results in a complete disappearance of the UCST behavior in the measurable temperature range of 0 to 100 °C. The results are in accordance with studies on zwitterionic hydrogels where a strong decrease of UCST-type T_c is observed with increasing crosslinking density [55,318-320]. Interestingly, Willcock and colleagues propose a model of reduced effective molar mass of branched polymer chains in order to describe the influence of branching on their thermoresponsive behavior. The thermodynamic theory of polymers in solution states that in general the UCST increases with increasing molecular weight of the chains due to a decrease of the entropy of mixing [51]. Thus, an effectively lower chain length for branched polymers could well explain a significant decrease in UCST with increasing branching. However, the very simple model neglects the steric constraint of the branched polymer chains, which can lead to a dramatic change in the attractive polymer–polymer interactions governing the UCST behavior.

This phenomenon is also illustrated by Zhang et al. on a star-shaped copolymer consisting of a zwitterionic as well as a cationic block grafted on a hydrophobic cyclodextrine core [321]. Due to the UCST behavior of the zwitterionic polymer, an increase in temperature causes the zwitterionic block to collapse around the cationic segment, which results in the formation of an outer corona of sticky patches. While this particular behavior occurs in all 12-arm star copolymers, an UCST behavior of the zwitterionic block is completely suppressed due to steric constraints, when the grafting density and thus the number of arms is increased to 17. Interestingly, the high local density of polymer segments within the star architecture also influences screening effects of the zwitterionic block by added salts. Known as the antipolyelectrolyte effect, salt ions can shield charges in zwitterionic polymers. This leads to an increase in solubility and thus a sharp drop in UCST until the thermoresponsive behavior eventually disappears completely even at relatively low ionic strength [50,281,322]. This phenomenon still hinders the wide use of zwitterionic polymers in physiological media for biomedical applications, although they have long been known for their sharp and reversible UCST-type behavior in water. However, the high local density of polymer segments within the star polymer leads to a limitation of shielding effects, resulting in a salt tolerance of up to 20 mM NaCl, which is more than 10 times higher than that of linear zwitterionic polymers ($c \approx 0.7$–2 mM) [321]. Furthermore, the association behavior of the star polymers in aqueous solution could be specifically influenced via the grafting density as well as the arm length. While association processes were strongly suppressed for high grafting densities, increasingly large spherical aggregates were detected below the critical phase transition temperature ($T <$ UCST) with increasing arm length of the star poly-

mers. Benefits and limitations of star-shaped topologies on the UCST behavior of polymers are summarized in Table 2.

Block copolymers forming micellar structures

Polymers with LCST or UCST behavior can undergo a single-phase transition upon variation of temperature (coil-to-globule transition), which is often attributed with switching between a hydrophilic and a hydrophobic physicochemical state [51,52]. However, if several thermoresponsive segments are linked to form a block copolymer, sequential transitions between more than two states can be obtained. Often, two blocks of the same (LCST–LCST, UCST–UCST) or different responsivities (UCST–LCST) are linked to form a so-called dual thermoresponsive block copolymer [55,323-325]. Sequential transitions of the individual blocks allow reversible switching between hydrophilic, amphiphilic and hydrophobic states of the copolymer. In aqueous solutions, the block copolymer can consequently be present either in fully dissolved state (hydrophilic) as well as within self-assembled micelles (amphiphilic) or as macroscopic aggregates (hydrophobic). Moreover, when generating multiblock copolymers with more than two different thermoresponsive segments, an increasingly complex thermoresponsiveness with an increasing number of structural phase transitions can be obtained. For a triblock copolymer, 12 different structural modes should be conceivable due to different arrangement possibilities of the UCST/LCST blocks [323,324]. Sugihara et al. succeeded in preparing a LCST–LCST–LCST triblock copolymer showing a reversible multistage morphology transformation from sol (T < 20 °C) to individual micelles (20 °C < T < 41 °C) towards physical gelation (41 °C < T < 61 °C) and precipitation (T > 64 °C) [326]. However, even in the case of a diblock copolymer, the thermoresponsive phase transitions are strongly influenced by a variety of parameters such as length and interaction of the different blocks, polymer concentration, but also by the selected solvent and added salt ions [325]. This results in a large variety of self-assembly scenarios, which gives rise to a broad range of micellar structures. In the following, we will limit ourselves to dual thermoresponsive block copolymers and refer the interested reader to further literature on multi-block copolymers [323].

According to the segments they contain, dual thermoresponsive block copolymers can be classified into four different categories [55]. If similar responsive blocks are used, LCST–LCST as well as UCST–UCST systems can be generated. If different types of segments are combined, LCST–UCST copolymers are created in which either LCST > UCST or LCST < UCST is present. In all systems, sequential phase transitions of the individual blocks occur, resulting in a conformational change of the entire block copolymer. Above and below the critical micelle concentration (CMC), different structural scenarios arise according to the composition of the copolymer, which were summarized schematically by Kotsuchibashi et al. (Figure 10, part A) [324]. While multiple LCST–LCST systems have already been studied, often using at least one PNIPAAm block, to the best of our knowledge there has been no report of a UCST–UCST system so far [55,324]. In addition to the still significantly lower number of available UCST systems, this is probably also due to the more complex phase behavior of UCST polymers. Since the phase behavior is determined by oriented intra- and intermolecular interactions, gaining precise control over distinguishable critical transition temperatures for each block is particularly difficult. Even in UCST–LCST systems, the selection and control of the UCST block is usually more challenging compared to the LCST counterpart [325]. Despite all obstacles, UCST–LCST systems are particularly interesting because they offer the self-assembly of so-called inside-out switchable micelles. With increasing temperature, a copolymer of the type UCST < LCST can transform from a micellar structure with the UCST segment in the core, via fully dissolved unimers, to a micelle with the LCST block in the solvophobic core. Turbidimetry can be used to measure the high optical transmittance of the dissolved unimers at intermediate temperatures, as well as the turbidity of the solution due to the micelle structures at low (T < UCST) and high temperatures (T > LCST) (Figure 10, part B). Similarly, copolymers of the

Table 2: Benefits and limitations arising from a star topology on the thermoresponsiveness of UCST-type polymers.

Benefits	Limitations
• Often very sharp phase transitions (small temperature window, in which transitions takes place). • Often low concentration dependence of the transition temperature. • High density of functional groups (beneficial for the implementation of a secondary external trigger). • Grafting density and arm length of the star architecture can be used to control T_c as well as the aggregation behavior. • Impact of the antipolyelectrolyte effect reduced for zwitterionic star polymers (increased salt tolerance). • Excellent rheological properties (low viscosity).	• T_c can drop significantly if steric restrictions of the star topology hamper attractive polymer–polymer interactions. • T_c is strongly dependent on the grafting density and the arm length of the star polymer, but is difficult to predict (general trends may vary depending on the chemical composition of the star polymer).

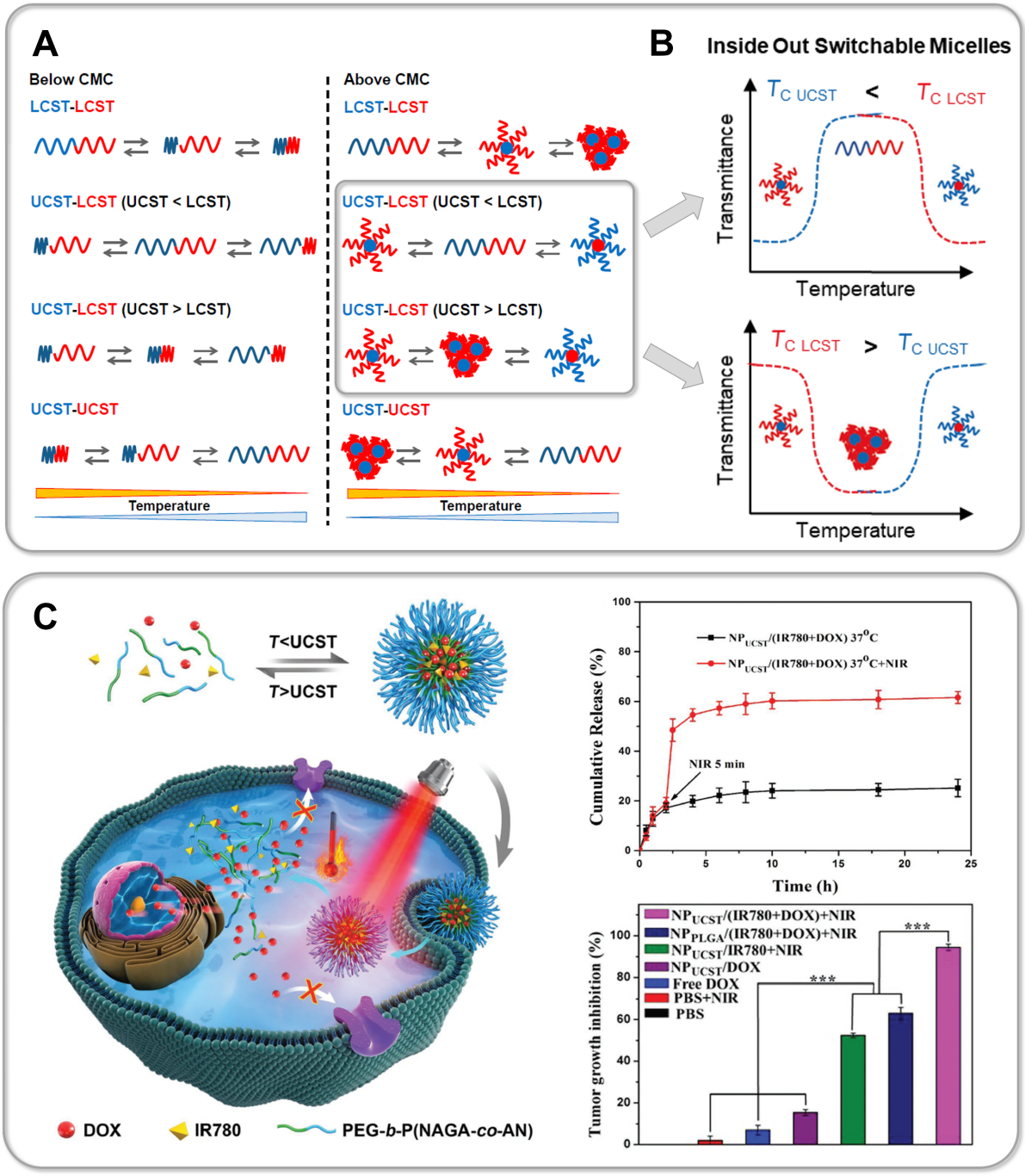


Figure 10: Part A contains a schematic demonstration of conformational transitions of dual-thermoresponsive block copolymers above and below the critical micelle concentration (CMC) adapted from Kotsuchibashi et al. [324]. The temperature-dependent self-assembly of UCST–LCST block copolymers into inside-out switchable micelles, whose characteristic transmittance curves are schematically pictured in part B, is of particular interest. In part C, the use of UCST block copolymers as smart nanocarriers for drug delivery is exemplified by the work of Deng et al. [330]. The UCST-based disassembly of micelles triggered by near-infrared radiation onto the internalized photosensitizer IR780, which causes the on demand drug release of doxorubicin hydrochloride (DOX) into the cancer cell, is shown schematically on the left. Based on the successful application of the NIR trigger leading to a burst release of DOX (upper right), excellent tumor growth inhibition is registered within in vivo studies using a mouse model (bottom right).
Figure 10A was adapted from [324] (© 2016 Kotsuchibashi, Y. et al., published by MDPI, Basel, Switzerland, distributed under the terms of the Creative Commons Attribution 4.0 International License, https://creativecommons.org/licenses/by/4.0). Figure 10B was redrawn from [55]. Figure 10C was adapted from [330], Deng et al., “Let There be Light: Polymeric Micelles with Upper Critical Solution Temperature as Light-Triggered Heat Nanogenerators for Combating Drug-Resistant Cancer”, *Small,* with permission from John Wiley and Sons. Copyright © 2018 WILEY-VCH Verlag GmbH & Co. KGaA, Weinheim. This content is not subject to CC BY 4.0.

UCST > LCST type also self-assemble into switchable micelles, though connected via an aggregated state at intermediate temperatures [55,325]. Thus, in both scenarios, without varying the chemical composition of the copolymer, a simple thermal stimulus can be exploited to provide different types of microdomains in the core as well as a switchable micelle corona interacting with the solvent [280]. The unique properties of such dual responsive block copolymers therefore have a great potential for application in the field of biosensing, smart drug delivery, emulsification systems as well as in smart rheology [55,325]. For the first time such an UCST–LCST copolymer was synthesized by Arotçaréna et al. in 2002 [327] fusing an LCST exhibiting nonionic PNIPAAm block and a zwitterionic poly(*N,N*-dimethyl-*N*-(3-(methacrylamido)propyl)ammoniopropane sulfonate) (PSPP) block, showing UCST type behavior. While the PNIPAAm block exhibited a constant $T_{c\ LCST}$ of around 32 °C, which differed only slightly from the homopolymer, varying the length of the zwitterionic block shifted the $T_{c\ UCST}$ between 9 and 19 °C. However, slightly broader phase transitions of the different blocks in the copolymer were observed compared to the homopolymers. The characteristic inside-out switching of the self-assembled micelles was detected via viscosity and fluorescence measurements as well as ^{1}H NMR and turbidimetry. In a recent feature article, Papadakis and colleagues also profoundly discuss diblock copolymers consisting of a nonionic PNIPAAm and a zwitterionic poly(sulfobetaine) block [325]. The comparison of the cloud points T_c (LCST/UCST) of the homopolymers $PNIPAAm_{200}$ and $PSPP_{430}$ with the block copolymer $PSPP_{430}$-$PNIPAAm_{200}$ showed interesting variations due to the respective nature of the thermoresponsive block. While the $T_{c\ LCST}$ of the block copolymer of 32.3 ± 0.5 °C is not changed, a decrease in the $T_{c\ UCST}$ of the copolymer by about 8 K to 21.2 ± 0.5 °C is observed [328]. Whereas the UCST transition is strongly affected by the polymer architecture and the presence of the LCST block, conversely the nonionic PNIPAAm segment behaves rather unaffected by the UCST type block. This illustrates that the double thermoresponsive behavior of a block copolymer is not a simple superposition of the phase behavior of the fused homopolymers [325]. This should be taken into account when designing novel structures for future smart applications. Vishnevetskay et al. also demonstrate that only the UCST behavior of a PSPP–PNIPAAm block copolymer was dependent on ionic strength (addition of NaBr) and polymer concentration, while the LCST transition was unchanged [328]. This is consistent with the original findings of Arotçaréna et al. as well as further studies on block copolymers of varying segment length and structural derivatives of PNIPAAm and PSPP [325,327]. Usually, a decrease in the $T_{c\ UCST}$ of the zwitterionic block is observed with increasing ionic strength, as well as a decreasing length of the UCST block, which is in accordance with the well-known behavior of zwitterionic homopolymers. Moreover, Vishnevetskay et al. recently succeeded in exploiting the high sensitivity of the UCST block to secondary external triggers for selectively switching between two self-assembly routes of the thermoresponsive block copolymer [322]. By combining a sufficiently long zwitterionic block of poly(4-((3-methacrylamidopropyl)dimethylammonio)butane-1-sulfonate) (PSBP) with a PNIPAAm segment, a block copolymer was generated ($PSBP_{245}$-b-$PNIPAAm_{105}$), in which the $T_{c\ UCST}$ is shifted above the $T_{c\ LCST}$ under salt-free conditions (UCST > LCST). Consequently, thermoresponsive switching of the inside-out micelles proceeds via an aggregated intermediate state. Upon addition of NaBr, the $T_{c\ UCST}$ continuously decreases in contrast to the $T_{c\ LCST}$. When a critical concentration of 16 mM salt is exceeded, the $T_{c\ UCST}$ drops below the $T_{c\ LCST}$ (UCST < LCST). The assembly behavior of the block copolymer now changes and the transition between the inverse micelles occurs via fully solubilized unimers (Figure 10, part B). The sophisticated use of this orthogonal trigger superimposing the thermoresponse of the block copolymer offers promising opportunities especially in the field of smart carrier systems as well as emulsifiers. For the development of novel carriers, it is also interesting to note that the properties of the solvophobic micelle core can vary greatly depending on whether it is formed by the phase-separated UCST block (T < UCST, LCST) or the LCST block (T > LCST, UCST). In the case of a block copolymer synthesized by Hildebrand et al. the zwitterionic UCST block in the collapsed micelle core still had a high polarity and therefore contained large amounts of water, while the collapsed PNIPAAm core, present at high temperatures, was highly dehydrated [280]. The different microdomains thus formed in the micelle cores could be potentially used for selective solubilization as well as a triggered release of certain compounds, such as drugs. Furthermore, Cummings et al. were able to covalently anchor an analogous copolymer to the enzyme chymotropsin via surface-initiated RAFT polymerization [329]. The structural collapse of the zwitterionic UCST block at low temperatures, as well as of the PNIPAAm LCST block at high temperatures were successfully exploited to modulate the substrate affinity of the enzyme within the bioconjugate. The anchored polymer shell led to an increased stability of the enzyme by variation of the temperature, pH, and proteatic degradation, resulting in a stable bioconjugate for more than 8 h at pH 1.0 in the presence of stomach protease.

Recently, the discovery of novel UCST polymers has led to advancements in thermoresponsive block copolymers [331,332]. Zhang et al. [333], Käfer et al. [334], and Zhou et al. [335] succeeded in embedding the nonionic UCST-type copolymer P(AAm-*co*-AN) into dual thermoresponsive (UCST–LCST) systems, which were complemented either by a

PDMAEMA, PEG or PNIPAAm LCST block. In contrast to the use of zwitterionic polymers, a reversible, sharp UCST phase transition of the P(AAm-*co*-AN) block could be detected in pure water as well as buffer solutions of elevated ionic strength. The transition temperature could be controlled by the AN content of the copolymer. The UCST behavior very clearly reflected the known responsive behavior of pure P(AAm-*co*-AN) and was only slightly affected by the corresponding LCST block. In all examples, characteristic self-assembled in-side out micelles were detected via turbidity measurements as well as dynamic light scattering (DLS), and AFM. According to the relative position of UCST and LCST, a transition between the inverted micelles via fully solubilized unimers was detected for copolymers with a PNIPAAm or a PDMAEMA block, respectively (UCST < LCST), whereas Käfer et al. observed an aggregated transition state using a PEG block (UCST > LCST) [334].

The development of dual thermoresponsive block copolymers has attracted considerable academic interest in recent years due to the complexity of the phase transitions and the obtainable self-assembled structures. However, copolymers containing an UCST block as the only responsive unit have already been characterized more comprehensively and are currently leading towards smart applications, especially in the field of triggered drug release systems for cancer therapy. Based on the pioneering work of Li et al. [336] in 2015, in recent years (2016–2020) several research groups succeeded in developing the first UCST-based drug delivery nanocontainers showing excellent results in their application in vitro as well as within in vivo studies [272,330,337-341]. Due to their robust phase behavior under biologically relevant conditions (pH, ionic strength, etc.), block copolymers with nonionic UCST segments of P(AAm-AN) [272,336-341] or PNAGA [314] exhibiting a transition temperature of ≈43 °C were used in all studies. The major advantage of these novel systems, compared to their LCST-based counterparts, is the temporally and spatially very well controllable supply of heat needed for the responsive phase transition of the UCST polymers, thus leading to an on-demand release of the active drug molecules. In addition to the chemotherapeutic agent, usually doxorubicin, a photothermal agent such as cyanine dye IR780 is incorporated into the micelles. After accumulation of the micelles in the tumor tissue via the EPR effect, heat can be generated by temporal, local irradiation of an NIR laser (often λ = 808 nm, t < 5 min). This local hyperthermia can already produce enhanced tumor necrosis, it also leads to a phase transition of the UCST polymer block, which results in a disassembly of the micelles and a triggered local release of the drug (Figure 10, part C). Low leakage rates of the drug in the micellar "off-state" as well as rapid and often >70% on-demand release demonstrate the excellent properties of these nanocarriers, which in some cases are superior compared to well-known LCST-based systems [336,338]. In vivo studies in mouse models generally demonstrate both high accumulation of UCST-type micelles in the tumor tissue as well as excellent anticancer efficiency of the combined photothermal chemotherapy, which is often reflected in a significant reduction of cell viability and tumor size. The modular structure of the UCST block copolymers allowed Zhan et al. [338] as well as Yang et al. [339] to incorporate another responsive block with responsiveness towards reactive oxygen species or reduced pH in the tumor tissue, which lead to synergistic anticancer efficiencies. Furthermore, Yang et al. [341] succeeded in integrating the anticancer agent doxorubicin hydrochlorid (DOX) in the form of a pro-drug in the UCST block copolymer via a thermolabile linker, thus minimizing unwanted drug leakage below the UCST.

In this chapter we analyzed the behavior of block copolymers, containing at least one UCST-type block supplemented by other responsive or nonresponsive segments with particular focus on their temperature dependent self-assembly into micelles. Finally, in analogy to star polymers (Table 2), we summarize benefits and limitations of this topology and the resulting UCST-based thermoresponsive behavior (Table 3).

UCST polymers grafted to flat substrates

To apply thermoresponsive polymers for an intelligent control of surface properties the polymer chains need to be anchored to a substrate material. Thus, the temperature behavior of such systems is no longer just an interplay of the polymer chemistry of free chains and the surrounding solvent, but is largely determined by the assembly of the chains as well as the interaction between the polymer and the support material [124,342]. While in numerous reviews about the behavior of grafted LCST polymers it is shown that the grafting architecture not only influences the value of the critical phase transition temperature but often broadens the responsive transition as well, there are only few experimental studies on grafted UCST polymers so far. In the following, we would like to summarize the existing studies and draw conclusions for future applications of grafted UCST polymers. However, we would also like to point out that many topological effects, although some of them are very promising, are not well understood and exploited in applications yet.

The first polymer brush to demonstrate UCST behavior was fabricated in 2006 by Azzaroni et al. [90], using surface-initiated ATRP, homogeneous and patterned zwitterionic brushes on gold and silicon substrates were synthesized from [2-(methacryloyloxy)ethyl]dimethyl(3-sulfopropyl)ammonium hydroxide (MEDSAH). While extensive studies of zwitterionic polymers in bulk as well as in solution were available at that time [343], the fundamental work of Azzaroni et al. provides the first

Table 3: Benefits and limitations arising from UCST based block copolymers and their assembly into switchable micelles.

Benefits	Limitations
• Often, steric restrictions in self-assembled block copolymer micelles are smaller than in covalently fused star polymers, therefore the UCST block usually resembles more strongly the phase behavior of the linear homopolymer. However, a shift in $T_{c\ UCST}$ caused by the attached copolymer strongly depends on the UCST mechanism (ionic, non-ionic). • Dual thermoresponsive block copolymers (UCST-LCST) offer the self-assembly into in inside-out switchable micelles containing different microdomains in one polymer, which carries high potential for smart nanocarriers. • Despite of the thermoresponsive transition, precipitation can be strongly suppressed, especially in contrast to homopolymers. • First successful in vivo studies of UCST block copolymers as drug delivery systems for cancer therapy. Temporally, localized heat can be generated easily, which provides an advantage over LCST based systems requiring cooling. Combined photo-thermal and chemotherapy yields synergistic effects. • The modular structure of block copolymers can be extended to further blocks with specific properties.	• In particular, dually thermoresponsive block copolymers can have very complex phase transitions/assembly patterns. • Often the thermoresponsive behavior of the UCST segment is more strongly influenced by other segments than vice versa

insight into how these polymers behave within dense layers assembled on a surface [90]. The preparation of brushes of different layer thicknesses as well as their extensive characterization by means of contact angle measurements, Auger electron spectroscopy and AFM allows for the first time to identify molecular self-assembly processes within the brush. Accompanied by a sharp increase in the contact angle against water, Azzaroni and colleagues show that brushes with low film thickness (d < 50 nm) exist within a nonassociated state, while at high film thicknesses (up to 100 nm) inter- and intrachain ionic bridges are formed within an avalanche-type association process resulting in a supercollapsed state of the brush (Figure 11, part A) [90]. The thickness-dependent association states resulted in hydrophilic surfaces with an advancing water contact angle of about $\theta_{AW} \approx 12°$ for thin brushes, while for thick brushes θ_{AW} increased up to ≈79° (at d = 180 nm) and thus a pronounced hydrophobicity was detected. AFM measurements on patterned brushes confirmed that strong swelling and thus hydration of thin brushes occurs (d_{air} = 50 nm < h_{water} = 150 nm), while supercollapsed thick films hardly showed any swelling behavior with the film thickness being effectively constant both in air (d = 90 nm) and under water (h = 96 nm). Derived from theoretical studies, describing a high sensitivity of the electrostatic microenvironment of zwitterionic polymers to their conformation [344], Azzaroni et al. suggest that, in particular, the increase in chain length and thus the increasing number of potential ion pairings per grafting site enables the transition of the brush to a supercollapsed state [90]. However, further studies by Cheng et al. in 2008 show that additionally to a sufficient molecular weight the grafting density of the brush is a key factor [345]. For densely grafted polymer brushes the critical layer thickness for a supercollapsed state was relatively low, whereas for brushes with low grafting density higher layer thicknesses were required.

Temperature-dependent contact angle measurements, performed by Azzaroni et al., confirmed for the first time the UCST-based hydrophobic-to-hydrophilic transition of zwitterionic supercollapsed brushes (d = 180 nm) in which θ_{AW} decreased from 79° to 58° during a temperature increase from 22 °C to 52 °C (Figure 11, part A) [90]. Repeated temperature cycling indicated that this UCST transition is completely reversible and the magnitude of the effect is comparable to the well-established LCST transition of PNIPAAm brushes [347]. However, it is interesting to note that the UCST-type transition temperature of the zwitterionic brushes of ≈40 to 50 °C is significantly higher than that of comparable free polymer chains in solution (≈30 °C) [343]. The authors suggest that this is caused by trace impurities (<0.5 mol %) of inorganic salts arising from ATRP polymerization. However, based on the meanwile extensively studied antipolyelectrolyte effect [50], it is reasonable to assume that the presence of monovalent salts leads to a decrease in UCST. Therefore, we assume that the significantly increased transition temperature is due to the confined arrangement of the polymer chains within the brush structure thus promoting ion pair formation. Cheng et al. also observed similar high transition temperatures of zwitterionic brushes [345]. They also demonstrate that during the UCST transition densely grafted brushes show a low switching amplitude of ≈10–15° while a change in contact angle of up to 35° was measured for

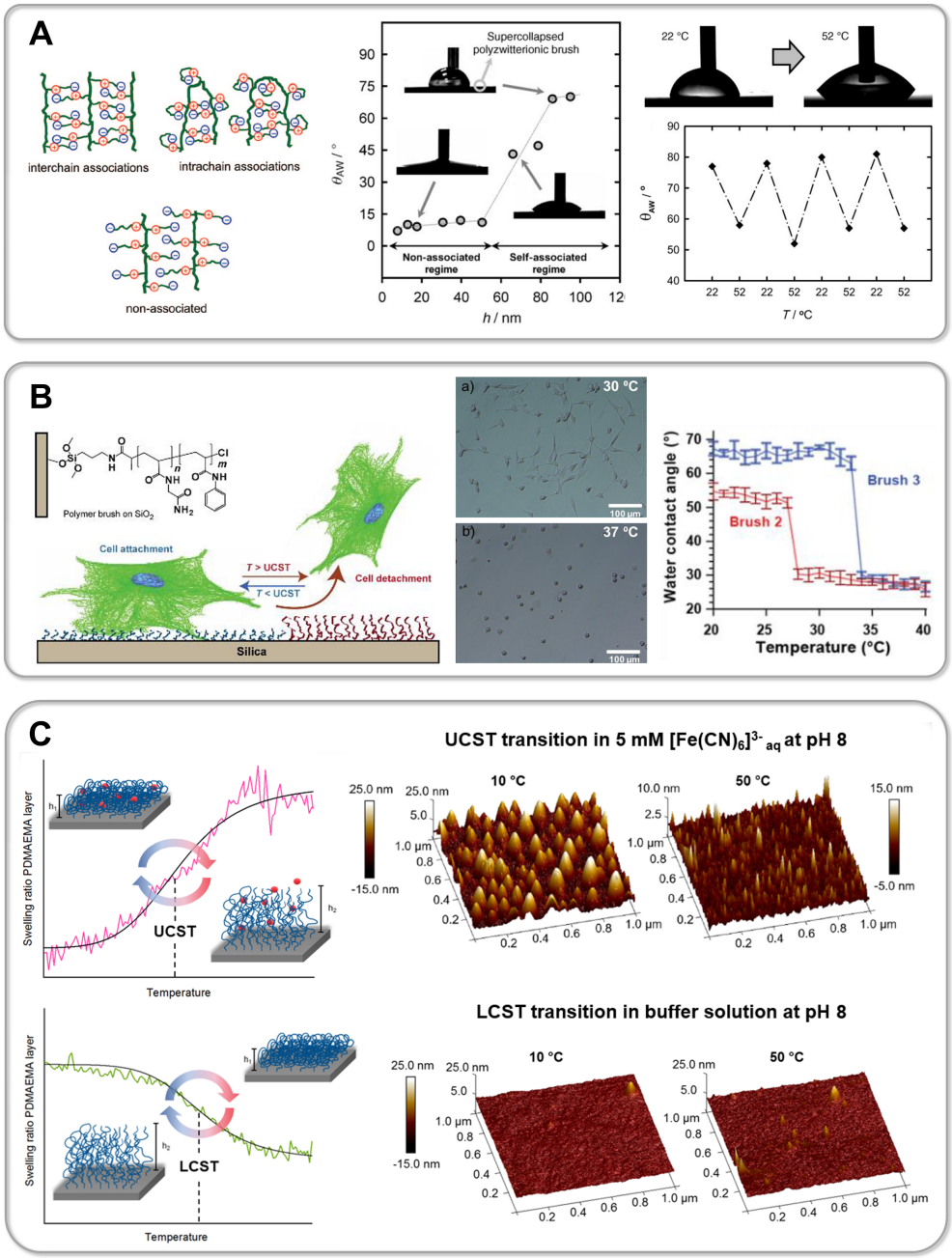


Figure 11: Part A pictures zwitterionic brushes grafted from silicon substrates obtaining a nonassociated, hydrophilic state at small brush thicknesses compared to thick brushes exhibiting hydrophobic surface properties due to a supercollapsed state based on inter- and intrachain associations (left). Temperature-dependent contact angle measurements of supercollapsed zwitterionic brushes by Azzaroni et al. (right) [90]. Part B shows the UCST-mediated cell adhesion of a silicon substrate coated with PNAGA brushes from Xue et al. [346]. Microscopic images herein monitor the cell-adhesive state at 30 °C (T < UCST) and the cell-repulsive state obtained at an elevated temperature of 37 °C (T > UCST) (right). Part C demonstrates the switchable character of PDMAEMA brushes prepared by Flemming et al. [300,301], which exhibit a LCST transition in presence of monovalent salts (bottom), whereas an UCST transition can be induced in the presence of multivalent ions like $[Fe(CN)_6]^{3-}$ (top). Spectroscopic in situ ellipsometry monitors the temperature-dependent swelling of the brushes (left), while in situ AFM images capture the surface properties of the brushes (right). Homogeneous brush surfaces are observed during the LCST transition, while the induced UCST transition is characterized by the appearance of pinned micelles with entrapped multivalent ions. Figure 11A was adapted from [90], O. Azzaroni et al., "UCST Wetting Transitions of Polyzwitterionic Brushes Driven by Self-Association", *Angew. Chem. Int. Ed.*, with permission from John Wiley and Sons. Copyright © 2006 WILEY-VCH Verlag GmbH & Co. KGaA, Weinheim. This content is not subject to CC BY 4.0. Figure 11B was adapted with permission of The Royal Society of Chemistry from [346] ("Upper critical solution temperature thermo-responsive polymer brushes and a mechanism for controlled cell attachment" by X. Xue et al., *J. Mater. Chem. B*, vol. 5, issue 25, © 2017); permission conveyed through Copyright Clearing Center, Inc. This content is not subjected to CC BY 4.0. Figure 11C (left) was adapted with permission from [300]. Copyright 2020 American Chemical Society. This content is not subject to CC BY 4.0. Figure 11C (right) was adapted with permission from [301]. Copyright 2020 American Chemical Society. This content is not subject to CC BY 4.0.

diluted brushes. Thus, the brush conformation determines not only the phase transition temperature itself, but also the macroscopic switching efficiency. A similarly large UCST-based switching effect was obtained by Yuan et al. using quaternized PDMAEMA brushes grafted from a graphene oxide sheet [348]. Upon increasing the temperature from 5 °C to 60 °C, a decrease in the static water contact angle (θ_{SW}) from ≈68° to ≈43° ($\Delta\theta_{SW} \approx 25°$) was detected. Interestingly, comparable nonquaternized PDMAEMA brushes, inherently exhibiting LCST behavior, showed an inversed switching effect with a slightly lower switching amplitude of $\Delta\theta_{SW} \approx 20°$. Recently, Chen et al. (2020) reported the adaptive wettability of an UCST-based surface with an extremely high switching amplitude and a very fast response rate [349]. Switching from a hydrophobic state at 30 °C with a θ_{SW} of ≈103° to a hydrophilic surface at 80 °C with a θ_{SW} of ≈60° ($\Delta\theta_{SW} \approx -43°$) occurred with a maximum response rate of ≈11° s^{-1}. The reversible switching behavior is superior in all parameters to those of known LCST-based PNIPAAm systems. However, it should be noted that the developed interface is a multicomponent system. Chen et al. used a porous aluminum oxide substrate with 100 nm sized nanopores, which was coated with both the UCST copolymer P(AAm-*co*-AN) and a fluorosilane (1*H*,1*H*,2*H*,2*H*-perfluorooctyltriethoxysilane; PFOTES). Based on reference studies on flat substrates as well as coatings containing only the single component (P(AAM-*co*-AN) or PFOTES), it became evident that the excellent UCST-based switching of the multicomponent system arises from synergistic effects. In particular, porosity greatly improved the UCST-based switching efficiency.

In addition to successfully adapting the wettability of a surface, Shen et al. [350] were able to generate a temperature-dependent ion permeability for energy storage devices containing nonaqueous electrolytes. For this purpose, a graphene oxide sheet was coated with zwitterionic poly(sulfobetaine) brushes using surface-initiated ATRP. While the Li ion flux is almost unimpeded below the UCST with the brushes obtaining a collapsed conformation, at elevated temperatures the unfolding zwitterionic chains begin to interact more and more with the surrounding electrolyte. The ion flux and the specific capacity for Li ions is reversibly reduced by more than 50%, when the temperature is increased from 20 °C to 80 °C. The responsive mechanism thus effectively prevents a thermal runaway, which is still a fundamental problem in the use of lithium ion batteries. In addition to the application of grafted UCST polymers in electronic systems as well as within switchable gating membranes [351], in recent years there has been a growing interest to develop UCST-based surfaces for controlled cell adhesion within cell manufacturing and regenerative medicine [346,352,353]. Xue et al. succeeded in preparing two different types of UCST-based thermoresponsive surfaces for controlled cell attachment between 2017 and 2018 [346,352]. In the first study, a PNAGA-based surface was investigated, in which the critical transition temperature could be controlled by means of random copolymerization with the hydrophobic monomer poly(*N*-phenylacrylamide). In the second case, ureido-modified poly(L-ornithine)-*co*-poly(L-citrulline)-based polypeptides were used, whose T_c could be controlled via the proportion of ureido-modified functionalities. In both systems, a temperature-dependent UCST switching behavior of the surfaces could be detected in terms of changing water contact angles. Furthermore, controlled cell adhesion was verified in both cases using fibroblasts of the cell line NIH-3T3. For the PNAGA system, cells were first incubated for 20 h on the cell adhesive collapsed brush structure at 30 °C ($T < T_{c\ UCST}$), which had a θ_{SW} of ≈65° (Figure 11, part B). After applying the temperature trigger, i.e., increasing the temperature to 37 °C ($T > T_{c\ LCST}$), ≈94% of the cells can be released due to the conformational change of the brushes to the stretched, hydrophilic state ($\theta_{SW}(T = 37\ °C) \approx 30°$). Among the released cells ≈98% were still viable. Although, in contrast to LCST systems, the cell release occurs upon increasing the temperature, a cell-adhesive state consistently occurs for collapsed polymer chains ($T <$ UCST, $T >$ LCST) whereas a cell-repulsive state is present for stretched chains ($T >$ UCST, $T <$ LCST). However, considering the polypeptide-based UCST system, cell adhesion occurs at high temperatures ($T = 39$ °C; $T >$ UCST) in the swollen polymer state, while subsequently about ≈65% of the grown cells were released during the collapse of the thermoresponsive polypeptides upon temperature reduction to 37 °C. The viability of the released cells was similarly high (≈96%) [352]. Despite extensive characterization of the surfaces, the authors were unable to elucidate the fundamental differences in the temperature-dependent cell adhesion of the two UCST systems, although they both rely on nonionic hydrogen bonding. This compelling example demonstrates clearly, that the complex UCST behavior of polymers, especially when anchored to surfaces, is not sufficiently well understood yet. In order to improve this, fundamental mechanistic studies are of particular importance.

Based on preliminary theoretical studies, Murakami et al. investigated the thermoresponse of polystyrene (PS) brushes in cyclohexane [354,355], which is one of the fundamental and well known systems exhibiting UCST behavior. They observed a shift of the binodal line and thus the UCST to lower temperatures of the PS brush system compared to PS chains in solution both in Monte Carlo simulations as well as within experimental data. They attribute this behavior to the spatial restrictions of the polymer chains within the brush structure, which hampers segregation. Interestingly, they also describe in detail a revers-

ible formation of characteristic microdomain structures of the brushes below their critical transition temperature. This unique feature, leading to a structuring of the brush surface, partially resembles the microphase separation of diblock copolymer brushes. Murakami et al. showed that different types of microdomains can be reversibly formed via tuning of the grafting density [354]. While for densely grafted brushes (σ = 0.38 chains/nm^2) the formation of microdomains is strongly suppressed by the steric restrictions and a homogeneous surface is obtained below $T_{c\ UCST}$ (10 °C), island- (σ = 0.020 chains/nm^2), bicontinous- (σ = 0.027 chains/nm^2) and hole-shaped (σ = 0.055 chains/nm^2) microdomains appear at low grafting densities. While around 20–30 nm large PS-rich islands of segregated polymer chains are formed in a PS poor matrix at σ = 0.020 chains/nm^2, inversely at higher grafting densities domains of lower PS density (holes) are formed in a PS-rich matrix. In all cases, however, due to the UCST behavior of the brushes, the roughness decreases sharply with increasing temperature and the nanostructuring of the surface disappears above $T_{c\ UCST}$.

Recently, we were able to develop a novel multi-responsive coating with counterion inducible UCST, which we have subjected to extensive mechanistic in situ investigations (Figure 11, part C) [300,301]. Herein, the water-soluble polyelectrolyte PDMAEMA is covalently anchored to a silicon substrate using an effective grafting-to approach. The obtained 5–12 nm thick (dry state) "Guiselin" brushes exhibit LCST behavior in the presence of monovalent salt ions, which is typical for PDMAEMA. However, upon addition of the multivalent ion $[Fe(CN)_6]^{3-}$, an induced UCST behavior of the brushes was detected. Using spectroscopic in situ ellipsometry, it was possible to monitor this unique temperature-dependent swelling behavior of the brushes in aqueous media for the first time. Moreover, applying in situ ATR-FTIR spectroscopy enabled monitoring of the temperature-dependent electrostatic interactions between the polycationic PDMAEMA brushes and the anionic complex, which govern the molecular mechanism of the induced UCST transition. Due to its polyelectrolyte structure (pK_a ≈ 7.0– 7.5) PDMAEMA also exhibits responsiveness to both pH and ionic strength. Exploiting the highly charged state of the polycation under acidic conditions enabled shifting of the $T_{c\ UCST}$ to 40.7 ± 2.0 °C at pH 5, whereas a significantly lower $T_{c\ UCST}$ of 34.0 ± 1.2 °C was observed for the brushes at pH 8. Interestingly, under basic conditions this value is significantly higher than in comparable studies of free polymer chains in solution, where a $T_{c\ UCST}$ (at pH 8) of 24 °C was detected via turbidity. Since Plamper et al. [293]. were also able to detect an increase in the induced $T_{c\ UCST}$ for star PDMAEMA compared to linear PDMAEMA, it can be assumed that the steric restrictions of the polymer chains and the resulting high local polymeric segment density in these architectures are responsible for a shift in T_c.

Moreover, by varying the concentration of monovalent NaCl or multivalent $[Fe(CN)_6]^{3-}$ ions, both of the critical transition temperatures ($T_{c\ LCST}$ and $T_{c\ UCST}$) as well as the switching amplitude of the brushes (change in degree of swelling), the width of the phase transition and its reversibility could be controlled. A linear dependence of T_c on the logarithmic ionic strength was observed for the LCST transition of the brushes, allowing to adjust the T_c between 26 °C and 60 °C by increasing the NaCl concentration from 0.001 mM to 100 mM. In addition, a complex pattern of very sharp, jump-like transitions of the brushes at intermediate ionic strength (1–100 mM NaCl) versus a broad transition at low and high concentrations of NaCl were observed, which resembled a theoretical model for thermoresponsive polyelectrolyte microgels [356]. However, for the induced UCST transition of the brushes, an increase in T_c and particularly sharp phase transitions were observed at high concentrations of the multivalent ion. A maximum film thickness change due to thermoresponsive switching of ≈98% (from ≈24 nm to ≈48 nm) was achieved at a concentration of 100 mM $[Fe(CN)_6]^{3-}$. Despite all this, however, it is also an extremely sensitive brush where even a low concentration of 0.001 mM multivalent ions leads to a domination of the PDMAEMA inherent LCST behavior and an induced UCST response with an increase in brush thickness with increasing temperature is detected instead.

In addition, applying temperature-dependent in situ AFM revealed fundamental structural differences between UCST and LCST transitions of the nanoscopic coating. Whereas homogeneous surfaces were detected both below and above the $T_{c\ LCST}$ in monovalent salt solutions, pinned PDMAEMA micelles with entrapped multivalent counterions were observed during the induced UCST transition (Figure 11, part C) [301].

While the occurrence of such nanostructures is consistent with recently developed theoretical models [292,357], the in situ study demonstrated for the first time that the characteristic dimensions of the pinned micelles (diameter and height) can be specifically controlled by the superimposed multi-responsive behavior of PDMAEMA towards environmental triggers like temperature or pH value. Moreover, in contrast to the PS-based system of Murakami et al. in which the formation of microdomains solely occurs below the $T_{c\ UCST}$ of the brushes, the structure of pinned micelles persists even above the $T_{c\ UCST}$ due to strong electrostatic interactions with the multivalent ions [354]. The use of grafted UCST-type polymers therefore represents a promising, novel bottom-up strategy to generate and control nanopatterns in aqueous environment, which is an im-

portant tool to tailor surface properties of flat substrates but also provides new perspectives for the colloidal stability of grafted nanoparticles. While the effect of multivalent ions on free polyelectrolyte chains has been extensively studied in the past, it was only in 2017 that Lee et al. demonstrated a Ca^{2+}-induced UCST behavior of grafted polyelectrolyte brushes on silica particles for the first time [358]. Before going into more detail on grafted particles in the next chapter, we would first like to summarize benefits and limitations of UCST exhibiting brushes on flat substrates (Table 4).

UCST polymers grafted to (nano-)particles

In addition to anchoring UCST-type thermoresponsive polymers on flat substrates, they can also be immobilized on (nano-)particles forming a responsive corona. The functional shell allows to regulate surface properties of the particles in response to environmental triggers, paving the way to novel sensors and drug delivery systems, adaptable lubricants as well as providing colloidal stability or controlled assemblies of nanoparticles [117,359]. Similarly, to the situation at flat substrates, the grafting density and thus the alignment of immobilized polymer chains has a large impact on the thermoresponse of coated nanoparticles. However, the shape of the particle and its curvature additionally define the steric constraints of the grafted polymer chains. Especially for particles with small diameters (≈1– 50 nm), the free volume available to each of the grafted polymer chains is strongly dependent on the curvature of the particle, even considering a constant grafting density on the particle surface. The complex interplay of particle curvature, as well as grafting density and chain length of the grafted polymers determines the local segment density in the particle corona, which significantly determines the thermoresponsive behavior as well as the temperature-dependent colloidal stability of the particles [115]. Due to the large number of available studies in which LCST-type polymers were used to generate responsive nanoparticles, Gibson and O'Reilly, have already been able to critically illuminate some fundamental differences and trends between the thermoresponsive behavior of responsive nanoparticles compared to polymeric brushes on flat substrates or free chains in solution [115]. However, this approach remains somewhat limited due to the lack of experimental studies for polymers with UCST behavior. However, in the following we would like to discuss the still small number of individual works on UCST-based responsive nanoparticles highlighting compelling advantages as well as remaining challenges of these novel systems in order to set the stage for a more systematic, fundamental discussion in the future.

In very recent studies, Beltrán-Osuna et al. extensively characterized the thermoresponsive behavior of mesoporous silica particles (95 ± 15 nm particle diameter, 2.8 nm pore size) grafted with zwitterionic poly(sulfobetaine methacrylate) (PSBMA) brushes using surface-initiated ATRP [360,361]. DLS measurements of the dispersed particles in aqueous solution showed a sudden increase of the hydrodynamic radius D_h upon an increase in temperature, which confirmed the UCST behavior of the responsive particle shell (Figure 12, part A). For all investigated grafting densities (0.16–0.51 chains/nm^2) as well as molar masses (6500 g/mol ≤ M_n ≤ 32 000 g/mol) of the zwitterionic brushes this structural transition from a collapsed state at low temperature to a stretched hydrophilic state at high temperature was registered. The largest switching amplitude with an increase from D_h = 109 ± 7 nm for T < 40 °C to D_h = 194 ± 6 nm at T ≈ 60 °C, was observed for the polymer brush with the highest molecular weight and the highest

Table 4: Benefits and limitations of UCST exhibiting brushes grafted onto the surface of flat substrates.

Benefits	Limitations
• Adaptive surface properties can be obtained in a resource-efficient manner by a nanoscopic polymeric coating. • Often, a shift in $T_{c\ UCST}$ to higher temperatures is observed for ionic UCST polymers in a sterically restrictive brush structure, while the $T_{c\ UCST}$ of non-ionic polymers more closely resembles that of free polymer chains. • Wetting of a surface can be modulated by temperature. UCST based systems demonstrate reproducible and in some cases switching characteristics superior to well-known LCST systems. In addition, the heat required for a UCST transition can usually be provided more easily, than the cooling which is required for LCST based coatings. • Controlled cell adhesion can be obtained with UCST exhibiting coatings. • Anchoring UCST-type polymers to surfaces can lead to adaptive nanostructuring in the form of microdomains, e.g., as pinned micelles in the presence of multivalent ions	• Frequently, a broadening of the UCST phase transition is observed due to the steric constraints of the grafted polymer chains. • A temperature-dependent characterization of grafted polymers is usually more challenging than the analysis of free polymer chains in solution.

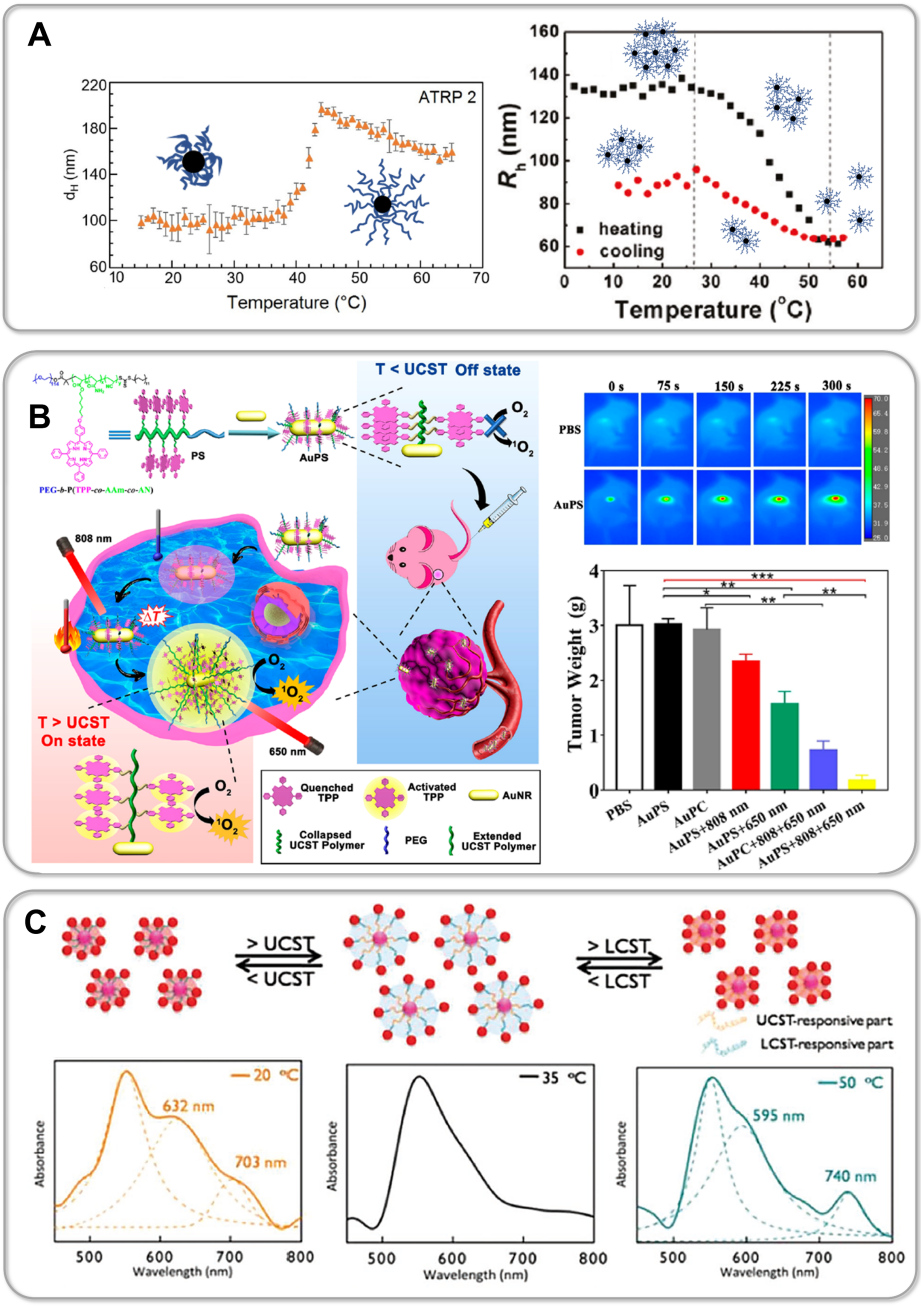


Figure 12: Part A pictures the UCST phase transition of zwitterionic polymers grafted on the surface of mesoporous silica particles. Upon an increase in temperature, this can either lead to an increasing hydrodynamic diameter of the particles due to the swelling of the particle shell as detected by Béltran-Osuna et al. [360] (left) or can proceed via associated states of the particles, resulting in a decreasing hydrodynamic radius as monitored by Dong et. al. [362] (right). Part B demonstrates a hybrid nanomaterial synthesized by Huang et al. [276], which combines an UCST exhibiting copolymer, containing (P(AAm-co-AN), and gold nanorods (left). In vivo NIR radiation of 4T1 tumor-bearing mice leads to plasmonic heating in presence of the nanomaterial (AuPS) in comparison to the injected PBS buffer reference (PBS) as pictured in the IR thermal images (upper right). The subsequently induced conformational transition of the UCST polymer leads to an activation of the photothermal therapy via embedded porphyrin units, which results in a significant reduction of the tumor volume (bottom, right). Part C shows the first core-satellite structure embedding a dual thermoresponsive polymeric linker synthesized by Han et al. in 2018 [365]. The spacing between the gold nanoparticle core and its satellites can be controlled via the thermoresponsive transitions (UCST and LCST), thus leading to a dynamic modulation of the optical properties. Figure 12A (left) was adapted from [360] with the permission of AIP Publishing. © 2020 Á. A. Beltrán-Osuna, J. L. Gómez-Ribelles, J. E. Perilla. Published under license by AIP Publishing. This content is not subject to CC BY 4.0. Figure 12A (right) was adapted with permission from [362]. Copyright 2011 American Chemical Society. This content is not subject to CC BY 4.0. Figure 12B was adapted with permission from [276]. Copyright 2019 American Chemical Society. This content is not subject to CC BY 4.0. Figure 12C was adapted from [365], F. Han et al., “Reversible Thermoresponsive Plasmonic Core-Satellite Nanostructures That Exhibit Both Expansion and Contraction (UCST and LCST)”, Macromol. Rapid Commun., with permission from John Wiley and Sons. Copyright © 2018 WILEY-VCH Verlag GmbH & Co. KGaA, Weinheim. This content is not subject to CC BY 4.0.

grafting density. At high molar masses a broadening of the temperature-dependent phase transition was observed, which is a well-known phenomenon of linear zwitterionic polymers, but occurs there at a considerably higher molecular weight of the polymers [311]. The linear increase of the phase transition temperature with increasing molecular weight of the zwitterionic polymers, which was found here is in good agreement with linear polymers [311]. Beltrán-Osuna et al. found this shifts the $T_{c\ UCST}$ from ≈34 °C for M_n = 6.5 kDa to ≈52 °C for M_n ≈ 32 kDa [360]. This universal dependence is also confirmed for grafted brushes on classical nonporous silica particles [362,363] as well as gold nanoparticles [364], and is also consistent with zwitterionic brushes confined to flat substrates [90]. However, it is interesting to note that, at comparable molecular weight of the polymers, the $T_{c\ UCST}$ for these brush systems is significantly increased compared to free linear chains in solution. Beltrán-Osuna et al. attribute this to the reduction of conformational freedom in these structures, which enhances electrostatic attractions governing the UCST transition [360]. Furthermore, it is pointed out that the local segmental density of the polymer within the brush structure is very high. According to estimates by Durand-Gasselin et al., investigating zwitterionic brushes on gold nanoparticles with similar grafting densities of ≈0.2 chains/nm^2, a weight fraction of ≈60 wt % polymer can be achieved within the particle corona [364]. Although it has long been known for zwitterionic polymers in solution that the $T_{c\ UCST}$ initially increases significantly in the range up to ≈10 wt % [343], Yu et al. were able to clarify in a recent study that at very high polymer concentrations of 10–40 wt % an extensive decrease of the $T_{c\ UCST}$ can be observed [320]. The authors attribute this to the high viscosity of the solutions and thus limited mobility of the polymer chains, which hinders the formation of attractive polymer interactions essential for UCST behavior. However, in several independent studies it was found that the high local segment density in zwitterionic brushes inversely leads to a strong increase in $T_{c\ UCST}$. Considering different architectures, we conclude that in particular the relative alignment of the polymer chains is crucial for the location of the transition temperature. On the one hand, in zwitterionic brush architectures on flat substrates as well as on particles, the parallel arrangement of the chains often leads to increased ion pair formation and thus increases the $T_{c\ UCST}$ compared to free linear chains. On the other hand, steric constraints in zwitterionic star polymers as well as branched structures or block copolymers usually hamper attractive electrostatic interactions, which leads to a decrease in $T_{c\ UCST}$.

In addition to the shift of the transition temperature, the spatially directed interactions, that govern the thermoresponsiveness of these polymers, can lead to different macroscopic outcomes of the phase transition even in apparently similar architectures. In this context, the colloidal stability of nanoparticles with a thermoresponsive polymeric shell is not only very sensitive to the interplay of particle curvature, grafting density and chain length for grafted LCST polymers, as already discussed in detail by Gibson and O'Reilly, but often leads to contradictory observations for UCST based systems as well [115]. While studies on zwitterionically grafted mesoporous silica [360], polystyrene particles [366] and gold nanoparticles [364], respectively, report an increase in D_h of dispersed particles during the UCST transition, similar work on classical as well as mesoporous silica particles with a zwitterionic corona show a temperature-dependent assembly behavior that leads oppositely to a decreasing D_h upon an increase in temperature [362,363,367]. For the first case, Polzer et al. demonstrated via cryo-TEM analysis that the zwitterionic particle corona takes the form of a highly condensed phase at the particle surface supplemented by a diluted layer consisting of individual chains that extend far into the surrounding solution at low temperatures (T < UCST) [366]. Nevertheless, even at low temperatures, colloidal stability of the particles is achieved both in water and upon addition of up to 2 mol/L NaCl. Upon heating, a drastic swelling of the responsive particle shell is detected even in the presence of salts. The UCST transition is moreover reproducible and reversible during several heating/cooling cycles without any detectable particle aggregation, which was similarly observed by Beltrán-Osuna et al. [360] and Durand-Gasselin et al. [364]. In contrast, Dong et al. [362,363] and Paramelle et al. [367] show in their work that below the $T_{c\ UCST}$ intrachain associations between the zwitterionic groups lead to particle aggregation and result in the formation of a translucent physical gel (Figure 12, part A). Only by increasing the temperature these attractive associations can be transcended, resulting in an excellently dispersed state of the particles at $T > T_{c\ UCST}$. Although in this scenario a comparable $T_{c\ UCST}$ is reported in both the heating and cooling cycle, D_h does not return to its initial value leading to enhanced aggregation upon multiple temperature cycles. While for LCST-based thermally responsive nanoparticles the grafting density seems to be the key parameter determining the colloidal stability [115], both the grafting density and the molar mass of zwitterionic polymers in the particulate UCST systems summarized here seem to play only a subordinate role. Rather, a sufficiently high particle concentration in solution seems to be decisive for the occurrence of aggregation processes [360]. Moreover, Durand-Gasselin et al. show that aggregation below the $T_{c\ UCST}$ can also be induced by the presence of free polymer chains in solution via a depletion flocculation mechanism [364].

Paramelle et al. show that particles with UCST responsive shells can be exploited for a triggered release of the hydrophilic

model compound rhodamine B (RhB) [367]. For this purpose, porous hollow silica nanocapsules modified with zwitterionic brushes were first loaded with RhB at $T > T_{c\ UCST}$. Subsequent cooling of the particles in solution leads to a collapse of the brushes at $T < T_{c\ UCST}$, which reversibly closes the pores of the particles and efficiently encapsulates RhB. Finally, conjugation of 5 nm gold nanoparticles on the brush surface enables plasmonic heating via laser stimulation (λ = 532 nm), which achieves a photothermally induced burst release of RhB from the capsules during the UCST transition of the zwitterionic particle shell. Interestingly, via plasmonic heating, a rapid release of RhB could be registered within 60 min, while thermal heating resulted in a leakage of RhB up to a time period of 6 h. Hei at el. showed that the robust UCST behavior of P(AAm-*co*-AN) brushes can also be exploited for the controlled release of the anticancer drug DOX from mesoporous silica nanoparticles [368]. By varying the AN content of the copolymer from around ≈7 to 13 mol %, the $T_{c\ UCST}$ could be adjusted between 32–50 °C, similar to micellar carriers. Temperature cycling between 25 °C and 42 °C achieved a step wise release of the loaded DOX from the grafted particles via gating of the porous channels through the conformational changes of the UCST brushes. Moreover, in vitro studies demonstrate the effective uptake of the responsive particles into breast tumor cells and the triggered release of DOX at elevated temperature leading to a reduction in cell viability of more than 20% (42 °C vs 37 °C). A similar burst release of DOX molecules from grafted mesoporous silica particles was recently reported by Hu et al. using the UCST polymer PNAGA [369]. By additionally incorporating a photosensitizer (indocyanine green) into the carrier system, it was possible to trigger the localized generation of heat via NIR irradiation. In analogy to micellar systems, a synergistic effect of this combined chemo- and photothermal therapy could be observed. In a recent work, Amoli-Diva et al. [370] and Huang et al. [276] developed P(AAM-*co*-AN)-based nanocarriers, in which the UCST copolymer was coupled to bimetallic Au-Ag nanoparticles and gold nanorods, respectively. In both cases, laser irradiation and thus excited surface plasmon resonance within the metallic components effectively generated localized heat for the UCST transition of the copolymer. The same approach was successfully applied for responsive hydrogels consisting of (PAAm-*co*-AN) and spherical gold particles or gold nanorods, respectively [371,372]. Here, plasmonic heating represents an advantageous alternative to the use of conventional organic photosensitizers which are often applied in micellar P(AAm-*co*-AN) carriers. Aggregation-induced quenching of the photosensitizer as well as its unselective activation and cytotoxicity can be avoided by plasmonic heating with metallic nanoparticles. The $T_{c\ UCST}$ values of the pure block copolymer P(AAm-*co*-AN) and the nanocarrier systems developed by Amoli-Diva et al. and Huang et al. agree well. The systems show in all cases reproducible and reversible UCST transitions with a slightly lower sensitivity and broader phase transition for the carrier systems. Nevertheless, Amoli-Diva et al. succeeded in reducing the cell viability of breast tumor cells by up to ≈30% via plasmonic heating of the nanocarrier and the triggered release of the anticancer drug letrozole from the P(AAm-*co*-AN) particle corona. Huang et al., on the other hand, exploited an on demand generation of reactive oxygen species (ROS) for targeting tumor cells via the incorporation of porphyrin units into the UCST block copolymer (Figure 12, part B). The collapsed state of the thermoresponsive polymer at $T < T_{c\ UCST}$ initially generates a quenched "off" state of the porphyrin units via π–π stacking. After incorporation of the carrier into the tumor tissue, UCST-based stretching of the polymer chains can be obtained via plasmonic heating of the gold nanorods, which subsequently switch the porphyrin units in a ROS-generating “on” state. Both in vitro and in vivo studies show that minimal toxicity of the nanocarrier can be ensured in the “off” state, for example during blood circulation, but also high cell toxicity is achieved in the “on” state after incorporation into breast tumor cells (4T1). In addition to the development of smart carrier systems, UCST polymers are also gaining interest for the controlled self-assembly of nanoparticles. Among other external stimuli, the temperature-responsive self-assembly (TRSA) of polymer-grafted nanoparticles is a particularly promising method, although it has been conducted almost exclusively with LCST exhibiting polymers in the past [373]. Despite of early work on polystyrene brushes grafted from iron oxides nanoparticles, as well as PNAGA grafted onto gold nanoparticles qualitatively demonstrating UCST-based TRSA [374,375], only recently, extensive studies by Tao et al. provide a broader insight in UCST type polymeric ligands for responsive nanoparticles [373]. The utilized ≈21 nm large gold nanoparticles, which were coated with polystyrene ligands, demonstrate a temperature-dependent reversible and reproducible self-assembly into clusters in a water/THF mixture. When the temperature decreased from 36 °C to 21 °C, the particles initially formed small clusters that subsequently grew into larger assemblies, resulting in both a drop in extinction due to partial precipitation as well as a strong red shift of the characteristic localized surface plasmon resonance peak in the UV–vis spectrum. However, upon subsequent increase in temperature, the formed clusters/precipitates were able to dissociate into individual dispersed nanoparticles, thus reversibly modulating their optical properties. Furthermore, by varying the composition of the THF/water mixture the $T_{c\ UCST}$ can be tuned, which provides a second external trigger for controlling the solvent quality and thus the particle assembly. Interestingly, comparison of free PS chains in solution shows that the $T_{c\ UCST}$ of the particles is much lower and, moreover, the particles react much more sensitive to changes in

solvent composition. Han et al. successfully fabricated a responsive hybrid core-satellite nanostructure containing an UCST-type polymeric linker for the first time in 2018 (Figure 12, part C) [365]. Well defined nanostructures of this type, though containing LCST-based polymeric linkers between the core and its satellites, have been reported before by Rossner et al. [376] and Han et al. [377]. Unlike these examples the use of UCST polymers not only enables to trigger a single-phase transition, but also, by combination with a LCST-type polymer, enables a dual-thermoresponsive behavior of a core-satellite nanostructure for the first time. The gap distance between the core and its satellites, determining the surface plasmon resonance coupling, can therefore be modulated by two distinct thermoresponsive transitions (UCST and LCST) of the polymeric linker, allowing to tune the optical properties of the assembly dynamically. For this purpose, Han and colleagues synthesized a block copolymer from a zwitterionic betanized PDMAPMA unit with $T_{c\ UCST} \approx 25$ °C and a poly(DEGA-*co*-OEGA) segment with a $T_{c\ UCST}$ of ≈45 °C. Similar to what was discussed in detail about double stimuli responsive block copolymers earlier, a shift in the $T_{c\ UCST}$ of the block copolymer is detected in comparison to the UCST of the homopolymer ($T_{c\ UCST}$ betanized PDMAPMA ≈37 °C), while the LCST behavior of the block copolymer strongly resembles that of the incorporated LCST segment ($T_{c\ LCST}$ poly(DEGA-*co*-OEGA) ≈ 45 °C). After successfully embedding the obtained block copolymer in the core-satellite structure composed of gold nanoparticles, DLS measurements demonstrate the dual-thermoresponsiveness of the assembly. While below the UCST at 20 °C a small hydrodynamic radius D_h of 163.4 ± 3.1 nm is detected due to the collapse of the UCST block within the polymeric linker, an increased D_h of 174.1 ± 2.7 nm is reported at an elevated temperature of 35 °C (T > UCST). Further increasing the temperature to 50 °C (T > LCST), which causes the thermoresponsive transition of the LCST segment, results again in a decreased D_h of 161.2 ± 3.1 nm. The reversible change of the distance between the core and the satellites via temperature cycles successfully controls the plasmonic coupling of the assembly and offers a high potential as a so-called plasmonic ruler, but also for the application as responsive SERS sensor as well as for advanced bioimaging. Finally, we would like to summarize the benefits and limitations of particles grafted with UCST polymers (Table 5).

Conclusion

The present review focused on the correlation of the thermoresponsitivity of polymers with morphological patterns as well as arrangement and conformation of the polymer chains. The consideration included star polymers, polymeric micelles and polymers covalently attached to flat substrates and particles. The focus of our considerations was on polymer systems exhibiting UCST behavior because this temperature-induced phase transition is underrepresented in the literature so far, in contrast to polymers having an LCST. Starting from a basic theoretical consideration and a description of the characteristics of the four included polymer arrangements, the influence of the specific polymeric architectures on the UCST behavior is described. Therefore, the review article provides a deeper understanding of temperature triggered responsive phase transitions that goes beyond previous reviews, which were focused on the description of the macromolecular structure of UCST-type polymers but not on polymer architectures that lead to spatially constrained assemblies. It is demonstrated, that a limited mobility of the polymer chains has a strong impact on the phase transition temperature itself, but also on the sharpness, switching amplitude and reversibility of the UCST transition. Interesting and promising effects, such as amplified secondary triggers in

Table 5: Benefits and limitations arising from UCST exhibiting polymers grafted onto the surface of (nano-)particles.

Benefits	Limitations
• Metallic nanoparticles enable plasmonic heating in order to trigger the UCST transition of the polymeric particle shell. Under light irradiation, heat can thus be generated in a localized and temporally controlled manner without the use of typically cytotoxic organic photosensitizers. This approach provides high potential for novel drug delivery systems and sensor applications. • The UCST transition of the particle shell can be used either for a targeted assembly of particles (TRSA) or for providing colloidal stability of particles in a large temperature window. • Within particle assemblies, e.g., gold nanoparticle based core-satellite structures, UCST exhibiting polymeric linkers enable a dynamic modulation of the optical properties via plasmonic coupling.	• Even with supposedly analogous particle architectures, the temperature-dependent colloidal stability or assembly behavior can vary strongly (Figure 12, part A) and is therefore difficult to predict. Because of the small number of available studies, the reasons for these variations are not sufficiently understood until now.

star polymers, inside-out switchable micelles of block copolymers, nanostructured coatings with switchable wettability, as well as the targeted release of drug molecules from grafted nanoparticles via plasmonic heating can be obtained exclusively with these sterically constrained architectures, but not by using free polymer chains in solution. Furthermore, it is pointed out that the temporally and spatially well-controllable supply of heat via irradiation of photosensitizers or plasmonic particles required for UCST-type transitions, offers tremendous advantages over well-known LCST-based systems demanding conventional cooling. Even though interest in UCST polymers continues to grow strongly and more and more novel structures with this characteristic have been synthesized, it is also obvious that the mechanistic understanding of these polymers is still insufficient, often leading to contradictory macroscopic observations even for apparently analogous architectures. More detailed academic studies of UCST-type polymers, both theoretically and experimentally, are required to enable a broad use of these promising polymers in real-life applications as novel sensors, smart coatings, or medical carrier systems.

Abbreviations

AAm, acrylamide; AFM, atomic force microscopy; AN, acrylonitrile; ATR-FTIR, attenuated total reflection-Fourier-transform infrared spectroscopy; ATRP, atom transfer radical polymerization; CMC, critical micelle concentration; CMP, critical mixing point; DEGA-*co*-OEGA, di(ethylene glycol) ethyl ether acrylate)-*co*-(oligoethylene glycol acrylate); DLS, dynamic light scattering; DNA, deoxyribonucleic acid; DOX, doxorubicin hydrochlorid; EPR, electron paramagnetic resonance; LCST, lower critical solution temperature; GA-polyHMPA, glycolamide-modified poly(*N*-(2-hydroxypropyl)methacrylamide); Gly, glycine; GMA, glycidyl methacrylate; HPG, hyperbranches poly(glycol); IDPs, disordered proteins; LBL, Langmuir–Blodgett layer; NIR, near-infrared; NMR, nuclear magnetic resonance; MEDSAH, [2-(methacryloyloxy)ethyl]dimethyl(3-sulfopropyl)ammonium hydroxide; OEGA, oligoethylene glycol acrylate; PAA, poly(acrylic acid); PAm, poly(acrylamide); PAMPT, poly(3-acrylamidopropyl)trimethylammonium chloride); PBIEM, 2-(2-bromoisobutyryloxy)ethyl methacrylate; PBMA, poly(butylmethacrylate); PBuOX, poly(2-butyl-2-oxazoline); PBOX, poly(2-(3-butinyl)-2-oxazoline); PCL, poly(ε-caporlactone); PCPOX, poly(2-cyclopropyl-2-oxazoline); PDEAAM, poly(*N,N*-diethylacrylamide); PDEAEAM, poly(*N*-(2-diethylamino)ethyl acrylamide)); PDEAEMA, poly(2-(diethylamino)ethyl methacrylate)); PDEGA, poly(di(ethylene glcol)ethyl ether acrylate); PDEGMA, poly(di(ethylene glycol)monoethyl ether methacrylate); PDMAAm, poly(*N,N*-dimethyl acrylamide); PDMAEMA, poly(2-(dimethylamino)ethyl methacrylate); PDMAPMA, poly(*N*,*N*-dimethylaminopropyl methacrylamide); PDMAPS, poly(*N*,*N*′-dimethyl(methacryloylethyl)ammonium propanesulfonate); PEI, polyethyleneimine; PEG, poly(ethylene glycol); PEGMA, poly(ethylene glycol)monomethyl ether)methacrylate; PEtOX, poly(2-ethyl-2-oxazoline); PFOTES, 1*H*,1*H*,2*H*,2*H*-perfluorooctyltriethoxysilane; PHEA, poly(2-hydroxyethyl acrylate); P(HPEI-IBAm), poly(hyperbranched polyethyleneimine isobutyramide); PHPMA, poly(2-hydroxypropyl methacrylamide); PLAMA, poly(2-lactobionamidoethyl methacrylate); PLys, poly(L-lysine); PIPOZ, poly(2-isopropyl-2-oxazoline); PMAPMA, poly(2-(*N*-methyl-*N*-(4-pyridyl)amino)ethyl methacrylate); PMDM, poly(2-(2-methoxyethoxy)ethyl methacrylate); PMEMA, poly(2-(*N*-morpholine)ethyl methacrylate)); $PMEO_2MA$, poly(di(ethylene oxid) mehyl ether methacrylate); PMeOX, poly(2-methyl-2-oxazoline); PMAA, poly(metacrylic acid); PMMA, poly(methyl methacrylate); PMPC, poly(2-methacryloyloxyethyl phosphorylcholine); PMPEG, poly(monomethoxy poly(ethylene glycol)); PNAGA, poly(*N*-acryloyl glycinamide); PNIPAAm, poly(*N*-isopropyl methacrylamide); PNMA, poly(*N*-methylolacrylamide); PNTBA, poly(*N*-*tert*-butylacrylamide); PNVCL, poly(*N*-vinyl caprolactam); PNVP, poly(*N*-vinyl-2-pyrolidone); POEGMA, poly((ethylene glycol) methyl ether methacrylate); POEOMA, poly(oligo(ethylene oxide)methacylate); poly(AAm-*co*-MDO), poly(acrylamide-*co*-2-methylene-1,3-dioxepane); POX, poly(2-oxazoline); PP, polypropylene; PPE, poly(phosphoester); PPO, poly(propylene oxide); PPropOX, poly(2-*n*-propyl-2-oxazoline); Pro, proline; PS poly(styrene); PSBMA, poly(sulfobetaine methacrylate); PSBP, poly(4-((3-methacrylamidopropyl) dimethylammonio) butane-1-sulfonate); PSPP, poly(*N,N*-dimethyl-*N*-(3-(methacrylamido)propyl) ammoniopropane sulfonate); PtBMA, poly(tert-butyl methacrylate); PTEGDA, poly(tetra(ethylene glycol)diacrylate)); PTEGMMA, poly(methoxytri(ethylene glycol) methacrylate); PVAc, poly(vinyl acetate); PVCL, poly(*N*-vinylcaprolactam); PVIm, poly(vinylimidazole); PVME, poly(vinyl methyl ether); P4VP, poly(4-vinylpyridine); RAFT, reversible addition-fragmentation chain transfer; RhB, rhodamine B; ROS, reactive oxygen species; SERS, surface-enhanced Raman spectroscopy; SPIO, supraparamagnetic iron oxide; SPOC, poly(L-ornithin-*co*-L-citrullin); TEM, transmission electron microscopy; THF, tetrahydrofuran; TRSA, temperature-responsive self-assembly; UCNP, rare-earth upconversion nanoparticles; UCST, upper critical solution temperature; UV–vis, ultraviolet-visible spectroscopy; WCA, water contact angle.

Funding

P. Flemming and A. S. Münch gratefully acknowledge the funding from Federal Ministry for Economic Affairs and Energy (BMWi) of Germany (AiF-IGF 19895 BR) and Federal Ministry of Education and Research (BMBF) of Germany (grant number 03SF0475B).

ORCID® iDs

Patricia Flemming - https://orcid.org/0000-0002-1294-1321
Alexander S. Münch - https://orcid.org/0000-0002-8398-9277
Andreas Fery - https://orcid.org/0000-0001-6692-3762
Petra Uhlmann - https://orcid.org/0000-0001-9298-4083

References

1. Ganesh, V. A.; Baji, A.; Ramakrishna, S. *RSC Adv.* **2014,** *4,* 53352–53364. doi:10.1039/c4ra10631h
2. Roy, D.; Brooks, W. L. A.; Sumerlin, B. S. *Chem. Soc. Rev.* **2013,** *42,* 7214–7243. doi:10.1039/c3cs35499g
3. Mendes, P. M. *Chem. Soc. Rev.* **2008,** *37,* 2512–2529. doi:10.1039/b714635n
4. Ward, M. A.; Georgiou, T. K. *Polymers (Basel, Switz.)* **2011,** *3,* 1215–1242. doi:10.3390/polym3031215
5. Wei, M.; Gao, Y.; Li, X.; Serpe, M. J. *Polym. Chem.* **2017,** *8,* 127–143. doi:10.1039/c6py01585a
6. Gandhi, A.; Paul, A.; Sen, S. O.; Sen, K. K. *Asian J. Pharm. Sci.* **2015,** *10,* 99–107. doi:10.1016/j.ajps.2014.08.010
7. Stuart, M. A. C.; Huck, W. T. S.; Genzer, J.; Müller, M.; Ober, C.; Stamm, M.; Sukhorukov, G. B.; Szleifer, I.; Tsukruk, V. V.; Urban, M.; Winnik, F.; Zauscher, S.; Luzinov, I.; Minko, S. *Nat. Mater.* **2010,** *9,* 101–113. doi:10.1038/nmat2614
8. Cao, P.-F.; Mangadlao, J. D.; Advincula, R. C. *Polym. Rev. (Philadelphia, PA, U. S.)* **2015,** *55,* 706–733. doi:10.1080/15583724.2015.1040553
9. Cao, Z.-Q.; Wang, G.-J. *Chem. Rec.* **2016,** *16,* 1398–1435. doi:10.1002/tcr.201500281
10. Francis, R.; Gopalan, G. P.; Sivadas, A.; Joy, N. Properties of Stimuli-Responsive Polymers. In *Biomedical Applications of Polymeric Materials and Composites;* Francis, R.; Kumar, D. S., Eds.; Wiley-VCH: Weinheim, Germany, 2016; pp 187–231. doi:10.1002/9783527690916.ch8
11. Dai, S.; Ravi, P.; Tam, K. C. *Soft Matter* **2008,** *4,* 435–449. doi:10.1039/b714741d
12. Schmaljohann, D. *Adv. Drug Delivery Rev.* **2006,** *58,* 1655–1670. doi:10.1016/j.addr.2006.09.020
13. Xiang, T.; Lu, T.; Zhao, W.-F.; Zhao, C.-S. *Langmuir* **2019,** *35,* 1146–1155. doi:10.1021/acs.langmuir.8b01719
14. Kwak, G.; Lee, W.-E.; Jeong, H.; Sakaguchi, T.; Fujiki, M. *Macromolecules* **2009,** *42,* 20–24. doi:10.1021/ma802506x
15. Vandamme, T. F.; Lenourry, A.; Charrueau, C.; Chaumeil, J.-C. *Carbohydr. Polym.* **2002,** *48,* 219–231. doi:10.1016/s0144-8617(01)00263-6
16. Itoh, Y.; Matsusaki, M.; Kida, T.; Akashi, M. *Biomacromolecules* **2006,** *7,* 2715–2718. doi:10.1021/bm060289y
17. Zhao, Y. *Macromolecules* **2012,** *45,* 3647–3657. doi:10.1021/ma300094t
18. Jochum, F. D.; Theato, P. *Polymer* **2009,** *50,* 3079–3085. doi:10.1016/j.polymer.2009.05.041
19. Pietsch, C.; Schubert, U. S.; Hoogenboom, R. *Chem. Commun.* **2011,** *47,* 8750–8765. doi:10.1039/c1cc11940k
20. Shiga, T. Deformation and Viscoelastic Behavior of Polymer Gels in Electric Fields. *Neutron Spin Echo Spectroscopy Viscoelasticity Rheology;* Advances in Polymer Science, Vol. 134; Springer: Berlin, Heidelberg, 1997; pp 131–163. doi:10.1007/3-540-68449-2_2
21. Filipcsei, G.; Fehér, J.; Zrınyi, M. *J. Mol. Struct.* **2000,** *554,* 109–117. doi:10.1016/s0022-2860(00)00564-0
22. Szabó, D.; Szeghy, G.; Zrínyi, M. *Macromolecules* **1998,** *31,* 6541–6548. doi:10.1021/ma980284w
23. Keng, P. Y.; Shim, I.; Korth, B. D.; Douglas, J. F.; Pyun, J. *ACS Nano* **2007,** *1,* 279–292. doi:10.1021/nn7001213
24. Czaun, M.; Hevesi, L.; Takafuji, M.; Ihara, H. *Chem. Commun.* **2008,** 2124–2126. doi:10.1039/b717721f
25. Schattling, P.; Jochum, F. D.; Theato, P. *Polym. Chem.* **2014,** *5,* 25–36. doi:10.1039/c3py00880k
26. Islam, M. R.; Lu, Z.; Li, X.; Sarker, A. K.; Hu, L.; Choi, P.; Li, X.; Hakobyan, N.; Serpe, M. J. *Anal. Chim. Acta* **2013,** *789,* 17–32. doi:10.1016/j.aca.2013.05.009
27. Roy, D.; Cambre, J. N.; Sumerlin, B. S. *Prog. Polym. Sci.* **2010,** *35,* 278–301. doi:10.1016/j.progpolymsci.2009.10.008
28. Liu, F.; Urban, M. W. *Prog. Polym. Sci.* **2010,** *35,* 3–23. doi:10.1016/j.progpolymsci.2009.10.002
29. Shim, M. S.; Kwon, Y. J. *Adv. Drug Delivery Rev.* **2012,** *64,* 1046–1059. doi:10.1016/j.addr.2012.01.018
30. Hoffman, A. S. *Adv. Drug Delivery Rev.* **2013,** *65,* 10–16. doi:10.1016/j.addr.2012.11.004
31. Bajpai, A. K.; Shukla, S. K.; Bhanu, S.; Kankane, S. *Prog. Polym. Sci.* **2008,** *33,* 1088–1118. doi:10.1016/j.progpolymsci.2008.07.005
32. Oliveira, M. B.; Mano, J. F. Natural-Based and Stimuli-Responsive Polymers for Tissue Engineering and Regenerative Medicine. *Polymers in Regenerative Medicine;* John Wiley & Sons: Hoboken, NJ, USA, 2014; pp 49–90. doi:10.1002/9781118356692.ch2
33. Municoy, S.; Álvarez Echazú, M. I.; Antezana, P. E.; Galdopórpora, J. M.; Olivetti, C.; Mebert, A. M.; Foglia, M. L.; Tuttolomondo, M. V.; Alvarez, G. S.; Hardy, J. G.; Desimone, M. F. *Int. J. Mol. Sci.* **2020,** *21,* 4724. doi:10.3390/ijms21134724
34. Wang, Z.; Liu, X.; Wu, Y.; Liu, B.; Wang, Z.; Zhang, J.; Liu, K.; Yang, B. *J. Mater. Chem. C* **2018,** *6,* 10861–10869. doi:10.1039/c8tc02049c
35. Parasuraman, D.; Serpe, M. J. *ACS Appl. Mater. Interfaces* **2011,** *3,* 2732–2737. doi:10.1021/am2005288
36. Hu, J.; Liu, S. *Macromolecules* **2010,** *43,* 8315–8330. doi:10.1021/ma1005815
37. Zhang, Q. M.; Serpe, M. J. Responsive Polymers as Sensors, Muscles, and Self-Healing Materials BT. In *Polymer Mechanochemistry;* Boulatov, R., Ed.; Springer International Publishing: Cham, Switzerland, 2015; pp 377–424. doi:10.1007/128_2015_626
38. Hu, L.; Zhang, Q.; Li, X.; Serpe, M. J. *Mater. Horiz.* **2019,** *6,* 1774–1793. doi:10.1039/c9mh00490d
39. Cui, H.; Zhao, Q.; Wang, Y.; Du, X. *Chem. – Asian J.* **2019,** *14,* 2369–2387. doi:10.1002/asia.201900292
40. Peng, S.; Bhushan, B. *RSC Adv.* **2012,** *2,* 8557–8578. doi:10.1039/c2ra20451g
41. Chen, W.-L.; Cordero, R.; Tran, H.; Ober, C. K. *Macromolecules* **2017,** *50,* 4089–4113. doi:10.1021/acs.macromol.7b00450
42. Nath, N.; Chilkoti, A. *Adv. Mater. (Weinheim, Ger.)* **2002,** *14,* 1243–1247. doi:10.1002/1521-4095(20020903)14:17<1243::aid-adma1243>3.0.co;2-m
43. Stetsyshyn, Y.; Raczkowska, J.; Harhay, K.; Gajos, K.; Melnyk, Y.; Dąbczyński, P.; Shevtsova, T.; Budkowski, A. *Colloid Polym. Sci.* **2021,** *299,* 363–383. doi:10.1007/s00396-020-04750-0
44. Hoogenboom, R. Temperature-responsive polymers: properties, synthesis and applications. In *Smart Polymers and their Applications;* Aguilar, M. R.; San Román, J., Eds.; Woodhead Publishing: Cambridge. UK, 2014; pp 15–44. doi:10.1533/9780857097026.1.15

45. Teotia, A. K.; Sami, H.; Kumar, A. Thermo-Responsive Polymers: Structure and Design of Smart Materials. Zhang, Z., Ed.; Woodhead Publishing: Cambridge. UK, 2015; pp 3–43.
46. Zhang, Q.; Weber, C.; Schubert, U. S.; Hoogenboom, R. *Mater. Horiz.* **2017,** *4,* 109–116. doi:10.1039/c7mh00016b
47. Somcynsky, T. *Polym. Eng. Sci.* **1982,** *22,* 58–63. doi:10.1002/pen.760220203
48. Halperin, A.; Kröger, M.; Winnik, F. M. *Angew. Chem., Int. Ed.* **2015,** *54,* 15342–15367. doi:10.1002/anie.201506663
49. Aseyev, V.; Tenhu, H.; Winnik, F. M. Non-ionic Thermoresponsive Polymers in Water. In *Self Organized Nanostructures of Amphiphilic Block Copolymers II;* Müller, A.; Borisov, O., Eds.; Advances in Polymer Science, Vol. 242; Springer: Berlin, Heidelberg, 2011; pp 29–89. doi:10.1007/12_2010_57
50. Niskanen, J.; Tenhu, H. *Polym. Chem.* **2017,** *8,* 220–232. doi:10.1039/c6py01612j
51. Seuring, J.; Agarwal, S. *Macromol. Rapid Commun.* **2012,** *33,* 1898–1920. doi:10.1002/marc.201200433
52. Bansal, K. K.; Upadhyay, P. K.; Saraogi, G. K.; Rosling, A.; Rosenholm, J. M. *eXPRESS Polym. Lett.* **2019,** *13,* 974–992. doi:10.3144/expresspolymlett.2019.85
53. Zhang, Q.; Hoogenboom, R. *Prog. Polym. Sci.* **2015,** *48,* 122–142. doi:10.1016/j.progpolymsci.2015.02.003
54. Seuring, J.; Agarwal, S. *ACS Macro Lett.* **2013,** *2,* 597–600. doi:10.1021/mz400227y
55. Zhao, C.; Ma, Z.; Zhu, X. X. *Prog. Polym. Sci.* **2019,** *90,* 269–291. doi:10.1016/j.progpolymsci.2019.01.001
56. Zarrintaj, P.; Jouyandeh, M.; Ganjali, M. R.; Hadavand, B. S.; Mozafari, M.; Sheiko, S. S.; Vatankhah-Varnoosfaderani, M.; Gutiérrez, T. J.; Saeb, M. R. *Eur. Polym. J.* **2019,** *117,* 402–423. doi:10.1016/j.eurpolymj.2019.05.024
57. Mokhtarinia, K.; Masaeli, E. *Eur. Polym. J.* **2020,** *141,* 110076. doi:10.1016/j.eurpolymj.2020.110076
58. Sponchioni, M.; Capasso Palmiero, U.; Moscatelli, D. *Mater. Sci. Eng., C* **2019,** *102,* 589–605. doi:10.1016/j.msec.2019.04.069
59. Bordat, A.; Boissenot, T.; Nicolas, J.; Tsapis, N. *Adv. Drug Delivery Rev.* **2019,** *138,* 167–192. doi:10.1016/j.addr.2018.10.005
60. Le, P. N.; Huynh, C. K.; Tran, N. Q. *Mater. Sci. Eng., C* **2018,** *92,* 1016–1030. doi:10.1016/j.msec.2018.02.006
61. Li, Z.; Chen, Y.; Yang, Y.; Yu, Y.; Zhang, Y.; Zhu, D.; Yu, X.; Ouyang, X.; Xie, Z.; Zhao, Y.; Li, L. *Front. Bioeng. Biotechnol.* **2019,** *7,* 293. doi:10.3389/fbioe.2019.00293
62. Chen, T.; Ferris, R.; Zhang, J.; Ducker, R.; Zauscher, S. *Prog. Polym. Sci.* **2010,** *35,* 94–112. doi:10.1016/j.progpolymsci.2009.11.004
63. Tang, L.; Wang, L.; Yang, X.; Feng, Y.; Li, Y.; Feng, W. *Prog. Mater. Sci.* **2021,** *115,* 100702. doi:10.1016/j.pmatsci.2020.100702
64. Ramakrishna, S. N.; Cirelli, M.; Kooij, E. S.; Klein Gunnewiek, M.; Benetti, E. M. *Macromolecules* **2015,** *48,* 7106–7116. doi:10.1021/acs.macromol.5b01556
65. Lüdecke, D.; Lüdecke, C. *Thermodynamik: Physikalisch-chemische Grundlagen der thermischen Verfahrenstechnik;* Springer: Berlin, Heidelberg, 2013.
66. Atkins, P.; De Paula, J.; Walters, V. *Physical Chemistry;* W. H. Freeman, 2006.
67. Flory, P. J. *J. Chem. Phys.* **1941,** *9,* 660. doi:10.1063/1.1750971
68. Flory, P. J. *J. Chem. Phys.* **1942,** *10,* 51–61. doi:10.1063/1.1723621
69. Huggins, M. L. *J. Chem. Phys.* **1941,** *9,* 440. doi:10.1063/1.1750930
70. Huggins, M. L. *J. Phys. Chem.* **1942,** *46,* 151–158. doi:10.1021/j150415a018
71. Baulin, V. A.; Halperin, A. *Macromolecules* **2002,** *35,* 6432–6438. doi:10.1021/ma020296o
72. Bekiranov, S.; Bruinsma, R.; Pincus, P. *Phys. Rev. E* **1997,** *55,* 577–585. doi:10.1103/physreve.55.577
73. Solc, K.; Koningsveld, R. *J. Phys. Chem.* **1992,** *96,* 4056–4068. doi:10.1021/j100189a027
74. Schäfer-Soenen, H.; Moerkerke, R.; Berghmans, H.; Koningsveld, R.; Dušek, K.; Šolc, K. *Macromolecules* **1997,** *30,* 410–416. doi:10.1021/ma960114o
75. De Sousa, H. C.; Rebelo, L. P. N. *J. Polym. Sci., Part B: Polym. Phys.* **2000,** *38,* 632–651. doi:10.1002/(sici)1099-0488(20000215)38:4<632::aid-polb15>3.0.co;2-q
76. Vimalchand, P.; Donohue, M. D. *J. Phys. Chem.* **1989,** *93,* 4355–4360. doi:10.1021/j100347a088
77. Beaucage, G.; Stein, R. S.; Koningsveld, R. *Macromolecules* **1993,** *26,* 1603–1608. doi:10.1021/ma00059a018
78. Staverman, A. J.; van Santen, J. H. *Recl. Trav. Chim. Pays-Bas* **1941,** *60,* 76–84. doi:10.1002/recl.19410600202
79. Staverman, A. J. *Recl. Trav. Chim. Pays-Bas* **1941,** *60,* 640–649. doi:10.1002/recl.19410600903
80. Flory, P. J. *J. Chem. Phys.* **1944,** *12,* 425–438. doi:10.1063/1.1723887
81. Scott, R. L.; Magat, M. *J. Chem. Phys.* **1945,** *13,* 172–177. doi:10.1063/1.1724018
82. Richon, D.; Mohammadi, A. H. *Open Thermodyn. J.* **2008,** *2,* 13–16. doi:10.2174/1874396x00802010013
83. Zhang, Q.; Schattling, P.; Theato, P.; Hoogenboom, R. *Polym. Chem.* **2012,** *3,* 1418–1426. doi:10.1039/c2py20073b
84. Zhang, Q.; Hong, J.-D.; Hoogenboom, R. *Polym. Chem.* **2013,** *4,* 4322–4325. doi:10.1039/c3py00659j
85. Monge, S.; Antoniacomi, S.; Lapinte, V.; Darcos, V.; Robin, J.-J. *Polym. Chem.* **2012,** *3,* 2502–2507. doi:10.1039/c2py20309j
86. Sahn, M.; Yildirim, T.; Dirauf, M.; Weber, C.; Sungur, P.; Hoeppener, S.; Schubert, U. S. *Macromolecules* **2016,** *49,* 7257–7267. doi:10.1021/acs.macromol.6b01371
87. Weber, C.; Rogers, S.; Vollrath, A.; Hoeppener, S.; Rudolph, T.; Fritz, N.; Hoogenboom, R.; Schubert, U. S. *J. Polym. Sci., Part A: Polym. Chem.* **2013,** *51,* 139–148. doi:10.1002/pola.26332
88. Vasantha, V. A.; Jana, S.; Parthiban, A.; Vancso, J. G. *Chem. Commun.* **2014,** *50,* 46–48. doi:10.1039/c3cc44407d
89. Ilčíková, M.; Tkáč, J.; Kasák, P. *Polymers (Basel, Switz.)* **2015,** *7,* 2344–2370. doi:10.3390/polym7111518
90. Azzaroni, O.; Brown, A. A.; Huck, W. T. S. *Angew. Chem., Int. Ed.* **2006,** *45,* 1770–1774. doi:10.1002/anie.200503264
91. Chen, L.; Honma, Y.; Mizutani, T.; Liaw, D.-J.; Gong, J. P.; Osada, Y. *Polymer* **2000,** *41,* 141–147. doi:10.1016/s0032-3861(99)00161-5
92. Seuring, J.; Bayer, F. M.; Huber, K.; Agarwal, S. *Macromolecules* **2012,** *45,* 374–384. doi:10.1021/ma202059t
93. Seuring, J.; Agarwal, S. *Macromol. Chem. Phys.* **2010,** *211,* 2109–2117. doi:10.1002/macp.201000147
94. Seuring, J.; Agarwal, S. *Macromolecules* **2012,** *45,* 3910–3918. doi:10.1021/ma300355k
95. Xu, Z.; Liu, W. *Chem. Commun.* **2018,** *54,* 10540–10553. doi:10.1039/c8cc04614j

96. Sun, W.; Wu, P. *Phys. Chem. Chem. Phys.* **2018,** *20,* 20849–20855. doi:10.1039/c8cp04147d
97. Schild, H. G. *Prog. Polym. Sci.* **1992,** *17,* 163–249. doi:10.1016/0079-6700(92)90023-r
98. Lin, S.-Y.; Chen, K.-S.; Liang, R.-C. *Polymer* **1999,** *40,* 2619–2624. doi:10.1016/s0032-3861(98)00512-6
99. Katsumoto, Y.; Tanaka, T.; Sato, H.; Ozaki, Y. *J. Phys. Chem. A* **2002,** *106,* 3429–3435. doi:10.1021/jp0124903
100. Qiu, X.; Koga, T.; Tanaka, F.; Winnik, F. M. *Sci. China: Chem.* **2013,** *56,* 56–64. doi:10.1007/s11426-012-4781-9
101. Müller, A. H. E.; Borisov, O., Eds. *Self Organized Nanostructures of Amphiphilic Block Copolymers II;* Advances in Polymer Science; Springer: Berlin, Heidelberg, 2011. doi:10.1007/978-3-642-22297-9
102. Kuckling, D.; Wycisk, A. *J. Polym. Sci., Part A: Polym. Chem.* **2013,** *51,* 2980–2994. doi:10.1002/pola.26696
103. Ren, J. M.; McKenzie, T. G.; Fu, Q.; Wong, E. H. H.; Xu, J.; An, Z.; Shanmugam, S.; Davis, T. P.; Boyer, C.; Qiao, G. G. *Chem. Rev.* **2016,** *116,* 6743–6836. doi:10.1021/acs.chemrev.6b00008
104. Kotrchová, L.; Kostka, L.; Etrych, T. *Physiol. Res. (Prague, Czech Repub.)* **2018,** *67* (Suppl. 2), S293–S303. doi:10.33549/physiolres.933978
105. Zhang, Y.; Yan, J.; Avellan, A.; Gao, X.; Matyjaszewski, K.; Tilton, R. D.; Lowry, G. V. *ACS Nano* **2020,** *14,* 10954–10965. doi:10.1021/acsnano.0c03140
106. Patil, R. A.; Aloorkar, N. H.; Kulkarni, A. S.; Ingale, D. J. *Int. J. Pharm. Sci. Nanotechnol.* **2012,** *5,* 1675–1684. doi:10.37285/ijpsn.2012.5.2.3
107. Matyjaszewski, K.; Miller, P. J.; Pyun, J.; Kickelbick, G.; Diamanti, S. *Macromolecules* **1999,** *32,* 6526–6535. doi:10.1021/ma9904823
108. Wu, Z.; Liang, H.; Lu, J. *Macromolecules* **2010,** *43,* 5699–5705. doi:10.1021/ma100800b
109. Roovers, J.; Martin, J. E. *J. Polym. Sci., Part B: Polym. Phys.* **1989,** *27,* 2513–2524. doi:10.1002/polb.1989.090271209
110. Sun, X.-L.; Tsai, P.-C.; Bhat, R.; Bonder, E. M.; Michniak-Kohn, B.; Pietrangelo, A. *J. Mater. Chem. B* **2015,** *3,* 814–823. doi:10.1039/c4tb01494d
111. Vishnevetskaya, N. S.; Hildebrand, V.; Niebuur, B.-J.; Grillo, I.; Filippov, S. K.; Laschewsky, A.; Müller-Buschbaum, P.; Papadakis, C. M. *Macromolecules* **2017,** *50,* 3985–3999. doi:10.1021/acs.macromol.7b00356
112. Rösler, A.; Vandermeulen, G. W. M.; Klok, H.-A. *Adv. Drug Delivery Rev.* **2012,** *64,* 270–279. doi:10.1016/j.addr.2012.09.026
113. Wei, H.; Zhang, X.-Z.; Zhou, Y.; Cheng, S.-X.; Zhuo, R.-X. *Biomaterials* **2006,** *27,* 2028–2034. doi:10.1016/j.biomaterials.2005.09.028
114. Toomey, R.; Tirrell, M. *Annu. Rev. Phys. Chem.* **2008,** *59,* 493–517. doi:10.1146/annurev.physchem.59.032607.093623
115. Gibson, M. I.; O'Reilly, R. K. *Chem. Soc. Rev.* **2013,** *42,* 7204–7213. doi:10.1039/c3cs60035a
116. Ballauff, M.; Borisov, O. V. *Polymer* **2016,** *98,* 402–408. doi:10.1016/j.polymer.2016.05.014
117. Reimhult, E.; Schroffenegger, M.; Lassenberger, A. *Langmuir* **2019,** *35,* 7092–7104. doi:10.1021/acs.langmuir.9b00665
118. Milner, S. T.; Witten, T. A.; Cates, M. E. *Macromolecules* **1988,** *21,* 2610–2619. doi:10.1021/ma00186a051
119. De Gennes, P. G. *J. Phys. (Paris)* **1976,** *37,* 1445–1452. doi:10.1051/jphys:019760037012014450O
120. de Gennes, P. G. *Macromolecules* **1980,** *13,* 1069–1075. doi:10.1021/ma60077a009
121. Alexander, S. *J. Phys. (Paris)* **1977,** *38,* 983–987. doi:10.1051/jphys:01977003808098300
122. Skvortsov, A. M.; Pavlushkov, I. V.; Gorbunov, A. A.; Zhulina, Y. B.; Borisov, O. V.; Pryamitsyn, V. A. *Polym. Sci. USSR* **1988,** *30,* 1706–1715. doi:10.1016/0032-3950(88)90393-0
123. Zhulina, E. B.; Borisov, O. V.; Pryamitsyn, V. A.; Birshtein, T. M. *Macromolecules* **1991,** *24,* 140–149. doi:10.1021/ma00001a023
124. Lian, C.; Wang, L.; Chen, X.; Han, X.; Zhao, S.; Liu, H.; Hu, Y. *Langmuir* **2014,** *30,* 4040–4048. doi:10.1021/la5003429
125. Minko, S. *Polym. Rev. (Philadelphia, PA, U. S.)* **2006,** *46,* 397–420. doi:10.1080/15583720600945402
126. Grest, G. S.; Murat, M. *Macromolecules* **1993,** *26,* 3108–3117. doi:10.1021/ma00064a019
127. Flory, P. J. *J. Am. Chem. Soc.* **1965,** *87,* 1833–1838. doi:10.1021/ja01087a002
128. Karim, A.; Satija, S. K.; Douglas, J. F.; Ankner, J. F.; Fetters, L. J. *Phys. Rev. Lett.* **1994,** *73,* 3407–3410. doi:10.1103/physrevlett.73.3407
129. Baulin, V. A.; Halperin, A. *Macromol. Theory Simul.* **2003,** *12,* 549–559. doi:10.1002/mats.200350014
130. Erman, B.; Flory, P. J. *Macromolecules* **1986,** *19,* 2342–2353. doi:10.1021/ma00163a003
131. Baulin, V. A.; Zhulina, E. B.; Halperin, A. *J. Chem. Phys.* **2003,** *119,* 10977–10988. doi:10.1063/1.1619934
132. Yim, H.; Kent, M. S.; Mendez, S.; Lopez, G. P.; Satija, S.; Seo, Y. *Macromolecules* **2006,** *39,* 3420–3426. doi:10.1021/ma0520949
133. Yim, H.; Kent, M. S.; Satija, S.; Mendez, S.; Balamurugan, S. S.; Balamurugan, S.; Lopez, G. P. *Phys. Rev. E* **2005,** *72,* 051801. doi:10.1103/physreve.72.051801
134. Misra, S.; Varanasi, S.; Varanasi, P. P. *Macromolecules* **1989,** *22,* 4173–4179. doi:10.1021/ma00201a007
135. Zhulina, E. B.; Borisov, O. V.; Birshtein, T. M. *J. Phys. II* **1992,** *2,* 63–74. doi:10.1051/jp2:1992113
136. Israëls, R.; Leermakers, F. A. M.; Fleer, G. J.; Zhulina, E. B. *Macromolecules* **1994,** *27,* 3249–3261. doi:10.1021/ma00090a018
137. Borisov, O. V.; Zhulina, E. B.; Birshtein, T. M. *Macromolecules* **1994,** *27,* 4795–4803. doi:10.1021/ma00095a021
138. Guenoun, P.; Schalchli, A.; Sentenac, D.; Mays, J. W.; Benattar, J. J. *Phys. Rev. Lett.* **1995,** *74,* 3628–3631. doi:10.1103/physrevlett.74.3628
139. Zhu, M.-Q.; Wang, L.-Q.; Exarhos, G. J.; Li, A. D. Q. *J. Am. Chem. Soc.* **2004,** *126,* 2656–2657. doi:10.1021/ja038544z
140. Gibson, M. I.; Paripovic, D.; Klok, H.-A. *Adv. Mater. (Weinheim, Ger.)* **2010,** *22,* 4721–4725. doi:10.1002/adma.201001382
141. Ge, Z.; Cai, Y.; Yin, J.; Zhu, Z.; Rao, J.; Liu, S. *Langmuir* **2007,** *23,* 1114–1122. doi:10.1021/la062719b
142. Ge, Z.; Xu, J.; Hu, J.; Zhang, Y.; Liu, S. *Soft Matter* **2009,** *5,* 3932–3939. doi:10.1039/b907906h
143. Qu, Y.; Chang, X.; Chen, S.; Zhang, W. *Polym. Chem.* **2017,** *8,* 3485–3496. doi:10.1039/c7py00508c
144. Zhang, Y.; Liu, H.; Hu, J.; Li, C.; Liu, S. *Macromol. Rapid Commun.* **2009,** *30,* 941–947. doi:10.1002/marc.200800820
145. Li, J.; He, W.-D.; He, N.; Han, S.-C.; Sun, X.-L.; Li, L.-Y.; Zhang, B.-Y. *J. Polym. Sci., Part A: Polym. Chem.* **2009,** *47,* 1450–1462. doi:10.1002/pola.23254
146. Zhang, Y.; Liu, H.; Dong, H.; Li, C.; Liu, S. *J. Polym. Sci., Part A: Polym. Chem.* **2009,** *47,* 1636–1650. doi:10.1002/pola.23273
147. Li, C.; Ge, Z.; Liu, H.; Liu, S. *J. Polym. Sci., Part A: Polym. Chem.* **2009,** *47,* 4001–4013. doi:10.1002/pola.23461

148. Li, J.; He, W.-D.; Han, S.-c.; Sun, X.-l.; Li, L.-y.; Zhang, B.-y. *J. Polym. Sci., Part A: Polym. Chem.* **2009,** *47,* 786–796. doi:10.1002/pola.23195
149. Zhang, W.; Zhang, W.; Zhou, N.; Zhu, J.; Cheng, Z.; Zhu, X. *J. Polym. Sci., Part A: Polym. Chem.* **2009,** *47,* 6304–6315. doi:10.1002/pola.23673
150. Fazlalizadeh, F.; Massoumi, B.; Banaei, A.; Jaymand, M. *Polym. Sci., Ser. B* **2020,** *62,* 540–549. doi:10.1134/s1560090420050061
151. Xu, N.; Huang, X.; Yin, G.; Bu, M.; Pu, X.; Chen, X.; Liao, X.; Huang, Z. *RSC Adv.* **2018,** *8,* 15604–15612. doi:10.1039/c8ra02117a
152. Cao, M.; Han, G.; Duan, W.; Zhang, W. *Polym. Chem.* **2018,** *9,* 2625–2633. doi:10.1039/c8py00422f
153. ten Brummelhuis, N.; Schlaad, H. *Polym. Chem.* **2011,** *2,* 1180–1184. doi:10.1039/c1py00002k
154. Kurlykin, M. P.; Bursian, A. E.; Dudkina, M. M.; Ten'kovtsev, A. V. *Fibre Chem.* **2015,** *47,* 291–297. doi:10.1007/s10692-016-9681-x
155. Filippov, A. P.; Amirova, A. I.; Dudkina, M. M.; Tenkovtsev, A. V. *Int. J. Polym. Anal. Charact.* **2013,** *18,* 567–577. doi:10.1080/1023666x.2013.836925
156. Amirova, A. I.; Dudkina, M. M.; Tenkovtsev, A. V.; Filippov, A. P. *Colloid Polym. Sci.* **2015,** *293,* 239–248. doi:10.1007/s00396-014-3402-x
157. Plamper, F. A.; McKee, J. R.; Laukkanen, A.; Nykänen, A.; Walther, A.; Ruokolainen, J.; Aseyev, V.; Tenhu, H. *Soft Matter* **2009,** *5,* 1812–1821. doi:10.1039/b822143j
158. Zhu, W.; Nese, A.; Matyjaszewski, K. *J. Polym. Sci., Part A: Polym. Chem.* **2011,** *49,* 1942–1952. doi:10.1002/pola.24611
159. Vrijsen, J. H.; Van de Reydt, E.; Junkers, T. *J. Polym. Sci. (Hoboken, NJ, U. S.)* **2020,** *58,* 3402–3410. doi:10.1002/pol.20200634
160. Mendrek, B.; Żymełka-Miara, I.; Sieroń, Ł.; Fus, A.; Balin, K.; Kubacki, J.; Smet, M.; Trzebicka, B.; Sieroń, A. L.; Kowalczuk, A. *J. Mater. Chem. B* **2018,** *6,* 641–655. doi:10.1039/c7tb02748f
161. Kent, E. W.; Zhao, B. *Macromolecules* **2019,** *52,* 6714–6724. doi:10.1021/acs.macromol.9b01446
162. Yuan, Y.-Y.; Wang, J. *Colloids Surf., B* **2011,** *85,* 81–85. doi:10.1016/j.colsurfb.2010.10.044
163. Cortez-Lemus, N. A.; Licea-Claverie, A. *Polymers (Basel, Switz.)* **2017,** *10,* 20. doi:10.3390/polym10010020
164. Kalhapure, R. S.; Renukuntla, J. *Chem.-Biol. Interact.* **2018,** *295,* 20–37. doi:10.1016/j.cbi.2018.07.016
165. Nakayama, M.; Okano, T. *J. Drug Delivery Sci. Technol.* **2006,** *16,* 35–44. doi:10.1016/s1773-2247(06)50005-x
166. Wang, Y.; Wei, G.; Zhang, W.; Jiang, X.; Zheng, P.; Shi, L.; Dong, A. *J. Mol. Catal. A: Chem.* **2007,** *266,* 233–238. doi:10.1016/j.molcata.2006.11.014
167. Chaw, C.-S.; Chooi, K.-W.; Liu, X.-M.; Tan, C.-w.; Wang, L.; Yang, Y.-Y. *Biomaterials* **2004,** *25,* 4297–4308. doi:10.1016/j.biomaterials.2003.10.095
168. Pan, P.; Fujita, M.; Ooi, W.-Y.; Sudesh, K.; Takarada, T.; Goto, A.; Maeda, M. *Langmuir* **2012,** *28,* 14347–14356. doi:10.1021/la303128y
169. Neradovic, D.; van Nostrum, C. F.; Hennink, W. E. *Macromolecules* **2001,** *34,* 7589–7591. doi:10.1021/ma011198q
170. Chung, J. E.; Yokoyama, M.; Yamato, M.; Aoyagi, T.; Sakurai, Y.; Okano, T. *J. Controlled Release* **1999,** *62,* 115–127. doi:10.1016/s0168-3659(99)00029-2
171. Cammas, S.; Suzuki, K.; Sone, C.; Sakurai, Y.; Kataoka, K.; Okano, T. *J. Controlled Release* **1997,** *48,* 157–164. doi:10.1016/s0168-3659(97)00040-0
172. Chung, J. E.; Yokoyama, M.; Aoyagi, T.; Sakurai, Y.; Okano, T. *J. Controlled Release* **1998,** *53,* 119–130. doi:10.1016/s0168-3659(97)00244-7
173. Luo, S.; Hu, X.; Zhang, Y.; Ling, C.; Liu, X.; Chen, S. *Polym. J.* **2011,** *43,* 41–50. doi:10.1038/pj.2010.93
174. Hoogenboom, R.; Schlaad, H. *Polym. Chem.* **2017,** *8,* 24–40. doi:10.1039/c6py01320a
175. Lorson, T.; Lübtow, M. M.; Wegener, E.; Haider, M. S.; Borova, S.; Nahm, D.; Jordan, R.; Sokolski-Papkov, M.; Kabanov, A. V.; Luxenhofer, R. *Biomaterials* **2018,** *178,* 204–280. doi:10.1016/j.biomaterials.2018.05.022
176. Trinh, L. T. T.; Lambermont-Thijs, H. M. L.; Schubert, U. S.; Hoogenboom, R.; Kjøniksen, A.-L. *Macromolecules* **2012,** *45,* 4337–4345. doi:10.1021/ma300570j
177. Korchagina, E. V.; Qiu, X.-P.; Winnik, F. M. *Macromolecules* **2013,** *46,* 2341–2351. doi:10.1021/ma302666e
178. Hruby, M.; Filippov, S. K.; Panek, J.; Novakova, M.; Mackova, H.; Kucka, J.; Vetvicka, D.; Ulbrich, K. *Macromol. Biosci.* **2010,** *10,* 916–924. doi:10.1002/mabi.201000034
179. Luxenhofer, R.; Schulz, A.; Roques, C.; Li, S.; Bronich, T. K.; Batrakova, E. V.; Jordan, R.; Kabanov, A. V. *Biomaterials* **2010,** *31,* 4972–4979. doi:10.1016/j.biomaterials.2010.02.057
180. San Miguel, V.; Limer, A. J.; Haddleton, D. M.; Catalina, F.; Peinado, C. *Eur. Polym. J.* **2008,** *44,* 3853–3863. doi:10.1016/j.eurpolymj.2008.07.056
181. Gotzamanis, G.; Tsitsilianis, C. *Polymer* **2007,** *48,* 6226–6233. doi:10.1016/j.polymer.2007.08.042
182. Laga, R.; Janoušková, O.; Ulbrich, K.; Pola, R.; Blažková, J.; Filippov, S. K.; Etrych, T.; Pechar, M. *Biomacromolecules* **2015,** *16,* 2493–2505. doi:10.1021/acs.biomac.5b00764
183. Schroffenegger, M.; Reimhult, E. Thermoresponsive Core-Shell Nanoparticles and Their Potential Applications. In *Comprehensive Nanoscience and Nanotechnology,* 2nd ed.; Andrews, D. L.; Lipson, R. H.; Nann, T., Eds.; Academic Press: Oxford, UK, 2019; pp 145–170. doi:10.1016/b978-0-12-803581-8.10431-x
184. Mai, B. T.; Fernandes, S.; Balakrishnan, P. B.; Pellegrino, T. *Acc. Chem. Res.* **2018,** *51,* 999–1013. doi:10.1021/acs.accounts.7b00549
185. Liu, T.-Y.; Hu, S.-H.; Liu, D.-M.; Chen, S.-Y.; Chen, I.-W. *Nano Today* **2009,** *4,* 52–65. doi:10.1016/j.nantod.2008.10.011
186. Zhang, J. L.; Srivastava, R. S.; Misra, R. D. K. *Langmuir* **2007,** *23,* 6342–6351. doi:10.1021/la0636199
187. Liu, C.; Guo, J.; Yang, W.; Hu, J.; Wang, C.; Fu, S. *J. Mater. Chem.* **2009,** *19,* 4764–4770. doi:10.1039/b902985k
188. You, Y.-Z.; Kalebaila, K. K.; Brock, S. L.; Oupický, D. *Chem. Mater.* **2008,** *20,* 3354–3359. doi:10.1021/cm703363w
189. Su, Y.; Ojo, O. F.; Tsengam, I. K. M.; He, J.; McPherson, G. L.; John, V. T.; Valla, J. A. *Langmuir* **2018,** *34,* 14608–14616. doi:10.1021/acs.langmuir.8b02714
190. Gotoh, Y.; Suzuki, H.; Kumano, N.; Seki, T.; Katagiri, K.; Takeoka, Y. *New J. Chem.* **2012,** *36,* 2171–2175. doi:10.1039/c2nj40368d
191. Lien, Y.-H.; Wu, T.-M.; Wu, J.-H.; Liao, J.-W. *J. Nanopart. Res.* **2011,** *13,* 5065–5075. doi:10.1007/s11051-011-0487-8
192. Lai, J. J.; Hoffman, J. M.; Ebara, M.; Hoffman, A. S.; Estournès, C.; Wattiaux, A.; Stayton, P. S. *Langmuir* **2007,** *23,* 7385–7391. doi:10.1021/la062527g

193. Balasubramaniam, S.; Pothayee, N.; Lin, Y.; House, M.; Woodward, R. C.; St. Pierre, T. G.; Davis, R. M.; Riffle, J. S. *Chem. Mater.* **2011,** *23,* 3348–3356. doi:10.1021/cm2009048
194. Zhang, S.; Zhang, L.; He, B.; Wu, Z. *Nanotechnology* **2008,** *19,* 325608. doi:10.1088/0957-4484/19/32/325608
195. Gehan, H.; Fillaud, L.; Chehimi, M. M.; Aubard, J.; Hohenau, A.; Felidj, N.; Mangeney, C. *ACS Nano* **2010,** *4,* 6491–6500. doi:10.1021/nn101451q
196. Yusa, S.-i.; Fukuda, K.; Yamamoto, T.; Iwasaki, Y.; Watanabe, A.; Akiyoshi, K.; Morishima, Y. *Langmuir* **2007,** *23,* 12842–12848. doi:10.1021/la702741q
197. Chakraborty, S.; Bishnoi, S. W.; Pérez-Luna, V. H. *J. Phys. Chem. C* **2010,** *114,* 5947–5955. doi:10.1021/jp910417g
198. Jones, S. T.; Walsh-Korb, Z.; Barrow, S. J.; Henderson, S. L.; del Barrio, J.; Scherman, O. A. *ACS Nano* **2016,** *10,* 3158–3165. doi:10.1021/acsnano.5b04083
199. Ji, Y.; Lin, X.; Zhang, H.; Wu, Y.; Li, J.; He, Q. *Angew. Chem., Int. Ed.* **2019,** *58,* 4184–4188. doi:10.1002/anie.201812860
200. Salmaso, S.; Caliceti, P.; Amendola, V.; Meneghetti, M.; Magnusson, J. P.; Pasparakis, G.; Alexander, C. *J. Mater. Chem.* **2009,** *19,* 1608–1615. doi:10.1039/b816603j
201. Schweizerhof, S.; Demco, D. E.; Mourran, A.; Keul, H.; Fechete, R.; Möller, M. *Macromol. Chem. Phys.* **2017,** *218,* 1600495. doi:10.1002/macp.201600495
202. Hamner, K. L.; Maye, M. M. *Langmuir* **2013,** *29,* 15217–15223. doi:10.1021/la4037887
203. Lü, T.; Zhang, S.; Qi, D.; Zhang, D.; Zhao, H. *J. Alloys Compd.* **2016,** *688,* 513–520. doi:10.1016/j.jallcom.2016.07.262
204. Liu, G.; Wang, D.; Zhou, F.; Liu, W. *Small* **2015,** *11,* 2807–2816. doi:10.1002/smll.201403305
205. Li, P.; Liu, L.; Zhou, J.; Zhao, L.; Fan, H.; Huang, X. *RSC Adv.* **2017,** *7,* 50643–50647. doi:10.1039/c7ra10859a
206. Davaran, S.; Akbarzadeh, A.; Nejati-Koshki, K.; Alimohammadi, S.; Farajpour Ghamari, M.; Mahmoudi Soghrati, M.; Rezaei, A.; Ahmad Khandaghi, A. *J. Encapsulation Adsorpt. Sci.* **2013,** *03,* 108–115. doi:10.4236/jeas.2013.34013
207. de la Rosa, V. R.; Zhang, Z.; De Geest, B. G.; Hoogenboom, R. *Adv. Funct. Mater.* **2015,** *25,* 2511–2519. doi:10.1002/adfm.201404560
208. Schroffenegger, M.; Zirbs, R.; Kurzhals, S.; Reimhult, E. *Polymers (Basel, Switz.)* **2018,** *10,* 451. doi:10.3390/polym10040451
209. Kurzhals, S.; Gal, N.; Zirbs, R.; Reimhult, E. *Nanoscale* **2017,** *9,* 2793–2805. doi:10.1039/c6nr08654c
210. Wiedmann, S.; Kerscher, B.; Lienert, C.; Böcherer, D.; Mülhaupt, R. *Macromolecules* **2020,** *53,* 6703–6710. doi:10.1021/acs.macromol.0c00267
211. Hu, Z.; Cai, T.; Chi, C. *Soft Matter* **2010,** *6,* 2115–2123. doi:10.1039/b921150k
212. Housni, A.; Zhao, Y. *Langmuir* **2010,** *26,* 12933–12939. doi:10.1021/la1017856
213. Yavuz, M. S.; Citir, M.; Cavusoglu, H.; Demirel, G. *ChemNanoMat* **2017,** *3,* 496–502. doi:10.1002/cnma.201700081
214. Strozyk, M. S.; Chanana, M.; Pastoriza-Santos, I.; Pérez-Juste, J.; Liz-Marzán, L. M. *Adv. Funct. Mater.* **2012,** *22,* 1436–1444. doi:10.1002/adfm.201102471
215. Huang, H.; He, L. *J. Mater. Sci. Chem. Eng.* **2016,** *4,* 18–23. doi:10.4236/msce.2016.41004
216. Hannecart, A.; Stanicki, D.; Vander Elst, L.; Muller, R. N.; Lecommandoux, S.; Thévenot, J.; Bonduelle, C.; Trotier, A.; Massot, P.; Miraux, S.; Sandre, O.; Laurent, S. *Nanoscale* **2015,** *7,* 3754–3767. doi:10.1039/c4nr07064j
217. Louguet, S.; Rousseau, B.; Epherre, R.; Guidolin, N.; Goglio, G.; Mornet, S.; Duguet, E.; Lecommandoux, S.; Schatz, C. *Polym. Chem.* **2012,** *3,* 1408–1417. doi:10.1039/c2py20089a
218. Liu, X.-Y.; Cheng, F.; Liu, Y.; Liu, H.-J.; Chen, Y. *J. Mater. Chem.* **2010,** *20,* 360–368. doi:10.1039/b915313f
219. Liu, X.-Y.; Cheng, F.; Liu, Y.; Li, W.-G.; Chen, Y.; Pan, H.; Liu, H.-J. *J. Mater. Chem.* **2010,** *20,* 278–284. doi:10.1039/b916125b
220. Bhattacharjee, R. R.; Chakraborty, M.; Mandal, T. K. *J. Phys. Chem. B* **2006,** *110,* 6768–6775. doi:10.1021/jp056675b
221. Kitano, H.; Kondo, T.; Suzuki, H.; Ohno, K. *J. Colloid Interface Sci.* **2010,** *345,* 325–331. doi:10.1016/j.jcis.2009.10.004
222. Kitano, H.; Kago, H.; Matsuura, K. *J. Colloid Interface Sci.* **2009,** *331,* 343–350. doi:10.1016/j.jcis.2008.11.058
223. Nomura, K.; Makino, H.; Nakaji-Hirabayashi, T.; Kitano, H.; Ohno, K. *Colloid Polym. Sci.* **2015,** *293,* 851–859. doi:10.1007/s00396-014-3476-5
224. Jiang, X.; Wang, B.; Li, C. Y.; Zhao, B. *J. Polym. Sci., Part A: Polym. Chem.* **2009,** *47,* 2853–2870. doi:10.1002/pola.23375
225. Kuroki, H.; Tokarev, I.; Minko, S. *Annu. Rev. Mater. Res.* **2012,** *42,* 343–372. doi:10.1146/annurev-matsci-070511-155044
226. Zhuang, P.; Dirani, A.; Glinel, K.; Jonas, A. M. *Langmuir* **2016,** *32,* 3433–3444. doi:10.1021/acs.langmuir.6b00448
227. Nagase, K.; Yamato, M.; Kanazawa, H.; Okano, T. *Biomaterials* **2018,** *153,* 27–48. doi:10.1016/j.biomaterials.2017.10.026
228. Adam, S.; Koenig, M.; Rodenhausen, K. B.; Eichhorn, K.-J.; Oertel, U.; Schubert, M.; Stamm, M.; Uhlmann, P. *Appl. Surf. Sci.* **2017,** *421,* 843–851. doi:10.1016/j.apsusc.2017.02.078
229. Yim, H.; Kent, M. S.; Satija, S.; Mendez, S.; Balamurugan, S. S.; Balamurugan, S.; Lopez, G. P. *J. Polym. Sci., Part B: Polym. Phys.* **2004,** *42,* 3302–3310. doi:10.1002/polb.20169
230. Koenig, M.; Rodenhausen, K. B.; Rauch, S.; Bittrich, E.; Eichhorn, K.-J.; Schubert, M.; Stamm, M.; Uhlmann, P. *Langmuir* **2018,** *34,* 2448–2454. doi:10.1021/acs.langmuir.7b03919
231. Balamurugan, S.; Mendez, S.; Balamurugan, S. S.; O'Brien, M. J., II; López, G. P. *Langmuir* **2003,** *19,* 2545–2549. doi:10.1021/la026787j
232. Mizutani, A.; Kikuchi, A.; Yamato, M.; Kanazawa, H.; Okano, T. *Biomaterials* **2008,** *29,* 2073–2081. doi:10.1016/j.biomaterials.2008.01.004
233. Choi, S.; Choi, B.-C.; Xue, C.; Leckband, D. *Biomacromolecules* **2013,** *14,* 92–100. doi:10.1021/bm301390q
234. Divandari, M.; Pollard, J.; Dehghani, E.; Bruns, N.; Benetti, E. M. *Biomacromolecules* **2017,** *18,* 4261–4270. doi:10.1021/acs.biomac.7b01313
235. Gehan, H.; Mangeney, C.; Aubard, J.; Lévi, G.; Hohenau, A.; Krenn, J. R.; Lacaze, E.; Félidj, N. *J. Phys. Chem. Lett.* **2011,** *2,* 926–931. doi:10.1021/jz200272r
236. Takahashi, H.; Nakayama, M.; Yamato, M.; Okano, T. *Biomacromolecules* **2010,** *11,* 1991–1999. doi:10.1021/bm100342e
237. Wang, Y.; Kotsuchibashi, Y.; Liu, Y.; Narain, R. *ACS Appl. Mater. Interfaces* **2015,** *7,* 1652–1661. doi:10.1021/am508792k
238. Xiao, Q.; Li, Y.; Li, F.; Zhang, M.; Zhang, Z.; Lin, H. *Nanoscale* **2014,** *6,* 10179–10186. doi:10.1039/c4nr02497d
239. Gong, K.; Marshall, B. D.; Chapman, W. G. *J. Chem. Phys.* **2013,** *139,* 094904. doi:10.1063/1.4819957

240. Furchner, A.; Kroning, A.; Rauch, S.; Uhlmann, P.; Eichhorn, K.-J.; Hinrichs, K. *Anal. Chem. (Washington, DC, U. S.)* **2017,** *89,* 3240–3244. doi:10.1021/acs.analchem.7b00208
241. Varma, S.; Bureau, L.; Débarre, D. *Langmuir* **2016,** *32,* 3152–3163. doi:10.1021/acs.langmuir.6b00138
242. Cole, M. A.; Voelcker, N. H.; Thissen, H.; Horn, R. G.; Griesser, H. J. *Soft Matter* **2010,** *6,* 2657–2667. doi:10.1039/b926441h
243. Chin, H.-Y.; Wang, D.; Schwartz, D. K. *Macromolecules* **2015,** *48,* 4562–4571. doi:10.1021/acs.macromol.5b00729
244. Yu, Y.; Kieviet, B. D.; Liu, F.; Siretanu, I.; Kutnyánszky, E.; Vancso, G. J.; de Beer, S. *Soft Matter* **2015,** *11,* 8508–8516. doi:10.1039/c5sm01426c
245. Jadhav, S. A.; Nisticò, R.; Magnacca, G.; Scalarone, D. *RSC Adv.* **2018,** *8,* 1246–1254. doi:10.1039/c7ra11869d
246. Imato, K.; Nagata, K.; Watanabe, R.; Takeda, N. *J. Mater. Chem. B* **2020,** *8,* 2393–2399. doi:10.1039/c9tb02958c
247. Dai, W.; Zheng, C.; Zhao, B.; Chen, K.; Jia, P.; Yang, J.; Zhao, J. *J. Mater. Chem. B* **2019,** *7,* 2162–2168. doi:10.1039/c8tb03061h
248. Ista, L. K.; López, G. P. *J. Ind. Microbiol. Biotechnol.* **1998,** *20,* 121–125. doi:10.1038/sj.jim.2900490
249. Zhu, X.; Yan, C.; Winnik, F. M.; Leckband, D. *Langmuir* **2007,** *23,* 162–169. doi:10.1021/la061577i
250. Plunkett, K. N.; Zhu, X.; Moore, J. S.; Leckband, D. E. *Langmuir* **2006,** *22,* 4259–4266. doi:10.1021/la0531502
251. Elliott, L. C. C.; Jing, B.; Akgun, B.; Zhu, Y.; Bohn, P. W.; Fullerton-Shirey, S. K. *Langmuir* **2013,** *29,* 3259–3268. doi:10.1021/la305088k
252. Montagne, F.; Polesel-Maris, J.; Pugin, R.; Heinzelmann, H. *Langmuir* **2009,** *25,* 983–991. doi:10.1021/la803729p
253. Ishida, N.; Biggs, S. *Macromolecules* **2010,** *43,* 7269–7276. doi:10.1021/ma101113g
254. Bradley, C.; Jalili, N.; Nett, S. K.; Chu, L.; Förch, R.; Gutmann, J. S.; Berger, R. *Macromol. Chem. Phys.* **2009,** *210,* 1339–1345. doi:10.1002/macp.200900081
255. Shivapooja, P.; Ista, L. K.; Canavan, H. E.; Lopez, G. P. *Biointerphases* **2012,** *7,* 32. doi:10.1007/s13758-012-0032-z
256. Kroning, A.; Furchner, A.; Aulich, D.; Bittrich, E.; Rauch, S.; Uhlmann, P.; Eichhorn, K.-J.; Seeber, M.; Luzinov, I.; Kilbey, S. M., II; Lokitz, B. S.; Minko, S.; Hinrichs, K. *ACS Appl. Mater. Interfaces* **2015,** *7,* 12430–12439. doi:10.1021/am5075997
257. Kurkuri, M. D.; Nussio, M. R.; Deslandes, A.; Voelcker, N. H. *Langmuir* **2008,** *24,* 4238–4244. doi:10.1021/la703668s
258. Psarra, E.; König, U.; Ueda, Y.; Bellmann, C.; Janke, A.; Bittrich, E.; Eichhorn, K.-J.; Uhlmann, P. *ACS Appl. Mater. Interfaces* **2015,** *7,* 12516–12529. doi:10.1021/am508161q
259. Sudre, G.; Siband, E.; Gallas, B.; Cousin, F.; Hourdet, D.; Tran, Y. *Polymers (Basel, Switz.)* **2020,** *12,* 153. doi:10.3390/polym12010153
260. Li, J.-J.; Zhou, Y.-N.; Luo, Z.-H. *Polymer* **2014,** *55,* 6552–6560. doi:10.1016/j.polymer.2014.10.025
261. Idota, N.; Ebara, M.; Kotsuchibashi, Y.; Narain, R.; Aoyagi, T. *Sci. Technol. Adv. Mater.* **2012,** *13,* 064206. doi:10.1088/1468-6996/13/6/064206
262. Liu, X.; Ye, Q.; Song, X.; Zhu, Y.; Cao, X.; Liang, Y.; Zhou, F. *Soft Matter* **2011,** *7,* 515–523. doi:10.1039/c0sm00682c
263. Rollason, G.; Davies, J. E.; Sefton, M. V. *Biomaterials* **1993,** *14,* 153–155. doi:10.1016/0142-9612(93)90230-y
264. Saitoh, T.; Sekino, A.; Hiraide, M. *Anal. Chim. Acta* **2005,** *536,* 179–182. doi:10.1016/j.aca.2004.12.050
265. Ernst, O.; Lieske, A.; Jäger, M.; Lankenau, A.; Duschl, C. *Lab Chip* **2007,** *7,* 1322–1329. doi:10.1039/b708619a
266. Ryma, M.; Blöhbaum, J.; Singh, R.; Sancho, A.; Matuszak, J.; Cicha, I.; Groll, J. *ACS Biomater. Sci. Eng.* **2019,** *5,* 1509–1517. doi:10.1021/acsbiomaterials.8b01588
267. Johnson, E. C.; Willott, J. D.; de Vos, W. M.; Wanless, E. J.; Webber, G. B. *Langmuir* **2020,** *36,* 5765–5777. doi:10.1021/acs.langmuir.0c00424
268. Gao, X.; Kučerka, N.; Nieh, M.-P.; Katsaras, J.; Zhu, S.; Brash, J. L.; Sheardown, H. *Langmuir* **2009,** *25,* 10271–10278. doi:10.1021/la901086e
269. Wang, B.; Ye, Z.; Xu, Q.; Liu, H.; Lin, Q.; Chen, H.; Nan, K. *Biomater. Sci.* **2016,** *4,* 1731–1741. doi:10.1039/c6bm00587j
270. Weiss, M. S.; Palm, G. J.; Hilgenfeld, R. *Acta Crystallogr., Sect. D: Biol. Crystallogr.* **2000,** *56,* 952–958. doi:10.1107/s0907444900006685
271. Zhang, Z.; Li, H.; Kasmi, S.; Van Herck, S.; Deswarte, K.; Lambrecht, B. N.; Hoogenboom, R.; Nuhn, L.; De Geest, B. G. *Angew. Chem., Int. Ed.* **2019,** *58,* 7866–7872. doi:10.1002/anie.201900224
272. Jiang, D.; Chen, C.; Xue, Y.; Cao, H.; Wang, C.; Yang, G.; Gao, Y.; Wang, P.; Zhang, W. *ACS Appl. Mater. Interfaces* **2019,** *11,* 37121–37129. doi:10.1021/acsami.9b12889
273. Audureau, N.; Coumes, F.; Guigner, J.-M.; Nguyen, T. P. T.; Ménager, C.; Stoffelbach, F.; Rieger, J. *Polym. Chem.* **2020,** *11,* 5998–6008. doi:10.1039/d0py00895h
274. Asadujjaman, A.; Kent, B.; Bertin, A. *Soft Matter* **2017,** *13,* 658–669. doi:10.1039/c6sm02262f
275. Otsuka, C.; Wakahara, Y.; Okabe, K.; Sakata, J.; Okuyama, M.; Hayashi, A.; Tokuyama, H.; Uchiyama, S. *Macromolecules* **2019,** *52,* 7646–7660. doi:10.1021/acs.macromol.9b00880
276. Huang, B.; Tian, J.; Jiang, D.; Gao, Y.; Zhang, W. *Biomacromolecules* **2019,** *20,* 3873–3883. doi:10.1021/acs.biomac.9b00963
277. Kertsomboon, T.; Agarwal, S.; Chirachanchai, S. *Macromol. Rapid Commun.* **2020,** *41,* 2000243. doi:10.1002/marc.202000243
278. Zhao, C.; Lu, J.; Zhu, X. X. *ACS Appl. Polym. Mater.* **2020,** *2,* 256–262. doi:10.1021/acsapm.9b00779
279. Shimada, N.; Sasaki, T.; Kawano, T.; Maruyama, A. *Biomacromolecules* **2018,** *19,* 4133–4138. doi:10.1021/acs.biomac.8b01152
280. Hildebrand, V.; Laschewsky, A.; Päch, M.; Müller-Buschbaum, P.; Papadakis, C. M. *Polym. Chem.* **2017,** *8,* 310–322. doi:10.1039/c6py01220e
281. Li, M.; Zhuang, B.; Yu, J. *Chem. – Asian J.* **2020,** *15,* 2060–2075. doi:10.1002/asia.202000547
282. Paschke, S.; Lienkamp, K. *ACS Appl. Polym. Mater.* **2020,** *2,* 129–151. doi:10.1021/acsapm.9b00897
283. Lewoczko, E. M.; Wang, N.; Lundberg, C. E.; Kelly, M. T.; Kent, E. W.; Wu, T.; Chen, M.-L.; Wang, J.-H.; Zhao, B. *ACS Appl. Polym. Mater.* **2021,** *3,* 867–878. doi:10.1021/acsapm.0c01191
284. Wang, N.; Seymour, B. T.; Lewoczko, E. M.; Kent, E. W.; Chen, M.-L.; Wang, J.-H.; Zhao, B. *Polym. Chem.* **2018,** *9,* 5257–5261. doi:10.1039/c8py01211c
285. Blackman, L. D.; Gunatillake, P. A.; Cass, P.; Locock, K. E. S. *Chem. Soc. Rev.* **2019,** *48,* 757–770. doi:10.1039/c8cs00508g
286. Flory, P. J.; Osterheld, J. E. *J. Phys. Chem.* **1954,** *58,* 653–661. doi:10.1021/j150518a014
287. Noh, M.; Kang, S.; Mok, Y.; Choi, S. J.; Park, J.; Kingma, J.; Seo, J.-H.; Lee, Y. *Chem. Commun.* **2016,** *52,* 509–512. doi:10.1039/c5cc08005c

288. Kohno, Y.; Saita, S.; Men, Y.; Yuan, J.; Ohno, H. *Polym. Chem.* **2015,** *6,* 2163–2178. doi:10.1039/c4py01665c
289. Yoshimitsu, H.; Kanazawa, A.; Kanaoka, S.; Aoshima, S. *Macromolecules* **2012,** *45,* 9427–9434. doi:10.1021/ma301746u
290. Wu, Y.; Wang, X.; Ling, Y.; Tang, H. *RSC Adv.* **2015,** *5,* 40772–40778. doi:10.1039/c5ra04541j
291. Ge, C.; Liu, S.; Liang, C.; Ling, Y.; Tang, H. *Polym. Chem.* **2016,** *7,* 5978–5987. doi:10.1039/c6py01287f
292. Yu, J.; Jackson, N. E.; Xu, X.; Morgenstern, Y.; Kaufman, Y.; Ruths, M.; de Pablo, J. J.; Tirrell, M. *Science* **2018,** *360,* 1434–1438. doi:10.1126/science.aar5877
293. Plamper, F. A.; Ballauff, M.; Müller, A. H. E. *J. Am. Chem. Soc.* **2007,** *129,* 14538–14539. doi:10.1021/ja074720i
294. Zhang, Q.; Tosi, F.; Üğdüler, S.; Maji, S.; Hoogenboom, R. *Macromol. Rapid Commun.* **2015,** *36,* 633–639. doi:10.1002/marc.201400550
295. Zheng, J. Y.; Tan, M. J.; Thoniyot, P.; Loh, X. J. *RSC Adv.* **2015,** *5,* 62314–62318. doi:10.1039/c5ra12816a
296. Gao, J.; Zhai, G.; Song, Y.; Jiang, B. *J. Appl. Polym. Sci.* **2008,** *107,* 3548–3556. doi:10.1002/app.26683
297. Xu, Y.; Bolisetty, S.; Drechsler, M.; Fang, B.; Yuan, J.; Ballauff, M.; Müller, A. H. E. *Polymer* **2008,** *49,* 3957–3964. doi:10.1016/j.polymer.2008.06.051
298. Agarwal, S.; Zhang, Y.; Maji, S.; Greiner, A. *Mater. Today* **2012,** *15,* 388–393. doi:10.1016/s1369-7021(12)70165-7
299. Wang, X.; Berger, R.; Ramos, J. I.; Wang, T.; Koynov, K.; Liu, G.; Butt, H.-J.; Wu, S. *RSC Adv.* **2014,** *4,* 45059–45064. doi:10.1039/c4ra07623k
300. Flemming, P.; Müller, M.; Fery, A.; Münch, A. S.; Uhlmann, P. *Macromolecules* **2020,** *53,* 1957–1966. doi:10.1021/acs.macromol.9b02666
301. Flemming, P.; Janke, A.; Simon, F.; Fery, A.; Münch, A. S.; Uhlmann, P. *Langmuir* **2020,** *36,* 15283–15295. doi:10.1021/acs.langmuir.0c02711
302. Begam, N.; Matsarskaia, O.; Sztucki, M.; Zhang, F.; Schreiber, F. *Soft Matter* **2020,** *16,* 2128–2134. doi:10.1039/c9sm02329a
303. Matsarskaia, O.; Braun, M. K.; Roosen-Runge, F.; Wolf, M.; Zhang, F.; Roth, R.; Schreiber, F. *J. Phys. Chem. B* **2016,** *120,* 7731–7736. doi:10.1021/acs.jpcb.6b04506
304. Prather, L. J.; Weerasekare, G. M.; Sima, M.; Quinn, C.; Stewart, R. J. *Polymers (Basel, Switz.)* **2019,** *11,* 649. doi:10.3390/polym11040649
305. Kim, H.; Jeon, B.-j.; Kim, S.; Jho, Y.; Hwang, D. S. *Polymers (Basel, Switz.)* **2019,** *11,* 691. doi:10.3390/polym11040691
306. Quiroz, F. G.; Chilkoti, A. *Nat. Mater.* **2015,** *14,* 1164–1171. doi:10.1038/nmat4418
307. Liu, D.; Sun, J. *Polymers (Basel, Switz.)* **2020,** *12,* 2973. doi:10.3390/polym12122973
308. Xing, C.; Shi, Z.; Tian, J.; Sun, J.; Li, Z. *Biomacromolecules* **2018,** *19,* 2109–2116. doi:10.1021/acs.biomac.8b00240
309. Xu, W.; Ledin, P. A.; Shevchenko, V. V.; Tsukruk, V. V. *ACS Appl. Mater. Interfaces* **2015,** *7,* 12570–12596. doi:10.1021/acsami.5b01833
310. Li, Z.; Li, H.; Sun, Z.; Hao, B.; Lee, T.-C.; Feng, A.; Zhang, L.; Thang, S. H. *Polym. Chem.* **2020,** *11,* 3162–3168. doi:10.1039/d0py00318b
311. Shih, Y.-J.; Chang, Y. *Langmuir* **2010,** *26,* 17286–17294. doi:10.1021/la103186y
312. Hu, L.; Wan, Y.; Zhang, Q.; Serpe, M. J. *Adv. Funct. Mater.* **2020,** *30,* 1903471. doi:10.1002/adfm.201903471
313. Qi, M.; Li, K.; Zheng, Y.; Rasheed, T.; Zhou, Y. *Langmuir* **2018,** *34,* 3058–3067. doi:10.1021/acs.langmuir.7b04255
314. Zhou, Q.; Palanisamy, A.; Albright, V.; Sukhishvili, S. A. *Polym. Chem.* **2018,** *9,* 4979–4983. doi:10.1039/c8py00939b
315. Fujihara, A.; Itsuki, K.; Shimada, N.; Maruyama, A.; Sagawa, N.; Shikata, T.; Yusa, S.-I. *J. Polym. Sci., Part A: Polym. Chem.* **2016,** *54,* 2845–2854. doi:10.1002/pola.28183
316. Palanisamy, A.; Albright, V.; Sukhishvili, S. A. *Chem. Mater.* **2017,** *29,* 9084–9094. doi:10.1021/acs.chemmater.7b02748
317. Albright, V.; Palanisamy, A.; Zhou, Q.; Selin, V.; Sukhishvili, S. A. *Langmuir* **2019,** *35,* 10677–10688. doi:10.1021/acs.langmuir.8b02535
318. Willcock, H.; Lu, A.; Hansell, C. F.; Chapman, E.; Collins, I. R.; O'Reilly, R. K. *Polym. Chem.* **2014,** *5,* 1023–1030. doi:10.1039/c3py00998j
319. Ning, J.; Li, G.; Haraguchi, K. *Macromolecules* **2013,** *46,* 5317–5328. doi:10.1021/ma4009059
320. Yu, J.; Liu, Y.; Song, S.; Gao, G.; Liu, F. *Polym. J.* **2017,** *49,* 767–774. doi:10.1038/pj.2017.51
321. Zhang, M.; Shen, W.; Xiong, Q.; Wang, H.; Zhou, Z.; Chen, W.; Zhang, Q. *RSC Adv.* **2015,** *5,* 28133–28140. doi:10.1039/c5ra02115d
322. Vishnevetskaya, N. S.; Hildebrand, V.; Nizardo, N. M.; Ko, C.-H.; Di, Z.; Radulescu, A.; Barnsley, L. C.; Müller-Buschbaum, P.; Laschewsky, A.; Papadakis, C. M. *Langmuir* **2019,** *35,* 6441–6452. doi:10.1021/acs.langmuir.9b00241
323. Kotsuchibashi, Y. *Polym. J.* **2020,** *52,* 681–689. doi:10.1038/s41428-020-0330-0
324. Kotsuchibashi, Y.; Ebara, M.; Aoyagi, T.; Narain, R. *Polymers (Basel, Switz.)* **2016,** *8,* 380. doi:10.3390/polym8110380
325. Papadakis, C. M.; Müller-Buschbaum, P.; Laschewsky, A. *Langmuir* **2019,** *35,* 9660–9676. doi:10.1021/acs.langmuir.9b01444
326. Sugihara, S.; Kanaoka, S.; Aoshima, S. *J. Polym. Sci., Part A: Polym. Chem.* **2004,** *42,* 2601–2611. doi:10.1002/pola.20121
327. Arotçaréna, M.; Heise, B.; Ishaya, S.; Laschewsky, A. *J. Am. Chem. Soc.* **2002,** *124,* 3787–3793. doi:10.1021/ja012167d
328. Vishnevetskaya, N. S.; Hildebrand, V.; Niebuur, B.-J.; Grillo, I.; Filippov, S. K.; Laschewsky, A.; Müller-Buschbaum, P.; Papadakis, C. M. *Macromolecules* **2016,** *49,* 6655–6668. doi:10.1021/acs.macromol.6b01186
329. Cummings, C.; Murata, H.; Koepsel, R.; Russell, A. J. *Biomacromolecules* **2014,** *15,* 763–771. doi:10.1021/bm401575k
330. Deng, Y.; Käfer, F.; Chen, T.; Jin, Q.; Ji, J.; Agarwal, S. *Small* **2018,** *14,* 1802420. doi:10.1002/smll.201802420
331. Palanisamy, A.; Sukhishvili, S. A. *Macromolecules* **2018,** *51,* 3467–3476. doi:10.1021/acs.macromol.8b00519
332. Aliakseyeu, A.; Albright, V.; Yarbrough, D.; Hernandez, S.; Zhou, Q.; Ankner, J. F.; Sukhishvili, S. A. *Soft Matter* **2021,** *17,* 2181–2190. doi:10.1039/d0sm01997f
333. Zhang, H.; Tong, X.; Zhao, Y. *Langmuir* **2014,** *30,* 11433–11441. doi:10.1021/la5026334
334. Käfer, F.; Liu, F.; Stahlschmidt, U.; Jérôme, V.; Freitag, R.; Karg, M.; Agarwal, S. *Langmuir* **2015,** *31,* 8940–8946. doi:10.1021/acs.langmuir.5b02006
335. Zhou, C.; Chen, Y.; Huang, M.; Ling, Y.; Yang, L.; Zhao, G.; Chen, J. *New J. Chem.* **2021,** *45,* 5925–5932. doi:10.1039/d0nj06153k
336. Li, W.; Huang, L.; Ying, X.; Jian, Y.; Hong, Y.; Hu, F.; Du, Y. *Angew. Chem., Int. Ed.* **2015,** *54,* 3126–3131. doi:10.1002/anie.201411524
337. Hui, L.; Qin, S.; Yang, L. *ACS Biomater. Sci. Eng.* **2016,** *2,* 2127–2132. doi:10.1021/acsbiomaterials.6b00459

338. Zhan, X.; Nie, X.; Gao, F.; Zhang, C.; You, Y.-Z.; Yu, Y. *Biomater. Sci.* **2020,** *8,* 5931–5940. doi:10.1039/d0bm01324b
339. Yang, Z.; Cheng, R.; Zhao, C.; Sun, N.; Luo, H.; Chen, Y.; Liu, Z.; Li, X.; Liu, J.; Tian, Z. *Theranostics* **2018,** *8,* 4097–4115. doi:10.7150/thno.26195
340. Tian, J.; Huang, B.; Li, H.; Cao, H.; Zhang, W. *Biomacromolecules* **2019,** *20,* 2338–2349. doi:10.1021/acs.biomac.9b00321
341. Yang, J.; Zhai, S.; Qin, H.; Yan, H.; Xing, D.; Hu, X. *Biomaterials* **2018,** *176,* 1–12. doi:10.1016/j.biomaterials.2018.05.033
342. Murdoch, T. J.; Humphreys, B. A.; Johnson, E. C.; Webber, G. B.; Wanless, E. J. *J. Colloid Interface Sci.* **2018,** *526,* 429–450. doi:10.1016/j.jcis.2018.04.086
343. Schulz, D. N.; Peiffer, D. G.; Agarwal, P. K.; Larabee, J.; Kaladas, J. J.; Soni, L.; Handwerker, B.; Garner, R. T. *Polymer* **1986,** *27,* 1734–1742. doi:10.1016/0032-3861(86)90269-7
344. Kramarenko, E. Y.; Erukhimovich, I. Y.; Khokhlov, A. R. *Macromol. Theory Simul.* **2002,** *11,* 462–471. doi:10.1002/1521-3919(20020601)11:5<462::aid-mats462>3.0.co;2-k
345. Cheng, N.; Brown, A. A.; Azzaroni, O.; Huck, W. T. S. *Macromolecules* **2008,** *41,* 6317–6321. doi:10.1021/ma800625y
346. Xue, X.; Thiagarajan, L.; Braim, S.; Saunders, B. R.; Shakesheff, K. M.; Alexander, C. *J. Mater. Chem. B* **2017,** *5,* 4926–4933. doi:10.1039/c7tb00052a
347. Sun, T.; Wang, G.; Feng, L.; Liu, B.; Ma, Y.; Jiang, L.; Zhu, D. *Angew. Chem., Int. Ed.* **2004,** *43,* 357–360. doi:10.1002/anie.200352565
348. Yuan, W.; Wang, J.; Shen, T.; Ren, J. *Mater. Lett.* **2013,** *107,* 243–246. doi:10.1016/j.matlet.2013.06.028
349. Chen, L.; Yang, T.; Niu, Y.; Mu, X.; Gong, Y.; Feng, Y.; de Rooij, N. F.; Wang, Y.; Li, H.; Zhou, G. *Chem. Commun.* **2020,** *56,* 2837–2840. doi:10.1039/c9cc09479b
350. Shen, J.; Han, K.; Martin, E. J.; Wu, Y. Y.; Kung, M. C.; Hayner, C. M.; Shull, K. R.; Kung, H. H. *J. Mater. Chem. A* **2014,** *2,* 18204–18207. doi:10.1039/c4ta04852k
351. Chu, L.-Y.; Li, Y.; Zhu, J.-H.; Chen, W.-M. *Angew. Chem.* **2005,** *117,* 2162–2165. doi:10.1002/ange.200462687
352. Xue, X.; Thiagarajan, L.; Dixon, J. E.; Saunders, B. R.; Shakesheff, K. M.; Alexander, C. *Materials* **2018,** *11,* 95. doi:10.3390/ma11010095
353. Shimada, N.; Saito, M.; Shukuri, S.; Kuroyanagi, S.; Kuboki, T.; Kidoaki, S.; Nagai, T.; Maruyama, A. *ACS Appl. Mater. Interfaces* **2016,** *8,* 31524–31529. doi:10.1021/acsami.6b07614
354. Murakami, D.; Norizoe, Y.; Higaki, Y.; Takahara, A.; Jinnai, H. *Macromolecules* **2016,** *49,* 4862–4866. doi:10.1021/acs.macromol.6b00151
355. Norizoe, Y.; Jinnai, H.; Takahara, A. *EPL* **2013,** *101,* 16006. doi:10.1209/0295-5075/101/16006
356. Polotsky, A. A.; Plamper, F. A.; Borisov, O. V. *Macromolecules* **2013,** *46,* 8702–8709. doi:10.1021/ma401402e
357. Jackson, N. E.; Brettmann, B. K.; Vishwanath, V.; Tirrell, M.; de Pablo, J. J. *ACS Macro Lett.* **2017,** *6,* 155–160. doi:10.1021/acsmacrolett.6b00837
358. Lee, J.; Moesari, E.; Dandamudi, C. B.; Beniah, G.; Chang, B.; Iqbal, M.; Fei, Y.; Zhou, N.; Ellison, C. J.; Johnston, K. P. *Macromolecules* **2017,** *50,* 7699–7711. doi:10.1021/acs.macromol.7b01243
359. Sun, J.-T.; Yu, Z.-Q.; Hong, C.-Y.; Pan, C.-Y. *Macromol. Rapid Commun.* **2012,** *33,* 811–818. doi:10.1002/marc.201100876
360. Beltrán-Osuna, Á. A.; Gómez-Ribelles, J. L.; Perilla, J. E. *J. Appl. Phys.* **2020,** *127,* 135106. doi:10.1063/1.5140707
361. Beltrán-Osuna, Á. A.; Ródenas-Rochina, J.; Gómez Ribelles, J. L.; Perilla, J. E. *Polym. Adv. Technol.* **2019,** *30,* 688–697. doi:10.1002/pat.4505
362. Dong, Z.; Mao, J.; Yang, M.; Wang, D.; Bo, S.; Ji, X. *Langmuir* **2011,** *27,* 15282–15291. doi:10.1021/la2038558
363. Dong, Z.; Mao, J.; Wang, D.; Yang, M.; Wang, W.; Bo, S.; Ji, X. *Macromol. Chem. Phys.* **2014,** *215,* 111–120. doi:10.1002/macp.201300552
364. Durand-Gasselin, C.; Koerin, R.; Rieger, J.; Lequeux, N.; Sanson, N. *J. Colloid Interface Sci.* **2014,** *434,* 188–194. doi:10.1016/j.jcis.2014.07.048
365. Han, F.; Soeriyadi, A. H.; Gooding, J. J. *Macromol. Rapid Commun.* **2018,** *39,* 1800451. doi:10.1002/marc.201800451
366. Polzer, F.; Heigl, J.; Schneider, C.; Ballauff, M.; Borisov, O. V. *Macromolecules* **2011,** *44,* 1654–1660. doi:10.1021/ma102927c
367. Paramelle, D.; Gorelik, S.; Liu, Y.; Kumar, J. *Chem. Commun.* **2016,** *52,* 9897–9900. doi:10.1039/c6cc04187f
368. Hei, M.; Wang, J.; Wang, K.; Zhu, W.; Ma, P. X. *J. Mater. Chem. B* **2017,** *5,* 9497–9501. doi:10.1039/c7tb02429k
369. Hu, W.; Bai, X.; Wang, Y.; Lei, Z.; Luo, H.; Tong, Z. *J. Mater. Chem. B* **2019,** *7,* 5789–5796. doi:10.1039/c9tb01071h
370. Amoli-Diva, M.; Sadighi-Bonabi, R.; Pourghazi, K.; Hadilou, N. *J. Pharm. Sci.* **2018,** *107,* 2618–2627. doi:10.1016/j.xphs.2018.05.025
371. Zhang, H.; Guo, S.; Fu, S.; Zhao, Y. *Polymers (Basel, Switz.)* **2017,** *9,* 238. doi:10.3390/polym9060238
372. Amoli-Diva, M.; Sadighi-Bonabi, R.; Pourghazi, K. *Mater. Sci. Eng., C* **2017,** *76,* 242–248. doi:10.1016/j.msec.2017.03.038
373. Tao, H.; Galati, E.; Kumacheva, E. *Macromolecules* **2018,** *51,* 6021–6027. doi:10.1021/acs.macromol.8b01058
374. Kaiser, A.; Schmidt, A. M. *J. Phys. Chem. B* **2008,** *112,* 1894–1898. doi:10.1021/jp076218q
375. Liu, F.; Agarwal, S. *Macromol. Chem. Phys.* **2015,** *216,* 460–465. doi:10.1002/macp.201400497
376. Rossner, C.; Glatter, O.; Vana, P. *Macromolecules* **2017,** *50,* 7344–7350. doi:10.1021/acs.macromol.7b01267
377. Han, F.; Vivekchand, S. R. C.; Soeriyadi, A. H.; Zheng, Y.; Gooding, J. J. *Nanoscale* **2018,** *10,* 4284–4290. doi:10.1039/c7nr09218k

License and Terms

This is an Open Access article under the terms of the Creative Commons Attribution License (https://creativecommons.org/licenses/by/4.0). Please note that the reuse, redistribution and reproduction in particular requires that the author(s) and source are credited and that individual graphics may be subject to special legal provisions.

The license is subject to the *Beilstein Journal of Organic Chemistry* terms and conditions: (https://www.beilstein-journals.org/bjoc/terms)

The definitive version of this article is the electronic one which can be found at: https://doi.org/10.3762/bjoc.17.138

BEILSTEIN JOURNAL OF ORGANIC CHEMISTRY

Post-functionalization of drug-loaded nanoparticles prepared by polymerization-induced self-assembly (PISA) with mitochondria targeting ligands

Janina-Miriam Noy, Fan Chen and Martina Stenzel*

Full Research Paper

Open Access

Address:
School of Chemistry, University of New South Wales, Sydney NSW 2052, Australia

Email:
Martina Stenzel* - M.Stenzel@unsw.edu.au

* Corresponding author

Keywords:
micelle; mitochondria; phosphorylcholine; PISA; polymerization-induced self-assembly

Beilstein J. Org. Chem. **2021,** *17,* 2302–2314.
https://doi.org/10.3762/bjoc.17.148

Received: 28 June 2021
Accepted: 19 August 2021
Published: 03 September 2021

This article is part of the thematic issue "Polymer chemistry: fundamentals and applications".

Guest Editor: B. V. K. J. Schmidt

© 2021 Noy et al.; licensee Beilstein-Institut.
License and terms: see end of document.

Abstract

Herein, the postfunctionalization of different non-fouling PISA particles, prepared from either poly(oligo ethylene glycol methyl ether methacrylate) (pPEGMA) and the anticancer drug PENAO (4-(*N*-(*S*-penicillaminylacetyl)amino)phenylarsenonous acid) or zwitterionic 2-methacryloyloxyethyl phosphorylcholine (MPC) and PENAO were reported. Both PISA particles were reacted with triphenylphosphonium (TPP) as mitochondria targeting units in order to evaluate the changes in cellular uptake or the toxicity of the conjugated arsenic drug. Attachment of TPP onto the PISA particles however was found not to enhance the mitochondrial accumulation, but it did influence overall the biological activity of pMPC-based particles in 2D and 3D cultured sarcoma SW982 cells. When TPP was conjugated to the pMPC PISA particles more cellular uptake as well as better spheroid penetration were observed, while TPP on PEG-based PISA had only little effect. It was hypothesized that TPP on the micelle surface may not be accessible enough to allow mitochondria targeting, but more structural investigations are required to elucidate this.

Introduction

Targeting mitochondria is a promising strategy for the development of new anticancer drugs [1]. Among them, organoarsenical drugs have shown great promise as these drugs inhibit the function of mitochondria while showing overall reduced systemic toxicity. PENAO (4-(*N*-(*S*-penicillaminylacetyl)amino)phenylarsenonous acid) [2,3], a trivalent arsenical drug, was developed by Hogg and co-workers and is currently in clinical trials [4]. PENAO triggers cell apoptosis by targeting the ANT protein, which is located in the mitochondria. More specifically, PENAO binds to the thiols located on the ANT peptide loops Cys^{57} and Cys^{257}, which results in the formation of stable cyclic dithioarsinite complexes [5]. Arsenic drugs do not only

bind to mitochondrial protein, but also chelates other cysteine-containing species. Several hundred good binding sites for trivalent arsenicals in each organ have been proposed [6,7], and more than 50 arsenic-binding proteins could be identified and analysed by Zhang et al. [8] and Yan et al. [9] using *p*-phenylarsenoxide-based agents. This can also lead to deactivation of the drug as these organoarsenic drugs react readily with blood proteins, in particular transferrin [10]. In order to limit premature inactivation of the arsenic drugs, a range of nanoparticles have been developed to enhance stability, thus increase activity [11,12]. These nanoparticles have been decorated with targeting ligands to enhance the accumulation of the drug in cancer tissue. The activity of arsenic drugs could, however, also be enhanced by targeting mitochondria inside the cells, the target of action of arsenic drugs.

To the current date, one of the most effective methods to specifically target the mitochondria is the covalent attachment of mitochondrial penetrating molecules to carrier systems [13,14]. Several mitochondriotropic moieties such as dequalinium (DQA), triphenylphosphonium (TPP), and mitochondrial penetrating peptides and proteins have been linked to nanotechnology. DQA and TPP are both cationic and lipophilic molecules and therefore able to easily pass the mitochondrial membrane [15-19]. TPP is the most-studied mitochondrial targeting agent and has shown to accumulate 1000 times more in the mitochondrial matrix than in the cytosol [20]. TPP derivatives were attached to PEGylated poly(ε-caprolactone) (PCL), and corresponding micellar formulation enabled the delivery of coenzyme Q10 (CoQ10) to the mitochondria [21]. In addition, PEGylated TPP-conjugated poly(lactic-*co*-glycolic acid) nanoparticles have shown to increase mitochondrial accumulation when more positive zeta potentials were obtained [22], and when the TPP-nanoparticles were loaded with drugs, significantly better antitumour activities were acquired [23-27], highlighting TPP's desirable influence on the therapeutic efficiency.

Micelles are ideal carriers when designing a nanoparticle with an abundance of functional groups on the surface, which could be conjugated with targeting ligands such as TPP. Moreover, they have already been used to successfully deliver arsenic drugs [28-32], highlighting their suitability as a potential vehicle to deliver these drugs. Disadvantage is however the multistep procedure to generate micelles ranging from the synthesis of block copolymers to the self-assembly into micelles, often in low dilution, making the process inefficient. Micelles obtained by the PISA process can in contrast generate large amounts of nanoparticles in a reproducible manner. PISA nanoparticles have been frequently investigated as drug carriers. The challenge is often how to entrap the drug during the self-assembly process. Addition of drugs during the PISA process is possible [33,34], but it needs to be taken into account that the drug can interfere with the block copolymer aggregation. Alternatively, the use of reactive polymers for the polymerization creates a functional anchor to enable post-functionalization of the PISA nanoparticles with drugs such as doxorubicin [35,36]. In a different strategy, drug conjugated monomers can be directly used in the polymerization, eliminating the post-modification step [28,37-39].

In order to use micelles, prepared by PISA or traditional techniques, for targeting specific receptors, it is necessary that these materials are low-fouling, thus repel non-specific protein absorption. Su et al. [40] investigated the effects of a protein corona on active and passive targeting using 20 different types of PEGylated gold nanoparticles, which were decorated with cyclic RGD (arginylglycylaspartic acid) peptides. As a result, the active targeting efficiency on a protein covered nanoparticle was significantly reduced compared to a non-protein bounded nanoparticle. Stealth like nanoparticle surfaces, such as surfaces covered with polyethylene glycol or phosphorylcholine, are therefore attractive for biological applications, as they have the ability to repel proteins and therefore reduce the possibility of macrophage clearance [41]. Therefore, in this study we will use poly(2-methacryloyloxyethyl phosphorylcholine) (pMPC) and poly(oligo ethylene glycol methyl ether methacrylate) (pPEGMA) as protein-repellent polymers in order to ensure that the formation of the protein corona is reduced.

In earlier studies we have shown the polymerization-induced self-assembly is an excellent tool to generate nanoparticles with conjugated PENAO in situ [28]. We described how the zwitterionic 2-methacryloyloxyethyl phosphorylcholine (MPC), copolymerized with 4-(*N*-(*S*-penicillaminylacetyl)amino)phenylarsonous acid methacrylamide, which is PENAO reacted with a polymerizable group, can be used as a stabilizing block for the subsequent PISA reaction with methyl methacrylate (MMA) [42]. We also showed how small changes to the stabilizing block can cause changes in the self-assembly process [43]. Moreover, a second nanoparticle based on poly(oligo ethylene glycol methyl ether methacrylate) (pPEGMA) was generated as both polymers, pPEGMA and pMPC display protein-repellent properties [44,45]. In this paper, we aimed at comparing the effect of nanoparticles with and without triphenylphosphonium (TPP) as mitochondria targeting units. In order to keep the aggregation number, and therefore the size of the nanoparticle, constant, we opted to post-functionalize the nanoparticles with TPP to facilitate the study of the effect of TPP only. Aim of this project is to explore if the attachment of mitochondria targeting ligands can enhance the activity of PENAO using the nanoparticles that were recently described in our group [28,42].

Results and Discussion

Synthesis of Micelles by PISA

Initially two nanoparticles were prepared that had comparable particle sizes, which enabled not only comparison of nanoparticles with and without TPP, but also the effect of the shell material, pPEGMA and pMPC. The synthesis of p(MPC-*co*-PENAO)-*b*-p(MMA) and p(PEGMA-*co*-PENAO)-*b*-p(MMA) nanoparticles has been described in our earlier publication [28]. Initially, the monomer 4-(*N*-(*S*-penicillaminylacetyl)amino)phenylarsonous acid methacrylamide was prepared by reaction of PENAO with methacylic anhydride [29] and then copolymerized with MPC or PEGMA using CPADB-OH (2-hydroxyethyl 4-cyano-4-((phenylcarbonothioyl)thio)pentanoate) as RAFT agent. This RAFT agent is based on the well-studied 4-cyano-4-((phenylcarbonothioyl)thio)pentanoic acid, but it was modified with ethylene glycol. During the polymerization of the water-soluble polymers, fluorescein *O*-methacrylate was added at a ratio of CTA to fluorescent monomer of 1:0.3. This means more that three out of ten polymer chains will be labelled, which is sufficient for cell work. The water-soluble polymer was then chain-extended via PISA using MMA at a various feed ratio of MMA and RAFT agent using earlier procedures [42], resulting in nanoparticles with hydroxy functionalities located on the surface. In earlier studies it was observed that shorter MPC blocks result in more bioactive PISA nanoparticles [28]. Therefore, the relative short MPC block ($p(MPC_{17}$-*co*-$PENAO_4)$, **MP2**) was selected, which was reacted with MMA in water–methanol to yield nanoparticles of around 76 nm (Table 1). In order to identify a matching nanoparticle of similar size with a PEG surface, a range of polymerizations with various concentrations had to be carried out. As described earlier, a range of PISA particles had to be prepared in order to generate two particles of similar size [42]. In general, it was necessary to use longer blocks based on PEGMA in order to achieve similar particles sizes, which was discussed in detail elsewhere [42]. Here, the best two candidates as discussed in reference [42] were used.

Both systems, $p(PEGMA_{63}$-*co*-$PENAO_7)$-*b*-$p(MMA)_{2838}$ **PPM-NP4** and $p(MPC_{17}$-*co*-$PENAO_4)$-*b*-$p(MMA)_{1485}$ **MPM-NP2**, resulted in spherical core-shell nanoparticles with sizes of around 80 nm (Table 1). It is evident that it is not possible to compare two nanoparticles with similar repeating units or similar molecular weight as both polymers, pMPC and p(PEGMA), influence the PISA polymerization in different ways. However, the chosen particles are comparable in size and drug loading content (DLC, Table 1). These nanoparticles were already described in [42], but they are included in this publication for convenience of the reader.

Modification with TPP

The PISA particles with excess hydroxy groups on the surface were subsequently modified with the water-soluble TPP derivate, TPP-COOH ((4-carboxybutyl)triphenylphosphonium bromide), which was chosen as a target agent for the herein conducted studies, and covalently coupled to **PPM-NP** and **MPM-NP** particles. The reaction was conducted in aqueous medium, using 5 equiv excess of TPP-COOH to RAFT-end group. The pH was first adjusted to 5.2 at the start of the reaction and after 45 min tuned to 8.3 to allow maximum conjugation efficiency. After removing excess TPP-COOH and coupling reagents via dialysis in Milli-Q water, the particles were adjusted to 4 mg mL^{-1} and analysed using DLS experiments and TEM microscopy (Figure 1). The attachment of TPP-COOH to the micelle variants resulted in an increase in hydrodynamic diameter from approximately 85 nm to 136 nm for the PEG micelles and from 75 nm to 138 nm for the zwitterionic counterparts. However, no major change in dispersities was detected and well-defined nanoparticles (PdI < 0.078) were formed. Furthermore, the surface charge became less negative for both particle systems (**PPM-NP4** = −14.1 mV, **PPM-NP4-TPP** = −4.7 mV; **MPM-NP2** = −15.6 mV, **MPM-NP2-TPP** = −5.1 mV) (Table 2), confirming the successful attachment of the positively charged mitochondria agent.

No quantitative elucidation via NMR spectroscopy or UV–vis measurement was possible due to the extremely high molecular weights of the particles. The NMR spectra in D_2O showed only very broad peaks of low intensity and no aromatic peaks, indicative of TPP attachment, were detected. This could of course mean that TPP has either not reacted, is buried inside the shell

Table 1: Summary of the pPEGMA and pMPC block copolymers prepared by PISA at 70 °C including the hydrodynamic diameter D_h and particle size distribution PdI obtained by DLS and the drug loading content (DLC) calculated using DLC = m(PENAO)/[m(PENAO) + m(polymer)]. The table here contains the two nanoparticles used in this work. The full table describing several nanoparticles can be found in [42].

Particles	[MMA]:[PP/MP]:[I]	Time (h)	Conv.[a] (%)	D_h (nm)	PdI	DLC (%)
$p(PEGMA_{63}$-*co*-$PENAO_7)$-*b*-$p(MMA)_{2838}$ **PPM-NP4**	5000:1:0.2 **PP3**	4.5	57	85.4 ± 0.9	0.067	0.79
$p(MPC_{17}$-*co*-$PENAO_4)$-*b*-$p(MMA)_{1485}$ **MPM-NP2**	1500:1:0.2 **MP2**	6	99	75.9 ± 1.2	0.094	0.89

[a]Determined by ^{1}H NMR spectroscopy.

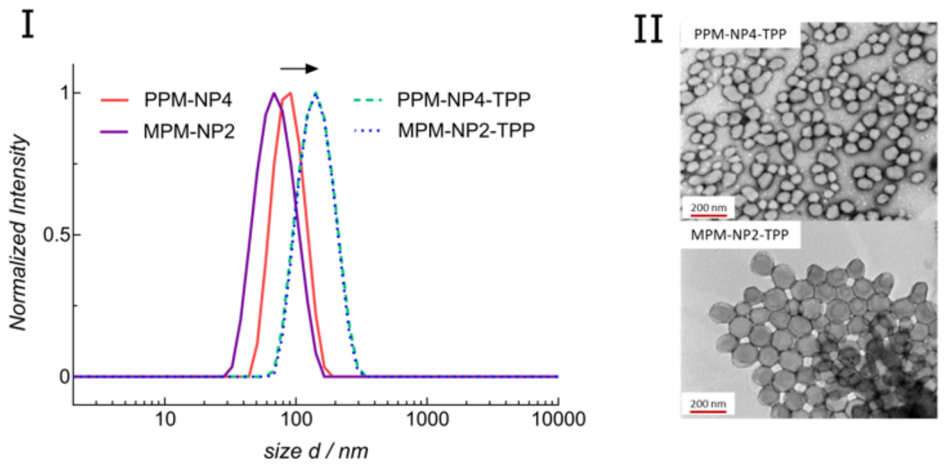


Figure 1: (I) DLS of **PPM-NP4**, **MPM-NP2**, **PPM-NP4-TPP** and **MPM-NP2-TPP** and (II) TEM of **PPM-NP4-TPP** and **MPM-NP2-TPP** (stained with uranyl acetate). Note: The curves of **PPM-NP4-TPP** and **MPM-NP2-TPP** are overlapping.

Table 2: Summary of **PPM-NP4** and **MPM-NP2** before and after attachment of TPP-COOH.

Particles	D_h^a (nm)	PdI[a]	D_h^b (nm)	PdI[b]	ζ^a (mV)	ζ^b (mV)	cmc[a] (μM)	cmc[b] (μM[1])
PPM-NP4/PPM-NP4-TPP	85.4 ± 0.9	0.067	136.3 ± 0.5	0.078	−14.1	−4.7	2.3	6.5
MPM-NP2/PPM-NP2-TPP	75.9 ± 1.2	0.094	137.5 ± 1.5	0.074	−15.6	−5.1	5.6	14.6

[a]Before TPP attachment. [b]After TPP attachment.

or NMR is not sufficiently sensitive to detect the attachment of an end group in large nanoparticles. In any case, this approach was inconclusive. Hence, the copolymer **PP3** (p(PEGMA$_{63}$-*co*-PENAO$_7$) was used as a model compound and reacted with TPP-COOH under the same conditions as described above. The conjugation product was analysed using ^{1}H and ^{31}P NMR spectroscopy. The ^{31}P NMR spectrum (Figure 2a) shows a peak at 23.07 ppm which belongs to the phosphorus of the triphenylphosphonium moiety. Furthermore, the additional peaks in the region between 7.5–8.2 ppm in the ^{1}H NMR spectrum (Figure 2b) can be associated to the phenyl protons of the TPP residue. The integration cannot be calculated using the methylene signal adjacent to the ester of PEGMA at δ = 4.1 ppm as this peak will overlap with the ethylene glycol spacer to TPP. Instead, the methyl signal 3.4 ppm was used. As the polymer has 63 PEGMEMA repeating units, the intensity of this peak is 189, which should be equivalent to the 15 aromatic peaks of TPP. This signal overlaps with 7 × 4 aromatic peaks belonging to PENAO. Care needs to be taken here as this is also the region of the aromatic group of the RAFT agent although there is no direct overlap. Full TPP endchain modification therefor equates to an intensity ratio of 43 (δ = 7.5–8.2 ppm) to 189 (δ = 3.4 ppm), which is equivalent to the signal intensity of 2.91 (δ = 3.4 ppm) to 0.68 (δ = 7.5–8.2 ppm) shown in Figure 2, suggesting complete modification.

The integration for the peak at the region (g, h and i) increased by 0.26 in number, suggesting that approximately one TPP group per chain was attached. The model reaction using **PP3** revealed that the conjugation of TPP-COOH to the polymer proceeded in a quantitative manner and can be used as a good indication for the reaction efficiency between the hydroxy residue of the RAFT-end group and the carboxylic group of the TPP molecule. It was assumed that the particle systems show similar reactivity profiles and resulted in high TPP attachment as depicted in Scheme 1. However, that still slightly negative zeta potentials were obtained, indicates that somewhat lower conjugation products were achieved. This is not surprising as the introduction of positive charges on the surface will introduce stress to the system due to strong repulsive forces, thus the complete reaction is prevented. At this stage, it is difficult to determine how many end groups were actually modified as typical techniques such as NMR are not sensitive enough to detect small changes on the polymer end groups. At this point it can be argued that it would be easier to prepare a TPP-modified RAFT agent as this would be the only way to ensure high end group

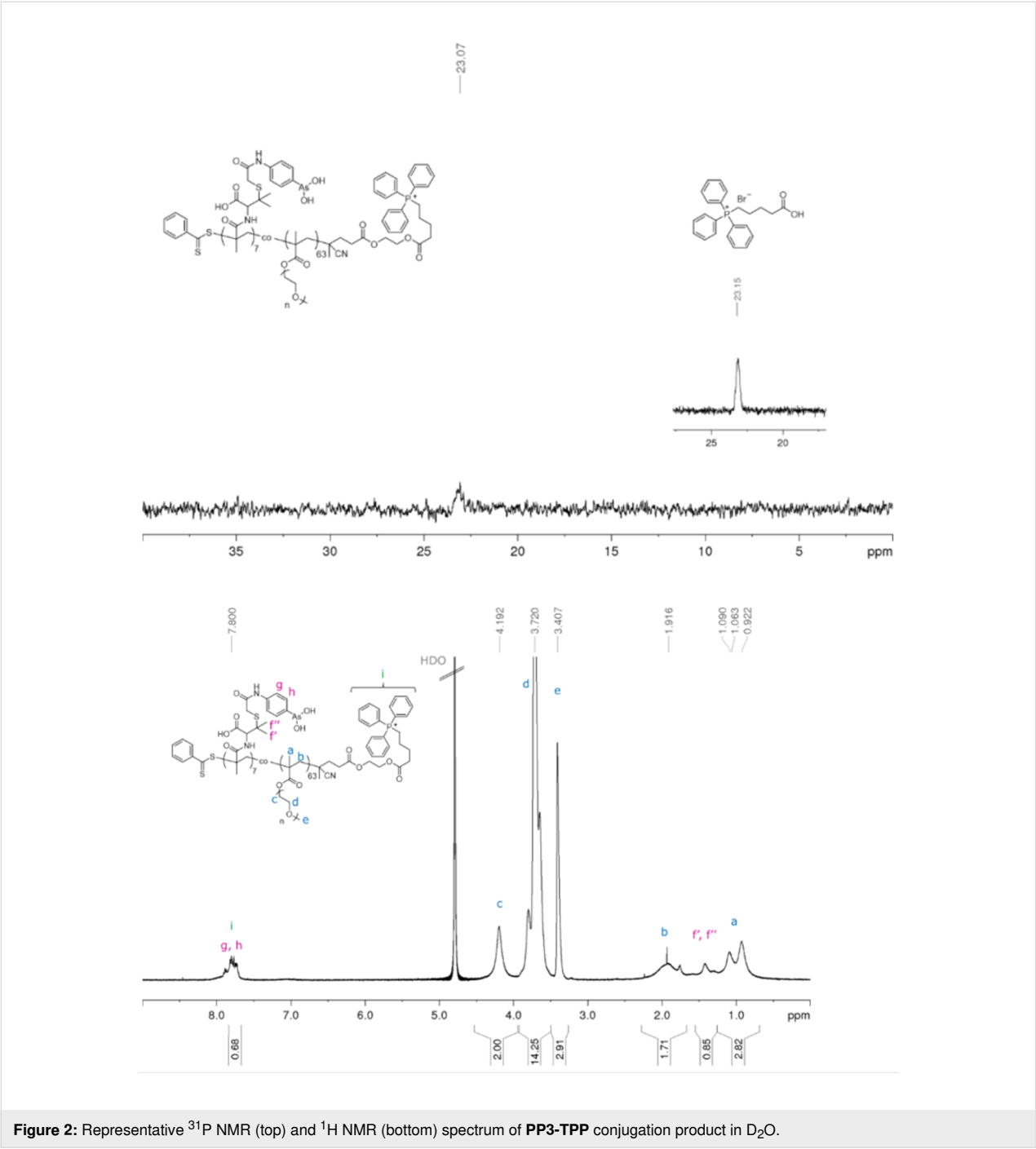
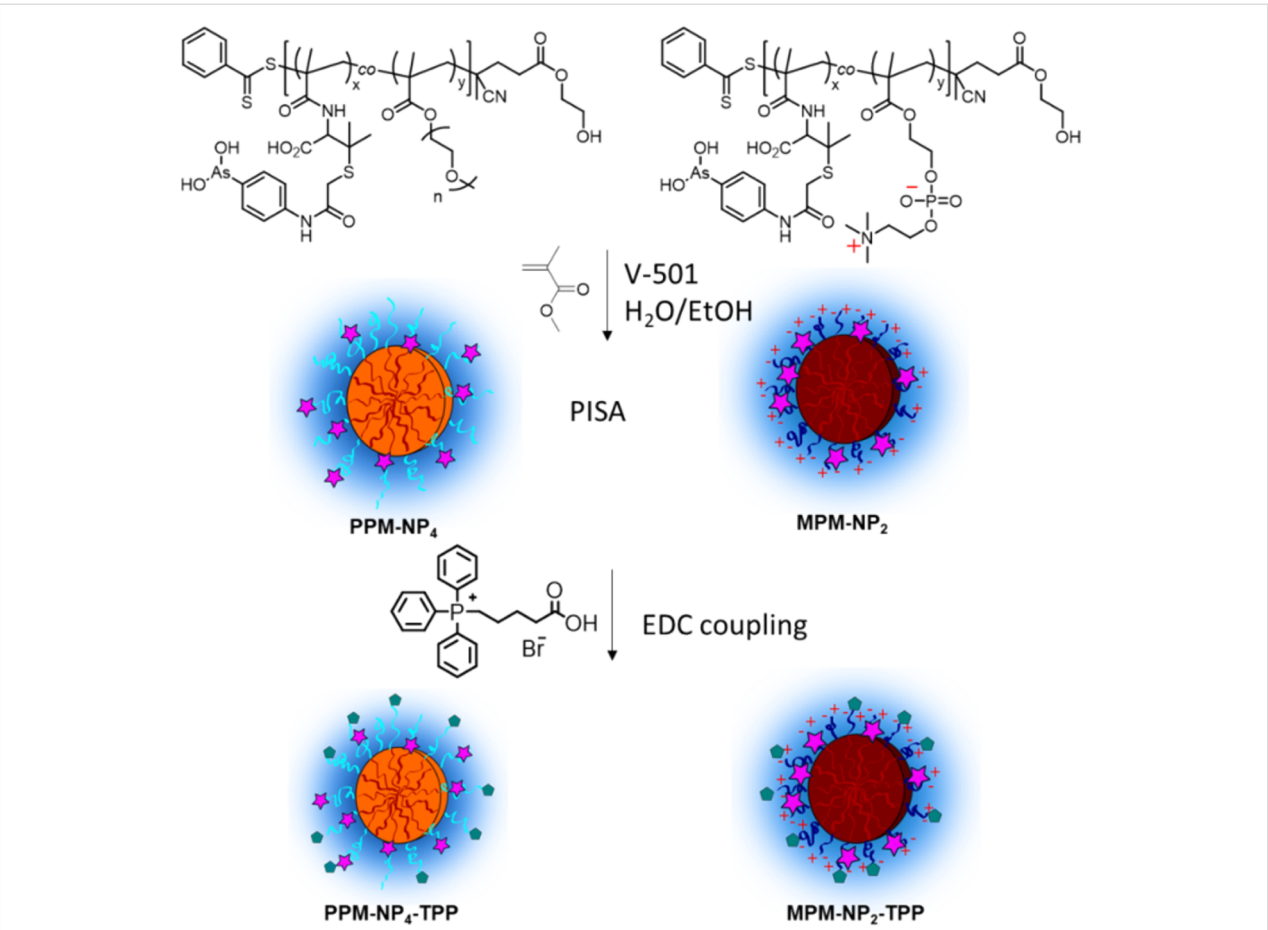


Figure 2: Representative ^{31}P NMR (top) and ^{1}H NMR (bottom) spectrum of **PP3-TPP** conjugation product in D_2O.

fidelity. This is of course true, but it also needs to be considered that the presence of the end group will influence the PISA process and results in aggregation numbers and particle sizes that are very different to the ones obtained with unmodified RAFT agent.

Due to the observed change in size after ligand attachment, the stability of the particles to disassembly was analysed by measuring the scattering intensity for different polymer concentrations (c = 0–100 μM) and the critical micelle concentration (cmc) values were determined from the intercept point of the linear regressions as shown in Supporting Information File 1, Figure S1. **PPM-NP4** demonstrated a slightly lower cmc value (cmc = 2.3 μM) compared to **MPM-NP2** (cmc = 5.6 μM), thus is the most stable. After TPP conjugation to the surface of the nanoparticles, the stability for both micelle variants decreased by approximately 2.5-fold (Table 2). Furthermore, the more neutral zeta potentials of the TPP-conjugated particles influ-



Scheme 1: Synthesis of TPP-based PISA particles based on zwitterionic 2-methacryloyloxyethyl phosphorylcholine (**PPM-NP4-TPP**) and poly(oligo ethylene glycol methyl ether methacrylate) (pPEGMA) with a pMMA core and pendant PENAO drugs (pink stars). The synthesis of the nanoparticles was described earlier [28,42], here, the postmodification with TPP was explored. Parts of the scheme were adapted from ref. [28], © 2018 American Chemical Society. This content is not subject to CC BY 4.0.

ences the stability of particles to aggregation. High zeta potentials – positive or negative – result typically in less aggregated particle systems [20,46].

Biological characterization

The mitochondria target containing nanoparticles **PPM-NP4-TPP** and **MPM-NP2-TPP** were further analysed using 3D spheroid tumour models [47]. The samples were incubated with 143B and SW982 cells and the penetration profiles of the micelles were investigated using laser scanning confocal microscopy. After 3 hours of incubation, the penetration profiles of the micelles into the spheroids can be visualized as seen in Figure 3. The PEG-based micelle, **PPM-NP4-TPP**, reveals no significant change in fluorescence compared to the non TPP-conjugated micelle, **PPM-NP4** (green and red curves respectively, Figure 3A II and B II)). No dominant improvement in spheroid penetration could therefore be detected. Interestingly, for **MPM-NP2-TPP** significant higher fluorescence intensities were measured, when the TPP-micelle was subjected to 143B and SW982 MCTS (Figure 3). As a result, high spheroid uptake and deep spheroid penetration were observed, particularly into the soft tissue sarcoma spheroids, indicating that the TPP conjugation improved the internalization into tumours for **MPM-NP2-TPP**, despite being slightly less stable than the non-conjugate micelles.

The TPP-particles were further investigated for spheroid growth inhibition using the SW982 MCTS model. The spheroids were treated with the nano-objects at a drug concentration c = 11.25 µM and the size and morphology of the MCTS were traced after 3 and 6 days. The chosen concentration was based on IC_{50} values of various PENAO formulations measured in earlier works, which typically ranged around this value. Both treated spheroids led to smaller tumour MCTS compared to the control (Figure 4). No dominant optical difference could be detected between the nanoparticle samples. Therefore, the optical cell density of **PPM-NP4-TPP** and **MPM-NP2-TPP** treated spheroids was elucidated via the APH assay after 6 days

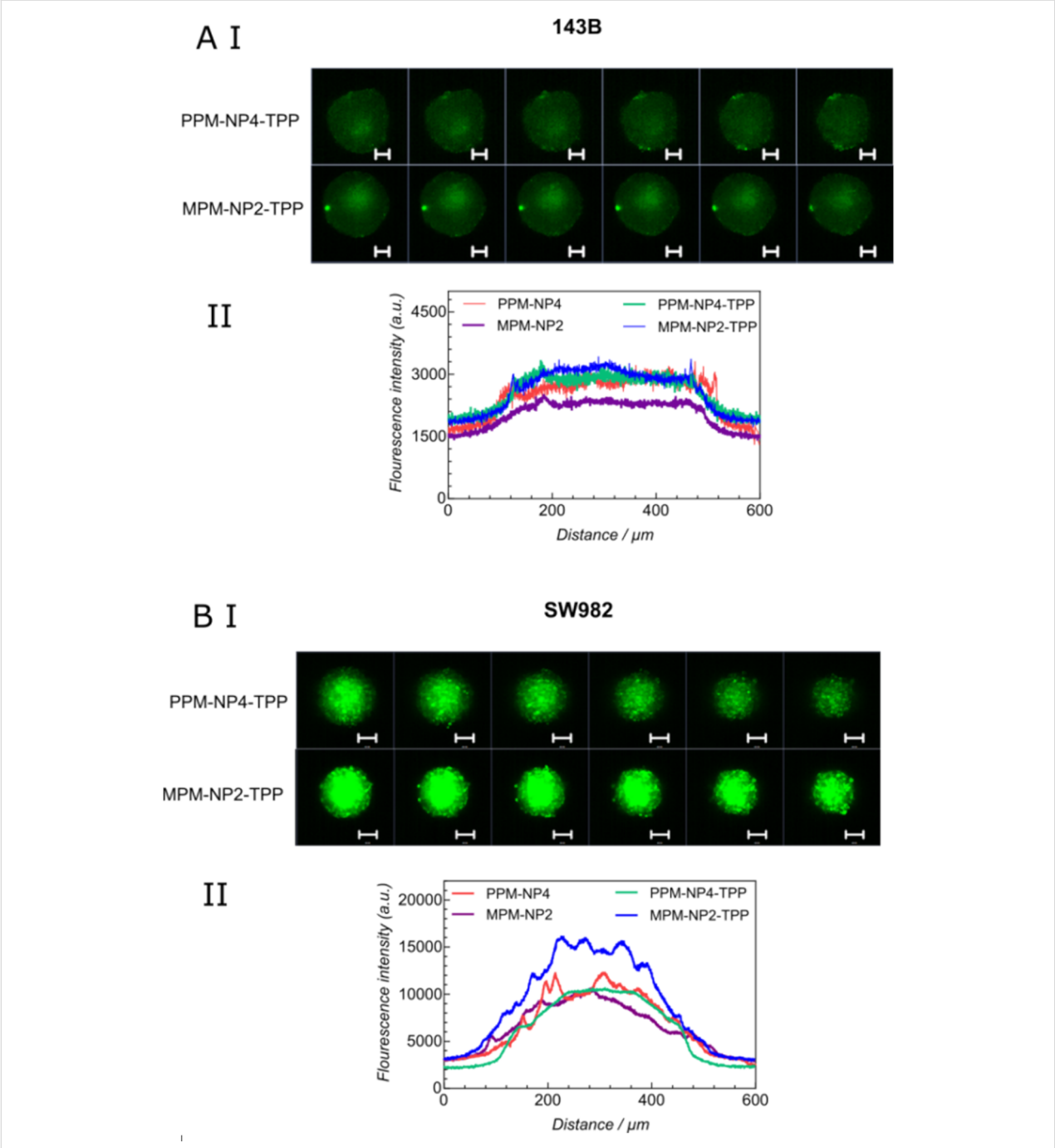


Figure 3: Penetration of **PPM-NP4-TPP** and **MPM-NP2-TPP** micelles and fluorescence intensity profile on (A I, II) 143B and (B I, II) SW982 spheroids (scale bars = 300 µm). The results of the nanoparticles without TPP have been reported earlier [42]. This figure was adapted with permission from [42], Noy et al., Direct Comparison of Poly(ethylene glycol) and Phosphorylcholine Drug-Loaded Nanoparticles In Vitro and In Vivo, *Biomacromolecules* **2020,** *21,* 2320–2333. Copyright 2020 American Chemical Society. This content is not subject to CC BY 4.0.

of treatment and compared with each other and with the previous obtained optical densities of **PPM-NP4** and **MPM-NP2** treated MCTS (Figure 5). As already seen in the images in Figure 4, the cell viability of the micelle-treated spheroids is lower than that of the control. No improvement in treatment was achieved for the **PPM-NP4-TPP** micelles, which is in agreement with the 3D penetration studies. On the other hand, the zwitterionic **MPM-NP2-TPP** particles induced more cell death and represent a lower optical cell density for SW982 MCTS. This outcome reveals that the attachment of TPP to zwitterionic particles accelerated its anticancer performance in terms of spheroid uptake and tumour growth inhibition, while

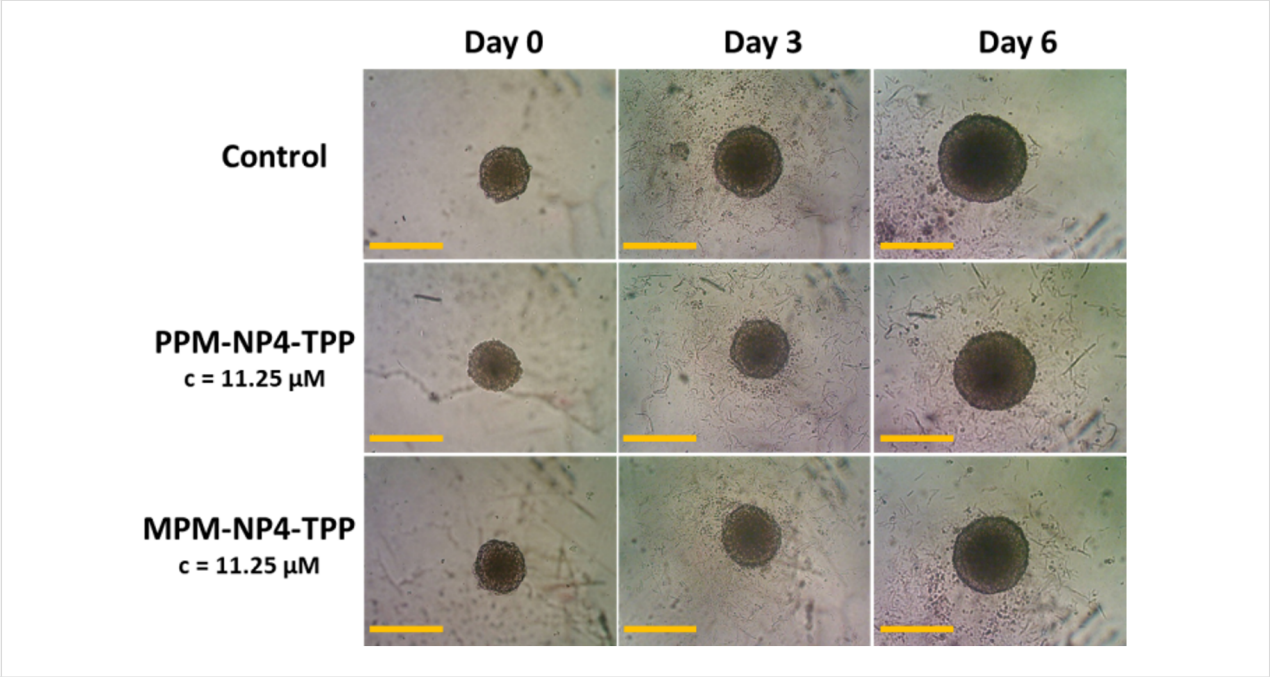


Figure 4: Growth effects of **PPM-NP4-TPP** and **MPM-NP2-TPP** on SW982 spheroids after 3 and 6 days of incubation (*c*(drug) = 11.25 µM, scale bar 300 µm).

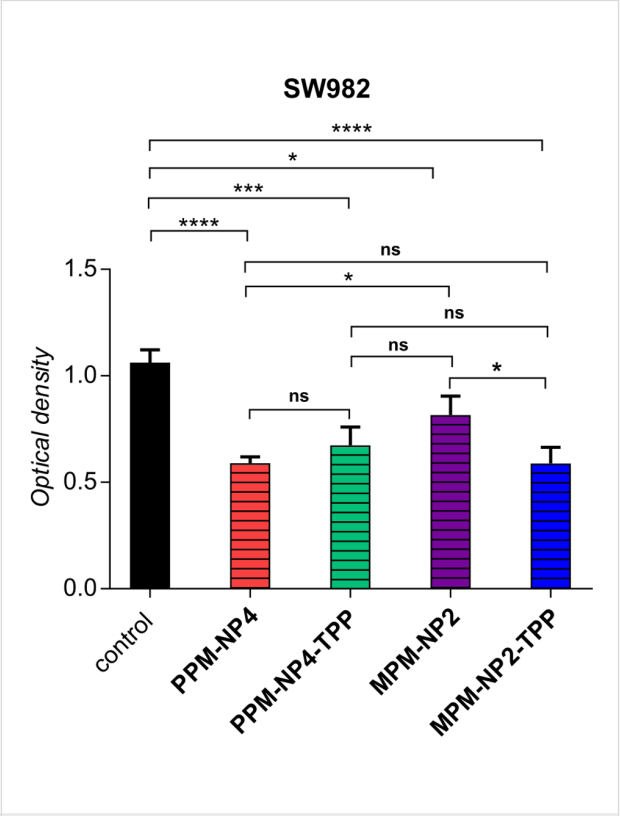


Figure 5: Cell viability of SW982 spheroids after 6 days treatment with **PPM-NP4**, **PPM-NP-TPP**, **MPM-NP2** and **MPM-NP2-TPP** (*c*(drug) = 11.25 µM). Data represent means ± SD, *n* = 6. *, significant difference, $P < 0.05$; **, significant difference, $P < 0.01$; ***, significant difference, $P < 0.001$; ****, significant difference, $P < 0.0001$.

no anticancer enhancement was detected when the PEGylated micelle was conjugated with a mitochondrial agent. In conclusion, the conjugation of TPP to **MPM-NP2** gave the zwitterionic drug particles similar anticancer efficiency than that of the non-conjugated **PPM-NP4** micelles.

The co-localization of the TPP-variants into the mitochondria, lysosomes and nuclei were analysed using laser scanning confocal microscopy. Surprisingly, there was no improvement in mitochondria localization for the employed samples, despite carrying a mitochondria target on its surface according to the the Pearson correlation coefficient shown in Table 3. Moreover, **PPM-NP4-TPP** represents notable lower co-localization into the mitochondria than **PPM-NP4** (Figure 6 and Supporting Information File 1, Figure S2), which is supported by the calculation of the Pearson's correlation coefficient (Table 3). The Pearson's correlation coefficient – which is a statistical formula that calculates the correlation between two variables – decreases in number for the **PPM-NP4-TPP** micelles, indicating that less nanoparticles were accumulated within the mitochondria. It also shows a slightly lower number for the localization into the lysosomes, stating that overall lower cell internalization was achieved by the TPP-conjugated PEG micelle. Also the zwitterionic TPP-micelle led to no enhanced accumulation into the mitochondria (Figure 6 and Table 3) after 3 hours of incubation. However, an increase in lysosomal localization was observed and calculated. No co-localization was detected within the nuclei for both particle systems.

Table 3: Summary mitochondrial and lysosomal co-localization of **PPM-NP4**, **PPM-NP4-TPP**, **MPM-NP2** and **MPM-NP2-TPP** in SW982.

Organelles	Particles	Overlap coefficient[a]	Correlation R[b]	Correlation R × R[c]
mitochondria	**PPM-NP4**	0.62	0.10	0.01
	PPM-NP4-TPP	0.56	0.04	0
	MPM-NP2	0.43	−0.04	0
	MPM-NP2-TPP	0.38	−0.13	0.02
lysosomes	**PPM-NP4**	0.79	0.56	0.31
	PPM-NP4-TPP	0.77	0.48	0.23
	MPM-NP2	0.80	0.52	0.27
	MPM-NP2-TPP	0.84	0.63	0.4

[a]Manders overlap coefficient, [b]Pearson's correlation coefficient, [c]Coefficient of determination.

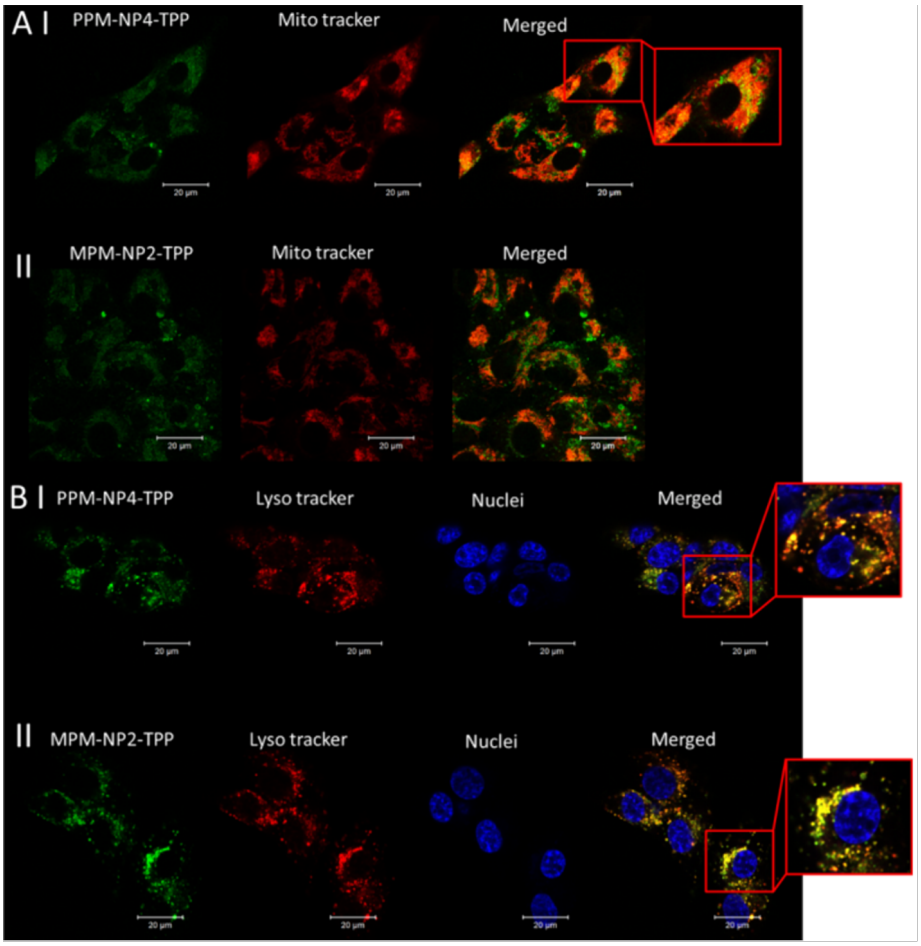


Figure 6: Cell localization of **PPM-NP4-TPP** (I) and **MPM-NP2-TPP** (II) into (A) mitochondria and (B) lysosomes und nuclei of SW982 cells. The particles carry fluorescein (green), the mitochondria and lysosomes were stain with Mito and Lyso Tracker, respectively (red) and the nuclei was stained with Hoechst 33342 (blue). Merged images show co-localisation (yellow fluorescence).

It seems therefore that TTP conjugation reduces the uptake by PEG-coated nanoparticles, but slightly, although not significantly increases the uptake in pMPC particles. We hypothesize that in both particles the nanoparticles remain in the lysosomes, but do not seem to escape the lysosomes to reach the mitochondria. However, the particles were still found to be active and inhibit

the cell proliferation of human synovial sarcoma SW982 cells (Figure 7). All four PISA particles displayed an enhanced cytotoxicity compared to free PENAO using SW982. While PENAO's cytotoxicity arises mainly from crosslinking two cysteine loops in the mitochondrial ANT protein, the here employed systems seem to not only rely on that reaction to introduce cell apoptosis, as all particle systems are cytotoxic regardless of reaching the mitochondria or not. The mitochondria contain indeed several vicinal protein thiols that readily react with trivalent arsenicals, however, it has been shown that various other proteins, enzymes and receptors bind to As(III) molecules [8,9]. It is on the other hand interesting that the zwitterionic micelles represent overall better anticancer efficiency when TPP is attached, while the PEG micelle performance is better without added TPP. The **PPM-NP4-TPP** micelle represents more than a 2-fold decrease in cytotoxicity, thus being less toxic compared to **PPM-NP4** micelle, while **MPM-NP2-TPP** displays slightly lower IC_{50} values than that of **MPM-NP2** (Figure 7). This is in agreement with the uptake results as **PPM-NP4-TPP** displays lower uptake while **MPM-NP2-TPP** displays higher uptake compared to the TPP-free PISA nanoparticle. It needs to be considered that these results here are unique to this cell line and different results can be obtained when using other cell lines. Such a study should include healthy cell lines such as cell lines of the immune system to ensure that the mitochondria binding ligand does not induce any damaging effects to these cell lines.

Many studies have reported that attaching targeting ligands on nanoparticle or liposome surfaces play a key role in overcoming biological barriers and reducing targeting effects. Active targeting or retention can increase cellular internalization as well as accumulation at the diseased tissues by targeting specific over-expressed receptors in cancer cells. However, to this date it is still debateable if active retention truly causes this "homing" effect. It has been shown that due to increased protein corona formation on a target agent carrying nanoparticle surface, the interaction between ligand and targeting agent is inhibited and resulted consequently in significant lower nanoparticle targeting efficiency [48,49].

This study demonstrates that every small change to nanoparticle design can result in unpredictable outcomes, illustrating the complexity in understanding and designing efficient drug-delivery systems in biological environments. It needs to be considered that TPP, despite its positive charge, still carries large phenyl groups that render the surface hydrophobic. While this can affect protein adsorption, it is more important to understand how TPP is presented on the surface of these PISA particles. In order for TPP to fulfil its function, the surrounding of the ligand needs to be considered. Cartoons are widely used in the drug delivery literature, often showing the targeting ligand readily available above a micelle shell of ordered polymer brushes. This assumes that the targeting ligand is well protruding out of the surface, which is usually not the case when the ligand was attached to endfunctionality of a micelle and is not attached to a longer chain. Chan and co-workers have shown that the binding of biorecognition molecules on a PEG nanoparticle to its target only works when the PEG chain length is less than the polymer chain to which the ligand is attached.

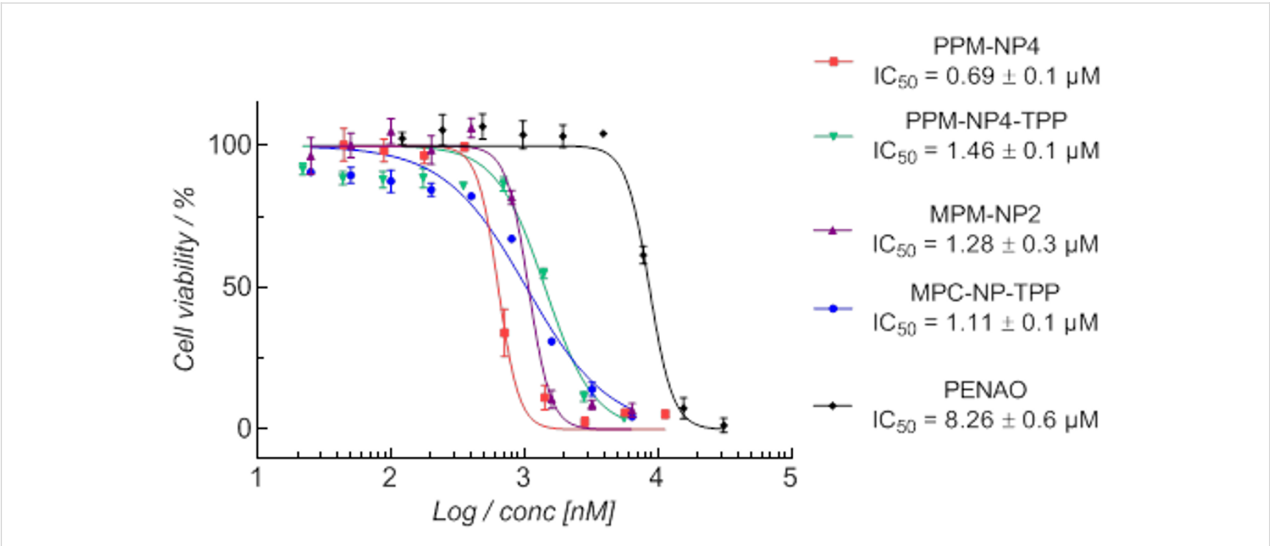


Figure 7: Cytotoxicity study of **PPM-NP4-TPP** and **MPM-NP2-TPP** on SW982 cells in relation to the concentration of PENAO present. The results of the nanoparticles without TPP have been reported earlier [42]. This figure was adapted with permission from [42], Noy et al., Direct Comparison of Poly(ethylene glycol) and Phosphorylcholine Drug-Loaded Nanoparticles In Vitro and In Vivo, *Biomacromolecules* **2020,** *21,* 2320–2333. Copyright 2020 American Chemical Society. This content is not subject to CC BY 4.0.

Otherwise, the long PEG chain will intercept ligand binding [50]. It is also reasonable to think that TPP is barely visible on the surface at all. The hydrophobic phenyl group might redirect towards the hydrophobic core, disappearing into the polymer shell. Moreover, the targeting ligand might introduce changes to the shell structure that is not evident with the characterization carried out here. It has been shown that the presence of hydrophobic groups in the surface can reduce the hydration and limit cellular uptake [51,52]. It is therefore evident that more studies such as in-depth scattering studies are needed to fully elucidate the structure of the micelle [53]. Although TPP is present, it may not be fully available on the surface to display a significant mitochondria targeting effect.

Conclusion

A triphenylphosphonium (TPP) mitochondria agent was attached to PISA nanoparticles with the aim to improve overall mitochondrial accumulation and therefore anticancer efficiency. However, having TPP on the nanoparticle surfaces only enhanced tumor penetration and cytotoxicity for the zwitterionic micelles, while no positive effect was seen for the PEGylated micelles. More importantly, no increased mitochondria targeting ability was observed for both micelles. While the attachment of TPP clearly influenced the biological behaviour, this behaviour may simply stem from the fact that TPP interacts with the shell or, thanks to the hydrophobic phenyl groups, even with the core of the micelle. More in-depth studies are necessary to answer the question if TPP is readily available on the surface of the micelle and if the presence of the polymer around TPP may interfere with binding to the mitochondria.

Experimental

The synthesis of polymers and PISA particles and the biological experiments are described elsewhere [28,42], but the procedure has been added to Supporting Information File 1 for convenience.

Attachment of TPP-COOH to **PPM-NP4** and **MPM-NP2**

In a typical experiment, (4-carboxybutyl)triphenylphosphonium bromide (TPP-COOH) (0.10 mg, 0.00022 mmol, 5 equiv to RAFT end group) was added to a 5 mg mL^{-1} particle solution before *N*-(3-dimethylaminopropyl)-*N*′-ethylcarbodiimide hydrochloride (EDC·HCl) (0.034 mg, 0.00022 mmol, 5 equiv to RAFT end group) and *N*-hydroxysuccinimide (NHS) (0.025 mg, 0.00022 mmol, 5 equiv to RAFT end group) were added (stock solutions were made in Milli-Q water and 25 μL of stock solution were added accordingly). The pH was corrected to 5.2 using 0.1 M NaOH or 0.1 M HCl solution. The solution was stirred for 45 min and the pH was adjusted to 8.3 and the solution was stirred for 3 days at room temperature. The particles were purified by dialysis in Milli-Q water with frequent solvent change (regenerated cellulose membranes, MW cut-off 6000–8000 g mol^{-1}) and analysed via DLS experiments and TEM microscopy.

Control experiment: attachment of TPP-COOH to **PP3** copolymer

For the control experiment, **PP3** (19.30 mg, 0.85 mmol of RAFT end group, 1 equiv) was dissolved in 1.5 mL of Milli-Q water and TPP-COOH (1.88 mg, 4.25 mmol, 5 equiv to RAFT end group), EDC·HCl (0.82 mg, 4.25 mmol, 5 equiv to RAFT end group) and NHS (0.49 mg, 4.25 mmol, 5 equiv to RAFT end group) were added to the polymer solution (the educts were added as stock solutions in Milli-Q water (100 μL), respectively) and the pH was adjusted to 5.2 using 0.1 M NaOH or 0.1 M HCl solution. After 45 min, the pH was corrected to 8.2 and the reaction was left to stir at room temperature for 3 days. The polymer was purified by dialysis in Milli-Q water with frequent solvent change (regenerated cellulose membranes, MW cut-off 6000–8000 g mol^{-1}) and the product was then lyophilized and analysed using NMR spectroscopy.

^{1}H NMR (300 MHz, D_2O) δ_H (ppm) 8.0 (1H, aromatic RAFT), 7.8–7.9 (7 × 4H, aromatic PENAO and 15H TPP), 7.7 (2H, aromatic RAFT), 7.55 (2H, aromatic RAFT), 4.1–4.2 (36 × 2H + 2H, CH_2-C=O of p(PEGMA) and RAFT agent), 3.80 (36 × 2H, CH_2-CH_2-O), 3.72 (36 × 2H × (~5)H + 7H, C*H*-N of PENAO and CH_2-O of p(PEGMA)), 3.64 (2 × 7H, S-C**H**$_2$-C=O of PENAO), 3.46 (36 × 3H, OCH_3), 1.7–2.1 (140H, CH_2 backbone), 1.5 (7 × 6H, CH_3 PENAO), 0.7–1.2 (210H, CH_3 backbone).

Supporting Information

Supporting Information File 1

Analytical techniques, in vitro experiments, polymer synthesis, analysis of critical micelle concentration, and fluorescence microscopy of non-TPP micelles.
[https://www.beilstein-journals.org/bjoc/content/supplementary/1860-5397-17-148-S1.pdf]

Acknowledgements

The authors would like to acknowledge the NMR and microscopy facility within the Mark Wainwright Analytical Centre at the University of New South Wales for NMR support.

Funding

The authors would also like to thank the Australian Government and the Australian Research Council for funding.

ORCID® iDs

Martina Stenzel - https://orcid.org/0000-0002-6433-4419

References

1. Fulda, S.; Galluzzi, L.; Kroemer, G. *Nat. Rev. Drug Discovery* **2010,** *9,* 447–464. doi:10.1038/nrd3137
2. Dilda, P. J.; Decollogne, S.; Weerakoon, L.; Norris, M. D.; Haber, M.; Allen, J. D.; Hogg, P. J. *J. Med. Chem.* **2009,** *52,* 6209–6216. doi:10.1021/jm9008339
3. Dilda, P. J.; Hogg, P. J. *Cancer Treat. Rev.* **2007,** *33,* 542–564. doi:10.1016/j.ctrv.2007.05.001
4. Decollogne, S.; Joshi, S.; Chung, S. A.; Luk, P. P.; Yeo, R. X.; Nixdorf, S.; Fedier, A.; Heinzelmann-Schwarz, V.; Hogg, P. J.; Dilda, P. J. *Gynecol. Oncol.* **2015,** *138,* 363–371. doi:10.1016/j.ygyno.2015.06.018
5. Park, D.; Chiu, J.; Perrone, G. G.; Dilda, P. J.; Hogg, P. J. *Cancer Cell Int.* **2012,** *12,* No. 11. doi:10.1186/1475-2867-12-11
6. Kitchin, K. T.; Wallace, K. *J. Inorg. Biochem.* **2008,** *102,* 532–539. doi:10.1016/j.jinorgbio.2007.10.021
7. Kitchin, K. T.; Wallace, K. *Toxicol. Appl. Pharmacol.* **2005,** *206,* 66–72. doi:10.1016/j.taap.2004.12.010
8. Zhang, X.; Yang, F.; Shim, J.-Y.; Kirk, K. L.; Anderson, D. E.; Chen, X. *Cancer Lett.* **2007,** *255,* 95–106. doi:10.1016/j.canlet.2007.03.025
9. Yan, X.; Li, J.; Liu, Q.; Peng, H.; Popowich, A.; Wang, Z.; Li, X.-F.; Le, X. C. *Angew. Chem., Int. Ed.* **2016,** *55,* 14051–14056. doi:10.1002/anie.201608006
10. Zhang, X.; Cornelis, R.; De Kimpe, J.; Mees, L.; Lameire, N. *Clin. Chem.* **1998,** *44,* 141–147. doi:10.1093/clinchem/44.1.141
11. Tanaka, J.; Davis, T. P.; Wilson, P. *Macromol. Rapid Commun.* **2018,** *39,* 1800205. doi:10.1002/marc.201800205
12. Akhtar, A.; Wang, S. X.; Ghali, L.; Bell, C.; Wen, X. *J. Biomed. Res.* **2017,** *31,* 177–188. doi:10.7555/jbr.31.20160059
13. Qin, J.; Gong, N.; Liao, Z.; Zhang, S.; Timashev, P.; Huo, S.; Liang, X.-J. *Nanoscale* **2021,** *13,* 7108–7118. doi:10.1039/d1nr01068a
14. Liew, S. S.; Qin, X.; Zhou, J.; Li, L.; Huang, W.; Yao, S. Q. *Angew. Chem., Int. Ed.* **2021,** *60,* 2232–2256. doi:10.1002/anie.201915826
15. Cho, D. Y.; Cho, H.; Kwon, K.; Yu, M.; Lee, E.; Huh, K. M.; Lee, D. H.; Kang, H. C. *Adv. Funct. Mater.* **2015,** *25,* 5479–5491. doi:10.1002/adfm.201501422
16. Qu, Q.; Ma, X.; Zhao, Y. *Nanoscale* **2015,** *7,* 16677–16686. doi:10.1039/c5nr05139h
17. Weissig, V.; Lizano, C.; Torchilin, V. P. *J. Liposome Res.* **1998,** *8,* 391–400. doi:10.3109/08982109809035542
18. Weissig, V. *Pharm. Res.* **2011,** *28,* 2657–2668. doi:10.1007/s11095-011-0556-9
19. Di, X.; Wang, D.; Zhou, J.; Zhang, L.; Stenzel, M. H.; Su, Q. P.; Jin, D. *Nano Lett.* **2021,** *21,* 1651–1658. doi:10.1021/acs.nanolett.0c04281
20. Wang, Z.; Guo, W.; Kuang, X.; Hou, S.; Liu, H. *Asian J. Pharm. Sci. (Amsterdam, Neth.)* **2017,** *12,* 498–508. doi:10.1016/j.ajps.2017.05.006
21. Sharma, A.; Soliman, G. M.; Al-Hajaj, N.; Sharma, R.; Maysinger, D.; Kakkar, A. *Biomacromolecules* **2012,** *13,* 239–252. doi:10.1021/bm201538j
22. Marrache, S.; Dhar, S. *Proc. Natl. Acad. Sci. U. S. A.* **2012,** *109,* 16288–16293. doi:10.1073/pnas.1210096109
23. Yue, C.; Yang, Y.; Zhang, C.; Alfranca, G.; Cheng, S.; Ma, L.; Liu, Y.; Zhi, X.; Ni, J.; Jiang, W.; Song, J.; de la Fuente, J. M.; Cui, D. *Theranostics* **2016,** *6,* 2352–2366. doi:10.7150/thno.15433
24. Hou, J.; Yu, X.; Shen, Y.; Shi, Y.; Su, C.; Zhao, L. *Nanoscale Res. Lett.* **2017,** *12,* No. 158. doi:10.1186/s11671-017-1931-1
25. Khatun, Z.; Choi, Y. S.; Kim, Y. G.; Yoon, K.; Nurunnabi, M.; Li, L.; Lee, E.; Kang, H. C.; Huh, K. M. *Biomacromolecules* **2017,** *18,* 1074–1085. doi:10.1021/acs.biomac.6b01324
26. Blaikie, F. H.; Brown, S. E.; Samuelsson, L. M.; Brand, M. D.; Smith, R. A. J.; Murphy, M. P. *Biosci. Rep.* **2006,** *26,* 231–243. doi:10.1007/s10540-006-9018-8
27. Neuzil, J.; Dyason, J. C.; Freeman, R.; Dong, L.-F.; Prochazka, L.; Wang, X.-F.; Scheffler, I.; Ralph, S. J. *J. Bioenerg. Biomembr.* **2007,** *39,* 65–72. doi:10.1007/s10863-006-9060-z
28. Noy, J.-M.; Cao, C.; Stenzel, M. *ACS Macro Lett.* **2019,** *8,* 57–63. doi:10.1021/acsmacrolett.8b00853
29. Noy, J.-M.; Lu, H.; Hogg, P. J.; Yang, J.-L.; Stenzel, M. *Bioconjugate Chem.* **2018,** *29,* 546–558. doi:10.1021/acs.bioconjchem.8b00032
30. Zhang, Q.; Vakili, M. R.; Li, X.-F.; Lavasanifar, A.; Le, X. C. *Biomaterials* **2014,** *35,* 7088–7100. doi:10.1016/j.biomaterials.2014.04.072
31. Zhang, Q.; Vakili, M. R.; Li, X.-F.; Lavasanifar, A.; Le, X. C. *Mol. Pharmaceutics* **2016,** *13,* 4021–4033. doi:10.1021/acs.molpharmaceut.6b00362
32. Tanaka, J.; Moriceau, G.; Cook, A.; Kerr, A.; Zhang, J.; Peltier, R.; Perrier, S.; Davis, T. P.; Wilson, P. *Macromolecules* **2019,** *52,* 992–1003. doi:10.1021/acs.macromol.8b02459
33. Karagoz, B.; Boyer, C.; Davis, T. P. *Macromol. Rapid Commun.* **2014,** *35,* 417–421. doi:10.1002/marc.201300730
34. Zhang, W.-J.; Hong, C.-Y.; Pan, C.-Y. *Macromol. Rapid Commun.* **2019,** *40,* 1800279. doi:10.1002/marc.201800279
35. Qiu, L.; Xu, C.-R.; Zhong, F.; Hong, C.-Y.; Pan, C.-Y. *ACS Appl. Mater. Interfaces* **2016,** *8,* 18347–18359. doi:10.1021/acsami.6b04693
36. Karagoz, B.; Esser, L.; Duong, H. T.; Basuki, J. S.; Boyer, C.; Davis, T. P. *Polym. Chem.* **2014,** *5,* 350–355. doi:10.1039/c3py01306e
37. Phan, H.; Taresco, V.; Penelle, J.; Couturaud, B. *Biomater. Sci.* **2021,** *9,* 38–50. doi:10.1039/d0bm01406k
38. Zhang, W.-J.; Hong, C.-Y.; Pan, C.-Y. *Biomacromolecules* **2016,** *17,* 2992–2999. doi:10.1021/acs.biomac.6b00819
39. Wright, D. B.; Proetto, M. T.; Touve, M. A.; Gianneschi, N. C. *Polym. Chem.* **2019,** *10,* 2996–3000. doi:10.1039/c8py01539b
40. Su, G.; Jiang, H.; Xu, B.; Yu, Y.; Chen, X. *Mol. Pharmaceutics* **2018,** *15,* 5019–5030. doi:10.1021/acs.molpharmaceut.8b00612
41. Suk, J. S.; Xu, Q.; Kim, N.; Hanes, J.; Ensign, L. M. *Adv. Drug Delivery Rev.* **2016,** *99,* 28–51. doi:10.1016/j.addr.2015.09.012
42. Noy, J.-M.; Chen, F.; Akhter, D. T.; Houston, Z. H.; Fletcher, N. L.; Thurecht, K. J.; Stenzel, M. H. *Biomacromolecules* **2020,** *21,* 2320–2333. doi:10.1021/acs.biomac.0c00257
43. Cao, C.; Chen, F.; Garvey, C. J.; Stenzel, M. H. *ACS Appl. Mater. Interfaces* **2020,** *12,* 30221–30233. doi:10.1021/acsami.0c09054
44. Leng, C.; Hung, H.-C.; Sun, S.; Wang, D.; Li, Y.; Jiang, S.; Chen, Z. *ACS Appl. Mater. Interfaces* **2015,** *7,* 16881–16888. doi:10.1021/acsami.5b05627
45. Settanni, G.; Schäfer, T.; Muhl, C.; Barz, M.; Schmid, F. *Comput. Struct. Biotechnol. J.* **2018,** *16,* 543–550. doi:10.1016/j.csbj.2018.10.012
46. Honary, S.; Zahir, F. *Trop. J. Pharm. Res.* **2013,** *12,* 265–273. doi:10.4314/tjpr.v12i2.20

47. Lu, H.; Stenzel, M. H. *Small* **2018,** *14,* 1702858. doi:10.1002/smll.201702858
48. Mirshafiee, V.; Mahmoudi, M.; Lou, K.; Cheng, J.; Kraft, M. L. *Chem. Commun.* **2013,** *49,* 2557–2559. doi:10.1039/c3cc37307j
49. Reineke, J. *J. Controlled Release* **2018,** *273,* 180–183. doi:10.1016/j.jconrel.2018.01.016
50. Dai, Q.; Walkey, C.; Chan, W. C. W. *Angew. Chem., Int. Ed.* **2014,** *53,* 5093–5096. doi:10.1002/anie.201309464
51. Lu, M. X.; Khine, Y. Y.; Chen, F.; Cao, C.; Garvey, C. J.; Lu, H. X.; Stenzel, M. H. *Biomacromolecules* **2019,** *20,* 273–284. doi:10.1021/acs.biomac.8b01406
52. Cao, C.; Zhao, J. C.; Lu, M. X.; Garvey, C. J.; Stenzel, M. H. *Biomacromolecules* **2019,** *20,* 1545–1554. doi:10.1021/acs.biomac.8b01707
53. Stenzel, M. H. *Angew. Chem., Int. Ed.* **2021,** *60,* 2202–2206. doi:10.1002/anie.202010934

License and Terms

This is an Open Access article under the terms of the Creative Commons Attribution License (https://creativecommons.org/licenses/by/4.0). Please note that the reuse, redistribution and reproduction in particular requires that the author(s) and source are credited and that individual graphics may be subject to special legal provisions.

The license is subject to the *Beilstein Journal of Organic Chemistry* terms and conditions: (https://www.beilstein-journals.org/bjoc/terms)

The definitive version of this article is the electronic one which can be found at: https://doi.org/10.3762/bjoc.17.148

BEILSTEIN JOURNAL OF ORGANIC CHEMISTRY

Exfoliated black phosphorous-mediated CuAAC chemistry for organic and macromolecular synthesis under white LED and near-IR irradiation

Azra Kocaarslan[1], Zafer Eroglu[2,3], Önder Metin[*2] and Yusuf Yagci[*1,4]

Full Research Paper

Open Access

Address:
[1]Department of Chemistry, Istanbul Technical University, Maslak, 34469 Istanbul, Turkey, [2]Department of Chemistry, Koç University, Sarıyer, 34450, Istanbul, Turkey, [3]Department of Nanoscience and Nanoengineering, Atatürk University, 25240 Erzurum, Turkey and [4]King Abdulaziz University, Faculty of Science, Chemistry Department, 21589 Jeddah, Saudi Arabia

Email:
Önder Metin[*] - ometin@ku.edu.tr; Yusuf Yagci[*] - yusuf@itu.edu.tr

* Corresponding author

Keywords:
black phosphorus; click chemistry; heterogeneous photocatalyst; near infrared; phosphorene

Beilstein J. Org. Chem. **2021,** *17,* 2477–2487.
https://doi.org/10.3762/bjoc.17.164

Received: 14 July 2021
Accepted: 20 September 2021
Published: 23 September 2021

This article is part of the thematic issue "Polymer chemistry: fundamentals and applications".

Guest Editor: B. V. K. J. Schmidt

© 2021 Kocaarslan et al.; licensee Beilstein-Institut.
License and terms: see end of document.

Abstract

The development of long-wavelength photoinduced copper-catalyzed azide–alkyne click (CuAAC) reaction routes is attractive for organic and polymer chemistry. In this study, we present a novel synthetic methodology for the photoinduced CuAAC reaction utilizing exfoliated two-dimensional (2D) few-layer black phosphorus nanosheets (BPNs) as photocatalysts under white LED and near-IR (NIR) light irradiation. Upon irradiation, BPNs generated excited electrons and holes on its conduction (CB) and valence band (VB), respectively. The excited electrons thus formed were then transferred to the Cu^{II} ions to produce active Cu^{I} catalysts. The ability of BPNs to initiate the CuAAC reaction was investigated by studying the reaction between various low molar mass alkyne and azide derivatives under both white LED and NIR light irradiation. Due to its deeper penetration of NIR light, the possibility of synthesizing different macromolecular structures such as functional polymers, cross-linked networks and block copolymer has also been demonstrated. The structural and molecular properties of the intermediates and final products were evaluated by spectral and chromatographic analyses.

Introduction

For the last decade, click chemistry has been recognized as an indispensable part of synthetic chemistry due to its easiness of application, efficiency to produce the targeted products with very high yields and little or no byproducts under a variety of conditions, and high interconnected group tolerance. Since the introduction of click chemistry by Sharpless [1,2] and Mendal [3], many studies have been dedicated to better understanding of the concept and expanding its scope to be applied in various

fields of chemistry including bioconjugation [4], drug discovery [5], materials science [6-9] and so on [10]. The development of the use of light in click chemistry has set a milestone as a new and effective method for the synthesis of macromolecules [11]. Initiation of this reaction photocatalytically provides many advantages for the synthetic methodologies including bioconjugation, labeling, surface functionalization, dendrimer synthesis, polymer synthesis, and polymer modification by adding spatial and temporal control [12,13].

In recent years, heterogeneous photocatalysts have been performed in many photosynthetic reactions since they provide a more reasonable and easy way to synthesize the targeted products compared to the classical homogenous photocatalysts. In this respect, 2D materials offer great potential due to converting the inexhaustible energy of sunlight into chemical and electrical energy along with having a less environmental impact. After the discovery of the photocatalytic effect of 2D materials under UV light [14,15] the heterogeneous photocatalysts have been successfully applied in both small- and large-scale synthesis such as organic reactions [16,17], free radical polymerization (FRP) [18-20], controlled radical polymerization (CRP) [21,22], CuAAC chemistry [23-25], and thiol–ene chemistry [26,27]. However, most of the conventional 2D materials have a wide bandgap that requires UV light irradiation for their activation. Since 94% of the rays from the sun are not sufficient to activate these conventional semiconductor materials, many strategies have been proposed to design photocatalysts that can harvest in a wide spectrum of sunlight, especially in the NIR region [28,29]. In particular, the development of new photocatalyst systems that absorb the incident light from the sun at much longer wavelengths have aroused widespread interest [30-33]. However, the most of the NIR photocatalysts applied exhibit relatively low catalytic efficiency due to their low absorption characteristics and require complicated synthetic procedures. In this respect, it is worth to mention that elemental 2D materials with a proper bandgap and charge mobilities have been shown to act as photocatalysts in several reactions [34,35]. Exfoliated black phosphorus (BP), the most stable allotrope of phosphorus, has been shown as a highly efficient photocatalyst possessing superior features in many respects [36,37]. BP, a vital semiconductor 2D material with excellent physicochemical properties such as high carrier mobility, tunable optical absorption, and novel electronic band structure, fills the gap between graphene and wide bandgap semiconductors [35,38]. Furthermore, BP shows a layer thickness tunable bandgap ranging between 0.3 and 2.1 eV. Therefore, BPNs can efficiently be applied as a photoredox catalyst with broadband solar absorption [34,38-40].

The use of 2D materials for the photoinitiated electron transfer reactions with Cu^{II} catalysts for the photoinduced atom transfer radical polymerization (ATRP) and CuAAC reactions prompted us to develop a new photoredox system that works under NIR irradiation for the CuAAC reaction. In this work, we report a new synthetic strategy to the photochemical reduction of Cu^{II} to Cu^{I} for the CuAAC reaction using BPNs as the photo-initiator under NIR light.

Results and Discussion

The detailed preparation and characterization of the initial BP crystals and BPNs were previously reported [40]. BPNs were tested as NIR photoinitiator for the CuAAC reactions of low molar mass compounds and polymers possessing antagonist azide and alkyne functionalities (Figure 1).

The optical absorption spectra of BPNs, copper(I) chloride ($Cu^{I}Cl$, 0.05 mmol) and copper(II) chloride ($Cu^{II}Cl_2$,

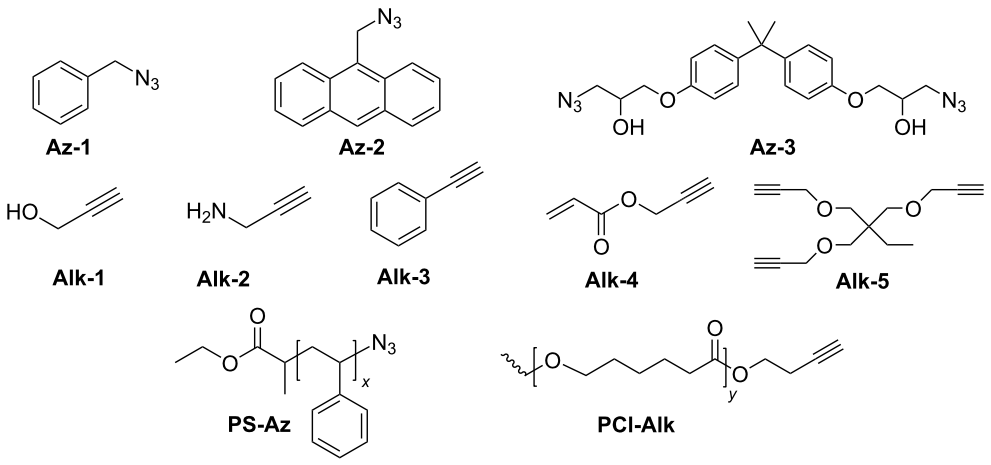


Figure 1: Structures of azide and alkyne functional molecules and polymers used in the photoinduced CuAAC reactions.

0.05 mmol) are shown in Figure 2. As can be seen, the BPNs displayed an excellent wide range of light absorption region up to 1000 nm. In this regard, BPNs are the only light absorbing component in the NIR region where Cu^{II} is completely transparent.

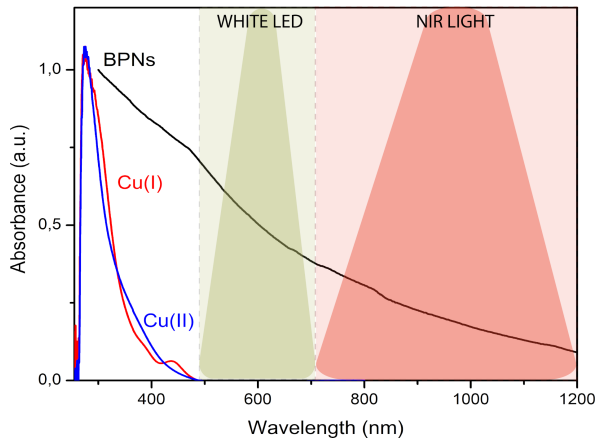


Figure 2: UV–vis spectra of $Cu^{I}Cl$, $Cu^{II}Cl_2$ and BPNs.

Initially, the model reaction between benzyl azide (**Az-1**) and phenylacetylene (**Alk-3**) in the presence of copper(II) chloride/*N*,*N*,*N*',*N*',*N*''-pentamethyldiethylenetriamine ($Cu^{II}Cl_2$/PMDETA) and exfoliated BPNs under the white LED irradiation was performed (Figure 3). The reaction was followed by ^{1}H NMR spectroscopy during the click process. The decrease of the acetylene proton at 4.42 ppm and appearance of the new signal at 8.67 ppm corresponding to the triazole moiety confirmed successful click reaction under white LED exposure conditions after 4 h (Figure 3a). Kinetic studies conducted by ^{1}H NMR analysis confirmed that the click reaction between benzyl azide and phenylacetylene resulted in almost complete conversion within 4 h white LED irradiation (Figure 3b). In this connection, it should be pointed out that the reaction proceeds also in dark almost at the same rate (Supporting Information File 1, Figure S4). This is an expected observation because there is no back reaction to reform Cu(II). Similar observations were reported by the other photoinduced CuAAC reactions [41].

In order to demonstrate the functional group tolerance, the extent of the reaction was investigated on various alkyne groups using benzyl azide under both white LED and NIR light irradiation. The results presented in Table 1 revealed that NIR-light-triggered click reactions produced the corresponding products with slightly higher yields favored by the higher penetration of NIR light to the reaction media containing heterogeneously dispersed BPNs. Compared with propargyl alcohol (**Alk-1**) and propargyl acrylate (**Alk-4**), the rate of clicking slightly decreased in the case of propargylamine (**Alk-2**), but still gave high yields. Therefore, it can be concluded that **Alk-2** and **Alk-1** exhibit relatively lower efficiency probably due to the additional coordination of the Cu^{I} catalyst. Notably, the reaction with **Alk-4** gave higher yields with both light sources.

In the light of previous studies, a photoinduced electron transfer mechanism presented in Scheme 1 can be proposed. Upon the light irradiation, BPNs absorb the light and generate a single electron which was transferred from the conduction band to the

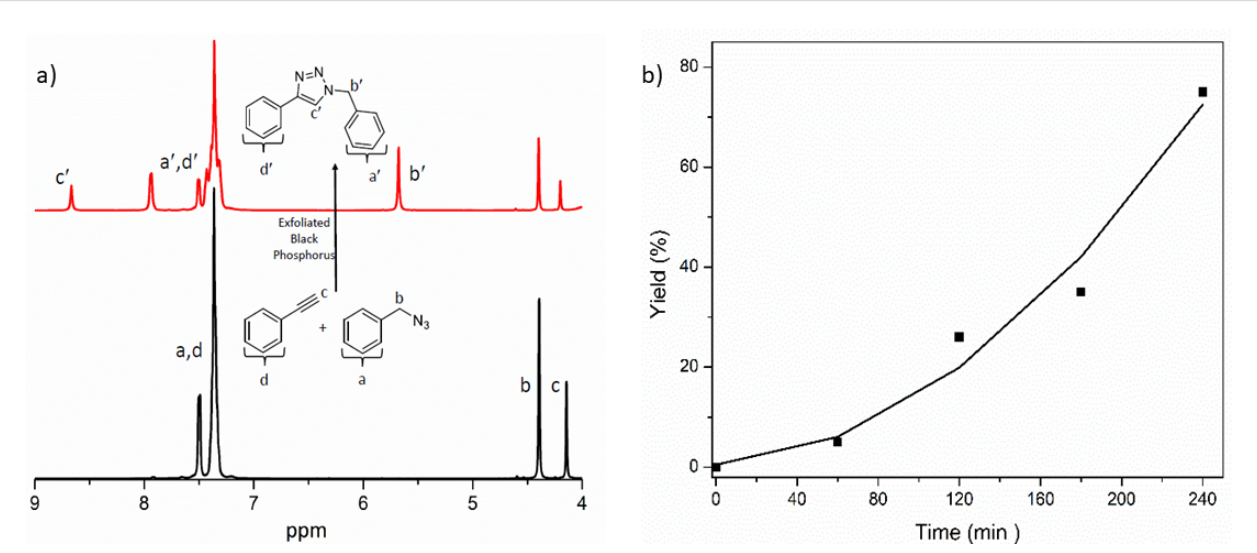
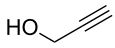
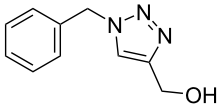
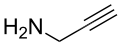
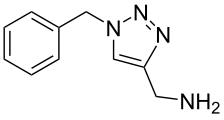
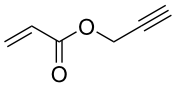
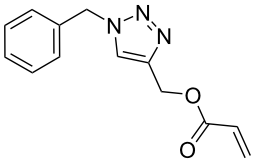


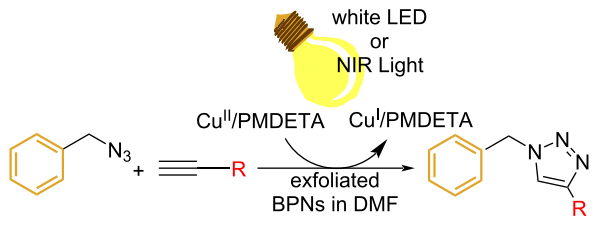
Figure 3: a) ^{1}H NMR spectra of the model reaction between benzyl azide (**Az-1**) and phenylacetylene (**Alk-3**) before (black) and after (red) irradiation. b) Conversion-time plot as measured by ^{1}H NMR spectroscopy through integration of the acetylene proton around 4.42 ppm.

Table 1: Photoinduced CuAAC between benzyl azide and various alkynes[a] using exfoliated BPNs[b] in DMSO-d_6 = 1 g/L.

Run	R—	Product	White LED Yield[c]	NIR Light Yield[c]
1			43	98
2			65	69
3			90	95

[a]All reactions were carried out in a NMR tube in a room temperature in the presence of $Cu^{II}Cl_2$/PMDETA. [b]Reaction time = 4 h. [c]Conversions were determined by ^{1}H NMR spectroscopy.

Cu^{II} complex to form Cu^{I} capable of catalyzing the click reaction in a conventional manner.



Scheme 1: Proposed mechanism for photoinduced CuAAC reaction using exfoliated BPNs.

The applicability of the described click reaction to synthetic polymer chemistry was also demonstrated. For this purpose, polymer functionalization by using alkyne functional poly(ε-caprolactone) (**PCL-Alk**) and 9-(azidomethyl)anthracene (**Az-2**) as click components was investigated. The detailed ^{1}H NMR spectrum of the resulting anthracene functional polymer (**PCL-Anth**) exhibited the characteristic signals of triazole and benzylic protons at 5.5 ppm and 8.70 ppm, respectively (Figure 4a). The obtained polymer has similar absorption characteristic to bare anthracene (Figure 4b). The fluorescence spectrum of diluted solution of **PCL-Anth** in THF excited at λ_{exc} = 350 nm showed the characteristic emission bands of the excited (singlet) anthracene at 595, 655, and 725 nm (Figure 4c). These observations clearly confirmed the successful chain-end functionalization.

In addition, block copolymer formation via NIR activated CuAAC process between the polymers having antagonist click components, namely, polystyrene azide (**PS-Az**) and **PCL-Alk**, was investigated. At the end of irradiation in the presence of exfoliated BPNs and $Cu^{II}Cl_2$/PMDETA, polystyrene-*b*-poly(ε-caprolactone) (**PS-*b*-PCL**) is selectively formed (Scheme 2).

Figure 5a displays the GPC traces of precursors **PS-Az**, **PCL-Alk**, and the block copolymer **PS-*b*-PCL**. As it can be seen, the trace of **Ps-*b*-PCL** block copolymer was clearly shifted to higher molecular weight region without contamination of the precursor polymers. The ^{1}H NMR spectrum of the block copolymer displayed the characteristic peaks of both macromolecular segments. Additionally, the methylene protons adjacent to the triazole ring at 7.48 ppm were noted (Figure 5b). These results indicated that structurally diverse polymers formed by different polymerization mechanisms can readily be linked just by a simple NIR-induced CuAAC reaction.

The macromolecular scope was further extended to the preparation of cross-linked materials. Thus, the formulations containing bisphenol A di(3-azido-2-hydroxypropan-1-ol) ether (**Az-3**), and 1-(prop-2-yn-1-yloxy)-2,2-bis((prop-2-yn-1-yloxy)methyl)butane (**Alk-5**) as multifunctional click components were irradiated in the presence of BPNs and Cu^{II} ligand under NIR light. The gelation was completed after 24 h (Scheme 3).

The photocuring process was also followed by differential scanning calorimetry (DSC). The DSC thermogram shows two exo-

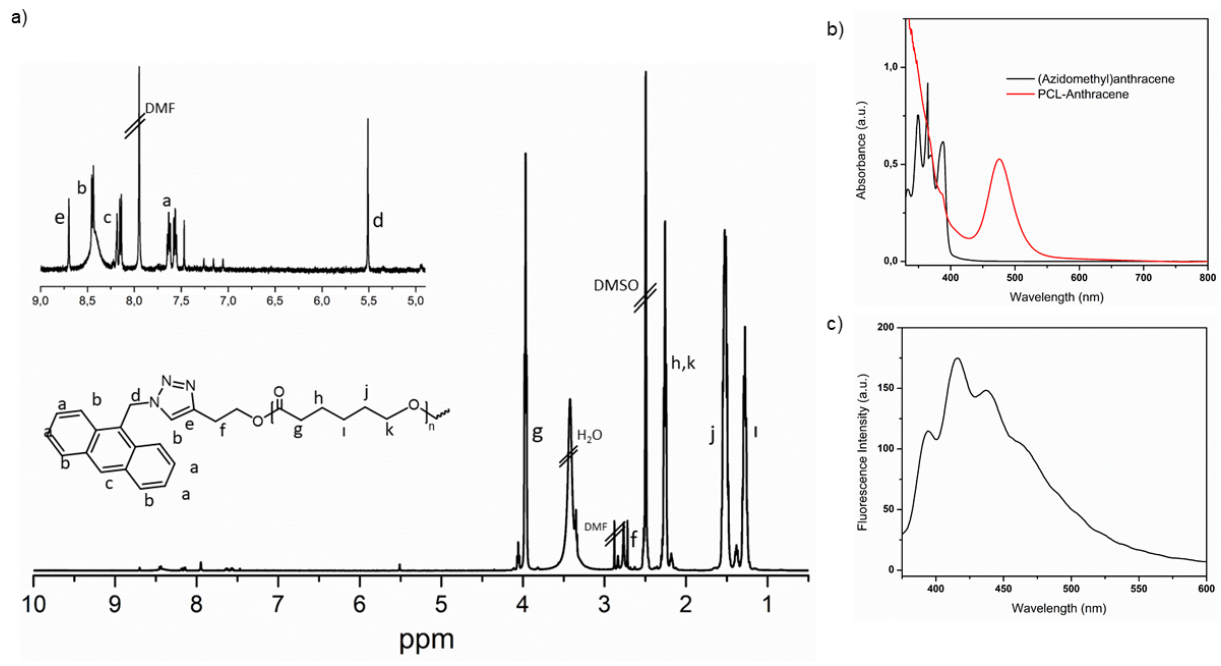
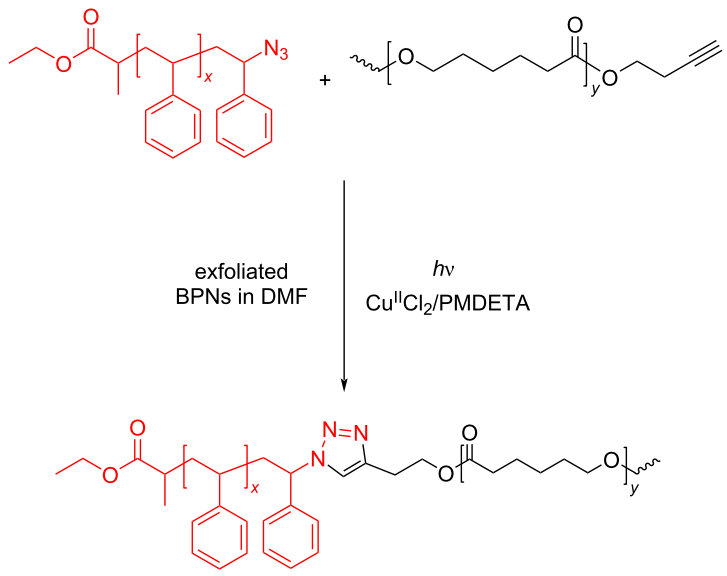


Figure 4: a) ^{1}H NMR spectrum of chain end modified **PCL-Anth**; b) UV–vis spectra of (azidomethyl)anthracene (black) and **PCL-Anth** (red); c) fluorescence emission spectrum of **PCL-Anth**.



Scheme 2: Synthesis of **PS-*b*-PCL** block copolymer via exfoliated BPNs-mediated photoinduced CuAAC reaction.

thermic peaks at 220.38 and 241.74 °C, corresponding to the photo click cure reaction in two stages (Figure 6a). Since a complete reaction of all the azide groups could not occur during the dynamic ramping of temperature, the residual azide groups decomposed at higher temperature. The IR spectrum of the cross-linked polymer further demonstrates the formation of a triazole ring by the decrease of the azide peak at 2100 cm^{-1} (Figure 6b).

Representative TEM images recorded at different magnifications of the resulting cross-linked polymer are shown in Figure 7. From the TEM images, it can be concluded that the

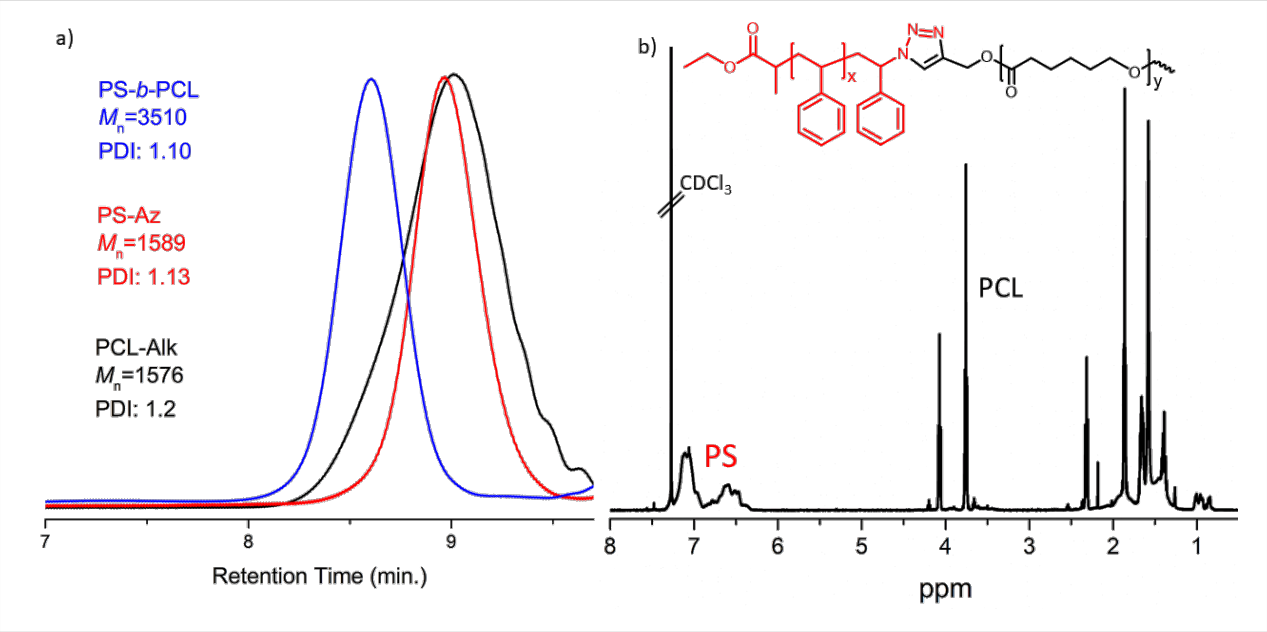
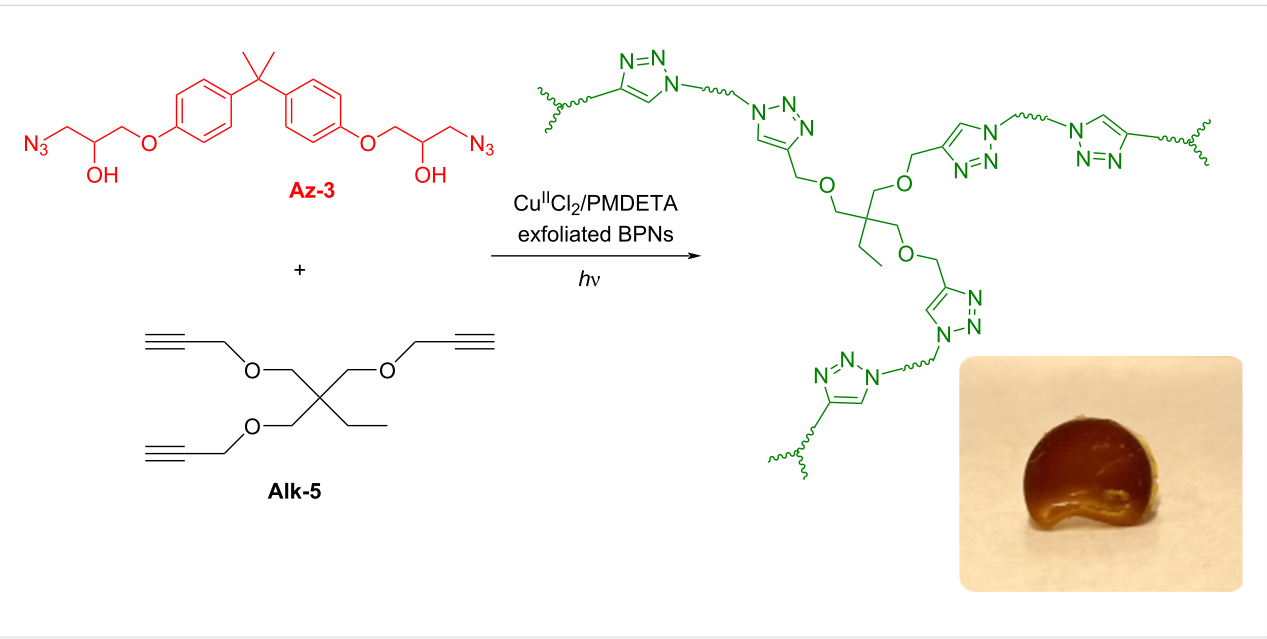


Figure 5: a) GPC traces of **PS-Az**, **PCL-Alk** and block copolymer (**Ps-*b*-PCL**) b) ^{1}H NMR spectrum of the block copolymer (**Ps-*b*-PCL**).



Scheme 3: Preparation of the cross-linked polymer by CuAAC reaction using multifunctional monomers, **Az-3** and **Alk-5**.

process leads to the formation of BPNs-embedded cross-linked polymers. The darker regions circled with yellow dashed line in Figure 6a were attributed to the BPNs while the other relatively lighter regions were ascribed to the cross-linked polymer. To further prove the existence of BPNs in the cross-linked structure, a high-angle annular dark-field scanning TEM (HAADF-STEM) image and the associated elemental mapping images for C, N, and P were recorded and depicted in Figure 7c and 7d. The elemental mapping images adequately demonstrated the presence and the distribution of P atoms that are attributed to BPNs in the cross-linked polymer in addition to C and N atoms (Figure 7d). In contrast to the cross-linked polymer, the distribution of BPNs in the block copolymer structure could not be visualized by TEM, HAADF-STEM, and elemental mapping images (Supporting Information File 1, Figures S5 and S6). This behavior is expected since BPNs are immobilized between the interconnected chains in the cross-linked structure.

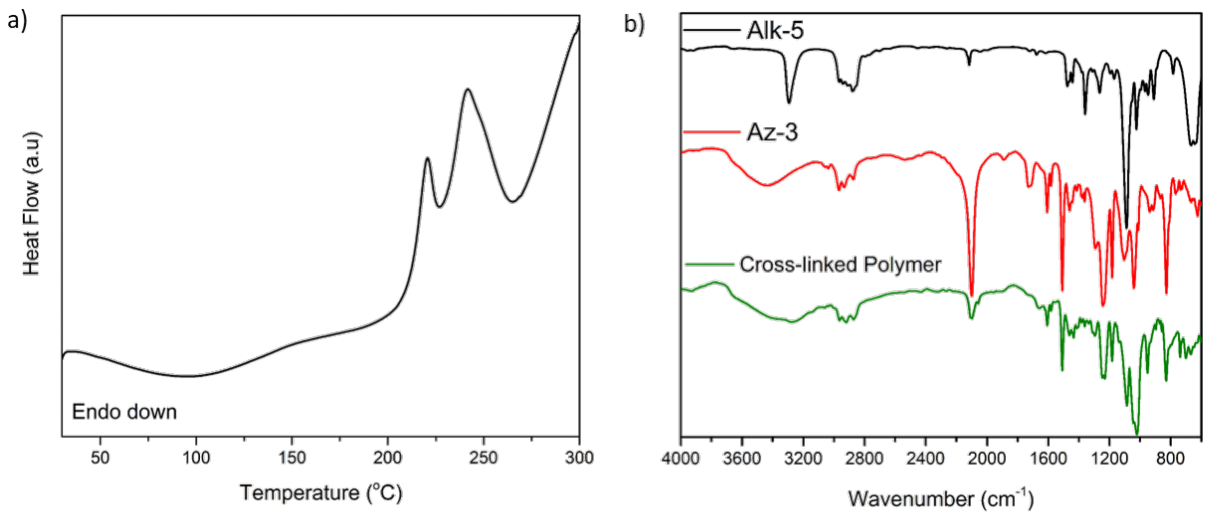


Figure 6: a) DSC thermogram of photoinduced synthesis of nanocomposite networks (heating rate: 10 °C/min). b) FTIR spectra of **Alk-5**, **Az-3** monomers and the corresponding cross-linked polymer.

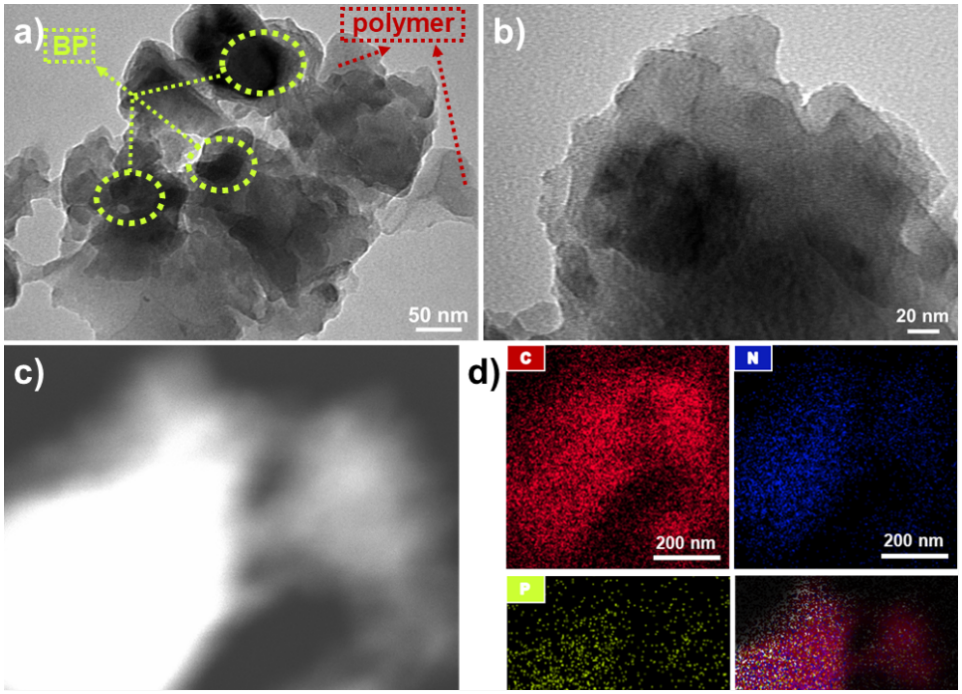


Figure 7: (a, b) TEM images of cross-linked polymer at two different magnifications, c) HAADF-STEM image and d) the associated EDS elemental mapping images of the cross-linked polymer.

Conclusion

In conclusion, we have demonstrated the use of BPNs as an efficient photoinitiator for the photoinduced CuAAC reactions under white LED and NIR light irradiation. The described method is applicable to organic and macromolecular syntheses. NIR irradiation appeared to be more efficient compared to the while LED due to the higher penetration in the dispersed media. In macromolecular syntheses, polymer chain-end functionalization, block copolymer formation of structurally different polymers and cross-linking polymerization can successfully be achieved by using suitably selected click components. This new method would dramatically extend the applications of photoin-

duced CuAAC reactions, particularly when the components are light sensitive at short wavelength region and spatial control is required.

Experimental

Materials

Red phosphorus (98.9%), tin (99.5%), and tin(IV) iodide (95%) were purchased from Alfa Aesar. Ethyl alcohol (absolute) was obtained from Sigma-Aldrich. Dimethyl sulfoxide (DMSO) was purchased from Merck. All chemicals and solvents were used as received without further purification for synthesis of black phosphorus. Benzyl bromide (Merck), phenylacetylene (Sigma), propargylamine (Sigma), propargyl alcohol (Sigma), *d*-dimethyl sulfoxide, (DMSO-d_6, Merck), *N*,*N*,*N*',*N*'',*N*''-pentamethyldiethylenetriamine (PMDETA, Aldrich), sodium azide (NaN_3, Panreac), copper(II) chloride ($Cu^{II}Cl_2$, Merck), black phosphorus, dimethyl sulfoxide (DMSO) was used as received. Propargyl acrylate (Sigma), styrene (Merck) were purified before by using a basic alumina column to remove the inhibitor and then stored in the fridge. ε-Caprolactone (Merck), and stannous octoate (Aldrich) were dried with CaH_2 under vacuum.

Characterizations

^{1}H NMR spectra were recorded at room temperature at 500 MHz on an Agilent VNMRS 500 spectrometer. Gel permeation chromatography (GPC) measurements were performed on a TOSOH EcoSEC GPC system equipped with an auto sampler system, a temperature-controlled pump, a column oven, a refractive index (RI) detector, a purge and degasser unit and a TSKgel superhZ2000, 4.6 mm ID × 15 cm × 2cm column. Tetrahydrofuran was used as an eluent at a flow rate of 1.0 mL/min at 40 °C. The refractive index detector was calibrated with polystyrene standards having narrow molecular-weight distributions. The data were analyzed using Eco-SEC analysis software. A Hitachi HT7700 (TEM) with EXALENS (120 kV) working at a high-resolution (HR) mode was used to obtain transmission electron microscopy (TEM) images, high-angle annular dark field (HAADF) scanning transmission microscope (STEM) images and the associated EDS elemental mapping images.

Synthesis of black phosphorus crystals and preparation of its nanosheets

Black phosphorus (BP) was prepared using a modified low-pressure chemical vapor transport method [40,42,43]. For the synthesis, 500 mg of red phosphorus, 20 mg of Sn and 10 mg of SnI_4 were placed into a quartz ampoule with the dimensions of 20 cm length and 1.5 cm width. The air was evacuated by vacuum, and the ampoule was left to dry at least for 30 min under vacuum. The sealed ampoule was placed horizontally in a muffle furnace. The applied heating program was as follows: firstly, the temperature raised to 893 K in 5 h and kept at this temperature for 5 h. Next, the temperature was lowered to 758 K in the span of 6 h and the temperature was kept at this temperature for 2 h. Finally, the oven was cooled to 393 K in 5 h, and it was left for natural cooling afterwards. After the heating process, the ampoule was cracked in dry toluene and the crystalline BP was separated. In order to remove surface impurities, the BP crystals were transferred into absolute ethanol and sonicated for 30 minutes. The sonicated crystals were carefully transferred to a Schlenk tube and dried under vacuum. The Schlenk tube was filled with argon and crushed under inert atmosphere. The produced BP crystals were stored under vacuum.

BP nanosheets were prepared by the liquid phase exfoliation of BP crystals. A specific amount of BP was dispersed thoroughly in DMSO by a sonication bath (200 W) for 10 h at 6 °C. The resulting BP nanosheets dispersion was kept under an inert atmosphere for the further use.

Preparation of azide and alkyne derivatives

Synthesis of benzyl azide (**Az-1**)

A literature procedure was used [44]. Product was obtained pale yellow oil, yield 96%. ^{1}H NMR (500 MHz, DMSO-d_6) δ 7.43–7.34 (m, 5H, -C_6H_5), 4.43 (s, 2H, CH_2-N_3). FTIR: 2108 cm^{-1}.

Synthesis of (azidomethyl)anthracene (**Az-2**)

A literature procedure was used [45]. 9-Hydroxymethylanthracene (7.40 mmol, 1 equiv) was added to DCM (50 mL) and cooled to 0 °C. Then, $SOCl_2$ (1.5 equiv) was slowly introduced to the reaction media and allowed to warm up to room temperature while being stirred for 1 h. The solvent was removed under vacuum and the residue redissolved in DMF (10 mL). Following dissolution of the compound, NaN_3 (1.5 equiv) was added, and the reaction was stirred at 50 °C. After 1 h, the reaction mixture was allowed to cool down, diluted with water and extracted with EtOAc. The combined organic phases were washed with brine, dried with anhydrous $MgSO_4$, filtered, and concentrated under vacuum. Brownish yellow crystalline solid, yield = 93%. ^{1}H NMR (500 MHz, DMSO-d_6) δ 8.70 (s, 1H), 8.44 (dd, 2H), 8.14 (dd, 2H), 7.64 (td, 2H), 7.56 (td, 2H), 5.51 (s, 2H); ^{13}C{^{1}H} NMR (DMSO-d_6, 125 MHz) δ 131.39, 130.72, 129.51, 129.06, 127.28, 126.96, 125.88, 124.51, 45.96.

Synthesis of bisphenol A di(3-azido-2-hydroxypropan-1-ol) ether (**Az-3**)

Diazido monomer, bisphenol A di(3-azido-2-hydroxypropan-1-ol) (**Az-3**) was synthesized according to a described method [46]. **Az-3** was obtained as light yellowish viscous oil and was directly used without further purification, yield 98%. ^{1}H NMR (500 MHz, $CDCl_3$) δ 7.15 (m, 4H), 6.82 (m, 4H), 4.16 (m, 2H),

4.0 (dd, 4H), 3.51 (m, 4H), 1.65 (s, 6H); $^{13}C\{^1H\}$ NMR ($CDCl_3$, 125 MHz) δ 131.38, 130.67, 129.51, 129.09, 127.26, 126.83, 125.80, 45.93.

Synthesis of 1-(prop-2-yn-1-yloxy)-2,2-bis((prop-2-yn-1yloxy)methyl)butane (**Alk-5**)

A literature procedure was followed [47]. The crude obtained product was then purified using column chromatography to give a clear oil, yield 70%. ^1H NMR (500 MHz, DMSO-d_6) δ 0.80 (t, 3H, CH_3), 1.30 (q, 2H, CH_2-CH_3), 3.30 (s, 6H, CH_2), 4.10 (d, 6H, CH_2-alkyne); $^{13}C\{^1H\}$ NMR (DMSO-d_6, 125 MHz) δ 7.84 (1C, CH_3), 23.33 (1C, CH_2), 42.82 (1C, C), 58.39 (3C, CH_2-alkyne), 70.13 (3C, CH_2), 77.24 (3C, CH_2), 80.83 (3C, C, alkyne).

Synthesis of ω-azido terminated polystyrene (**PS-Az**)

ω-Bromo functional polystyrene was synthesized by ATRP according to a reported procedure [48]. In a flask equipped with a magnetic stirrer, PS-Br (1 equiv) and sodium azide (5 equiv) were dissolved in 5 mL DMF. The reaction mixture was stirred at room temperature 24 h, then precipitated in 10-fold excess of methanol, filtered and dried in vacuum to yield PS-N_3. Yield 95% ($M_{n,GPC}$: 1589 g·mol^{-1}, M_w/M_n: 1.13). FTIR: 2096 cm^{-1}.

Synthesis of acetylene-terminated poly(ε-caprolactone) (**PCL-Alk**)

Acetylene-terminated PCL-Alk was synthesized according to a modified procedure [49]. To a Schlenk tube, 3-butyn-1-ol was dissolved in ε-caprolactone and heated to 110 °C under nitrogen. After the reaction mixture warmed up homogeneously, one drop of tin octoate was added to the reaction media and the solution was stirred for 3 hours. The obtained polymer was dissolved in chloroform and precipitated in methanol:water (2:1) to yield poly(ε-caprolactone). White solid, (85%) $M_{n,GPC}$: 1576 g·mol^{-1}, M_w/M_n: 1.2. FTIR: 2102 cm^{-1}.

Photoinduced CuAAC reactions

Synthesis of organic molecules

For the first step of the reaction an appropriate amount of black phosphorus was exfoliated in DMSO-d_6. In a typical experiment, exfoliated BP in DMSO-d_6 (0.5 mL) and azide compound (1 mmol, 1 equiv) were added to a NMR tube containing $Cu^{(II)}Cl_2$ (0.05 equiv), PMDETA (0.1 equiv). After 5 min, alkyne derivative (1 mmol, 1 equiv) was added slowly to the NMR tube. The reaction tube was irradiated by using a Philips 150 W PAR38E E27 halogen pressure glass type bulb with strong IR-A (NIR) emission. The light intensity inside the reaction tube was ≈200 mW·cm^{-2}. The light bulb was attached to the top of a photoreactor setup equipped with a large air cooling fan and the reaction temperature was kept constant at room temperature (24−25 °C). ^1H NMR spectra were recorded 4 h later.

Synthesis of anthracene functional poly(ε-caprolactone) (**PCL-Anth**)

The same process as in the block copolymerization was applied. **Az-2** (19.27 mg, 1 equiv), **PCL-Alk** (1 equiv), $CuCl_2$ (1 equiv) and PMDETA (1 equiv) were placed in a Schlenk tube. The tube was degassed by three freeze pump-thaw cycles. Then the tube was irradiated under NIR light for 48 h. After the given time, the mixture was diluted with THF and the copper complex was removed by passing through a neutral alumina column. Excess amount of THF was evaporated by a rotary evaporator. After precipitation of the mixture to cold methanol, the polymer was collected by filtration and dried under vacuum overnight. ^1H NMR was demonstrated in Figure 4.

Synthesis of polystyrene-*b*-poly(ε-caprolactone) (**PS-*b*-PCL**)

Firstly, under dark conditions BP was exfoliated in dry DMF by a sonic bath for 8 h at 10 °C. Subsequently, the solution was transferred into a centrifuge at 2500 rpm for 15 min. Terminally, this exfoliated BPNs with **PS-Az** (200 mg, 1 equiv), $Cu^{II}Cl_2$ (1 equiv), PMDETA (1 equiv) and **PCL-Alk** (1 equiv) were placed in a Schlenk tube. The tube was degassed by three freez-pump thaw cycles. Then the tube was irradiated with NIR light 48 h. At the end of the reaction, the mixture diluted THF and the copper complex was removed by passing it through a neutral alumina column. Excess amount of THF was evaporated by a rotary evaporator. After precipitation of the mixture to cold methanol, the polymer was collected by filtration and dried under vacuum overnight. $M_{n,GPC}$: 3510 g·mol^{-1}, M_w/M_n: 1.10.

Synthesis of cross-linked polymer

Az-3 and **Alk-5** was mixed in equal ratio (1 equiv) with $Cu^{II}Cl_2$ (0.05 equiv) and PMDETA (0.1 equiv) in a small transparent vial and 300 μL BPNs in DMF was added to the vial, then irradiated 4 h. After the gelation was completed, the gel was placed in DCM for 24 h hours, then filtered and dried 24 h in a vacuum oven.

Supporting Information

Supporting Information File 1

Characterisation data: ^1H NMR spectra of **Alk-1**, **Alk-2** and **Alk-3**, TEM, HAADF-STEM and associated EDS elemental mapping of **PS-*b*-PCL**.
[https://www.beilstein-journals.org/bjoc/content/supplementary/1860-5397-17-164-S1.pdf]

Funding

One of the authors, A. K., would like to thank the Council of Higher Education of Turkey for 100/2000 CoHE Doctoral Scholarship and TUBITAK 2211-A National Graduate Scholarship. Z. E. thanks to the Council of Higher Education (CoHE) and The Scientific and Technological Research Council of Turkey (TUBITAK) for Ph.D. scholarships (CoHE/100-2000 and TUBITAK 2211-C). The authors would like to thank to the Scientific and Technological Research Council of Turkey (Project Number: 120C121) and Istanbul Technical University Research Fund (Project Number: 42851).

ORCID® iDs

Zafer Eroglu - https://orcid.org/0000-0002-0601-2526
Önder Metin - https://orcid.org/0000-0003-1622-4992

References

1. Kolb, H. C.; Finn, M. G.; Sharpless, K. B. *Angew. Chem., Int. Ed.* **2001,** *40,* 2004–2021. doi:10.1002/1521-3773(20010601)40:11<2004::aid-anie2004>3.0.co;2-5
2. Rostovtsev, V. V.; Green, L. G.; Fokin, V. V.; Sharpless, K. B. *Angew. Chem.* **2002,** *114,* 2708–2711. doi:10.1002/1521-3757(20020715)114:14<2708::aid-ange2708>3.0.co;2-0
3. Tornøe, C. W.; Christensen, C.; Meldal, M. *J. Org. Chem.* **2002,** *67,* 3057–3064. doi:10.1021/jo011148j
4. Lutz, J.-F.; Börner, H. G. *Prog. Polym. Sci.* **2008,** *33,* 1–39. doi:10.1016/j.progpolymsci.2007.07.005
5. Kolb, H. C.; Sharpless, K. B. *Drug Discovery Today* **2003,** *8,* 1128–1137. doi:10.1016/s1359-6446(03)02933-7
6. Lutz, J.-F. *Angew. Chem., Int. Ed.* **2007,** *46,* 1018–1025. doi:10.1002/anie.200604050
7. Xi, W.; Scott, T. F.; Kloxin, C. J.; Bowman, C. N. *Adv. Funct. Mater.* **2014,** *24,* 2572–2590. doi:10.1002/adfm.201302847
8. Johnson, J. A.; Finn, M. G.; Koberstein, J. T.; Turro, N. J. *Macromol. Rapid Commun.* **2008,** *29,* 1052–1072. doi:10.1002/marc.200800208
9. Kempe, K.; Krieg, A.; Becer, C. R.; Schubert, U. S. *Chem. Soc. Rev.* **2012,** *41,* 176–191. doi:10.1039/c1cs15107j
10. Moses, J. E.; Moorhouse, A. D. *Chem. Soc. Rev.* **2007,** *36,* 1249–1262. doi:10.1039/b613014n
11. Adzima, B. J.; Tao, Y.; Kloxin, C. J.; DeForest, C. A.; Anseth, K. S.; Bowman, C. N. *Nat. Chem.* **2011,** *3,* 256–259. doi:10.1038/nchem.980
12. Tasdelen, M. A.; Yagci, Y. *Angew. Chem., Int. Ed.* **2013,** *52,* 5930–5938. doi:10.1002/anie.201208741
13. Doran, S.; Murtezi, E.; Barlas, F. B.; Timur, S.; Yagci, Y. *Macromolecules* **2014,** *47,* 3608–3613. doi:10.1021/ma5007039
14. Lan, Y.; Lu, Y.; Ren, Z. *Nano Energy* **2013,** *2,* 1031–1045. doi:10.1016/j.nanoen.2013.04.002
15. Sangermano, M.; Rodriguez, D.; Gonzalez, M. C.; Laurenti, E.; Yagci, Y. *Macromol. Rapid Commun.* **2018,** *39,* 1800250. doi:10.1002/marc.201800250
16. Franchi, D.; Amara, Z. *ACS Sustainable Chem. Eng.* **2020,** *8,* 15405–15429. doi:10.1021/acssuschemeng.0c05179
17. Yanalak, G.; Doganay, F.; Eroglu, Z.; Kucukkececi, H.; Aslan, E.; Ozmen, M.; Bas, S. Z.; Metin, O.; Hatay Patir, I. *Appl. Surf. Sci.* **2021,** *557,* 149755. doi:10.1016/j.apsusc.2021.149755
18. Dadashi-Silab, S.; Bildirir, H.; Dawson, R.; Thomas, A.; Yagci, Y. *Macromolecules* **2014,** *47,* 4607–4614. doi:10.1021/ma501001m
19. Kiskan, B.; Zhang, J.; Wang, X.; Antonietti, M.; Yagci, Y. *ACS Macro Lett.* **2012,** *1,* 546–549. doi:10.1021/mz300116w
20. Kaya, K.; Kiskan, B.; Kumru, B.; Schmidt, B. V. K. J.; Yagci, Y. *Eur. Polym. J.* **2020,** *122,* 109410. doi:10.1016/j.eurpolymj.2019.109410
21. Dadashi-Silab, S.; Tasdelen, M. A.; Kiskan, B.; Wang, X.; Antonietti, M.; Yagci, Y. *Macromol. Chem. Phys.* **2014,** *215,* 675–681. doi:10.1002/macp.201400063
22. Dadashi-Silab, S.; Atilla Tasdelen, M.; Mohamed Asiri, A.; Bahadar Khan, S.; Yagci, Y. *Macromol. Rapid Commun.* **2014,** *35,* 454–459. doi:10.1002/marc.201300704
23. Gao, T.; Su, X.; Xu, H.; Hu, H.; Zeng, C.; Gao, Y. *ChemistrySelect* **2020,** *5,* 15010–15014. doi:10.1002/slct.202004130
24. Samuel, A. G.; Nagarajan, K.; Cidhuraj, K.; Gopal, B.; Chakravarty, S.; Selvaraj, V.; Lourdusamy, E.; Bhagavathsingh, J. *Appl. Organomet. Chem.* **2020,** *34,* e6017. doi:10.1002/aoc.6017
25. Dadashi-Silab, S.; Kiskan, B.; Antonietti, M.; Yagci, Y. *RSC Adv.* **2014,** *4,* 52170–52173. doi:10.1039/c4ra09954k
26. Shen, Z.-Y.; Li, L.-Y.; Li, Y.; Wang, C.-C. *J. Colloid Interface Sci.* **2011,** *354,* 196–201. doi:10.1016/j.jcis.2010.10.023
27. Colucci, G.; Mana, S.; Conzatti, L.; Sangermano, M. *Surf. Coat. Technol.* **2012,** *206,* 2719–2724. doi:10.1016/j.surfcoat.2011.12.007
28. Mokbel, H.; Graff, B.; Dumur, F.; Lalevée, J. *Macromol. Rapid Commun.* **2020,** *41,* 2000289. doi:10.1002/marc.202000289
29. Dietlin, C.; Schweizer, S.; Xiao, P.; Zhang, J.; Morlet-Savary, F.; Graff, B.; Fouassier, J.-P.; Lalevée, J. *Polym. Chem.* **2015,** *6,* 3895–3912. doi:10.1039/c5py00258c
30. Li, Z.; Zou, X.; Shi, F.; Liu, R.; Yagci, Y. *Nat. Commun.* **2019,** *10,* 3560. doi:10.1038/s41467-019-11522-0
31. Kocaarslan, A.; Tabanli, S.; Eryurek, G.; Yagci, Y. *Angew. Chem., Int. Ed.* **2017,** *56,* 14507–14510. doi:10.1002/anie.201707944
32. Suerkan, A.; Alkan, E. A.; Kaya, K.; Udum, Y. A.; Toppare, L.; Yagci, Y. *Prog. Org. Coat.* **2021,** *154,* 106189. doi:10.1016/j.porgcoat.2021.106189
33. Kütahya, C.; Zhai, Y.; Li, S.; Liu, S.; Li, J.; Strehmel, V.; Chen, Z.; Strehmel, B. *Angew. Chem., Int. Ed.* **2021,** *60,* 10983–10991. doi:10.1002/anie.202015677
34. Zhu, M.; Osakada, Y.; Kim, S.; Fujitsuka, M.; Majima, T. *Appl. Catal., B* **2017,** *217,* 285–292. doi:10.1016/j.apcatb.2017.06.002
35. Ling, X.; Wang, H.; Huang, S.; Xia, F.; Dresselhaus, M. S. *Proc. Natl. Acad. Sci. U. S. A.* **2015,** *112,* 4523–4530. doi:10.1073/pnas.1416581112
36. Han, C.; Li, Y.-H.; Li, J.-Y.; Qi, M.-Y.; Tang, Z.-R.; Xu, Y.-J. *Angew. Chem.* **2021,** *133,* 8041–8049. doi:10.1002/ange.202015756
37. Li, Y.; Wang, H.; Zhang, X.; Wang, S.; Jin, S.; Xu, X.; Liu, W.; Zhao, Z.; Xie, Y. *Angew. Chem., Int. Ed.* **2021,** *60,* 12891–12896. doi:10.1002/anie.202101090
38. Kalay, E.; Küçükkeçeci, H.; Kilic, H.; Metin, Ö. *Chem. Commun.* **2020,** *56,* 5901–5904. doi:10.1039/d0cc01874k
39. Eken Korkut, S.; Küçükkeçeci, H.; Metin, Ö. *ACS Appl. Mater. Interfaces* **2020,** *12,* 8130–8139. doi:10.1021/acsami.9b18917

40. Kocaarslan, A.; Eroglu, Z.; Yilmaz, G.; Metin, O.; Yagci, Y. *ACS Macro Lett.* **2021,** *10,* 679–683. doi:10.1021/acsmacrolett.1c00298
41. Kütahya, C.; Yagci, Y.; Strehmel, B. *ChemPhotoChem* **2019,** *3,* 1180–1186. doi:10.1002/cptc.201900012
42. Tiouitchi, G.; Ali, M. A.; Benyoussef, A.; Hamedoun, M.; Lachgar, A.; Benaissa, M.; Kara, A.; Ennaoui, A.; Mahmoud, A.; Boschini, F.; Oughaddou, H.; El Kenz, A.; Mounkachi, O. *Mater. Lett.* **2019,** *236,* 56–59. doi:10.1016/j.matlet.2018.10.019
43. Zhao, M.; Qian, H.; Niu, X.; Wang, W.; Guan, L.; Sha, J.; Wang, Y. *Cryst. Growth Des.* **2016,** *16,* 1096–1103. doi:10.1021/acs.cgd.5b01709
44. Wilkening, I.; del Signore, G.; Hackenberger, C. P. R. *Chem. Commun.* **2011,** *47,* 349–351. doi:10.1039/c0cc02472d
45. Borissov, A.; Lim, J. Y. C.; Brown, A.; Christensen, K. E.; Thompson, A. L.; Smith, M. D.; Beer, P. D. *Chem. Commun.* **2017,** *53,* 2483–2486. doi:10.1039/c7cc00727b
46. Gong, T.; Adzima, B. J.; Baker, N. H.; Bowman, C. N. *Adv. Mater. (Weinheim, Ger.)* **2013,** *25,* 2024–2028. doi:10.1002/adma.201203815
47. Baranek, A.; Song, H. B.; McBride, M.; Finnegan, P.; Bowman, C. N. *Macromolecules* **2016,** *49,* 1191–1200. doi:10.1021/acs.macromol.6b00137
48. Arslan, M.; Yilmaz, G.; Yagci, Y. *Polym. Chem.* **2015,** *6,* 8168–8175. doi:10.1039/c5py01465d
49. Hoogenboom, R.; Moore, B. C.; Schubert, U. S. *Chem. Commun.* **2006,** 4010–4012. doi:10.1039/b608313g

License and Terms

This is an Open Access article under the terms of the Creative Commons Attribution License (https://creativecommons.org/licenses/by/4.0). Please note that the reuse, redistribution and reproduction in particular requires that the author(s) and source are credited and that individual graphics may be subject to special legal provisions.

The license is subject to the *Beilstein Journal of Organic Chemistry* terms and conditions: (https://www.beilstein-journals.org/bjoc/terms)

The definitive version of this article is the electronic one which can be found at: https://doi.org/10.3762/bjoc.17.164

BEILSTEIN JOURNAL OF ORGANIC CHEMISTRY

In-depth characterization of self-healing polymers based on π–π interactions

Josefine Meurer‡[1,2], Julian Hniopek‡[3,4,5], Johannes Ahner[1,2], Michael Schmitt[3,4], Jürgen Popp[3,4,5], Stefan Zechel[1,2], Kalina Peneva[1,2] and Martin D. Hager*[1,2]

Full Research Paper

Open Access

Address:
[1]Laboratory of Organic and Macromolecular Chemistry (IOMC), Friedrich Schiller University Jena, Humboldstr. 10, 07743 Jena, Germany, [2]Jena Center for Soft Matter (JCSM), Friedrich Schiller University Jena, Philosophenweg 7, 07743 Jena, Germany, [3]Institute of Physical Chemistry (IPC), Friedrich Schiller University Jena, Helmholtzweg 4, 07743 Jena, Germany, [4]Abbe Center of Photonics (ACP), Friedrich Schiller University Jena, Albert-Einstein-Straße 6, 07745 Jena, Germany and [5]Leibniz Institute of Photonic Technology (IPHT), e. V. Jena, Albert-Einstein-Straße 9, 07745 Jena, Germany

Email:
Martin D. Hager* - martin.hager@uni-jena.de

* Corresponding author ‡ Equal contributors

Keywords:
characterization of polymers; π–π-interactions; self-healing polymers; supramolecular polymers

Beilstein J. Org. Chem. **2021,** *17,* 2496–2504.
https://doi.org/10.3762/bjoc.17.166

Received: 03 July 2021
Accepted: 14 September 2021
Published: 29 September 2021

This article is part of the thematic issue "Polymer chemistry: fundamentals and applications".

Guest Editor: B. V. K. J. Schmidt

© 2021 Meurer et al.; licensee Beilstein-Institut.
License and terms: see end of document.

Abstract

The self-healing behavior of two supramolecular polymers based on π–π-interactions featuring different polymer backbones is presented. For this purpose, these polymers were synthesized utilizing a polycondensation of a perylene tetracarboxylic dianhydride with polyether-based diamines and the resulting materials were investigated using various analytical techniques. Thus, the molecular structure of the polymers could be correlated with the ability for self-healing. Moreover, the mechanical behavior was studied using rheology. The activation of the supramolecular interactions results in a breaking of these noncovalent bonds, which was investigated using IR spectroscopy, leading to a sufficient increase in mobility and, finally, a healing of the mechanical damage. This scratch-healing behavior was also quantified in detail using an indenter.

Introduction

Damage inflicted on different materials is omnipresent. Consequently, nature established a mechanism dealing with this problem [1]. The regeneration after a damage is one of nature´s great abilities. For instance, a broken bone is healed [2] and sometimes even whole limbs can be regenerated as known from the amphib axolotl [3]. Additionally, nonliving natural materials can also be healed such as mussel byssus threads [4]. This specific process is based on reversible interactions, which are integrated in the chemical structure of the proteins of the thread [5]. Zinc–histidine metal complexes which are part of the protein's

structure enable the material to regenerate its mechanical performance after a damage event [1,6].

Besides the examples of self-healing/regeneration that exist in Nature, the general concept could also be transferred to different synthetic materials. Hereby, two concepts can be distinguished. In extrinsic self-healing materials, a material flow is achieved by the encapsulation of microcapsules [7] or microchannels [8] filled with liquid healing agent. In contrast, intrinsic self-healing [9] and, thus, regeneration of the materials without any additional required healing agents, can be obtained by the integration of dynamic covalent bonds or [10], as known from Nature, by supramolecular ones [11,12]. In previous studies, several of these interactions were already applied such as metal–ligand interactions [13,14], hydrogen bonds [15,16] or halogen bonds [17]. Furthermore, π–π interactions also feature a reversible behavior and were therefore utilized for the design of different self-healing polymers [18-20]. In this context, mainly the interaction between π-electron-deficient diimide groups and π-electron-rich pyrene moieties was applied resulting in a very strong and stable supramolecular bond [21,22]. The noncovalent interaction was found to be reversible and, therefore, enabled healing of scratches [18].

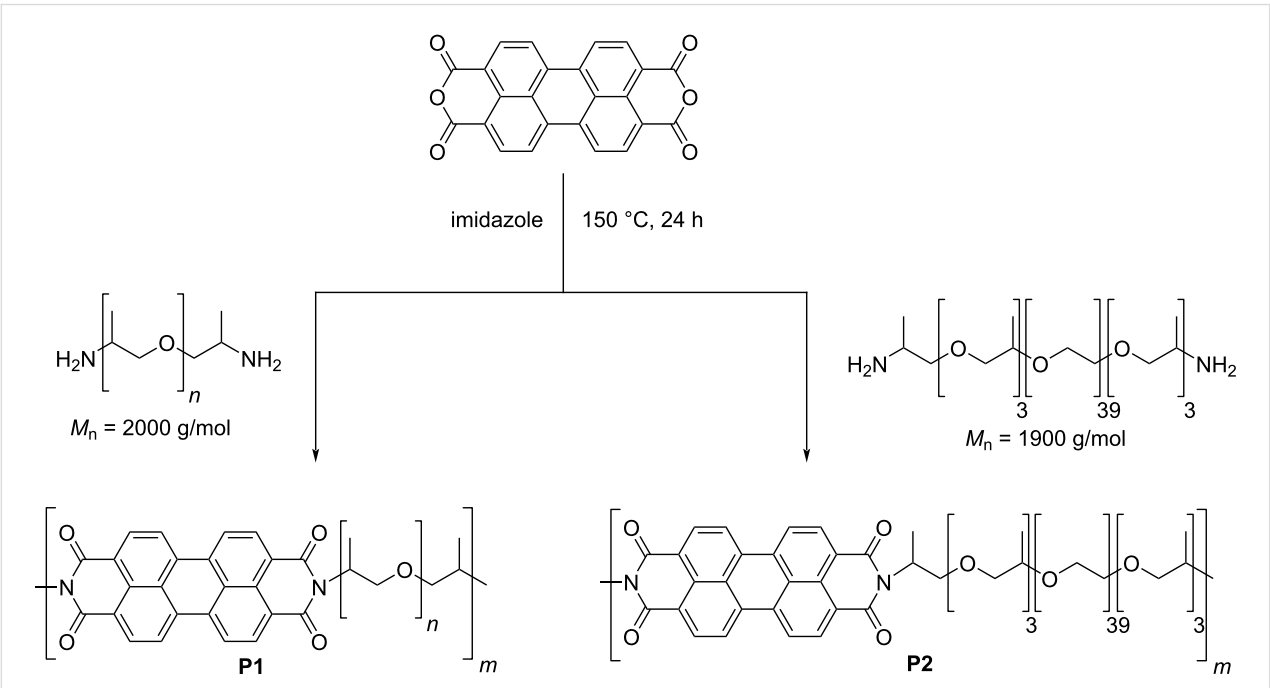
However, little is known about the exact healing mechanism on the molecular scale and the correlation to the macroscopic properties of such polymers. For this purpose, the current study will focus on the design of polymers containing π–π interactions and the quantification of the healing behavior as well as the in-depth characterization of the molecular behavior and the macroscopic properties, which reveals new insights into the self-healing materials based on π–π interactions.

Results and Discussion

Polymer synthesis

For the synthesis of supramolecular polymers based on π-π interactions a literature reported procedure was utilized (see Scheme 1), which described the synthesis of polypropylene glycol-based polymers featuring aromatic diimides [23]. Following the procedure, perylene-3,4,9,10-tetracarboxylic dianhydride was converted with poly(propylene glycol) bis(2-aminopropyl ether) with a molar mass of approximately 2000 g/mol resulting in polymer **P1**. In order to study the influence of the polymer backbone on the material's properties, the diamine containing polymer was exchanged to a triblock copolymer of poly(propylene glycol)-*block*-poly(ethylene glycol)-*block*-poly(propylene glycol) (PPG_3-PEG_{39}-PPG_3) featuring also two amine groups as end groups. The molar mass of this reactant was 1900 g/mol. The conversion with perylene-3,4,9,10-tetracarboxylic dianhydride resulted in polymer **P2**. In both synthesis protocols imidazole was applied as a catalyst in order to obtain higher molar masses.

Subsequently, both polymers were characterized regarding their structure. For this purpose, size exclusion chromatography (SEC) was performed revealing a molar mass of



Scheme 1: Schematic representation of the polymer synthesis of **P1** and **P2**.

M_n = 11,400 g/mol for **P1** and M_n = 17,400 g/mol for **P2** with respect to a PEG-standard. The SEC traces of both polymers are depicted in Supporting Information File 1. Furthermore, the polymers were analyzed using NMR spectroscopy. Herein, all signals could be assigned to both moieties within the polymers, the perylene and the polymer backbone. All spectra are shown in Supporting Information File 1.

Characterization of the polymers

After the synthesis of the polymers, the material and structural properties were analyzed in detail in order to study the molecular behavior and to correlate these results later with the healing behavior of the polymers. Firstly, the thermal properties of both polymers were investigated via differential scanning calorimetry (DSC) and thermogravimetric analysis (TGA). The TGA revealed a high thermal stability up to a temperature of 370 °C (for curves see Supporting Information File 1). The temperature was determined at a residual mass of 95%. The DSC on the other hand indicates several thermal transitions (see Figure 1). Both polymers feature a glass transition temperature (T_g) at −58 °C (**P1**) and −51 °C (**P2**), respectively. Furthermore, the polymers have an endothermic transition at 129 °C (**P1**) and 126 °C (**P2**). This transition is associated with the activation of the perylene domains, which was also reported in literature [23]. During cooling, the reformation of the perylene domain was also observed. Finally, **P2** featured a second endothermic transition at 13 °C, which is based on the melting of the short PEG-block [24].

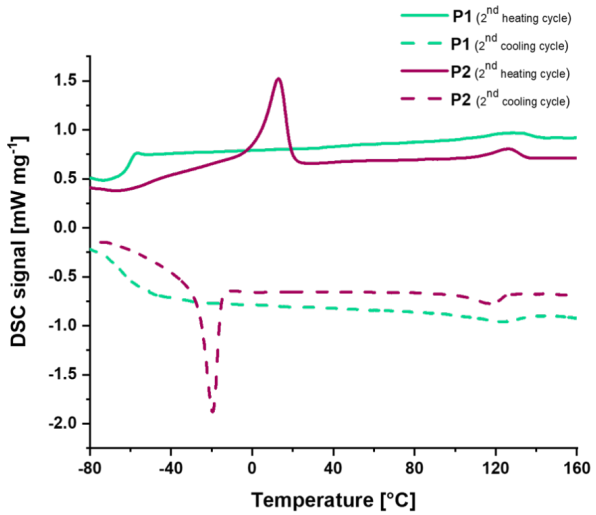


Figure 1: DSC-analysis of the polymers **P1** and **P2** (second heating and cooling cycle; 20 K/min for heating and cooling) with a glass transition temperature (T_g) at –58 °C (**P1**) and –51 °C (**P2**) and the endothermic transition at 129 °C (**P1**) and 126 °C (**P2**). In addition, **P2** shows a T_m at 13 °C.

Furthermore, both polymers were characterized via rheology and dynamic mechanical thermo-analysis (DMTA). The DMTA of **P1** and **P2** is depicted in Figure 2, revealing a network structure below temperatures of 120 °C. Above this temperature, a sharp transition (within a very small temperature range) and a significant drop of storage and loss modulus could be observed. Accordingly, this transition is associated with the endothermic signal measured in the DSC and based on the activation of the π–π interactions. Such a behavior could also be observed for other supramolecular polymers; however, the temperature window, in which the drop of the storage and loss moduli occurred, is rather small compared to other self-healing supramolecular polymers, e.g., metallopolymers [25].

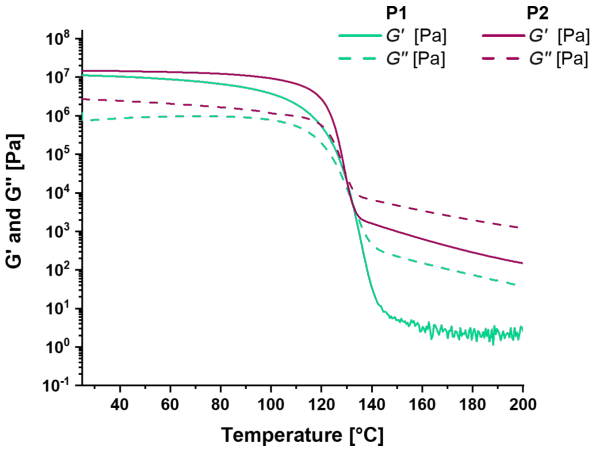


Figure 2: DMTA analysis of **P1** and **P2** showing the transition at around 130 °C due to the reversible π–π interactions.

Supramolecular polymers feature certain temperature ranges, in which the noncovalent bond is activated. The degree of reversibility can be determined by the supramolecular bond lifetime [26]. For example, a study regarding ionomers revealed a strong correlation of the bond lifetime with the healing behavior [27]. A similar behavior was also observed for metallopolymers [13]. Consequently, the polymers **P1** and **P2** were also studied by frequency sweeps at certain temperatures (see Figure 3). At temperatures below the endothermic transition at 125–130 °C, no crossover of G' and G'' could be observed indicating no active supramolecular bonds. Furthermore, at this temperature (80 °C) G' is higher than G'' indicating a network structure of the polymers. This finding correlates with the DSC results, since the π–π interactions are not activated and, therefore, the polymer network is intact.

Within the transition, the frequency sweeps revealed a crossover of storage and loss modulus showing the activation of

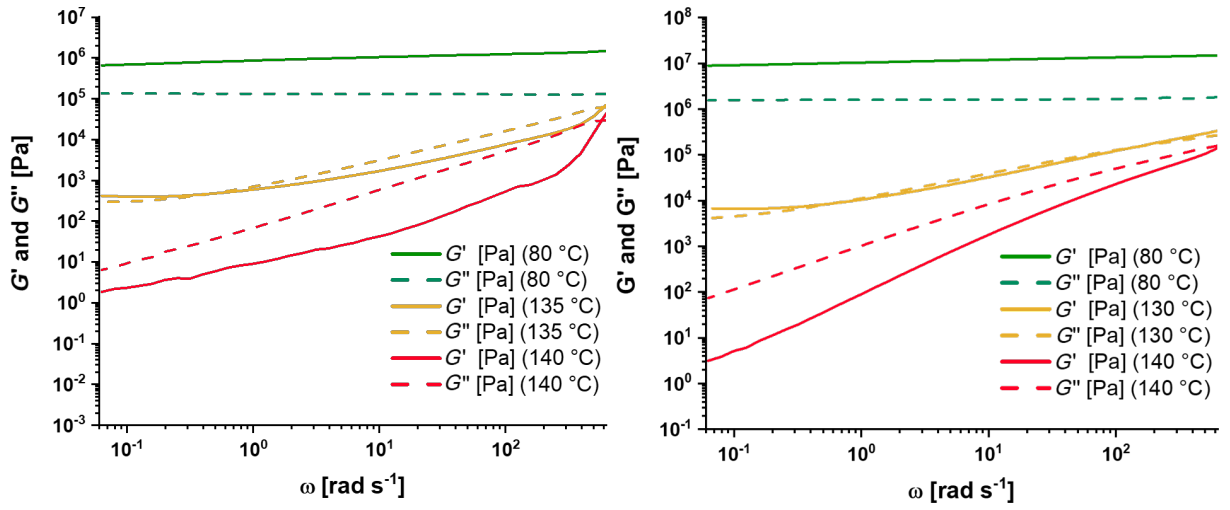


Figure 3: Frequency sweeps of polymers **P1** (left) and **P2** (right).

the π–π interactions, which goes hand in hand with the DSC results. Thus, a dynamic network structure could be revealed. The supramolecular bond lifetime was determined to be 15.87 s at 135 °C (**P1**) and 10.18 s at 130 °C (**P2**), respectively. The calculation was performed according to literature and Equation 1 [27].

$$\text{Supramolecular bond lifetime} = 1/\text{frequency}\left(\text{crossover}\right) \quad (1)$$

However, at higher temperatures also no crossover could be observed, which is also in line with findings for other supramolecular bonds like ionic interactions [27]. In this temperature range, G'' is higher than G' showing that the polymer is uncrosslinked. Thus, the mobility is very high, which is a precondition for the healing.

To get further insight into the molecular behavior of **P1** and **P2**, temperature dependent IR spectroscopy experiments of drop casted films of the respective polymers were carried out. The respective polymers were heated to 150 °C and an IR spectrum was recorded every 20 K. Afterwards the polymers were air cooled and further spectra at 100, 70, and 25 °C were recorded.

Figure 4 displays the aromatic C=C (1570–1605 cm^{-1}) and C=O stretching (1640–1710 cm^{-1}) region of the infrared spectra of **P1** recorded during heating. These regions are specific to the perylene moieties in the polymers and, therefore, allow a direct observation of the π–π interactions in the polymer. Both the C=C and C=O vibrations are sensitive to the electron density in the perylene systems, which changes depending on the strength of π–π interactions [28-30].

During heating, the C=C stretching vibrations located at 1578 and 1594 cm^{-1} show opposite behavior regarding their wavenumber position: While the band at 1578 cm^{-1} shifts to slightly higher wavenumbers (indicating more electron density in the perylene rings), the band at 1594 cm^{-1} shifts to slightly lower frequencies (indicating less electron density in the perylene rings). This seemingly counterintuitive behavior can be explained by the fact that the perylene-moieties act as both π-donors and -acceptors. Weakening of π–π interactions therefore results in higher electron densities in some part of the perylene moiety, while in other parts the electron density decreases. The C=O vibrations at 1656 and 1698 cm^{-1} on the other hand both shift to higher wavenumbers, indicating a strengthening of the carbon-oxygen bond. This is caused by a weakening of inter-perylene C–H–O interactions that also contribute to the stacking behavior [28,29], which in turn increases the electron density in the C=O bond.

In addition to these shifts in band positions, all bands show noticeable broadening during heating, which is most significant for the C=O vibration at 1656 cm^{-1}. This indicates a broader distribution of species contributing to the IR spectrum, which is consistent with increased mobility of the perylene moieties which allows for more possible geometries. Furthermore, it is evident that the broadening of the band shows an intensive increase at 150 °C. This nonlinear behavior indicates a drastic change in molecular structure around this temperature range, which corresponds to the observed signals in the DSC measurements and the findings of the DMTA analysis. The slight difference in temperature can be explained by the different experimental setups (open system for IR measurements, closed system

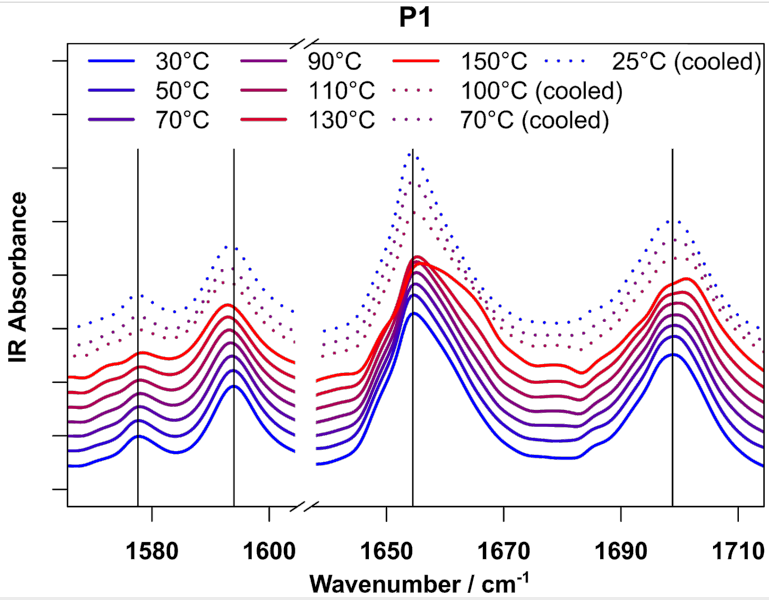


Figure 4: Temperature dependent IR spectra of **P1** drop casted on KBr in the C=C (1570–1605 cm^{-1}) and C=O stretching region (1640–1710 cm^{-1}). During heating, slight shifts in the position of all bands (1578 cm^{-1}: +1 cm^{-1}; 1594: −1.5 cm^{-1}; 1656 cm^{-1}: +0.8 cm^{-1}; 1698: +1.5 cm^{-1}. These shifts are partially reversed while cooling the polymer, indicating a reversible cause for the shifts. Additionally, all bands exhibit broadening during heating, especially noticeable at 150 °C, indicating a broader distribution of species contributing to the IR spectrum.

for DSC) and the different sample preparations as well as different applied heating rates.

For **P2,** the observations (see Supporting Information File 1) are generally the same; however; these changes are much weaker for lower temperatures. While for **P1** a slight band shift can be observed even for 50 and 70 °C, **P2** only shows noticeable shifts at higher temperature. This aspect is consistent with the higher rigidity of **P2** at lower temperatures, caused by the presence of a second phase transition of the PEG moieties observed in the DSC. Nevertheless, at 150 °C, **P2** also shows the clear broadening of bands, which is consistent with the very similar positions for the perylene π–π interaction signal in the DSC.

All these findings clearly support that at increased temperatures the perylene–perylene π–π interactions are significantly weakened, which increases the mobility of the chains. Furthermore, the reversible nature of these processes is indicated by the recovery of the band shifts and band broadenings upon cooling of the polymers to room temperature.

Self-healing behavior

Finally, the healing behavior of the polymers was studied in detail. For this purpose, an established method was applied enabling the detailed analysis of the scratch healing behavior by investigating the volume of the scratch [31,32]. A scratch was introduced into the material by using an indenter, afterwards, the sample was twisted to 90° and the profile was measured using an indenter resulting in the possibility to calculate the volume of the scratch. The subsequent heating at a certain temperature (80 °C, 125 °C or 150 °C) resulted in a healing behavior, which was quantified afterwards by measuring the profile again.

Using this approach, **P1** was studied first and the results are summarized in Table 1. For **P1**, a nearly complete healing at 150 °C was observed for the first scratch (see Figure 5) and a partial healing for the second scratch (see Supporting Information File 1). The healing behavior at 80 °C was significantly lower compared to 150 °C (see Supporting Information File 1) and the scratch could still be detected after 36 h at 80 °C. Furthermore, the healing was studied at 125 °C, which corresponds to the temperature, at which the change of the mechanical properties and flow behavior was started (see results of DMTA). Hereby, a partial healing was also observed (healing efficiency 50.64%, for pictures see Supporting Information File 1). Looking closer at the 3D-profiles, it can be seen that the depth of the scratch was reduced by more than 60% (from max. 64 µm to max. 23 µm). However, the width and the length of the scratch is nearly unchanged. Thus, the overall healing efficiency is lower compared to the reduction of the scratch depth.

In contrast, the analysis of the healing behavior of **P2** was just impossible. The scratching of the material resulted in no measurable scratch, which is presumably associated with the melting of the PEG-block at temperatures below room tempera-

Table 1: Overview of the healing of **P1**.

Scratch	Healing time/ temperature	Volume before healing [µm³]	Volume after healing [µm³]	Healing efficiency[a]
1	18 h; 150 °C	120,934,901	41,574	99.97%
2	18 h; 150 °C	33,233,081	8,757,225	73.65%
3[b]	18 h; 80 °C	23,741,395	12,086,157	49.09%
	18 h; 80 °C	12,086,157	11,194,985	7.37%
4	18 h; 125 °C	22,119,541	10,917,396	50.64%

[a]The healing efficiency was calculated based on a literature reported equation [31,32]. [b]The third scratch was healed at 80 °C for 18 h and afterwards, it was further healed again for 18 h at 80 °C. The overall healing efficiency is 52.85%.

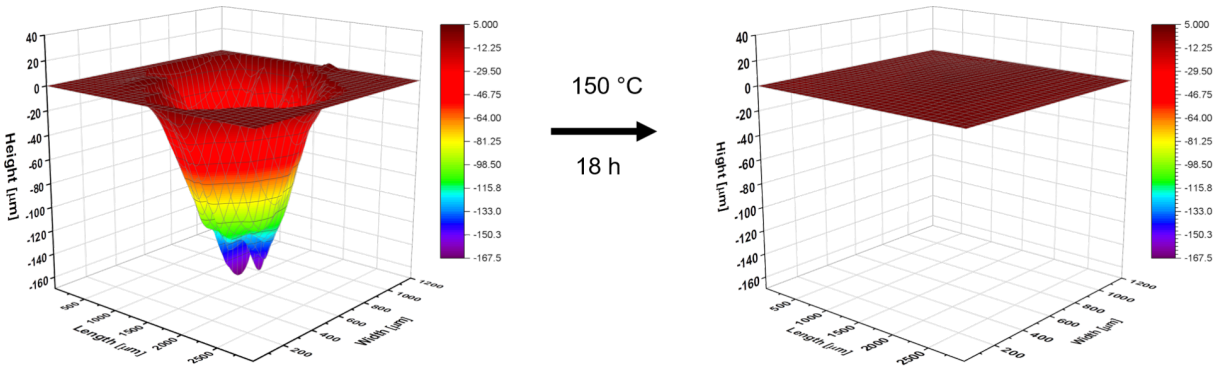


Figure 5: Schematic representation of the first healing of **P1** at 150 °C.

ture (see Supporting Information File 1). Thus, the material seems to feature a highly efficient elastic recovery (see Supporting Information File 1 for the "scratch" analysis) resulting in a (fast) crack closure behavior without the necessity of activating the supramolecular π–π interactions. Consequently, the healing of **P2** could not be analyzed in detail since the polymer backbone seems to influence the mobility behavior of the material significantly.

The observed healing behavior of **P1** goes hand in hand with the structural analysis of the material before. Since the healing behavior is based on π–π interactions, a sufficient healing could only be observed at temperatures above the activation of the π–π interactions. At temperatures below the activation, the healing was incomplete and presumably associated with the elastic recovery of the material. Consequently, for the first time, a correlation between the structure behavior of polymers featuring reversible π–π interactions and the healing behavior could be obtained.

Conclusion

Supramolecular polymers based on π–π interactions were synthesized and characterized in detail. The mechanical and thermal behavior was studied revealing an activation of the supramolecular interactions at 125 °C. This finding could also be verified by temperature-depending IR-spectroscopy indicating a broadening of the aromatic signals at 150 °C, which correlates to the changes of the molecular structure. Furthermore, the scratch healing was analyzed in detail showing that only one of the two polymers studied, polymer **P1** is able to heal scratches in a sufficient manner at temperature higher than the activation of the π–π interaction. In contrast, polymer **P2** could not be damaged in a sufficient manner (under the utilized conditions) due to the polymer design. In particular, the poly(ethylene glycol) block resulted in a sufficient elastic recovery. Consequently, the material could not be analyzed via scratch testing in sufficient manner.

The current study reveals a strong correlation between the molecular structure of the supramolecular building units and the healing behavior of such polymers. Thus, the polymer backbone influences the healing behavior of the materials significantly and, consequently, this aspect is also highly important for the design of novel self-healing materials. However, further studies are required in order to understand the influence of the utilized polymer backbone in more detail.

Experimental

Materials and instrumentation

All chemicals were used as received from Sigma-Aldrich (Darmstadt, Germany) if not otherwise stated. The dialysis tubings were purchased from Spectrum Labs (Spectra/PorTM, pre-wetted tubing, 3.5 kDa) and were rinsed with water before use.

Nuclear magnetic resonance spectra were measured using a Bruker AC 300 (300 MHz) spectrometer at 298 K (Billerica, MA, USA). The chemical shift is given in parts per million (ppm on δ scale) related to a deuterated solvent.

Elemental analysis was performed utilizing a Vario El III (Elementar, Langenselbold, Germany).

Size exclusion chromatography measurements were performed utilizing the following setup: Shimadzu with CBM-20A (system controller), DGU-14A (degasser), LC-20AD (pump), SIL-20AHT (auto sampler), CTO-10AC vp (oven), SPD-20A (UV detector), RID-10A (RI detector), PSS SDV guard/1000 Å/ 1,000,000 Å (5 µm particle size) chloroform/isopropanol/triethylamine [94/2/4] with 1 mL/ min at 40 °C, poly(ethylene glycol) (standard).

Differential scanning calorimetry was measured on a Netzsch DSC 204 F1 Phoenix instrument (Selb, Germany) under a nitrogen atmosphere with a heating rate of 20 K min^{-1} (first and second heating cycle) and 10 K min^{-1} (third heating cycle). In general, the first cycle is used as annealing step, which deletes the thermal history of the sample, and thus is neglected.

Thermo gravimetric analysis was carried under nitrogen atmosphere using a Netzsch TG 209 F1 Iris (Selb, Germany) with a heating rate of 10 K min^{-1} from 25 to 600 °C. The thermo gravimetric analysis revealed degradation temperatures above 370 °C for all synthesized polymers.

All dynamic mechanical analysis (DMA) experiments were performed on a MCR 301 rheometer (SN80386674) from Anton Paar (Graz, Austria) using a convection temperature device CTD 450 which covers a broad temperature range of −100 to 450 °C. For measurements and the export of data the Rheocompas- software was used.

The temperature sweeps (DMTA) and frequency sweeps (FS) were measured with a plate-plate setup (D-PP15-SN0). The sample was heated to 150 °C and the sample gap was set to 1 mm. For the DMTA, the samples were cooled to 25 °C and heated up to 200 °C with a heating rate of 2 °C/min under a frequency (f) of 1 Hz with 1% shear strain (γ). For the frequency sweeps, the sample was firstly annealed at the desired temperature (80, 130 (**P2**) or 135 (**P1**) and 140 °C). Afterwards, the frequency was decreased in a logarithmic profile from 100 up to 0.01 Hz at a strain of 1%.

All infrared (IR) spectra were recorded on a Nicolet iS5 FTIR spectrometer (Thermo Fisher Scientific, Waltham, Massachusetts, United States of America), equipped with potassium bromide windows and beam splitter. The sample temperature was controlled with a temperature cell and temperature controller combination (TFC-M13-3 / ATC-024-1, Harrick Scientific Products, Pleasantville, New York, United States of America), which provides a heated sample chamber suitable for 12 mm windows.

To collect IR spectra of the samples, first KBr windows were prepared directly before the measurement by pressing 200 mg dry spectroscopic grade KBr (Merck KGaA, Darmstadt, Germany) into a ∅ 12 mm-form under vacuum and 7 MPa pressure. The window was subsequently transferred into the temperature cell and secured with a lockring and teflon seals. A background spectrum with 32 scans and 4 cm^{-1} spectral resolution was recorded. 1 mg of the respective sample was dissolved in 100 µL spectroscopic grade $CHCl_3$ (Uvasol®, Merck KGaA, Darmstadt, Germany) and 20 µL drop casted onto the window. To record the IR spectra of the samples, the temperature cell was heated to the respective temperature (30–150 °C in 20 °C steps) and left to equilibrize for 2 minutes. Afterwards, a sample spectrum with 32 scans was recorded.

All graphics were generated with GNU R (version 4.0.2) [33] without further preprocessing of the spectra.

The preparation of the samples and the self-healing experiments (including evaluation of the data) were performed according to literature [31]. In the first step, the sample was hot pressed (at 150 °C, at about 2 t for 3 minutes) in a special manufactured mold. The pressed polymer samples were embedded in epoxy resin consisting of Epoxy Resin L and Hardener CL from R&G Faserverbundstoffe GmbH, followed by grinding of the sample with sandpaper (P60 to P2500).

The self-healing scratch tests were performed on an Anton Paar Micro scratch tester MST3 on a STeP 4 platform. The instrument was equipped with 10 µm and 50 µm Rockwell C indenters and the optical images were taken with the lenses MPlan N 5×/0.10/FN22. The scratches were performed with a 50 µm Rockwell indenter, 1500 mN normal force and 15 passages on a length of 2000 µm and a scratch speed of 30,000 µm/min. Subsequently, the scratch was imaged by the microscope in panorama mode. The sample was turned 90° in order to

measure the profile of the scratch. Therefore, 150 scratches along the scratch (every 20 µm) were performed with a 10 µm Rockwell indenter with the following parameters: 3 mN normal force, 200 µm/min scratch speed, length 1600 µm (**P1**) or 600 µm (**P2**).

For the visualization and evaluation of the scratch profile data recorded by the MST3, a Python-based GUI controlled program was developed, which mainly uses the well-established data analysis library pandas as well as the SciPy and NumPy libraries for linear algebra, integration and interpolation.

Polymer synthesis

The polymer synthesis was adapted from literature [23] and is reported briefly in the following.

P1: Perylene-3,4,9,10-tetracarboxylic dianhydride (1.02 g, 2.60 mmol), poly(propylene glycol) bis(2-aminopropyl ether) (M_n = 2000 g/mol; 5.2 g, 2.60 mmol) and imidazole (18 g, 264.39 mmol) were mixed in a round bottom flask under nitrogen atmosphere. Afterwards, the reaction mixture was heated to 150 °C for 17 h. After cooling to room temperature, water and chloroform were added to the mixture. The organic phase was washed two times with water, dried over sodium sulfate and concentrated. The residual was dissolved in tetrahydrofuran and dialyzed for three days with solvent exchange two times per day (MWCO: 3500 g/mol). After the solvent evaporation, a dark violet polymer could be obtained. ^{1}H NMR (300 MHz, $CDCl_3$) δ 8.74–8.45 (m, 8H, perylene-*H*), 4.27–3.12 (m, 143H, PPG: O*CH*$_2$, C*H*), 1.46–0.81 (m, 140H, PPG: C*H*$_3$) ppm; SEC (PEG standard): M_n = 11,400 g/mol, M_w = 27,600 g/mol, Đ = 2.43 (RI detector), M_n = 11,800 g/mol, M_w = 25,000 g/mol, Đ = 2.12 (UV detector); elemental analysis: found: C: 63.81, H: 9.06, N: 1.48; expected: C: 64.04, H: 9.04, N: 1.18.

P2: Perylene-3,4,9,10-tetracarboxylic dianhydride (1.02 g, 2.60 mmol), poly(propylene glycol)-*block*-poly(propylene glycol)-*block*-poly(propylene glycol) bis(2-aminopropyl ether) (M_n = 1900 g/mol; 4.94 g, 2.60 mmol) and imidazole (18 g, 264.39 mmol) were mixed in a round bottom flask under nitrogen atmosphere. Afterwards, the reaction mixture was heated to 150 °C for 17 h. After cooling to room temperature, water and chloroform were added to the mixture. The organic phase was washed two times with water and one time with brine, dried over sodium sulfate and concentrated. The residual was dissolved in a 1:1 mixture of chloroform and tetrahydrofuran and dialyzed for two days with solvent exchange two times per day (MWCO: 3500 g/mol). After the solvent evaporation, a dark violet polymer could be obtained. ^{1}H NMR (300 MHz, $CDCl_3$) δ 8.86–8.31 (m, 8H, perylene-*H*), 4.29–3.15 (m, 185H, PPG-*H* (O*CH*$_2$, C*H*) PEG-*H* (O*CH*$_2$)), 1.46–0.91 (m, 9H, PPG: C*H*$_3$) ppm; SEC (PEG standard): M_n = 17,400 g/mol, M_w = 34,100 g/mol, Đ = 1.95 (RI detector), M_n = 18,200 g/mol, M_w = 35,100 g/mol, Đ = 1.92 (UV detector); Elemental analysis: found: C: 57.94, H: 7.97, N: 1.50; expected: C: 58.71, H: 8.21, N: 1.14.

Supporting Information

Supporting Information File 1

Additional data.
[https://www.beilstein-journals.org/bjoc/content/supplementary/1860-5397-17-166-S1.pdf]

Funding

The authors would like to thank the Deutsche Forschungsgemeinschaft (DFG, HA606/7-1 and 36459901 – Collaborative Research Center (CRC) “CataLight” (Transregio SFB TRR 234, Projektnummer 364549901, projects A3, C2) and the Carl-Zeiss foundation (Perspektiven 2019) for financial support.

ORCID® iDs

Julian Hniopek - https://orcid.org/0000-0002-8652-8812
Michael Schmitt - https://orcid.org/0000-0002-3807-3630
Jürgen Popp - https://orcid.org/0000-0003-4257-593X
Martin D. Hager - https://orcid.org/0000-0002-6373-6600

References

1. Harrington, M. J.; Speck, O.; Speck, T.; Wagner, S.; Weinkamer, R. Biological Archetypes for Self-Healing Materials. *Self-healing Materials;* Advances in Polymer Science, Vol. 273; Springer: Cham, Switzerland, 2015; pp 307–344. doi:10.1007/12_2015_334
2. McKibbin, B. *J. Bone Jt. Surg., Br. Vol.* **1978,** *60-B,* 150–162. doi:10.1302/0301-620x.60b2.350882
3. Kragl, M.; Knapp, D.; Nacu, E.; Khattak, S.; Maden, M.; Epperlein, H. H.; Tanaka, E. M. *Nature* **2009,** *460,* 60–65. doi:10.1038/nature08152
4. Vaccaro, E.; Waite, J. H. *Biomacromolecules* **2001,** *2,* 906–911. doi:10.1021/bm0100514
5. Xu, Q.; Xu, M.; Lin, C.-Y.; Zhao, Q.; Zhang, R.; Dong, X.; Zhang, Y.; Tian, S.; Tian, Y.; Xia, Z. *Adv. Sci.* **2019,** *6,* 1902043. doi:10.1002/advs.201902043
6. Zechel, S.; Hager, M. D.; Priemel, T.; Harrington, M. J. *Biomimetics* **2019,** *4,* 20. doi:10.3390/biomimetics4010020
7. White, S. R.; Sottos, N. R.; Geubelle, P. H.; Moore, J. S.; Kessler, M. R.; Sriram, S. R.; Brown, E. N.; Viswanathan, S. *Nature* **2001,** *409,* 794–797. doi:10.1038/35057232
8. Toohey, K. S.; Sottos, N. R.; Lewis, J. A.; Moore, J. S.; White, S. R. *Nat. Mater.* **2007,** *6,* 581–585. doi:10.1038/nmat1934
9. Garcia, S. J. *Eur. Polym. J.* **2014,** *53,* 118–125. doi:10.1016/j.eurpolymj.2014.01.026

10. Dahlke, J.; Zechel, S.; Hager, M. D.; Schubert, U. S. *Adv. Mater. Interfaces* **2018,** *5,* 1800051. doi:10.1002/admi.201800051
11. Campanella, A.; Döhler, D.; Binder, W. H. *Macromol. Rapid Commun.* **2018,** *39,* 1700739. doi:10.1002/marc.201700739
12. Yang, Y.; Urban, M. W. *Adv. Mater. Interfaces* **2018,** *5,* 1800384. doi:10.1002/admi.201800384
13. Bode, S.; Enke, M.; Bose, R. K.; Schacher, F. H.; Garcia, S. J.; van der Zwaag, S.; Hager, M. D.; Schubert, U. S. *J. Mater. Chem. A* **2015,** *3,* 22145–22153. doi:10.1039/c5ta05545h
14. Mozhdehi, D.; Ayala, S.; Cromwell, O. R.; Guan, Z. *J. Am. Chem. Soc.* **2014,** *136,* 16128–16131. doi:10.1021/ja5097094
15. Cordier, P.; Tournilhac, F.; Soulié-Ziakovic, C.; Leibler, L. *Nature* **2008,** *451,* 977–980. doi:10.1038/nature06669
16. Zhou, Z.; Chen, S.; Xu, X.; Chen, Y.; Xu, L.; Zeng, Y.; Zhang, F. *Prog. Org. Coat.* **2021,** *154,* 106213. doi:10.1016/j.porgcoat.2021.106213
17. Tepper, R.; Bode, S.; Geitner, R.; Jäger, M.; Görls, H.; Vitz, J.; Dietzek, B.; Schmitt, M.; Popp, J.; Hager, M. D.; Schubert, U. S. *Angew. Chem., Int. Ed.* **2017,** *56,* 4047–4051. doi:10.1002/anie.201610406
18. Hart, L. R.; Nguyen, N. A.; Harries, J. L.; Mackay, M. E.; Colquhoun, H. M.; Hayes, W. *Polymer* **2015,** *69,* 293–300. doi:10.1016/j.polymer.2015.03.028
19. Mei, J.-F.; Jia, X.-Y.; Lai, J.-C.; Sun, Y.; Li, C.-H.; Wu, J.-H.; Cao, Y.; You, X.-Z.; Bao, Z. *Macromol. Rapid Commun.* **2016,** *37,* 1667–1675. doi:10.1002/marc.201600428
20. Burattini, S.; Colquhoun, H. M.; Greenland, B. W.; Hayes, W. *Faraday Discuss.* **2009,** *143,* 251–264. doi:10.1039/b900859d
21. Burattini, S.; Greenland, B. W.; Merino, D. H.; Weng, W.; Seppala, J.; Colquhoun, H. M.; Hayes, W.; Mackay, M. E.; Hamley, I. W.; Rowan, S. J. *J. Am. Chem. Soc.* **2010,** *132,* 12051–12058. doi:10.1021/ja104446r
22. Burattini, S.; Colquhoun, H. M.; Fox, J. D.; Friedmann, D.; Greenland, B. W.; Harris, P. J. F.; Hayes, W.; Mackay, M. E.; Rowan, S. J. *Chem. Commun.* **2009,** 6717–6719. doi:10.1039/b910648k
23. Higaki, Y.; Kiyoshima, Y.; Suzuki, K.; Kabayama, H.; Ohta, N.; Seo, Y.; Takahara, A. *RSC Adv.* **2017,** *7,* 46195–46200. doi:10.1039/c7ra08910d
24. Lai, W.-C.; Chang, C.-W.; Hsueh, C.-Y. *Polymer* **2021,** *213,* 123196. doi:10.1016/j.polymer.2020.123196
25. Meurer, J.; Hniopek, J.; Bätz, T.; Zechel, S.; Enke, M.; Vitz, J.; Schmitt, M.; Popp, J.; Hager, M. D.; Schubert, U. S. *Adv. Mater. (Weinheim, Ger.)* **2021,** *33,* 2006655. doi:10.1002/adma.202006655
26. Aida, T.; Meijer, E. W.; Stupp, S. I. *Science* **2012,** *335,* 813–817. doi:10.1126/science.1205962
27. Bose, R. K.; Hohlbein, N.; Garcia, S. J.; Schmidt, A. M.; van der Zwaag, S. *Phys. Chem. Chem. Phys.* **2015,** *17,* 1697–1704. doi:10.1039/c4cp04015e
28. Ding, L.; Schulz, P.; Farahzadi, A.; Shportko, K. V.; Wuttig, M. *J. Chem. Phys.* **2012,** *136,* 054503. doi:10.1063/1.3681164
29. Mattson, M. A.; Green, T. D.; Lake, P. T.; McCullagh, M.; Krummel, A. T. *J. Phys. Chem. B* **2018,** *122,* 4891–4900. doi:10.1021/acs.jpcb.8b02355
30. Ji, H.-F.; Majithia, R.; Yang, X.; Xu, X.; More, K. *J. Am. Chem. Soc.* **2008,** *130,* 10056–10057. doi:10.1021/ja803079w
31. Dahlke, J.; Kimmig, J.; Abend, M.; Zechel, S.; Vitz, J.; Schubert, U. S.; Hager, M. D. *NPG Asia Mater.* **2020,** *12,* 13. doi:10.1038/s41427-019-0190-2
32. Abend, M.; Tianis, L.; Kunz, C.; Zechel, S.; Gräf, S.; Müller, F. A.; Schubert, U. S.; Hager, M. D. *Polym. Test.* **2020,** *90,* 106699. doi:10.1016/j.polymertesting.2020.106699
33. R Core Team. https://www.R-project.org/ (accessed Sept 6, 2021).

License and Terms

This is an Open Access article under the terms of the Creative Commons Attribution License (https://creativecommons.org/licenses/by/4.0). Please note that the reuse, redistribution and reproduction in particular requires that the author(s) and source are credited and that individual graphics may be subject to special legal provisions.

The license is subject to the *Beilstein Journal of Organic Chemistry* terms and conditions: (https://www.beilstein-journals.org/bjoc/terms)

The definitive version of this article is the electronic one which can be found at: https://doi.org/10.3762/bjoc.17.166

BEILSTEIN JOURNAL OF ORGANIC CHEMISTRY

Cryogels: recent applications in 3D-bioprinting, injectable cryogels, drug delivery, and wound healing

Luke O. Jones, Leah Williams, Tasmin Boam, Martin Kalmet, Chidubem Oguike and Fiona L. Hatton*

Review

Open Access

Address:
Department of Materials, Loughborough University, Loughborough, LE11 3TU, UK

Email:
Fiona L. Hatton* - f.hatton@lboro.ac.uk

* Corresponding author

Keywords:
3D-bioprinting; cryogels; drug delivery; injectable cryogel; macroporous hydrogel; wound healing

Beilstein J. Org. Chem. **2021,** *17,* 2553–2569.
https://doi.org/10.3762/bjoc.17.171

Received: 30 June 2021
Accepted: 21 September 2021
Published: 14 October 2021

This article is part of the thematic issue "Polymer chemistry: fundamentals and applications".

Guest Editor: B. V. K. J. Schmidt

© 2021 Jones et al.; licensee Beilstein-Institut.
License and terms: see end of document.

Abstract

Cryogels are macroporous polymeric structures formed from the cryogelation of monomers/polymers in a solvent below freezing temperature. Due to their inherent interconnected macroporosity, ease of preparation, and biocompatibility, they are increasingly being investigated for use in biomedical applications such as 3D-bioprinting, drug delivery, wound healing, and as injectable therapeutics. This review highlights the fundamentals of macroporous cryogel preparation, cryogel properties that can be useful in the highlighted biomedical applications, followed by a comprehensive review of recent studies in these areas. Research evaluated includes the use of cryogels to combat various types of cancer, for implantation without surgical incision, and use as highly effective wound dressings. Furthermore, conclusions and outlooks are discussed for the use of these promising and durable macroporous cryogels.

Introduction

Gels can be defined as polymer networks that are expanded throughout their whole volume by a fluid. In the case of hydrogels, the network component is a hydrophilic polymer, and the swelling agent is water [1]. However, their lack of interconnected macropores and elasticity, required properties for a variety of biomedical applications, has demanded the development of cryogels. Cryogels are a class of hydrogels formed below the freezing point of the solvent. Following a cycle of freeze–thawing, a supermacroporous interconnected structure is formed [2]. The uniform porous structure facilitates cell proliferation and waste exchange, e.g., in a scaffold for tissue engineering applications [3]. Novel biomedical and biotechnical applications of cryogels can also be found in controlled drug delivery, carriers for cell immobilization, sensors, biosepara-

tion, purification, and wound dressing [4-6]. Here we discuss the preparation of cryogels, their properties and applications, focussing on recent reports of cryogels in emerging applications, including bioprinting, injectable cryogels, drug delivery, and wound healing, as investigations in these key areas have intensified in recent years. Previous reviews discuss the biomedical applications of cryogels, specifically composite cryogels [7] and biodegradable cryogels [8], while injectable cryogels have also been reviewed by Eggermont et al. [9] and Çimen et al. [10]. Here, we provide an update on the most recent literature relating to drug delivery and injectable cryogels, and we discuss 3D printing and wound healing in detail.

Review

1. Cryogel synthesis

Cryogels are produced by a cryogelation process, see Figure 1. While this process is relatively universal, differences exist in the initial materials used, hence resulting in either chemically or physically crosslinked cryogels [11-13]. Firstly, a reaction mixture is prepared consisting of monomers/small molecule precursors, polymeric precursors, or a combination of the two (Figure 1) and solvent (e.g., water).). It is worth noting that while we refer to water as the solvent here and in Figure 1, other solvents can be used, providing they have an appropriate melting/freezing temperature. Typically, the reagents will comprise only 5–20% of the reaction mixture. Often an initiator may also be required to initiate the polymerisation of the monomers/small molecule precursors. The solution is then cooled to below the freezing point of water, whereby ice crystals form. Importantly, here the solvent (water) solidifies (freezes) and forms solid solvent porogens within the structure allowing the polymer network to form around these crystals, templating the porous structure of the final cryogel. In chemically crosslinked cryogels (Figure 1a), the monomers polymerise and crosslink (in the presence of a crosslinker) around the ice crystals to form a network. In physically crosslinked cryogels (Figure 1b), once the solution is cooled below the freezing temperature the polymeric precursors can form chain entanglements and/or crystalline regions to form physical crosslinks between the chains. After thawing, the cryogel is formed and porous structure is retained. Often in physically crosslinked systems more than one freeze–thaw cycle is required to result in a free-standing cryogel. Common cryogel compositions include natural polymers such as gelatin and chitosan, and synthetic acrylamide-based polymers and poly(vinyl alcohol) (PVA) [12-14]. The reader is directed to a recent review by Thakor and co-workers which discusses cryogel synthesis in greater depth [15].

2. Cryogel properties

Cryogels are macroporous hydrogels with interconnected porosity, with high swelling capacities and large surface areas. Ultimately, many of the final cryogel properties are dependent on the choice of polymer/monomer composition used. However, other factors such as crosslinking, pore size, wall thickness, and incorporation of fillers or additives also affect the cryogel properties. Cryogel wall thickness and density, pore size and pore size distribution can be influenced by the method used for preparation, for example, by increasing the freezing rate smaller pores can be observed [13]. Final cryogel properties including biocompatibility, mechanical and thermal properties, and degradability are influenced by a variety of factors. Perhaps the

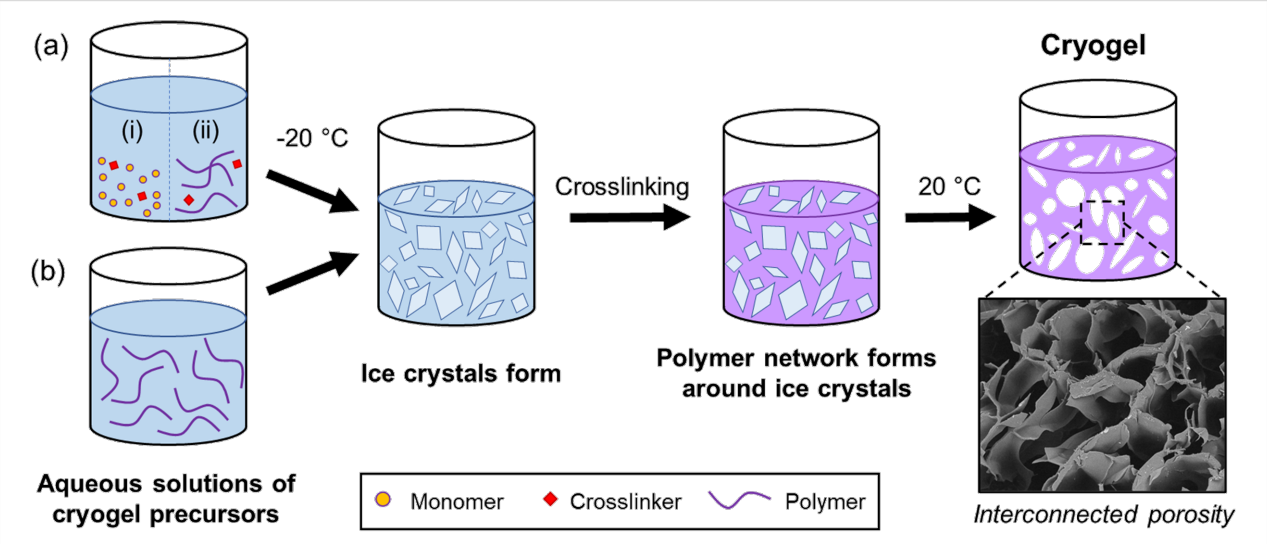


Figure 1: Schematic representation of the process of aqueous cryogel formation, using (a) monomers/small molecule (i) or polymeric precursors (ii) to form chemically crosslinked cryogels, or (b) polymeric precursors to form physically crosslinked cryogels. Temperatures are indicative of those typically used for aqueous cryogel formation.

most important factor is the chemical composition as this determines whether the cryogel is biocompatible or degradable and to some extent influences the mechanical and thermal properties of the cryogel. Mechanical properties are mainly influenced by porosity and degree of crosslinking, while crosslinking also influences biocompatibility and degradability. In chemically crosslinked cryogels the mechanical properties can be influenced by the degree of crosslinking (ratio of monomer to crosslinking agent), while the degree of crosslinking is tuned in physically crosslinked cryogels by varying the number of freeze–thaw cycles.

Pore size, wall thickness, and wall density are of significant importance for cryogels properties [16]. Thicker walls and higher wall densities typically result in improved mechanical properties and are influenced by the concentration of monomer or precursors used as well as the type of crosslinking in the cryogel. Moreover, the processing conditions used when synthesising cryogels have a vast effect on the internal structure. An accelerated freezing rate or reduction in cryogelation temperature will lead to smaller pore sizes throughout the cryogel. This is because the solvent freezes at a faster rate, allowing only a small amount of crystal growth [13,14]. Ivanov et al. researched the production of poly(acrylamide) (PAAm) cryogels and found that reducing the freezing temperature by 15 °C caused an average 30 μm decrease in pore size diameter [14,17]. In contrast, it has been reported that with cryogels crosslinked with glutaraldehyde, the freezing temperature does not affect the pore size [13].

An additional consideration is that during cryogelation a temperature gradient will be present. The exterior of the sample will be first exposed to the cold temperature, leading to enhanced freezing rates and smaller pore sizes compared to the inner cryogel material, resulting in a heterogeneous pore size distribution, see Figure 2 [18]. This has led to concerns over producing cryogels with dimensions greater than 25 mm [19]. Although, a report by Macková et al. outlines the benefits of graduated pore size distribution in hydrogels used in tissue engineering, since many human body tissues also exhibit a heterogeneous morphology [20]. This finding was further reiterated by Sen et al., who also explored heterogeneous pore size distribution for tissue engineering applications [21]. Cryostructuring, including directional freezing of cryogels, has been used to achieve varying degrees of porosity and aligned porosity or anisotropy within cryogels. This approach to cryogel preparation has recently been discussed in a review by Shiekh et al. [22] where different cryogel formats were also considered.

Chemical crosslinking can provide satisfying and tailored mechanical properties, however toxic compounds are used as crosslinking agents, which can be difficult to extract and can impair the biocompatibility [4]. Instead, with physical crosslinking, no organic solvents or toxic crosslinking agents are used, therefore no danger of residue left in the final material, which makes this method highly important for biomedical applications [4,5]. As the production is easier, it also results in lower cost. According to Zhang et al., the challenge has been to obtain satisfactory properties without any chemical modification, while retaining the biocompatibility, biodegradability, and bioactivity [4]. However, Bagri et al. confirm that physically crosslinked PVA cryogels show even greater mechanical strength than their chemically crosslinked counterparts [23]. Therefore, it is achievable to obtain similar properties with physical crosslinking, yet the matter of reproducibility and scalability remains an issue.

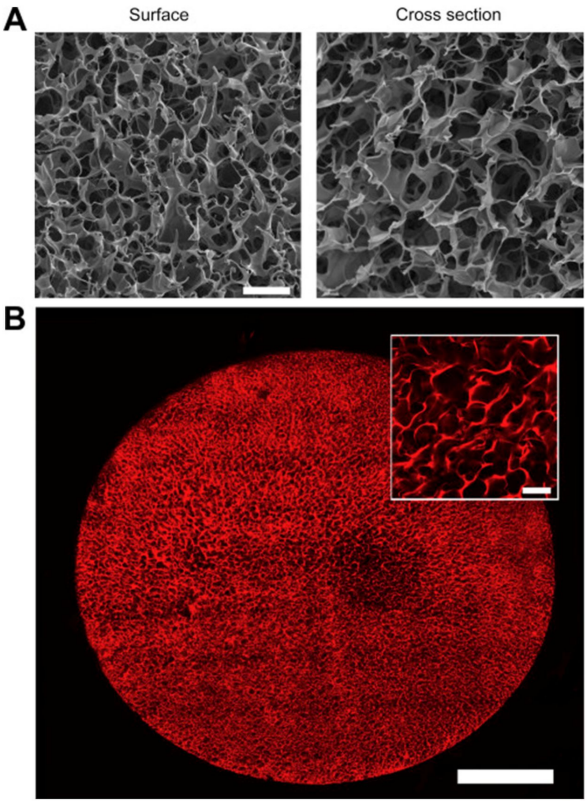


Figure 2: Microarchitecture of gelatin cryogels. (A) Surface and cross-sectional SEM micrographs of highly porous 1.0% (w/v) gelatin cryogels (scale bar = 50 μm). (B) 2-photon imaging at a depth of 150 μm below the surface of a rhodamine-gelatin cryogel (scale bar = 1 mm). The inset shows a magnified view at the centre of the scaffold diameter (scale bar = 100 μm). Images are representative of at least 5 gels imaged using each modality. Reprinted from [18], Biomaterials, vol. 35, issue 8, by S. T. Koshy; T. C. Ferrante; S. A. Lewin; D. J. Mooney, "Injectable, porous, and cell-responsive gelatin cryogels", 2477–2487, Copyright (2014), with permission from Elsevier. This content is not subject to CC BY 4.0.

To assess the mechanical performance of cryogels, compression testing is frequently carried out [12,13]. It has been reported that 99.8% compression can be achieved on continual occasions without any adverse effects, though this was for cryogels based on silk fibroin which is known for its elastic nature [14,24]. In contrast, other reports have cited lower compressibility values in the region of 50–75% [12,25]. It has been found that decreasing the pore size will increase the compressive strength [26], though in contrast to this Dispinar et al. found that increased porosity resulted in higher compressive stresses being achieved. Further to this, compressive strain was found to increase with porosity [25], suggesting that the brittle nature observed for some hydrogels may be due to their lack of macropores [27,28]. One such application where a low compressive strain would not be desirable is if the cryogel was to be injectable (see section 5.2). It has therefore been suggested that the ideal porosity for injectable cryogels is 91%. This figure was the suggested value for cryogels composed of methacrylated gelatin, therefore the value will change slightly with different chemical constituents [18].

For various applications of cryogels, degradation of the material is required, yet in many cases the cryogel is still required to perform some functionality during degradation. Therefore, it would be beneficial if the mechanical properties of the cryogel were measured throughout its degradation [25,29]. It has been suggested that during degradation of cryogels, the walls of the cryogel decrease in thickness and are in some cases broken. This analysis was made for enzyme-degraded cryogels, so it is unclear whether the process is likely to occur for cryogels degraded by other mechanisms such as disulphide cleavage [30,31] and hydrolysis [8]. It has also been found that degradation of chitosan/dextran cryogels resulted in an average increase in pore size, possibly due to thinning of the pore walls and reduction in crosslinks [32]. In general, mechanical property analysis of degraded cryogels is a topic largely overlooked by current literature, despite the importance of it for applications such as scaffold materials [29]. A recent review article by Savina et al. highlights biodegradable cryogels and their applications, including a variety of biocompatible polysaccharide-based cryogels [8].

3. Stimuli-responsive cryogels

Stimuli-responsive properties are often desirable for biomaterials used in drug-delivery applications. Here, we focus on temperature and solution pH response of cryogels as detailed below.

3.1. Temperature-responsive cryogels

This is a property which can easily be applied and manipulated through careful polymer selection. For example, altering the ratio of hydrophobic and hydrophilic polymers in the final cryogel structure can allow for fine tuning of the responsive behaviour [33,34].

At specific and unique temperatures, phase changes occur to a temperature-responsive polymer, physically changing the properties and/or morphology. Often it can be characterised in terms of swelling, as the solubility of a polymer within a solvent, or solvation state, changes with temperature in thermally responsive cryogels. This leads to variation in cryogel volume, as at differing temperatures the nature of intra- and intermolecular hydrogen bonding changes, leading to variations on how hydrated the cryogel is, triggering a volume phase transition [34,35]. Changes in solubility can be described by the upper critical solution temperature (UCST) and lower critical solution temperatures (LCST). The UCST is the temperature at which a polymer becomes soluble upon heating, and the LCST is the temperature at which polymers become insoluble upon heating. Any LCST or UCST behaviour can be identified from a polymer/solvent phase diagram, if it has both one-phase and two-phase regions [34,36].

Most commonly, the physical change in properties induced is used when transferring from room temperature to another environment (i.e., body temperature). This leads to potential applications such as injectable biodegradable scaffolds in tissue engineering, or utilising the changing surface properties for in vitro cell culture applications [36-38]. Furthermore, a polymer in cryogel form which exhibits LCST behaviour at below the body temperature of ≈37 °C would be suitable to use for medicinal applications in humans, as it would be insoluble at above these temperatures (i.e., normal body environment) and so would retain its structure when introduced to the human body, and not degrade or dissolve straight away. Poly(*N*-isopropylacrylamide) (PNIPAM) is a well-known example of a thermo-responsive polymer, which exhibits a phase transition close to body temperature and has been used in cryogels to infer temperature responsive behaviour [11,33,39]. Thermoresponsive cryogels comprising oligoethylene glycol have also been reported with dual shape memory behaviour [40]. Natural polymers such as cellulose derivatives, chitosan, gelatin, and dextran exhibit temperature-responsive properties and have been used in cryogels.

3.2. pH-Responsive cryogels

The degree of swelling is affected by the chemical composition of the cryogel, and the nature of the medium, such as pH, ionic strength, and swelling medium composition [34,41]. This affects the interactions of pH-sensitive polymers (both polymer–solvent and polymer–polymer interactions), as functional groups on the polymer chains can have weak acidic characteristics if they release protons, or weak basic characteristics

if they accept protons, in response to changes in pH. This can come about from even small variations in solution pH, depending on the degree of ionisation and pK_a value (index to express acidity of weak acids) of the polymer [35]. Polymers responsive to pH can be classified by the functional groups present within their polymerised structure [35,41,42]. Including (i) polyacids with weakly acidic groups (i.e., -COOH or -SO_3H), (ii) polybases with weakly basic groups (i.e., -NH_2), and (iii) polyamphoterics with both weakly acidic and weakly basic groups.

The scientific community is especially interested in using these properties in specific drug-delivery systems; the potential of using polysaccharide-based specific drug-delivery systems in the colon has been explored [43], as within the colon are many polysaccharides and a large number of bacteria which secrete enzymes [41]. Within this work, varying the concentration of various pH-sensitive polymers was considered in terms of swelling, and it was shown that abrupt changes in swelling could be obtained at a specific pH while using materials compatible with the colon. Also, assessing swelling as a function of NaCl concentration began to explore osmotic interactions of hydrogels, adding to the consideration of environmental conditions and providing data in a region often overlooked in these types of studies.

A great range of pH changes are faced when a foreign material travels through the human system. For example, for an orally administered drug-delivery device to release therapeutic agents in the colon, it must withstand a range of conditions as it passes through the body, including pH 6.2–7.3 in the mouth, pH 7 in the oesophageal tract, pH 1.5–3.5 in the stomach, pH 6 in the small intestine to pH 7.4 (terminal ileum) to 5.7 (caecum), and then a final pH 6.1–7.5 in the colon [44]. Often, in order for the therapeutic agent to reach the target site, specific barriers to variable pH must be designed for. Furthermore, a response to pH can be utilised to release the therapeutic agent at a site of specific acidity, thus ensuring targeted delivery.

Poly(acrylic acid)-based cryogels have been investigated as a pH oscillator in oscillatory bromate-sulphite-ferrocyanide reactions as potential soft materials for energy generation [45]. Boyaci and Orakdogen reported pH-responsive cryogels based on the monomer *N*,*N*-dimethylaminoethyl methacrylate (DMAEMA), crosslinked with acrylamido-2-methylpropanosulphonic acid (AMPS), where the swelling of the cryogels was heavily dependent on solution pH [46]. pH-Responsive cryogels have also been prepared comprising polyamidoamine (PAMAM) dendrimers, whereby the cryogels were stable under acidic conditions, and degrade at physiological solution pH (7.4) [47].

3.3. Dual temperature and pH-responsive cryogels

During cryogel design and production a diverse range of starting monomers and/or polymers can be used, selected for desired properties to be exhibited in the final polymer matrix. Therefore, it is possible to combine thermo-responsive and pH-responsive properties through cryogelation techniques, resulting in a cryogel which responds to both changes in environmental temperature and pH. For example, grafting thermally responsive PNIPAM to a backbone of pH-responsive chitosan to produce a cryogel responsive to both temperature and pH has been explored in some detail [48-52], and the application as a drug-delivery system in the intestine has also been considered [12,13,34,35,42]. In particular, the work by Huang et al. demonstrated not only those systems responsive to both pH and temperature can be successfully produced using techniques which are scalable in theory to an industrial level, but also that these properties can be tailored to result in long-term release of therapeutic agents in environments modelling the human body [51]. A further example of multi-stimuli responsive cryogels includes the work by Dragan et al., who prepared semi-interpenetrating polymer networks (semi-IPN) hydrogels comprising DMAEMA and either potato starch or anionically modified polystyrene via a cryogelation procedure [53]. These materials were investigated as drug-delivery systems (DDS) and the release profile was strongly influenced by the pH. The authors suggested that due to a low release of the drug at pH 1.3, and an increase in release rate at pH 7.4, the material could be a potential for targeting release in the colon.

4. Other cryogel applications

For cryogel biomedical applications not discussed in section 5, including cell separation, tissue engineering scaffolds, bioreactors and capturing of target molecules, the reader is directed to a recent review by Bakhshpour et al. [54]. In addition to the biomedical applications discussed in detail below, cryogels have a variety of potential uses in fields such as tissue engineering [12], chromatography, and separation applications. For example, for the filtration of biologically relevant molecules [19,42], wastewater treatment [55,56], biosensors [57], as actuators [58,59], as carbon super-capacitators, anodic component of lithium-ion batteries, and devices for low-pressure H_2 storage have also been explored [60].

5. Biomedical applications

Cryogels are of major interest in several fields of research, through offering new solutions and improvements to current systems and procedures. Their interconnected porosity in the micrometre scale, superior mechanical strength, and stability in comparison to hydrogels, thermodynamic compatibility with water (and thus also aqueous solutions), and being able to produce them from biocompatible materials make these materi-

als ideal for cell culture and tissue engineering [12,16,38,42]. Furthermore, post-synthesis modifications can be performed to enhance attachment from certain objects, for example proteins from the extracellular matrix (ECM) in tissue engineering, cell culture and microbiology, or specific chemicals to aid in chemical, environmental, and medicinal filtration, and purification applications [5,19,42,60,61]. This also aids cell immobilisation, putting cryogels forward for potential use in bioreactors [5,42]. Cells can be included within the cryogel matrix, and shown benefits of doing this include reinforcing the matrix, increasing rigidity, and accelerating formation of pores [16,60,62].

Cryogels offer solutions to obstacles in current medicinal and therapeutic practices. In particular, specific isolation and characterisation of stem cells in cell-based therapies, detection of low levels of biomarkers in the blood (i.e., tumour cells, pathogenic microorganisms, etc.) for disease diagnosis, and general isolation of biological substances for clinical and environmental microbiology hold opportunities for cryogels [13,42,61]. They also allow for the processing of cell and virus suspensions and support microbiological research in studying interactions between different biological substances (i.e., cell–virus interactions) [38].

Highly dense polymeric structures in the walls result in cryogels having high elasticities, making them suitable for applications of a cyclic nature such as storage and sterilisation of biomedical materials, biocatalysts, bioreactors, actuators, biosensors, and more. They exhibit stability during repetitive freezing and thawing, and dehydrate/rehydrate and undergo cyclic compression without losing mechanical integrity [5,12,13,60]. Possessing shape memory allows for dehydration and storing; rehydration before use restores their original shape [37,60].

Here, we discuss emerging areas for cryogel application, including recent advancements in the use of cryogels in 3D printing, injectable cryogels, drug delivery and wound healing applications. It should be noted that whilst this section contains reference to tissue engineering, expansive detail on the subject matter is beyond the scope of this review.

5.1. 3D-Bioprinting of cryogels

3D-printing of biomaterials, or bioprinting, enables the control of the size, porosity, and geometry of the final product tailored to the requirements of the individual patient, e.g., potential scaffold fabrication from cryogels in tissue engineering [63]. It is extremely important to consider the viscosity and injectability of the material for limitations on deposition mechanisms, e.g., the maximum deposition force and/or syringe tip size (0.8 mm used for hydrogels) for certain printers, place restrictions on highly viscous materials. These material properties have a direct influence on the final printing resolution. The resolution should be adequate for millimetre-sized defects (common in most in vivo tissue-engineering work in small animal models) [64].

Kim and co-workers reported a method in 2009, whereby a 3D-plotting system was coupled to a cryogenic refrigeration system [65,66]. Using these systems 3D scaffolds were prepared by printing collagen layers first on the cryogenic stage, where they froze immediately. To prevent clogging, the nozzle tip was covered with silicone rubber. The fabricated scaffolds were investigated with dermal applications in mind, and keratinocytes and fibroblasts were shown to migrate and differentiate within the scaffolds. They further reported the development of 3D-printed cryogels based on alginate with hierarchical structures for hard tissue applications [67].

More recently, in 2018 Serex et al. developed a microfabricated dispensing probe that allowed for the mixing of cryogel monomeric components immediately prior to printing [68]. They demonstrated the ability to control pore sizes by altering the temperature of the frozen bed used and the temperature of the dispensing probe. Successfully 3D-printed sodium carboxymethyl cellulose (CMC)-based cryogels were subsequently coated with collagen to promote cell adhesion. Cultivation and spreading of fibroblast NOR-10 cells were achieved within the cryogels, suggesting promise for tissue engineering applications.

Building upon this work, hierarchical injectable cryogels were developed by Braschler and co-workers, based upon 3D additive manufacturing techniques [69]. They report 3D-printed structures which could be used for minimally invasive cell delivery (see Figure 3). Moreover, hierarchical structures with varying local pore sizes were obtained by tuning the substrate temperature during printing, which led to control over vascularisation density in vivo.

Biçen Ünlüer et al. recently reported the use of biocompatible gelatin–hyaluronic acid (Gel-HA)-based 3D-printed cryogels, which demonstrated biocompatibility without the need for additional coating [70]. In this work, the Gel-HA based bioink was 3D-printed to give a free-standing structure which was subsequently frozen to prepare the cryogel, prior to freeze drying. While this approach offers less control over the process than that reported by Serex, Braschler and co-workers, it does not require the cold stage necessary for cryogelation to occur during printing. Hybrid collagen/chitosan bioinks have also been investigated for their printability for producing cryogel scaffolds [71]. These cryogels form crosslinks through physical interactions, hence no additional crosslinking was required.

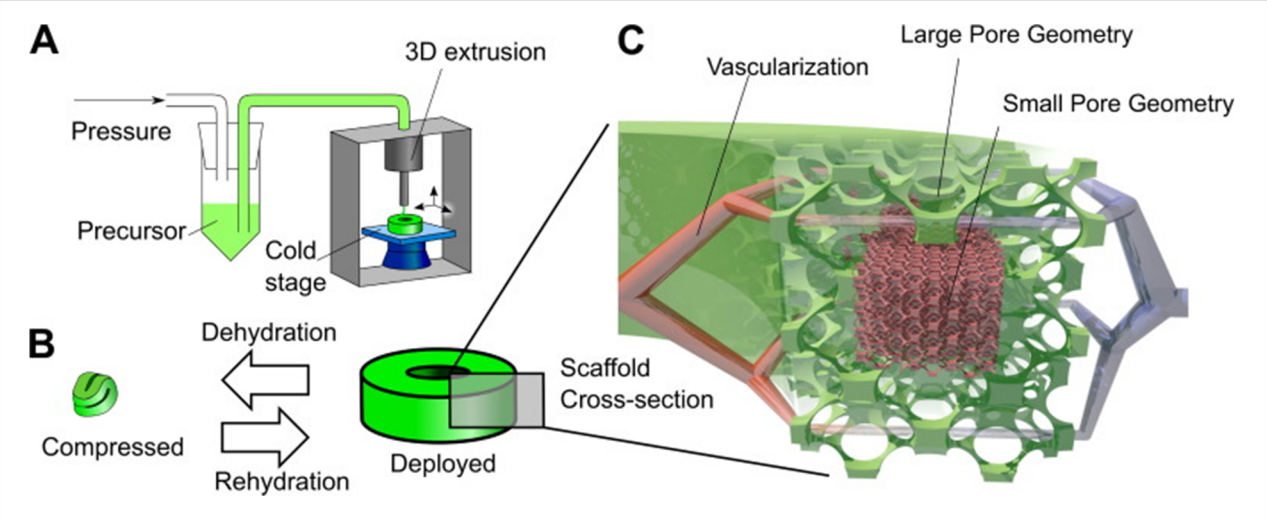


Figure 3: Principle of 3D-cryogel printing. A) Illustration of 3D-printing of cryogels. B) Illustration of the 4D shape change. By withdrawing fluid, the cryogel was highly dehydrated and compressed; in addition, surface tension drove surface-minimising folding. Upon rehydration, the cryogel returned to its original shape and volume via shape memory. C) Illustration of the hierarchical scaffold organisation. Local pore size variation was used to preferentially drive in vitro cellular organisation and in vivo vascularisation to areas with large pores. Reprinted from [69], Acta Biomaterialia, vol. 76, by A. Béduer; N. Piacentini; L. Aeberli; A. Da Silva; C. A. Verheyen; F. Bonini; A. Rochat; A. Filippova; L. Serex; P. Renaud; T. Braschler, "Additive manufacturing of hierarchical injectable scaffolds for tissue engineering", 71–79, Copyright (2018) Acta Materialia Inc., with permission from Elsevier. This content is not subject to CC BY 4.0.

Some difficulties arise when designing 3D-printed cryogels. While precise resolution may be achieved, there is some difficulty maintaining porous structures when stacking multiple layers, specifically the fusion of layer contact points without scaffold collapse. The vertical pores remain intact, but horizontal pores in hydrogel scaffolds might collapse due to material softness [64]. Shick et al. also pointed out the limitation in fabricating scaffolds with high porosity and complex internal structures, for example in tissue engineering applications [63]. They report the processes being not yet developed enough to be used in clinical applications. However, with the use of novel materials and development of printing systems, progress can be made in achieving stable print structures for the ultra-high standards set by the human body.

5.2. Injectable cryogels

Implantable biomaterials are proposed as a viable solution when dealing with issues relating to either the delivery or recruitment of cells. Currently the methods used are implantable biomaterials or polymeric hydrogels [18]. The issue with implantable biomaterials is that the implantation process requires the fabrication of the biomaterial component, trained physicians, post-operation patient distress, potential scarring, risk of infection, and often causes inflammation at the site of surgical incision. These issues may inhibit the performance of the implant [18] or cause distrust in the patient and the implant which may lead to negative emotional experiences [72]. Polymeric hydrogels, however, can cause issues of their own, such as the risk of liquid presursors leaking from the implant site to other tissues, and posing difficulties in generating the desired implant geometry [73]. An alternative proposal is the use of cryogels. This process typically results in a biomaterial with a unique macroporous network, shape-memory properties, and exceptional flexibility allowing syringe injectability [9].

It has been suggested that cryogels are more suitable for this application, as opposed to hydrogels, as a greater number of cells can be contained within the structure. With an exemption for injectable supramolecular hydrogel systems, which have been demonstrated to perform very well even after injection [74-76], hydrogels in general have been cited as being too brittle to enable injection [27]. Injectable cryogels have been investigated as scaffolds, for drug delivery, and for wound-healing applications. Here we highlight recent advances in the development of these injectable systems relevant to the applications discussed.

5.2.1. Injectable cell scaffolding: Injectable cryogels may be able to provide a suitable scaffolding for the attachment, proliferation, and survival of cells in complicated operations. The macroporous structure is an attractive option due to its low toxicity and to control the release of compounds stored in the porous structure through one of four methods: diffusion-controlled, swelling-controlled, erosion-controlled, and stimulus-controlled [54].

A study by Koshy et al. reported a methacrylated gelatin (GelMA) cryogel implanted by injecting through a conven-

tional needle [18]. Gelatin was chosen for its inherent peptide sequences that facilitate cell adhesion and enzymatic degradation. Gelatin is also low cost and safe to use in human testing as shown in a work done by Nichol et al. [77]. The bulk mechanical behaviour, structure, and degradation of the cryogelated GelMA was tested, as well as the ability of these injected scaffolds to promote cell attachment, proliferation, and survival. Their results show that cryogels have a useful ability to retain their original shape even when extruded through a needle, this means that the cryogel does not leak out of the needle bore after being applied. The GelMA can then be implied with minimal intrusion to the patient which decrease the chance of trauma to the patient. Koshy et al. also report that in vitro and in vivo testing showed that cryogelated GelMA is cell and tissue compatible, although mild inflammation occurred during in vivo tests, however this is a common occurrence with biomaterials as shown by Mikos et al. [78]. Finally, the cryogel was capable of a controlled release of proteins. This allowed for a more controlled integration and movement of cells interconnecting with pores of the gel. These cell-attracting properties suggest that the use of cryogelated GelMA as a method for cell-integrated scaffolding and protein release for applications in biomaterials-based therapy is a viable option. Similar work was carried out by Lai et al. [79], whereby the polymerisation of GelMA was carried out using carboxybetaine methacrylate (CBMA) as a co-monomer. With the incorporation of CBMA, these hydrogels demonstrated better mechanical properties, a slower degradation rate, and a controlled drug release rate compared with the GelMA alone. The properties of the GelMA/CBMA hydrogels could also be adjusted by varying the ratio of CBMA to GelMA which gives it a high degree of customisability.

The use of cryogels in neuroscience applications is gaining interest due to their soft and spongey properties [80]. Newland et al. recently reported on the use of injectable PEG/heparin-containing cryogels with nerve growth factor to promote the growth of neurite cells [81]. Through the use of template-assisted photopolymerisation, cylindrical cryogels were formed as high aspect ratios are desired for bridging across regions when whole neural pathways or large brain areas are targeted.

5.2.2. Injectable nanocomposite cryogels: Nanocomposite cryogels comprise a typical cryogel with nanoparticulate fillers incorporated into the structure. Addition of nanoparticles is often conducted to impart specific properties, such as improving mechanical properties or provide therapeutic properties such as antimicrobial properties. A work reported by Koshy et al. in 2018 was testing the use of injectable nanocomposite cryogels for versatile protein-drug delivery [37]. Injectable and porous cryogels were prepared using a bio-orthogonal click chemistry crosslinking approach with alginate employing tetrazine-norbornene coupling. Laponite nanoparticles were then incorporated within the walls of the cryogel. The results showed the so-called "click alginate" was able to produce cryogels with an interconnected porous structure, and high deformability allowing it to be used through a 16-gauge needle. The pore size range was between 50–300 μm, and small concentrations of laponite found in the gel wall helped with sustained release of a number of proteins with diverse properties [37].

Injectable nanocomposite cryogels have also appeared in research as a method to combat cancer. Bauleth-Ramos et al. used acetalated dextran nanoparticles in an injectable cryogel to combat the negative effects of chemotherapy and even suggested this approach as a potential method of vaccination (Figure 4) [82]. The injectable alginate cryogel was loaded with several therapeutic compounds, including spermine-modified acetalated dextran nanoparticles (Sp-AcDEX NPs). The Sp-AcDEX NPs were released over time to provide therapeutic effects with the nanoparticles aiding in accumulation in the tumour tissue. The reported results were found to be promising, as this method helped induce immunogenic cell death in tumour cells whilst also accumulating drug payloads into the tumour. Further testing was said to be targeted towards the use of the cryogel as an approach to delay or prevent cancer recurrence through the induction of in situ cancer vaccination mediated by antigens and danger signals released from the apoptotic cancer cells [82].

Additional to the work done by Bauleth-Ramos et al., a biomaterial-based vaccination system has been developed by Bencherif et al. [27]. It used minimal extracorporeal manipulation to provide in situ enhancement of dendritic cell (DC) numbers, a physical space where DCs interface with transplanted tumour cells, and an immunogenic additive. Cryogels were injected into mice to localise transplanted tumour cells and deliver immunomodulatory factors. After 4 days of cellular investigation, it was revealed that sponges loaded with 1.5 μg of granulocyte macrophage colony stimulating factor (GM-CSF) led to a significant increase in the total number of cells, and more particularly infiltration by DCs. The works done by Bauleth-Ramos et al. [82] and Bencherif et al. [27] suggest that the cryogels may help to combat against cancers.

Injectable composite cryogels based on GelMA, and cellulose nanocrystals (CNC) or polyamidoamine (PAMAM) dendrimers have been shown to be effective for minimally invasive drug delivery [83]. The reinforced cryogels main function was to provide scaffolding for cell growth and also incorporated the anti-inflammatory corticosteroid drug betamethasone sodium phosphate (BSP) for delivery when implanted. While optimum formulations were identified with the PAMAM dendrimer

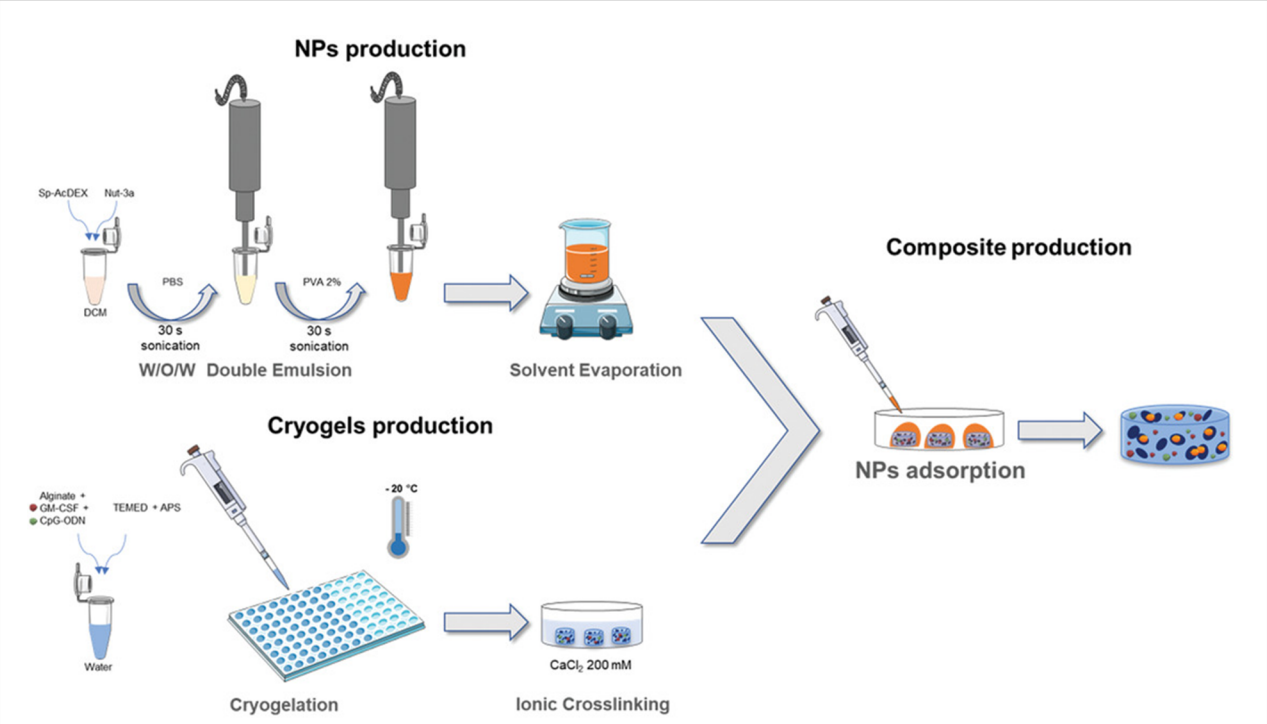


Figure 4: Illustration of the production of the injectable multifunctional composite, comprised of alginate cryogels loaded with GM-CSF and CpG-ODN and Sp-AcDEX NPs loaded with Nut-3a. Nut-3a loaded Sp-AcDEX NPs were produced by double emulsion technique and alginate cryogels were prepared by double crosslinking (covalent and ionic). The composite was prepared by allowing the Sp-AcDEX NPs to adsorb into freshly prepared alginate cryogels. Figure 4 was reproduced from [82], T. Bauleth-Ramos et al., "Acetalated Dextran Nanoparticles Loaded into an Injectable Alginate Cryogel for Combined Chemotherapy and Cancer Vaccination", Adv. Funct. Mater., with permission from John Wiley and Sons. Copyright © 2019 WILEY-VCH Verlag GmbH & Co. KGaA, Weinheim. This content is not subject to CC BY 4.0.

present, the release of BSP was relatively high within a 24-hour period, indicating that further development is needed to achieve sustained release with this system.

After reviewing the recent diverse work currently being achieved in the field of injectable cryogels we can identify that the use of cryogel is not only novel but also extremely effective and easily achievable. Potential risks arise in the use of injectable gels which occur in the presence of not fully polymerised gels being injected into patients. The non-polymerised precursors can cause free radical damage or react with proteins in the human body containing thiols and amino groups [84]. Further toxicity research would be required for all of these cryogels to fully understand how they react in the human body as opposed to animal substitutes.

However, the use of injectable cryogels is a subject matter that has yet to be fully studied. Use of hydrogels in these areas is well known, while cryogels offer most of the benefits that hydrogels can offer with a few added benefits such as their inherent porosity and open macroporous structure which can remain intact after injection [13]. The potential to incorporate nanoparticles within cryogels is also an area of interest due to the interesting properties and chemical interactions both materials have. Bauleth-Ramos et al. even went a step further to combine the nanoparticles healing effects with the cryogel sustained release formulation. Potential fields of study here could include the increase in injectable cryogels that guide drugs (due to the pinpoint injection method and chemical sensitivity [82]) and nanoparticles to targeted sites maximising the efficiency of healing in modern day medicine.

5.3. Cryogels in drug delivery

Polymers are commonly used in drug-delivery applications as they can improve bioavailability of hydrophobic drugs and facilitate a controlled release of the drug. This leads to numerous benefits, including the increased time spent in the therapeutic zone, which allows the drug to be effective but is below the level considered toxic [85]. Drug-delivery systems (DDS) demand safe and effective treatment, and in the majority of cases a long-term target specific treatment would be favoured over general multi-dose pharmaceuticals. Cryogels have been identified as a good material of choice for the development of DDS, as properties can be tailored to meet the exact requirements necessary for a treatment. A major motivation for drug delivery is to produce a system that is a low-cost alternative to

current methods, whilst retaining similar if not better performance. Cryogels' inexpensive preparation and storage make them desirable for replacing currently used DDS where appropriate [73,82]. Moreover, stimuli-responsive cryogels can also be used to control drug release under specific conditions. There are also some emerging areas where cryogels are proving to be uniquely equipped for certain tasks due to their adaptability and physical-chemical properties [18].

Macroporous polymeric gels with their unique heterogeneous open-porous structure open new perspectives for the development of innovative systems for biomedical and pharmaceutical applications. Cryotropic gelation is an efficient method for the preparation of super-macroporous polymer hydrogels. They have large pore sizes which can easily contain samples and additives whilst also retaining biocompatible structures [86]. Some reports focus on the use of model drug compounds [87-89], or newly synthesised antimicrobial compounds [90], for example. Here, we highlight recent examples whereby a drug of clinical relevance has been investigated using cryogels for delivery.

Kostova et al. published research on the novel approach of using cryogels with poly(ethoxytriethyleneglycol acrylate) (PETEGA) in 2011 (see Figure 5) [91]. They reported that the addition of the drug verapamil hydrochloride had no effect on the polymerisation of the cryogel, as gel yields close to 100% were obtained. The verapamil hydrochloride carried via PETEGA cryogels possessed sustained release over a period of more than 8 h, which is attributed to the hydrophobic state of the polymer network at physiological temperature and the method of drug immobilisation. Additionally, cryogels based on other polymers such as polyacrylamide (PAAm), PNIPAM and poly(2-hydroxyethyl methacrylate) (PHEMA), obtained via the same method reported by Kostava et al., have shown similar effects as reported by Petrov et al. in 2007 [30] and 2009 [92].

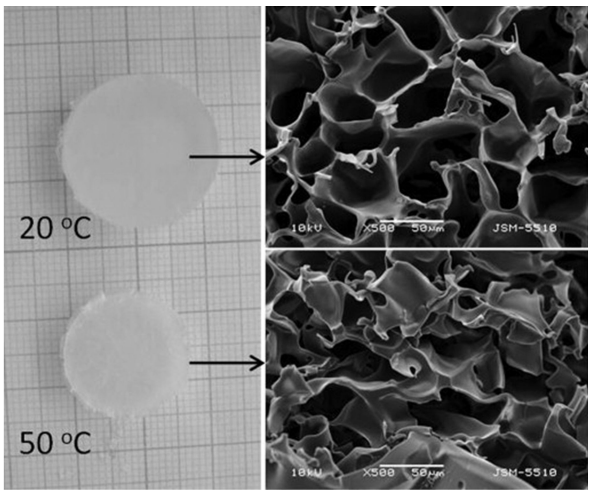


Figure 5: Digital and SEM photographs of PETEGA cryogel at 20 °C (top) and 50 °C (bottom), synthesised via UV irradiation of a moderately frozen system (10 mass % solution of ETEGA; temperature of freezing –20 °C; 5 mass % H_2O_2 and 30 mass % PEGDA to the monomer). Reprinted from [91], Polymer, vol. 52, issue 5, by B. Kostova; D. Momekova; P. Petrov; G. Momekov; N. Toncheva-Moncheva; C. B. Tsvetanov; N. Lambov, "Poly(ethoxytriethyleneglycol acrylate) cryogels as novel sustained drug release systems for oral application", 1217–1222, Copyright (2011), with permission from Elsevier. This content is not subject to CC BY 4.0.

More recently, cryogels have been used to tackle diseases such as cancer. Aliperta et al. have used cryogels in the sustained release of bispecific antibodies for cancer immunotherapy [93], combining stem cells with a biopolymeric cryogel DDS. Human mesenchymal stromal cells (MSCs) were gene-modified to secrete anti-CD33-anti-CD3 bispecific antibodies (bsAb) to be used for the treatment of acute myeloid leukaemia (AML). Macroporous star-shaped poly(ethylene glycol) (starPEG)-heparin cryogels were prepared by combining hydrogel network formation via chemical cross-linking of starPEG and heparin at 4 °C and pH 8. The initial tests were reported to be a success with rapid and efficient transport of nutrients and therapeutic bsAbs via the interconnected macropores, however, more testing is required on its effects on long lasting T cells. Similar positive results were attained by Tam et al., who synthesized biomimetic cryogels whilst also analysing the mechanism of their formation [7,94]. They examined the effects of mono/disaccharide additives on the size of pores and how they interact with polysaccharide polymers to alter cryogel pore size and mechanical properties. In addition, Tam et al. demonstrated the optical transparency with three-dimensional spatial control of immobilised bioactive growth factors using multiphoton patterning and cellular response to immobilised ligands as shown in Figure 6 [94].

Researchers are working on the design of effective and low-cost gel-based DDS. Biopolymeric porous gels can be derived from natural materials such as chitosan. Dinu et al. prepared macroporous structures based on chitosan and clinoptilolite by cryogelation [95]. The group investigated and tested their potential as a DDS using diclofenac sodium and indomethacin as the drugs. They reported the cumulative release of diclofenac sodium from the monoliths lower than 5% at pH 1.2 and higher than 70% at pH 7.4. In addition, they reported cumulative release 6% of indomethacin within the first hour in phosphate buffered saline (PBS) from composite cryogels.

Lima et al. presented an interesting partnership of cryogels with ceramics for a DDS [96]. Polyvinyl alcohol and polyacrylic acid were used as the precursor to the cryogel, and integrated within

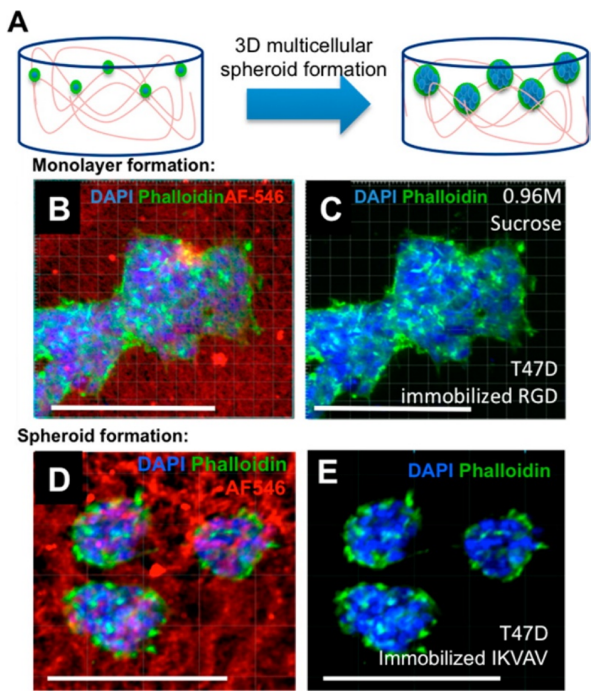


Figure 6: Cell morphology of T47D breast cancer cells cultured in HA cryogels. (A) Schematic representation of cells cultured on HA cryogels resulting in formation of 3D multicellular spheroids. Fluorescently labelled cryogels (red) immobilised with (B, C) RGD peptides result in cell monolayers whereas cryogels immobilised with (D, E) IKVAV peptides result in cellular spheroids. Scale bars represent 200 μm. Reprinted with permission from [94]. Copyright 2016 American Chemical Society. This content is not subject to CC BY 4.0.

the ceramic. They produced a layer-by-layer structure by adding both cryogels and ceramics into a mould, and a physical crosslinker was used to realise the drug theophylline after stimuli had been achieved. Due to the layer system, drug release could occur without diffusion of the subsequent layers, controlling the speed of the release in the ceramic cryogel. In addition, the ceramic can enhance the mechanical properties of composite within the cryogel and can be tailored for specific drugs and drug-release profiles [96].

The drug aripiprazole used to treat schizophrenia was recently investigated for delivery using cryogels comprising β-cyclodextrin (β-CD) functionality [97]. The cryogels were synthesised by photochemical crosslinking of *N*,*N*-dimethylacrylamide (DMA) and β-CD triacrylate (Figure 7) and aripiprazole was incorporated through inclusion inside the hydrophobic β-CD domains. The release of aripiprazole was monitored at pH 1.2 and 6.8, targeting oral delivery, with different release profiles depending on the ratio of DMA/β-CD.

The antifungal agent voriconazole was incorporated into a physically crosslinked cryogel comprising PVA and chitosan grafted with NIPAAm (CS-*g*-PNIPAM) for mucosal applications [98]. Cell culture assays confirmed that the cryogels were non-toxic and the release profiles of voriconazole from a CS-*g*-PNIPAM/PVA 75/25 gel showed release of up to 80% of the encapsulated drug over a period of 8 hours. Sustained release of diclofenac over two weeks was studied using natural biopolymer kefiran cryogels [99]. Kefiran is a biocompatible water-soluble branched polysaccharide, isolated from kefir grains. Scaffolds were prepared by cryogelation of a 2% w/v aqueous solution of the kefiran, without the need for any crosslinking agents. Release of diclofenac, a non-steroidal anti-inflammatory drug, was low with 15% of the drug released after 2 weeks. However, this could result in a sustained release over longer

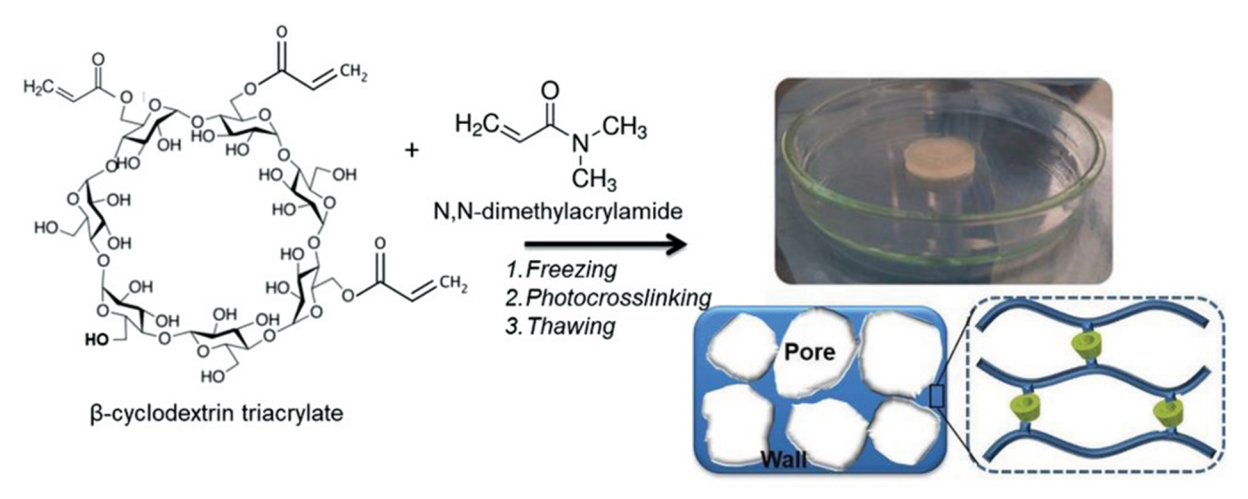


Figure 7: Preparation of PDMA/β-CD cryogel via cryogenic treatment and photochemical crosslinking in frozen state. Figure 7 was reproduced from [97], Y. Danov et al., "Cryogel Carriers Comprising β-Cyclodextrin Moieties for Improved Solubilization and Delivery of Aripiprazole", Macromol. Chem. Phys., with permission from John Wiley and Sons. Copyright © 2021 Wiley-VCH GmbH. This content is not subject to CC BY 4.0.

time periods which would require further investigation. Doxorubicin release from heparin-containing cryogel microcarriers was investigated by Newland et al. [100]. Highly sulphated heparin was used to exploit electrostatic interactions between anionic sulphate groups and the primary amine group present in doxorubicin which confers a positive charge under physiological conditions. This interaction was confirmed by in silico modelling. While the carriers did not show any cytotoxicity, cell viability was reduced in the presence of the doxorubicin-loaded cryogels, suggesting delivery of the drug was successful. These cryogels were also injected into mice, adjacent to an orthotopic breast cancer tumour, impeding tumour growth and metastasis.

Several groups have reported on the use of composite cryogels for drug delivery, whereby the active ingredient is encapsulated within a particle, such as polymeric micelles [101] or microneedles [102], embedded within the cryogel. Therapeutic agents may not necessarily be represented solely by drug molecules. Recent examples of other types of therapeutic cargos used for delivery by cryogels include fertilizers for agrochemical applications [103], peptides [104], proteins [37], and growth factors [81,105,106]. For example, Lee et al. reported the use of a double cryogel structure for the delivery of growth factor for enhanced bone regeneration [105].

5.4. Cryogels in wound healing

The skin acts as a protective barrier against the environment with immunologic and sensorial functions [7]. As of now, the way of dealing with extensive skin loss would be wound dressing, autografts, and allographs but there is a lot of room for improvement. Cryogels can cause cell migration which shows promise to solving these problems and enhancing skin substitutes [7]. An optimal bio-scaffold would have to be biocompatible, biodegradable, have a high pore connectivity and swelling ratio as its function is to promote cell growth and act as a nucleus for cell migration. Moreover, ideally it would also promote hemostasis, the physiological process that stops bleeding. Certain cryogels have the potential to provide all the ideal criteria listed above; this is brought about by careful consideration of the material chemistry and processing techniques. Pore connectivity is needed as it facilitates metabolic and oxygen transport. When cryogels are fully hydrated, they often exhibit a soft consistency which in turn creates low interfacial tension. This low interfacial tension minimises irritation to surrounding tissue post-implantation. This theory has been put into practice because Priya et al, investigated the ability of cryogels to mimic various layers of skin [107]. A polyvinylpyrrolidone-iodine cryogel was used as the top layer to impart antiseptic properties, while the bottom regenerative layer comprised a gelatin cryogel. When the cryogel had been implanted into rabbits which had sustained wounds, the animals with cryogels implanted showed faster and more productive wound healing compared to the untreated rabbits and a complete skin regeneration occurred after 4 weeks with no inflammatory response.

Most reports of cryogels used in wound-healing applications use a naturally occurring biopolymer such as gelatin and/or chitosan in combination with other components. Gelatin and chitosan are known to be biocompatible [108,109], and while gelatin is known to promote cell adhesion [108], chitosan owns haemostatic properties [109]. Neres Santos et al. produced PVA/gelatin cryogels incorporated with manuka honey in the matrix for wound-healing applications [110]. The manuka honey was used to diffuse to the wound through controlled release from the cryogel matrix. Gelatin has also been suggested to be used as scaffolding material in absorbent pads for wound dressing and for surgical use [111]. Chhatri et al. developed physically crosslinked PVA/chitosan cryogels loaded with Savlon (antiseptic liquid) and suggested wound-healing applications for the material [112]. This theory is supported by literature that chitosan is known to accelerate the wound healing process in humans and providing antibacterial properties as well [113]. Physically crosslinked chitosan-gluconic acid cryogels have also been reported by Takei et al., who investigated applying differing methods of sterilisation, using either ethanol washing [114], or by autoclaving the cryogels [115]. Interestingly, the cryogels retained their haemostatic properties following autoclaving at 121 °C for 20 min, and showed comparable healing rates compared to ethanol sterilisation (Figure 8).

A unique take to the development of cryogels as injectable gels is the work achieved by Zhao et al. in developing an injectable antibacterial and conductive shape memory haemostatic cryogel [116]. The cryogel is based on carbon nanotubes (CNT) combined with methacrylated chitosan. Zhao et al. report that the cryogel has robust mechanical strength which is required to aid in wound healing. The shape recovery mechanism of the cryogel is also triggered by blood and has high absorption speed and uptake values, this would mean the cryogel works well for blood clotting purposes. Overall, it was tested against gelatin sponges and traditional gauze which it outperformed. Figure 9 shows the results of Zhao et al. in vivo experimentation. The effectiveness of the CNT-reinforced cryogel can be seen as it consistently is shown outperforming the gauze and/or gelatin sponges. The results concluded that cryogel QCSG/CNT4 was shown to have better haemostatic capability than QCSG/CNT0, and better in vivo wound-healing performance than Tegaderm™ film, gelatin sponge, gauze, and QCSG/CNT0 [116].

Cryogels comprising the natural biopolymers silk fibroin and chitosan, with tannic acid and ferric ions (Fe^{3+}) incorporated have been reported as multifunctional devices for wound

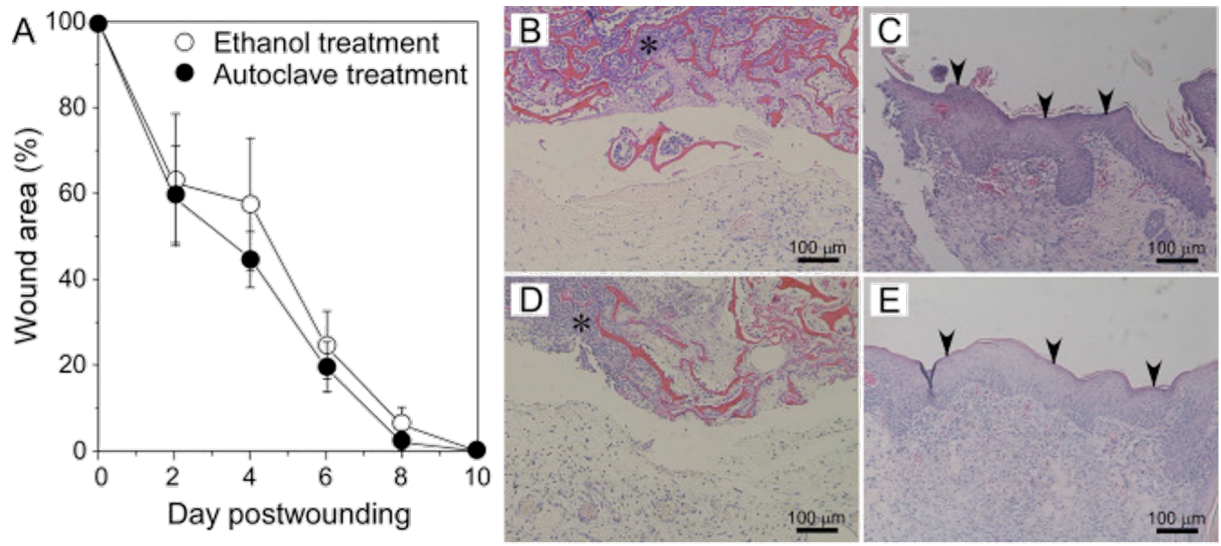


Figure 8: (A) Healing rate of wounds treated with autoclaved CG11 cryogels and those treated with 70% ethanol. (B–E) Hematoxylin and eosin-stained sections of wound tissues treated with autoclaved CG11 cryogels (B, C) and those treated with 70% ethanol (D, E) at 2 days (B, D) and 10 days post wounding (C, E). Reprinted from [115], Journal of Bioscience and Bioengineering, vol. 125, issue 4, by T. Takei; S. Danjo; S. Sakoguchi; S. Tanaka; T. Yoshinaga; H. Nishimata; M. Yoshida, "Autoclavable physically-crosslinked chitosan cryogel as a wound dressing", 490–495, Copyright (2018) The Society for Biotechnology, Japan, with permission from Elsevier. This content is not subject to CC BY 4.0.

healing providing hemostasis, exudate absorbance, antibacterial effects, and promotion of cell proliferation [117]. The tannic acid and ferric ions provide photothermal properties whereby under near infrared (NIR) radiation the temperature increased to enhance the antimicrobial properties, while also showing good hemostasis properties such as blood absorption and clotting, and cell proliferation. Chitosan has also been used by Meena et al. for producing cryogels for haemostatic applications, with locust bean gum (LBG) incorporated to enhance mechanical properties and water absorption [32]. This chitosan/LBG semi-interpenetrating network cryogel was investigated for its swelling, degradation, and protein adsorption properties, demonstrating potential as a haemostatic dressing.

The healing of wounds to skin tissue takes place over a much shorter time scale than the regeneration of bone tissue in fractures and breaks [118,119]. It has been reported that the majority of skin tissue wounding will be healed up to the proliferative phase by 4–6 days depending on the size, location, and severity of the wound [120]. The application of a degradable cryogel with a higher rate of degradation may be preferable compared to the rate of degradation that would be required for other purposes such as severe tissue engineering or bone tissue applications. However, it has been suggested that for wound dressing applications degradation of the cryogels is not wanted, as it may result in small pieces of cryogel remaining in the wound [121]. If full degradation of the cryogel was to occur, this would not be a problem.

Conclusion

While cryogels have been investigated by researchers for decades, they are now finding applications in a broad range of biomedical settings due to their interconnected porosity and advantageous properties. A major advantage of cryogels is their low-cost manufacturing due to the medium of porogens commonly used being water, and relatively low amounts of reagent required. However, there are issues when considering scaling up cryogel syntheses.

The variability of cryogel compositions, dictated by the precursors used, as well as physical properties such as porosity, pore size distribution, wall thickness, and density have given researchers a plethora of tools with which to tune cryogels properties for separation, tissue engineering, for preparing printable and injectable cryogels, wound healing and drug delivery applications. Here, we have reviewed recent advances in the development of injectable cryogels and 3D printing with cryogels, and cryogel applications in wound healing and drug delivery. Showing that while 3D printing of cryogels is still in its infancy developments are being made to develop complex hierarchical structures, with potential to successfully mimic biological structures. This could have a huge impact on how we design scaffolds for tissue engineering and wound healing in the future. Furthermore, injectable cryogels have been an area of intense research in recent years, and injectables could pave the way for new and improved therapies with minimal invasive procedures for patients. Due to the structure of cryogels, they inherently

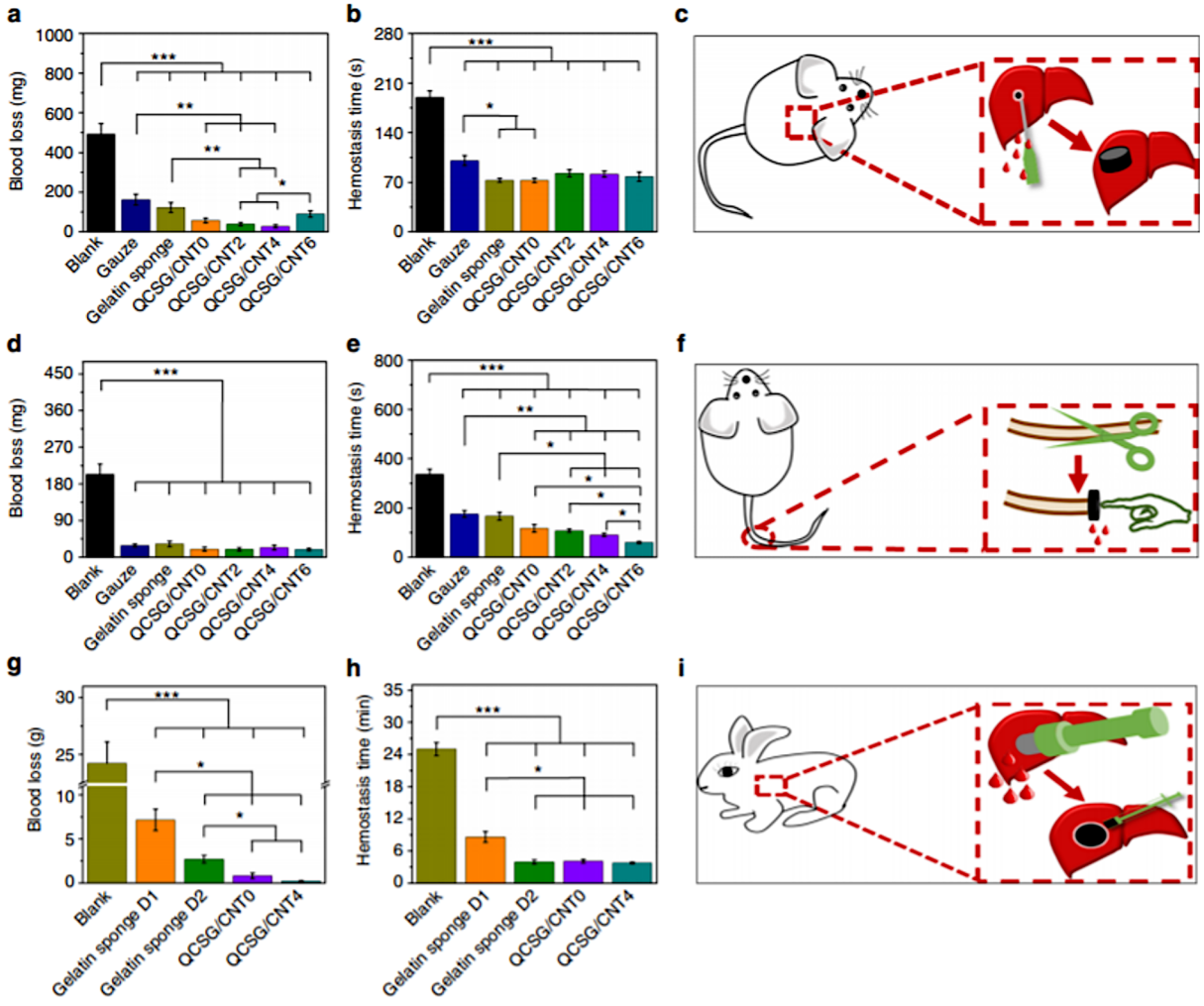


Figure 9: In vivo haemostatic capacity evaluation of the cryogels. Blood loss (a) and haemostatic time (b) in the mouse liver injury model. Schematic (c) represents the injury model for the mouse. Blood loss (d) and haemostatic time (e) in the mouse-tail amputation model. Schematic (f) represents the amputation model of the mouse tail. Blood loss (g) and haemostatic time (h) in the rabbit liver defect lethal noncompressible haemorrhage model. Schematic (i) represents the noncompressible haemorrhage model of the rabbit's liver. Reproduced from [116] (Copyright © 2018 X. Zhao et al., distributed under the terms of the Creative Commons Attribution 4.0 International License, https://creativecommons.org/licenses/by/4.0/).

have a high surface area and hence are a logical candidate for the release of therapeutics from the walls of the material. Similarly, they are excellent candidates for wound healing due to the ability of cryogels to swell and absorb water and provide a sterile environment for new tissue growth, supported by the porous structure.

However, after reviewing these areas of interest there is room for further investigation. For example, cryogels used in injectable gels for DDS is currently an emerging field. In the examples given previously there were no two methods that were similar and when authors compared the use of cryogels, there was mostly comparison to hydrogels rather than previously reported work involving cryogels. In the field of cryogels for drug delivery and wound healing there are several examples of systems that have demonstrated proof of principle. However, there are limited efforts dedicated to testing these on human test subjects which is required to learn the effects these potential drugs can have on humans whether long term or short term.

In the authors opinion, there is a huge positive outlook for the use of cryogels combatting cancer. Future research would be required to identify types of cancers that could be successfully treated using alternative methods such as cryogels, as opposed to well-known chemotherapies. Injectable nanocomposite cryogels have possible ties in cancer research and the potential to form vaccination against several types of cancer. More broadly, this platform may be useful for generating a range of T-cell effect responses from immunity to tolerance. The overall outlook for cryogels is incredibly positive and exciting as they

are a subset of materials which may have a huge impact in many areas of biomedical science and medicine, which we hope to see implemented in the coming years.

ORCID® iDs

Leah Williams - https://orcid.org/0000-0002-7169-8878
Martin Kalmet - https://orcid.org/0000-0002-6672-7865
Fiona L. Hatton - https://orcid.org/0000-0002-0105-7530

References

1. Jones, R. G.; Wilks, E. S.; Metanomski, W. V.; Kahovec, J.; Hess, M.; Stepto, R.; Kitayama, T. *Compendium of Polymer Terminology and Nomenclature;* The Royal Society of Chemistry: Cambridge, UK, 2009. doi:10.1039/9781847559425
2. Memic, A.; Colombani, T.; Eggermont, L. J.; Rezaeeyazdi, M.; Steingold, J.; Rogers, Z. J.; Navare, K. J.; Mohammed, H. S.; Bencherif, S. A. *Adv. Ther.* **2019,** *2,* 1800114. doi:10.1002/adtp.201800114
3. Bhat, S.; Kumar, A. *J. Biosci. Bioeng.* **2012,** *114,* 663–670. doi:10.1016/j.jbiosc.2012.07.005
4. Zhang, H.; Zhang, F.; Wu, J. *React. Funct. Polym.* **2013,** *73,* 923–928. doi:10.1016/j.reactfunctpolym.2012.12.014
5. Lozinsky, V. I.; Galaev, I. Y.; Plieva, F. M.; Savina, I. N.; Jungvid, H.; Mattiasson, B. *Trends Biotechnol.* **2003,** *21,* 445–451. doi:10.1016/j.tibtech.2003.08.002
6. Dragan, E. S. *Chem. Eng. J.* **2014,** *243,* 572–590. doi:10.1016/j.cej.2014.01.065
7. Saylan, Y.; Denizli, A. *Gels* **2019,** *5,* 20. doi:10.3390/gels5020020
8. Savina, I. N.; Zoughaib, M.; Yergeshov, A. A. *Gels* **2021,** *7,* 79. doi:10.3390/gels7030079
9. Eggermont, L. J.; Rogers, Z. J.; Colombani, T.; Memic, A.; Bencherif, S. A. *Trends Biotechnol.* **2020,** *38,* 418–431. doi:10.1016/j.tibtech.2019.09.008
10. Çimen, D.; Özbek, M. A.; Bereli, N.; Mattiasson, B.; Denizli, A. *Gels* **2021,** *7,* 38. doi:10.3390/gels7020038
11. Larsson, E.; Boujemaoui, A.; Malmström, E.; Carlmark, A. *RSC Adv.* **2015,** *5,* 77643–77650. doi:10.1039/c5ra12603g
12. Hixon, K. R.; Lu, T.; Sell, S. A. *Acta Biomater.* **2017,** *62,* 29–41. doi:10.1016/j.actbio.2017.08.033
13. Henderson, T. M. A.; Ladewig, K.; Haylock, D. N.; McLean, K. M.; O'Connor, A. J. *J. Mater. Chem. B* **2013,** *1,* 2682–2695. doi:10.1039/c3tb20280a
14. Okay, O.; Lozinsky, V. I. Synthesis and Structure–Property Relationships of Cryogels. In *Polymeric Cryogels;* Okay, O., Ed.; Advances in Polymer Science, Vol. 263; Springer: Cham, Switzerland, 2014; pp 103–157. doi:10.1007/978-3-319-05846-7_3
15. Razavi, M.; Qiao, Y.; Thakor, A. S. *J. Biomed. Mater. Res., Part A* **2019,** *107,* 2736–2755. doi:10.1002/jbm.a.36777
16. Plieva, F. M.; Karlsson, M.; Aguilar, M.-R.; Gomez, D.; Mikhalovsky, S.; Galaev', I. Y. *Soft Matter* **2005,** *1,* 303–309. doi:10.1039/b510010k
17. Ivanov, R. V.; Lozinsky, V. I.; Noh, S. K.; Han, S. S.; Lyoo, W. S. *J. Appl. Polym. Sci.* **2007,** *106,* 1470–1475. doi:10.1002/app.26559
18. Koshy, S. T.; Ferrante, T. C.; Lewin, S. A.; Mooney, D. J. *Biomaterials* **2014,** *35,* 2477–2487. doi:10.1016/j.biomaterials.2013.11.044
19. Ertürk, G.; Mattiasson, B. *J. Chromatogr. A* **2014,** *1357,* 24–35. doi:10.1016/j.chroma.2014.05.055
20. Macková, H.; Plichta, Z.; Hlídková, H.; Sedláček, O.; Konefal, R.; Sadakbayeva, Z.; Dušková-Smrčková, M.; Horák, D.; Kubinová, Š. *ACS Appl. Mater. Interfaces* **2017,** *9,* 10544–10553. doi:10.1021/acsami.7b01513
21. Sen, T.; Ozcelik, B.; Ozmen, M. M. *Int. J. Polym. Mater. Polym. Biomater.* **2019,** *68,* 411–416. doi:10.1080/00914037.2018.1452225
22. Shiekh, P. A.; Andrabi, S. M.; Singh, A.; Majumder, S.; Kumar, A. *Eur. Polym. J.* **2021,** *144,* 110234. doi:10.1016/j.eurpolymj.2020.110234
23. Bagri, L. P.; Bajpai, J.; Bajpai, A. K. *J. Macromol. Sci., Part A: Pure Appl. Chem.* **2009,** *46,* 1060–1068. doi:10.1080/10601320903252025
24. Ak, F.; Oztoprak, Z.; Karakutuk, I.; Okay, O. *Biomacromolecules* **2013,** *14,* 719–727. doi:10.1021/bm3018033
25. Dispinar, T.; Van Camp, W.; De Cock, L. J.; De Geest, B. G.; Du Prez, F. E. *Macromol. Biosci.* **2012,** *12,* 383–394. doi:10.1002/mabi.201100396
26. Bölgen, N.; Plieva, F.; Galaev, I. Y.; Mattiasson, B.; Pişkin, E. *J. Biomater. Sci., Polym. Ed.* **2007,** *18,* 1165–1179. doi:10.1163/156856207781554064
27. Bencherif, S. A.; Sands, R. W.; Ali, O. A.; Li, W. A.; Lewin, S. A.; Braschler, T. M.; Shih, T. Y.; Verbeke, C. S.; Bhatta, D.; Dranoff, G.; Mooney, D. J. *Nat. Commun.* **2015,** 6. doi:10.1038/ncomms8556
28. Muslumova, S.; Yetiskin, B.; Okay, O. *Gels* **2019,** *5,* 1. doi:10.3390/gels5010001
29. Zhang, H.; Zhou, L.; Zhang, W. *Tissue Eng., Part B* **2014,** *20,* 492–502. doi:10.1089/ten.teb.2013.0452
30. Petrov, P.; Petrova, E.; Tchorbanov, B.; Tsvetanov, C. B. *Polymer* **2007,** *48,* 4943–4949. doi:10.1016/j.polymer.2007.06.027
31. Petrov, P. D.; Tsvetanov, C. B. Cryogels via UV Irradiation. In *Polymeric Cryogels;* Okay, O., Ed.; Advances in Polymer Science, Vol. 263; Springer: Cham, Switzerland, 2014; pp 199–222. doi:10.1007/978-3-319-05846-7_5
32. Meena, L. K.; Raval, P.; Kedaria, D.; Vasita, R. *Bioact. Mater.* **2018,** *3,* 370–384. doi:10.1016/j.bioactmat.2017.11.005
33. Zhang, F.; Wu, W.; Zhang, X.; Meng, X.; Tong, G.; Deng, Y. *Cellulose* **2016,** *23,* 415–425. doi:10.1007/s10570-015-0799-4
34. Klouda, L.; Mikos, A. G. *Eur. J. Pharm. Biopharm.* **2008,** *68,* 34–45. doi:10.1016/j.ejpb.2007.02.025
35. Pasparakis, G.; Vamvakaki, M. *Polym. Chem.* **2011,** *2,* 1234–1248. doi:10.1039/c0py00424c
36. Gandhi, A.; Paul, A.; Sen, S. O.; Sen, K. K. *Asian J. Pharm. Sci.* **2015,** *10,* 99–107. doi:10.1016/j.ajps.2014.08.010
37. Koshy, S. T.; Zhang, D. K. Y.; Grolman, J. M.; Stafford, A. G.; Mooney, D. J. *Acta Biomater.* **2018,** *65,* 36–43. doi:10.1016/j.actbio.2017.11.024
38. O'Brien, F. J. *Mater. Today* **2011,** *14,* 88–95. doi:10.1016/s1369-7021(11)70058-x
39. Deng, Z.; Guo, Y.; Ma, P. X.; Guo, B. *J. Colloid Interface Sci.* **2018,** *526,* 281–294. doi:10.1016/j.jcis.2018.04.093
40. Zhang, X.; Liu, K.; Liu, J.; Ding, Y.; Li, W.; Zhang, A. *Eur. Polym. J.* **2020,** *141,* 110092. doi:10.1016/j.eurpolymj.2020.110092
41. Singh, B.; Chauhan, G. S.; Kumar, S.; Chauhan, N. *Carbohydr. Polym.* **2007,** *67,* 190–200. doi:10.1016/j.carbpol.2006.05.006
42. Galaev, I. Y.; Mattiasson, B. *Trends Biotechnol.* **1999,** *17,* 335–340. doi:10.1016/s0167-7799(99)01345-1
43. Kopeček, J. *J. Polym. Sci., Part A: Polym. Chem.* **2009,** *47,* 5929–5946. doi:10.1002/pola.23607

44. Fallingborg, J. *Dan. Med. Bull.* **1999,** *46,* 183–196.
45. Bilici, C.; Karayel, S.; Demir, T. T.; Okay, O. *J. Appl. Polym. Sci.* **2010,** *118,* 2981–2988. doi:10.1002/app.32693
46. Boyaci, T.; Orakdogen, N. *RSC Adv.* **2015,** *5,* 77235–77247. doi:10.1039/c5ra11634a
47. Wang, J.; Yang, H. *Sci. Rep.* **2018,** *8,* 7155. doi:10.1038/s41598-018-25456-y
48. Wang, Y.; Wang, J.; Ge, L.; Liu, Q.; Jiang, L.; Zhu, J.; Zhou, J.; Xiong, F. *J. Appl. Polym. Sci.* **2013,** *127,* 3749–3759. doi:10.1002/app.37648
49. Bao, H.; Li, L.; Leong, W. C.; Gan, L. H. *J. Phys. Chem. B* **2010,** *114,* 10666–10673. doi:10.1021/jp105041z
50. Seetapan, N.; Mai-ngam, K.; Plucktaveesak, N.; Sirivat, A. *Rheol. Acta* **2006,** *45,* 1011–1018. doi:10.1007/s00397-005-0055-1
51. Huang, C.-H.; Wang, C.-F.; Don, T.-M.; Chiu, W.-Y. *Cellulose* **2013,** *20,* 1791–1805. doi:10.1007/s10570-013-9951-1
52. Li, G.; Guo, L.; Wen, Q.; Zhang, T. *Int. J. Biol. Macromol.* **2013,** *55,* 69–74. doi:10.1016/j.ijbiomac.2012.12.048
53. Dragan, E. S.; Apopei Loghin, D. F.; Cocarta, A.-I.; Doroftei, M. *React. Funct. Polym.* **2016,** *105,* 66–77. doi:10.1016/j.reactfunctpolym.2016.05.015
54. Bakhshpour, M.; Idil, N.; Perçin, I.; Denizli, A. *Appl. Sci.* **2019,** *9,* 553. doi:10.3390/app9030553
55. Ingavle, G. C.; Baillie, L. W. J.; Zheng, Y.; Lis, E. K.; Savina, I. N.; Howell, C. A.; Mikhalovsky, S. V.; Sandeman, S. R. *Biomaterials* **2015,** *50,* 140–153. doi:10.1016/j.biomaterials.2015.01.039
56. Sheng, P. X.; Wee, K. H.; Ting, Y. P.; Chen, J. P. *Chem. Eng. J.* **2008,** *136,* 156–163. doi:10.1016/j.cej.2007.03.033
57. Lutz, J.-F. *J. Polym. Sci., Part A: Polym. Chem.* **2008,** *46,* 3459–3470. doi:10.1002/pola.22706
58. Ionov, L. *Mater. Today* **2014,** *17,* 494–503. doi:10.1016/j.mattod.2014.07.002
59. Feil, H.; Bae, Y. H.; Feijen, J.; Kim, S. W. *Macromolecules* **1993,** *26,* 2496–2500. doi:10.1021/ma00062a016
60. Mikhalovsky, S. V.; Savina, I. N.; Dainiak, M.; Ivanov, A. E.; Galaev, I. Y. Biomaterials/Cryogels. *Comprehensive Biotechnology,* 2nd ed.; Elsevier: Amsterdam, Netherlands, 2011; Vol. 5, pp 11–22. doi:10.1016/b978-0-08-088504-9.00432-3
61. Dainiak, M. B.; Galaev, I. Y.; Kumar, A.; Plieva, F. M.; Mattiasson, B. Chromatography of Living Cells Using Supermacroporous Hydrogels, *Cryogels*. In *Cell Separation;* Kumar, A.; Galaev, I. Y.; Mattiasson, B., Eds.; Advances in Biochemical Engineering/Biotechnology, Vol. 106; Springer: Berlin, Heidelberg, 2007; pp 101–127. doi:10.1007/10_2006_044
62. Kumar, A.; Mishra, R.; Reinwald, Y.; Bhat, S. *Mater. Today* **2010,** *13,* 42–44. doi:10.1016/s1369-7021(10)70202-9
63. Shick, T. M.; Abdul Kadir, A. Z.; Ngadiman, N. H. A.; Ma'aram, A. *J. Bioact. Compat. Polym.* **2019,** *34,* 415–435. doi:10.1177/0883911519877426
64. Lanza, R.; Langer, R.; Vacanti, J. P. *Principles of Tissue Engineering,* 4th ed.; Elsevier: Amsterdam, Netherlands, 2014. doi:10.1016/c2011-0-07193-4
65. Kim, G.; Ahn, S.; Yoon, H.; Kim, Y.; Chun, W. *J. Mater. Chem.* **2009,** *19,* 8817–8823. doi:10.1039/b914187a
66. Ahn, S.; Yoon, H.; Kim, G.; Kim, Y.; Lee, S.; Chun, W. *Tissue Eng., Part C* **2010,** *16,* 813–820. doi:10.1089/ten.tec.2009.0511
67. Jin Lee, H.; Kim, G. H. *RSC Adv.* **2012,** *2,* 7578–7587. doi:10.1039/c2ra20836a
68. Serex, L.; Braschler, T.; Filippova, A.; Rochat, A.; Béduer, A.; Bertsch, A.; Renaud, P. *Adv. Mater. Technol. (Weinheim, Ger.)* **2018,** *3,* 1700340. doi:10.1002/admt.201700340
69. Béduer, A.; Piacentini, N.; Aeberli, L.; Da Silva, A.; Verheyen, C. A.; Bonini, F.; Rochat, A.; Filippova, A.; Serex, L.; Renaud, P.; Braschler, T. *Acta Biomater.* **2018,** *76,* 71–79. doi:10.1016/j.actbio.2018.05.056
70. Biçen Ünlüer, Ö.; Emir Diltemiz, S.; Say, M. G.; Hür, D.; Say, R.; Ersöz, A. *Int. J. Polym. Mater. Polym. Biomater.* **2020,** 1–13. doi:10.1080/00914037.2020.1825083
71. Suo, H.; Zhang, J.; Xu, M.; Wang, L. *Mater. Sci. Eng., C* **2021,** *123,* 111963. doi:10.1016/j.msec.2021.111963
72. Matthews, K.; Matthews, C. A. Neurosurgery for Mental Disorder. *The ECT Handbook;* Cambridge University Press: Cambridge, UK, 2019; pp 140–148. doi:10.1017/9781911623175.016
73. Bencherif, S. A.; Sands, R. W.; Bhatta, D.; Arany, P.; Verbeke, C. S.; Edwards, D. A.; Mooney, D. J. *Proc. Natl. Acad. Sci. U. S. A.* **2012,** *109,* 19590–19595. doi:10.1073/pnas.1211516109
74. Chen, M. H.; Chung, J. J.; Mealy, J. E.; Zaman, S.; Li, E. C.; Arisi, M. F.; Atluri, P.; Burdick, J. A. *Macromol. Biosci.* **2019,** *19,* 1800248. doi:10.1002/mabi.201800248
75. Liu, M.; Cao, Z.; Zhang, R.; Chen, Y.; Yang, X. *ACS Appl. Mater. Interfaces* **2021,** *13,* 33874–33884. doi:10.1021/acsami.1c08285
76. Liu, Z.; Xu, G.; Wang, C.; Li, C.; Yao, P. *Int. J. Pharm.* **2017,** *530,* 53–62. doi:10.1016/j.ijpharm.2017.07.063
77. Nichol, J. W.; Koshy, S. T.; Bae, H.; Hwang, C. M.; Yamanlar, S.; Khademhosseini, A. *Biomaterials* **2010,** *31,* 5536–5544. doi:10.1016/j.biomaterials.2010.03.064
78. Babensee, J. E.; Anderson, J. M.; McIntire, L. V.; Mikos, A. G. *Adv. Drug Delivery Rev.* **1998,** *33,* 111–139. doi:10.1016/s0169-409x(98)00023-4
79. Lai, T. C.; Yu, J.; Tsai, W. B. *J. Mater. Chem. B* **2016,** *4,* 2304–2313. doi:10.1039/c5tb02518d
80. Eigel, D.; Werner, C.; Newland, B. *Neurochem. Int.* **2021,** *147,* 105012. doi:10.1016/j.neuint.2021.105012
81. Newland, B.; Newland, H.; Lorenzi, F.; Eigel, D.; Welzel, P. B.; Fischer, D.; Wang, W.; Freudenberg, U.; Rosser, A.; Werner, C. *ACS Chem. Neurosci.* **2021,** *12,* 1178–1188. doi:10.1021/acschemneuro.1c00005
82. Bauleth-Ramos, T.; Shih, T.-Y.; Shahbazi, M.-A.; Najibi, A. J.; Mao, A. S.; Liu, D.; Granja, P.; Santos, H. A.; Sarmento, B.; Mooney, D. J. *Adv. Funct. Mater.* **2019,** *29,* 1903686. doi:10.1002/adfm.201903686
83. Goodarzi, K.; Jonidi Shariatzadeh, F.; Solouk, A.; Akbari, S.; Mirzadeh, H. *Eur. Polym. J.* **2020,** *139,* 109992. doi:10.1016/j.eurpolymj.2020.109992
84. Young, S.; Wong, M.; Tabata, Y.; Mikos, A. G. *J. Controlled Release* **2005,** *109,* 256–274. doi:10.1016/j.jconrel.2005.09.023
85. Saikia, C.; Gogoi, P.; Maji, T. K. *J. Mol. Genet. Med.* **2015,** *S4,* 006.
86. Kumar, A., Ed. *Supermacroporous Cryogels: Biomedical and Biotechnological Applications;* CRC Press: Boca Raton, FL, USA, 2016. doi:10.1201/b19676
87. Evans, C.; Morimitsu, Y.; Hisadome, T.; Inomoto, F.; Yoshida, M.; Takei, T. *J. Biosci. Bioeng.* **2021,** *132,* 81–87. doi:10.1016/j.jbiosc.2021.03.008
88. Pacelli, S.; Di Muzio, L.; Paolicelli, P.; Fortunati, V.; Petralito, S.; Trilli, J.; Casadei, M. A. *Int. J. Biol. Macromol.* **2021,** *166,* 1292–1300. doi:10.1016/j.ijbiomac.2020.10.273

89. Boccia, A. C.; Scavia, G.; Schizzi, I.; Conzatti, L. *Molecules* **2020,** *25,* 2557. doi:10.3390/molecules25112557
90. Elsherbiny, D. A.; Abdelgawad, A. M.; El-Naggar, M. E.; El-Sherbiny, R. A.; El-Rafie, M. H.; El-Sayed, I. E.-T. *Int. J. Biol. Macromol.* **2020,** *163,* 96–107. doi:10.1016/j.ijbiomac.2020.06.251
91. Kostova, B.; Momekova, D.; Petrov, P.; Momekov, G.; Toncheva-Moncheva, N.; Tsvetanov, C. B.; Lambov, N. *Polymer* **2011,** *52,* 1217–1222. doi:10.1016/j.polymer.2011.01.049
92. Petrov, P.; Petrova, E.; Tsvetanov, C. B. *Polymer* **2009,** *50,* 1118–1123. doi:10.1016/j.polymer.2008.12.039
93. Aliperta, R.; Welzel, P. B.; Bergmann, R.; Freudenberg, U.; Berndt, N.; Feldmann, A.; Arndt, C.; Koristka, S.; Stanzione, M.; Cartellieri, M.; Ehninger, A.; Ehninger, G.; Werner, C.; Pietzsch, J.; Steinbach, J.; Bornhäuser, M.; Bachmann, M. P. *Sci. Rep.* **2017,** *7,* 42855. doi:10.1038/srep42855
94. Tam, R. Y.; Fisher, S. A.; Baker, A. E. G.; Shoichet, M. S. *Chem. Mater.* **2016,** *28,* 3762–3770. doi:10.1021/acs.chemmater.6b00627
95. Dinu, M. V.; Cocarta, A. I.; Dragan, E. S. *Carbohydr. Polym.* **2016,** *153,* 203–211. doi:10.1016/j.carbpol.2016.07.111
96. de Lima, G. G.; Traon, F.; Moal, E.; Canillas, M.; Rodriguez, M. A.; McCarthy, H. O.; Dunne, N.; Devine, D. M.; Nugent, M. J. D. *Polym. Compos.* **2018,** *39,* E210–E220. doi:10.1002/pc.24450
97. Danov, Y.; Georgieva, D.; Mihaylova, R.; Kostova, B.; Petrov, P. D. *Macromol. Chem. Phys.* **2021,** *222,* 2100004. doi:10.1002/macp.202100004
98. Cheaburu-Yilmaz, C. N.; Yilmaz, O.; Kose, F. A.; Bibire, N. *Polymers (Basel, Switz.)* **2019,** *11,* 1432. doi:10.3390/polym11091432
99. Radhouani, H.; Bicho, D.; Gonçalves, C.; Maia, F. R.; Reis, R. L.; Oliveira, J. M. *Mater. Today Commun.* **2019,** *20,* 100554. doi:10.1016/j.mtcomm.2019.100554
100. Newland, B.; Varricchio, C.; Körner, Y.; Hoppe, F.; Taplan, C.; Newland, H.; Eigel, D.; Tornillo, G.; Pette, D.; Brancale, A.; Welzel, P. B.; Seib, F. P.; Werner, C. *Carbohydr. Polym.* **2020,** *245,* 116504. doi:10.1016/j.carbpol.2020.116504
101. Momekova, D.; Ivanov, E.; Konstantinov, S.; Ublekov, F.; Petrov, P. D. *Polymers (Basel, Switz.)* **2020,** *12,* 1172. doi:10.3390/polym12051172
102. Saraswathy, K.; Agarwal, G.; Srivastava, A. *J. Appl. Polym. Sci.* **2020,** *137,* 49285. doi:10.1002/app.49285
103. Akbari, A.; Jafari, H.; Gohari, G.; Kheiri, G.; Mahdavinia, G. R. *Int. Nano Lett.* **2021,** in press. doi:10.1007/s40089-021-00344-y
104. Chambre, L.; Rosselle, L.; Barras, A.; Aydin, D.; Loczechin, A.; Gunbay, S.; Sanyal, R.; Skandrani, N.; Metzler-Nolte, N.; Bandow, J. E.; Boukherroub, R.; Szunerits, S.; Sanyal, A. *ACS Appl. Mater. Interfaces* **2020,** *12,* 56805–56814. doi:10.1021/acsami.0c17633
105. Lee, S. S.; Kim, J. H.; Jeong, J.; Kim, S. H. L.; Koh, R. H.; Kim, I.; Bae, S.; Lee, H.; Hwang, N. S. *Biomaterials* **2020,** *257,* 120223. doi:10.1016/j.biomaterials.2020.120223
106. Sultankulov, B.; Berillo, D.; Kauanova, S.; Mikhalovsky, S.; Mikhalovska, L.; Saparov, A. *Pharmaceutics* **2019,** *11,* 650. doi:10.3390/pharmaceutics11120650
107. Priya, S. G.; Gupta, A.; Jain, E.; Sarkar, J.; Damania, A.; Jagdale, P. R.; Chaudhari, B. P.; Gupta, K. C.; Kumar, A. *ACS Appl. Mater. Interfaces* **2016,** *8,* 15145–15159. doi:10.1021/acsami.6b04711
108. Su, K.; Wang, C. *Biotechnol. Lett.* **2015,** *37,* 2139–2145. doi:10.1007/s10529-015-1907-0
109. Croisier, F.; Jérôme, C. *Eur. Polym. J.* **2013,** *49,* 780–792. doi:10.1016/j.eurpolymj.2012.12.009
110. Neres Santos, A.; Duarte Moreira, A.; Piler Carvalho, C.; Luchese, R.; Ribeiro, E.; McGuinness, G.; Fernandes Mendes, M.; Nunes Oliveira, R. *Materials* **2019,** *12,* 559. doi:10.3390/ma12040559
111. Sharma, A.; Bhat, S.; Nayak, V.; Kumar, A. *Mater. Sci. Eng., C* **2015,** *47,* 298–312. doi:10.1016/j.msec.2014.11.031
112. Chhatri, A.; Bajpai, J.; Bajpai, A. K. *Biomatter* **2011,** *1,* 189–197. doi:10.4161/biom.19005
113. Wu, Y.-B.; Yu, S.-H.; Mi, F.-L.; Wu, C.-W.; Shyu, S.-S.; Peng, C.-K.; Chao, A.-C. *Carbohydr. Polym.* **2004,** *57,* 435–440. doi:10.1016/j.carbpol.2004.05.013
114. Takei, T.; Nakahara, H.; Ijima, H.; Kawakami, K. *Acta Biomater.* **2012,** *8,* 686–693. doi:10.1016/j.actbio.2011.10.005
115. Takei, T.; Danjo, S.; Sakoguchi, S.; Tanaka, S.; Yoshinaga, T.; Nishimata, H.; Yoshida, M. *J. Biosci. Bioeng.* **2018,** *125,* 490–495. doi:10.1016/j.jbiosc.2017.10.015
116. Zhao, X.; Guo, B.; Wu, H.; Liang, Y.; Ma, P. X. *Nat. Commun.* **2018,** *9,* 2784. doi:10.1038/s41467-018-04998-9
117. Yu, Y.; Li, P.; Zhu, C.; Ning, N.; Zhang, S.; Vancso, G. J. *Adv. Funct. Mater.* **2019,** *29,* 1904402. doi:10.1002/adfm.201904402
118. Cañedo-Dorantes, L.; Cañedo-Ayala, M. *Int. J. Inflammation* **2019,** 3706315. doi:10.1155/2019/3706315
119. Doblaré, M.; Garcıa, J. M.; Gómez, M. J. *Eng. Fract. Mech.* **2004,** *71,* 1809–1840. doi:10.1016/j.engfracmech.2003.08.003
120. Broughton, G., II; Janis, J. E.; Attinger, C. E. *Plast. Reconstr. Surg.* **2006,** *117,* 12S–34S. doi:10.1097/01.prs.0000225430.42531.c2
121. Takei, T.; Nakahara, H.; Tanaka, S.; Nishimata, H.; Yoshida, M.; Kawakami, K. *J. Mater. Sci.: Mater. Med.* **2013,** *24,* 2479–2487. doi:10.1007/s10856-013-4991-5

License and Terms

This is an Open Access article under the terms of the Creative Commons Attribution License (https://creativecommons.org/licenses/by/4.0). Please note that the reuse, redistribution and reproduction in particular requires that the author(s) and source are credited and that individual graphics may be subject to special legal provisions.

The license is subject to the *Beilstein Journal of Organic Chemistry* terms and conditions: (https://www.beilstein-journals.org/bjoc/terms)

The definitive version of this article is the electronic one which can be found at: https://doi.org/10.3762/bjoc.17.171

BEILSTEIN JOURNAL OF ORGANIC CHEMISTRY

Adjusting the length of supramolecular polymer bottlebrushes by top-down approaches

Tobias Klein[‡1,2], Franka V. Gruschwitz[‡1,2], Maren T. Kuchenbrod[1,2], Ivo Nischang[1,2], Stephanie Hoeppener[1,2] and Johannes C. Brendel[*1,2]

Letter

Open Access

Address:
[1]Laboratory of Organic and Macromolecular Chemistry (IOMC), Friedrich Schiller University Jena, Humboldtstraße 10, 07743 Jena, Germany and [2]Jena Center for Soft Matter (JCSM), Friedrich Schiller University Jena, Philosophenweg 7, 07743 Jena, Germany

Email:
Johannes C. Brendel[*] - johannes.brendel@uni-jena.de

* Corresponding author ‡ Equal contributors

Keywords:
distribution; dual centrifugation; filomicelles; self-assembly; ultrasonication

Beilstein J. Org. Chem. **2021,** *17,* 2621–2628.
https://doi.org/10.3762/bjoc.17.175

Received: 30 July 2021
Accepted: 29 September 2021
Published: 21 October 2021

This article is part of the thematic issue "Polymer chemistry: fundamentals and applications".

Guest Editor: B. V. K. J. Schmidt

© 2021 Klein et al.; licensee Beilstein-Institut.
License and terms: see end of document.

Abstract

Controlling the length of one-dimensional (1D) polymer nanostructures remains a key challenge on the way toward the applications of these structures. Here, we demonstrate that top-down processing facilitates a straightforward adjustment of the length of polyethylene oxide (PEO)-based supramolecular polymer bottlebrushes (SPBs) in aqueous solutions. These cylindrical structures self-assemble via directional hydrogen bonds formed by benzenetrisurea (BTU) or benzenetrispeptide (BTP) motifs located within the hydrophobic core of the fiber. A slow transition from different organic solvents to water leads first to the formation of µm-long fibers, which can subsequently be fragmented by ultrasonication or dual asymmetric centrifugation. The latter allows for a better adjustment of applied shear stresses, and thus enables access to differently sized fragments depending on time and rotation rate. Extended sonication and scission analysis further allowed an estimation of tensile strengths of around 16 MPa for both the BTU and BTP systems. In combination with the high kinetic stability of these SPBs, the applied top-down methods represent an easily implementable technique toward 1D polymer nanostructures with an adjustable length in the range of interest for perspective biomedical applications.

Introduction

Cylindrical polymer nanostructures in solution have received increasing attention during the last two decades, related to the high surface-to-volume ratio, which is particularly attractive for targeted carrier materials in biomedical applications. In addition, cylindrical drug delivery vehicles appear to be advantageous compared to the spherical analogues with regard to blood circulation time, drug loading, and tumor penetration abilities [1-3]. However, the straightforward preparation of cylindrical polymer aggregates with defined and reproducible length still remains challenging but represents a prerequisite for the desired applications in nanomedicine [4,5]. A key factor in this regard are formulation strategies, which allow a straightforward imple-

mentation into established processes that are, e.g., in accordance with good manufacturing practice (GMP) [6]. Approaches such as the crystallization-driven self-assembly (CDSA) or the synthesis of covalently bound cylindrical polymer brushes (CPBs) offer access to a defined fiber length [7-16]. However, they also suffer from disadvantages, such as significant experimental effort to evaluate suitable reaction procedures for the synthesis or the conditions for the assembly process, and are therefore often limited to specific materials. An alternative is the use of molecular motifs capable of forming directional supramolecular interaction forces, such as hydrogen bonds or π-interactions, to guide the one-dimensional (1D) assembly of established, commercial polymers in solution [17]. We recently reported the self-assembly of polyethylene oxide (PEO) polymers into cylindrical nanostructures, also called supramolecular polymer bottlebrushes (SPBs), based on the end group modification with hydrogen bond forming benzenetrisurea (BTU) and benzenetrispeptide (BTP) motifs [18-20]. The resulting amphiphilic character of the materials facilitated a control of the kinetic assembly, which provided access to stable nanostructures on a broad length range (<100 nm–2 µm). While the process enables a good adjustment of the length, it relies on a precise control of the assembly pathway and requires the use of organic solvents, such as THF and DMF, which limits the applicability in pharmaceutical formulations [21]. For an application in nanomedicine, a length in the range of 100–200 nm is particularly attractive to ensure cellular uptake and to access the known size window for a potential enhanced permeability and retention effect (EPR) [22,23]. As an alternative for the assembly pathway control, we opted to apply easy-to-use top-down approaches to tune the length distribution in a straightforward fashion over the above-mentioned length range of interest. While ultrasonication (US) represents a standard but rather harsh fragmentation technique, we additionally introduced dual asymmetric centrifugation (DAC) as an excellent alternative top-down method for effective, more controlled, and adaptable preparation of polymer nanostructures [24-28]. Both methods are applied for fragmentation of initially µm-long SPBs based on BTU–PEO and BTP–PEO conjugates. The resulting nanofibers were characterized in detail by cryogenic transmission electron microscopy (cryoTEM), as well as by asymmetrical flow field-flow fractionation measurements coupled to a UV detector and a multiangle laser light scattering detector (AF4–MALLS technique) to estimate the apparent structure length and the length distribution of the SPBs.

Results and Discussion

The general structure of the tested BTP and BTU is depicted in Figure 1 [19,20]. While the hydrogen bonding moieties are either urea-based or peptide-based (i.e., phenylalanine) units, the dodecyl chains act as hydrophobic shields to induce the amphiphilic assembly in water and prevent the surrounding water from interfering with the hydrogen bonds in the interior [29]. Attaching a hydrophilic PEO chain (2 kg·mol^{-1}), the compounds self-assemble into long fiber structures consisting of 2–4 lateral core units upon transfer into water, as reported previously [19-21]. A slow solvent change from a THF solution to water resulted in µm-long fibers in both cases (BTU or BTP).

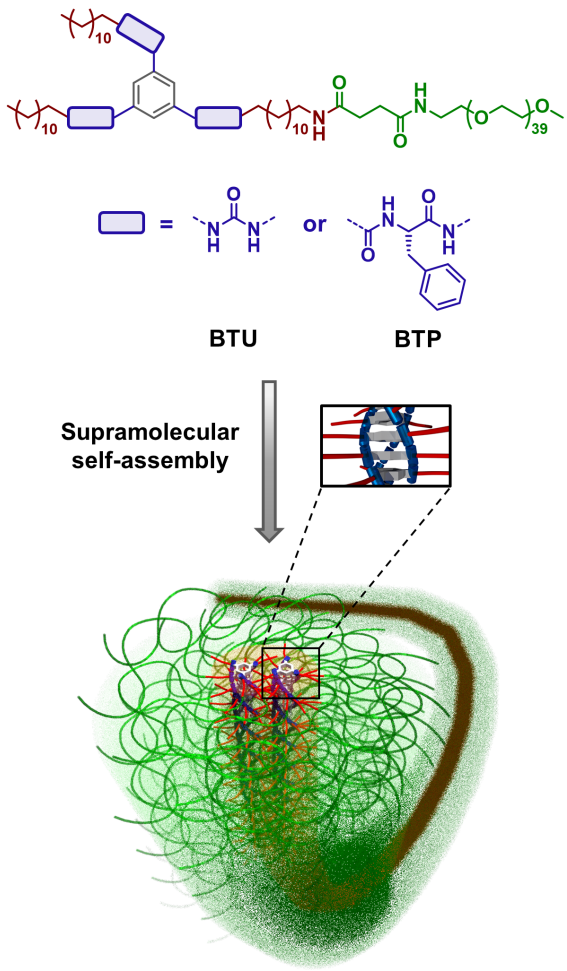


Figure 1: Schematic representation of the chemical structures of BTU and BTP and the supramolecular self-assembly of the compounds into SPBs.

An initial attempt to tune the fiber length by changing the initial organic solvent was not successful. As seen in the corresponding cryoTEM images (Figures S1–S6, Supporting Information File 1) as well as AF4 measurements (Figure S10, Supporting Information File 1), all tested organic solvents yielded similarly µm-long fibers, exemplifying the surprisingly minor influence of the initial organic solvent on the resulting fiber length. Alternatively, a targeted size below 1 µm can be achieved by top-

down strategies inducing strong shear forces. Typically, US is applied to fragment supramolecular structures [7,30-33]. However, US causes cavitation within the sample, the collapse of which is accompanied by very high local heating. Alternative approaches rely on inducing strong shear forces by strong mixers or dispersers. An interesting method in this regard is the use of DAC, which is also considered to be a speed-mix technology due to the rapid mixing of the sample [28]. In DAC, the sample holder performs an additional rotation besides the main rotor rotation, resulting in a continuous change of the direction of the centrifugal force [28]. This change induces a strong agitation of the solution and generates large shear forces. DAC has mainly been used to create drug composites but recently found application in the formulation of liposomes or the direct nanodispersion of pharmaceutically active ingredients [24-28]. The technique resembles nanomilling methods but allows a much smaller sample scale, which renders it particularly attractive for testing the suitability to fragment fiber-like supramolecular assemblies in solution [34].

We started with a rotational speed of 1,000 rpm and treated the initial fibers for 10 min using samples BTU DAC (10 min, 1,000 rpm) and BTP DAC (10 min, 1,000 rpm). This comparably mild treatment already caused a significant fragmentation of the µm-long fibers, resulting in structures of 50–200 nm length according to the cryoTEM images after 10 min of treatment (Figure 2). An average fiber length of 92 ± 51 nm and 74 ± 39 nm for BTU DAC (10 min, 1,000 rpm) and BTP DAC (10 min, 1,000 rpm), respectively, were apparent according to cryoTEM.

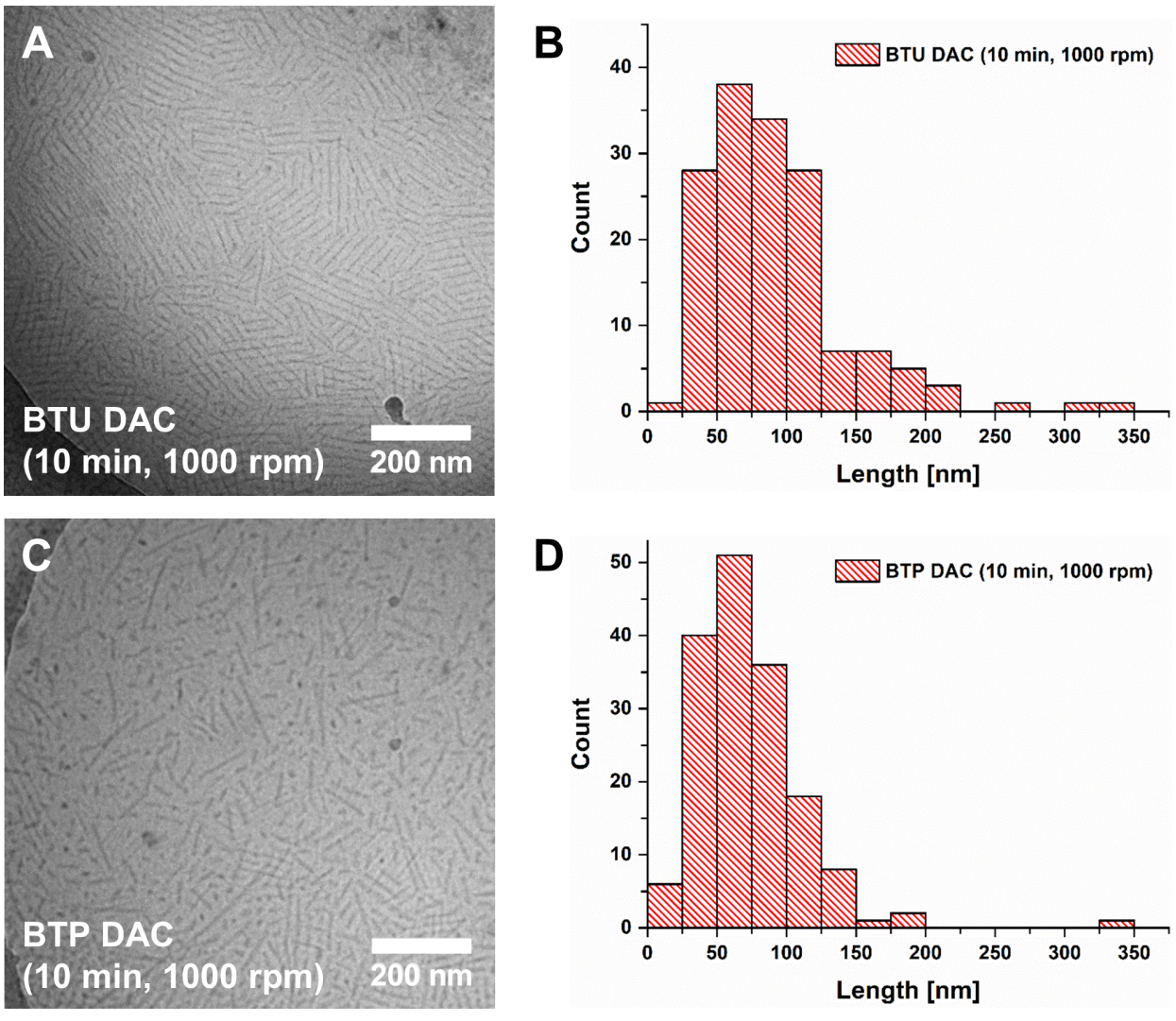


Figure 2: cryoTEM images of A) BTU DAC (10 min, 1,000 rpm) and C) BTP DAC (10 min, 1,000 rpm). The corresponding histograms B) and D) show the length distribution of BTU DAC (10 min, 1,000 rpm, B, mean length: 92 ± 51 nm) and BTP DAC (10 min, 1,000 rpm, D, mean length: 74 ± 39 nm).

This could further be supported by AF4 measurements (Figure 3A and 3B). Here, fibers featuring an average radius of gyration of $R_g \approx 20$ nm and a weight-average molar mass of $M_w = 3{,}099{,}000$ g·mol^{-1}, corresponding to a number of aggregation of $N_{agg} \approx 1{,}200$ and a length of 110 nm for BTU (assuming four units per cross-section), as well as a weight-average molar mass of $M_w = 4{,}406{,}000$ g·mol^{-1}, corresponding to a number of aggregation of $N_{agg} \approx 490$ and a length of 120 nm (assuming two units per cross-section) for BTP, could be observed after 10 min at 1,000 rpm (Figure S12A and S12B, Supporting Information File 1) [19,21].

As a consequence, we scrutinized the influence of time and rotation speed on the size of the fragments, which were analyzed by AF4 (Figure 3). First, samples were treated for 1, 5, and 10 min at a rotation speed of 1,000 rpm (Figure 3A and 3B as well as Figure S12A and S12B, Supporting Information File 1) to investigate if an extended exposure time can break up the aggregates even further. For BTU, the peak maximum of the UV trace was shifted from 60 min to 45 min already after 1 min of mixing (Figure 3A). After 5 min of centrifugation, no further change could be observed since the peak at this low elution time already corresponded to very small oligomers (Figure 3A). For BTP, a stronger downward shift of the peak maximum from 70 to 45 min could be observed after 1 min of mixing. Similar to BTU, the increase in centrifugation time to 5 min led to a more pronounced fragmentation, which was not further enhanced by prolonged DAC.

To determine the influence of the strength of the shear forces, we also increased or decreased the centrifugal speed to 2,500 and 500 rpm, respectively (Figure 3C and 3D). At 2,500 rpm, the fragmentation of the aggregates occurred more rapidly, and a significant shift in AF4 elution time was observed for both samples, BTU and BTP, within 1 min of DAC (Figure S11A and S11B, Supporting Information File 1). For BTU, the samples were further fragmented with extended time at this speed, and the smallest structures were obtained for BTU with

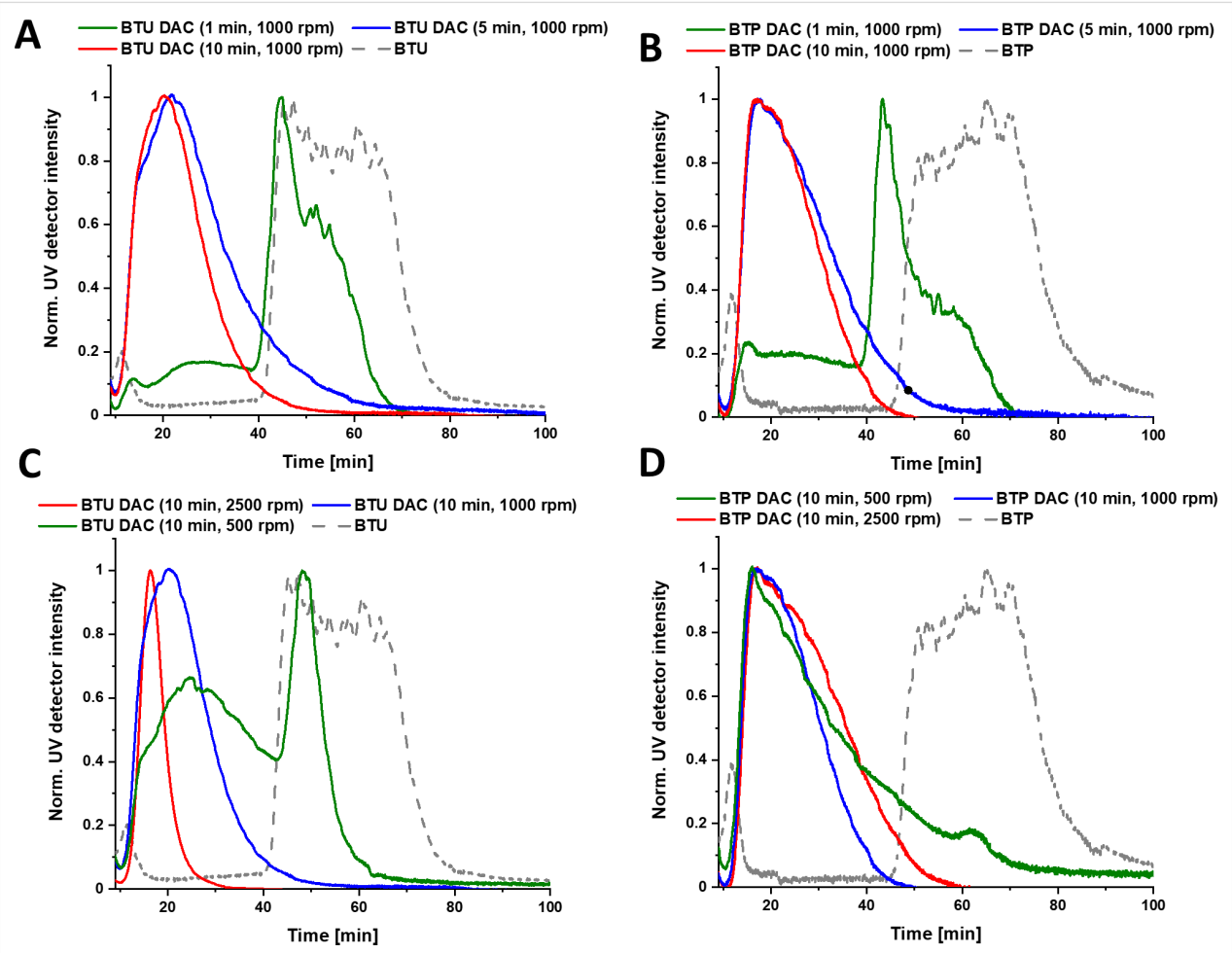


Figure 3: AF4 elution profiles showing the stability against dual centrifugation over different time ranges at a rotation speed of 1,000 rpm (A and B) and 2500 rpm (C and D) of BTU and BTP, respectively. Injection peaks are omitted for clarity.

R_g < 3 nm (Figure S12C, Supporting Information File 1). On the contrary, the reduction of the applied shear forces (500 rpm) limited the fragmentation rate for both samples. For BTU and after 10 min, a significant amount of the large structures (>40 min elution time) remained intact (Figure 3C and 3D as well as Figure S11C and S11D, Supporting Information File 1). Overall, DAC represents a straightforward technique to adjust the size of these supramolecular assemblies, which could easily be tuned by variation of rotational speed and treatment time. Nevertheless, the distribution of the aggregate size remained rather broad. Increasing the time of treatment, the length of the fibers appeared to approach a lower size limit depending on the speed of rotation, which became particularly apparent for the BTU compounds. Even an extended mixing time of 3 h at 2,500 rpm did not significantly change the observed distributions compared to 10 min treatment (Figure S13, Supporting Information File 1).

For comparison to more established techniques, we tested the impact of US on the same fibers. Initial tests on treating fibers within an ultrasound bath (≈11.5 W·L^{-1}) did not reveal any changes in the structure. Therefore, we decided to apply a US probe at higher power (200 W) and varied the exposure times (Figure 4).

Already after 1 s of US, a significant decrease in the length of the fibers could be seen for both samples (Figure 4A and 4C), substantiating the rather harsh forces induced by this technique at the applied conditions. A reduction of the applied power might represent a suitable way to further limit the shear forces

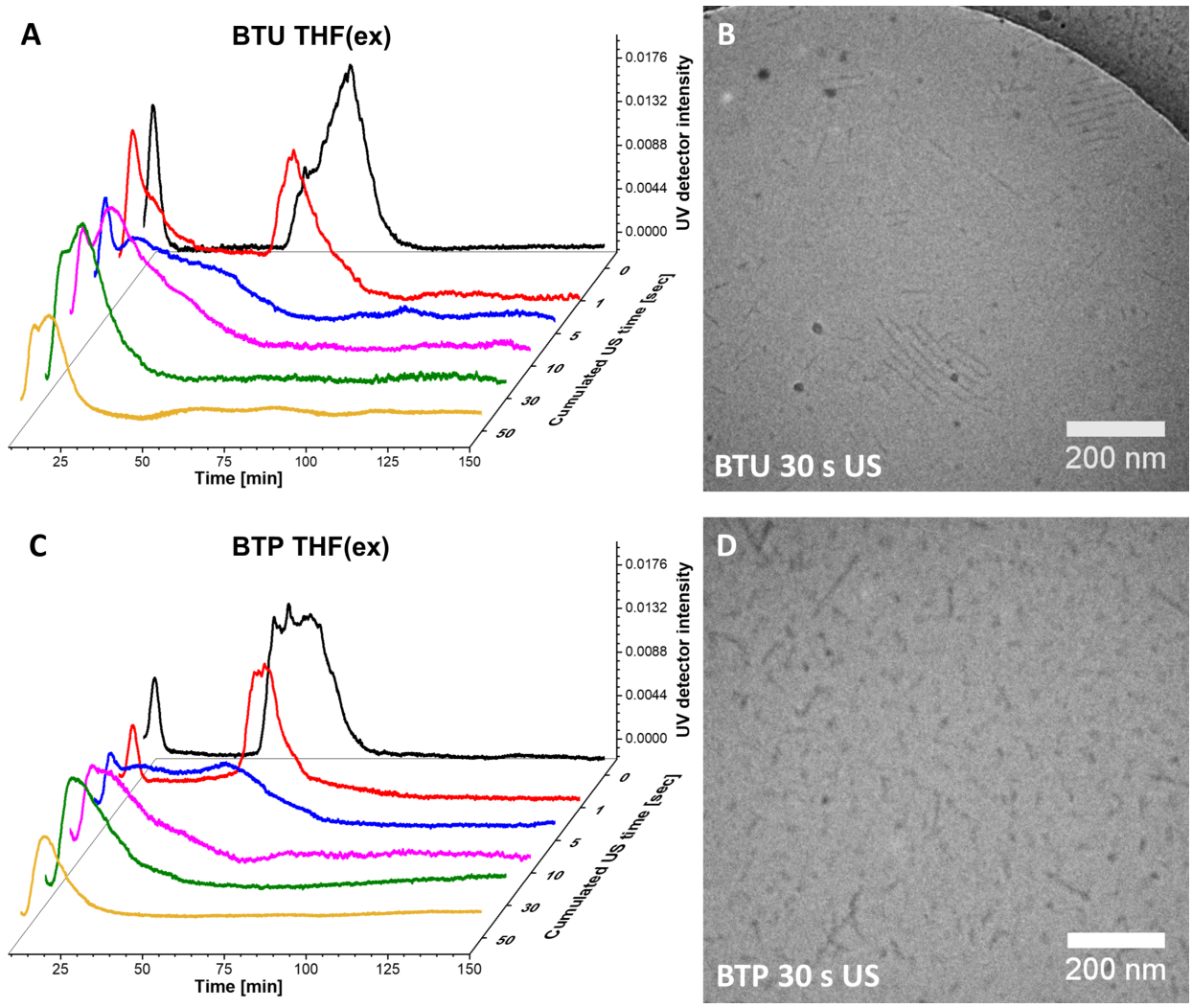


Figure 4: AF4–UV elution profiles after US for the cumulated time of 0 s (black), 1 s (red), 5 s (blue), 10 s (magenta), 30 s (green), and 50 s (yellow) for BTU (A) and BTP (C). The injection peaks were omitted for clarity. cryoTEM images of BTU (B) and BTP (D) after 30 s of US exposure (c = 1 mg·mL^{-1}).

on the sample and gain more control, but this was not further tested. The peak maxima at around 80 min (BTU) and 65 min (BTP) decreased slightly and shifted to a lower elution time. For the BTU sample, even a new peak was formed at 10 to 20 min, corresponding to the formation of short structures. Continuous US for a cumulated time of 5 s resulted in the disappearance of the main peaks and the appearance of a broad distribution ranging from 15 min to 70 min elution time for both samples. The severe broadening of the distribution and the immediate formation of very small structures suggests a shearing off of small fragments during US. A further increase of the time (up to 30 s) narrowed the length distribution once again, and only the small aggregates remained in solution, which appeared to be stable during further sonication (50 s of cumulated US time). The resulting fibers featured an average R_g value of ≈15 nm (Figure S14, Supporting Information File 1) and a weight-average molar mass of M_w = 3,633,000 g·mol^{-1}, corresponding to a number of aggregation of N_{agg} = 1400 and a length of 125 nm for BTU (assuming four units per cross-section). For BTP, a weight-average molar mass of M_w = 2,910,000 g·mol^{-1}, corresponding to a number of aggregation of N_{agg} = 440 and a length of 80 nm (assuming two units per cross-section) was calculated [19,21]. Correlating well with the AF4 results, cryoTEM images of both samples (Figure 4B and 1D) showed mainly short cylinders after a cumulated US time of 30 s, with an average fiber length of 124 ± 65 nm and 69 ± 41 nm for BTU and BTP, respectively (Figure S8, Supporting Information File 1). It is important to note that all obtained fibers remained unchanged over several months after the top-down processing, demonstrating the previously described excellent kinetic stability of these supramolecular aggregates (Figures S15 and S16, Supporting Information File 1) [21].

Inspired by work of Lamour et al., we estimated a similar limit length L_{lim} upon extensive US treatment [35]. This length allows an indirect estimation of the tensile strength σ* of our fibers according to

$$L_{lim} = \sqrt{\frac{d^2 \cdot \sigma^*}{2 \cdot \eta \cdot (\dot{R}_l / R_i)}}$$

where R_i is the radius of the cavitation bubble, $\dot{R}_l$ is the wall velocity of the collapsing bubble, d is the fiber diameter, and η is the viscosity of the solvent [36]. By assuming typical values for the wall velocity, bubble radius, and viscosity of the solvent, the equation simplifies [37,38] to

$$L_{lim} = 7 \cdot 10^{-4} \cdot d \cdot \sqrt{\sigma^*}$$

We exposed the BTU and BTP fibers to extended US (>1 h). No further scission could be observed after 2–3 h of US. AF4–MALLS measurements of the fibers after 3 h US revealed a M_w at the elution peak maximum of 843,000 g·mol^{-1} and 943,000 g·mol^{-1} for BTU and BTP, respectively (Figure S17, Supporting Information File 1). This translates to a fiber length of 29 nm for BTU by assuming a stacking distance of 0.36 nm and 4 molecules per cross-section [19], and 28 nm for BTP by assuming a similar stacking distance and 2 molecules per cross-section [21]. Based on a fiber diameter of 12 nm (estimated from small-angle X-ray scattering experiments) [19,20], the resulting tensile strength for both compounds was approximately 16 to 17 MPa (Table S1, Supporting Information File 1). This strength was in the range of Elastin filaments and significantly lower as, for instance, the tensile strength of amyloid fibrils [35,39]. Overall, the observed values for the fibers corresponded well to the sensitivity to shear forces. However, the core–shell structure of our supramolecular systems has to be considered in this regard. For example, significant steric strains induced by the polymer chains act on the core structure, limiting the strength of the supramolecular assembly.

Conclusion

In conclusion, the remarkable long-term stability of BTU–PEO and BTP–PEO fibers in water, which were prepared via bottom-up self-assembly, enabled us to apply two straightforward top-down approaches (US and dual asymmetric centrifugation) to tune the length distributions of the supramolecular fibers. Exposing the SPBs to US resulted in a rapid fragmentation of the fibers into small rod-like fragments. Dual asymmetric centrifugation, on the other hand, allowed to adjust the length distribution in a more controlled manner by adjusting the time and rotation speed. Thus, this study demonstrates that easy-to-use top-down methods can be a feasible approach to obtain some control over the length distributions of 1D polymer nanostructures, and thus this makes them more likely to be applied in biomedicine, where dimensional control is a prerequisite.

Supporting Information

Supporting Information File 1

Synthesis, procedures, and characterization.
[https://www.beilstein-journals.org/bjoc/content/supplementary/1860-5397-17-175-S1.pdf]

Acknowledgements

The authors thank Prof. Ulrich S. Schubert for his continuous support and access to excellent research facilities.

Funding

T. K., F. V. G., and J. C. B. thank the German Science Foundation (DFG) for generous funding within the Emmy Noether Programme (Project-ID: 358263073). cryoTEM investigations were performed at the electron microscopy facilities of the Jena Center for Soft Matter (JCSM), which were purchased with grants from the DFG and the European funds for Regional Development (EFRE). The funding of the collaborative research center PolyTarget, projects A05 and Z01 (Project-ID: 316213987 – SFB 1278), by the DFG is acknowledged.

ORCID® iDs

Tobias Klein - https://orcid.org/0000-0001-9404-7739
Johannes C. Brendel - https://orcid.org/0000-0002-1206-1375

References

1. Truong, N. P.; Whittaker, M. R.; Mak, C. W.; Davis, T. P. *Expert Opin. Drug Delivery* **2015,** *12,* 129–142. doi:10.1517/17425247.2014.950564
2. Toy, R.; Peiris, P. M.; Ghaghada, K. B.; Karathanasis, E. *Nanomedicine (London, U. K.)* **2014,** *9,* 121–134. doi:10.2217/nnm.13.191
3. Liu, Y.; Tan, J.; Thomas, A.; Ou-Yang, D.; Muzykantov, V. R. *Ther. Delivery* **2012,** *3,* 181–194. doi:10.4155/tde.11.156
4. Müllner, M. *Macromol. Chem. Phys.* **2016,** *217,* 2209–2222. doi:10.1002/macp.201600086
5. Truong, N. P.; Quinn, J. F.; Whittaker, M. R.; Davis, T. P. *Polym. Chem.* **2016,** *7,* 4295–4312. doi:10.1039/c6py00639f
6. Shkodra-Pula, B.; Vollrath, A.; Schubert, U. S.; Schubert, S. Polymer-based nanoparticles for biomedical applications. In *Frontiers of Nanoscience;* Parak, W. J.; Feliu, N., Eds.; Elsevier: Amsterdam, Netherlands, 2020; Vol. 16, pp 233–252. doi:10.1016/b978-0-08-102828-5.00009-7
7. Gilroy, J. B.; Gädt, T.; Whittell, G. R.; Chabanne, L.; Mitchels, J. M.; Richardson, R. M.; Winnik, M. A.; Manners, I. *Nat. Chem.* **2010,** *2,* 566–570. doi:10.1038/nchem.664
8. Finnegan, J. R.; Pilkington, E. H.; Alt, K.; Rahim, M. A.; Kent, S. J.; Davis, T. P.; Kempe, K. *Chem. Sci.* **2021,** *12,* 7350–7360. doi:10.1039/d1sc00938a
9. Finnegan, J. R.; He, X.; Street, S. T. G.; Garcia-Hernandez, J. D.; Hayward, D. W.; Harniman, R. L.; Richardson, R. M.; Whittell, G. R.; Manners, I. *J. Am. Chem. Soc.* **2018,** *140,* 17127–17140. doi:10.1021/jacs.8b09861
10. He, Y.; Eloi, J.-C.; Harniman, R. L.; Richardson, R. M.; Whittell, G. R.; Mathers, R. T.; Dove, A. P.; O'Reilly, R. K.; Manners, I. *J. Am. Chem. Soc.* **2019,** *141,* 19088–19098. doi:10.1021/jacs.9b09885
11. Street, S. T. G.; He, Y.; Jin, X.-H.; Hodgson, L.; Verkade, P.; Manners, I. *Chem. Sci.* **2020,** *11,* 8394–8408. doi:10.1039/d0sc02593c
12. Niederberger, A.; Pelras, T.; Manni, L. S.; FitzGerald, P. A.; Warr, G. G.; Müllner, M. *Macromol. Rapid Commun.* **2021,** *42,* 2100138. doi:10.1002/marc.202100138
13. Müllner, M.; Yang, K.; Kaur, A.; New, E. J. *Polym. Chem.* **2018,** *9,* 3461–3465. doi:10.1039/c8py00703a
14. Müllner, M.; Mehta, D.; Nowell, C. J.; Porter, C. J. H. *Chem. Commun.* **2016,** *52,* 9121–9124. doi:10.1039/c6cc00447d
15. Müllner, M.; Müller, A. H. E. *Polymer* **2016,** *98,* 389–401. doi:10.1016/j.polymer.2016.03.076
16. Müllner, M.; Dodds, S. J.; Nguyen, T.-H.; Senyschyn, D.; Porter, C. J. H.; Boyd, B. J.; Caruso, F. *ACS Nano* **2015,** *9,* 1294–1304. doi:10.1021/nn505125f
17. Gruschwitz, F. V.; Klein, T.; Catrouillet, S.; Brendel, J. C. *Chem. Commun.* **2020,** *56,* 5079–5110. doi:10.1039/d0cc01202e
18. Klein, T.; Ulrich, H. F.; Gruschwitz, F. V.; Kuchenbrod, M. T.; Takahashi, R.; Hoeppener, S.; Nischang, I.; Sakurai, K.; Brendel, J. C. *Macromol. Rapid Commun.* **2021,** *42,* 2000585. doi:10.1002/marc.202000585
19. Gruschwitz, F. V.; Fu, M.-C.; Klein, T.; Takahashi, R.; Higashihara, T.; Hoeppener, S.; Nischang, I.; Sakurai, K.; Brendel, J. C. *Macromolecules* **2020,** *53,* 7552–7560. doi:10.1021/acs.macromol.0c01361
20. Klein, T.; Ulrich, H. F.; Gruschwitz, F. V.; Kuchenbrod, M. T.; Takahashi, R.; Fujii, S.; Hoeppener, S.; Nischang, I.; Sakurai, K.; Brendel, J. C. *Polym. Chem.* **2020,** *11,* 6763–6771. doi:10.1039/d0py01185a
21. Gruschwitz, F. V.; Klein, T.; Kuchenbrod, M. T.; Moriyama, N.; Fujii, S.; Nischang, I.; Hoeppener, S.; Sakurai, K.; Schubert, U. S.; Brendel, J. C. *ACS Macro Lett.* **2021,** *10,* 837–843. doi:10.1021/acsmacrolett.1c00296
22. Maeda, H. *Adv. Drug Delivery Rev.* **2015,** *91,* 3–6. doi:10.1016/j.addr.2015.01.002
23. Maeda, H.; Nakamura, H.; Fang, J. *Adv. Drug Delivery Rev.* **2013,** *65,* 71–79. doi:10.1016/j.addr.2012.10.002
24. Krämer, W.; Schubert, R.; Massing, U. *Int. J. Pharm.* **2019,** *572,* 118753. doi:10.1016/j.ijpharm.2019.118753
25. Hagedorn, M.; Liebich, L.; Bögershausen, A.; Massing, U.; Hoffmann, S.; Mende, S.; Rischer, M. *Int. J. Pharm.* **2019,** *565,* 187–198. doi:10.1016/j.ijpharm.2019.04.082
26. Hagedorn, M.; Bögershausen, A.; Rischer, M.; Schubert, R.; Massing, U. *Int. J. Pharm.* **2017,** *530,* 79–88. doi:10.1016/j.ijpharm.2017.07.047
27. Hirsch, M.; Ziroli, V.; Helm, M.; Massing, U. *J. Controlled Release* **2009,** *135,* 80–88. doi:10.1016/j.jconrel.2008.11.029
28. Massing, U.; Cicko, S.; Ziroli, V. *J. Controlled Release* **2008,** *125,* 16–24. doi:10.1016/j.jconrel.2007.09.010
29. Krieg, E.; Bastings, M. M. C.; Besenius, P.; Rybtchinski, B. *Chem. Rev.* **2016,** *116,* 2414–2477. doi:10.1021/acs.chemrev.5b00369
30. Gädt, T.; Ieong, N. S.; Cambridge, G.; Winnik, M. A.; Manners, I. *Nat. Mater.* **2009,** *8,* 144–150. doi:10.1038/nmat2356
31. Rho, J. Y.; Cox, H.; Mansfield, E. D. H.; Ellacott, S. H.; Peltier, R.; Brendel, J. C.; Hartlieb, M.; Waigh, T. A.; Perrier, S. *Nat. Commun.* **2019,** *10,* 4708. doi:10.1038/s41467-019-12586-8
32. Steinlein, C.; Kreger, K.; Schmidt, H.-W. *Macromol. Mater. Eng.* **2019,** *304,* 1900258. doi:10.1002/mame.201900258
33. Guérin, G.; Wang, H.; Manners, I.; Winnik, M. A. *J. Am. Chem. Soc.* **2008,** *130,* 14763–14771. doi:10.1021/ja805262v
34. Peltonen, L.; Hirvonen, J. *J. Pharm. Pharmacol.* **2010,** *62,* 1569–1579. doi:10.1111/j.2042-7158.2010.01022.x
35. Lamour, G.; Nassar, R.; Chan, P. H. W.; Bozkurt, G.; Li, J.; Bui, J. M.; Yip, C. K.; Mayor, T.; Li, H.; Wu, H.; Gsponer, J. A. *Biophys. J.* **2017,** *112,* 584–594. doi:10.1016/j.bpj.2016.12.036
36. Huang, Y. Y.; Knowles, T. P. J.; Terentjev, E. M. *Adv. Mater. (Weinheim, Ger.)* **2009,** *21,* 3945–3948. doi:10.1002/adma.200900498
37. Nguyen, T. Q.; Liang, Q. Z.; Kausch, H.-H. *Polymer* **1997,** *38,* 3783–3793. doi:10.1016/s0032-3861(96)00950-0

38. Hennrich, F.; Krupke, R.; Arnold, K.; Rojas Stütz, J. A.; Lebedkin, S.; Koch, T.; Schimmel, T.; Kappes, M. M. *J. Phys. Chem. B* **2007,** *111,* 1932–1937. doi:10.1021/jp065262n
39. Paparcone, R.; Buehler, M. J. *Biomaterials* **2011,** *32,* 3367–3374. doi:10.1016/j.biomaterials.2010.11.066

License and Terms

This is an Open Access article under the terms of the Creative Commons Attribution License (https://creativecommons.org/licenses/by/4.0). Please note that the reuse, redistribution and reproduction in particular requires that the author(s) and source are credited and that individual graphics may be subject to special legal provisions.

The license is subject to the *Beilstein Journal of Organic Chemistry* terms and conditions: (https://www.beilstein-journals.org/bjoc/terms)

The definitive version of this article is the electronic one which can be found at: https://doi.org/10.3762/bjoc.17.175